

FINITE ELEMENT ANALYSIS OF COMPONENTS

SUBJECTED TO RATCHETTING AND CREEP

by

S. J. Hardy, B.Sc., C.Eng., M.I.Mech.E., A.I.E.D.

Thesis submitted to the University of Nottingham for the degree
of Doctor of Philosophy, May 1983.

IMAGING SERVICES NORTH

Boston Spa, Wetherby
West Yorkshire, LS23 7BQ
www.bl.uk

BEST COPY AVAILABLE.

VARIABLE PRINT QUALITY



IMAGING SERVICES NORTH

Boston Spa, Wetherby
West Yorkshire, LS23 7BQ
www.bl.uk

BEST COPY AVAILABLE.

**TEXT IN ORIGINAL IS
CLOSE TO THE EDGE OF
THE PAGE**



IMAGING SERVICES NORTH

Boston Spa, Wetherby

West Yorkshire, LS23 7BQ

www.bl.uk

**CONTAINS
PULLOUTS**

To

Susan, Elizabeth and Mark.

(They have put up with so much.)

SUMMARY

Many components in conventional and nuclear power plant, chemical plant and aero engines may be subjected to severe loading conditions, i.e. loads which cause reverse plasticity and/or incremental growth (Ratchetting). If operating temperatures are high, creep strains may also be significant and may exacerbate the ratchetting process. Also the residual stress fields associated with the cycling of load in the plastic region for a material will influence the accumulation of strain during the dwell periods between cycles when steady loading is sustained.

Some analytical solutions for the cyclic behaviour of simple components and loadings are available, however very little information on the effects of stress concentrations and complex loading conditions on ratchetting is published. A better understanding of the mechanisms of ratchetting for complex components and loadings is essential in order to identify characteristic behaviours which can be used to aid the design process for components in potential ratchetting situations.

A range of component geometries, uniform sections and stress concentrations, and loading conditions have been analysed by the finite element method to investigate ratchetting mechanisms and to obtain ratchet and dwell period strain data. The effects of stress concentrations, material behaviour models, loading conditions and stress redistribution due to creep on ratchetting mechanisms and strain accumulations are described. Dwell period creep effects are bounded by the 'no creep' (zero dwell period) condition on the one hand and by complete redistribution between cycles at the other extreme.

The results of the analyses have been successfully used to extend existing approximate design rules for simple components to these more

complex components and loadings. It has been shown that reasonable estimates (in some cases exact solutions) can be obtained from either a limited finite element analysis or by using approximate methods of solution.

Comparisons between experimental ratchetting data for two components made from a lead alloy material and equivalent finite element predictions are presented. Simple material behaviour models are used and the results highlight both the benefits and shortfalls of these models. Improvements to modelling techniques for more accurate predictions are suggested although it is shown that, in certain circumstances, more realistic material behaviour modelling is unwarranted.

CONTENTS

NOTATION AND ABBREVIATIONS

1. INTRODUCTION

2. LITERATURE SURVEY

2.1 Material Behaviour Models

2.1.1 Elastic-plastic behaviour

2.1.1.1 Simple models

2.1.1.2 Assessment of the 'simple' models

2.1.1.3 More complex models

2.1.1.4 Assessment of the more complex models

2.1.2 Creep behaviour

2.1.2.1 Creep under constant load

2.1.2.2 Creep under varying load

2.1.2.3 Multiaxial effects

2.1.3 Plasticity-creep interactions

2.2 Component Behaviour

2.2.1 Elastic-plastic behaviour

2.2.2 Elastic-plastic-creep behaviour

2.2.2.1 Steady load

2.2.2.2 Cyclic loading

2.2.2.2.1 Effect of creep on the shakedown
limits

2.2.2.2.2 Analytical and experimental
studies of ratchetting in the
presence of creep

2.2.2.2.3 Approximate solutions

2.3 Summary

2.3.1 Models for material behaviour

2.3.2 Cyclic behaviour of components

3. COMPONENT SELECTION

3.1 Introduction

3.2 Background to the Selection of Two Components for the Joint Experimental and Analytical Project

3.2.1 Choice of component with constant mechanical loading and cyclic mechanical loading

3.2.2 Choice of component with constant mechanical loading and cyclic thermal loading

3.2.2.1 'Hole-in-plate' component

3.2.2.2 Axisymmetric component with induction heating

3.2.2.3 Axisymmetric component with fluid heating

4. FLANGED TUBE

4.1 Introduction

4.2 Shank Analysis

4.2.1 Finite element model

4.2.2 Data

4.2.3 Thermal loading cycle

4.2.4 Cyclic thermal loading with constant axial load

4.2.4.1 'No creep' condition

4.2.4.1.1 Elastic-perfectly-plastic material model

Ratchetting mechanism

Effect of mean load on ratchetting behaviour

4.2.4.1.2 Linear hardening models

Ratchetting mechanism

Effects of mean load and E_p/E on ratchetting behaviour

4.2.4.2 Complete redistribution

4.2.4.2.1 Elastic-perfectly-plastic material model

Ratchetting mechanism

Effect of mean load on ratchetting behaviour

Creep during the dwell periods

4.2.4.2.2 Linear hardening models

Ratchetting mechanism

Effects of mean load and E_p/E on ratchetting behaviour

Creep during the dwell periods

4.3 Analysis of the Whole Component

4.3.1 Finite element model

4.3.2 Data

4.3.3 Axial loading

4.3.3.1 Elastic stresses

4.3.3.2 Elastic-plastic behaviour

4.3.3.3 Elastic-creep behaviour at constant axial load

4.3.4 Thermal loading cycle

4.3.5 Cyclic thermal loading with constant axial load

4.3.5.1 'No creep' condition

4.3.5.1.1 Elastic-perfectly-plastic material model

Ratchetting mechanism

Effect of mean load on ratchetting behaviour

4.3.5.1.2 Comparison between experimental results and finite element predictions

$P/P_L = 0.5$ (Figures 4.40 and 4.41)

$P/P_L = 0.7$ (Figures 4.42 and 4.43)

$P/P_L = 0.8$ (Figure 4.44)

4.3.5.2 Complete Redistribution (Elastic-perfectly-plastic material model)

Ratchetting mechanism

Effect of mean load on ratchetting behaviour

Creep during the dwell periods

4.3.5.3 Partial redistribution - comparison with experimental results

$P/P_L = 0.7$, 24 hour dwell period
(Figures 4.48 and 4.49)

$P/P_L = 0.7$, 120 hour dwell period
(Figures 4.50 and 4.51)

5. STEPPED BEAM

5.1 Introduction

5.2 Shank Analysis

5.2.1 Finite element model

5.2.2 Data

5.2.3 Bending cycle

5.2.4 Cyclic bending with constant axial load

5.2.4.1 'No creep' condition

5.2.4.1.1 Elastic-perfectly-plastic material model

Ratchetting mechanism

Effect of mean load and cyclic bending load on ratchetting behaviour

5.2.4.1.2 Linear hardening models

Ratchetting mechanism

Effects of mean load, bending load, hardening assumption and E_p/E on ratchetting behaviour

5.2.4.2 Complete redistribution

5.2.4.2.1 Elastic-perfectly-plastic material model

Ratchetting mechanism

Effects of mean load and cyclic bending load on ratchetting behaviour

Creep during the dwell periods

5.2.4.2.2 Linear hardening models

Ratchetting mechanism

Effects of mean load, bending load, hardening assumption and E_p/E on ratchetting behaviour

Creep during the dwell periods

5.3 Analysis of the Whole Component

5.3.1 Finite element model

5.3.2 Data

5.3.3 Axial loading

5.3.3.1 Elastic stresses

5.3.3.2 Elastic-plastic behaviour

5.3.3.3 Creep at sustained mean load

5.3.4 Application of bending moment

5.3.4.1 Elastic stresses

5.3.4.2 Elastic-plastic behaviour

5.3.5 Cyclic bending with sustained mean load

5.3.5.1 'No creep' condition

5.3.5.1.1 Elastic-perfectly-plastic material model

Ratchetting mechanism

Effects of mean load and bending load on ratchetting behaviour

5.3.5.1.2 Linear hardening models

5.3.5.1.3 Comparison between experimental results and finite element predictions

Actual moments

Curvature control

5.3.5.2 Complete redistribution (Elastic-perfectly-plastic material model)

Ratchetting mechanism

Effects of mean load and bending load on ratchetting behaviour

Creep during the dwell periods

5.4 Application of Ainsworth's Bounding Technique to the Shank

6. 'HOLE-IN-PLATE', CIRCULAR PLATE AND SHOULDERED TUBE COMPONENTS

6.1 Introduction

6.2 'Hole-in-plate' Component

6.2.1 Finite element model

6.2.2 Mechanical loading

6.2.2.1 Elastic stresses

6.2.2.2 Elastic-plastic behaviour

6.2.2.3 Creep at sustained mean load

6.2.3 Thermal loading cycle

6.2.4 Cyclic thermal loading with sustained mean load

6.2.4.1 'No creep' condition

Ratchetting mechanism

Effect of mean load on ratchetting
behaviour

6.2.4.2 Complete redistribution

Ratchetting mechanism

Effects of mean load on ratchetting
behaviour

Creep during the dwell periods

6.3 Circular Plate Component

6.3.1 Finite element model

6.3.2 Transverse pressure loading

6.3.2.1 Elastic stresses

6.3.2.2 Elastic-plastic behaviour

6.3.2.3 Creep at sustained mean load

6.3.3 Thermal loading cycle

6.3.4 Cyclic thermal loading with sustained transverse
pressure

6.3.4.1 'No creep' condition

Ratchetting mechanism

Effect of transverse pressure on
ratchetting behaviour

6.3.4.2 Complete redistribution

Ratchetting mechanism

Effect of transverse pressure on
ratchetting behaviour

Creep during the dwell periods

6.4 Shouldered Tube Components

6.4.1 Finite element model

6.4.2 Axial mechanical loading

- 6.4.2.1 Elastic stresses
- 6.4.2.2 Elastic-plastic behaviour
- 6.4.2.3 Creep at sustained mean load
- 6.4.3 Thermal loading cycle
- 6.4.4 Cyclic thermal loading with sustained axial load
 - 6.4.4.1 'No creep' condition
 - Ratchetting mechanism
 - Effects of mean load and thermal load on ratchetting behaviour
 - 6.4.4.2 Complete redistribution
 - Ratchetting mechanism
 - Effects of mean load and thermal load on ratchetting behaviour
 - Creep during the dwell periods

7. A CORRELATION OF THE RATCHETTING AND DWELL PERIOD BEHAVIOUR

7.1 Introduction

7.2 Elastic-Perfectly-Plastic Material Model (All 5 Components)

7.2.1 Mechanical and Thermal Loading Conditions

7.2.2 Ratchetting mechanisms

7.2.2.1 First cycle mechanism

7.2.2.2 Steady state, 'no creep' mechanism

7.2.2.3 Transient, 'no creep' mechanism

7.2.2.4 Steady state, 'complete redistribution' mechanism

7.2.3 Ratchet strains

7.2.3.1 Qualitative assessment

7.2.3.1.1 'No creep' condition

Uniform shank regions

Regions of stress concentration

Comparison between shank and fillet

- 7.2.3.1.2 Complete redistribution
 - Uniform shank regions
 - Regions of stress concentration
 - Comparison between shank and fillet
- 7.2.3.2 Quantitative correlation
 - 7.2.3.2.1 Bree's analysis
 - 'No creep' condition
 - Complete redistribution
 - 7.2.3.2.2 Cousseran analysis
 - 'No creep' condition
 - Complete redistribution
- 7.2.4 Dwell period strains
 - 7.2.4.1 Steady state strain rates
 - 7.2.4.2 Normalised increments of strain due to stress redistribution
- 7.3 Material Hardening Model (Flanged Tube and Stepped Beam)
 - 7.3.1 Ratchetting mechanisms
 - 7.3.1.1 Transient 'no creep' mechanism
 - 7.3.1.2 Transient complete redistribution mechanism
 - 7.3.2 Ratchet and dwell period strains
 - 7.3.2.1 'No creep' condition
 - 7.3.2.2 Ratchetting with creep
- 7.4 Effects of Partial Redistribution on Ratchet and Dwell Period Strains

8. DISCUSSION

- 8.1 Introduction
- 8.2 Detailed Studies of the Flanged Tube and Stepped Beam Shanks

8.3 Comparative Study of Components - Implications on Design

8.3.1 'No creep' case - ratchet and total accumulated strains

Finite element solutions

Approximate methods of solution

8.3.2 'Complete redistribution' case

8.3.2.1 Ratchet strains

Finite element solutions

Approximate methods of solution

8.3.2.2 Dwell period strains

Finite element solutions

Approximate methods of solution

8.3.2.3 Total accumulated strains

Finite element solutions

Approximate methods of solution

8.3.3 Notes on failure

8.4 Comparisons Between Experimental Results and Finite Element Predictions

8.5 Suggestions for Further Work

9. SUMMARY OF CONCLUSIONS

Acknowledgements

References

Appendix I THE NON-LINEAR FINITE ELEMENT PROGRAM

Appendix II JUSTIFICATION OF THE FINITE ELEMENT MESHES

NOTATION

A	constant
A,B,C,D,	positions on 'hole-in-plate' component (Figure 6.1)
	positions on circular plate component (Figure 6.21)
C	collapse region on Burgreen diagram (Figure 2.11)
C_p	specific heat
D	outside diameter
D_1, D_2	ratchetting regions on Burgreen diagram (Figure 2.11)
E	Young's Modulus
	elastic region on Bree diagram (Figure 2.10)
	elastic region on Burgreen diagram (Figure 2.11)
E_p	plastic modulus
K	curvature
L	length
M	moment
P	applied load
Q	activation energy
R	Boltzmann's constant
	radius
R_1, R_2	ratchetting regions on Bree diagram (Figure 2.10)
S_1, S_2	shakedown regions on Bree diagram (Figure 2.10)
	shakedown regions on Burgreen diagram (Figure 2.11)
T	temperature
V	efficiency index used by Cousseran et al (equation 2.12)
b	beam width
d	beam depth
	inside diameter

$f(), f_i()$	functions
h	surface heat transfer coefficient
k	thermal conductivity
m	time index in creep law
n	stress index in creep law
p	pressure
s	seconds
t	time
	thickness
x,y,z	co-ordinates
Γ	time function (equation 4.2)
Γ_R	time function for complete redistribution
$\Delta \epsilon$	increment of strain
ΔQ	secondary stress range used by Cousseran et al (equation 2.11)
ΔT	temperature difference
ϕ	diameter
α	coefficient of thermal expansion
δ	ratchet strain used by Bree (equations 2.7 & 2.8)
ϵ	strain
ν	Poisson's ratio
ρ	density
σ	stress
	primary stress
$\bar{\sigma}$	mean stress
σ_p	axial stress used by Bree (equations 2.7 & 2.8)
$\hat{\sigma}$	deviatoric stress
τ	shear stress

Other symbols are described where used.

Subscripts

A	axial
L	limit
R	radial
c	characteristic
col	collapse
eff	effective
m	meridional
max	maximum
n	normal
nom	nominal
p	pressure
ss	steady state
t, th	thermal
x,y,z	directions
y	yield
θ	hoop

Superscripts

c	creep
d	dwel
ine	inelastic
r	ratchet
t	total
*	effective

ABBREVIATIONS

Bi	Biot number
Fo	Fourier number
FC	first compressive surface for a beam (section 5.2.4)
FT	first tensile surface for a beam (section 5.2.4)

ICL	International Computers Limited
INC	increment number
RAD	radius
SCF	stress concentration factor
SR	secondary stress ratio used by Cousseran et al (equation 2.11)
UTS	ultimate tensile strength
YRI	yield range increment used by Jhansale (section 2.1.1.3)
conc	concentrated

CHAPTER ONE

1. INTRODUCTION

Many components in conventional and nuclear power plant, chemical plant and aero engines may be subjected to severe loading conditions, i.e. loads which cause reverse plasticity and/or incremental growth (Ratchetting). If operating temperatures are high, creep strain may also be significant. Ratchetting can lead to eventual failure of a component and has been identified as a potential problem in, for example, the design of Fast Breeder Reactor fuel element cladding (1, 2) where cladding failure and a possible release of gaseous fission products could have serious consequences.

Ratchetting is a build-up of inelastic strains and is one of the possible outcomes when engineering components are subjected to the combined effect of steady load, generally mechanical, and cyclic thermal or mechanical loading.

The onset of ratchetting depends on the relative magnitudes of the steady and variable loads. Creep straining, particularly in the dwell periods between successive thermal/mechanical cycles, may in addition to increasing the inelastic strains, exacerbate the ratchetting process. Also the modification of residual stress fields during transient loads will affect the subsequent steady load creep behaviour which can be significantly different to the creep behaviour of components subjected to steady load alone.

The safe design of such components should, in the first instance, be based on the avoidance of ratchetting. However, a

through-life accumulation of inelastic strains would be acceptable if within specified limits (eg.3). The latter option requires that the strains are estimated at the design stage. For simple components and loadings, design procedures exist which allow strain accumulations to be relatively easily calculated (eg. 1, 2, 4, 5). Also the effects of stress redistribution due to creep on ratchetting behaviour and the accumulation of creep strains during the dwell periods can be estimated (eg.1, 6, 7, 8, 9). For components which contain stress concentration regions, it has been shown (eg.10, 11) that ratchet strains in the stress concentration can be significantly larger than those in the uniform regions of the same component and also ratchetting can occur under less severe loading conditions. Cyclic behaviour with more complicated component geometries and/or loading conditions must be quantified and at the present time, simple design procedures for calculating 'ratchetting boundaries' and accumulated strains for complex components and loadings are not available. The finite element method provides a powerful technique for predicting component behaviour. However the accuracy of the prediction depends, to a large extent, on the accuracy with which the material behaviour for the variable load and temperature conditions is represented.

The main objectives of this project are:-

1. to identify the parameters which influence ratchetting behaviour and quantify the effects of varying these parameters.
2. to study the ratchetting mechanisms of a number of simple and more complex components with a variety of loadings and to quantify the effects of

(i) stress concentrations on ratchet strains

- (ii) stress redistribution due to creep on ratchetting behaviour, and
 - (iii) residual stress fields resulting from cyclic loads, on the subsequent steady load creep behaviour.
3. to assess and improve the analytical techniques for predicting ratchetting behaviour, in particular to suggest simple design procedures for complex ratchetting and creep problems.
 4. to compare analytical predictions of ratchetting behaviour with experimental results in order to identify
 - (i) the limitations of simple material models and
 - (ii) the important material behaviour characteristics which must be included to obtain accurate predictions of component behaviour.

Five components, some of which have both a uniform section (equivalent to a 'simple' component) and stress concentrations, subjected to a variety of steady and cyclic loads have been analysed. The components and their loadings are described below.

1. A flanged tube (thick tube with flange), having a uniform section and a stress concentration, subjected to steady axial mechanical loading and cyclic through-thickness axisymmetric temperature variation.
2. A stepped beam, having a uniform section and stress concentration, subjected to steady axial loading and cyclic bending.

3. A plate with a single hole, subjected to in-plane steady mechanical loading and cyclic heating and cooling of the hole surface.
4. A clamped circular plate subjected to transverse pressure loading and cyclic through-thickness temperature variation.
5. A shouldered tube (thin tube with shoulder) having a uniform section and stress concentration, subjected to steady axial mechanical loading and cyclic through-thickness axisymmetric temperature variation.

The ratchetting and creep behaviour of the components is examined and compared in order to identify simple, but conservative, design techniques for predicting the behaviour of real engineering components with similar geometries, loadings and material behaviour, particularly in regions of stress concentration. The flanged tube and stepped beam components have also been the subject of experimental investigations by Yahiaoui (12) in a parallel project and comparisons between the experimental results and analytical solutions are made. Also, the uniform regions of these two components have been studied in greater detail and the variation in ratchetting and creep behaviour with loading and material behaviour is examined.

The effects of creep on cyclic behaviour are bounded by the 'no-creep' case, where the effects of dwell period are ignored and the 'complete redistribution' case where complete redistribution to the steady load stationary^{*} state stress distribution is allowed between successive cycles of load. Generally, solutions for these two extreme cases only have been obtained. Where possible, the results have been normalised to be more generally applicable for a range of engineering materials.

* For proper definition, see reference 66.

Extensive use of the finite element method has been made. This has required significant development of existing finite element programs in order to perform elastic-plastic-creep analyses with complex loading conditions and material models. The finite element approach to non-linear problems and the present program capabilities, including details of the modifications, are discussed in Appendix 1.

A review of the literature, with particular emphasis on material behaviour models, existing prediction techniques and analytical and experimental results, is given in Chapter 2.

Chapter 3 describes the selection process for the components, particularly the flanged tube and stepped beam which were designed especially for the combined experimental and analytical projects and for which considerable preliminary work was carried out. The results for each component are presented and discussed in Chapters 4 - 6 and compared in Chapter 7. An overall discussion is given in Chapter 8 where the implications of the work are considered. Conclusions arising from the work are given in Chapter 9.

CHAPTER TWO

2. LITERATURE SURVEY

In predicting elastic-plastic-creep behaviour of components particularly under conditions of cyclic loading, the accuracy of prediction depends on the accuracy with which the true material behaviour is modelled. Section 2.1 describes some of the more common material models which are currently available, together with an assessment of their application to engineering materials. Section 2.2 gives a review of the literature relating to the behaviour of components under conditions of ratchetting and creep including approximate methods of solution. A general summary of the findings is given in Section 2.3.

2.1 Material Behaviour Models

2.1.1 Elastic-plastic behaviour

The elastic-plastic behaviour of materials under monotonic loading conditions is well documented (e.g. 13,14) and this section concentrates on a description of some of the more common models and their ability to describe the various phenomena associated with load reversal and cyclic loading.

e.g. reverse plasticity - regions within a component may suffer both tensile and compressive plastic deformation during a cycle of load. This can ultimately lead to failure due to fatigue.

cyclic hardening and softening - under strain controlled cyclic loading there may be an initial transitory stage while the stress range is changing, prior to a stable loop being established. A material may cyclically harden (increase in stress range) or soften (reduction in stress range) during this stage.

material ratchetting - the cyclic hardening and softening effects observed with strain controlled loading can lead to material

ratchetting under certain loading conditions. For example, in Figure 2.1 for a strain controlled cycle of range ϵ_R^t there is a cyclic stress relaxation, $\delta\sigma$, and hence for a stress controlled cycle an increment of plastic strain, $\delta\epsilon^p$, is accumulated in returning to the original stress. This material ratchetting results from the cyclic material behaviour and is in addition to the loading dependent structural ratchetting.

Uniaxial elastic-plastic behaviour is, in general, dependent on loading history since excursions into the plastic regime cause changes in the instantaneous yield stress and plastic modulus.

The modelling of multiaxial elastic and plastic behaviour using a yield criterion to define the limit of elasticity under any combination of stresses and a flow rule to determine the components of plastic strain after yielding is discussed in many references (e.g. 13). It is usually assumed that the von Mises effective stress and yield criterion and Prandtl-Reuss flow rules can be used to describe the behaviour of metals under multiaxial stress conditions. These models are used by the finite element program discussed in Appendix I. The von Mises yield criterion is assumed for describing multiaxial behaviour in this Chapter. The von Mises (or distortion energy) theory assumes that yielding will occur when the distortion energy reaches the distortion energy on yielding in simple tension or when

$$3\hat{\sigma}_{ij}\hat{\sigma}_{ij} \geq 2\sigma_y^2$$

where $\hat{\sigma}_{ij}$ is the deviatoric stress, or in terms of the stress components when

$$(\sigma_{xx} - \sigma_{yy})^2 + (\sigma_{yy} - \sigma_{zz})^2 + (\sigma_{zz} - \sigma_{xx})^2 + 6(\tau_{xy}^2 + \tau_{yz}^2 + \tau_{zx}^2) \geq 2\sigma_y^2$$

The Prandtl-Reuss flow rules are developed from the theory of plastic potential relating plastic strain increments to the stresses

$$d\epsilon_{ij}^p \propto \frac{\partial F(\sigma)}{\partial \tilde{\sigma}_{ij}} \quad \text{where } F(\sigma) \text{ is a function of all the stresses.}$$

If this function is the yield function then the plastic flow is determined by an 'associated flow rule'. The Prandtl-Reuss flow rules are associated flow rules based on the von Mises yield function and give

$$d\epsilon_{ij}^p = d\lambda \tilde{\sigma}_{ij}$$

where $d\lambda$ is a non-negative constant.

2.1.1.1 Simple Models

Figure 2.2 shows the variation of strain with stress for reversed loading for two of the simple models for a linear hardening material.

In the isotropic hardening model (13) the hardening produced in tension results in an equal hardening in compression (and vice versa) and is represented by the path ABCDE with compressive yield occurring when

$$\sigma = -\sigma_y'$$

In the π plane of principal stresses, for multiaxial states of stress, the initial yield surface is a circle centred on the origin of stress which expands uniformly with no change in origin as yielding occurs, as shown in Figure 2.3(a). For a multilinear representation of the uniaxial stress-strain relationship, the discontinuities are concentric circles. As loading increases the 'initial' yield surface expands to combine with the second surface. Further increases in loading cause expansion of the 'new' yield surface. There is no contraction when the loading is reversed.

The kinematic hardening model (15,16) assumes that the elastic stress range remains unchanged and a tensile hardening effect is offset by an equivalent softening of the material in compression. For kinematic hardening reversed loading is represented by path ABCFG in Figure 2.2 and compressive yielding occurs when

$$\sigma = \sigma_y' - 2\sigma_y.$$

Kinematic hardening requires a bilinear representation of the stress-strain curve, an elastic line and a single line model of the plastic behaviour. In a multiaxial stress field, the yield surface remains

a circle of diameter $2\sigma_y$ which translates in space as yielding occurs, see Figure 2.3(b).

In the absence of hardening, the isotropic and kinematic hardening models are identical, with a fixed yield stress and neither expansion nor translation of the yield surface. This is the elastic-perfectly-plastic model.

2.1.1.2 Assessment of the 'simple' models

The isotropic hardening model responses with uniaxial cyclic strain and stress control with a non-zero mean are shown in Figures 2.4(a) and (b) respectively. The hardening of the material eventually results in a 'shakedown' to purely elastic cycling for both strain and stress controlled loading. The model can describe cyclic hardening under strain controlled conditions. The kinematic hardening model results in a steady cyclic stress/strain loop after the first complete cycle for both strain and stress control as shown in Figure 2.5(a) and (b). The elastic-perfectly-plastic model also reaches a stable loop under strain controlled testing (stress controlled testing is not applicable because of collapse).

None of the three simple models can represent material ratchetting, however their constitutive equations can be readily incorporated into finite element programs.

2.1.1.3 More complex models

One of the earliest descriptions of a model for material behaviour under conditions of reversed and cyclic loading was suggested by Masing (17) who proposed a relationship between the monotonic stress-strain curve and the reversed loading curve. Masing's hypothesis is that the cyclic loading curves are geometrically similar to the monotonic curve, but scaled up by a factor of 2 and a

stable loop is reached after one cycle for both stress and strain control loading. Masing used an assembly of elastic-perfectly-plastic elements connected in parallel. Each element has a different yield stress and undergoes the same deformation. Under monotonic loading conditions, the result is a series of linear segments of reducing positive slope and the reversed loading curve is the same as the monotonic stress-strain curve scaled by a factor of 2 as shown in Figure 2.6. The model can be described as having a non-linear kinematic form.

The work hardening model of Mroz (18) uses a field of work-hardening moduli. The monotonic stress-strain curve is represented by a number of linear approximations. In stress space the discontinuities between the linear approximations are represented by a series of concentric circles which, for initially isotropic material, are centred on the origin. Loading in excess of the initial yield (first surface) produces a rigid body translation of that surface. The presence of a further yield surface upon increasing the load means that these two surfaces will translate together once contact is made between them. For the uniaxial loading case, shown in Figure 2.7 the elastic range (denoted by the first circle) is constant during unloading and twice the initial yield stress. The region between first and second surfaces has doubled and the model corresponds to the Masing hypothesis with the cyclic loading curve being twice the original monotonic curve.

For multiaxial loading, Mroz assumes that the surfaces cannot intersect and that once initial contact between surfaces is made the direction of straining changes with the inner surface sliding around the contact surface until the normals coincide. In a further paper Mroz (19) explains qualitatively how expansion and contraction

of the surfaces during plastic deformation, together with translation can be used to model transitory effects such as cyclic hardening and softening.

The 'overlay method' suggested by Zienkiewicz et al (20) is based on the Masing concept of parallel elements and is specifically designed for implementation into finite element programs without the need for complex constitutive relationships. A structure is made up of a number of overlaid sub-elements which can exhibit different material behaviours. The corresponding nodes of each sub-element coincide and identical strains are imposed on each of the sub-elements. In this way, complex material behaviours can be represented by simple but different material models attributed to each sub-element. For example a combination of elastic only and elastic-perfectly plastic sub-elements can be used to describe the kinematic hardening in a similar way to that shown in Figure 2.6 for the Masing model.

Goodman and Goodall (21) review some experimental tests on stainless steel at varying temperatures with particular interest being shown in type 316 stainless steel which is a candidate material for Fast Breeder Reactor components. Fixed strain range controlled cyclic tests on virgin material revealed a cyclic hardening effect for many cycles before a stable loop was achieved. However another fixed strain range cyclic test on a specimen with a previous loading history of controlled ratchetting resulted in a cyclic softening or 'memory decay' mechanism. Goodman and Goodall conclude that material behaviour depends on loading history as well as the operating temperature. They also emphasise the inability of the simple hardening models to adequately predict cyclic behaviour

(e.g. material ratchetting). They propose a 'saturation stress' model which incorporates both cyclic hardening and softening and will predict material ratchetting under conditions of stress cycling with a non-zero mean stress. The model assumes a constant yield range of twice the original virgin yield stress but the shape of the plastic curve depends on the instantaneous yield stress and a saturation stress parameter. This model appears to successfully represent the experimental observations of the stainless steel behaviour. However the equations developed by Goodman and Goodall refer only to uniaxial states of stress and the multiaxial generalisation is not considered.

Jhansale (22) examines experimental observations on a range of steels and aluminium which highlight the limitations of the simple hardening models. By considering the stable cyclic loops for these materials he concludes that the loops are identical in shape if a proportion of their elastic range is removed. He proposes a Yield Range Increment (YRI) parameter to normalise cyclic stress-strain behaviour with respect to the doubled monotonic loading curve postulation of Masing. For 'Masing materials', which achieve steady state conditions after the first cycle for both stress and strain controlled cycling, there is no change in the elastic range and the YRI is zero and independent of hysteresis loop size. For 'non-Masing materials', which display a transitory period, for a number of cycles, prior to achieving the steady state, the YRI is related to the size of the hysteresis loop. Increases and reductions in the YRI can be used to model cyclic hardening and softening respectively. The Jhansale model can therefore be used to model material ratchetting.

2.1.1.4 Assessment of the more complex models

The Goodman and Goodall and Jhansale models are of particular interest since they can predict material ratchetting which is apparent in many engineering materials and also in the lead alloy used by Yahiaoui (12). The Goodman and Goodall and Jhansale models differ in the way hardening and softening effects are produced. The Jhansale model assumes similarity of the cyclic curves and the hardening/softening effects are related to changes in the elastic range only. The Goodman and Goodall model has a constant elastic range with hardening/softening effects resulting from changes in the shape of the plastic region of the cyclic stress-strain curves.

Both models have been developed to describe the cyclic behaviour of actual engineering materials. Before choosing the more appropriate model for a particular material, it would be necessary to carry out experimental tests to see which model described the material behaviour more accurately. For example, superimposing experimental results for strain controlled testing at different strain ranges would highlight changes in elastic range (Jhansale) or shape of the plastic region (Goodman and Goodall).

A further factor in selecting a material model is the ease with which it can be used. In particular, if the finite element technique is being used, the capability of adapting the model for the computer program must be considered.

2.1.2 Creep behaviour

Above a temperature of about 0.3 of the absolute melting temperature, metals display the time dependent phenomenon of creep when under stress. Creep behaviour, including recovery and relaxation,

is described by many authors (e.g. 9), and this section concentrates on the modelling of creep behaviour.

2.1.2.1 Creep under constant load

The uniaxial creep test is widely used to obtain creep data for materials. A uniaxial specimen is allowed to creep under constant load and temperature. Typical creep curves for the lead alloy used by Yahiaoui (12) at room temperature are given in Figure 2.8. This shows the regions of primary & secondary creep. The primary stage marks a reduction in strain rate to a nominally constant value over the secondary stage. An apparent increase in strain rate in the tertiary stage is partially due to the now significant reduction in cross-sectional area. In addition, there is a true tertiary stage with increase in creep strain rate for constant stress. This is caused by the formation of microcracks at the grain boundaries. In order to obtain analytical solutions for complex structural behaviour it is necessary to determine a suitable creep law or model to represent the uniaxial material data, the most general being:-

$$\epsilon^c = f(\sigma, t, T) \quad (2.1)$$

It is generally assumed that the effects of stress, time and temperature are separable.

i.e.
$$\epsilon^c = f_1(\sigma), f_2(t), f_3(T).$$

(In the present work where comparison is made between experimental observations (12) and finite element predictions, the isothermal conditions during the dwell periods (i.e. when creep occurs) has simplified the material behaviour modelling considerably.) Penny and Marriott (9) give a review of the creep laws currently available.

The most commonly used creep law is the simple Norton-Bailey Power law (9) which combines the function of stress due to Norton with the time function proposed by Bailey.

$$\text{i.e. } \epsilon^c = A_1 \sigma^{n_1} t^{m_1} \quad (2.2)$$

where A_1 , n_1 and m_1 are material constants.

The suitability of the Power Law to represent the creep behaviour of the lead alloy material used in the experimental part of the current project is discussed by Yahiaoui (12); the results show a slight dependence of the constants n_1 and m_1 on the level of stress.

The sinh law is an alternative form of the stress function and when combined with the Bailey time function gives

$$\epsilon^c = A_2 \sinh \left[\frac{\sigma}{n_2} \right] t^{m_2} \quad (2.3)$$

The value of m in both the Norton-Bailey and sinh laws can be adjusted to model either the primary ($m < 1$), secondary ($m = 1$) or tertiary ($m > 1$) stages of creep. With a careful choice of constants, primary and a limited region of secondary creep can be approximately modelled.

Dorn (9) suggests that a combined function of time and temperature can be used and suggests a creep law in the form

$$\epsilon^c = f_1(\sigma), f_2(t e^{-Q/RT}) \quad (2.4)$$

The complexity of the creep law is significantly increased if tertiary stage creep is to be included. Very few models are available and one of the most commonly quoted is that due to Graham and Walles (9),

$$\epsilon^c = \sum_{i=1}^n C_i \sigma^{\alpha_i} t^{\beta_i} \quad (2.5)$$

where C_1 , α_1 and β_1 are constants.

It is claimed that the first four terms of the series are sufficient to describe the three stages of creep.

$$\text{i.e. } \epsilon^c = C_1 \sigma^{\alpha_1} t^{\beta_1} + C_2 \sigma^{\alpha_2} t + (C_3 \sigma^{\alpha_3} + C_4 \sigma^{\alpha_4}) t^3 \quad (2.6)$$

$$\epsilon^c = \epsilon^{\text{primary}} + \epsilon^{\text{secondary}} + \epsilon^{\text{tertiary}}$$

Obvious difficulties are encountered due to the number of constants (8 in the above expression) which have to be determined from experimental data.

The Kachanov brittle rupture theory (9), which provides an explanation for tertiary creep, assumes that there is a reduction in the effective cross sectional area of a tensile specimen as the material accumulates damage and hence an increase in the effective stress. The effective stress is related to the initial stress by a continuity parameter, ψ , which reduces from unity at $t = 0$ to zero when rupture occurs.

2.1.2.2 Creep under varying load

Although the constant load uniaxial creep data provides a basis for obtaining material creep laws, in practice the phenomenon of stress relaxation combined with possible changes in loading requires a model for predicting creep behaviour with varying stress.

Two models are commonly used:-

(a) Time hardening

It is assumed that the creep strain rate depends on the current stress level and the elapsed time, as shown in Figure 2.9.

(b) Strain hardening

It is assumed that the creep strain rate depends on current stress level and total creep strain, also shown in Figure 2.9.

Other more complex theories are available and are discussed by Penny and Marriott (9). It is generally agreed (e.g. 9, 23) that the strain hardening model is the more realistic of the simple theories.

2.1.2.3 Multiaxial effects

There is a requirement to model complex multiaxial behaviour using simple and more readily available uniaxial test data. The equivalent stress/equivalent strain method and associated flow rules for multiaxial creep are as described for plasticity in Section 2.1.1.

2.1.3 Plasticity-creep interactions

Fessler, Hyde and Webster (25) reported a number of tests showing the effects of plastic pre-strain on subsequent creep behaviour. Specimens were initially plastically pre-strained then allowed to creep at constant stress levels less than that required to induce the initial pre-strain. The resulting creep curves were compared with the virgin creep curve for the same constant stress level. The results generally indicate a large reduction in creep strain rates in the presence of plastic pre-strain and for a particular test, a period of reverse creep occurred prior to forward creep being re-established. However at high stress levels, there was a marked increase in the creep strain rate compared with the virgin curve. The authors also report on a test where creep, following initial plastic pre-strain, was interrupted by a further addition of plastic pre-strain which caused a small amount of reverse creep prior to forward creep. The specimen was then loaded incrementally up to failure and, when compared with the stress-strain behaviour for virgin material, showed an increase in the UTS.

2.2 Component Behaviour

2.2.1 Elastic-plastic behaviour

This section gives a review of the literature on the cyclic behaviour of components. Because of its straightforward nature, elastic-plastic behaviour under steady loading is not discussed.

The phenomenon of ratchetting was first investigated by Parkes (26, 27, 28, 29) who, in a series of publications, discusses the ratchetting behaviour of aircraft wings using a two bar structure model with elastic-perfectly-plastic material behaviour. The loading consists of cyclic thermal loads in addition to the normal wing loadings. One bar is kept at constant temperature while the other has a cyclic temperature range. The papers consider different aspects of the behaviour including the effects of a temperature dependent yield stress, the relative sizes of the bars and the effects of heat conduction in the bars.

Miller (4) uses a three bar assembly with both elastic-perfectly-plastic and linear hardening to develop relationships for the ratchet growth of such a model where the outer bars are subjected to cyclic thermal loading while the inner bar is kept at constant temperature, and all three bars experience a sustained mechanical load. The analysis shows that an elastic-perfectly-plastic material assumption results in a constant ratchet strain per cycle, whereas the hardening characteristics of the material result in decreasing increments of plastic strain for successive cycles and must ultimately result in purely elastic cycling once 'shakedown' is complete. Miller extends the analysis to a problem of ratchetting in a thin pressure vessel where constant internal pressure and cyclic heat fluxes combine to give cyclic elastic-plastic behaviour. He suggests design criteria for the avoidance of ratchetting (i.e. a shakedown formula) together with formulae for the prediction of ratchetting behaviour.

Probably the most important work in this field is that of Bree (1,2) in predicting the behaviour of a fuel can in a Fast Reactor due to the combined effects of internal pressure (due to the release of gaseous fission products during the decay process) and intermittent

high heat fluxes during start-up and shut down, particularly in emergency situations. The can is modelled by a slab of material experiencing uniaxial stress due to pressure combined with a through thickness temperature gradient which is time-dependent. Bree applies a rigorous analysis to the simple uniaxial model in order to investigate the modes of behaviour with an elastic-perfectly-plastic material assumption.

The 'Bree diagram' reproduced in Figure 2.10 defines the elastic, shakedown, cyclic plasticity and ratchetting regimes which depend on the normalised axial stress $\frac{\sigma_p}{\sigma_y}$ and normalised thermal stress $\frac{\sigma_t}{\sigma_y}$. The line $\frac{\sigma_t}{\sigma_y} (1 - \frac{\sigma_p}{\sigma_y}) = 1$ divides the shakedown and ratchetting regimes into S_1 and S_2 and R_1 and R_2 respectively where the suffix 1 denotes tensile yielding only and suffix 2 indicates combinations of mechanical and thermal stress which result in both tensile and compressive yielding.

In the R_1 region, an increment of ratchet strain, δ , is given by

$$\delta = \frac{2\sigma_t}{E} (1 - 2\sqrt{(\sigma_y - \sigma_p)/\sigma_t}) \quad (2.7)$$

and for the R_2 region

$$\delta = \frac{2\sigma_t}{E} \left(\frac{\sigma_p}{\sigma_y} - \frac{\sigma_y}{\sigma_t} \right) \quad (2.8)$$

Bree also investigated the effect of changes in yield stress between start-up and shut down due to the differences in temperature. The analysis assumes a greater yield stress on shut down (σ_y'), because of the reduced temperature, compared with the start up yield

stress (σ_y). Bree also considered a linear hardening material and equations for ratchet strain per cycle are given which are cycle dependent. The results show that ratchet strains are less than those for an elastic-perfectly-plastic material model.

Burgreen (5, 30, 31) also uses the two-bar assembly to investigate the regimes of cyclic behaviour due to combined axial load and cyclic thermal gradients for an elastic-perfectly-plastic material assumption. He carries out a similar analysis for a multi-bar assembly. Burgreen's analysis of a rectangular beam subjected to an axial load and cyclic bending moment is of particular relevance to this thesis. He uses an elastic-perfectly-plastic material model to investigate the cyclic behaviour of the component and the 'Burgreen diagram' reproduced in figure 2.11 shows the cyclic regimes which depend on the axial load normalised with respect to the limit load ($\frac{P}{P_L}$) and the moment normalised with respect to the yield moment ($\frac{M}{M_y}$). A particularly interesting feature of the diagram is the narrow band of ratchetting behaviour bounded by shakedown and collapse regimes, which highlights the large changes in ratchet strain associated with relatively small changes in steady and/or cyclic loads. The implication of this effect will be discussed in a later section when the finite element analysis of the stepped beam component is discussed.

Hyde (32) has analysed the ratchetting behaviour of a circular plate ($d/t = 21$) with radially moveable, direction fixed edges subjected to steady membrane loads, steady transverse pressure loading and cyclic through-thickness thermal loads. An elastic-perfectly-plastic material model is used. With zero steady transverse pressure, Hyde obtains results that are similar to those from Bree's (1) analysis.

When an additional steady transverse pressure is applied Hyde's results, which are limited to 3 cycles, show a reduction in ratchet strain between second and third cycles unlike the Bree model; the implication being that ratchetting will eventually stop.

Goodman and Goodall (21) have analysed a simply supported circular plate ($d/t = 40$) subjected to steady transverse pressure together with the application and removal of a linear radial temperature gradient with a uniform through thickness temperature. Kinematic hardening and elastic-perfectly-plastic material models were used and, in both cases, the increments of central deflection were reducing after 22 cycles, although at slow rate for the elastic-perfectly-plastic material model.

The use of the two and three bar structures to demonstrate the regimes of cyclic behaviour is common and other references include Gill (33), Ruiz (34) and Megahed (35). In particular, Megahed considers a two bar structure where the bars have different lengths and cross-sectional areas in order to simulate a stress concentration. He considers elastic-perfectly-plastic material behaviour together with isotropic and kinematic hardening materials. The most important conclusion in terms of this research concerns the effect of the simulated stress concentration. Megahed concludes that the presence of a stress concentration will considerably increase the ratchet strains.

Sagar and Payne (36) performed an analysis of the incremental collapse of a 'thick' cylinder under steady mechanical loading (axial tension and torsion) combined with cyclic thermal loading.

Finally, Edmunds and Beer (37) considered a number of situations which can result in incremental collapse and are particularly relevant

to the design of pressure vessels. The ratchetting and shakedown behaviour is studied by a simple slab model of a pressure vessel with constant follow-up stress and superimposed strain cycling (in the conjugate direction) and constant follow-up stress combined with cyclic bending strain for an elastic-perfectly plastic material model.

2.2.2 Elastic-plastic-creep behaviour

2.2.2.1 Steady load

Components subjected to steady loading may, depending on temperature, experience the effects of creep. In regions of uniform stress creep strain rates are also uniform with a subsequent uniform elongation of the component in the direction of the applied loads. However for more complex component geometries having non-uniform stress fields and for residual stress fields, creep strain rates are position dependent and in order to maintain equilibrium of stresses with the external loads and compatibility of strains throughout the structure, creep strains in regions of stress concentration will result in an overall reduction in stress; the opposite effect being experienced in regions of 'below average' stress. This interchange between elastic and creep strains is termed 'stress redistribution due to creep' and will eventually result in a new equilibrium stress field being established, known as the Stationary State Stress Distribution. The component is said to have experienced complete redistribution of stresses, and the transient creep behaviour is followed by steady state deformation at the Stationary State Stress. Marriott (8) has suggested an approximate method for quantifying transient creep by the superposition of a fraction of the elastic deformation on the steady state creep behaviour. The redistribution time is a

parameter used to characterise the time taken for the Stationary State Stress Distribution to be reached. It is general to specify a redistribution time based on stresses reaching a defined fraction of the Stationary State values. Calladine (38) uses the parameter t_{10} , the time for the maximum stress in a structure to be within 10% of its stationary state value, and proposes a formula

$$t_{10} = \frac{2.3}{n} t^*(\sigma_{\max}^*) \quad (2.9)$$

where $t^*(\sigma)$ denotes the time taken for the creep strain to be equal to the elastic strain when maintained at constant stress σ , σ_{\max}^* is the maximum stationary state stress, and n is the stress index in the creep law.

Bill and Mackenzie (39) propose a similar formula based on mean stress ($\bar{\sigma}$)

$$t_{10} = \gamma t^*(\bar{\sigma}) \quad (2.10)$$

where γ is a constant.

Kraus (23) discusses the redistribution of stresses due to creep and points out that closed form analytical solutions cannot in general be obtained. Although numerical methods, particularly the finite element method, are available, the high expense of running necessarily large computer programs highlights the advantages of approximate methods of solution.

The reference stress method was first investigated by Soderberg (40) in 1941 and has been actively developed in recent years. The reference stress is a parameter which can be used to predict stationary creep behaviour of a component and is relatively insensitive to the stress index, n , in the creep law. The advantage of

the Reference Stress Method is that stationary creep deformation can be predicted from uniaxial data at a single value of stress. Kraus (23) presents a detailed review of the development of the reference stress technique together with examples of the application of the method to engineering components. Hyde (41) presents a similar review together with an insight into the determination of reference stresses by experiment.

As an alternative to the Reference Stress Method, techniques have been developed for bounding the deformation in situations of elastic-creep and elastic-plastic-creep deformation. For elastic-creep behaviour Leckie and Martin (42) present bounds on creep deformation based on the principle of virtual work which has been extended by Leckie and Ponter (43) to include the effect of additional plastic strains. They found that effects of inherent plastic strains in elastic-creep behaviour was small so long as the selected stress fields have values of the ratio stress to yield stress which are less than $\frac{n}{n+1}$ at all points in the structure. (Where n is the stress index in the creep equation.)

2.2.2.2 Cyclic loading

The effects of creep on cyclic elastic-plastic behaviour is particularly important during the dwell periods between the cycles of load. In general, the duration of the transient is significantly shorter than the period between successive cycles. (e.g. for the nuclear fuel can problem analysed by Bree, severe cyclic thermal loads are experienced during the rapid start-up and shut down procedures and these are separated by long periods of full power operation). Creep during the dwell periods will cause a redistribution of the residual stresses which will affect the ratchet strains during the subsequent cycles.

2.2.2.2.1 Effect of creep on the shakedown limits

Creep during the dwell periods between cycles will, under sustained steady loading, cause a partial or complete redistribution of stress towards the stationary state stress distribution associated with the steady load. This in turn will modify the shakedown limits for the component and Ponter (44) obtains an analytical modified shakedown limit in the presence of creep which is $\frac{n}{n+1}$ times the shakedown limit for ratchetting without creep and concludes that effects of plastic straining can be ignored below this modified limit. Leckie (45) states that if Bree's (1) shakedown limit for the nuclear reactor fuel can is reduced by the $\frac{n}{n+1}$ factor then the contributions of plastic strains to the total accumulated strains are relatively insignificant.

2.2.2.2.2 Analytical and experimental studies of ratchetting in the presence of creep

Bree (1) considered the effect of complete redistribution during the dwell periods, using an elastic-perfectly-plastic model, where the residual stresses redistribute to that associated with the steady load; thus each cycle is identical to the first with an equal increment of ratchet strain. In his second paper, Bree (2) looks at the effects of partial redistribution. In both cases the shakedown regimes disappear with continued ratchetting occurring in all but the elastic region of the Bree diagram.

Anderson (46) carried out controlled curvature tests on bars of Type 304H stainless steel with creep occurring during the dwell periods at constant axial load in order to simulate the Bree thin tube problem, and thus verify Bree's conclusions on the interaction between dwell period creep and ratchetting behaviour. Cyclic thermal strains are simulated by bending the bars around two mandrels of

opposite curvature. He investigated load combinations on the ratchetting boundary and in the shakedown region of the original Bree Diagram (i.e. without creep). The results confirm Bree's conclusions that the effect of creep during the dwell periods is to move the ratchetting boundary for a particular cyclic load towards lower steady load levels since ratchetting was apparent for all load combinations.

Research into ratchetting with creep has been previously undertaken at the University of Nottingham by Hyde et al (10, 11). An axisymmetric shouldered tube component made of a lead alloy (1.1% Sb, 0.11% As) having both a uniform region (shank) and a stress concentration (fillet) has been subjected to constant axial mechanical load and cyclic through thickness thermal loading with creep during the dwell periods. The ratchetting behaviour in the shank and fillet is discussed and, comparisons between experimental results and finite element predictions of shank ratchet strains are made. The general observations are listed below.

1. The mechanical and thermal stress concentration factors in the fillet depress the ratchetting boundary.
2. For mean shank stresses below $0.94\sigma_y$ ratchet strains accumulated in the fillet were significantly larger than those in the shank and increased with increasing steady load.
3. For mean shank stresses above $0.94\sigma_y$ shank and fillet ratchet strains were of similar magnitude, relatively independent of mechanical load and significantly larger than those below $0.94\sigma_y$.
4. Finite element predictions using an isotropic hardening model and experimental results for shank ratchet strains were in reasonably good agreement.

5. A conservative estimate of ratchetting behaviour using the finite element technique can be made by assuming complete redistribution of stresses.
6. A plasticity-creep interaction model is required if accurate predictions of dwell period creep strains are required.

Inoue and Tanaka (47) compare analytical solutions for the ratchetting behaviour of a thin-walled tubular specimen (STB-35 low carbon steel) subjected to constant tensile stress superimposed on cyclic torsional strains at elevated temperature with experimental results. Ratchetting behaviour is investigated in terms of the translation and expansion of the yield surface and they conclude from both sets of results that the size and origin of the yield surface changes during an initial stage of reducing ratchet strains per cycle. A stationary state is eventually reached where the yield surface remains unchanged and ratchet strains per cycle tend towards a constant value.

Corum et al (48) report on ratchetting tests performed on pipes made from type 304 stainless steel. Cyclic thermal loading, induced by changes in the temperature of liquid sodium flowing through the bore, was superimposed on steady internal pressure. Dwell periods of 160 hours at steady internal pressure were allowed between successive thermal shocks and the ratchet strain reduced until ratchetting finally ceased.

Similar tests are reported by Yamamoto et al (49) with dwell periods of between 24 and 48 hours. In this case, the ratchet strains initially reduced but eventually reached a constant non-zero value.

Cousseran et al (50) have carried out ratchetting tests on thin tubes subjected to axial loading and strain controlled cyclic torsion. Type 304 and 316 stainless steel specimens were tested at room temperature and at 300°C. Initially, the material characteristics of the two steels were obtained at the test temperatures. The components were then subjected to creep ratchetting tests. The results of these tests are compared with experimental test data from other sources on an 'efficiency diagram' (see Figure 2.12) where secondary stress ratio, SR, is a function of the primary stress, σ , and the secondary stress range, ΔQ .

i.e.
$$SR = \frac{\Delta Q}{\sigma + \Delta Q} \quad (2.11)$$

and the efficiency index, V, is the ratio of primary stress to a notional effective stress, σ_{eff} ,

$$V = \frac{\sigma}{\sigma_{\text{eff}}} \quad (2.12)$$

The effective stress is defined as an equivalent primary stress which, over the same test duration, would produce the same inelastic strain as the combined primary and secondary stress for the ratchetting test. The effective stress is obtained from the material characteristics.

From Figure 2.12 it is seen that all the results appear to fall into a narrow band and a bound for the avoidance of ratchetting, based on the Bree (1) ratchetting boundary is suggested which is very conservative. Design limits on strain can be used in conjunction with the efficiency diagram to obtain acceptable levels of primary and secondary stress. It is suggested that less conservative estimates of allowable stress levels could be obtained if more experimental data were available.

2.2.2.2.3 Approximate Solutions

Ainsworth (7) presents a bounding technique for predicting creep ratchetting behaviour. From the principle of virtual work he obtains an upper bound for elastic-plastic-creep strains based on computations for elastic-plastic cycling in the absence of creep with an additional steady load in the direction of the required displacement. Consequently a detailed elastic-plastic-creep analysis can be avoided. Ainsworth obtained deformation bounds for a beam subjected to constant axial load and cyclic curvature and a pressurised tube subjected to repeated thermal shocks, which compare favourably with analytical solutions and experimental results respectively.

O'Donnell and Porowski (6) obtained a bound on creep strain for the Bree thin tube problem in the shakedown and reverse plasticity regions. The existence of a permanent elastic core for cyclic behaviour in these regions (which is also true in the presence of creep) is used to obtain an upper bound on creep strains using the maximum value of elastic core stress during a cycle. They show that elastic core stresses are a maximum after each start-up and uniform across the elastic core and hence any point in the core can be considered representative of creep across the whole section. The bound therefore only requires knowledge of the maximum elastic core stress and the uniaxial creep behaviour of the material at that stress and relevant operating temperature.

Leckie (45) presents a detailed review of bounding techniques for cyclic loading at elevated temperature. Theories for ratchetting and shakedown, with and without the effects of creep, are discussed.

2.3 Summary

2.3.1 Models for material behaviour

The choice of model for a particular material requires detailed information of the true cyclic behaviour if accurate predictions of component behaviour are to be obtained. In particular, the material ratchetting phenomenon of 316 Stainless Steel and the lead alloy used by Yahiaoui (12) can only be represented by models like Jhansale (22) and Goodman and Goodall (21). The Mroz (18,19) model describes cyclic material behaviour in a qualitative way. It has the disadvantage that it uses a linear approximation to the true stress-strain behaviour and cannot model the smooth transition between elastic and plastic regimes.

For the modelling of uniaxial creep data, the Norton-Bailey power law (9) is commonly used and requires a 'straight forward' determination of the material constants. This creep law has been adopted for the lead alloy model material used in both this combined project (12) and the previous project (10, 11, 25)

2.3.2 Cyclic behaviour of components

The references cited present analytical and experimental studies of component cyclic behaviour including the effects of creep, generally for simple geometries. Redistribution of stresses due to creep during the dwell periods is known to reduce the non-ratchetting regime and have an adverse effect on the accumulation of ratchet strains. The effects of creep during dwell periods on subsequent ratchetting behaviour is bounded by the 'no creep' condition and the case where complete redistribution of stresses to the steady state stress distribution occurs during each dwell period. There is only a limited amount of reported research on

the influence of stress concentrations on elastic-plastic or elastic-plastic-creep behaviour.

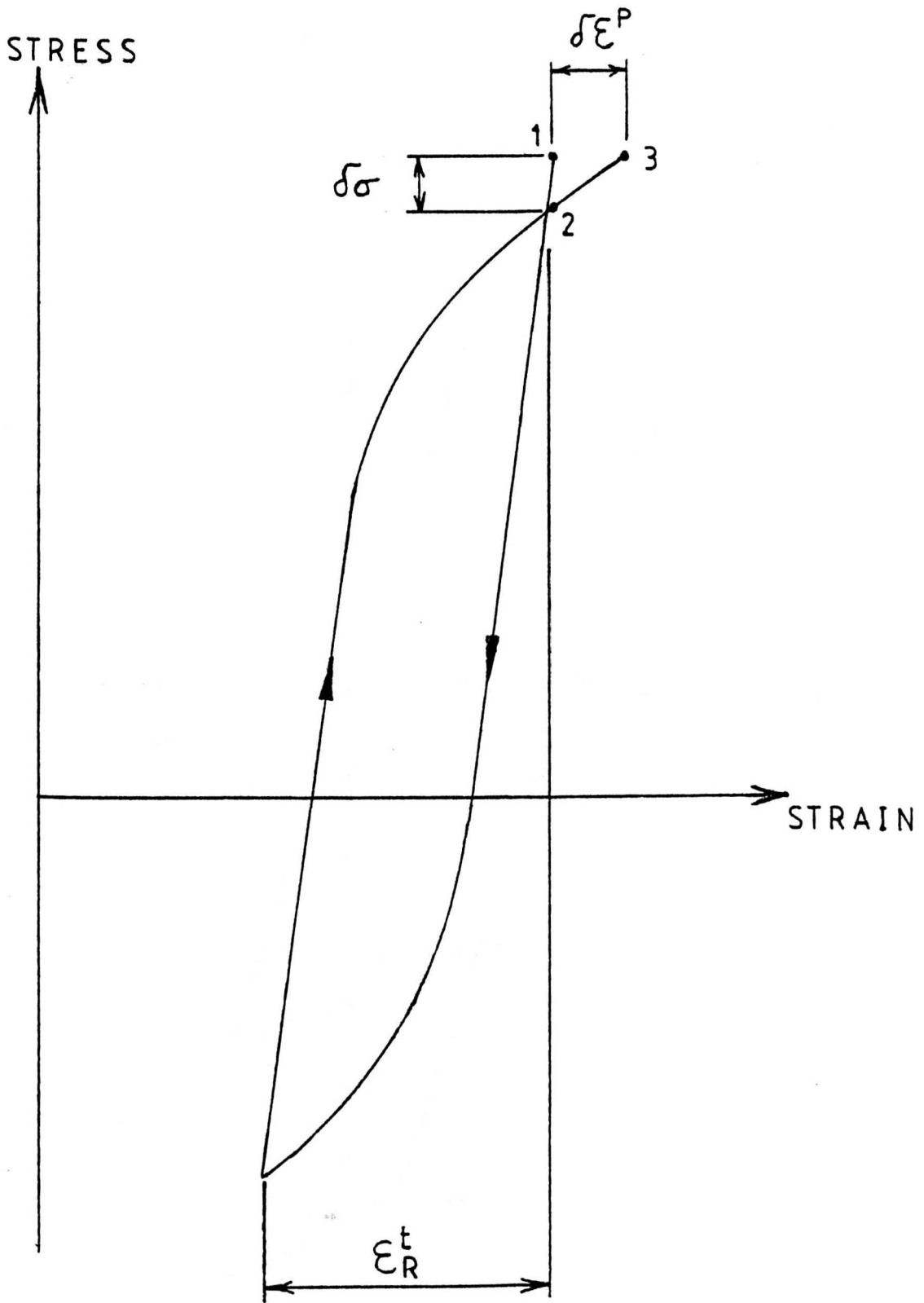


Figure 2.1 An example of Material Ratchetting.

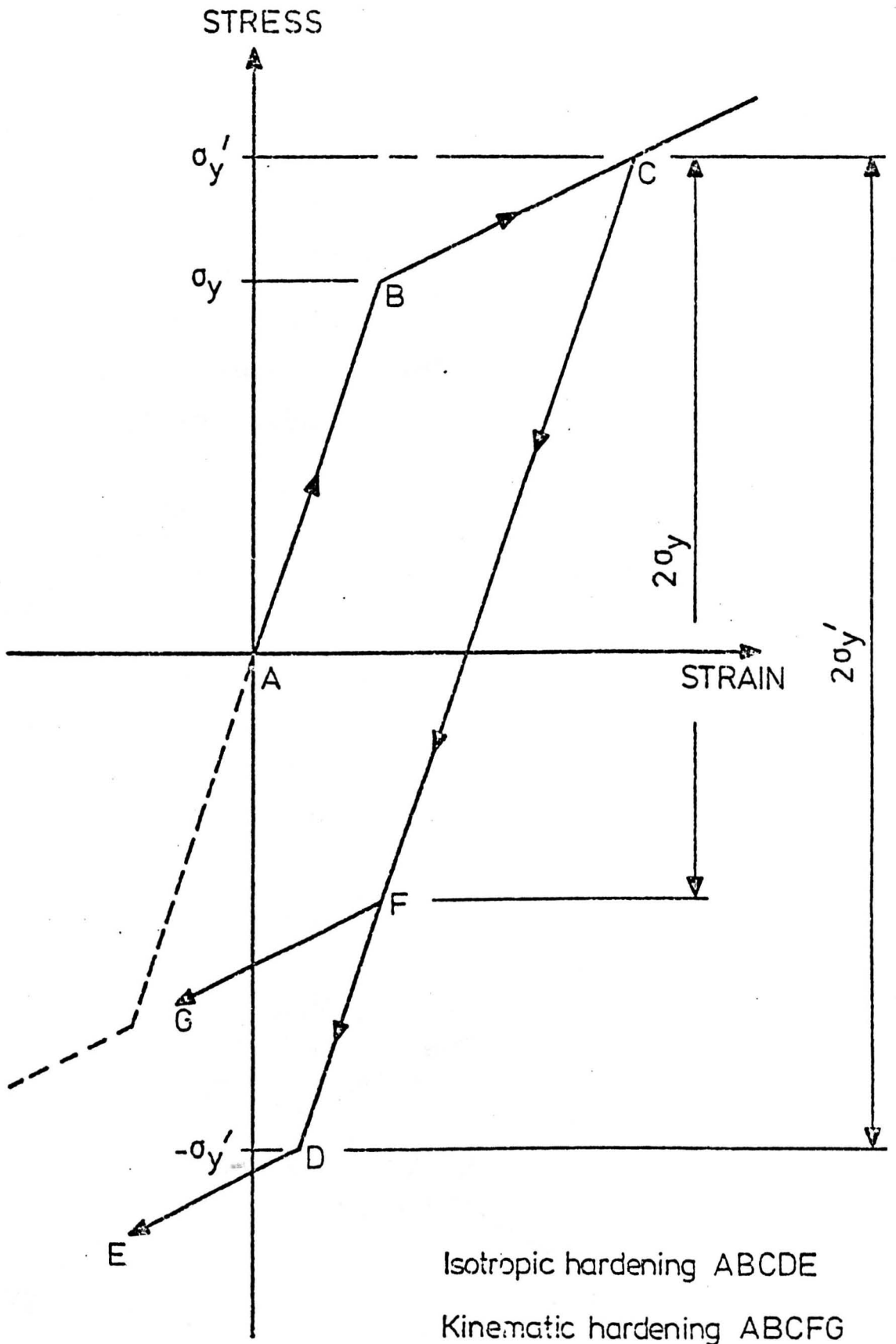
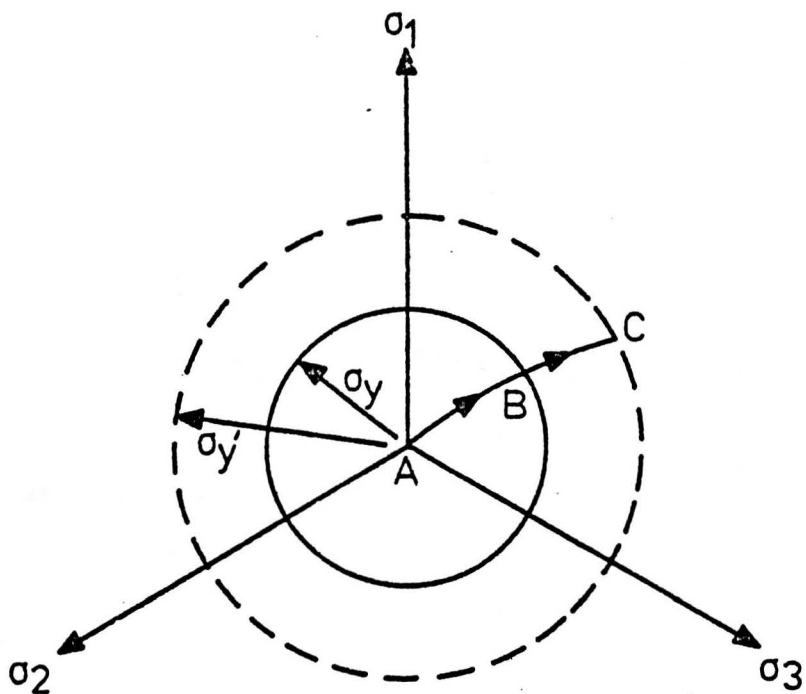
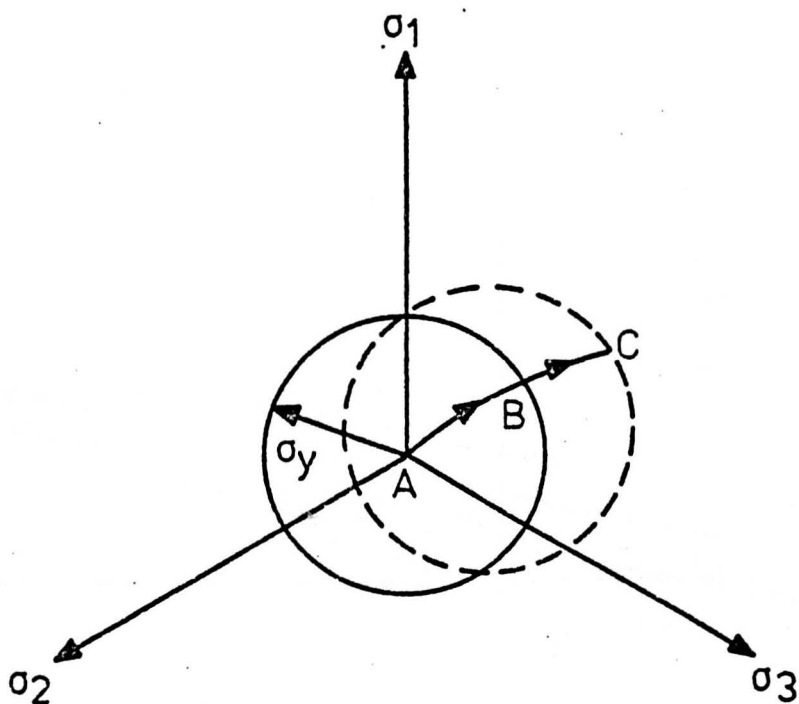


Figure 2.2 Uniaxial stress-strain relationships for Isotropic and Kinematic hardening models



a) Isotropic hardening



b) Kinematic hardening

Figure 2.3 Multiaxial representations of the Isotropic and Kinematic hardening models (see Figure 2.1 for notation)

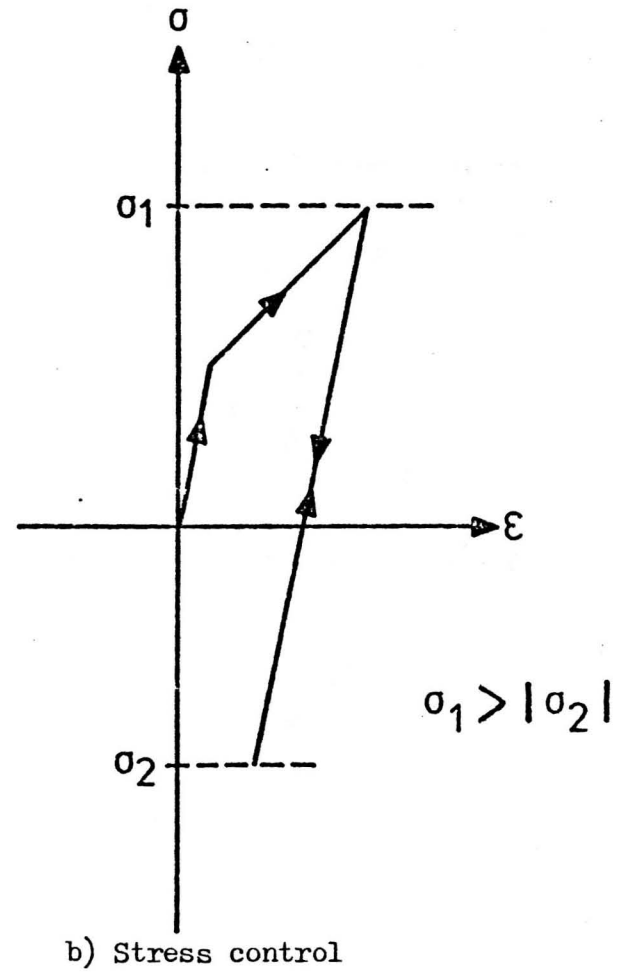
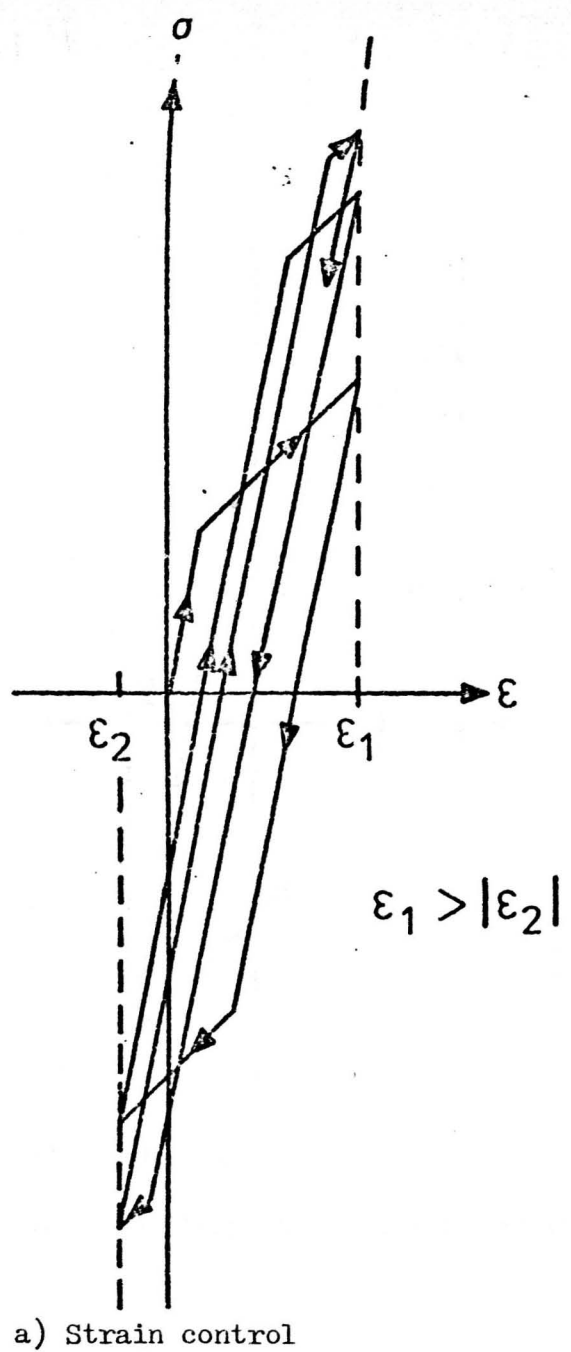
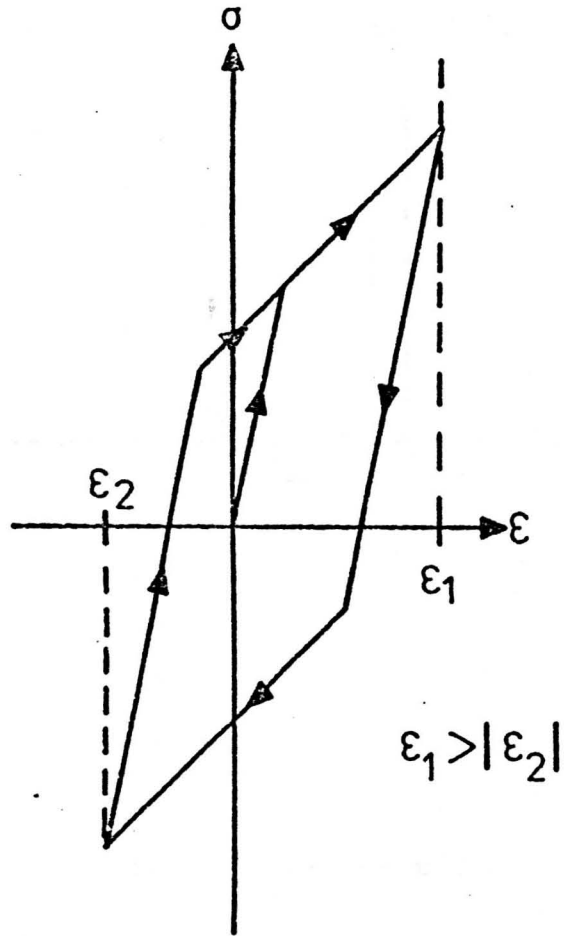
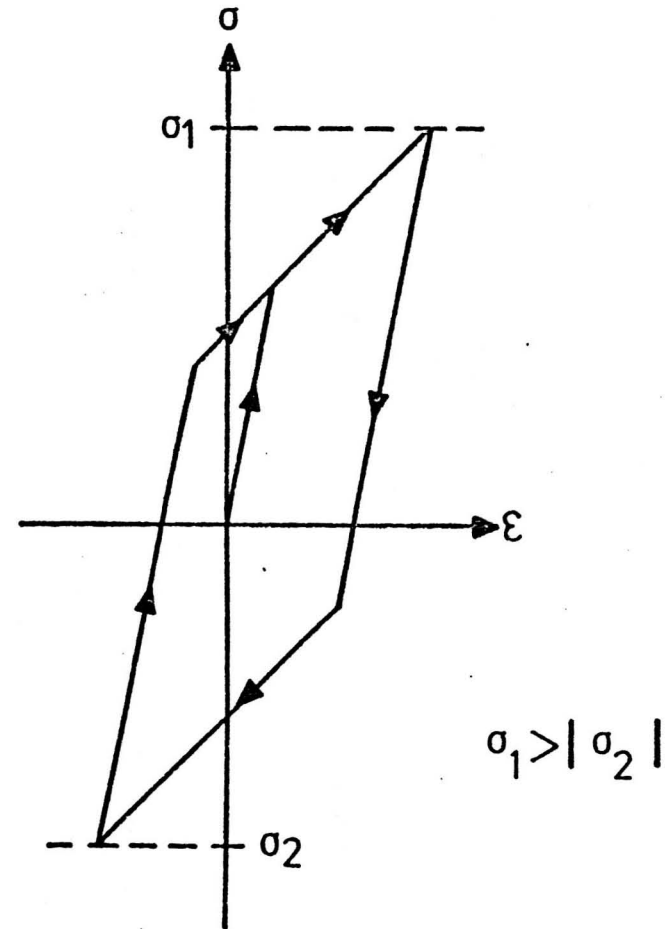


Figure 2.4 Response of the Isotropic hardening model with uniaxial cyclic strain and stress controlled loading



a) strain control



b) stress control

Figure 2.5 Response of the Kinematic hardening model with uniaxial cyclic strain and stress controlled loading

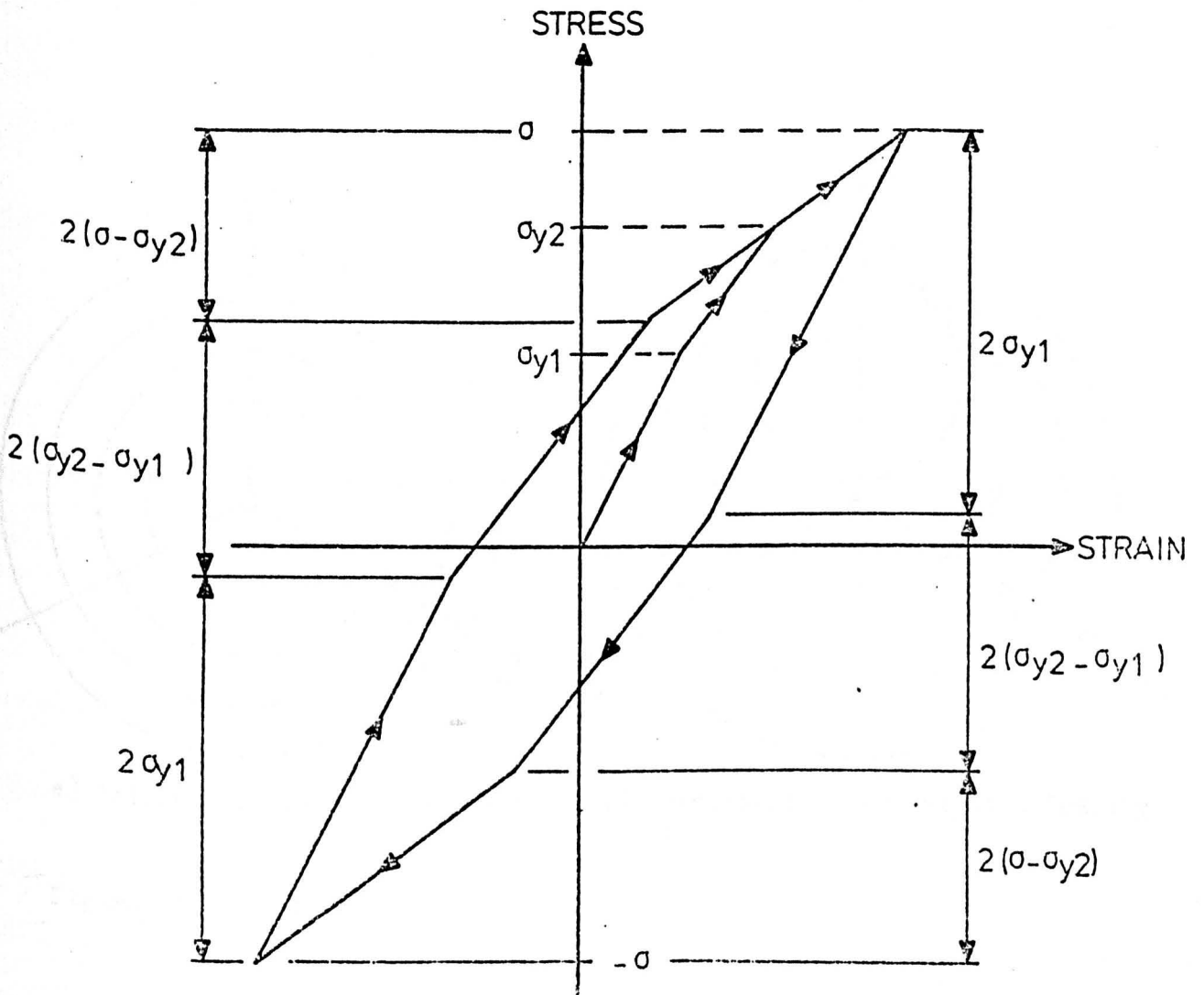
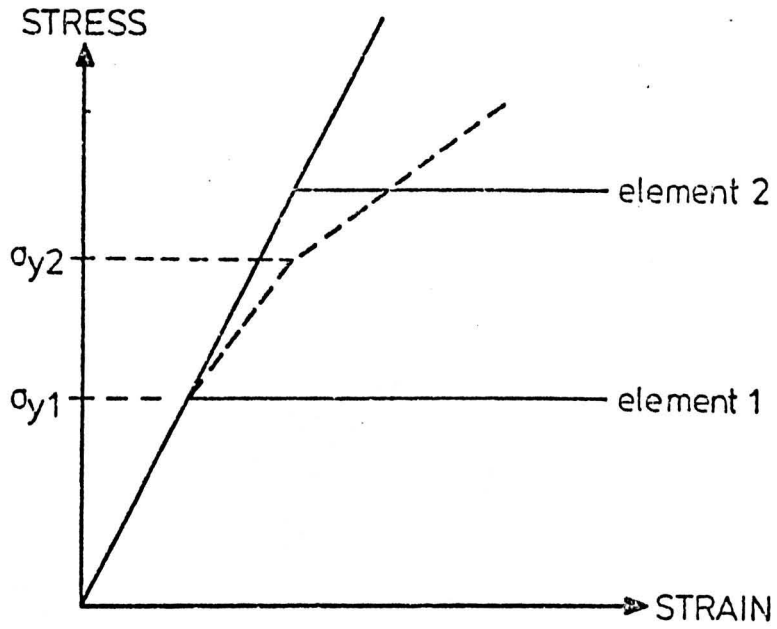
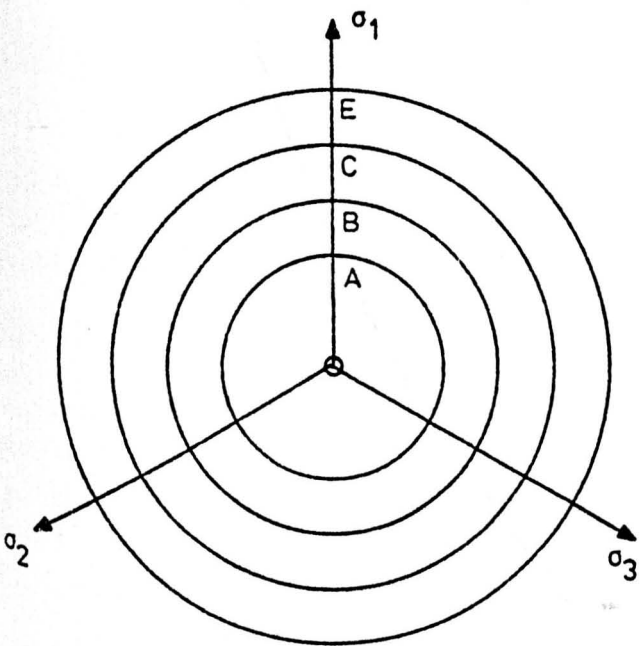
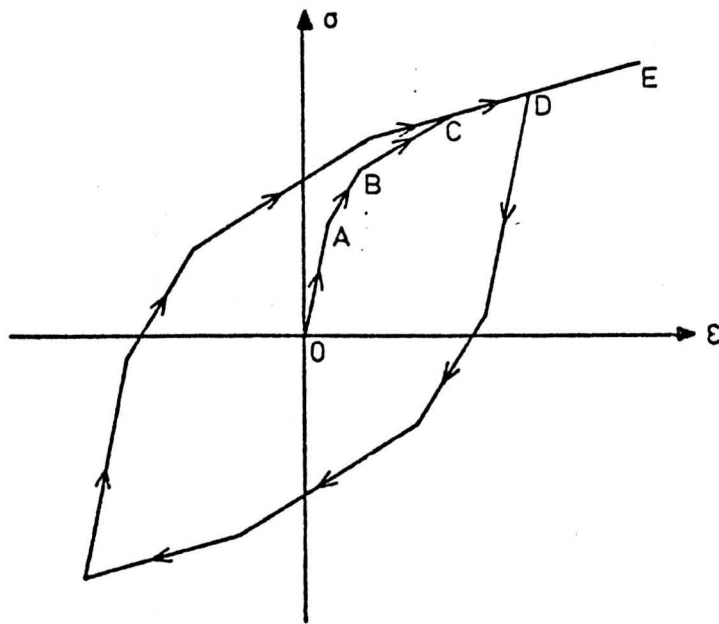
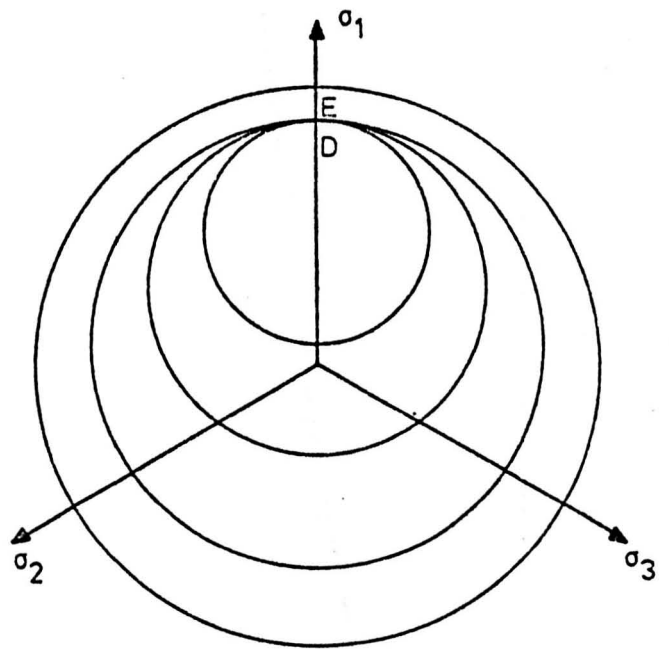


Figure 2.6 The Masing model (17)



a) initial isotropic conditions



b) conditions after uniaxial loading up to D

Figure 2.7 The Mroz model (18).

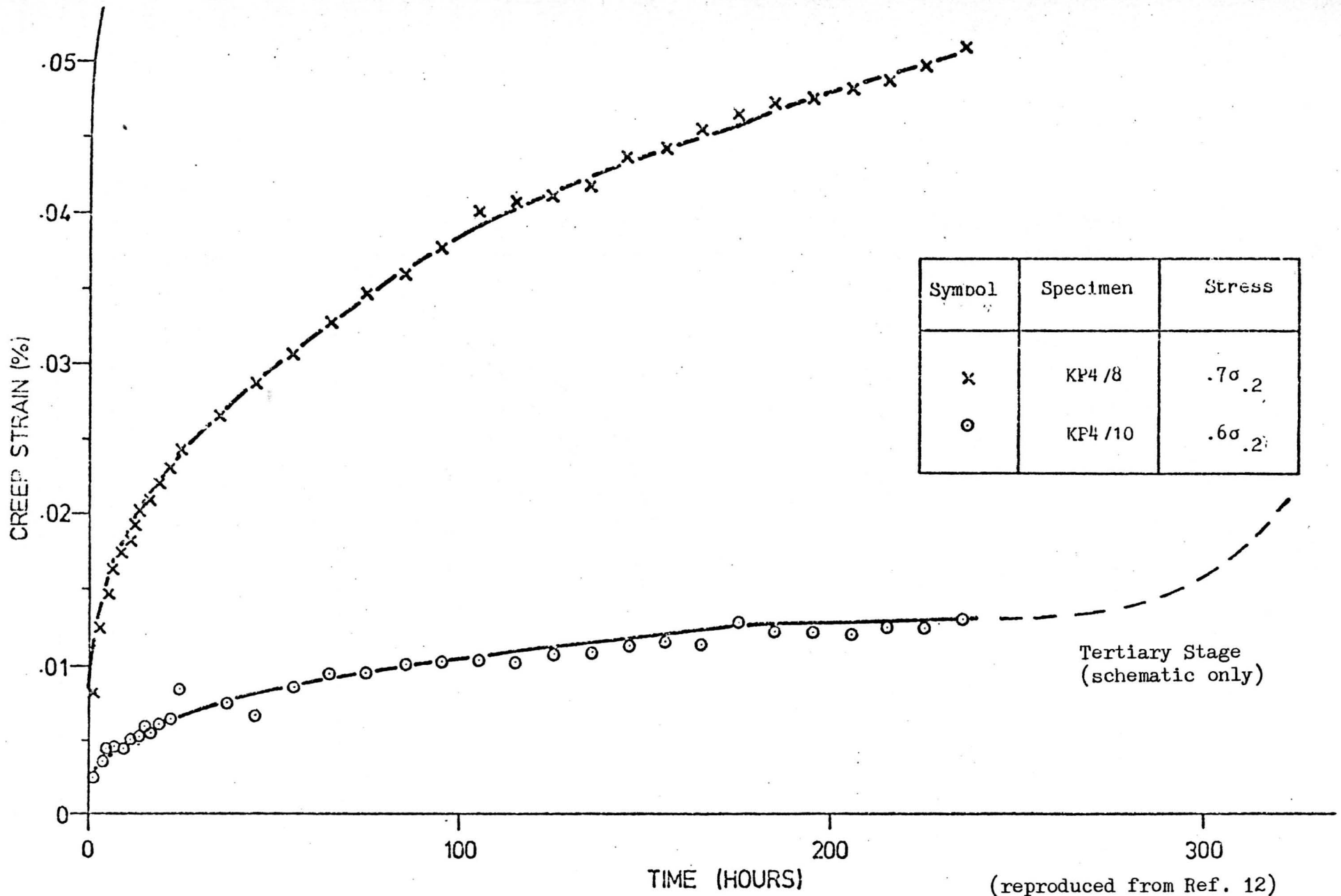


Figure 2.8 Typical Room Temperature Creep Curves for the Lead Alloy with Additional Schematic Representation of the Tertiary Creep Region

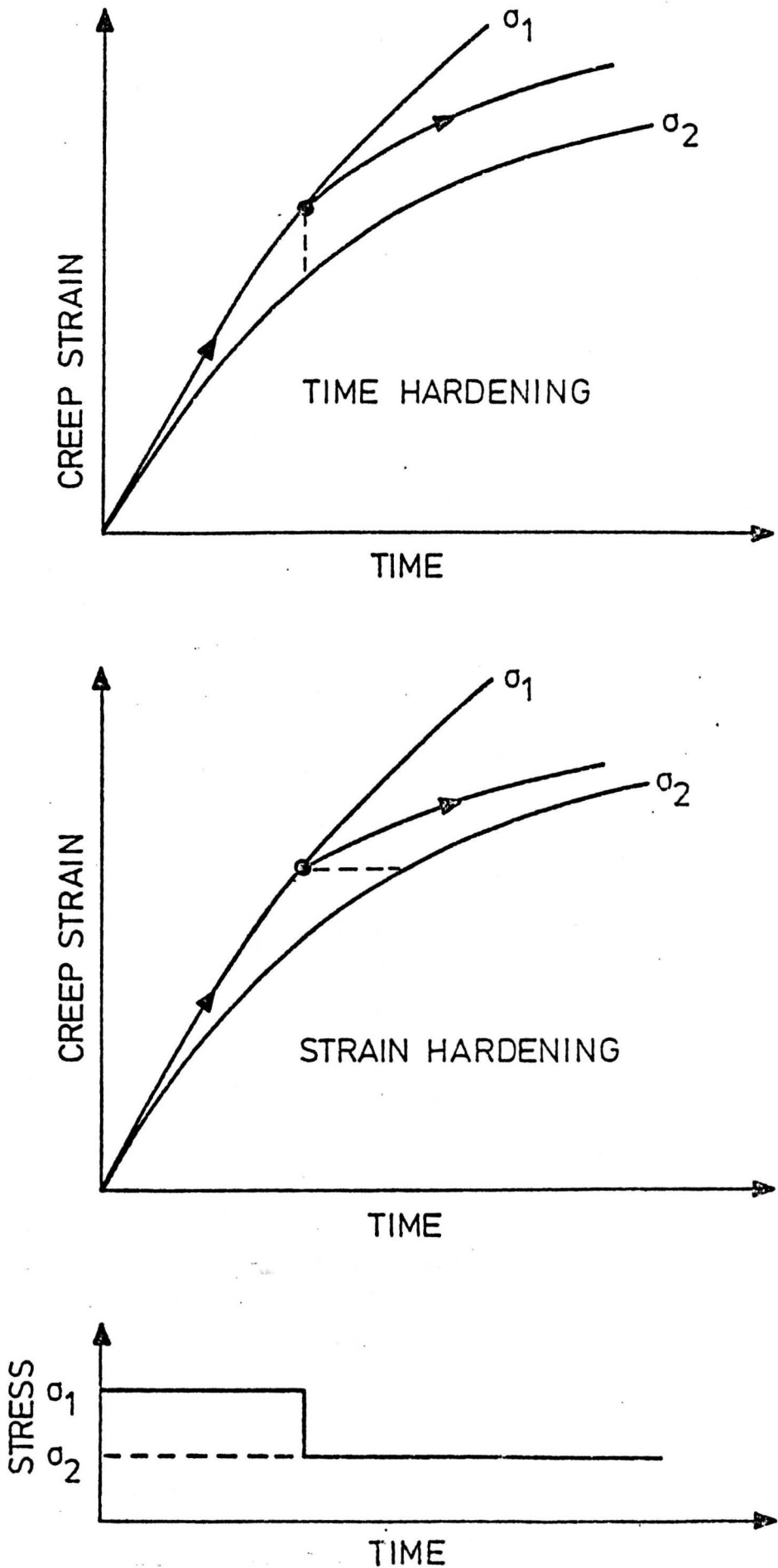


Figure 2.9 Examples of the time hardening and strain hardening models used for creep under varying load

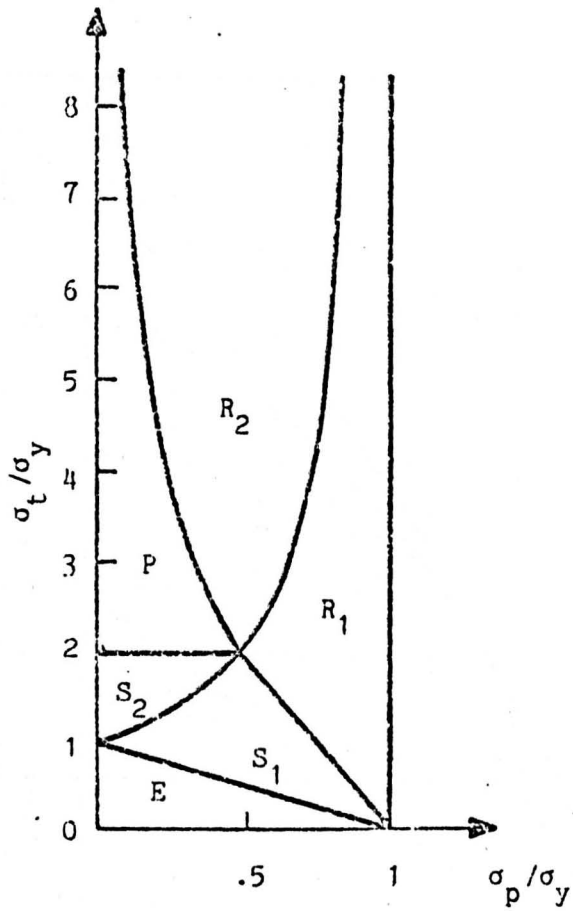


Figure 2.10 The Bree diagram (1)

- Regions:
- E - elastic cycling
 - P - reverse plasticity
 - S₁ and S₂ - shakedown
 - R₁ and R₂ - ratchetting

Regions: E - elastic
 S_1 and S_2 - shakedown
 D_1 and D_2 - ratchetting
 C - collapse

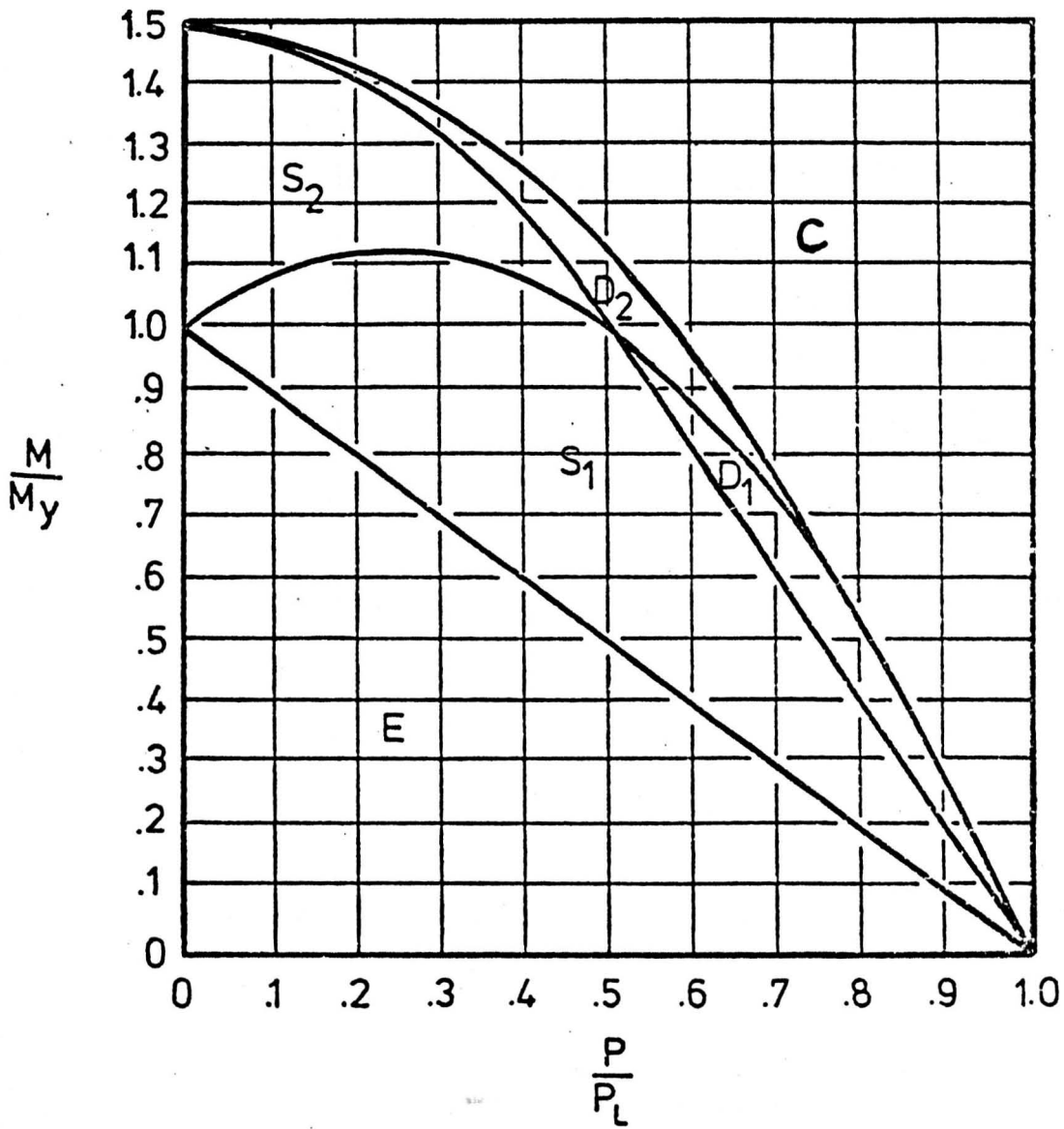


Figure 2.11 The Burgreen diagram (5)

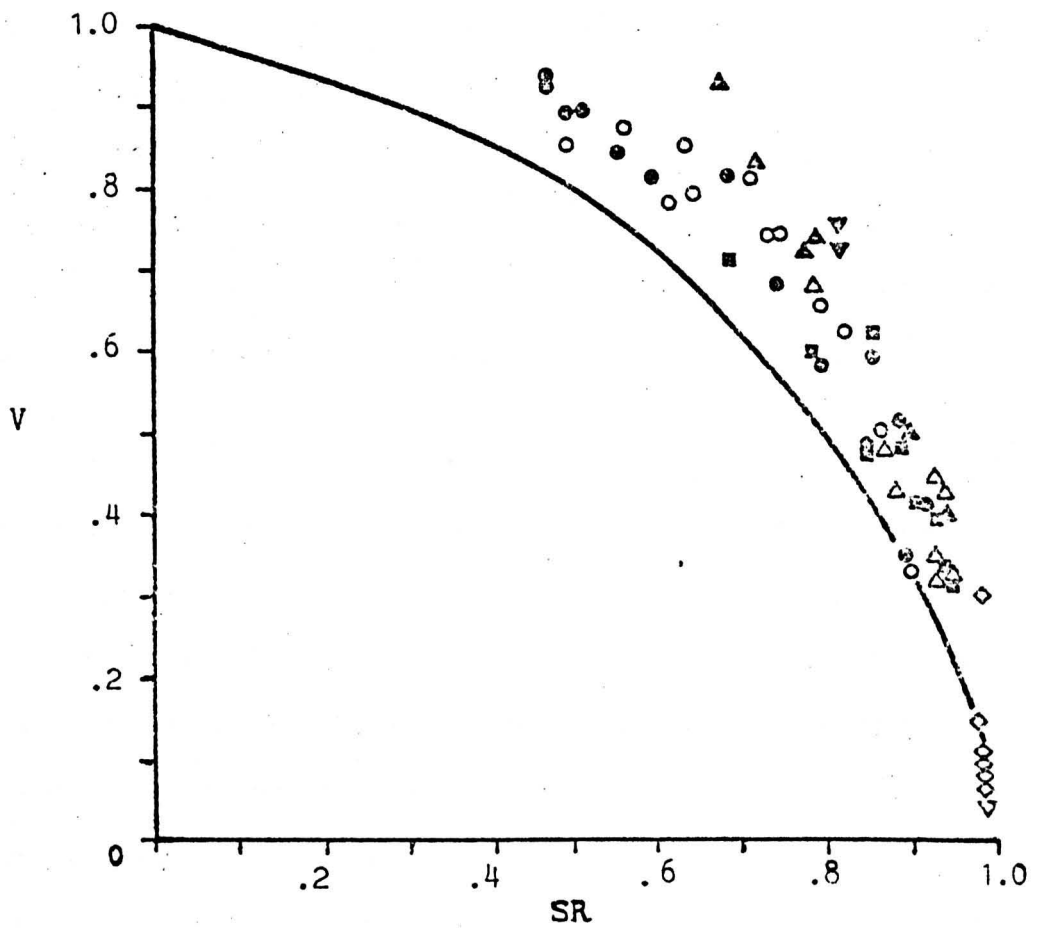


Figure 2.12 The Efficiency Diagram (50) showing experimental data points

CHAPTER THREE

3. COMPONENT SELECTION

3.1 Introduction

Five components subjected to the combined effects of steady and cyclic loading, both with and without the effects of creep were selected for the ratchetting behaviour study. They were chosen to provide a wide range of configurations and loadings which are representative of realistic engineering problems, and also to enable generalisations about the effects of geometry, loading and material behaviour to be made. The components, loadings and relevant figures are listed in Table 3.1. Detailed descriptions of the loadings are given in Chapters 4-6.

Three of the five components (flanged tube, stepped beam and shouldered tube) have both a uniform section (the shank) and stress concentrations in order that direct comparisons between the behaviour in uniform sections and stress concentrations can be made. The flanged tube and stepped beam components have been specifically developed for the combined experimental (12) and analytical projects. The final choice of these two components resulted from a preliminary investigation into suitable components taking into account both experimental and analytical requirements (51). The background to the subsequent choice of flanged tube and stepped beam components is given in section 3.2. Details of the experimental work is reported by Yahiaoui (12). The 'hole-in-plate' and circular plate components appeared in the initial list of possible candidates for the combined experimental and analytical project but were rejected in favour of the flanged tube and stepped beam, mainly on the grounds of experimental difficulty

(see section 3.2). The 'hole-in-plate' component is a 'classical' stress concentration problem which is closely related to the 'tube-plate' situation. The circular plate differs significantly from the other components in so far as the steady load induces tensile, compressive and shear stresses on ratchetting sections; in the other components the steady load stress on the ratchetting sections is dominantly tensile. The ratchetting behaviour of this component, in the absence of creep effects, has been studied by Goodman and Goodall (21) and Hyde (32). The shouldered tube, a thin tube with uniform shank and stress concentration, was developed for a previous project (25,52,53,54). The finite element mesh and temperature files (used to apply the thermal loading cycles - see Appendix I) for this component, and for the circular plate, were already available.

3.2 Background to the Selection of Two Components for the Joint Experimental and Analytical Project

In the initial stages of the project a considerable number of components were suggested as suitable for ratchetting tests. These are listed in Table 3.2 and they fall into two major loading categories:-

1. Constant mechanical loading with cyclic mechanical loading
2. Constant mechanical loading with cyclic thermal loading.

An early decision that at least one component of each loading type should be analysed in detail was made. The final choice of components depended largely on the following factors:-

- (a) ease of manufacture and testing;
- (b) ability to design a suitable loading rig for the purely mechanically loaded component;
- (c) the existence of a rig previously used for shouldered tube tests (54);
- (d) plane stress, plane strain or axisymmetric designs should be adopted to minimise computing costs and so that existing finite element programs could be used; and
- (e) the results should have some practical relevance and the components have both a uniform section and a stress concentration.

It was important that an early decision was made on the choice of components, since the design, manufacture and testing of rig(s) would take a significant portion of the available time (12). A new rig for the purely mechanically loaded component was essential and the choice of component was made the highest priority (section 3.2.1). If the existing shouldered tube rig was to be used for the mechanically/thermally loaded component then more time for a decision on a suitable component was available. Before deciding to modify the existing rig, other alternative components were briefly considered (section 3.2.2).

3.2.1 Choice of component with constant mechanical loading and cyclic mechanical loading

Within the constraints described above, particularly those relating to the experimental work in the joint project, it was considered that the most suitable candidate was a uniform thickness stepped beam with uniform rectangular cross-section in the shank

and stress concentration in the fillet. The loading would be cyclic in-plane bending superimposed on steady axial load. Analytical solutions in the shank are available for load controlled bending (5) and with strain controlled bending, the problem is analogous to the Bree model (1, 2). Factors considered in reaching the final shape of component were:-

- a) the nature and size of the stress raiser;
- b) the length of the shank required to ensure a uniform stress region; and
- c) the experimental limitation on overall length; including the clamping arrangement.

The final choice of component, the stepped beam, is shown in Figure 3.2. It has a shank depth of 25mm and a fillet radius of 7.5mm. This configuration results in photoelastically determined stress concentration factors in tension and pure bending of 1.66 and 1.38 respectively (55).

3.2.2 Choice of component with constant mechanical loading and cyclic thermal loading

The three most likely candidates were considered to be:-

- a) a 'hole-in-plate' component with radial heating of the hole surface;
- b) an axisymmetric component with induction heating; and
- c) an axisymmetric component with fluid heating.

Options a) and b) would require the design and manufacture of a new rig whereas the existing rig (54) could be modified for option c).

3.2.2.1 'Hole-in-plate' component

Preliminary finite element calculations were performed with the lead alloy material data to determine a suitable transient thermal load and to estimate the likely power requirement. It was found that a ramp change in hole surface temperature of 60°C in 10 seconds produced levels of thermal stress likely to cause ratchetting when combined with the stress distribution due to steady mechanical loading. However the power requirement would be in the range 90-140W. It was considered that this level of heating over the ~10mm thickness would be very difficult to achieve. A further disadvantage would be that the distribution of heat flux around the hole surface would vary as incremental growth caused changes in the shape of the hole and this would make finite element modelling of the transient difficult. The 'hole-in-plate' option was subsequently dropped in favour of an axisymmetric component.

3.2.2.2 Axisymmetric component with induction heating

Although induction heating results in rapid changes in temperature (and hence high thermal stresses) the high cost of a suitable power supply unit (~1½KW) was found to be a major drawback. Also it was anticipated that the strain gauge performance might be impaired by the effects of electro-magnetic induction. The induction heating option was dropped in favour of the fluid heating technique already developed for the shouldered tube (54).

3.2.2.3 Axisymmetric component with fluid heating

The component chosen for detailed analysis is the flanged tube shown in Figure 3.1. It is a thick cylinder ($D/d = 2$) with a flange; a uniform section in the shank and a stress concentration

in the fillet. Based on previous experience with strain gauging for the shouldered tube component, where water flowed along the outside surface as well as through the bore, it was decided to apply thermal loading by water flowing through the bore only. The outside surfaces would be open to the atmosphere and effectively insulated. The final dimensions of the component were based on:-

- a) the size limitations of the existing rig (54)
(i.e. overall length ~200mm);
- b) a length: bore machining limitation of 10:1;
- c) adequate strain gauging in the fillet region
using a band of 5 E.R.S. gauges;
- d) a small flange diameter to facilitate casting;
- e) a suitable length of shank to ensure uniform
stress conditions under steady axial and thermal
loading; and
- f) a suitable loading arrangement with no influence
on stress distributions in the shank and fillet.

Conditions e) and f) were investigated using a finite element model of the component and full details of the analysis are given elsewhere (51).

Table 3.1 Components and loadings

Component	Steady Loading	Cyclic Loading	Figure Number
Flanged tube	Axial tension	Through thickness axisymmetric temperature variation	3.1
Stepped beam	Axial tension	In-plane bending	3.2
'Hole-in-plate'	Tension	Heating and cooling of hole surface	3.3
Circular plate	Transverse pressure	Through thickness temperature variation	3.4
Shouldered tube	Axial tension	Through thickness axisymmetric temperature variation	3.5

Table 3.2 Components considered for joint experimental and analytical project

TYPE	LOADING	
	Steady	Varying
1. Plane stress/strain		
a] Rectangular bar	tension	bending [load controlled]
b] " "	"	thermal
c] Bree's problem	"	bending [curvature controlled]
d] Stepped beam	"	bending [load controlled]
e] Perforated strip, 1 hole	"	bending
f] " " " "	"	thermal
g] " " row of holes	"	bending
h] Perforated sheet, 1 hole	tension in x-direction	tension in y-direction
j] " " array of holes	"	" " "
k] " " " " "	"	thermal
2. Axisymmetric		
a] Plain drum head	pressure	thermal
b] " " "	"	conc. load
c] Axially bossed drum head	"	" "
d] " " " "	"	thermal
e] Drum head with axial nozzle	"	"
f] " " " " "	"	conc. load
g] Circular plate	tension	bending
h] " "	"	thermal
j] " "	"	pressure
k] Shouldered tube	"	thermal
l] Flanged tube	"	"

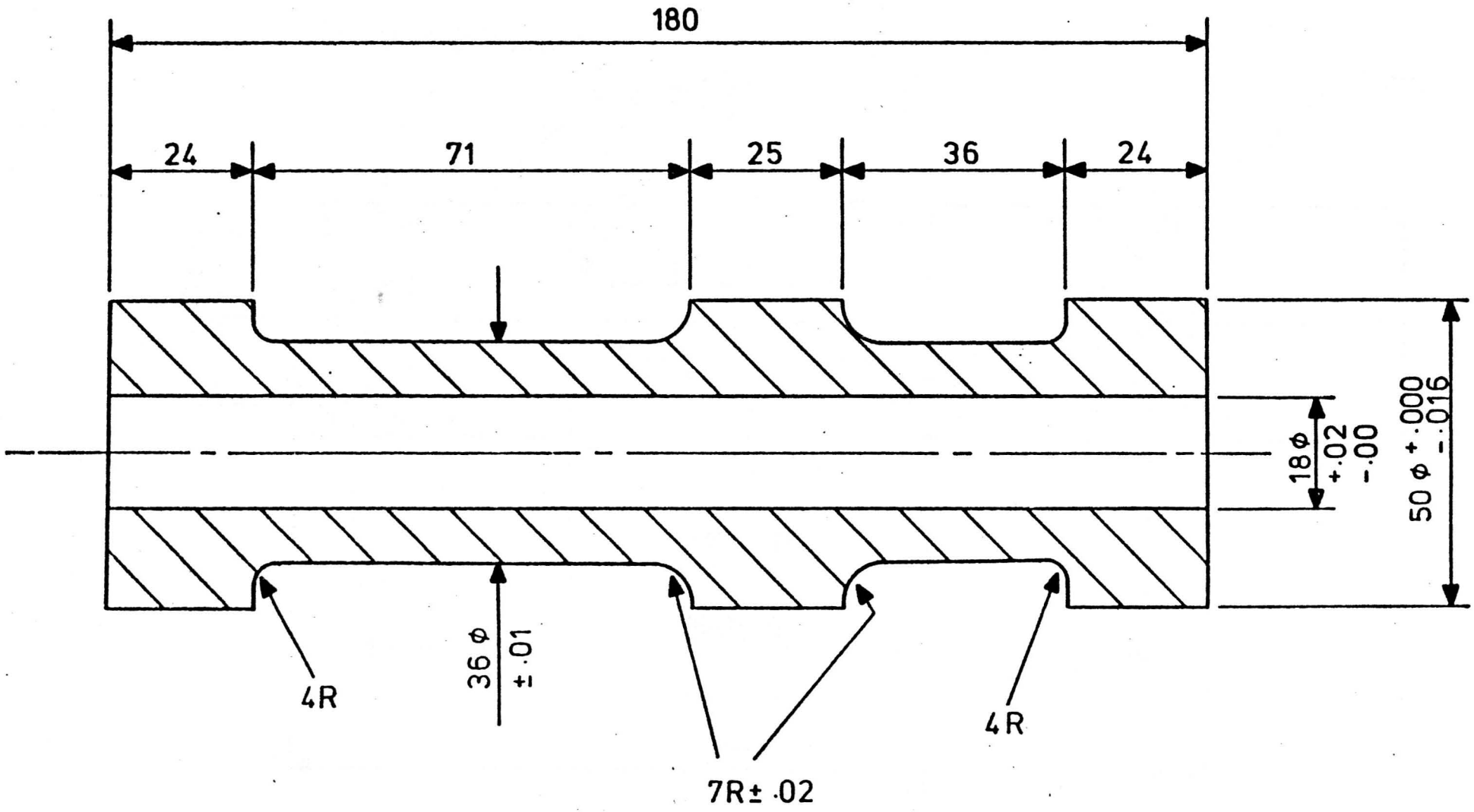


Figure 3.1 The flanged tube component. Dimensions in mm.

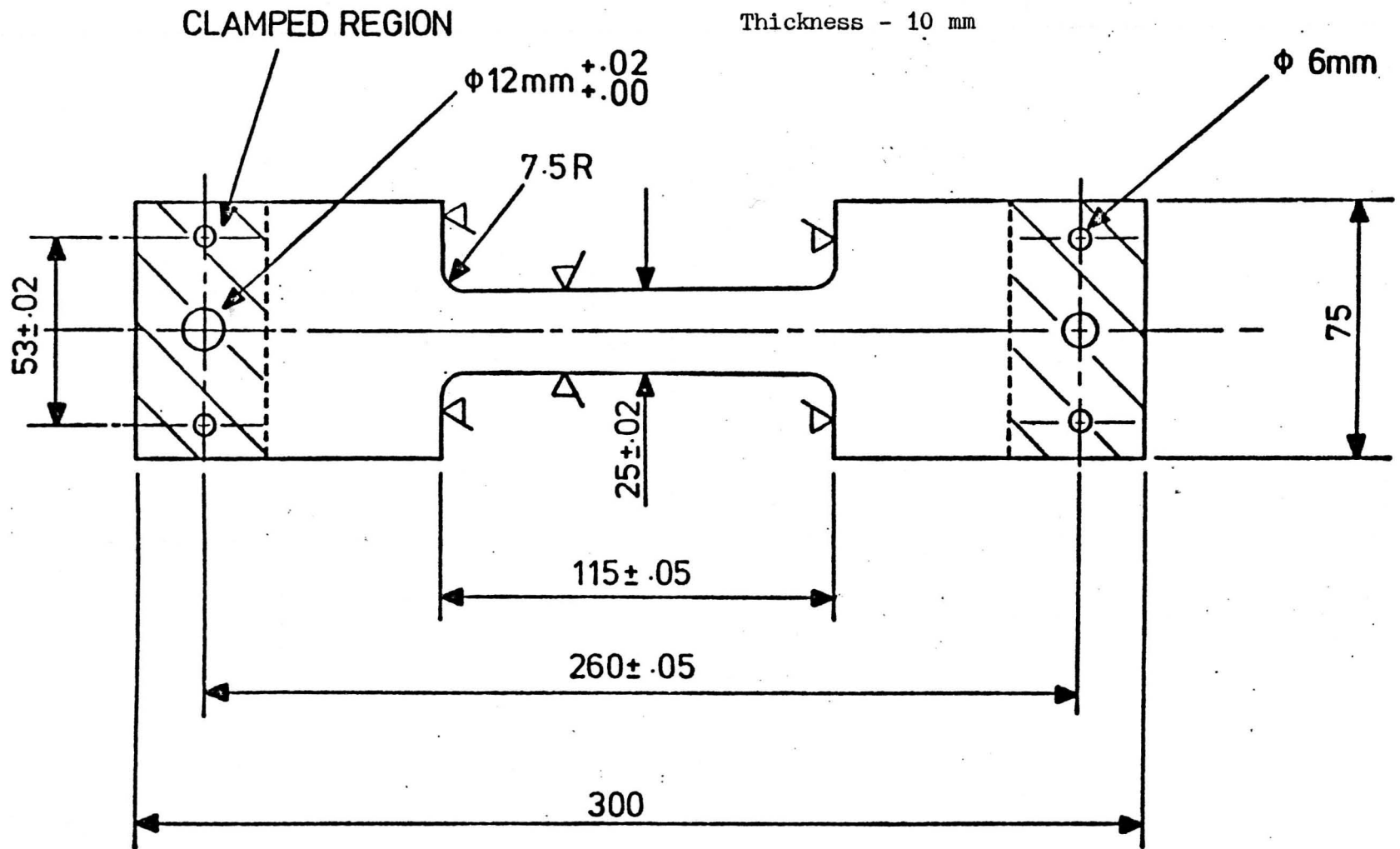
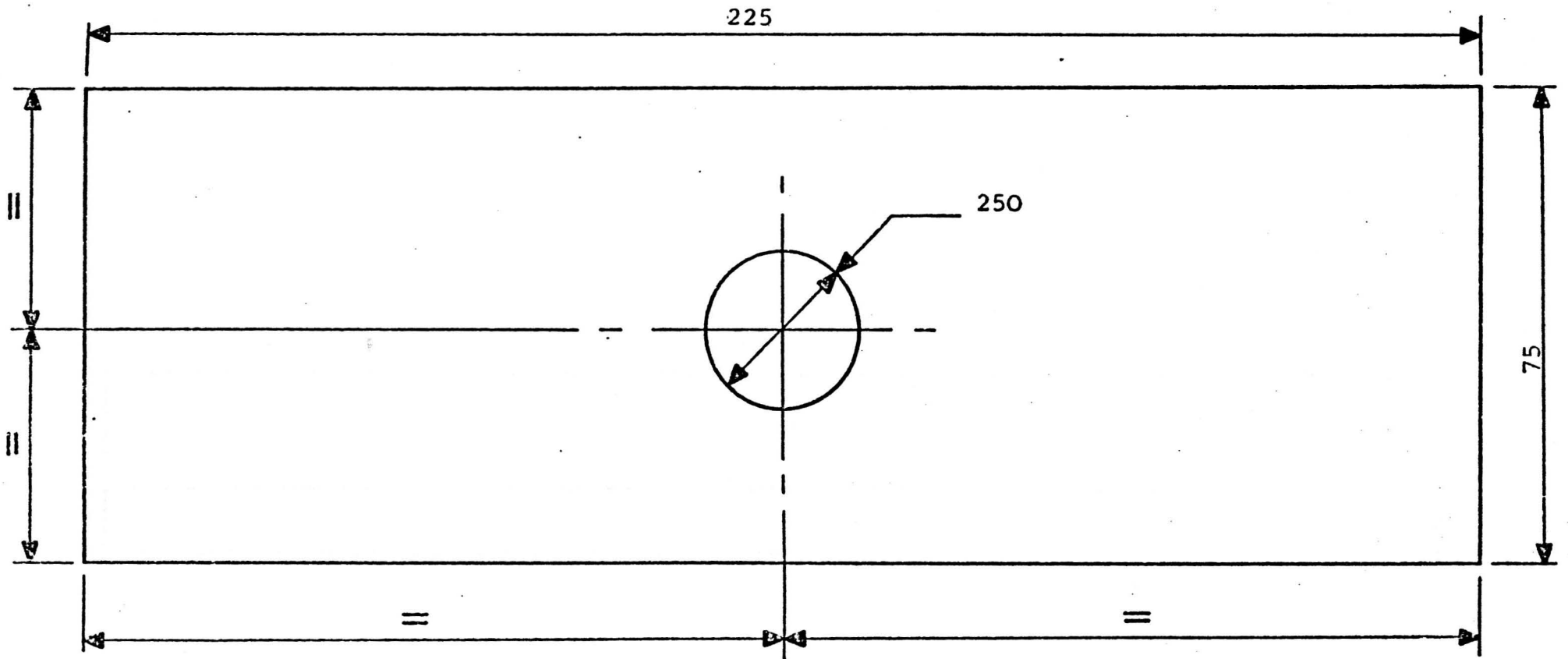


Figure 3.2 The stepped beam component. Dimensions in mm.



Thickness - 10 mm

Figure 3.3 The 'hole-in-plate' component. Dimensions in mm.

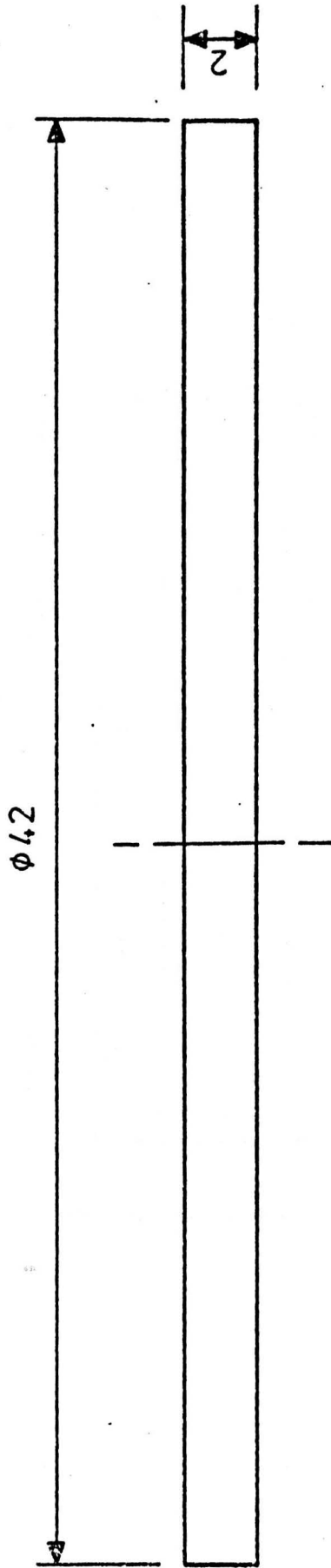


Figure 3.4 The circular plate component. Dimensions in mm.

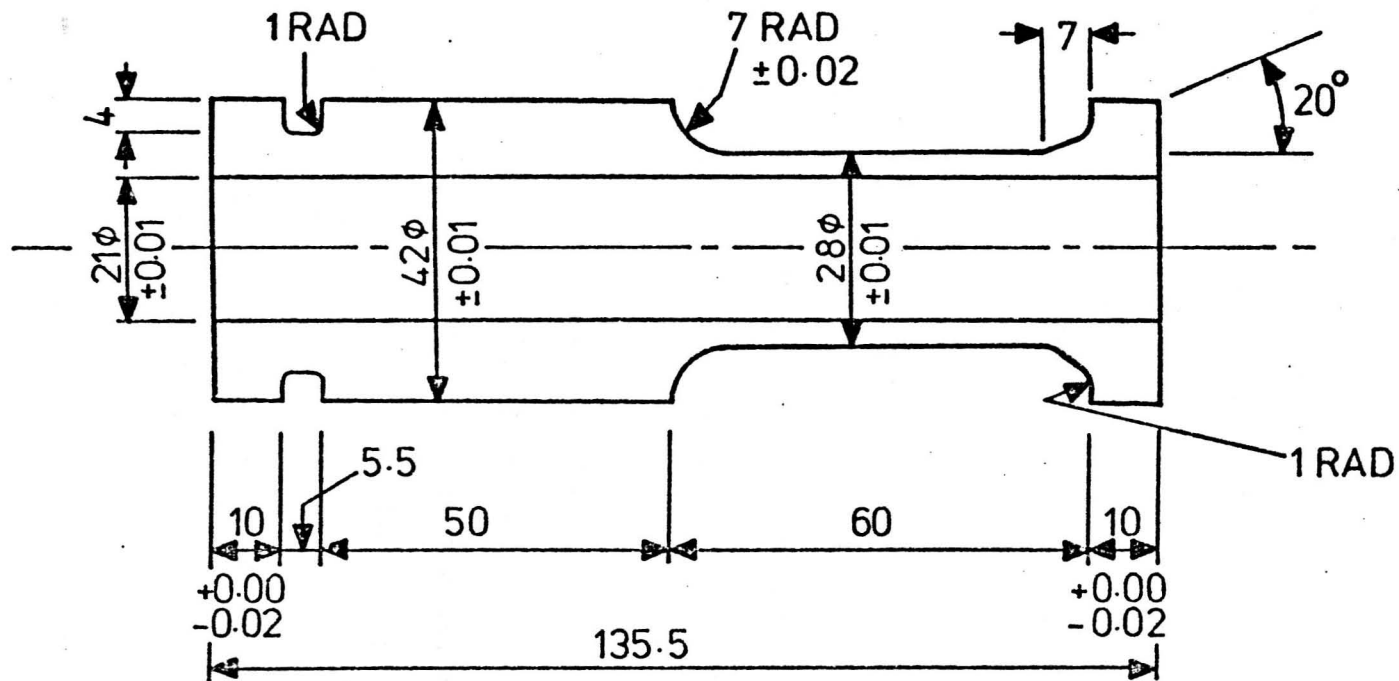


Figure 3.5 The shouldered tube component. Dimensions in mm.

CHAPTER FOUR

4. FLANGED TUBE

4.1 Introduction

The development of the flanged tube component (Figure 3.1) has been discussed in Section 3.2.2. The behaviour of the flanged tube under conditions of

- (i) steady mechanical axial load; and
- (ii) transient thermal loading

is discussed here.

When the two modes of loading are combined (i.e. steady mechanical axial load and cyclic variation in thermal loading) the component may display the phenomenon of ratchetting with creep in the dwell periods between thermal shocks affecting the ratchetting behaviour.

As a preliminary to the study of the whole component, a detailed study of the shank region is presented. This gives an insight into the component's behaviour using a simple finite element model and hence efficient use of computing time. Also it enables a wide range of loads and different material behaviour models to be examined. In addition to a description of the component behaviour, comparisons with the experimental results of Yahiaoui (12) are made.

4.2 Shank Analysis

4.2.1 Finite element model

A four element through thickness axisymmetric model of a 10 mm length of shank is used with constraints of constant axial displacement on one face and zero axial displacements on the other, using the axisymmetric 8-noded isoparametric elements.

4.2.2 Data

Basic material data is for the lead alloy used by Yahiaoui (12) with a Norton-Bailey Power law to define uniaxial creep behaviour

$$\epsilon^c = A \sigma^n t^m$$

and no interaction between creep and plastic strains. The data is summarised in Table 4.1. The elastic-perfectly-plastic, isotropic hardening and kinematic hardening models are used to define the material behaviour. Appendix I lists the 'standard' data used in the analysis.

4.2.3 Thermal loading cycle

A thermal loading for the shank (and hence whole component) was determined from the experimental results of Yahiaoui (12).

A thermal shock consists of:-

- (i) step increase in bore fluid temperature of 53.5°C,
- (ii) a transitory period of 20 seconds for conditions to stabilise with the bore fluid maintained at the increased temperature and all other surfaces assumed to be insulated,
- (iii) step reduction in bore fluid temperature of 53.5°C,
- (iv) as (ii) with bore fluid maintained at the original temperature.

The finite element predictions of through thickness temperature difference during the transient are compared with the experimental results in Figure 4.1. There is reasonable agreement between the results. The most severe conditions occur during the transient at $t \approx 0.5$ secs..

The incremental approach used in finite element plasticity calculations requires that thermal (and mechanical) loads are applied

incrementally and nodal temperature distributions at successive time increments up to 20 seconds for both halves of the thermal cycle were computed and stored on temperature files. To ensure that the most severe transient conditions were included, a small time increment of 0.1 seconds was used. This resulted in an unacceptable number of increments for each half cycle (i.e. 200). By considering the temperature/time distributions, these temperature files were edited down to an acceptable number of increments (i.e. 15) without affecting the severity of the transient. The times chosen were $t = 0.1$ to 1.1 s (in 0.1s steps), 2.1, 3.1, 4.1 and 20s. The temperature distributions during the first half of a thermal cycle are shown in Figure 4.2 which confirms that steady state conditions are effectively attained within 20s and also shows the non-linear characteristic through the thickness.

The resulting variations in elastic stresses (axial and hoop) are shown in Figure 4.3 up to and including the most severe condition ($t = 0.5$ s). From then on the stresses reduce to zero.

The increase in bore fluid temperature produces a compressive axial and hoop stress in the region of the bore and a tensile stress region towards the outside.

The equivalent linear temperature difference ΔT for the incremental temperature distributions have been obtained by the approach suggested by Yamamoto et al (49).

$$\text{i.e. } (\Delta T)_{\text{equivalent linear}} = \frac{12}{d^2} \int_{-d/2}^{+d/2} T(y) \cdot y \cdot dy$$

and a maximum value of 34.9°C occurs when $t = 0.5$ s. This yields a maximum normalised thermal stress of 0.97 using the Bree

d = wall thickness in above equation

y = distance from centre of the wall in above equation.

equation (1)

$$\text{i.e. } \frac{\sigma_t}{\sigma_y} = \frac{E \alpha \Delta T}{2(1-\nu) \sigma_y}$$

The maximum equivalent thermal stress range for a complete cycle, which includes both heating and cooling, is therefore 1.94.

4.2.4 Cyclic thermal loading with constant axial load

The behaviour of the shank with constant axial mechanical load and intermittent thermal shocks ((i) to (iv) in Section 4.2.3) is discussed in this section. The creep ratchetting behaviour is bounded by the 'no creep' condition (zero dwell period between shocks) and 'complete redistribution' (in this case the resulting stress distribution, after creep, is a uniform axial tensile stress). Elastic-perfectly-plastic and linear hardening models are considered; the numerical values of ratchet strain quoted are generally increments in the axial strain.

4.2.4.1 'No creep' condition

4.2.4.1.1 Elastic-perfectly-plastic material model

Ratchetting Mechanism

The axial and hoop stress distributions due to initial loading, at the most severe conditions during the first and second halves of the first thermal shock and at the end of the first thermal shock are shown in Figure 4.4 for an axial load of 0.7 of the limit load. For the first half of the shock there is no further plastic straining after $t = 0.6s$ and at the end of the half cycle the accumulated components of plastic strains are also shown in Figure 4.4. During the second half of the cycle yielding is again evident for the first 0.6 seconds and at the end of the first cycle plastic strains

have been accumulated over approximately $2/3$ of the section, with the residual stress distribution being significantly different from that due to initial loading. The ratchet strain for the first cycle is $0.107 \epsilon_y$. A steady cyclic state is established after the first cycle. The axial and hoop stress distributions during the second and subsequent cycles are shown in Figure 4.5. The whole section experiences some plastic straining during the complete cycle. Again plastic straining is only evident during the first 0.6 seconds of each half cycle. Also the residual stress distributions at the end of the cycle in Figure 4.5 are practically identical to those after the first cycle in Figure 4.4. This ratchetting mechanism is different from that of the 'Bree' tube for which a region around the mid thickness position remains at the yield stress throughout a complete cycle. The ratchetting process is continuous with the second and subsequent cycles contributing an equal amount to the accumulation of ratchet strain ($0.06 \epsilon_y$ for each cycle).

The accumulation of ratchet strains during the first ten cycles is shown in Figure 4.6 where the normalised accumulation of ratchet strain at the end of the j^{th} cycle is given by

$$\epsilon_j^r / \epsilon_y = \sum_{i=1}^j (\Delta \epsilon_i^r / \epsilon_y) \quad 4.1$$

and $\Delta \epsilon_i^r$ is the ratchet strain for the i^{th} cycle.

Effect of mean load on ratchetting behaviour

The discussion of the previous section has shown that the ratchetting behaviour of the flanged tube shank (with an elastic-perfectly-plastic material model) can be defined by two parameters; the first cycle ratchet strain and the constant ratchet strain in

subsequent cycles. The variation of these parameters with mean load is given in Table 4.2 (together with the equivalent results for complete redistribution which will be discussed later) and shown graphically in Figure 4.7. The ratchetting boundary appears to be at $\frac{P}{P_L} \simeq 0.68$ below which the first cycle ratchet strains are relatively small; above the ratchetting boundary both the first cycle and steady state ratchet strains increase very rapidly with increasing load. At mean loads above $\sim 0.72 P_L$ steady state ratchet strains are greater than in the first cycle.

4.2.4.1.2 Linear hardening models

For a bilinear representation of the monotonic stress-strain curve, a range of values for the ratio of plastic modulus to elastic modulus, $\frac{E_P}{E}$, has been considered which is intended to cover both the lead alloy (12) at around ambient temperature and 316 stainless steel at temperatures in the range 500-650°C (3). The range of values for $\frac{E_P}{E}$ is 0.01, 0.05 and 0.1. Both isotropic and linear kinematic hardening models were investigated; for all the load cases considered there was no significant difference in the results for the two models and hence the description 'linear hardening' is used. Detailed inspection of the finite element results showed that the two models gave very similar results because there was no significant reverse yielding for the thermal loading case investigated.

Ratchetting Mechanism

The mechanism of ratchetting with a linear hardening model is similar to that for the elastic-perfectly-plastic material model with the obvious exception that ratchetting is no longer a continuous process since shakedown will eventually occur when the increase

in yield stress is such that transient stresses are purely elastic. By comparison with the behaviour with an elastic-perfectly-plastic material model in Figures 4.4 and 4.5, the change in yield stress will result in cycle dependent residual stress distributions with a monotonic reduction in ratchet strain per cycle after the first non-representative cycle, as shown in Figure 4.8 for a mean load of 0.9 of the limit load (based on initial yield*). The results for an elastic-perfectly-plastic material model, taken from Table 4.2, are included. The magnitude of the ratchet strains and number of cycles to shakedown increase with decreasing $\frac{E_P}{E}$ and are bounded by the continuous ratchetting for $\frac{E_P}{E} = 0$ and the purely elastic model ($\frac{E_P}{E} = 1$) for which there is no ratchetting.

Effects of mean load and E_P/E on ratchetting behaviour

For hardening materials, the definition of ratchetting behaviour is more complex since ratchet strains vary from cycle to cycle. Figures 4.9 to 4.12 show the variation of normalised accumulated ratchet strains with mean load and $\frac{E_P}{E}$ after the 1st, 2nd, 5th and 10th cycles respectively. Figure 4.13 shows the total accumulated ratchet strains for $\frac{E_P}{E} = 0.05$ and 0.1 together with an indication of the number of cycles to shakedown. The equivalent results for $\frac{E_P}{E} = 0.01$ were not obtained because very many cycles would be required before ratchetting stops (as is apparent from Figure 4.8). Figure 4.13 shows that for mean loads below ~ 0.6 of the limit load, for which there is no ratchetting after the first cycle, there is no difference in the first cycle ratchet strain for $\frac{E_P}{E} = 0.05$ and 0.1 whereas for $\frac{P}{P_L} > 0.6$ the hardening of the material has a significant effect on the accumulated ratchet strain and cycles to shakedown.

* For consistency with the elastic-perfectly-plastic results, a limit load, based on the initial yield stress, is used throughout this document.

An alternative method for presenting the data, including the elastic-perfectly-plastic results is used in Figure 4.14. This plot enables the accumulated ratchet strain in 10 cycles to be estimated for a given material hardening and axial load.

The variation of normalised ratchet strains in the second cycle with mean load for various values of $\frac{E_P}{E}$ is shown in Figure 4.15. The ratchetting boundary for a given thermal loading is defined as the mean load below which there is no incremental growth after the first cycle. Figure 4.15 indicates a ratchetting boundary at $\frac{P}{P_L} \simeq 0.67$ which is relatively insensitive to the degree of material hardening for the range $0 \leq \frac{E_P}{E} \leq 0.1$.

4.2.4.2 Complete Redistribution

4.2.4.2.1 Elastic-perfectly-plastic material model

Ratchetting Mechanism

The axial and hoop stress distributions due to initial loading and during the first and second halves of the first thermal cycle are identical to those for the 'no creep' condition shown in Figure 4.4 for $\frac{P}{P_L} = 0.7$. However, between the end of the first thermal cycle and the beginning of the second thermal cycle, the stresses are allowed to completely redistribute to the stationary state stress distribution which is the same as the initial uniform stress distribution due to the mechanical loading. For the finite element computations, complete redistribution is assumed once the through thickness axial stress variation is within 1% of the mean stress. With an assumption of zero interaction between plastic and creep strains, the second and subsequent cycles will be identical to the first cycle with an equal increment of ratchet strain for each cycle. The accumulation of ratchet strains during the first ten

cycles for $\frac{P}{P_L} = 0.7$ is compared with the equivalent 'no creep' results in Figure 4.6. For this particular mean load, the 'complete redistribution' assumption provides the upper bound on ratchetting behaviour. The identical behaviour for all cycles under 'complete redistribution' leads to two important observations:-

1. for continued ratchetting it is not necessary for the whole section to suffer plastic deformation during a cycle (see Figure 4.4) as is the case under 'no creep' conditions;
2. if the first cycle produces any plastic deformation then the ratchetting process is continuous.

The second observation implies a shift in the ratchetting boundary to the elastic/plastic boundary. Ratchetting can only be avoided if the combination of mean axial load and cyclic thermal load leads to purely elastic behaviour.

Effect of mean load on ratchetting behaviour

The 'no creep' and 'complete redistribution' first cycle and steady state ratchet strains, for a range of axial loads 0 to $0.9 P_L$ are given in Table 4.2. As explained above, steady state 'complete redistribution' values are practically* the same as the first cycle 'no creep' values which are compared with the steady state 'no creep' values in Figure 4.7. It may be seen from Figure 4.7 that for values of $\frac{P}{P_L} < 0.72$ the creep in the dwell periods increases the steady state ratchet strain but above this value of $\frac{P}{P_L}$, the creep reduces the ratchet strains. This is because the complicated transient thermal loading conditions result in a residual stress distribution at the end of a thermal cycle which, for $\frac{P}{P_L} > 0.72$, is more favourable to ratchetting and leads to a larger ratchet strain in the subsequent cycle than

* within computational accuracy.

would be obtained with a uniform stress distribution resulting from complete stress redistribution. The residual equivalent stress distributions at the end of the first thermal cycle for various mean loads are shown in Figure 4.16; these do not provide any obvious explanation of the differences in behaviour for axial loads above and below $\frac{P}{P_L} = 0.72$.

Creep during the dwell periods

The normalised strains which accumulate during the dwell periods (ϵ^d) for the first 3 complete cycles for a mean load of $0.7 P_L$ are shown in Figure 4.17; the strains are plotted against time function Γ

$$\text{where } \Gamma = AE \sigma_{\text{nom}}^{n-1} t^m \quad 4.2$$

[A, n and m are constants in the creep law, σ_{nom} is the mean stress and t is the time]

The results are asymptotic to straight lines which all have the gradient of the 'virgin' creep curve at a constant stress equal to the mean stress. The exact gradient of these straight lines is therefore $\frac{P}{P_L}$.

$$\begin{aligned} \frac{d\left(\frac{\epsilon^d}{\epsilon_y}\right)}{d\Gamma} &= \frac{\text{'virgin' creep at } \sigma_{\text{nom}} \text{ in time } t \left[(A \sigma_{\text{nom}}^{n-1} t^m) / \epsilon_y \right]}{AE \sigma_{\text{nom}}^{n-1} t^m} \\ &= \frac{\sigma_{\text{nom}}}{\sigma_y} = \frac{P}{P_L} \quad 4.3 \end{aligned}$$

$\Delta \epsilon^d / \epsilon_y$ is the normalised increment of strain associated with stress redistribution and is equal for each dwell period since residual stress distributions at the start of each dwell period are the same. The variation in $\Delta \epsilon^d / \epsilon_y$ with mean load is

given in Table 4.3 and Figure 4.18. The values given are averages over 10 dwell periods. There appears to be very little variation in the increment with mean load and the absolute values are also very small. It should be noted that accurate predictions for $\Delta \epsilon^d / \epsilon_y$ are difficult both because of the small magnitude and because the predictions depend on an accurate determination of the steady state strain rate, $(\epsilon^d / \epsilon_y) / d\Gamma$, using a least squares fitting technique.

The variation in redistribution time with mean load is discussed in Section 4.2.4.2.2.

4.2.4.2.2 Linear hardening models

Ratchetting Mechanism

The mechanism is similar to that with an elastic-perfectly-plastic material as the stress redistributes to the initial uniform stress distribution during each dwell period. However, the increase in yield stress during a thermal shock results in a monotonic reduction in the ratchet strains produced by each successive thermal shock, including the first shock, with shakedown eventually occurring, as shown in Figure 4.19 for a mean load of $0.9 P_L$. The equivalent results for an elastic-perfectly-plastic material model are also included in the figure. From a comparison with the 'no creep' results in Figure 4.8, it may be seen that the 'no creep' condition leads to a greater accumulation of ratchet strain in the first ten cycles than the 'complete redistribution' condition for this particular mean load, particularly for low values of $\frac{E_P}{E}$. Although shakedown will eventually occur for a hardening material at all loading combinations, there can be a significant accumulation of ratchet strains.

Effects of mean load and E_p/E on ratchetting behaviour

The variation of normalised accumulated ratchet strains with mean load after the 1st, 2nd, 5th and 10th cycles are compared with the results for 'no creep' in Figures 4.9 to 4.12. At high mean loads the 'no creep' condition leads to a greater accumulation of ratchet strains, whereas the 'complete redistribution' condition provides the upper bound on ratchetting behaviour for smaller mean loads. The 'cross-over' value of $\frac{P}{P_L}$ may be seen to depend on both the number of cycles and on the hardening parameter, E_p/E . Considering the accumulation in 10 cycles, Figure 4.12, the cross-over value of $\frac{P}{P_L}$ increases from ~ 0.71 to ~ 0.90 for a change of $\frac{E_p}{E}$ from 0.01 to 0.1.

The variation of normalised accumulated ratchet strains in 10 cycles with mean load and $\frac{E_p}{E}$ may be seen in Figure 4.20. By comparison with the equivalent plot for the 'no creep' condition (Fig. 4.14) it may be seen that if the combination of mean load and $\frac{E_p}{E}$ results in an accumulation of more than twice the yield strain in 10 cycles then the 'no creep' condition is more severe, whereas if the accumulation of ratchet strains in 10 cycles is less than the yield strain, the complete redistribution case is more severe.

The total accumulated ratchet strains for $\frac{E_p}{E} = 0.05$ and 0.1 are compared with the equivalent results for 'no creep' in Figure 4.13. It is apparent that there is very little difference in total accumulated ratchet strains for the 'no creep' and 'complete redistribution' conditions. For small mean loads 'complete redistribution' leads to a significant increase in the number of cycles to achieve shakedown, but with only a small increase in the accumulation of ratchet strains. At higher mean loads, stress

redistribution has little effect on the total accumulation of ratchet strains or the number of cycles to shakedown.

Creep during the dwell periods

The normalised accumulated dwell period strain after the 1st, 5th and 10th dwell periods for the range of $\frac{E}{E_P}$ values (including elastic-perfectly-plastic) is shown in Figure 4.21 for a mean load of 0.9 of the limit load. It may be seen that the behaviour is practically independent of the degree of material hardening. The variation in time function for complete redistribution, Γ_R , with mean load and hardening assumption, including the elastic-perfectly-plastic results, is presented in Figure 4.22. As stated earlier, redistribution was assumed to be complete when the through thickness variations in stress were less than 1% of the mean stress. There is little variation in the time function for complete redistribution with $\frac{P}{P_L}$ and $\frac{E}{E_P}$. For $\frac{P}{P_L} = 0.3$ the creep strain rates are comparatively small and redistribution times are very large. It is considered reasonable to assume that the time function is independent of mean load and the degree of material hardening.

4.3 Analysis of the Whole Component

4.3.1 Finite element model

The 50 element, axisymmetric mesh used to model the flanged tube component is shown in Figure 4.23. Emphasis has been placed on adequate modelling of the fillet region while restricting the number of elements to 50. The right hand end of the mesh (flange centre plane) is constrained to have zero displacements in the axial direction. Axial loading is applied to the left hand end which has a constant axial displacement constraint. Axisymmetric, 8-noded, isoparametric elements are used. The justification for using this mesh is discussed in Appendix II. When surface stress or strain results are quoted, data has been obtained for the Gauss points nearest to the surface, shown in Figure 4.23

4.3.2 Data

The lead data given in Table 4.1 is used. An elastic-perfectly-plastic material assumption is used for investigating the ratcheting behaviour of the component. Where comparisons between finite element predictions and the experimental results of Yahiaoui (12) are made, more realistic multilinear representations of the lead alloy uniaxial stress-strain data, shown in Figure 4.24, are used. There is a significant difference in the stress-strain behaviour of the lead alloy at the extremes of the operating temperature range (i.e. 20°C and 76°C) and the bands of experimental data for both extremes are modelled. For these comparisons a Norton-Bailey Power Law for creep, with constants for the lead alloy obtained by Yahiaoui (12), is used,

$$\text{i.e. } \epsilon^c = 8.67 \times 10^{-58} \sigma^{7.36} t^{0.375} \quad (\sigma \text{ in N/m}^2, t \text{ in hours}) \quad 4.4$$

with a strain hardening assumption.

For a similar lead alloy, it has been shown that the von Mises yield criterion and Prandtl-Reuss flow rules are the most suitable of the common flow theories (41) and these theories have been used for this analysis.

4.3.3 Axial loading

4.3.3.1 Elastic stresses

The elastic stress distributions due to axial load along the shank outside surface and around the fillet are given in Figure 4.25 and along the bore surface are given in Figure 4.26. The values at the Gauss points nearest to these surfaces are plotted; the normal and shear stresses should be zero at the surface. For both surfaces the meridional stress is dominant and the highest stresses occur at the first Gauss point into the fillet. Extrapolating

fillet Gauss point stresses to the surface gives an elastic mechanical stress concentration factor of 1.53. Figure 4.27 shows the 'exaggerated' deformed shape for a mean axial load of $0.7 P_L$. The displacement scale is much greater than the dimension scale, hence the term 'exaggerated' deformed shape.

4.3.3.2 Elastic-plastic behaviour

The growth of the plastic zones with increasing axial load up to collapse for an elastic-perfectly-plastic material is shown in Figure 4.28. Yielding initiates in the fillet and this plastic zone grows in towards the shank. Yielding in the shank is not evident until very high loads are applied and the fully collapsed component still retains a large elastic region in the shank adjacent to the fillet. It would appear that the shank length is insufficient for fully uniform conditions to be reached. However the maximum stress variation of 1% is considered to be reasonable. The finite element predictions for elastic-plastic meridional strain distributions along the outside surface (based on the idealisation of stress-strain behaviour - Curve A in Figure 4.24) are compared with the experimental results of Yahiaoui (12) in Figure 4.29. Although there is good agreement at low mean load ($\frac{P}{P_L} = 0.72$), there is a significant difference at high mean loads ($\frac{P}{P_L} = 1.10$) when plastic strains are large. Other points of note from Figure 4.29 are:-

1. the finite element predictions indicate a shift in the point of maximum strain in the stress concentration with increasing load,
2. both finite element predictions and experimental results show the rate of increase of shank strain to be greater than those in the fillet so that for $\frac{P}{P_L} = 1.10$, shank strains exceed the peak values in the stress concentration.

4.3.3.3 Elastic-creep behaviour at constant axial load

The effects of creep on the meridional stress distribution along the outside and bore surfaces are shown in Figures 4.30 and 4.31 respectively. Creep has no effect on shank stress, whereas in the fillet region there is a considerable redistribution of stress and reduction in peak stress (Figures 4.30 and 4.31). Along the bore surface the transition between shank and flange stress is accentuated by creep and there is a reduction in the meridional stress in the region of the flange.

4.3.4 Thermal loading cycle

The thermal loading applied to the whole component is nominally identical to that used by Yahiaoui (12) in his experimental testing of the same component, and has been discussed in Section 4.2.3 for the analysis of the shank. The temperature files were created and edited in the same way as for those used in the shank analysis. The elastic thermal stresses during the first half of a thermal shock were computed in order to obtain a value for the thermal stress concentration factor in the fillet. Figure 4.32 shows the time variation of elastically calculated meridional thermal stresses along the shank outside surface and at the most severe point in the fillet. The thermal stress to yield stress ratios at Gauss points nearest to the surface in the shank and fillet are 0.5 and 0.83 respectively. Extrapolation of these peak conditions to the shank and fillet surfaces gives a thermal stress concentration factor of 1.81 in the fillet. Also peak fillet thermal stress occurs approximately 0.3 seconds after the peak has been reached in the shank.

4.3.5 Cyclic thermal loading with constant axial load

4.3.5.1 'No creep' condition

4.3.5.1.1 Elastic-perfectly-plastic material model

Ratchetting Mechanism

The regions of plastic growth during the first and second halves of the first thermal shock for $\frac{P}{P_L} = 0.7$ are shown in Figure 4.33. The first thermal shock produces an increment of ratchet strain in the shank and the maximum ratchet strain occurs at the 'peak fillet' position. There is an 'elastic core' throughout the component. After a few cycles a steady cyclic state is reached where each shock produces an equal amount of ratchet strain, both in the shank and at the 'peak fillet' position. The regions of additional plastic straining during the 10th thermal shock (i.e. steady cyclic state) are shown in Figure 4.34. Whereas the whole shank section suffers plastic deformation during the shock, the major portion of the flange remains elastic and there is a relatively small plastic zone adjacent to the bore. In the fillet region, strains are accumulated at a more rapid rate as can be seen in Figure 4.35, which shows the distribution of 10th shock meridional ratchet strains along the outside of the shank and around the fillet. Figure 4.36 shows the 'exaggerated deformed shape' at the end of this shock and the incremental deformation due to the 11th shock.

The largest strains occur in the fillet and the shank region adjacent to the fillet and result in considerable thinning of the section as well as axial strain. A small region of reverse plasticity is apparent from Figure 4.34 in the region of the bore surface. Reversed plasticity is defined by a change in the direction of plastic straining as illustrated in Figure 4.37 where components of plastic

strain are plotted in the π plane for point A in the reverse plasticity region (see Figure 4.34). The fourth thermal shock is shown in detail; there is an overall reduction in equivalent plastic strain during the first half of the thermal shock and an increase during the second half. Furthermore the directions of plastic straining during the first and second halves of the cycle are virtually opposite.

The accumulation of shank and peak fillet meridional ratchet strains during the first ten cycles for this mean load are shown in Figure 4.38. A steady cyclic state is reached in the fillet after ~ 6 cycles and from then on peak ratchet strain per cycle is constant, and greater than in the shank where the steady cyclic state is reached after the first cycle as discussed in Section 4.2.4.1.1.

Effect of mean load on ratchetting behaviour

Figure 4.39 shows the accumulation of shank and peak fillet meridional ratchet strains for a mean load of 0.5 of the limit load under which condition the steady state ratchet strains are zero in both the shank and fillet. The results for this loading condition, together with those for $\frac{P}{P_L} = 0.7$, are summarised in Table 4.4.

4.3.5.1.2 Comparison between experimental results and finite element predictions

Yahiaoui (12) has carried out experimental tests on flanged tube components with a range of axial loads and dwell periods between thermal shocks. In this section the results of 3 'rapid cycling' tests (i.e. ~ 15 minutes between shocks for steady state thermal conditions to be achieved) with negligible creep are compared with finite element predictions assuming a 'no creep' condition and using the material models given in Figure 4.24. Comparison between

the experimental results for tests with a significant dwell period and equivalent finite element predictions including creep are discussed in Section 4.3.5.3. The modelling of the thermal shocks has already been discussed in Sections 4.2.3 and 4.3.4.

The material models are based on uniaxial stress-strain data for the lead alloy at temperatures which are the extremes of the rig operating range, i.e. 20°C for the initial steady state condition prior to a thermal shock and 76°C at the intermediate steady state condition during the shock. This data is seen to fall into 2 discrete bands and the material is softer and resembles an elastic-perfectly-plastic material at the higher temperature.

Elastic-perfectly-plastic, isotropic and kinematic hardening models of the stress-strain data are used in the finite element computations. For the elastic-perfectly-plastic model a yield stress of 21.5 MN/m² is assumed based on the 0.2% proof stress of the material at 20°C and is seen to also be a reasonable model for the 76°C data (curve C, Figure 4.24). The isotropic and kinematic hardening models of the lower temperature data are curves A and B respectively in Figure 4.24. By definition, the kinematic hardening model is bilinear and is a reasonable model up to ~0.6% strain. The isotropic hardening model uses a three straight line representation of the data with a reduction in plastic modulus at 0.6% strain and is a reasonable 'fit' up to ~1.5% strain.

For the higher temperature data, curve D is used for both isotropic and kinematic hardening models and is a reasonable fit up to ~1.0% strain.

Finite element predictions of total strain and ratchet strain (in the shank and at the 'peak fillet' positions) and meridional strain distributions for $\frac{P}{P_L} = 0.5, 0.7$ and 0.8 are compared with

the experimental results in Figures 4.40 to 4.44.

The results are tabulated in Table 4.5. In Figures 4.40, 4.42 and 4.44 the two sets of experimental data are for diametrically opposed strain gauges, whereas average experimental results are given in Table 4.5 and Figures 4.41 and 4.43.

In all cases, the predictions with isotropic and kinematic hardening models of the same temperature data are very similar, as can be seen from Table 4.5. The predictions in Figures 4.40 to 4.44 are for the two extreme temperature kinematic hardening models. Inspection of the output indicated that there is no reverse plasticity with the kinematic hardening models and since strains are always less than 0.6% (i.e. the breakpoint between curve A for isotropic hardening and curve B for kinematic hardening) small discrepancies in the predictions are due to differences in the programming of the two models. Detailed comparisons of the experimental results and finite element predictions are given below. The implications of these results, in terms of modelling technique, are discussed in Chapter 8.

$P/P_T = 0.5$ (Figures 4.40 and 4.41)

The finite element predictions of ratchet strain are zero after a few cycles whereas the experimental results tend to a non-zero (albeit small) steady state value. Total strains are underestimated in all cases. In particular the first cycle ratchet strains, which dominate the total strains, are significantly underpredicted. Also the predictions with all models are very similar. From the strain distributions in Figure 4.41 it is seen that the ratio of peak fillet to mid shank total strains is approximately 2 after the 1st and 3rd shocks from both the experimental results and finite element predictions. After the 10th shock the experimental

value of the ratio has reduced to ~ 1.7 . From the finite element predictions, generally the distribution 'peaks' are at the first Gauss point into the fillet and the changes in strain in the fillet region are less severe than is apparent from the experimental results.

$$\frac{P}{P_L} = 0.7 \text{ (Figures 4.42 and 4.43)}$$

By comparing the experimental shank initial strain (0.075 - 0.11% in Figure 4.42) with the expected value from the uniaxial data (0.065% from Figure 4.24) it would appear that the tube material has a lower yield than the uniaxial data. Again the finite element predictions of ratchet strain and hence total strain are less than the experimental data. In the shank, the large first cycle experimental ratchet strain ($1281 \mu\epsilon$ from Table 4.5) is grossly underpredicted by the finite element models ($98 - 202 \mu\epsilon$ from Table 4.5) and the increase in ratchet strain between first and second cycles which is predicted by the hardening models is not apparent in the experimental results. The ratchet strain predictions at the 'peak fillet' position are generally closer to the experimental data than in the shank. The ratchet strain predictions with the hardening models must eventually reduce to zero, whereas the experimental ratchet strains appear to be tending towards a constant value which is almost an order of magnitude greater than the steady state ratchet strain predictions with the elastic-perfectly-plastic material model. For the experimental results in Figure 4.42 it can be seen that shank and peak fillet ratchet strains are very similar after ~ 4 cycles and this phenomenon is also predicted by the high plastic modulus kinematic hardening model (i.e. curve B). From the strain distributions in Figure 4.43

the 'peak fillet' strain prediction is again at the first Gauss point into the fillet and experimental strain distributions are more severe than the predicted results. The finite element results fail to predict the large reduction in shank ratchet strains adjacent to the fillet. The ratio peak fillet to mid shank total strain is overpredicted and, whereas the hardening models correctly predict a reduction in this ratio with successive cycles, the opposite effect is apparent with the elastic-perfectly-plastic model.

$P/P_L = 0.8$ (Figure 4.44)

The comparisons in Figure 4.44 are for the shank only since it was found that the fillet strain gauge readings were inaccurate due to unbonding of the gauges from the surface of the specimen. Differences between experimental results and the predictions are dominated by the large underprediction of the first cycle ratchet strain. The ratchet strain predictions with the kinematic hardening model using Curve D in Figure 4.24 are reasonably accurate for the 2nd to 4th cycles analysed. The experimental steady state ratchet strain of $\sim 0.05\%$ is well predicted by the elastic-perfectly-plastic model.

4.3.5.2 Complete Redistribution (Elastic-perfectly-plastic material model)

Ratchetting Mechanism

The regions of plastic straining during the first and second halves of the first thermal shock for $\frac{P}{P_L} = 0.7$ are the same as for the 'no creep' case shown in Figure 4.33.

Figure 4.45 illustrates a steady state cycle for the whole component, with a mean load of $0.7 P_L$, by showing the regions of additional plastic straining

during the 10th thermal shock, and may be compared with Figure 4.34 for the 'no creep' condition. Yielding commences in the bore region and is accompanied by a plastic zone initiating from the fillet which spreads into the shank during the first half of the cycle. There is no further yielding in the fillet during the second half of the thermal shock, where a plastic zone initiating in the bore spreads radially outwards before contracting to zero. A local region of reverse plasticity (see Section 4.3.5.1.1) is apparent in the bore. By comparison of Figures 4.34 and 4.45, the second half of the thermal shock has a similar effect for both 'no creep' and 'complete redistribution' cases, whereas the plastic zone growth during the first half of the thermal shock varies significantly between the two cases. The initial non-uniform residual strain field for 'no creep' case (for example see Figure 4.16) peaks around the mid-radius and 'compressive' yielding in the bore is accompanied by a 'tensile' yield zone in the 'core' and there is no initial yielding in the fillet. The initial stationary state stress distribution for 'complete redistribution' is less severe, particularly in the shank, and the yield zone initiates in the fillet in preference to the 'core'. There is a marked similarity between the overall region of plastic growth for the 'no creep' and 'complete redistribution' conditions.

The distribution of 10th shock meridional ratchet strains along the outside surface is shown in Figure 4.35. The peak fillet ratchet strains are larger than those in the shank and 'complete redistribution' leads to larger shank and fillet ratchet strains than are accumulated under 'no creep' conditions (Figure 4.38).

Figure 4.46 shows the 'exaggerated' deformed shape at the end

of the 10th dwell period and the incremental deformation during the 11th shock and dwell period.

Although there is a definite section thinning during the thermal shock (Figure 4.46(b)) the displacements are dominated by the dwell period behaviour and after 10 cycles there is little evidence of thinning in the total deformation (Figure 4.46(a)). Figures 4.36(b) and 4.46(b) give a direct comparison of ratchet deformation, allowing for the difference in displacement scales.

The accumulation of shank and peak fillet meridional ratchet strains during the first ten cycles for this mean load are shown in Figure 4.38. The constant ratchet strain per cycle in the shank has already been discussed. In the fillet, the ratchet strains in the second and subsequent cycles are the same and less than the first cycle ratchet strain because the stationary state stress distribution, after creep, at the start of the second and subsequent cycles is less favourable to ratchetting than the initial distribution due to axial loading at the start of the first cycle. Complete redistribution leads to greater accumulations of ratchet strains in the shank and fillet than for the 'no creep' condition.

Since both shank and fillet ratchet strains are constant after the first cycle, the ratchet strain distribution shown in Figure 4.35 is the steady state behaviour.

Effect of mean load on ratchetting behaviour

Figure 4.39 shows the accumulation of shank and peak fillet ratchet strains for a mean load of $0.5 P_L$ and again peak fillet steady state ratchet strains are apparent after the first cycle. For 'no creep', this combination of steady mechanical and cyclic thermal loading results in shakedown both in the shank and at the peak fillet position, however the ratchetting process is

continuous if complete redistribution occurs during the dwell periods. For the peak fillet position, if any plastic growth occurs during the second cycle then the ratchetting process is continuous. The results for this loading combination, together with $\frac{P}{P_L} = 0.7$, are summarised in Table 4.4.

Creep during the dwell periods

The strains which accumulate during the first dwell period in the shank and the 'peak ratchet strain' position, ϵ^d , are shown in Figure 4.47 for a mean load of 0.7 of the limit load. The behaviour in the fillet is similar to that for the shank already discussed in Section 4.2.4.2.1; that is the accumulation of dwell period strain is asymptotic to a straight line and with an increment of normalised strain, $(\Delta\epsilon^d/\epsilon_y)_{\text{fillet}}$, associated with the redistribution of stress. In the second and subsequent dwell periods, the strains are asymptotic to lines of the same gradient as for the first cycle with an equal increment of strain due to redistribution which is less than that for the first cycle. The peak fillet results together with the equivalent shank results from Table 4.3, for this mean load and $\frac{P}{P_L} = 0.5$ are given in Table 4.6. The gradient of the asymptotic line, $d(\epsilon^d/\epsilon_y)/d\Gamma$, is further normalised with respect to the mean load, $\frac{P}{P_L}$.

For all cases, the increment of strain due to redistribution is relatively small ($< 0.250 \times$ yield strain), and the normalised gradient, $\frac{d(\epsilon^d/\epsilon_y)/d\Gamma}{P/P_L}$, is independent of mean load.

4.3.5.3 Partial redistribution - comparison with experimental results

In addition to the comparisons between the experimental results for 'rapid cycling' and the finite element predictions assuming a 'no creep' condition discussed in Section 4.3.5.1.2, the results

of 2 tests with significant dwell periods between thermal shocks are compared with finite element predictions which include the effects of creep between shocks. The lead alloy material models described in Section 4.3.5.1.2 and shown in Figure 4.24 have been used together with the lead alloy material creep law from Table 4.1.

Figures 4.48 to 4.51 compare the experimental results and finite element predictions of total strain, ratchet strain and accumulated dwell period strain (in the shank and at the 'peak fillet' position) and meridional strain distributions for $\frac{P}{P_L} = 0.7$ with 24 hour and 120 hour dwell periods between thermal shocks. The results are tabulated in Table 4.7. The two sets of experimental total, ratchet and dwell period strains are for diametrically opposed strain gauges. Experimental strain distributions and the experimental data in Table 4.7 are average strain gauge results. The finite element predictions in Figures 4.48 to 4.51 are for the elastic-perfectly-plastic and two kinematic hardening models. Table 4.7 shows that the differences in predicted strains for the respective kinematic and isotropic hardening models are relatively small (see Section 4.3.5.1.2).

$\frac{P}{P_L} = 0.7$, 24 hour dwell period (Figures 4.48 and 4.49)

The predictions of total accumulated strains are in good agreement with the experimental results in the shank and at the 'peak fillet' positions; similarly the strain distributions. In particular, over the 8-10 cycles analysed, the predictions with curve D are in excellent agreement with the experimental data. For all models the dwell period strains are over-predicted, particularly during the first few (~ 3) dwell periods. In the shank this is

counterbalanced to a degree by the underprediction of ratchet strains. Ratchet strain predictions at the 'peak fillet' position are generally more accurate than in the shank. In the shank and at the 'peak fillet' position the experimental ratchet and dwell period strains approach a steady value after approximately 8-12 cycles.

$P/P_L = 0.7$, 120 hour dwell period (Figures 4.50 and 4.51)

Again, the finite element predictions of total strain are in good agreement with the experimental data, particularly for the kinematic (and isotropic) hardening model based on Curve D in Figure 4.24. Both the experimental values and finite element predictions of ratchet strain in the shank and at the 'peak fillet' position are very similar to those with the 24 hour dwell period between cycles (see Table 4.7) which implies an approach to 'complete redistribution' conditions between cycles.

In the shank the accuracy of the total strain predictions results from a balance of the underprediction of ratchet strains with the overprediction of dwell period strains. At the 'peak fillet' position the ratchet and dwell period strain predictions are in good agreement with the experimental data. Overall, the finite element predictions of dwell period strain accumulation are more accurate than the predictions with a 24 hour dwell period.

The finite element predictions of first cycle ratchet strain with zero and 120 hour initial dwell periods are compared with the average experimental results in Table 4.8. In the shank the initial 120 hour dwell period computation has no effect on the ratchet strain predictions as would be expected with a zero plasticity creep interaction model. However there is a marked reduction in the

equivalent experimental values. At the peak fillet position, the differences between finite element predictions with zero and 120 hour dwell periods is due to the stress redistribution during the initial dwell. The equivalent experimental 'peak fillet' results show a larger reduction due to the effect of the initial dwell period.

The results given in Table 4.8 are used in the discussion of plasticity-creep interaction modelling in Chapter 8.

Parameter	Value	Units
Young's Modulus	23.2×10^9	N/m ²
Yield stress*	21.5×10^6	N/m ²
Coefficient of expansion	28.84×10^{-6}	°C ⁻¹
Poisson's Ratio	0.44	-
Thermal conductivity	35.1	W/mK
Surface heat transfer coefficient	25.1×10^3	W/m ² K
Specific heat/unit volume	1.43×10^6	J/m ³ K
Creep Law Constants	A	-
	n	7.3
	m	0.375

* 0.2% proof stress

Table 4.1 Flanged tube material data

Normalised ratchet strain per cycle				
$\frac{P}{P_L}$	'No creep'		'Complete redistribution'	
	1st cycle	Steady state	1st cycle	Steady state
0	0	0	0	0
0.3	0.034	0	0.034	0.034
0.5	0.048	0	0.048	0.044
0.6	0.067	0	0.067	0.065
0.7	0.107	0.060	0.107	0.109
0.75	0.193	0.232	0.193	0.194
0.8	0.310	0.481	0.310	0.310
0.9	0.883	1.356	0.883	0.894

Table 4.2 Flanged tube shank ratchetting behaviour,
Elastic-perfectly-plastic material.

$\frac{P}{P_L}$	$\frac{\Delta \epsilon^d}{\epsilon_y}$
0.3	0.129
0.5	0.110
0.6	0.137
0.7	0.132
0.75	0.163
0.9	0.144

Table 4.3 Flanged Tube Shank - Variation of $\Delta \epsilon^d / \epsilon_y$ with mean load for an elastic-perfectly-plastic material assumption.

		Normalised ratchet strain per cycle			
		'No creep'		'Complete redistribution'	
		1st cycle	Steady state	1st cycle	Steady state
$\frac{P}{P_L}$	Position				
0.5	Shank	0.048	0	0.048	0.044
	Fillet	0.361	0	0.361	0.275
0.7	Shank	0.107	0.060	0.107	0.109
	Fillet	0.852	0.128	0.852	0.608

Table 4.4 Flanged Tube Ratchetting behaviour with an Elastic-Perfectly-Plastic material model.

PULLOUTS

P/P _L	Dwell period (hrs)	Cycle Number	Total Strain (μe)					Ratchet Strain (μe)					Dwell period strain (μe)				
			Average Experimental	Elastic-perfectly-plastic Curve C	Isotropic hardening Curve A	Kinematic hardening Curve B	Isotropic hardening Curve D	Kinematic hardening Curve D	Average Experimental	Elastic-perfectly-plastic Curve C	Isotropic hardening Curve A	Kinematic hardening Curve B	Isotropic hardening Curve D	Kinematic hardening Curve D	Average Experimental	Finite Element	
0.5	0	Init.	430	466	466	466	466	466	320	-	-	-	-	-	-	-	-
		1	750	510	504	521	525	529	210	44	38	55	59	63	0	0	0
		2	950	519	516	530	532	534	130	9	12	9	7	5	-10	0	0
		3	1069	528	520	532	533	536	97	9	4	2	1	2	-11	0	0
		4	1151	535	520	532	533	541	90	7	0	0	0	5	-15	0	0
		5	1217	535	520	532	536	541	77	0	0	0	-1	0	-25	0	0
		6	1273	535	520	532	535	541	72	0	0	0	0	0	-18	0	0
		7	1327	535	520	532	535	541	68	0	0	0	0	0	-14	0	0
		8	1381	535	520	532	535	541	61	0	0	0	0	0	-19	0	0
		9	1423	535	520	532	535	541	61	0	0	0	0	0	-20	0	0
10	1464	535	520	532	535	541	61	0	0	0	0	0	-	-	0		
0.7	0	Init.	934	653	652	652	652	652	-	-	-	-	-	-	-	-	-
		1	2215	751	840	844	854	855	1281	98	187	192	201	202	0	0	0
		2	3099	803	1082	1092	1154	1149	773	52	242	248	300	294	111	0	0
		3	3756	861	1270	1284	1432	1418	603	58	188	192	278	265	54	0	0
		4	4328	921	1421	1440	1688	1664	536	60	151	156	256	246	36	0	0
		5	4834	973	1542	1565	1925	1889	487	52	121	125	237	225	19	0	0
		6	5285	1033	1641	1672	2143	2097	423	60	99	107	218	208	28	0	0
		7	5697	1089	1724	1760	2350	2290	401	56	83	88	207	193	11	0	0
		8	6086	1142	1798	1838	2540	2470	376	53	74	78	190	180	13	0	0
		9	6453	1193	1857	1904	2721	2637	355	51	59	66	181	167	12	0	0
10	6806	1245	1907	1958	-	-	344	52	50	54	-	-	9	0	0		
0.8	0	Init.	1032	744	744	744	746	746	-	-	-	-	-	-	-	-	-
		1	2996	1029	1233	1237	1260	1260	1965	285	489	498	514	514	0	0	0
		2	4164	1495	1886	1873	2060	2060	1032	466	653	636	800	800	136	0	0
		3	5451	1955	2375	2345	2779	2779	846	460	489	472	719	719	150	0	0
		4	6257	2409	2639	2715	3432	3432	721	454	264	370	653	653	85	0	0
		5	7056	2860	3056	3007	748	748	748	451	417	292	292	292	51	0	0
		6	7754	3307	3304	3241	633	633	633	447	248	234	234	234	65	0	0
		7	8398	3754	3504	3426	597	597	597	447	200	185	185	185	47	0	0
		8	8998	4203	3669	3582	554	554	554	449	165	156	156	156	46	0	0
		9	9571	4649	3808	3710	537	537	537	446	139	128	128	128	32	0	0
10	10125	5090	3878	-	520	520	520	441	70	-	-	-	34	0	0		

Table 4.5(a) Flanged Tube. Comparisons between experimental 'rapid cycling' results and finite element predictions assuming 'no creep' conditions. Shank results.

P/P _L	Dwell period (hrs)	Cycle Number	Total Strain (μϵ)					Ratchet Strain (μϵ)					Dwell period strain (μϵ)			
			Average Experimental	Elastic-perfectly-plastic Curve C	Isotropic hardening Curve A	Kinematic hardening Curve B	Isotropic hardening Curve D	Kinematic hardening Curve D	Average Experimental	Elastic-perfectly-plastic Curve C	Isotropic hardening Curve A	Kinematic hardening Curve B	Isotropic hardening Curve D	Kinematic hardening Curve D	Average Experimental	Finite Element
0.5	0	Init.	693	552	552	552	552	552	-	-	-	-	-	-	-	-
		1	1490	887	926	923	1006	1006	797	335	374	371	454	454	0	0
		2	1784	943	999	981	1095	1089	298	56	73	58	89	83	- 4	0
		3	1936	968	1051	997	1116	1110	161	25	52	16	21	21	- 9	0
		4	2040	969	1070	1000	1129	1116	115	1	19	3	13	6	-11	0
		5	2122	969	1075	1000	1150	1138	106	0	5	0	0	22	-24	0
		6	2195	969	1075	1000	1148	1139	92	0	0	0	- 2	1	-19	0
		7	2258	969	1075	1000	1148	1139	83	0	0	0	0	0	-20	0
		8	2317	969	1075	1000	1148	1139	80	0	0	0	0	0	-22	0
		9	2373	969	1075	1000	1148	1139	70	0	0	0	0	0	-14	0
		10	2416	969	1075	1000	1148	1139	64	0	0	0	0	0	-21	0
0.7	0	Init.	1265	773	773	773	773	773	-	-	-	-	-	-	-	-
		1	2767	1563	1681	1677	1810	1812	1502	790	908	904	1037	1039	0	0
		2	3822	1898	2154	2138	2490	2476	1002	335	473	461	680	664	53	0
		3	4517	2129	2429	2403	2981	2949	687	231	275	265	491	473	8	0
		4	5080	2299	2609	2577	3369	3311	558	170	180	174	388	362	5	0
		5	5578	2447	2751	2710	3723	3643	500	148	142	133	354	332	- 2	0
		6	6007	2575	2858	2812	4043	3938	437	128	107	102	320	295	- 8	0
		7	6399	2695	2947	2896	4319	4189	401	120	89	84	276	261	- 9	0
		8	6763	2814	3020	2961	4587	4425	372	119	73	65	268	236	- 8	0
		9	7096	2932	3080	3008	4837	4641	347	118	60	47	250	216	-14	0
		10	7420	3048	3132	3051	-	-	329	116	52	43	-	-	- 5	0

Table 4.5(b) Flanged Tube. Comparisons between experimental 'rapid cycling' results and finite element predictions assuming 'no creep' conditions. Peak fillet results.

$\frac{P}{P_L}$	Position	$\frac{d(\epsilon^d/\epsilon_y)}{d\Gamma}$	$\frac{d(\epsilon^d/\epsilon_y)/d\Gamma}{P/P_L}$	$\Delta\epsilon^d/\epsilon_y$	
				1st cycle	Steady state
0.5	Shank	0.527	1.054	0.110	0.110
	Peak Fillet	0.350	0.701	0.250	0.176
0.7	Shank	0.742	1.060	0.132	0.132
	Peak Fillet	0.521	0.743	0.150	0.088

Table 4.6 Flanged Tube. Dwell period behaviour.

P/P _L	Dwell period (hrs)	Cycle Number	Total Strain (μe)						Ratchet Strain (μe)						Dwell Period Strain (μe)						
			Average Experimental	Elastic-perfectly-plastic Curve C	Isotropic hardening Curve A	Kinematic hardening Curve B	Isotropic hardening Curve D	Kinematic hardening Curve D	Average Experimental	Elastic-perfectly-plastic Curve C	Isotropic hardening Curve A	Kinematic hardening Curve D	Isotropic hardening Curve D	Kinematic hardening Curve D	Average Experimental	Elastic-perfectly-plastic Curve C	Isotropic hardening Curve A	Kinematic hardening Curve B	Isotropic hardening Curve D	Kinematic hardening Curve D	
0.7	24	Init.	987	773	773	773	X	773	-	-	-	-	-	-	166	-	-	-	-	-	
		1	2346	1680	1809	1812		1937	1135	695	824	827	952	166	212	212	212	212	212	211	
		2	3039	2260	2484	2452		2791	649	470	559	524	731	37	110	116	116	116	116	122	
		3	3511	2659	2903	2843		3401	444	332	358	325	534	42	67	61	66	66	66	76	
		4	3941	2966	3222	3140		3922	408	256	276	249	468	18	51	43	48	48	48	53	
		5	4361	3243	3473	3371		4370	402	235	217	193	404	25	42	34	38	38	38	44	
		6	4718	3496	3670	3550		4747	345	216	168	147	339	13	37	29	32	32	32	38	
		7	4992	3716	3842	3707		5102	268	188	148	130	321	12	32	24	27	27	27	34	
		8	5268	3933	3991	3834		5424	274	188	128	104	292	7	29	21	23	23	23	30	
		9	5538	4145	-	-		5704	273	186	-	-	252	4	26	-	26	-	-	-	28
		10	5790	4334	-	-		5976	256	165	-	-	246	4	24	-	24	-	-	-	26
0.7	120	Init.	944	773	773	773	773	-	-	-	-	-	-	-	-	-	-	-	-	-	
		1	2321	1788	1923	1924	2043	1012	674	809	810	929	364	341	341	341	341	341	341	341	
		2	3086	2482	2688	2659	3008	623	526	581	549	770	142	168	184	186	186	186	195		
		3	3620	2987	3194	3137	3718	435	402	409	373	598	99	103	97	105	105	112	116		
		4	4057	3390	3558	3485	4330	354	322	290	269	529	83	81	74	79	79	83	87		
		5	4473	3759	3854	3766	4867	372	309	246	212	463	44	60	50	69	69	74	72		
		6	4830	4092	4102	3998	5326	307	280	205	182	395	50	53	43	50	50	64	68		
		7	5133	4380	4303	4188	5754	267	240	164	147	372	36	48	37	43	43	56	61		
		8	5409	4668	4485	4353	6011	254	244	151	127	354	21	44	31	38	38	42	56		
		9	5703	4940	4642	4499	-	265	232	129	113	-	29	40	28	33	33	-	-		
		10	5943	-	-	-	-	218	-	-	-	-	22	-	-	-	-	-	-	-	

Table 4.7(b) Flanged Tube. Comparisons between experimental results and finite element predictions for cycling with 24 hour and 120 hour dwell periods. Peak fillet results.

P/P _L	Dwell period (hrs)	Cycle Number	Total Strain (μe)						Ratchet Strain (μe)						Dwell Period Strain (μe)						
			Average Experimental	Elastic-perfectly-plastic Curve C	Isotropic hardening Curve A	Kinematic hardening Curve B	Isotropic hardening Curve D	Kinematic hardening Curve D	Average Experimental	Elastic-perfectly-plastic Curve C	Isotropic hardening Curve A	Kinematic hardening Curve D	Isotropic hardening Curve D	Kinematic hardening Curve D	Average Experimental	Elastic-perfectly-plastic Curve C	Isotropic hardening Curve A	Kinematic hardening Curve B	Isotropic hardening Curve D	Kinematic hardening Curve D	
0.7	24	Init.	987	773	773	773	X	773	-	-	-	-	-	-	166	-	-	-	-	-	
		1	2346	1680	1809	1812		1937	1135	695	824	827	952	166	212	212	212	212	212	211	
		2	3039	2260	2484	2452		2791	649	470	559	524	731	37	110	116	116	116	116	122	
		3	3511	2659	2903	2843		3401	444	332	358	325	534	42	67	61	66	66	66	76	
		4	3941	2966	3222	3140		3922	408	256	276	249	468	18	51	43	48	48	48	53	
		5	4361	3243	3473	3371		4370	402	235	217	193	404	25	42	34	38	38	38	44	
		6	4718	3496	3670	3550		4747	345	216	168	147	339	13	37	29	32	32	32	38	
		7	4992	3716	3842	3707		5102	268	188	148	130	321	12	32	24	27	27	27	34	
		8	5268	3933	3991	3834		5424	274	188	128	104	292	7	29	21	23	23	23	30	
		9	5538	4145	-	-		5704	273	186	-	-	252	4	26	-	-	-	-	-	28
		10	5790	4334	-	-		5976	256	165	-	-	246	4	24	-	-	-	-	-	26
0.7	120	Init.	944	773	773	773	773	773	-	-	-	-	-	-	364	-	-	-	-	-	
		1	2321	1788	1923	1924	2043	1012	674	809	810	929	929	364	341	341	341	341	341	341	
		2	3086	2482	2688	2659	3008	623	526	581	549	770	760	142	168	184	186	195	195	195	
		3	3620	2987	3194	3137	3718	435	402	409	373	598	577	99	103	97	105	112	116	116	
		4	4057	3390	3558	3485	4330	354	322	290	269	529	505	83	81	74	79	83	87		
		5	4473	3759	3854	3766	4867	372	309	246	212	463	443	44	60	50	69	74	72		
		6	4830	4092	4102	3998	5326	307	280	205	182	395	366	50	53	43	50	64	68		
		7	5133	4380	4303	4188	5754	267	240	164	147	372	346	36	48	37	43	56	61		
		8	5409	4668	4485	4353	6011	254	244	151	127	354	316	21	44	31	38	42	56		
		9	5703	4940	4642	4499	-	265	232	129	113	-	-	29	40	28	33	-	-		
		10	5943	-	-	-	-	218	-	-	-	-	-	22	-	-	-	-	-		

Table 4.7(b) Flanged Tube. Comparisons between experimental results and finite element predictions for cycling with 24 hour and 120 hour dwell periods. Peak fillet results.

	Dwell Period (Hrs)	First cycle ratchet strain (%)	
		Average Experimental	Finite Element*
Shank	0	0.13	0.01 - 0.02
	120	0.05	0.01 - 0.02
Peak Fillet	0	0.15	0.08 - 0.10
	120	0.10	0.07 - 0.09

* range of values for the 5 material models

Table 4.8 Flanged Tube. Comparison between finite element predictions and experimental results. Effect of initial dwell period on 1st cycle ratchet strains.

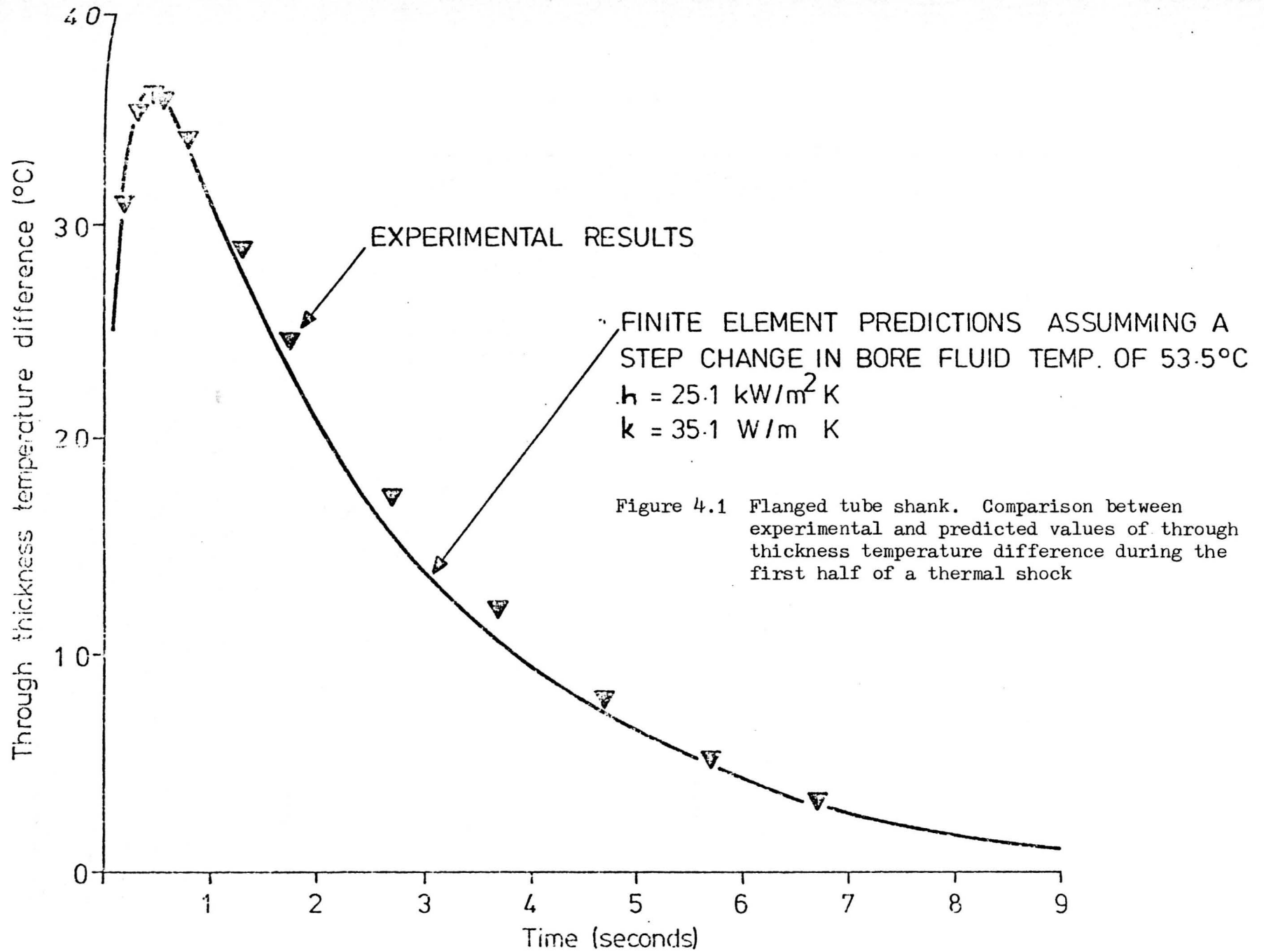


Figure 4.1 Flanged tube shank. Comparison between experimental and predicted values of through thickness temperature difference during the first half of a thermal shock

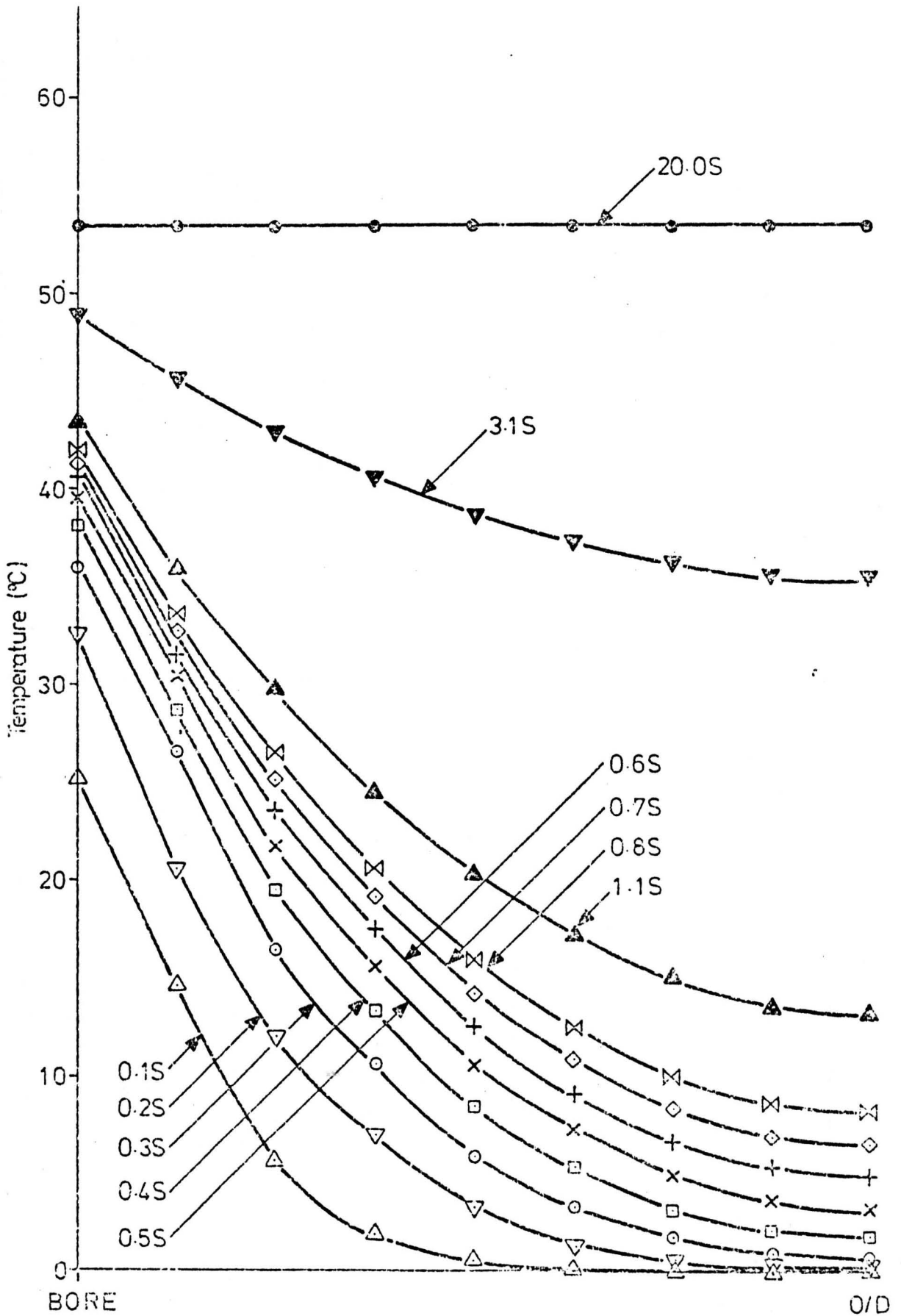


Figure 4.2 Flanged tube shank. Through-thickness temperature distributions during the first half of a thermal shock

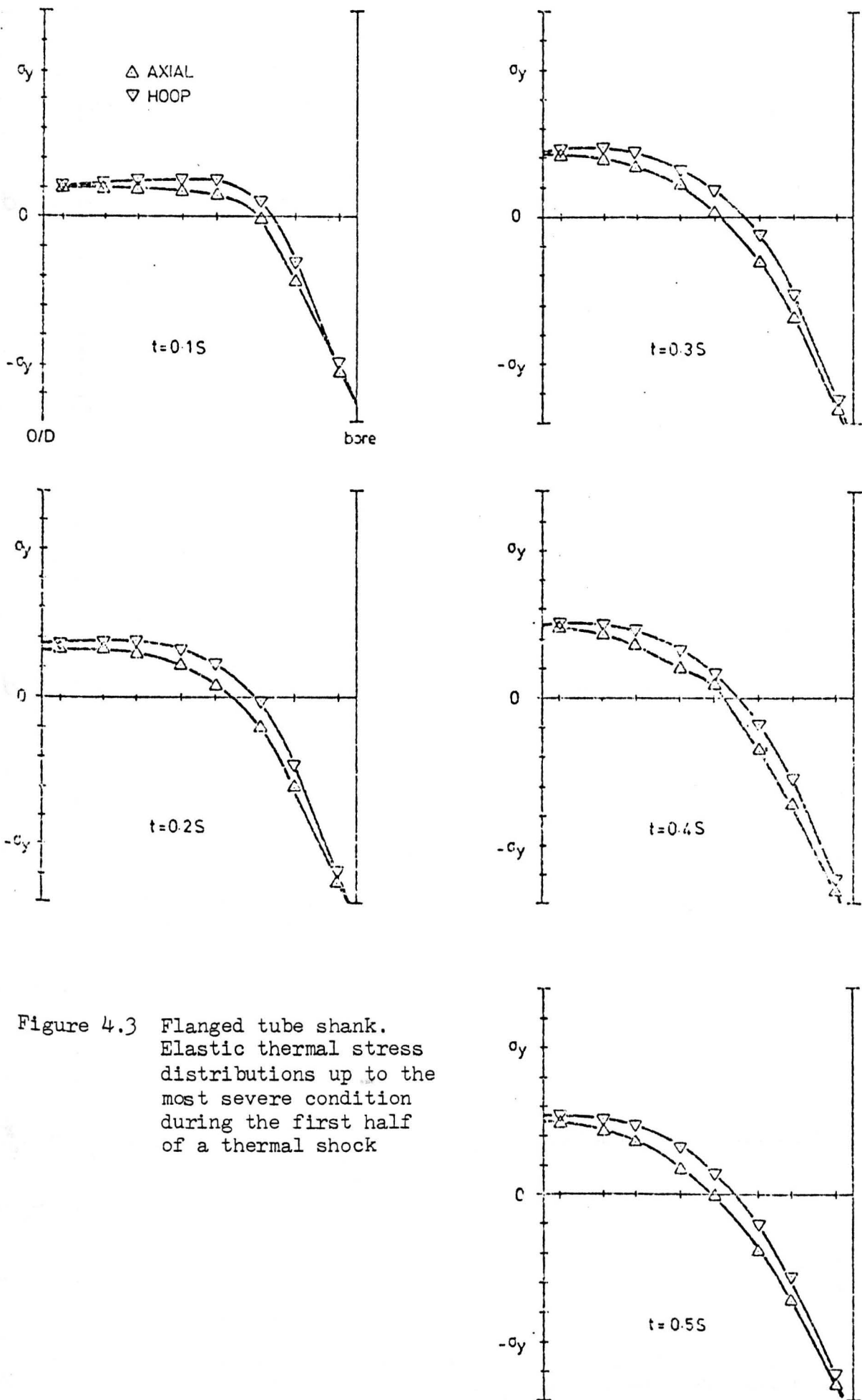
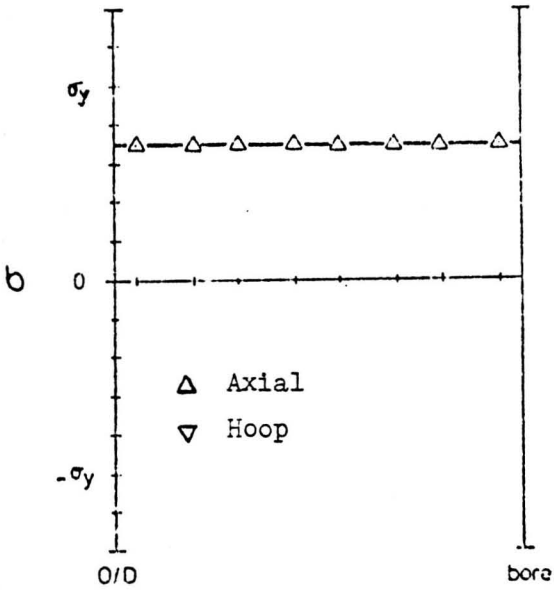
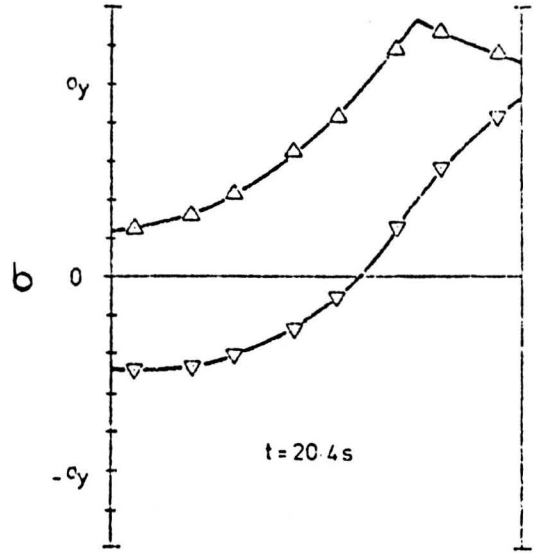


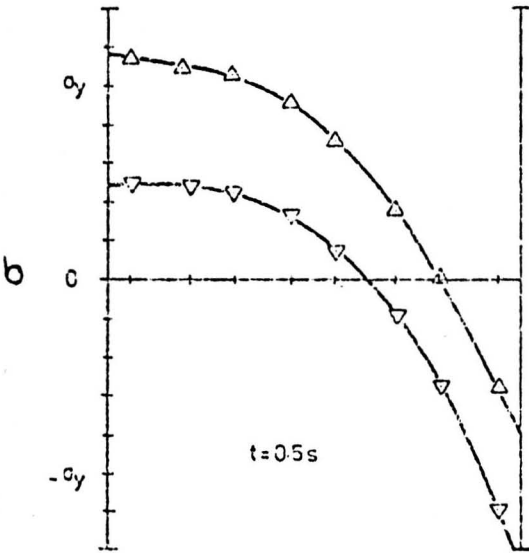
Figure 4.3 Flanged tube shank. Elastic thermal stress distributions up to the most severe condition during the first half of a thermal shock



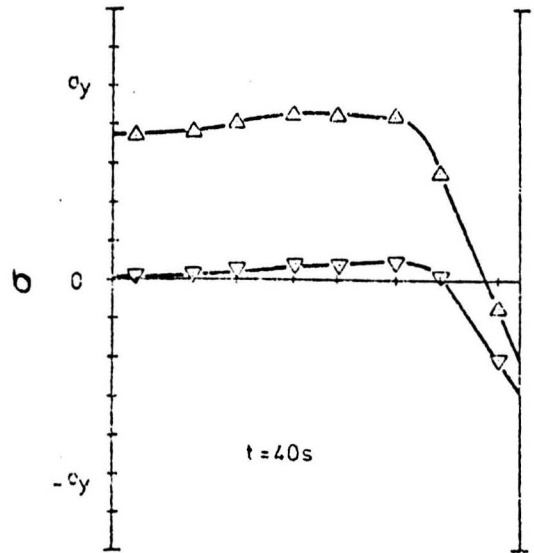
a) initial loading



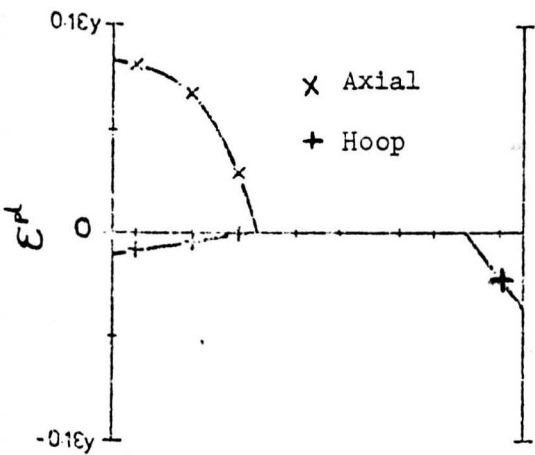
d) most severe conditions during second half of shock



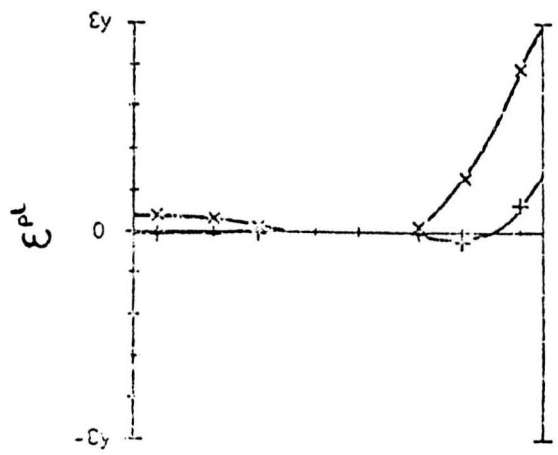
b) most severe conditions during first half of shock



e) end of shock



c) end of first half of shock



f) end of shock

Figure 4.4 Flanged tube shank (elastic-perfectly-plastic, $\sigma_t/\sigma_y = 1.94$, $P/P_L = 0.7$, 'no creep' conditions). Stress distributions due to initial loading and during the first thermal shock together with accumulated plastic strain distributions at the end of the first half and at the end of the first thermal shock.

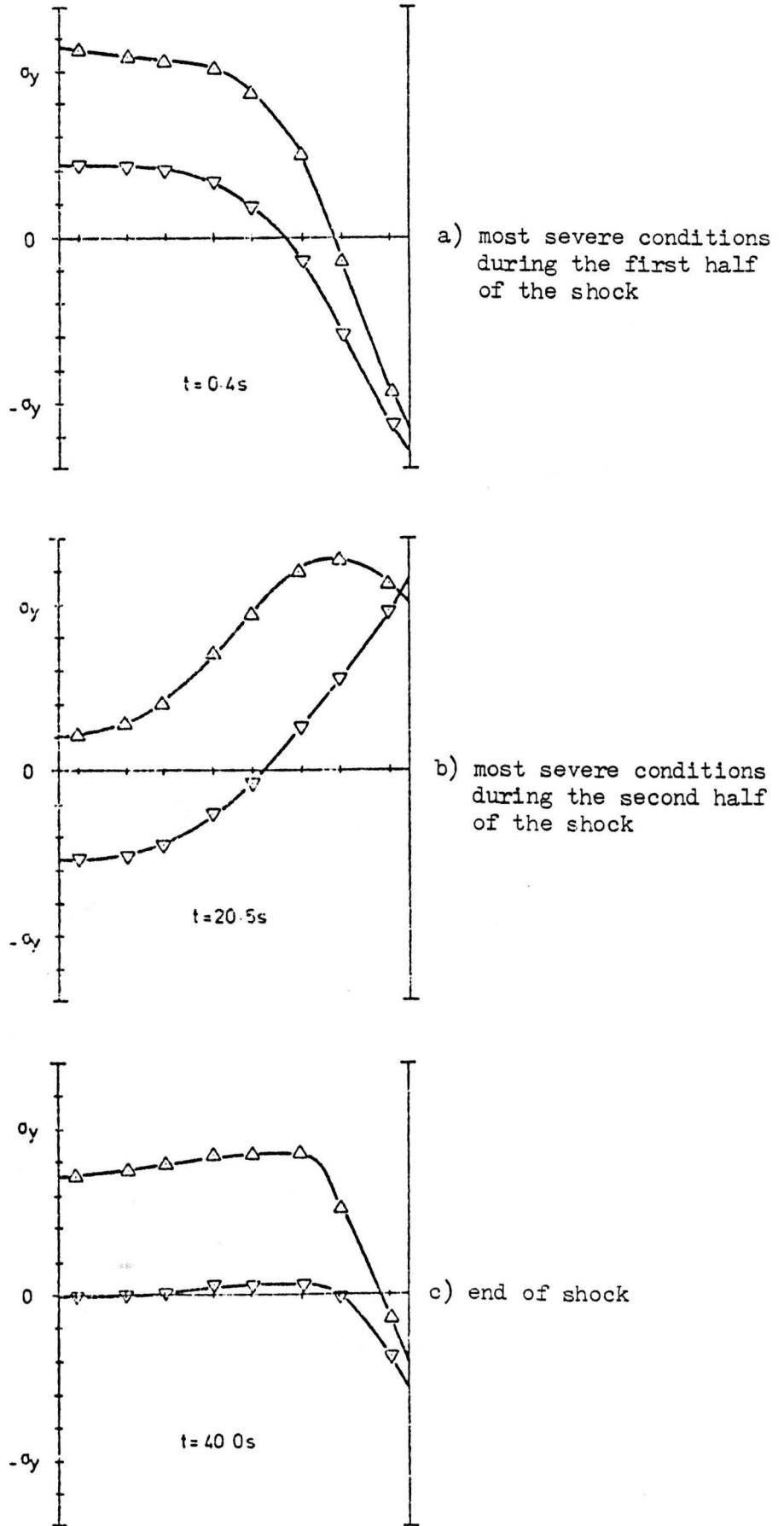


Figure 4.5 Flanged tube shank (elastic-perfectly-plastic, $\sigma_t/\sigma_y = 1.94$, $P/P_L = 0.7$, 'no creep' conditions). Stress distributions during the second and subsequent thermal shocks

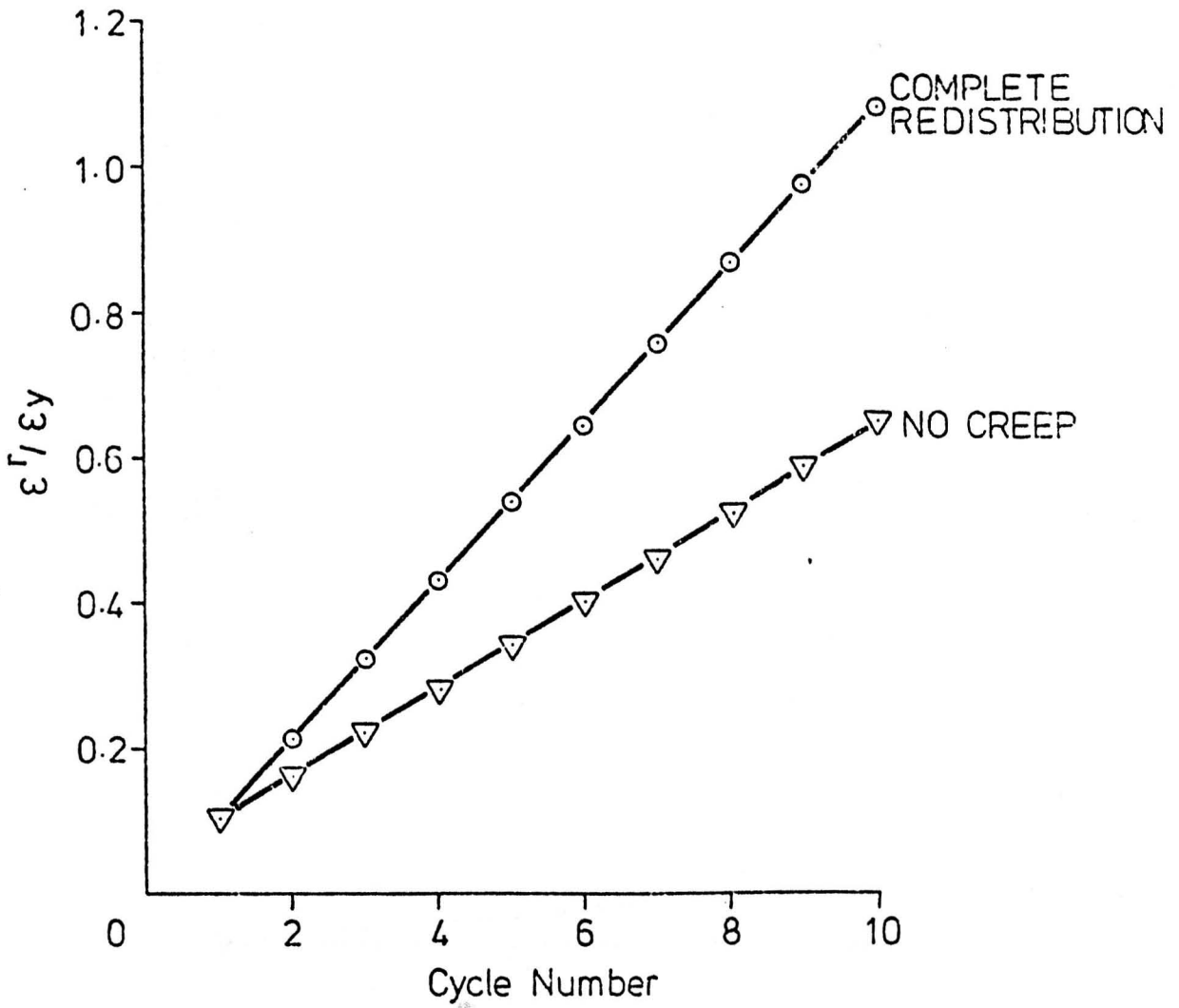


Figure 4.6 Flanged tube shank (elastic-perfectly-plastic, $\sigma_t / \sigma_y = 1.94$, $P/P_L = 0.7$). Accumulation of normalised ratchet strain during the first 10 cycles.

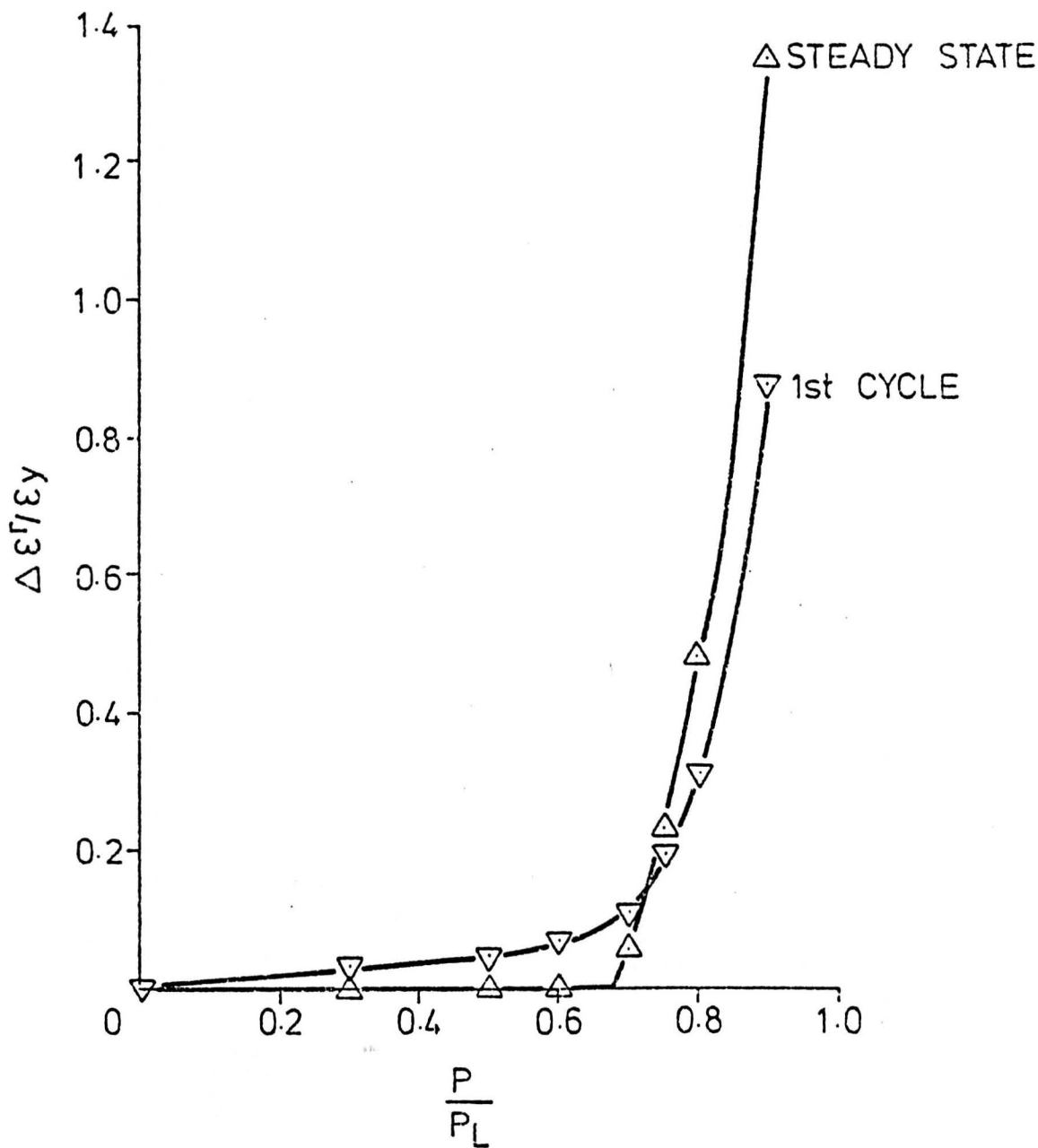


Figure 4.7 Flanged tube shank (elastic-perfectly-plastic, $\sigma_t / \sigma_y = 1.94$, 'no creep' conditions). Variation of normalised first cycle and steady state ratchet strains with mean load.

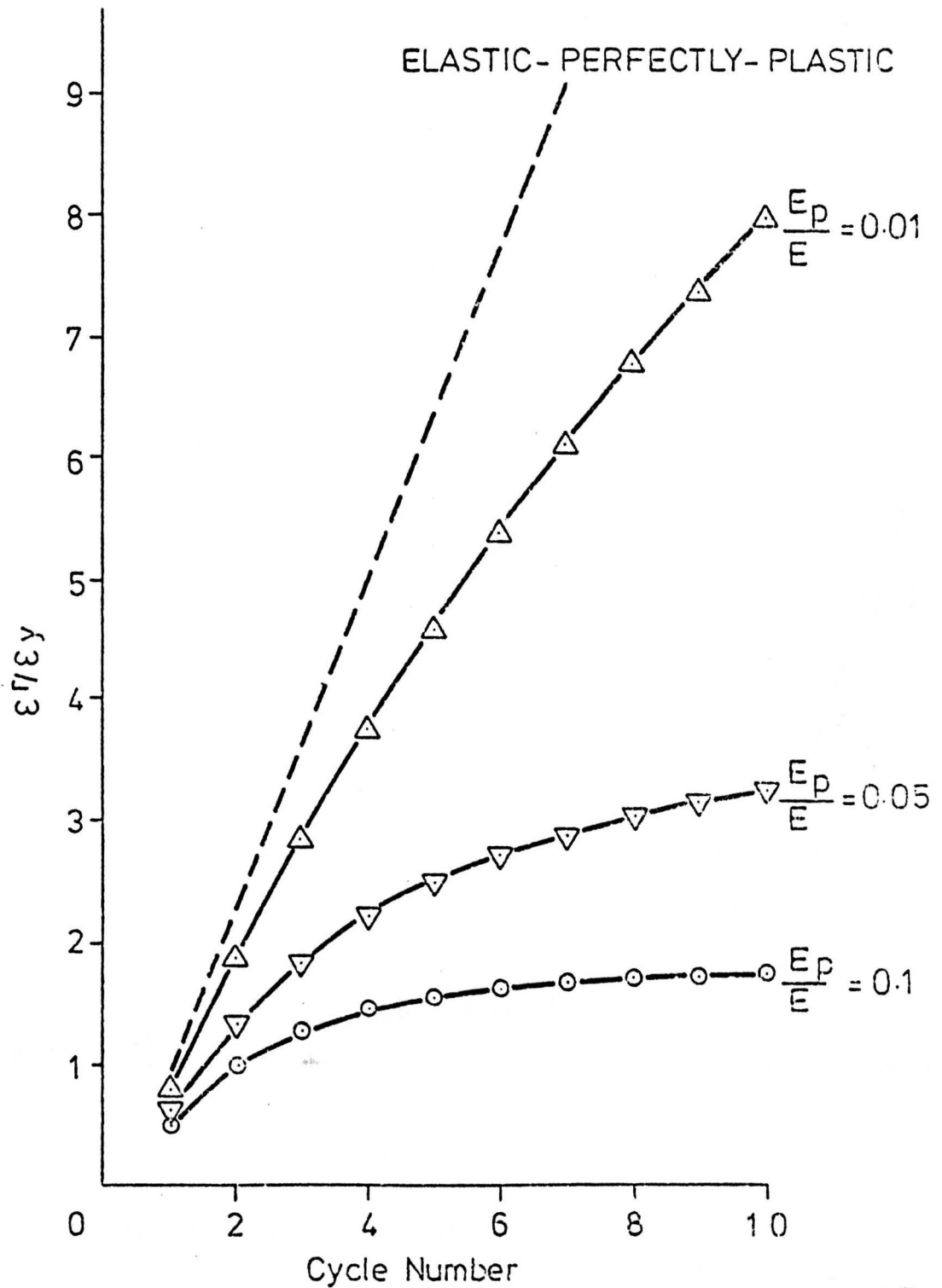


Figure 4.8 Flanged tube shank (Linear hardening, $\sigma_t/\sigma_y = 1.94$, $P/P_L = 0.9$, 'no creep' conditions). Accumulation of normalised ratchet strain during the first 10 cycles.

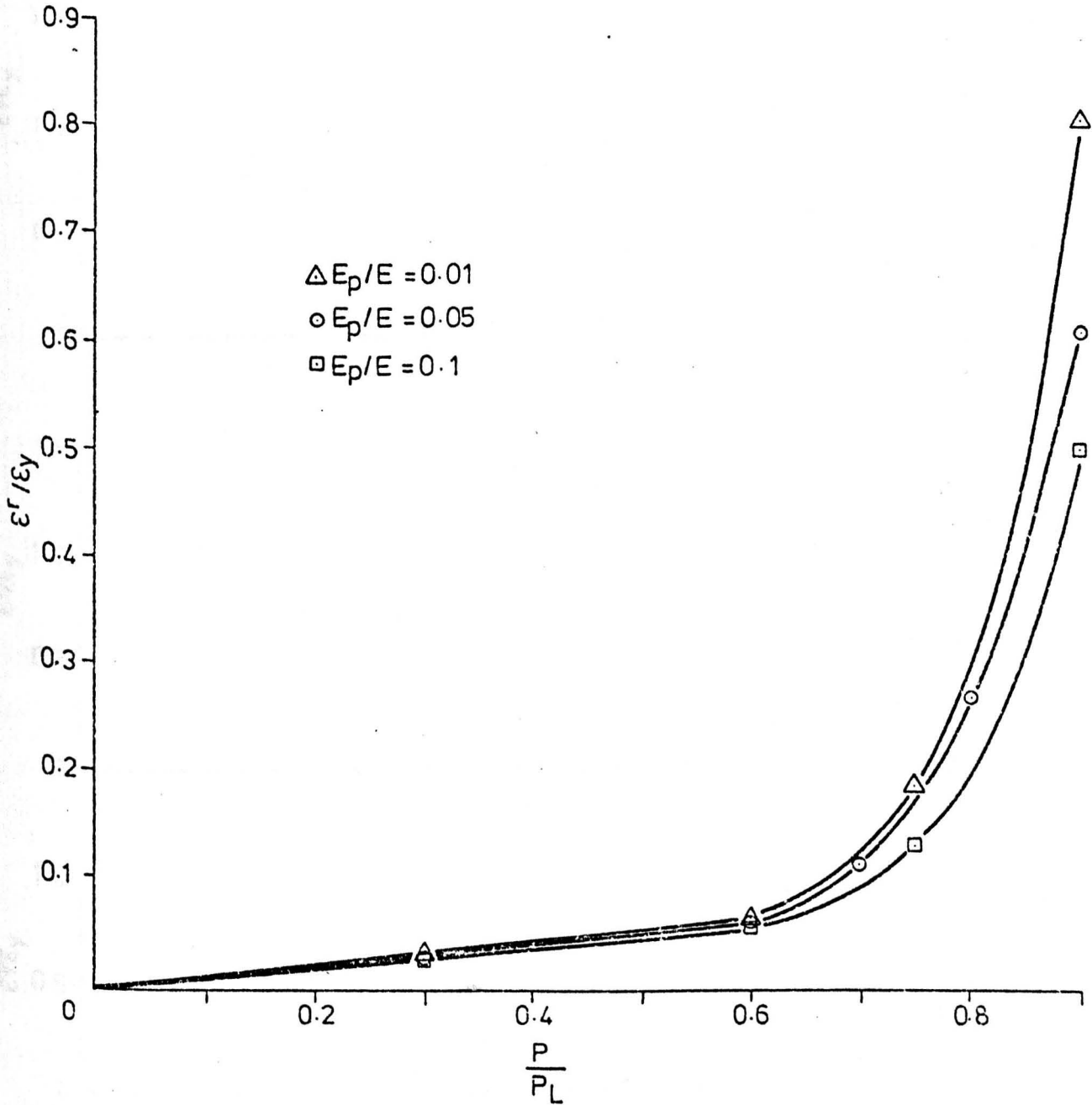


Figure 4.9 Flanged tube shank (Linear hardening, $\sigma_t / \sigma_y = 1.94$). Accumulation of normalized ratchet strain in the first cycle.

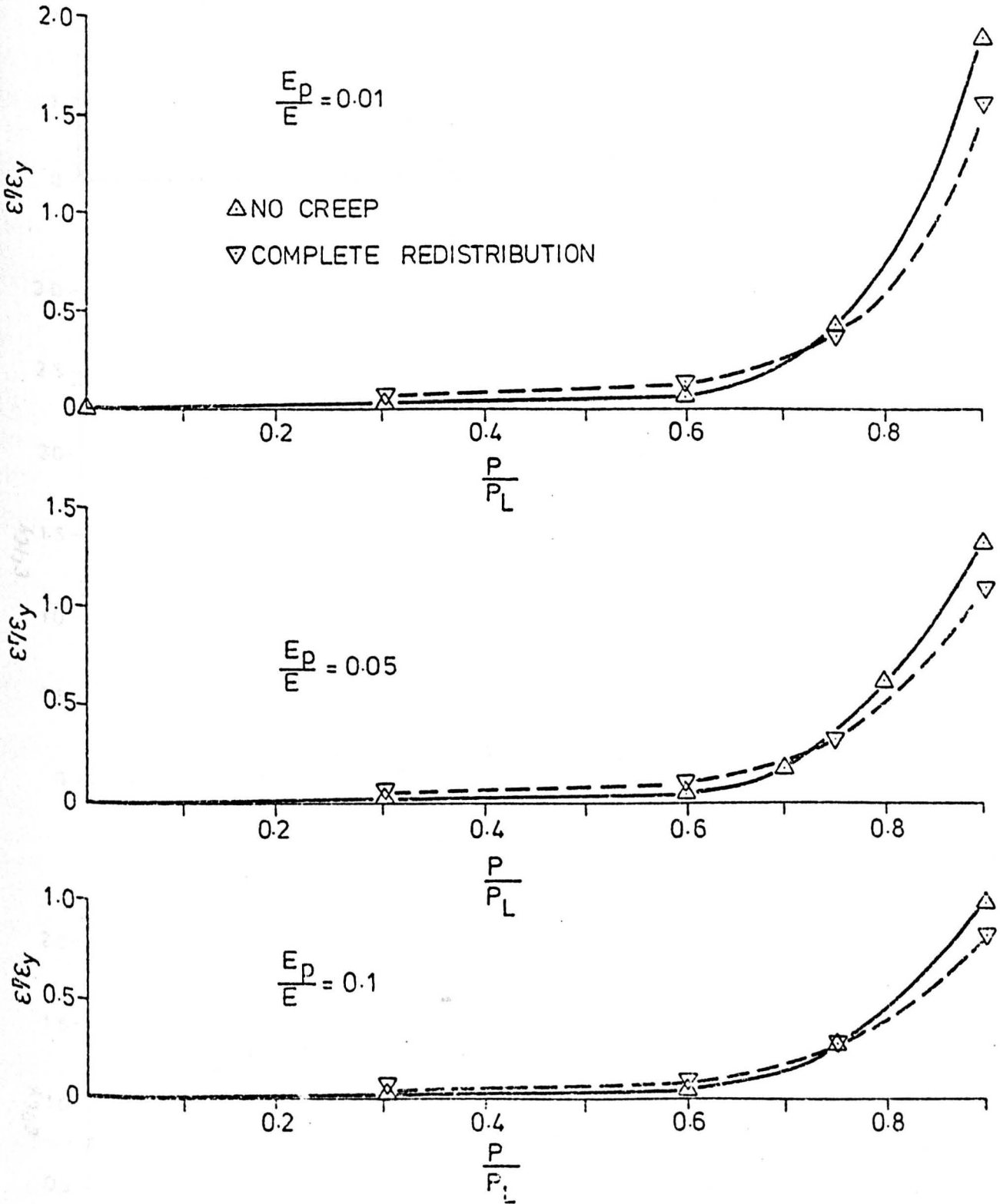


Figure 4.10 Flanged tube shank (Linear hardening, $\sigma_t/\sigma_y = 1.94$). Accumulation of normalised ratchet strain in the first 2 cycles

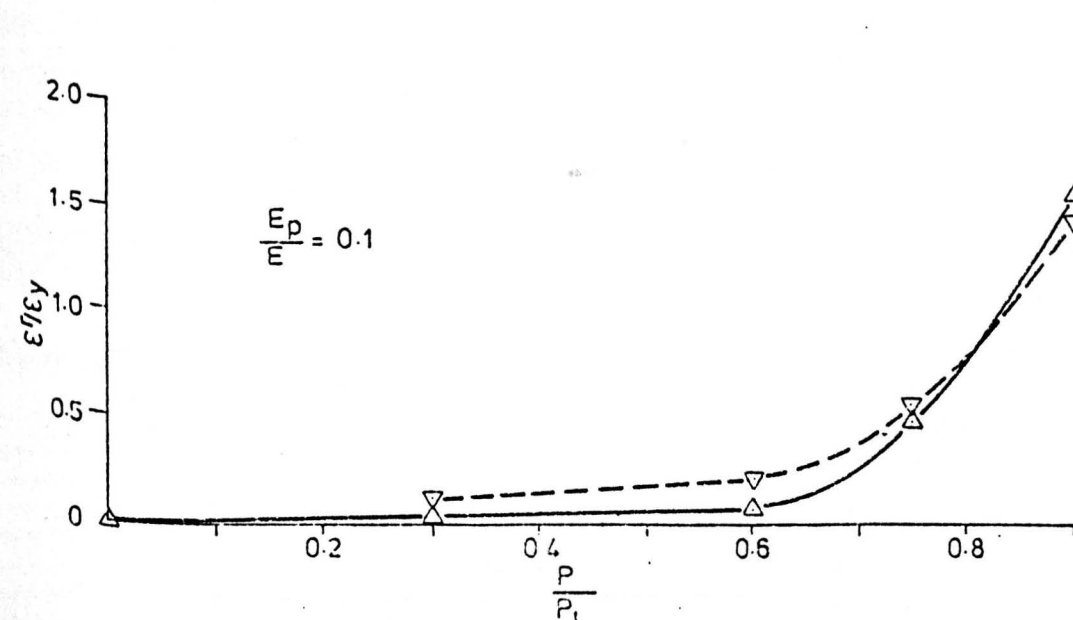
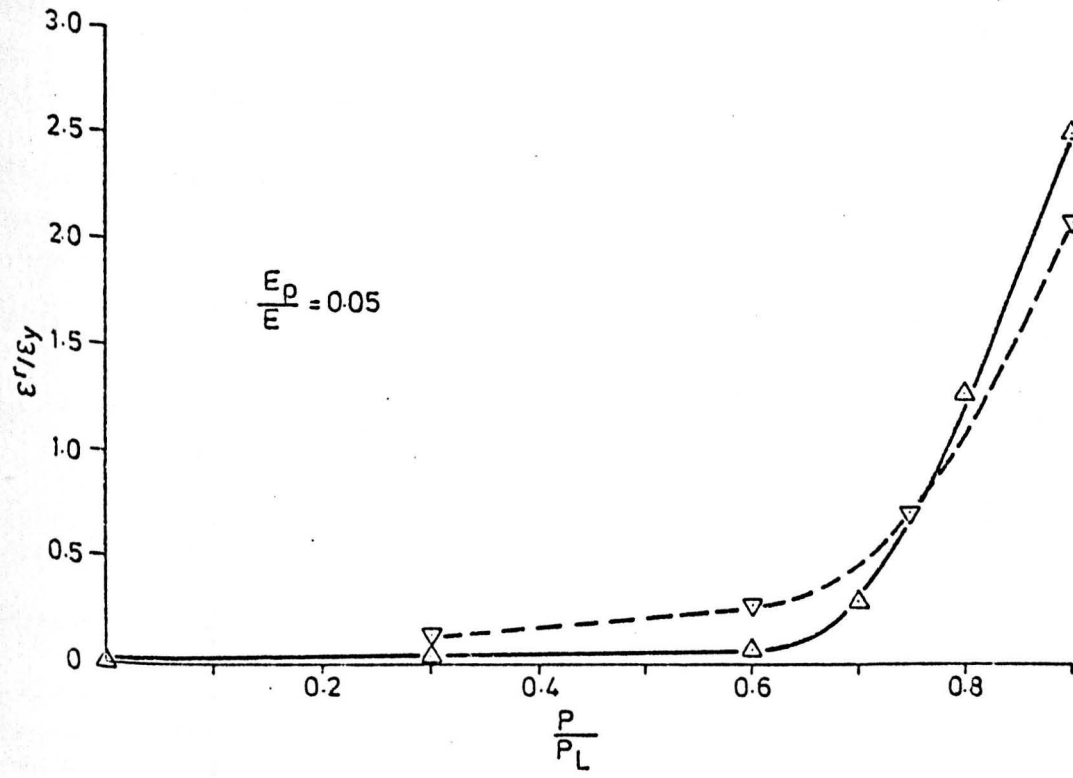
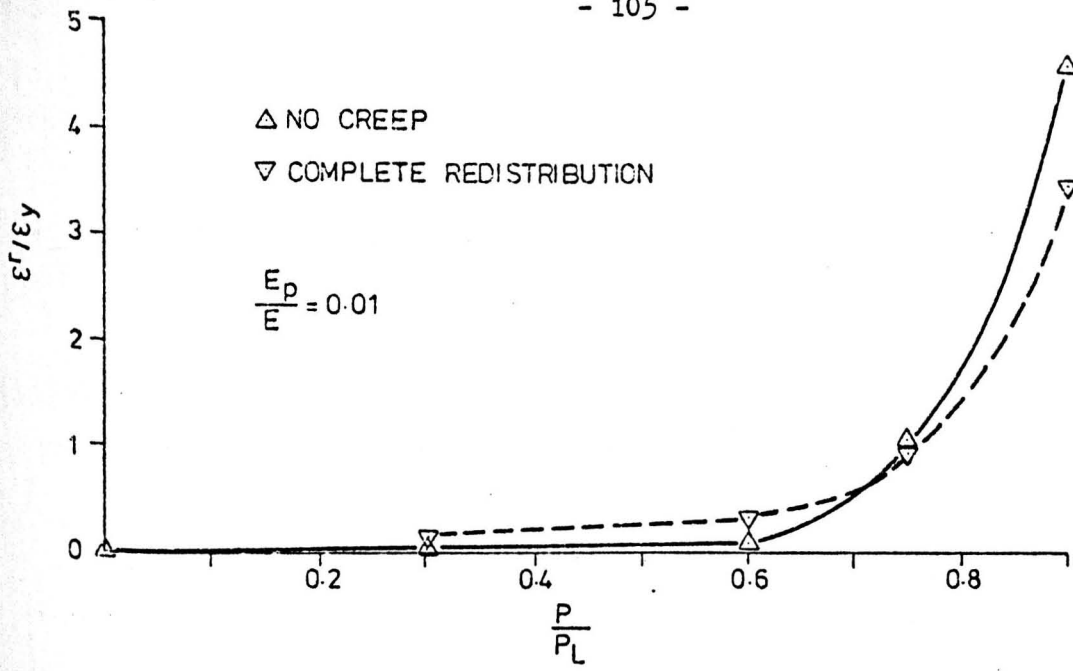


Figure 4.11 Flanged tube shank (Linear hardening, $\sigma_t/\sigma_y = 1.94$). Accumulation of normalised ratchet strain in the first 5 cycles.

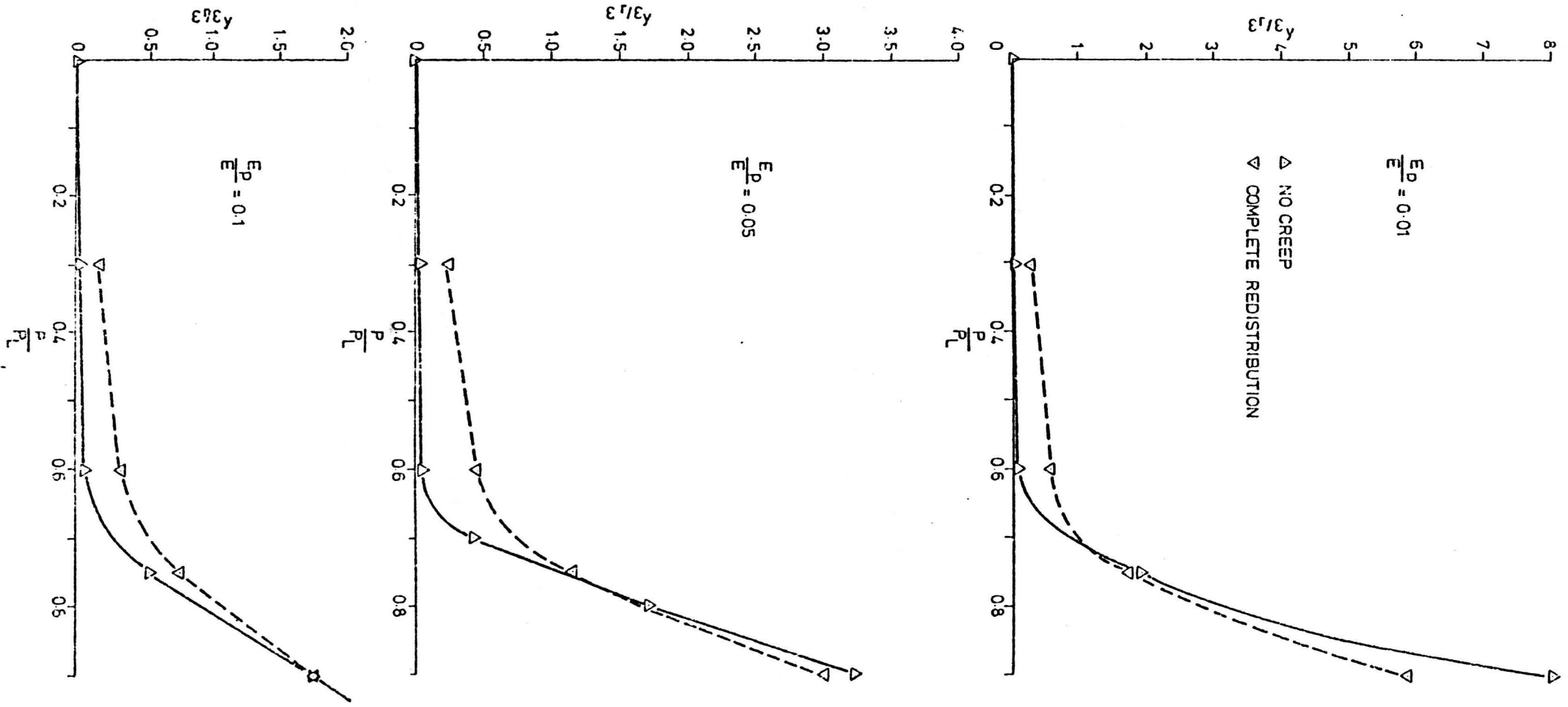


Figure 4.12 Flanged tube shank (Linear hardening, $\sigma_t/\sigma_y = 1.94$). Accumulation of normalised ratchet strain in the first 10 cycles.

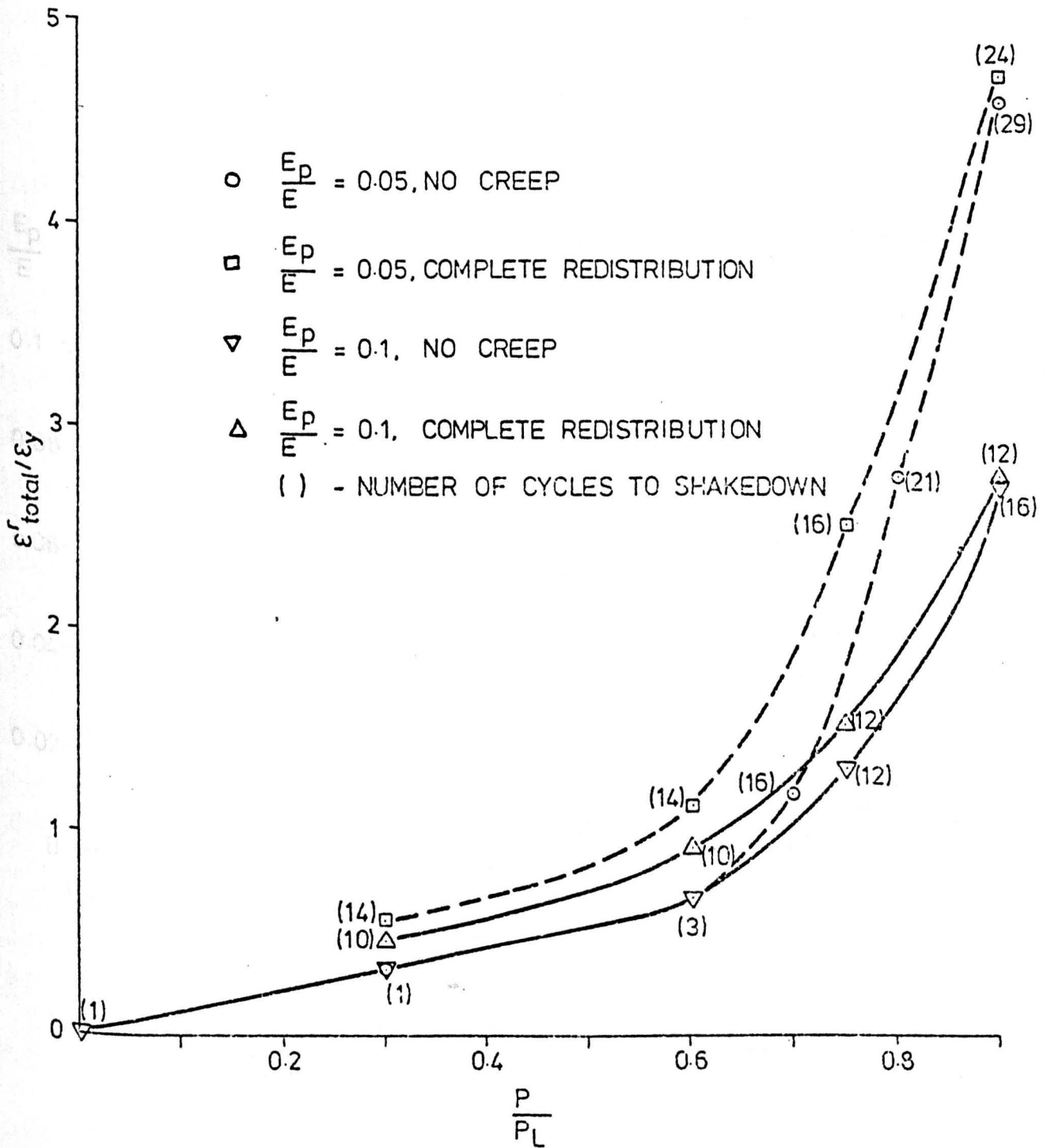


Figure 4.13 Flanged tube shank (Linear hardening, $\sigma_t/\sigma_y = 1.94$). Normalised total accumulated ratchet strains.

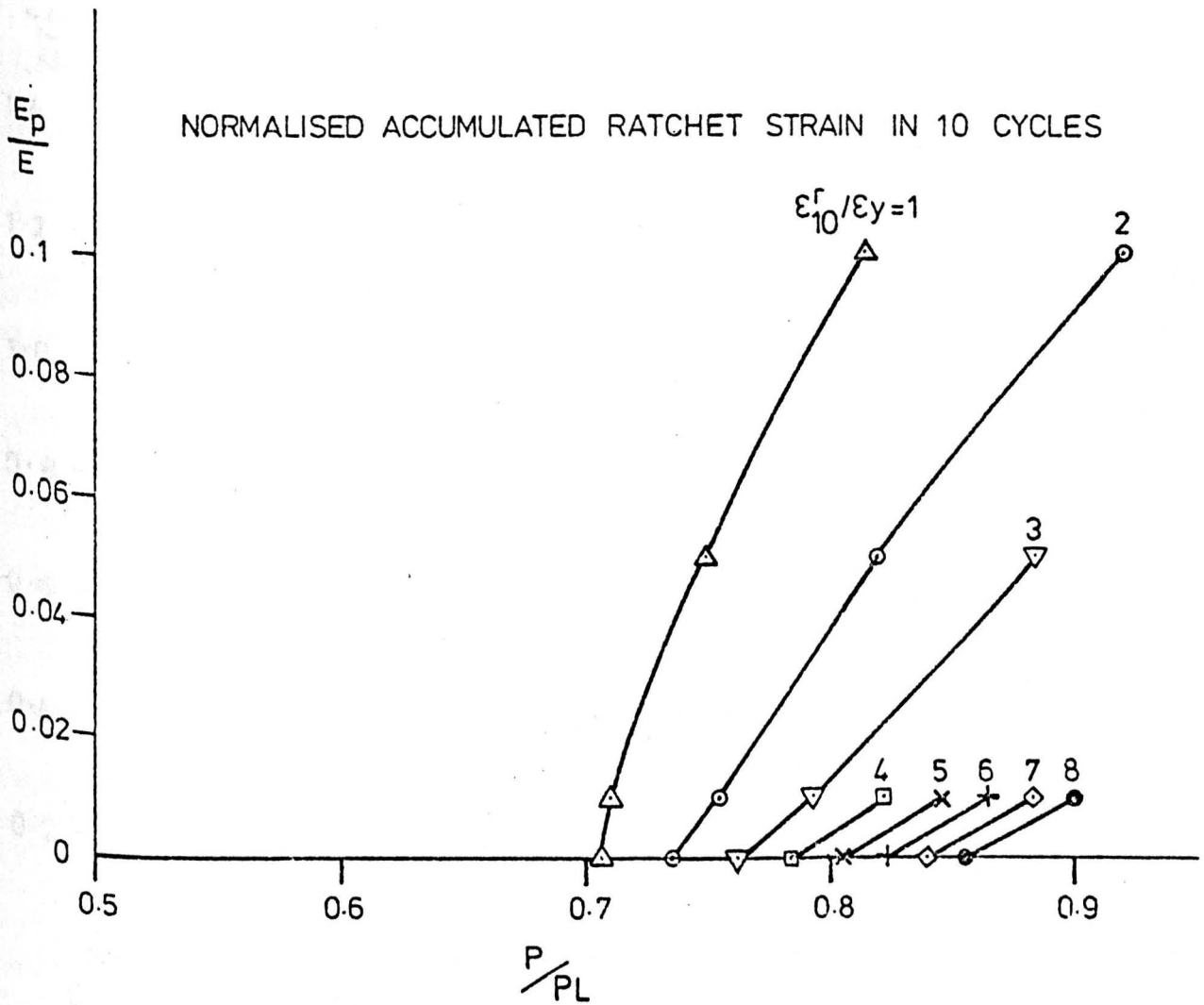


Figure 4.14 Flanged tube shank (elastic-perfectly-plastic and linear hardening, $\sigma_t / \sigma_y = 1.94$, 'no creep' conditions). Normalised accumulated ratchet strain in 10 cycles.

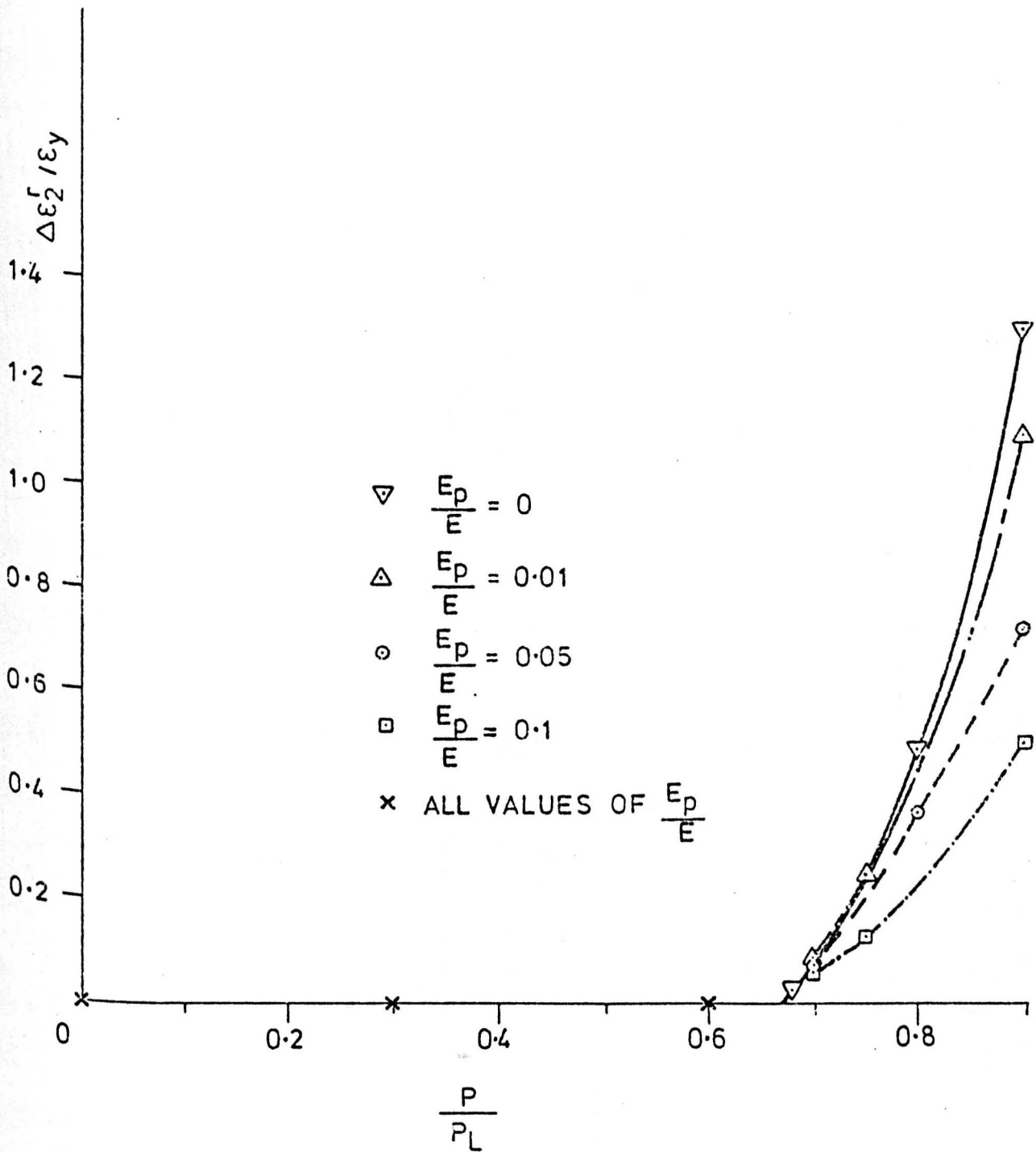


Figure 4.15 Flanged tube shank (elastic-perfectly-plastic and linear hardening, $\sigma_t/\sigma_y = 1.94$, 'no creep' conditions). Normalised ratchet strain in the 2nd cycle.

$$\triangleleft \frac{P}{P_L} = 0.3$$

$$\triangleright \frac{P}{P_L} = 0.7$$

$$+ \frac{P}{P_L} = 0.75$$

$$\circ \frac{P}{P_L} = 0.8$$

$$\times \frac{P}{P_L} = 0.9$$

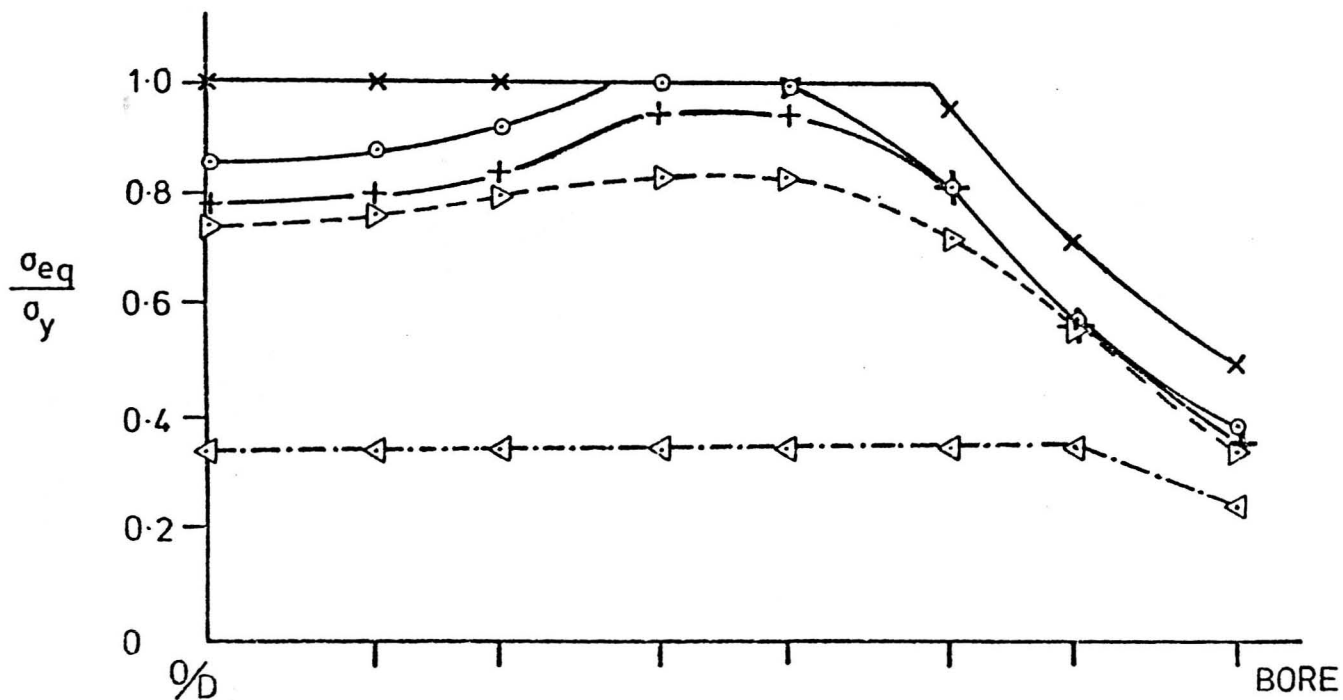


Figure 4.16 Flanged tube shank (elastic-perfectly-plastic, $\sigma_t/\sigma_y = 1.94$).
Distribution of residual equivalent stress at the end of the first thermal shock for a number of mean loads.

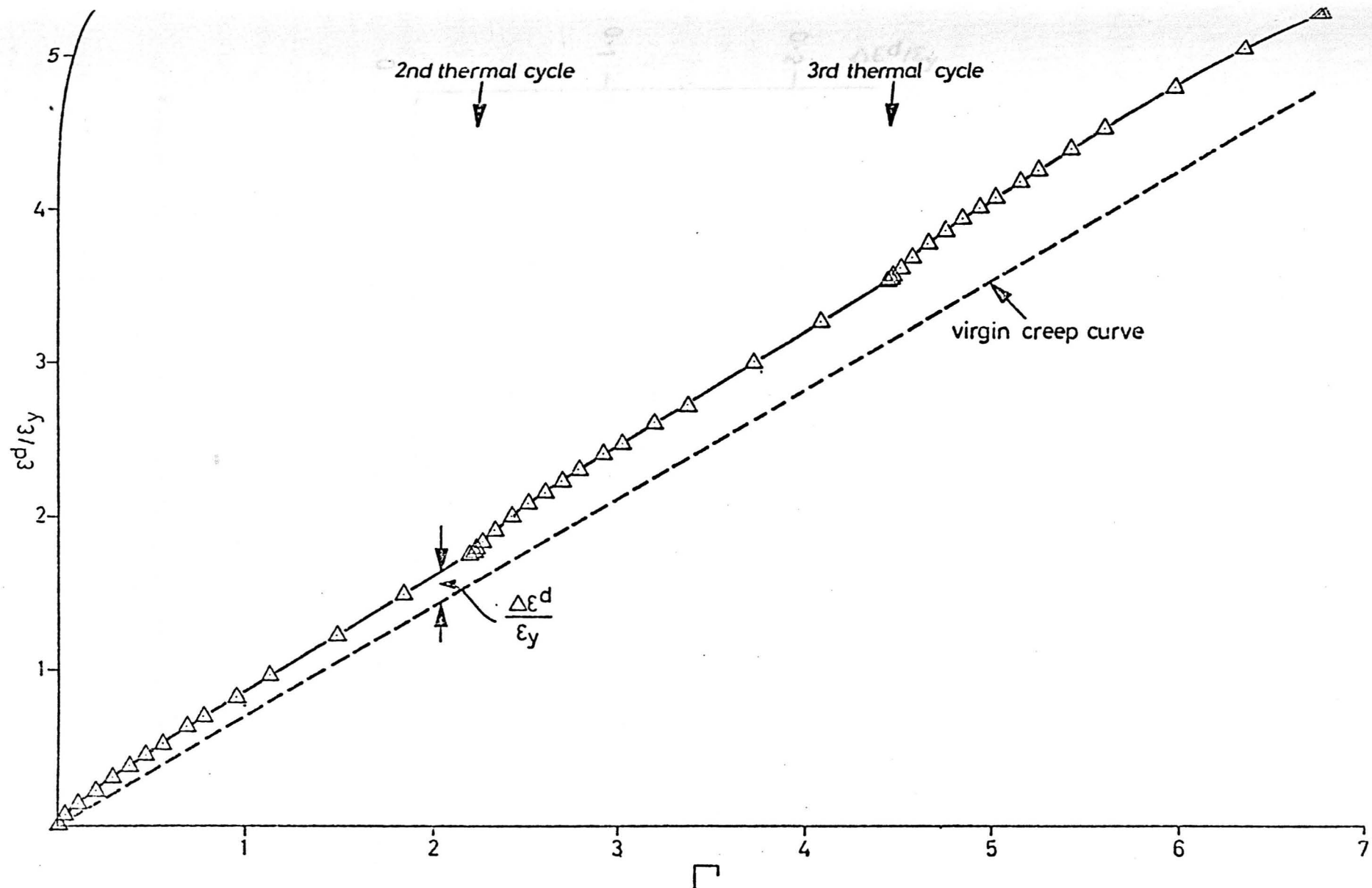


Figure 4.17 Flanged tube shank (elastic-perfectly-plastic, $\sigma_t/\sigma_y = 1.94$, $P/P_L = 0.7$, complete redistribution). Accumulation of normalised strain during the first 3 dwell periods.

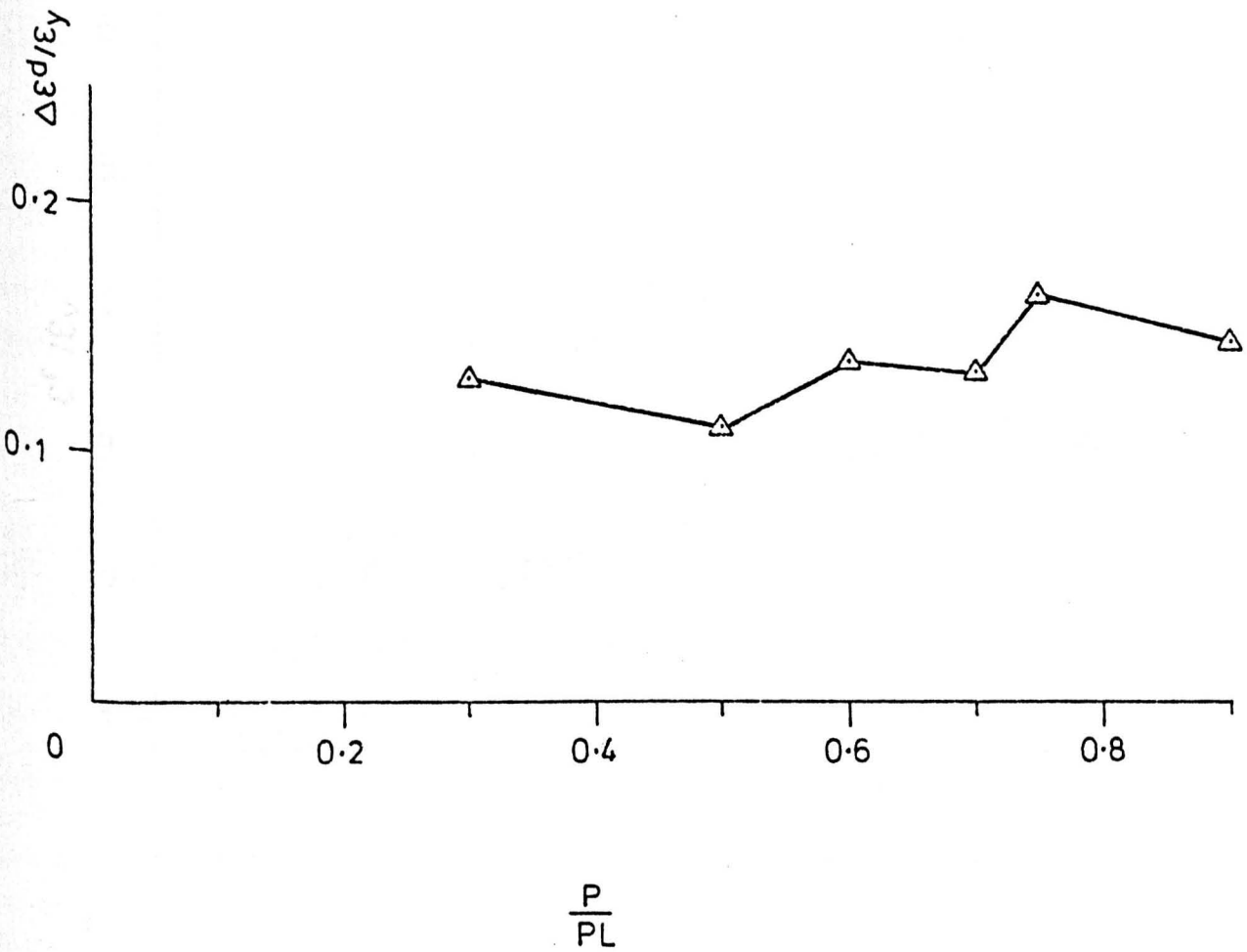


Figure 4.18 Flanged tube shank (elastic-perfectly-plastic, $\sigma_t / \sigma_y = 1.94$, complete redistribution). Variation in the normalised increment of dwell period strain due to stress redistribution with mean load.

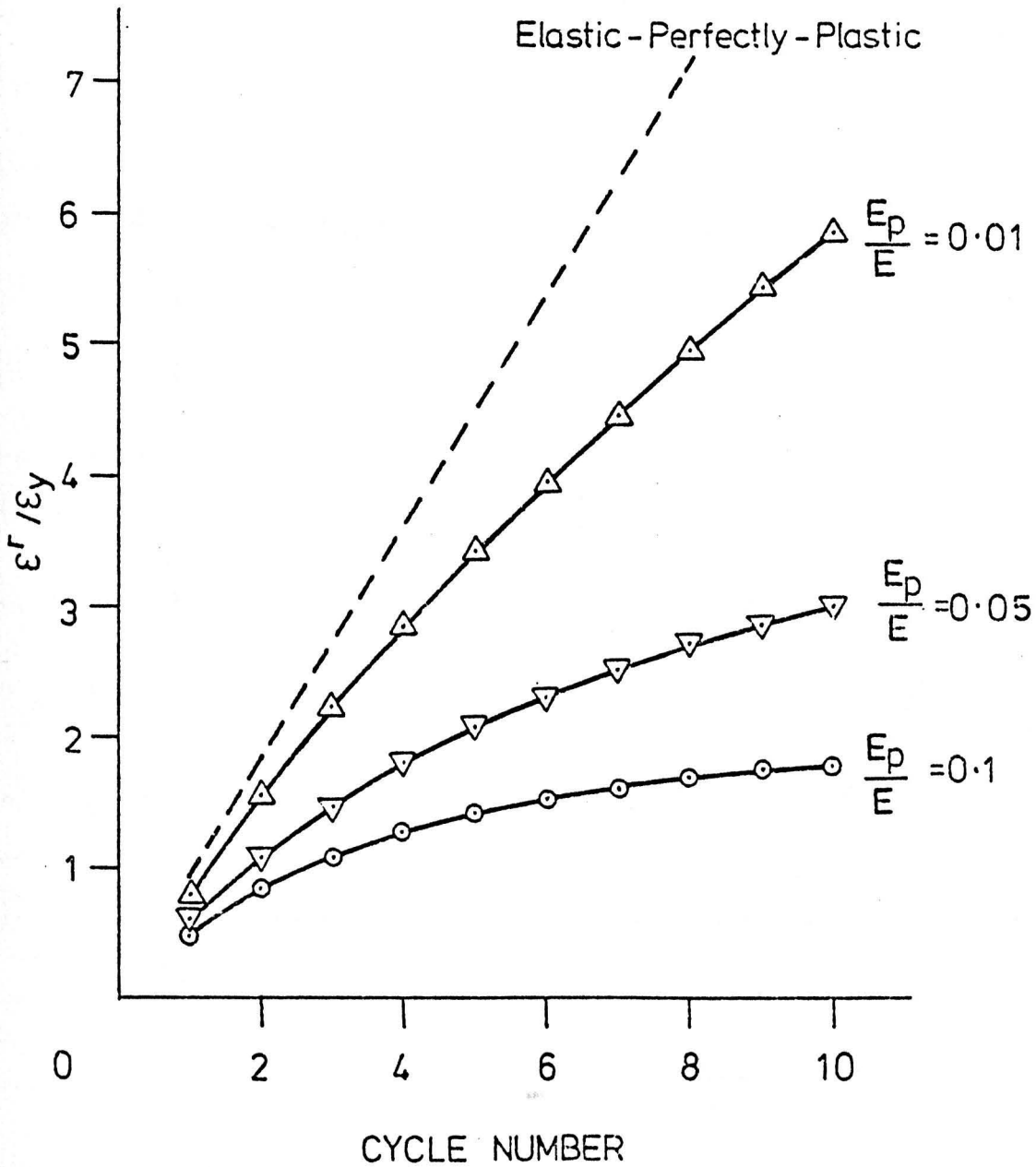


Figure 4.19 Flanged tube shank (Linear hardening, $\sigma_t/\sigma_y = 1.94$, $P/P_L = 0.9$, complete redistribution). Accumulation of normalised ratchet strain during the first 10 cycles.

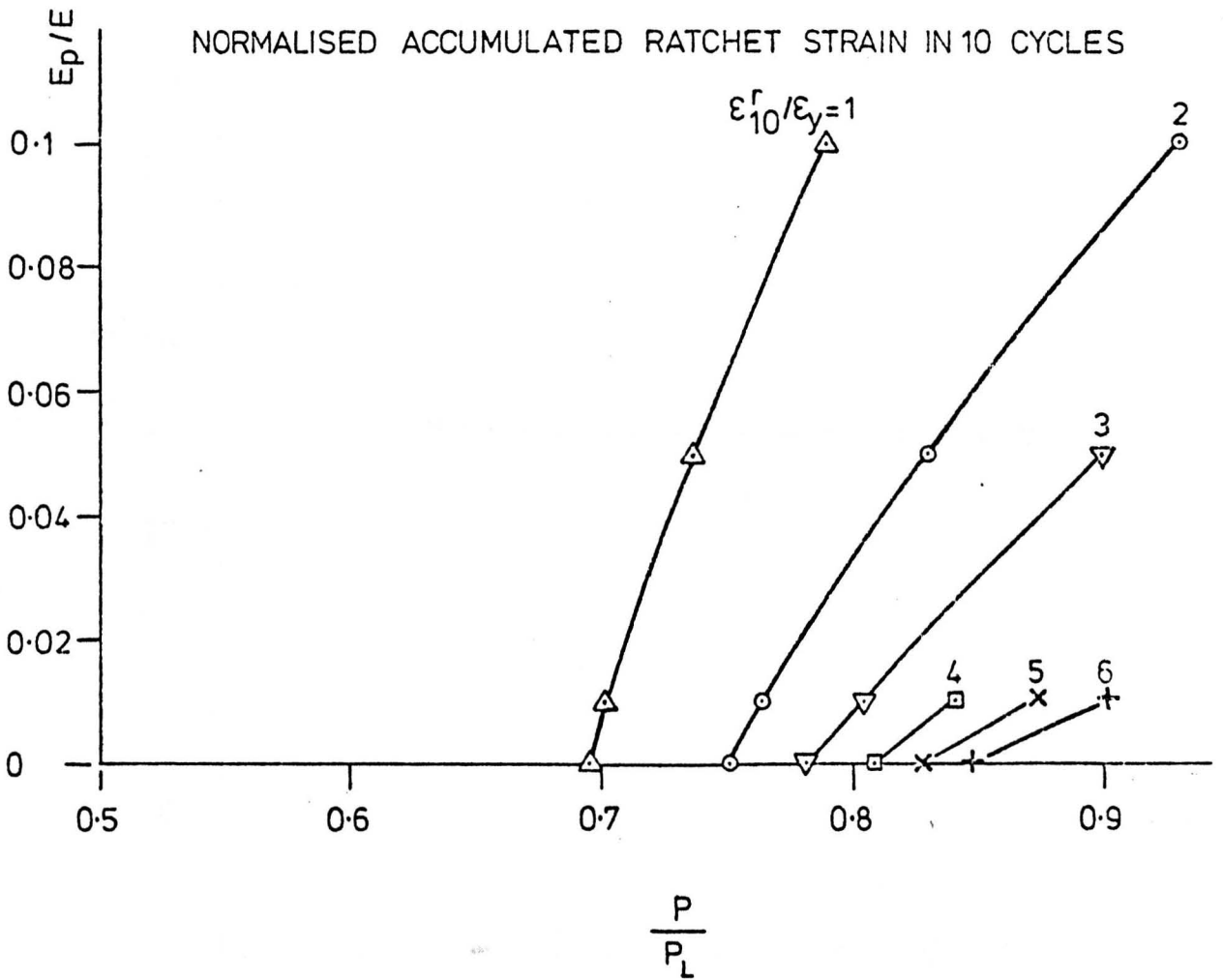


Figure 4.20 Flanged tube shank (elastic-perfectly-plastic and linear hardening, $\sigma_t/\sigma_y = 1.94$, complete redistribution). Normalised accumulated ratchet strain in 10 cycles.

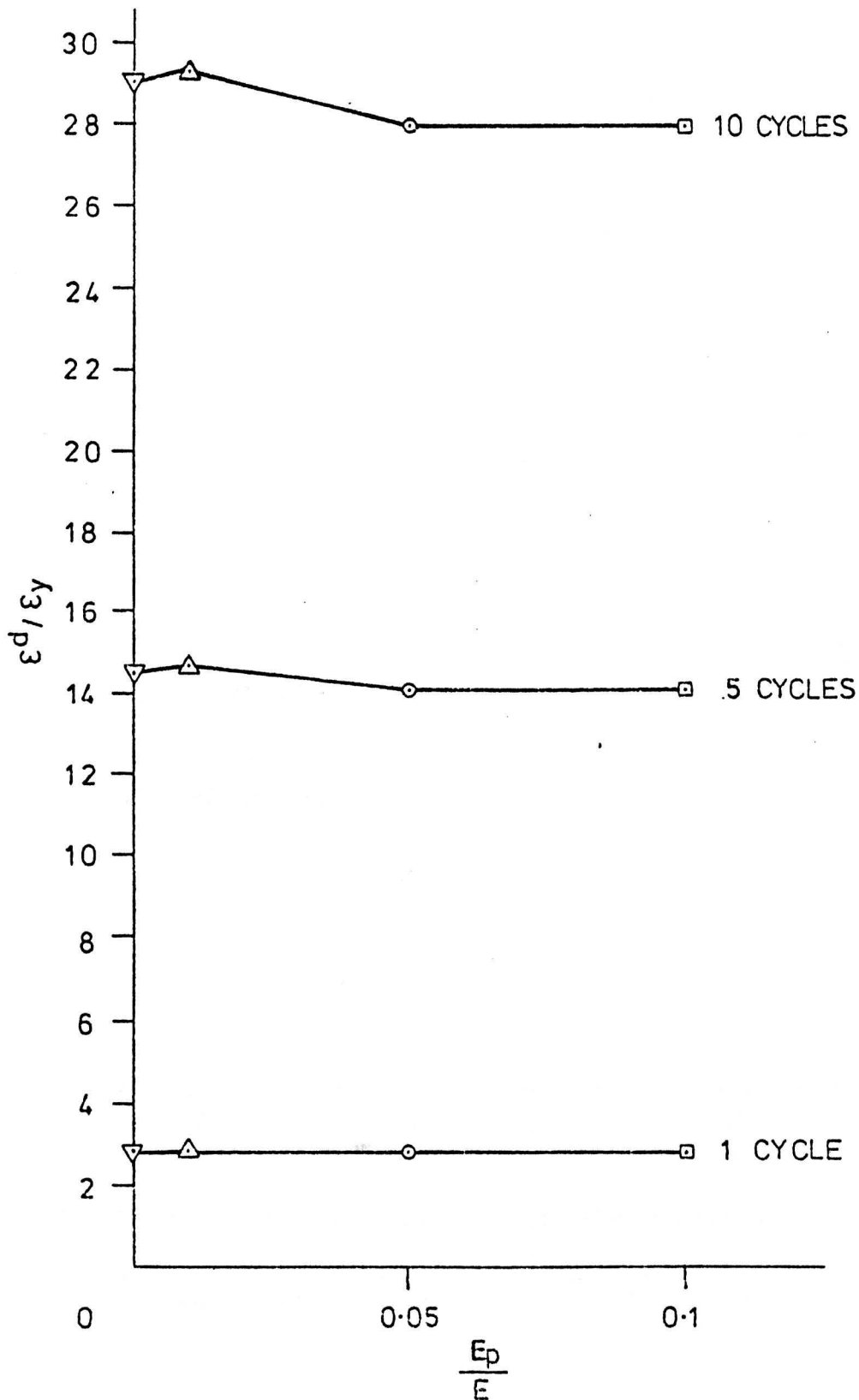


Figure 4.21 Flanged tube shank (elastic-perfectly-plastic and linear hardening, $\sigma_t/\sigma_y = 1.94$, $P/P_L = 0.9$, complete redistribution). Normalised accumulated dwell period strain after the 1st, 5th and 10th dwell periods.

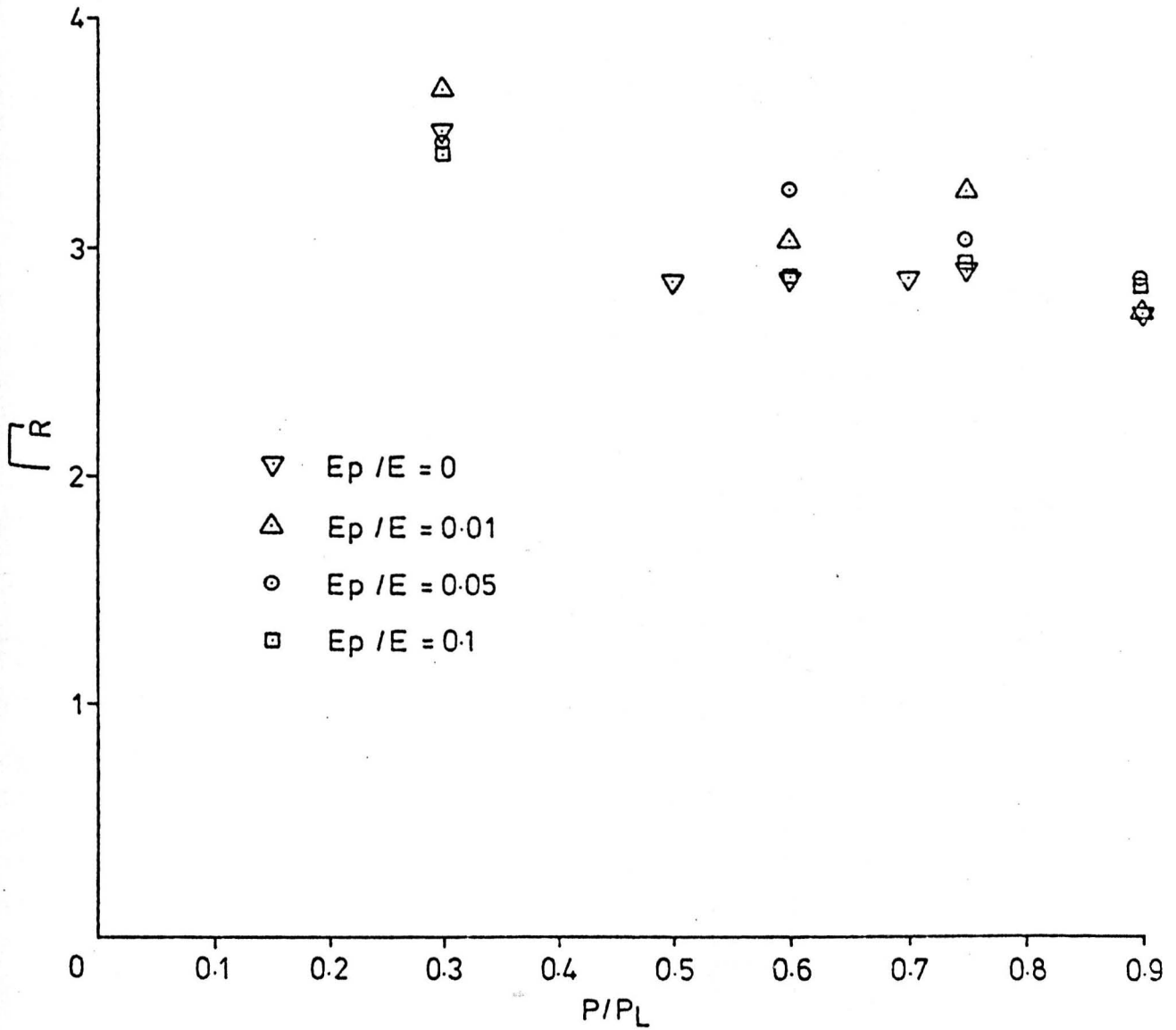


Figure 4.22 Flanged tube shank (elastic-perfectly-plastic and linear hardening, $\sigma_t/\sigma_y = 1.94$, complete redistribution). Variation in time function for complete redistribution with mean load and E_p/E .

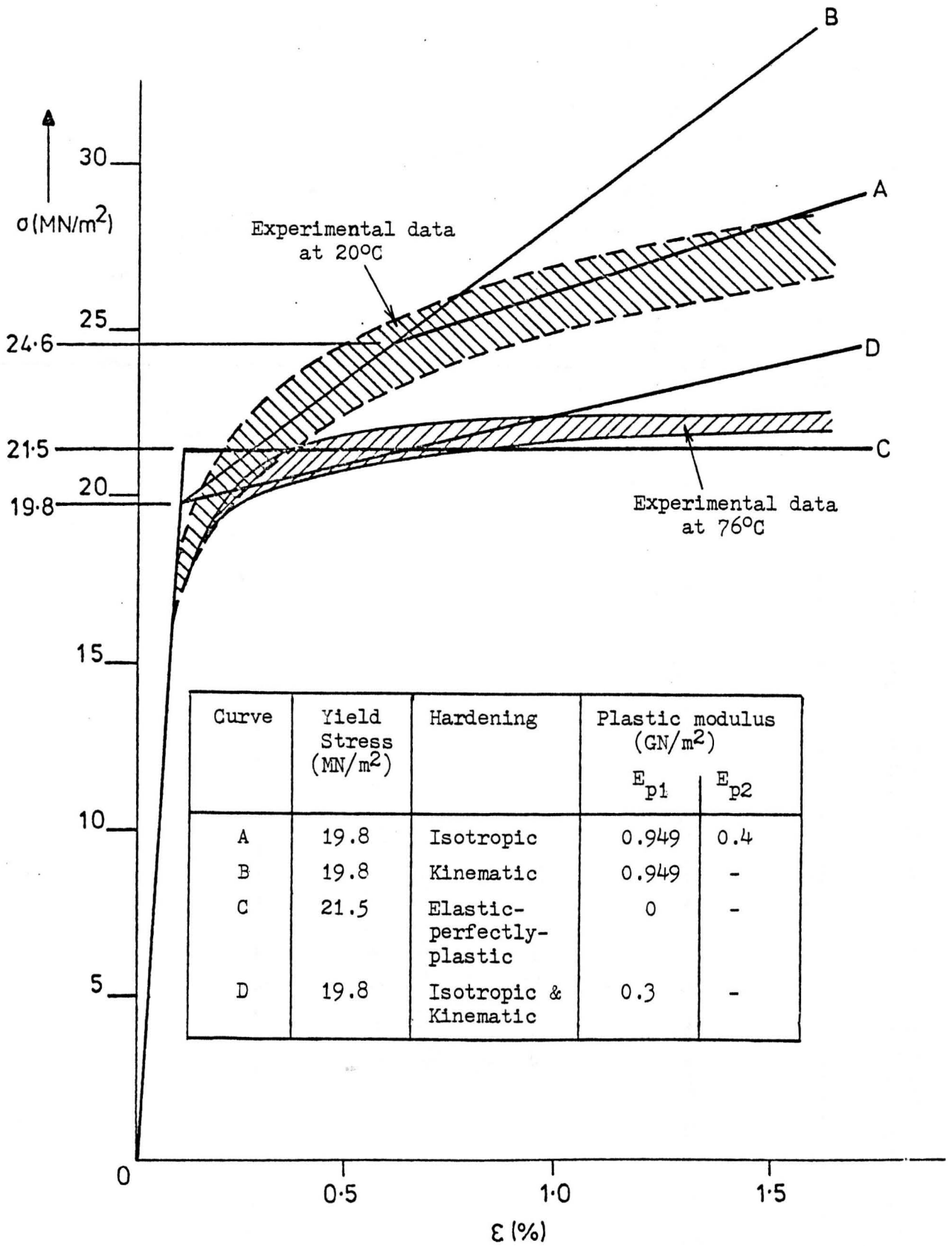


Figure 4.24 Modelling of lead alloy uniaxial stress-strain behaviour at 20°C and 76°C.

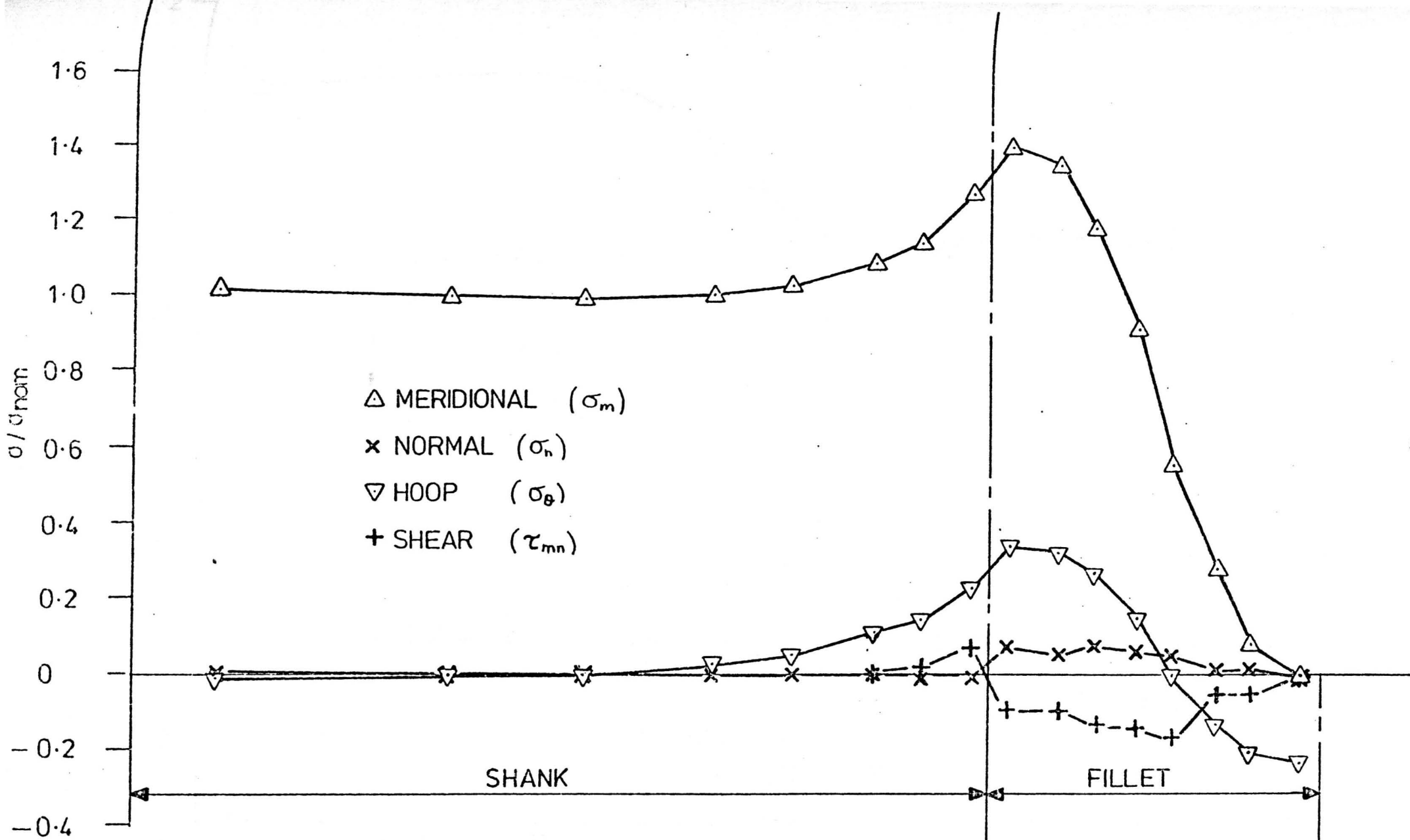


Figure 4.25 Flanged tube. Elastic stress distributions along the shank outside 'surface' and around the fillet due to an axial load. (see Figure 4.23).

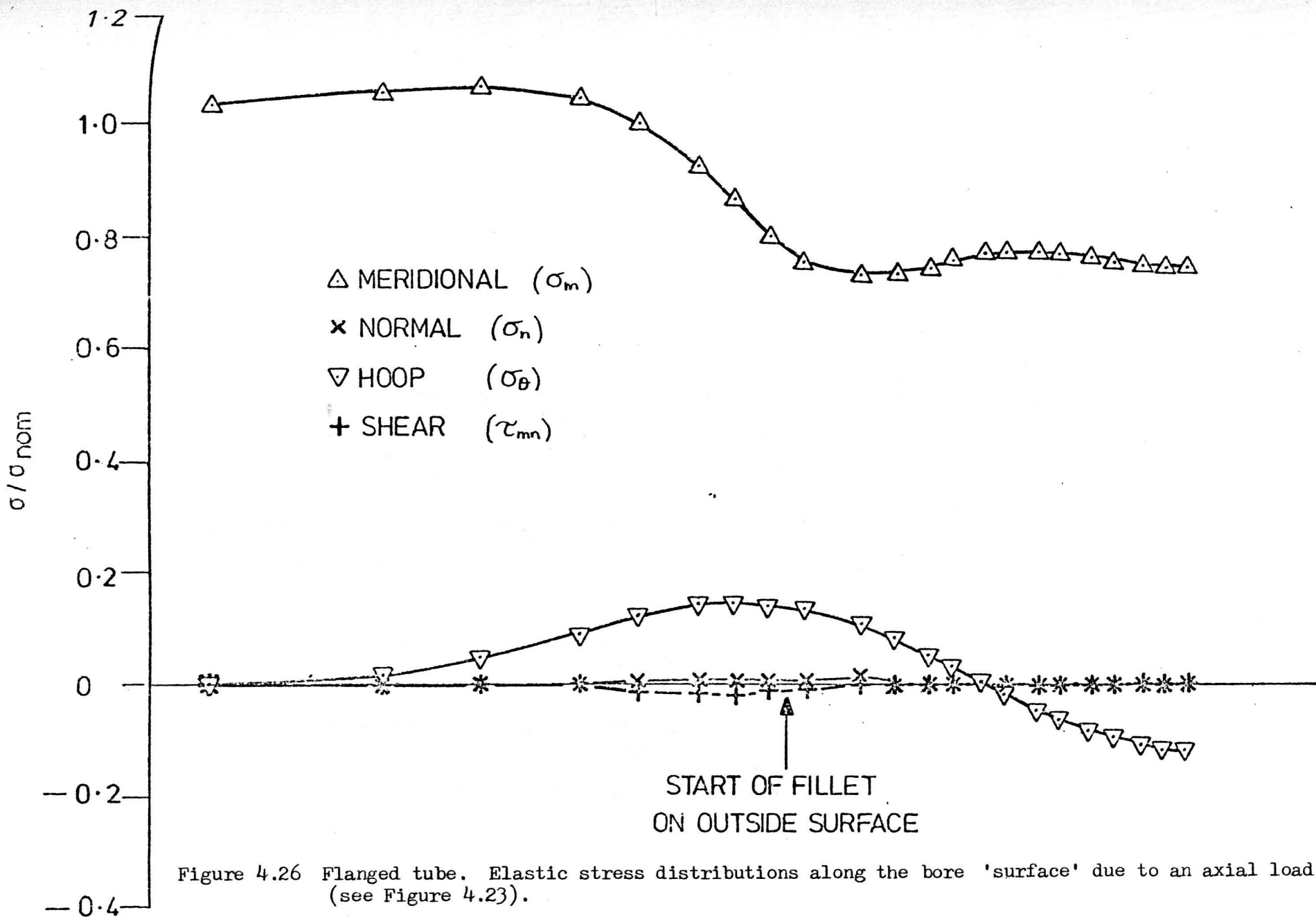


Figure 4.26 Flanged tube. Elastic stress distributions along the bore 'surface' due to an axial load. (see Figure 4.23).

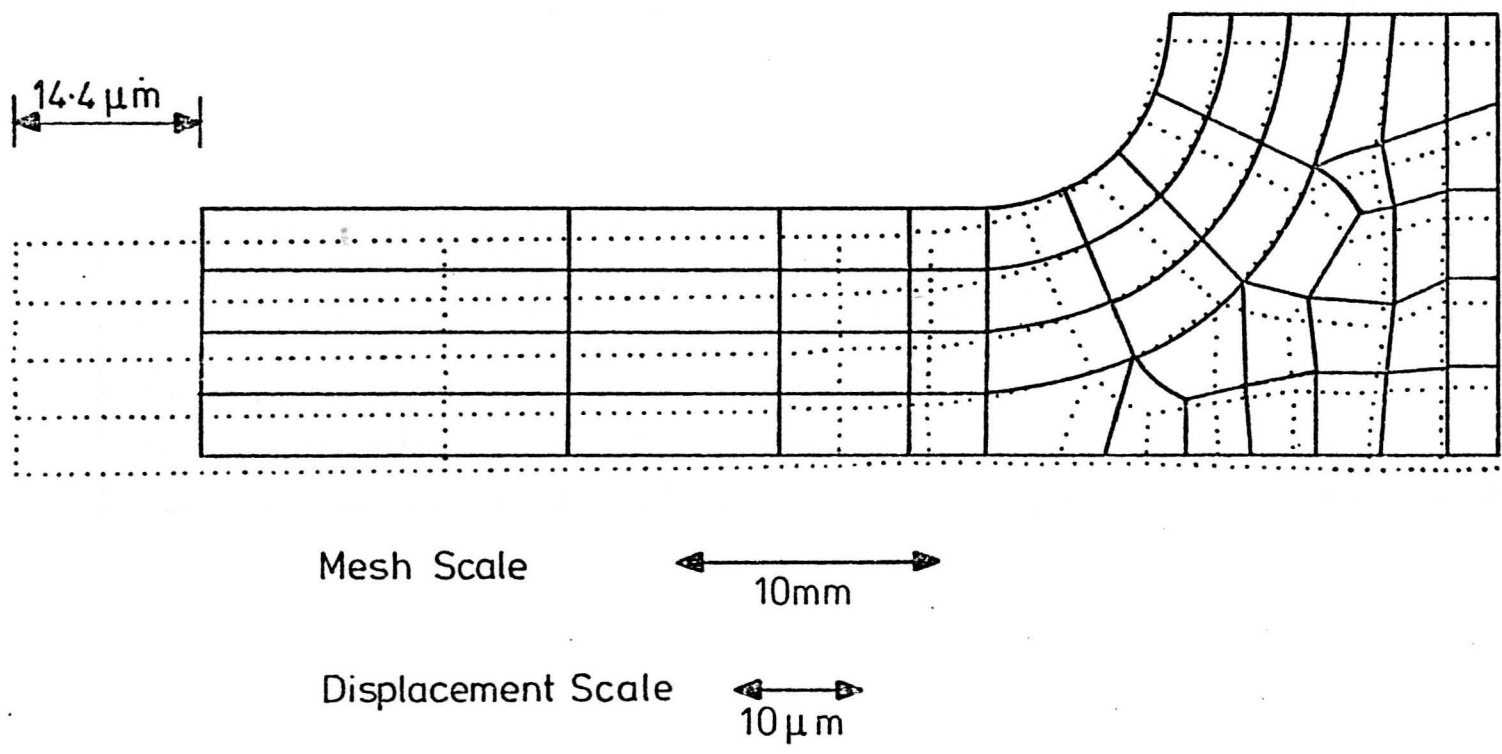


Figure 4.27 Flanged tube. 'Exaggerated' deformed shape for a mean load of 0.7 of the limit load.



$0.9 P_L$
 $0.99 P_L$
 P_L

WHERE P_L = LIMIT LOAD IN SHANK

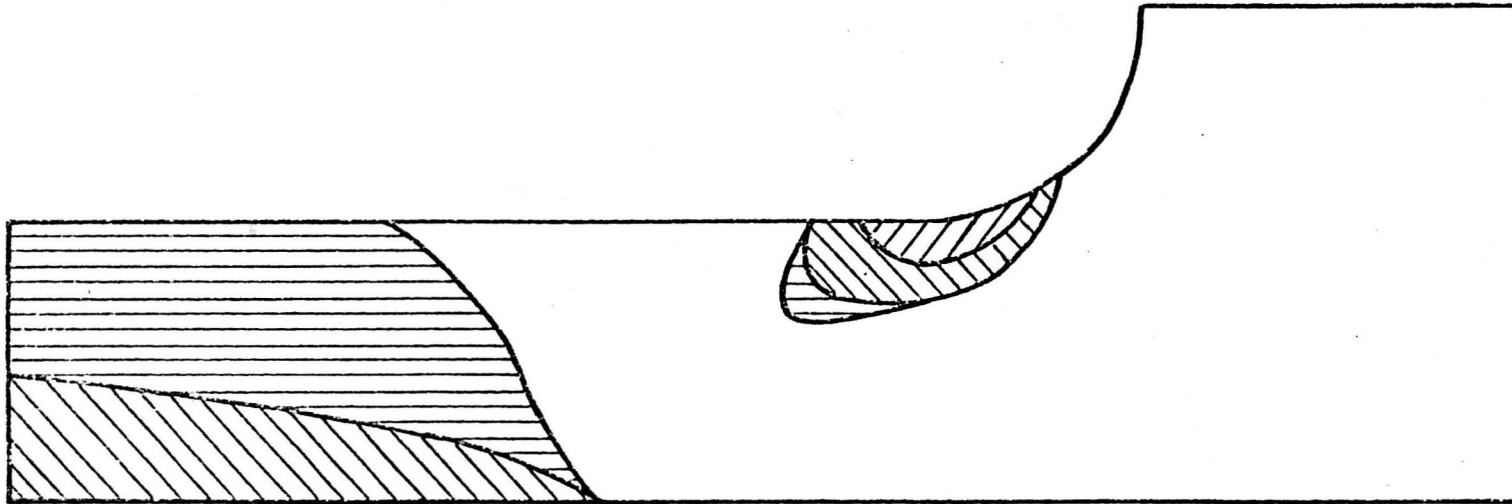


Figure 4.28 Flanged tube (elastic-perfectly-plastic). Growth of plastic zone with increasing axial load up to collapse.

$\epsilon_{XX}^t (\mu\epsilon \times 10^2)$

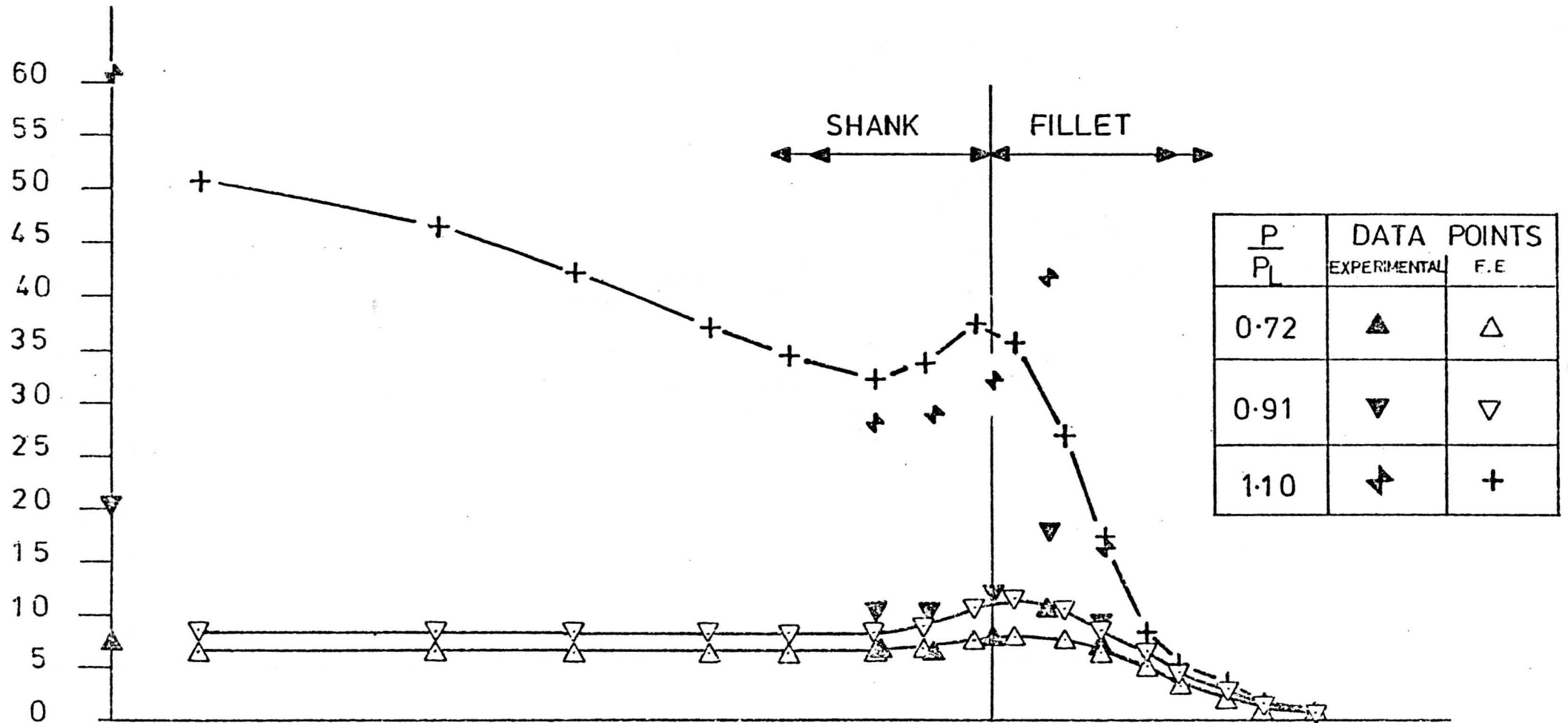


Figure 4.29 Flanged tube. Comparison between experimental results and finite element predictions (using curve A, Figure 4.24) of elastic-plastic meridional strain distributions along the outside 'surface' (see Figure 4.23).

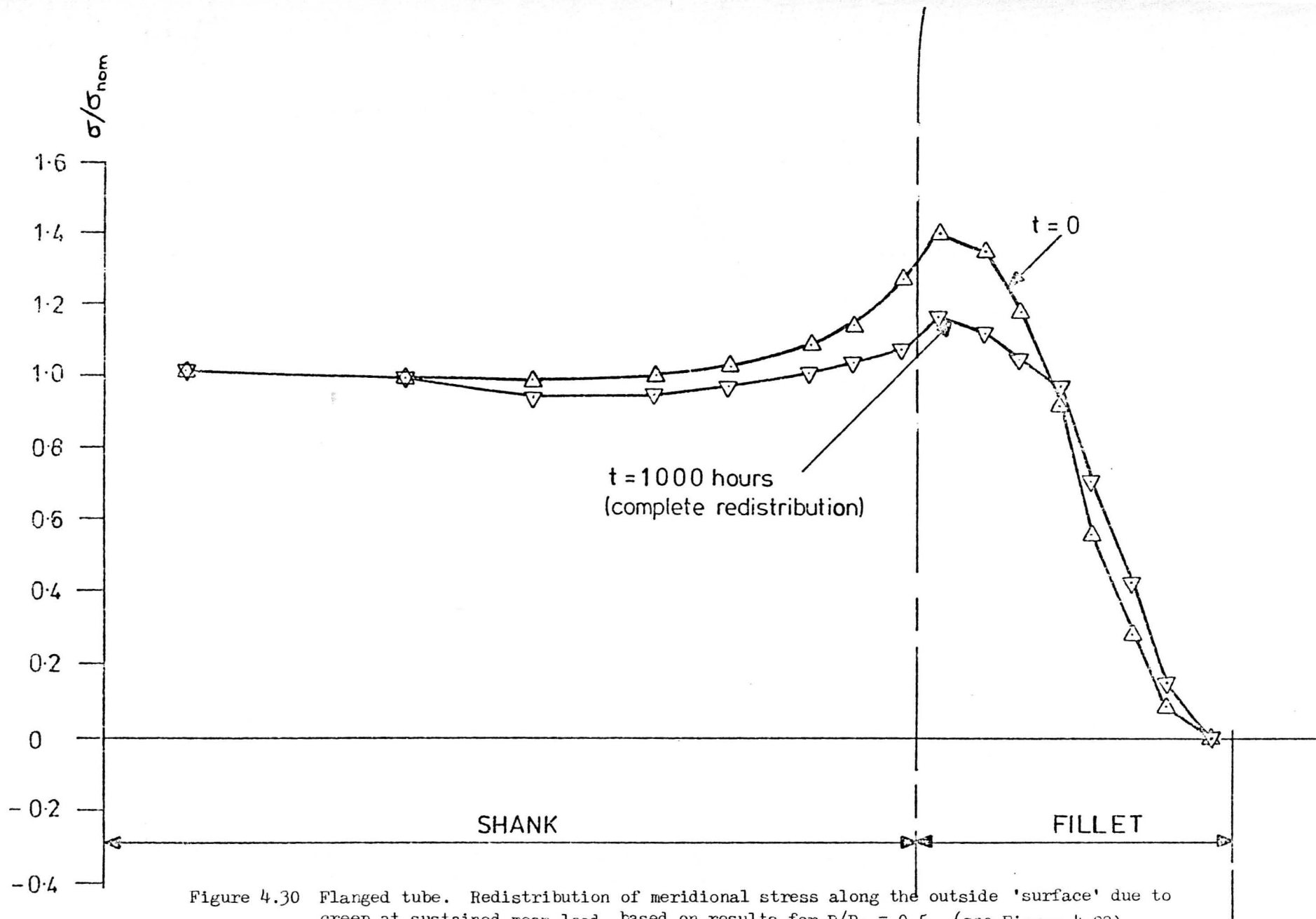


Figure 4.30 Flanged tube. Redistribution of meridional stress along the outside 'surface' due to creep at sustained mean load, based on results for $P/P_L = 0.5$. (see Figure 4.23)

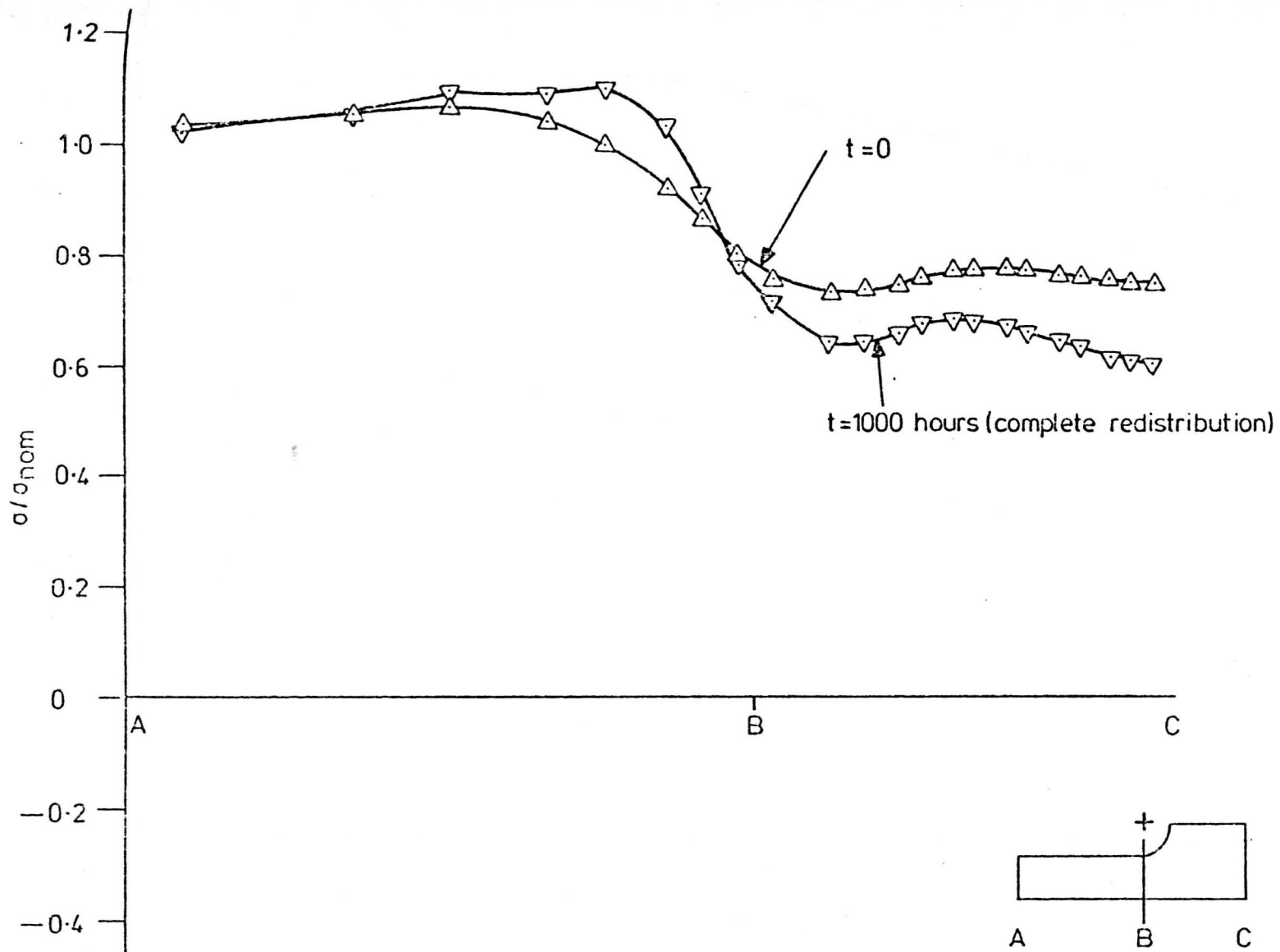


Figure 4.31 Flanged tube. Redistribution of meridional stress along the bore 'surface' due to creep at sustained mean load based on results for $P/P_L = 0.5$. (see Figure 4.23)

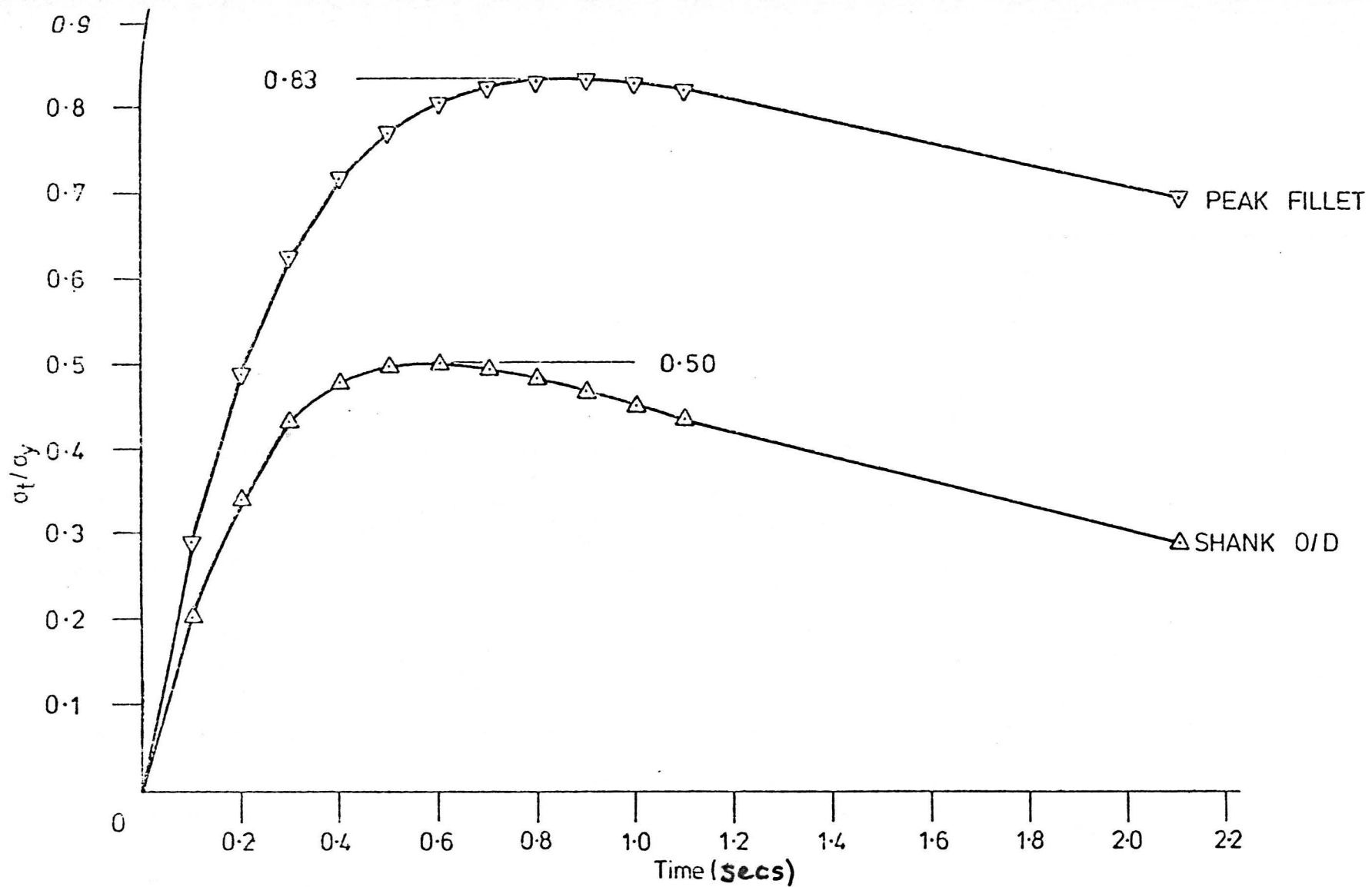
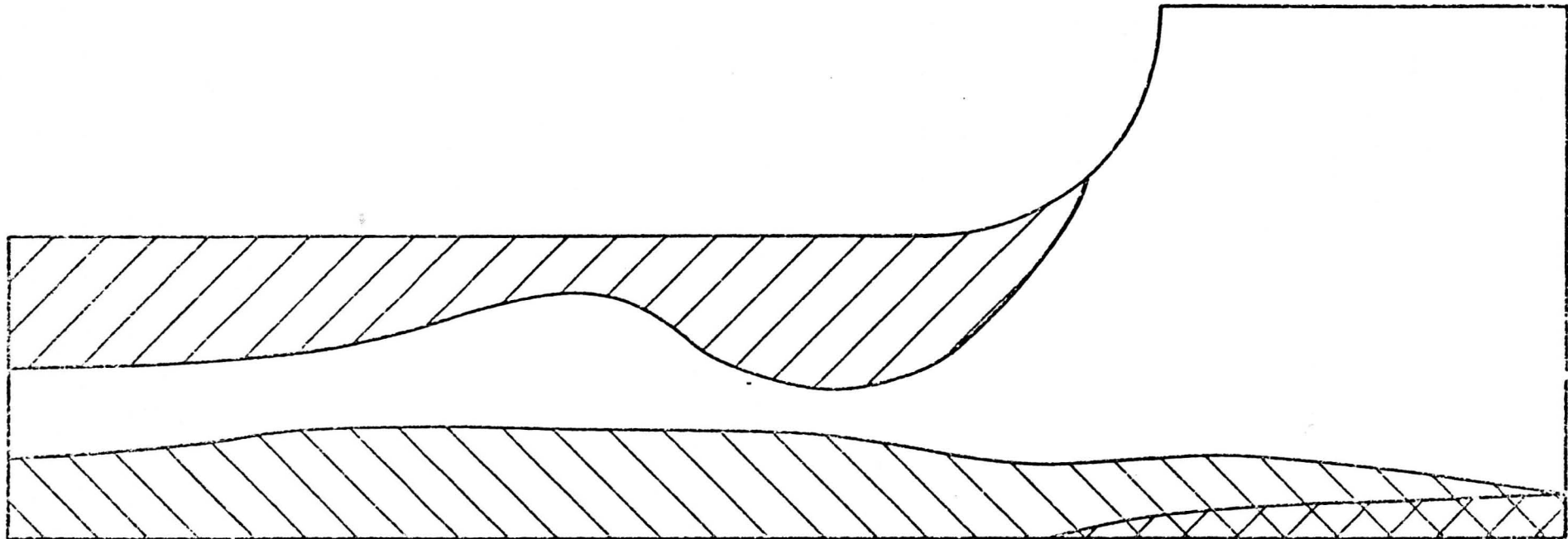


Figure 4.32 Flanged tube. Variation of elastic meridional thermal stress during the first half of a thermal shock.



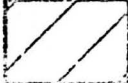
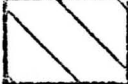
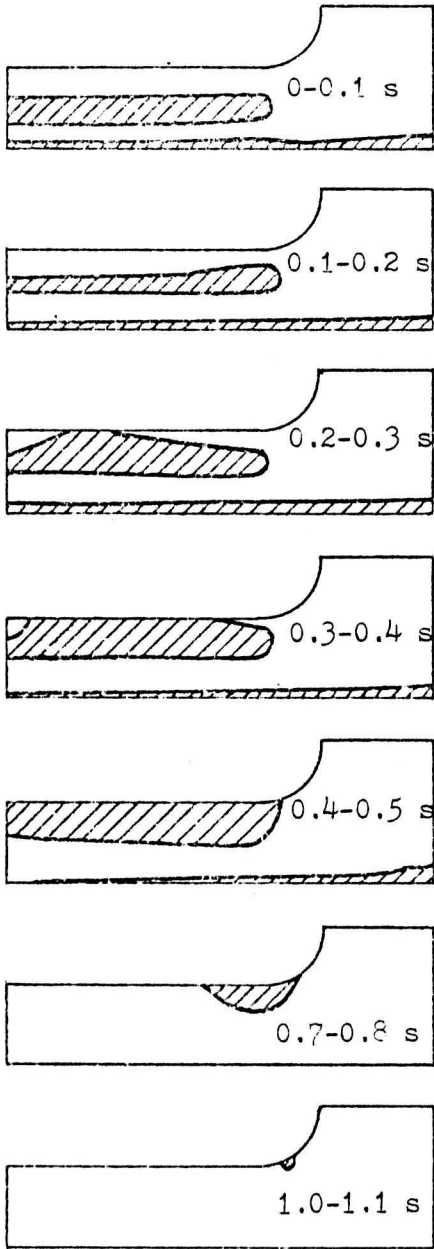
 1st half of cycle
 2nd half of cycle

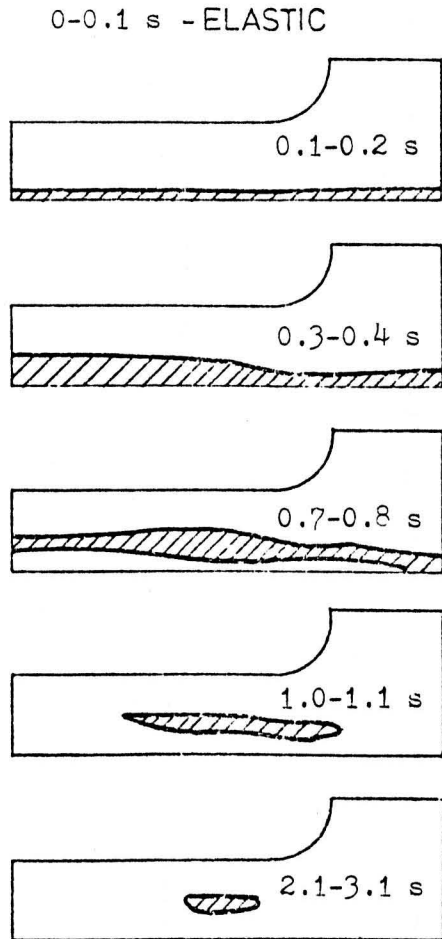
Figure 4.33 Flanged tube (elastic-perfectly-plastic, $\sigma_t/\sigma_y = 1.94$, $P/P_L = 0.7$, 'no creep' conditions). Regions of yielding during the first and second halves of the first thermal shock.

1st half of cycle (heating)



1.1 - 20 s ELASTIC

2nd half of cycle (cooling)



3.1-20 s - ELASTIC

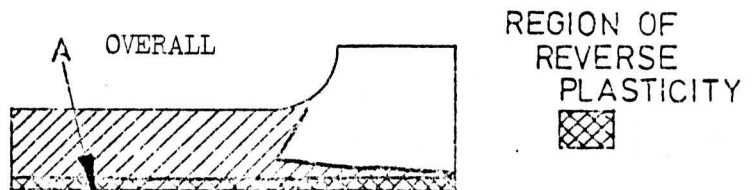


Figure 4.34 Flanged tube. (Elastic-perfectly-plastic, $\sigma_t/\sigma_y = 1.94$, $P/P_L = 0.7$, 'no creep' conditions). Regions of additional plastic straining during the 10th thermal cycle.

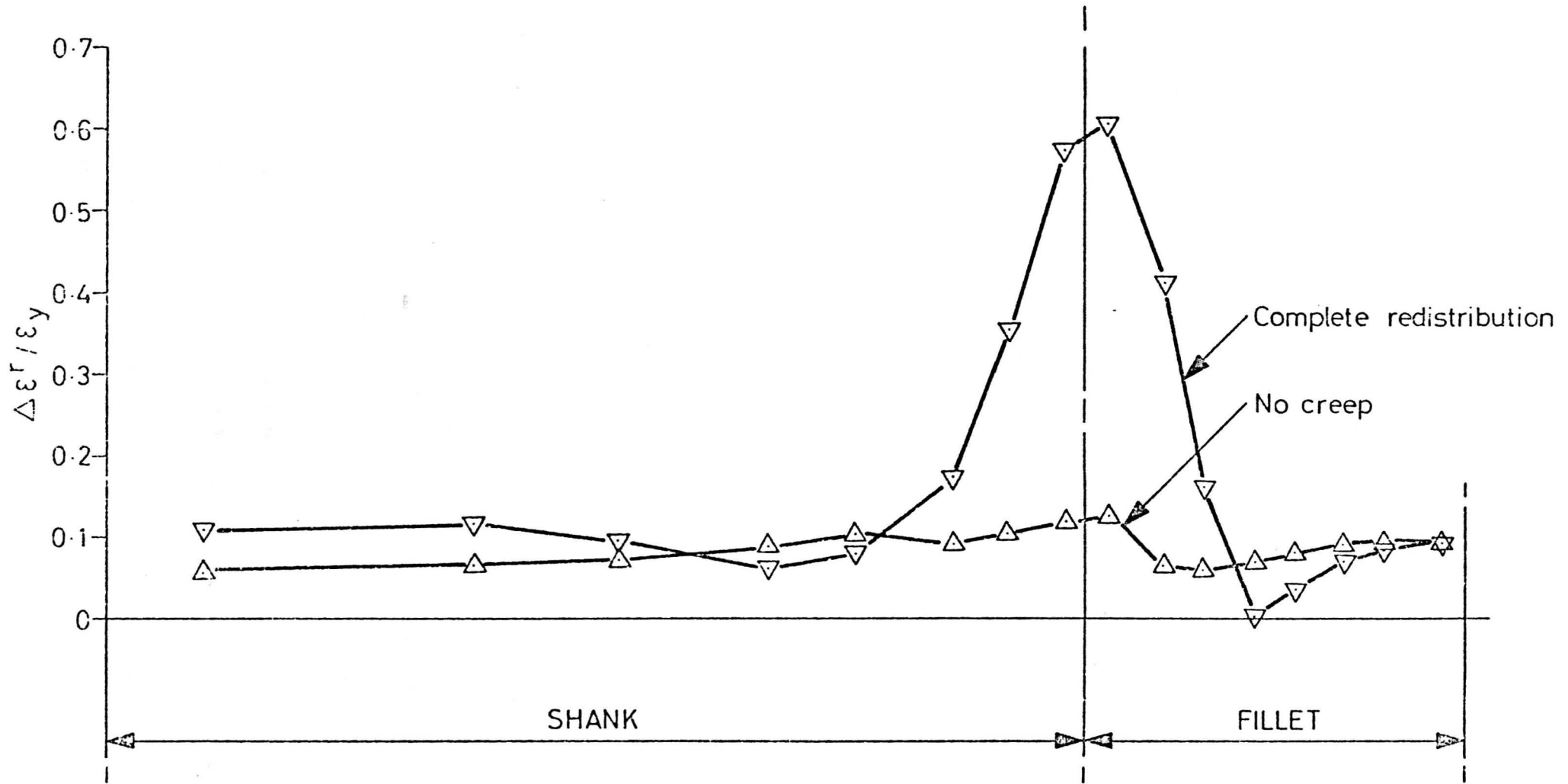
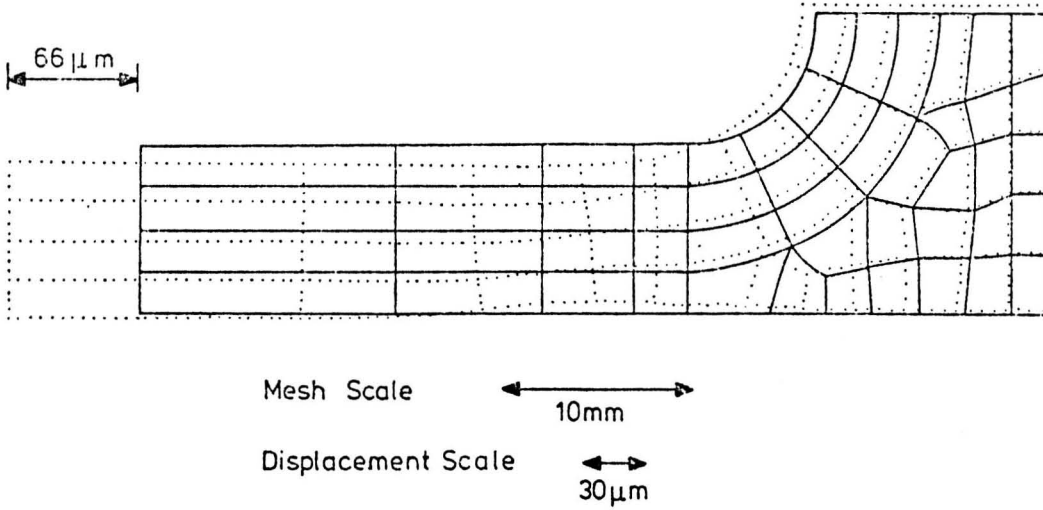


Figure 4.35 Flanged tube. (Elastic-perfectly-plastic, $\sigma_t/\sigma_y = 1.94$, $P/P_L = 0.7$).
 Distribution of steady state normalised meridional ratchet strain along the outside 'surface'.
 (see Figure 4.23).

a) end of the 10th shock



b) resulting from the 11th shock

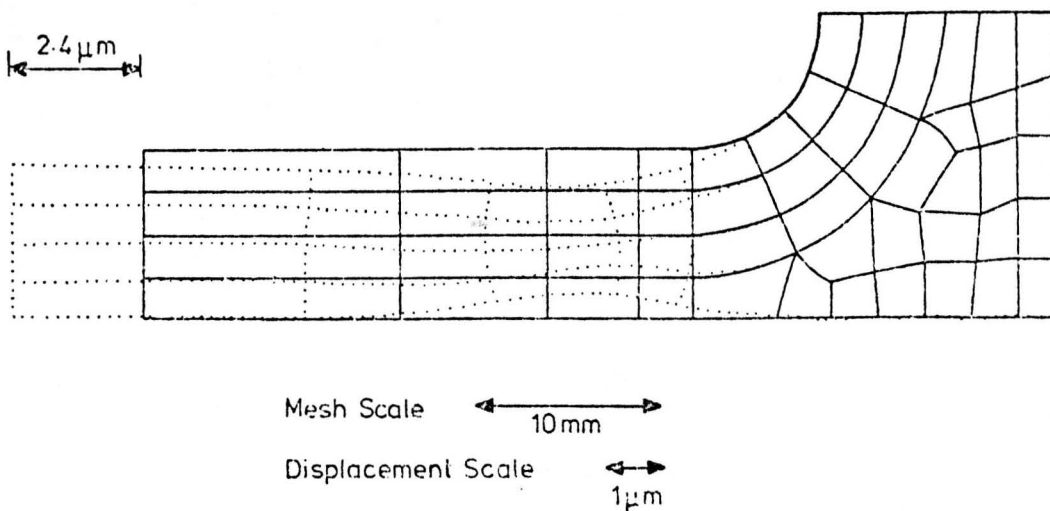


Figure 4.36 Flanged tube. (Elastic-perfectly-plastic, $\sigma_t/\sigma_y = 1.94$, $P/P_L = 0.7$, 'no creep' condition). 'Exaggerated' nodal displacements.

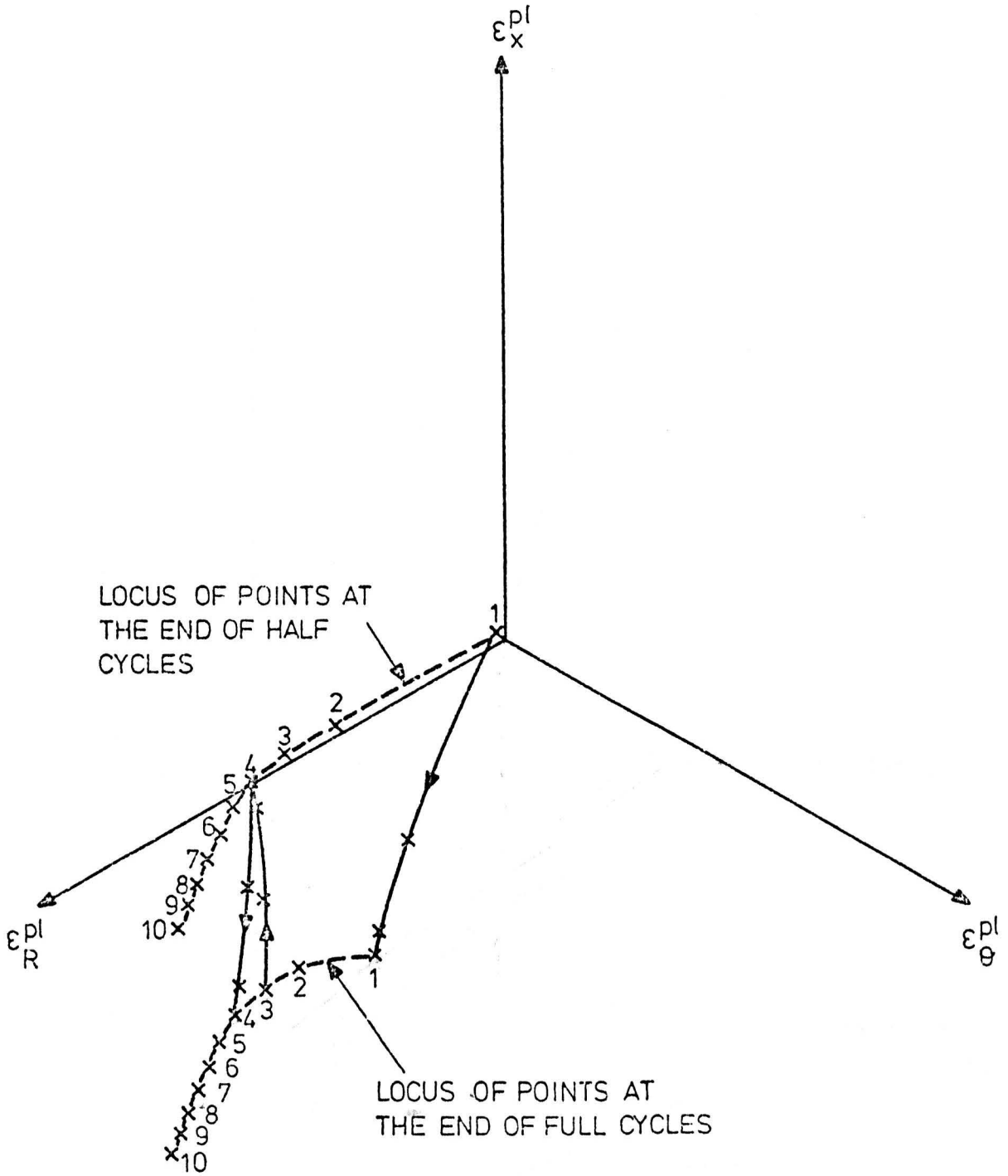


Figure 4.37 Flanged tube. (Elastic-perfectly-plastic, $\sigma_t/\sigma_y = 1.94$, $P/P_L = 0.7$, 'no creep' conditions). Cyclic variation in the components of plastic strain at point A in the reverse plasticity region (see Figure 4.34).

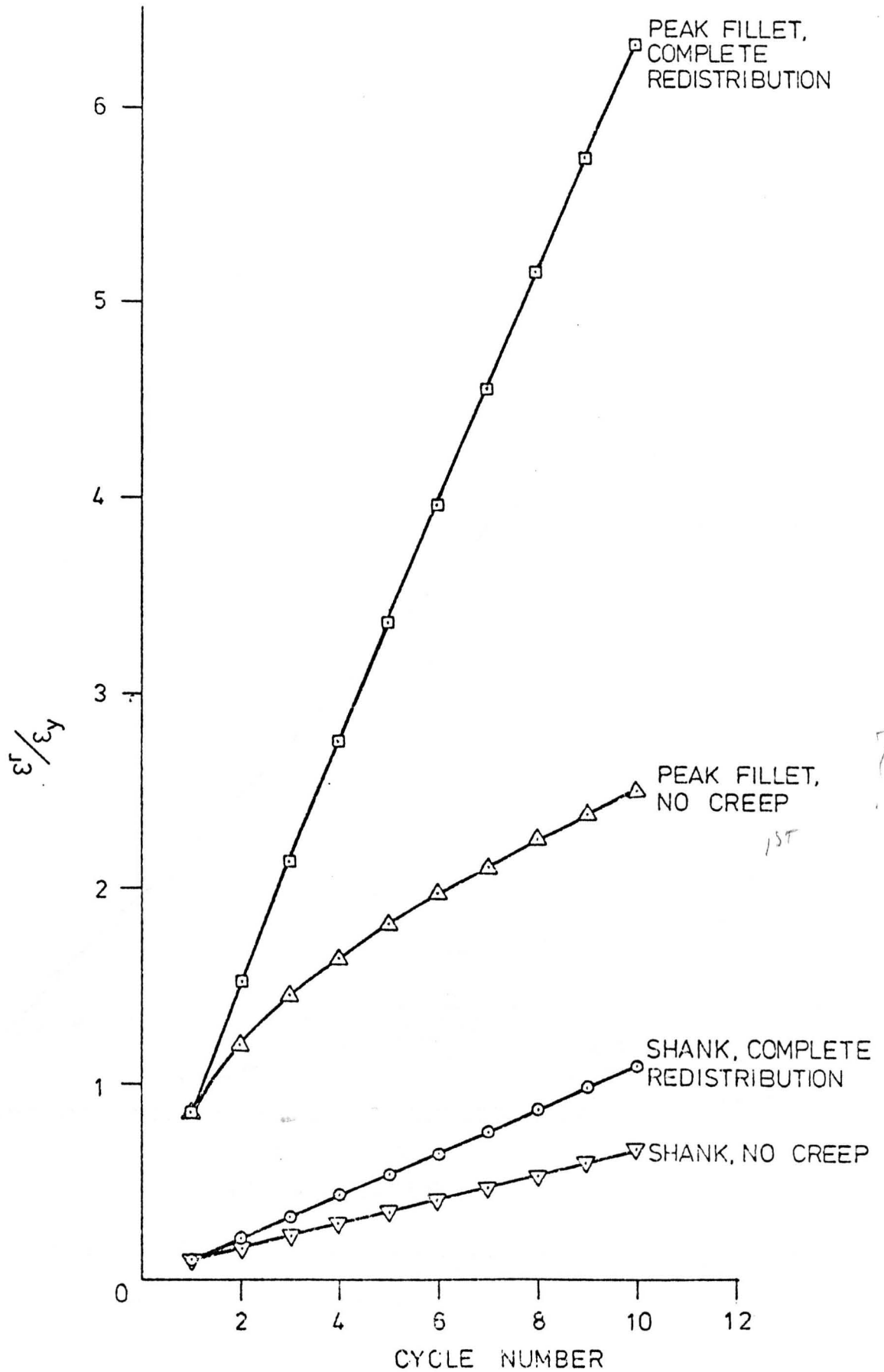


Figure 4.38 Flanged tube. (Elastic-perfectly-plastic, $\sigma_t/\sigma_y = 1.94$, $P/P_L = 0.7$). Accumulation of normalised ratchet strain during the first 10 cycles.

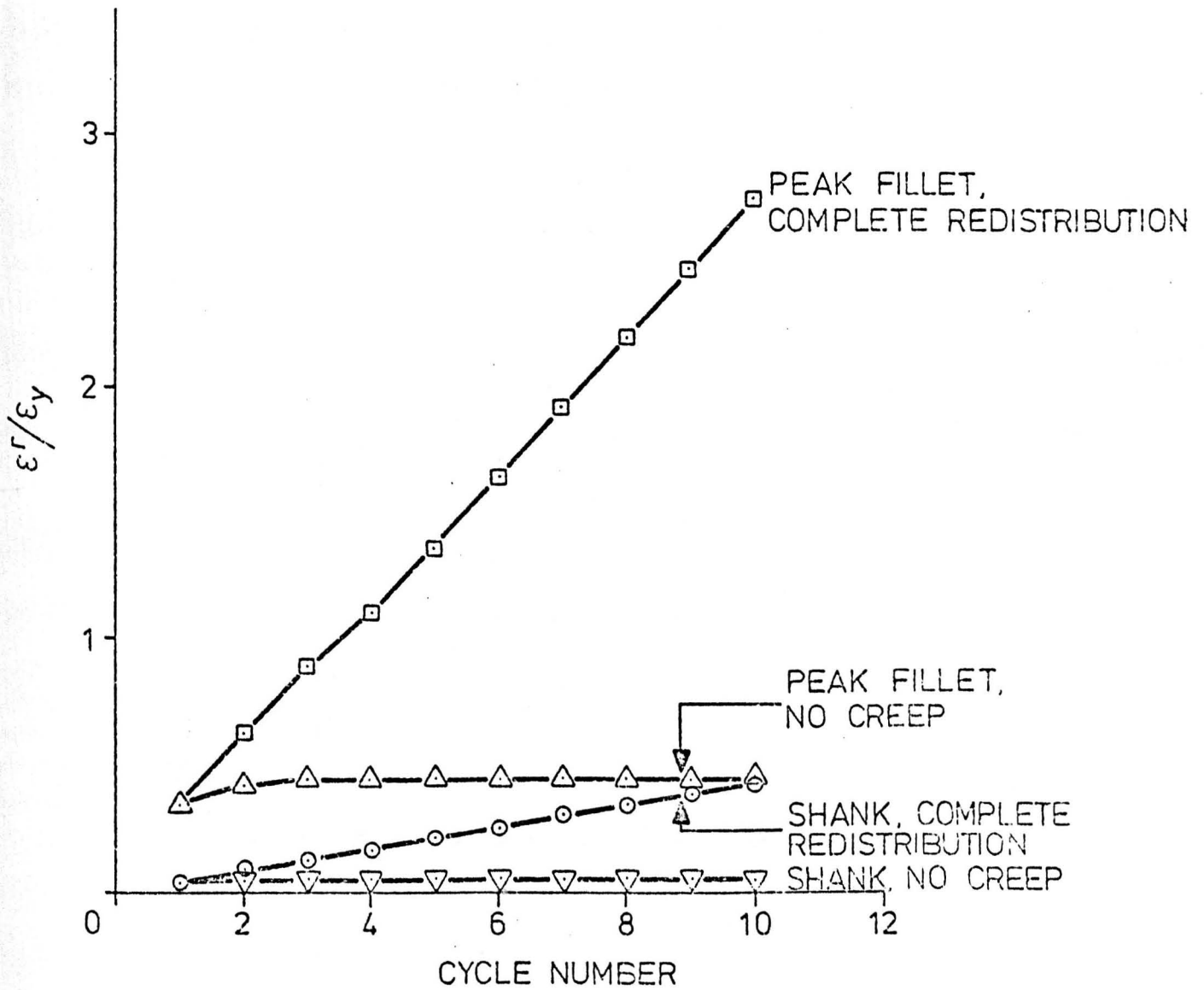


Figure 4.39 Flanged tube. (Elastic-perfectly-plastic, $\sigma_t/\sigma_y = 1.94$, $P/P_L = 0.5$). Accumulation of normalised ratchet strain during the first 10 cycles.

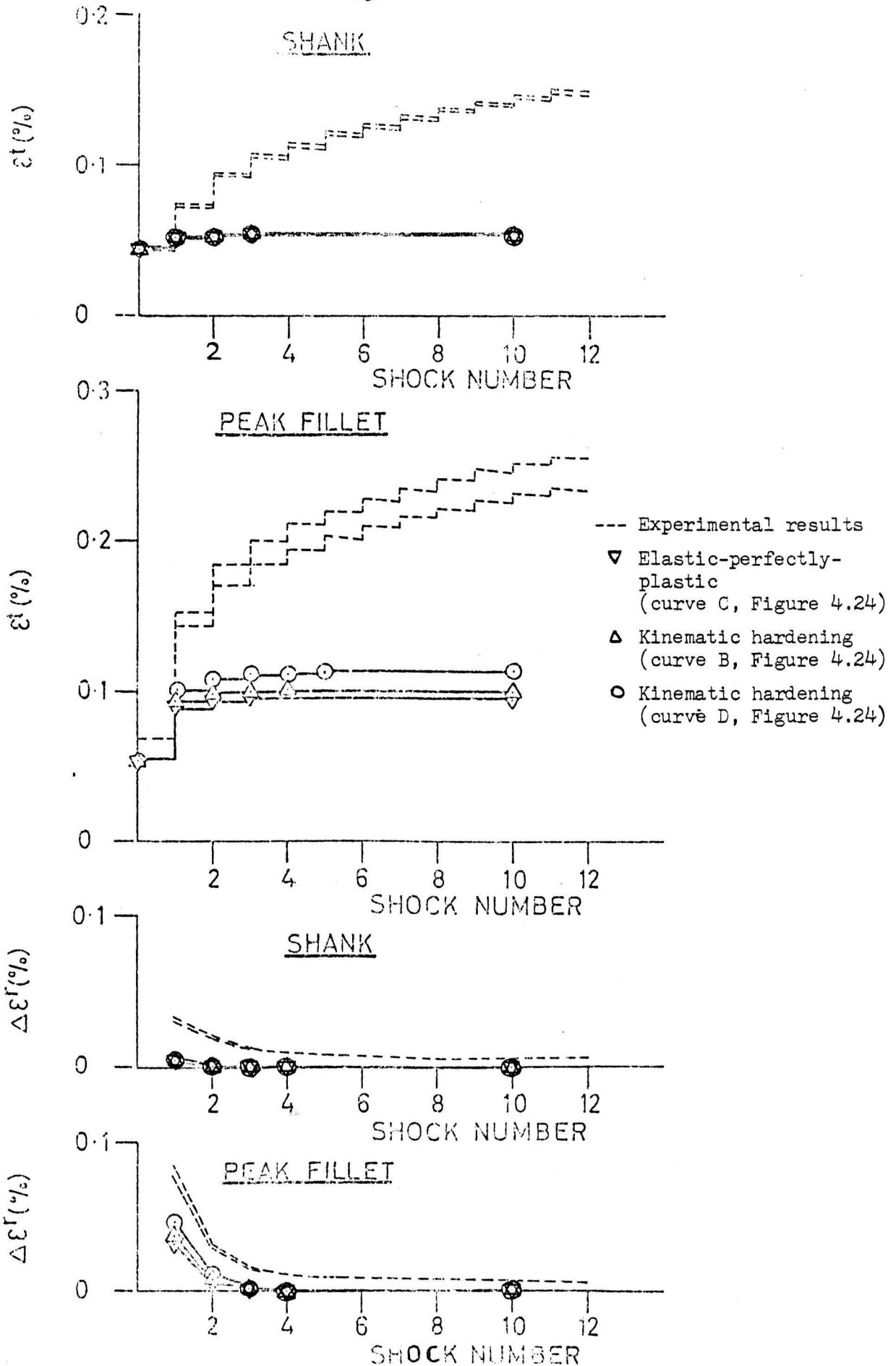


Figure 4.40 Flanged tube. Comparison between experimental results ($P/P_L = 0.5$, 'rapid cycling') and finite element predictions ($P/P_L = 0.5$, 'no creep' conditions) of total strain and ratchet strain.

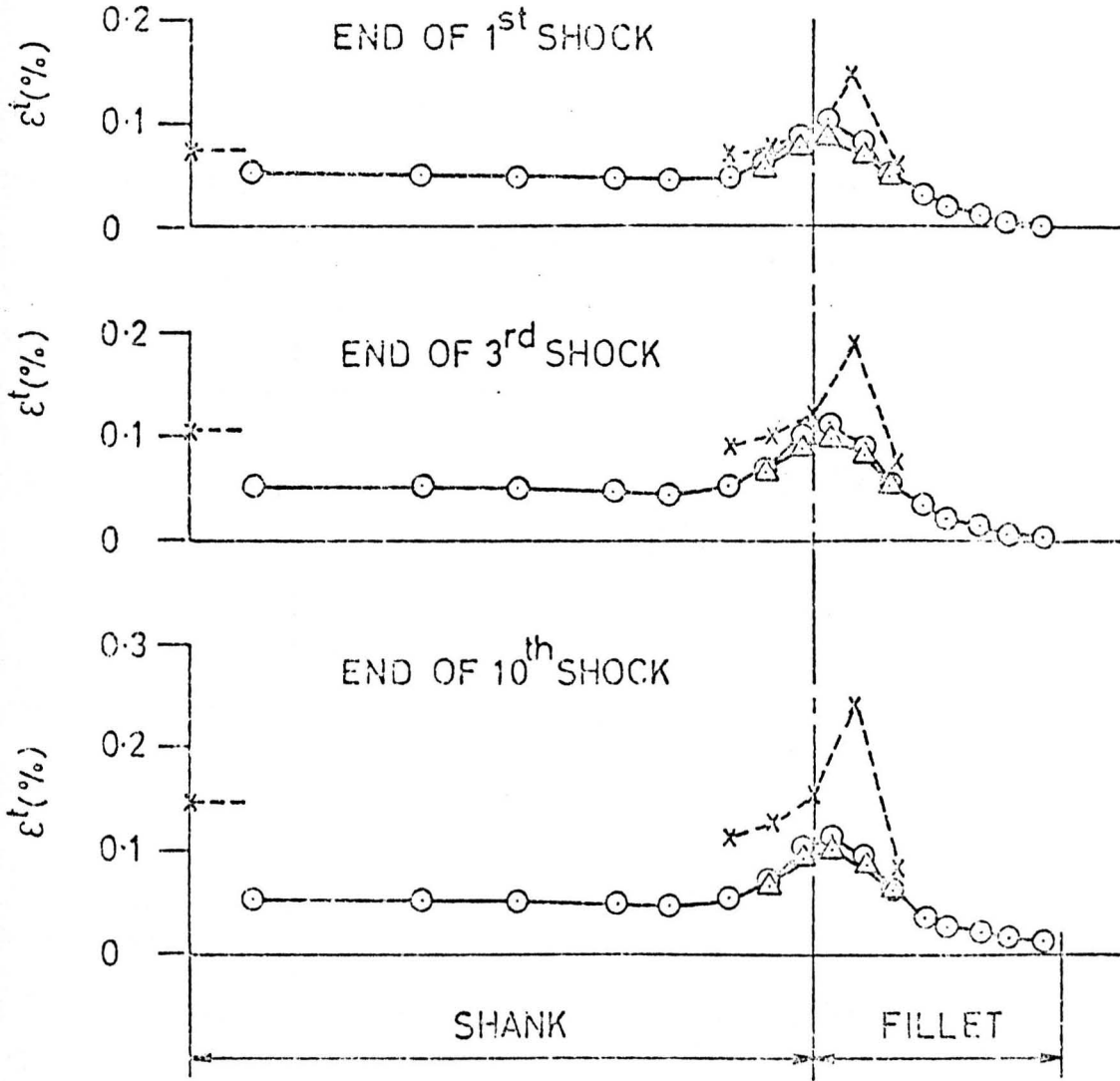


Figure 4.41 Flanged tube. Comparison between experimental results ($P/P_L = 0.5$, 'rapid cycling') and finite element predictions ($P/P_L = 0.5$, 'no creep' conditions) of total strain distributions along the outside surface. (See Figure 4.40 for notation).

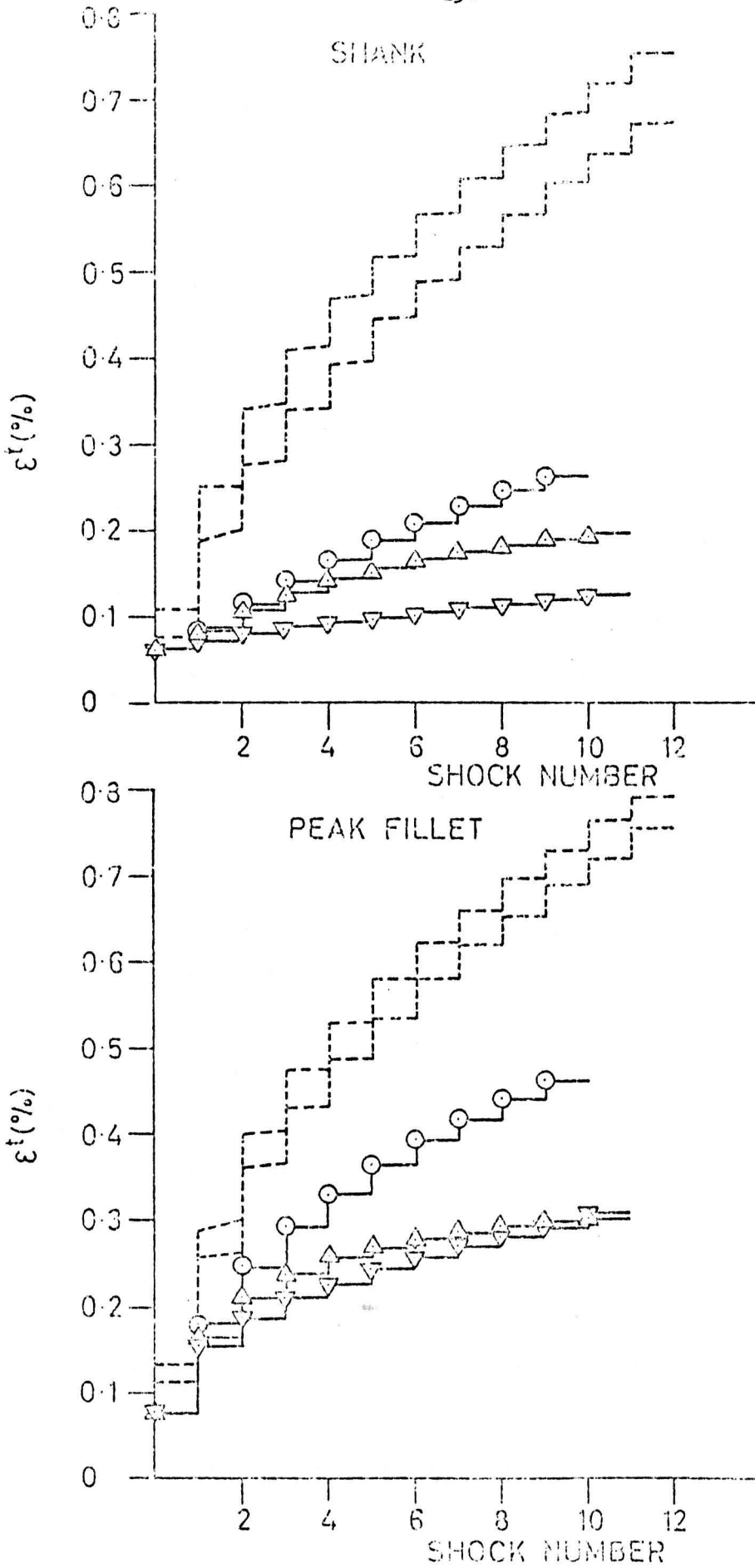


Figure 4.42(a) Flanged tube. Comparison between experimental results ($P/P_L = 0.7$, 'rapid cycling') and finite element predictions ($P/P_L = 0.7$, 'no creep' conditions) of total strain. (See Figure 4.40 for notation).

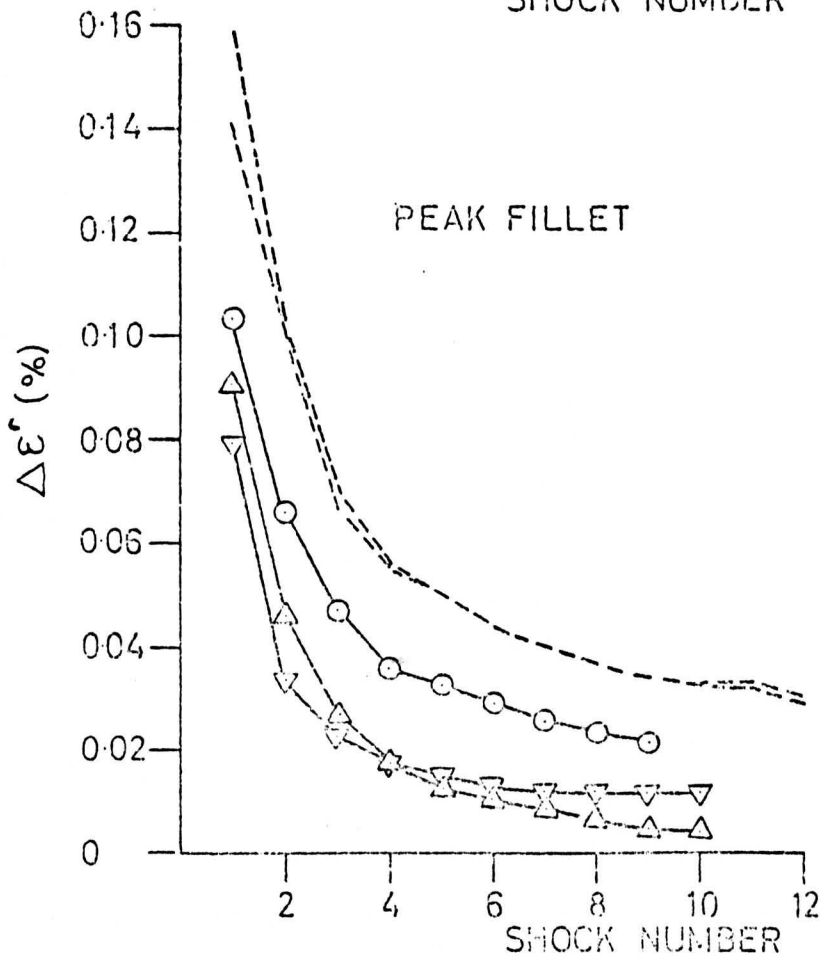
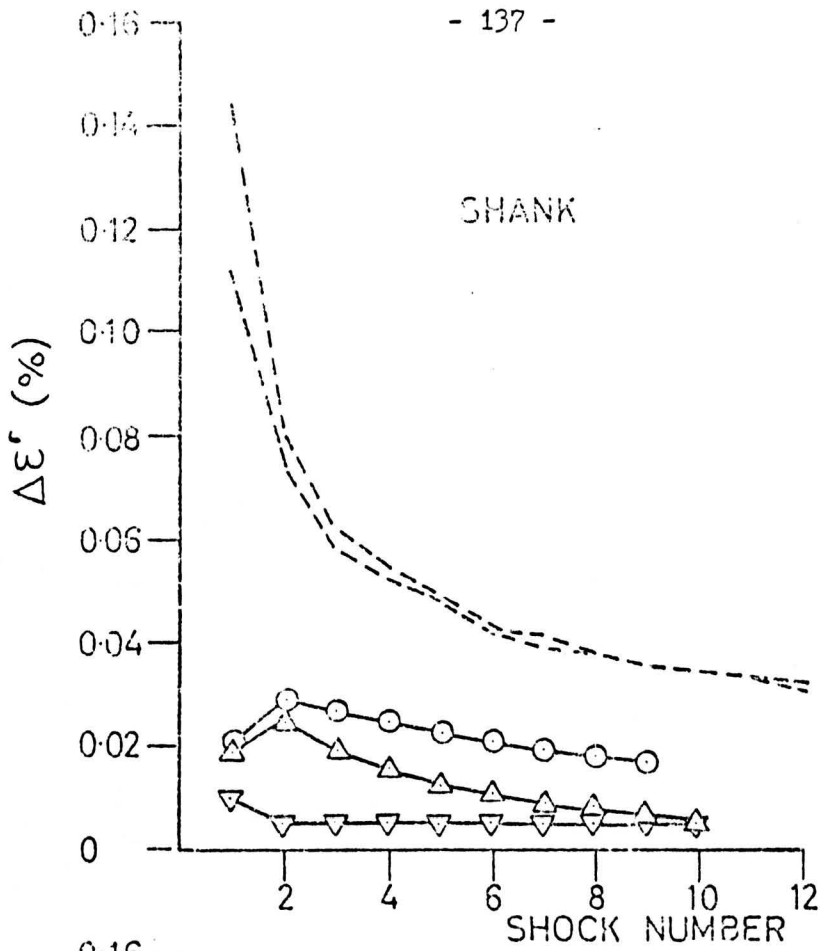


Figure 4.42(b) Flanged tube. Comparison between experimental results ($P/P_L = 0.7$, 'rapid cycling') and finite element predictions ($P/P_L = 0.7$, 'no creep' conditions) of ratchet strain. (See Figure 4.40 for notation).

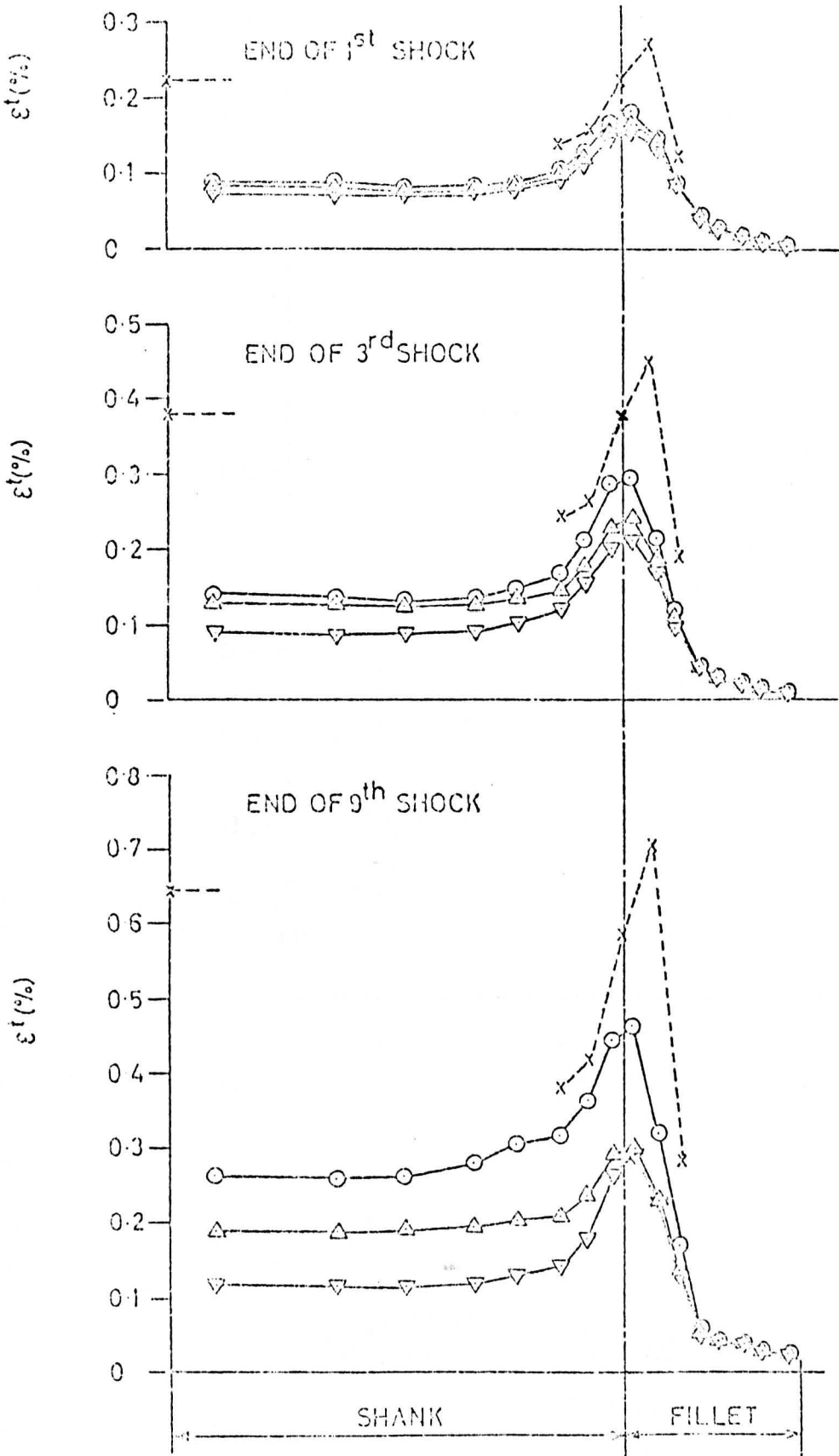


Figure 4.43 Flanged tube. Comparison between experimental results ($P/P_L = 0.7$, 'rapid cycling') and finite element predictions ($P/P_L = 0.7$, 'no creep' conditions) of total strain distributions along the outside surface (see Figure 4.40 for notation).

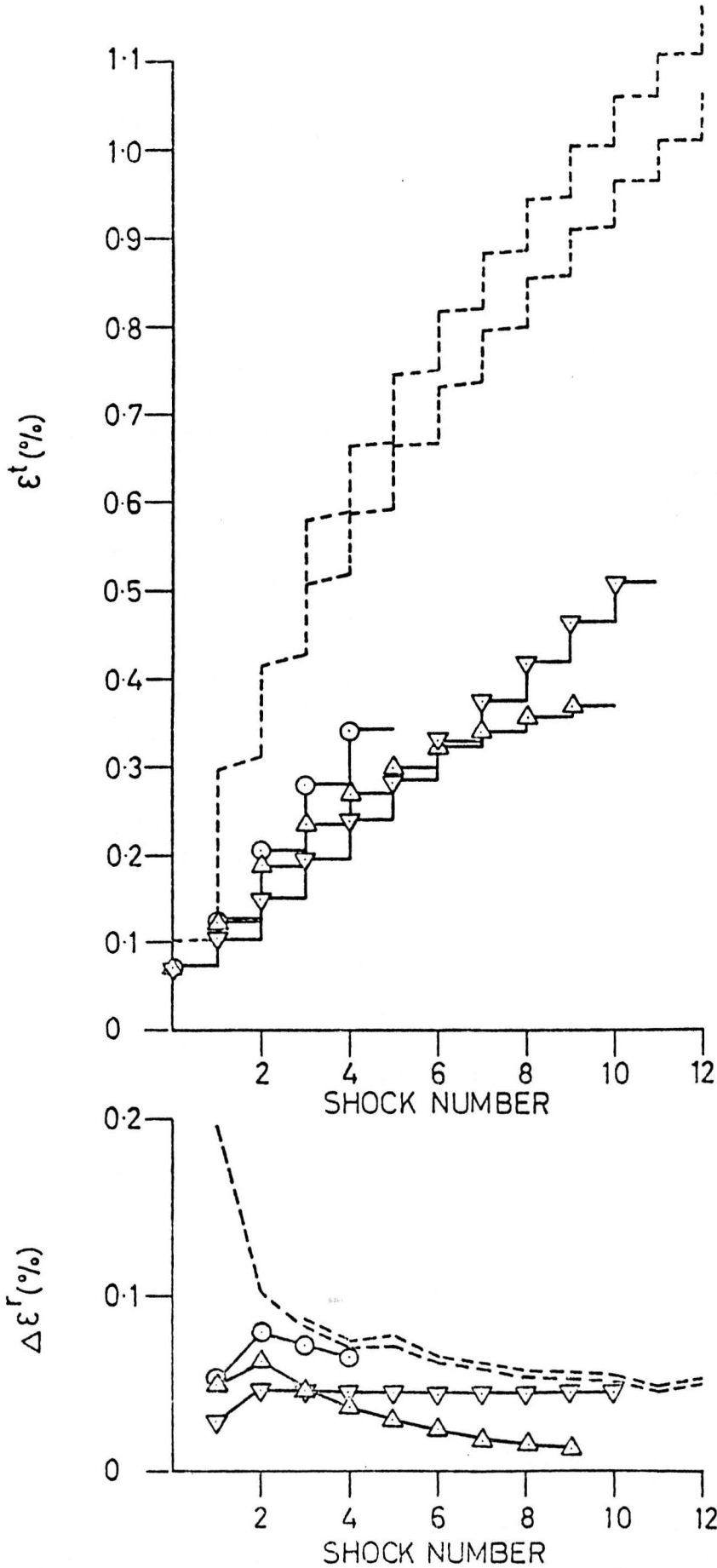
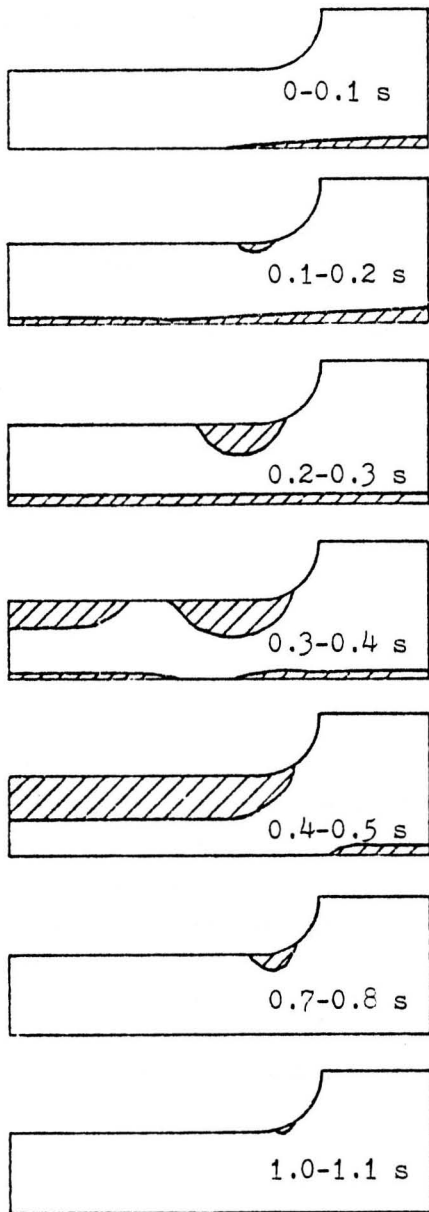


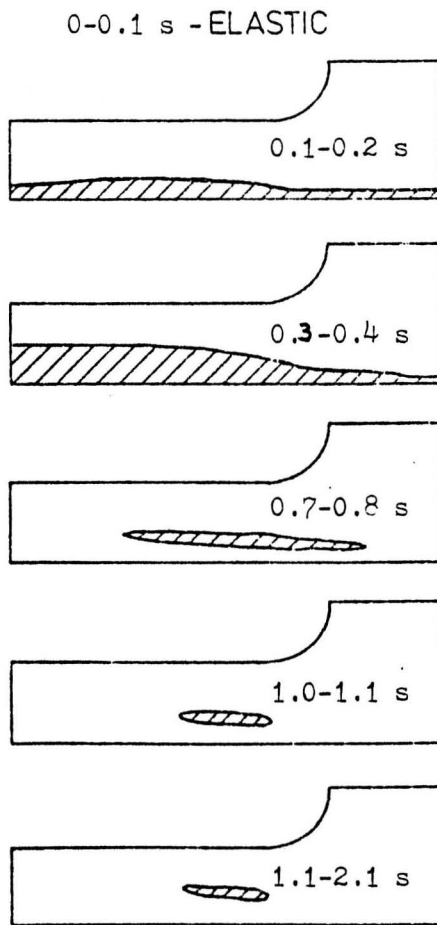
Figure 4.44 Flanged tube shank. Comparison between experimental results ($P/P_L = 0.8$, 'rapid cycling') and finite element predictions ($P/P_L = 0.8$, 'no creep') of total strain and ratchet strain. (See Figure 4.40 for notation).

1st half of cycle (heating)



1.1-20 s - ELASTIC

2nd half of cycle (cooling)



2.1-20 s - ELASTIC

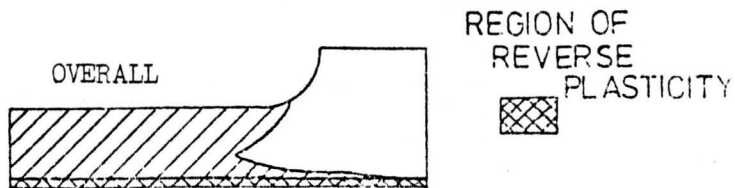
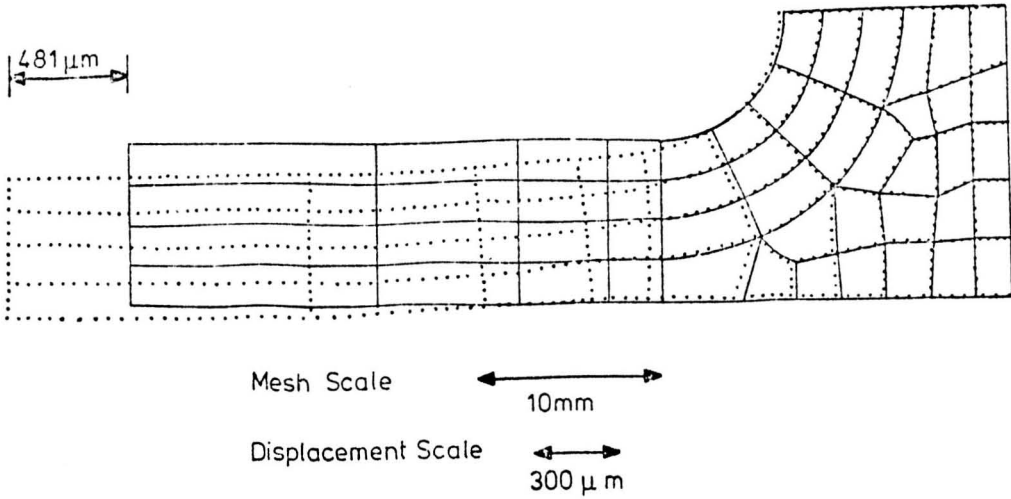
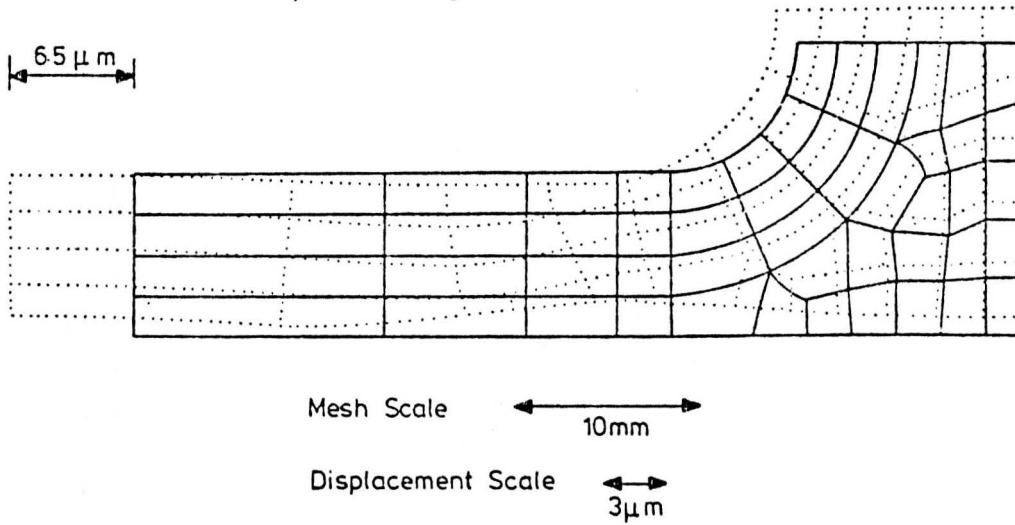


Figure 4.45 Flanged tube (Elastic-perfectly-plastic, $\sigma_t/\sigma_y = 1.94$, $P/P_L = 0.7$, complete redistribution). Regions of additional plastic straining during a steady state thermal cycle.

a) end of the 10th dwell period



b) resulting from the 11th shock



c) resulting from the 11th dwell period

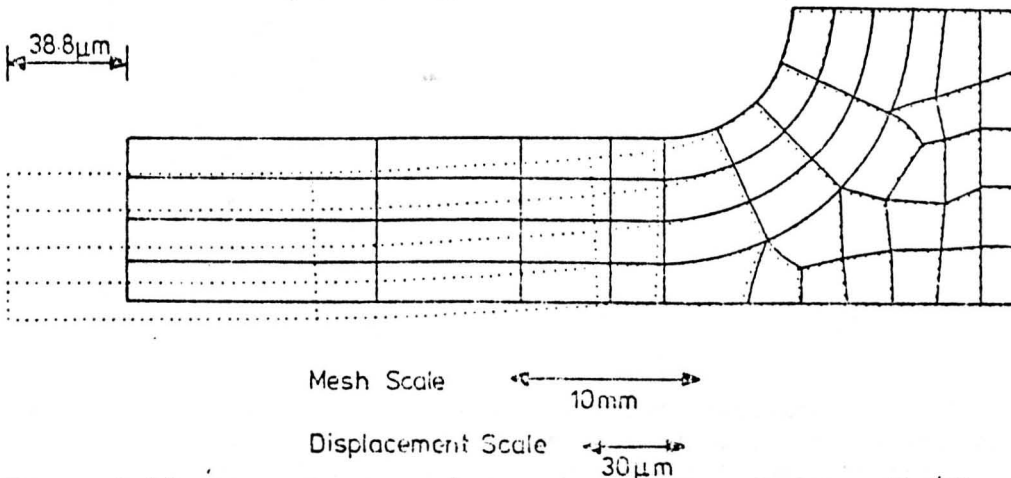


Figure 4.46 Flanged tube. (Elastic-perfectly-plastic, $\sigma_t/\sigma_{y1} = 1.94$, $P/P_L = 0.7$, complete redistribution). Exaggerated nodal displacements.

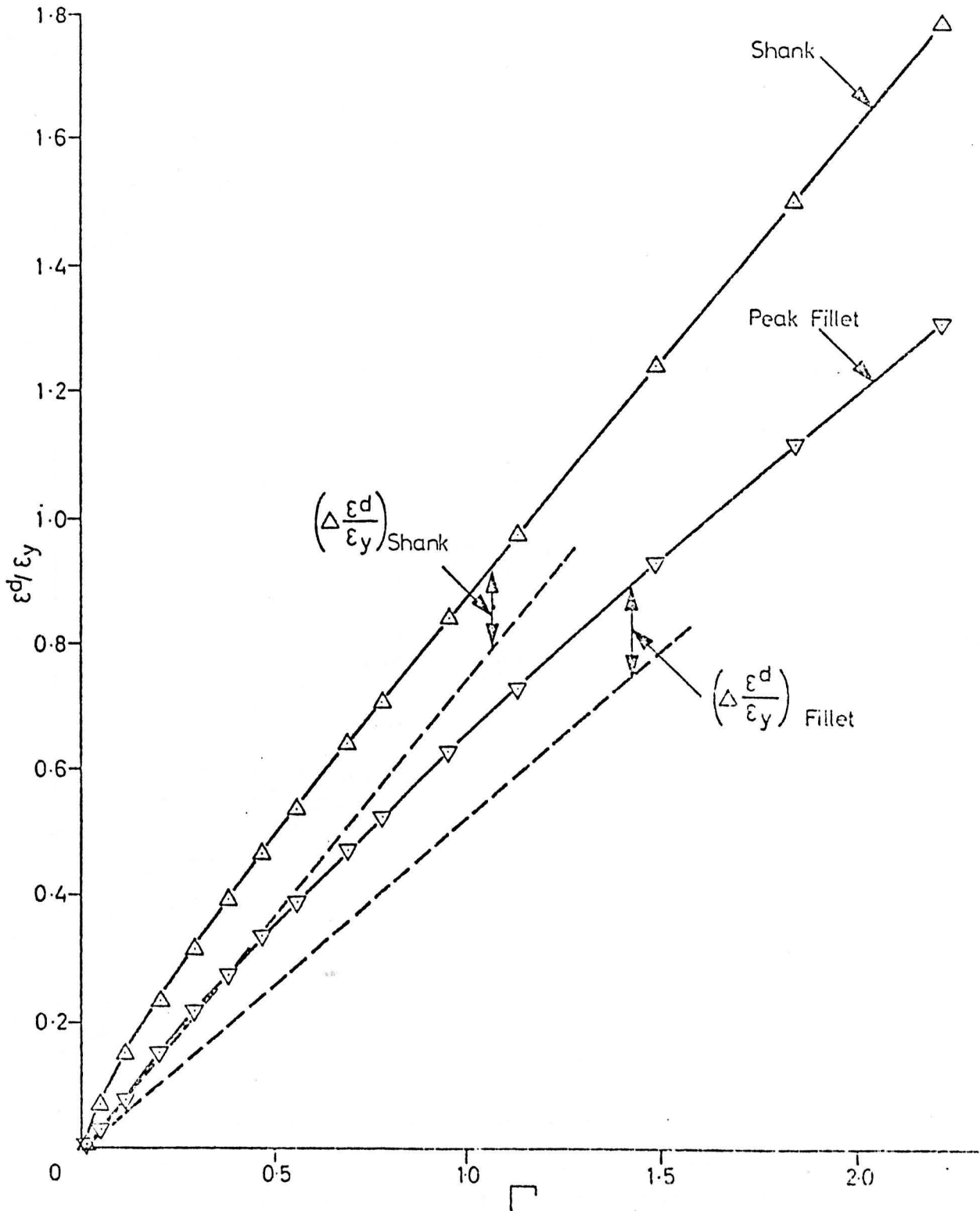


Figure 4.47 Flanged tube. (Elastic-perfectly-plastic, $\sigma_t/\sigma_y = 1.94$, $P/P_L = 0.7$, complete redistribution). Accumulation of normalised meridional strain during the first dwell period.

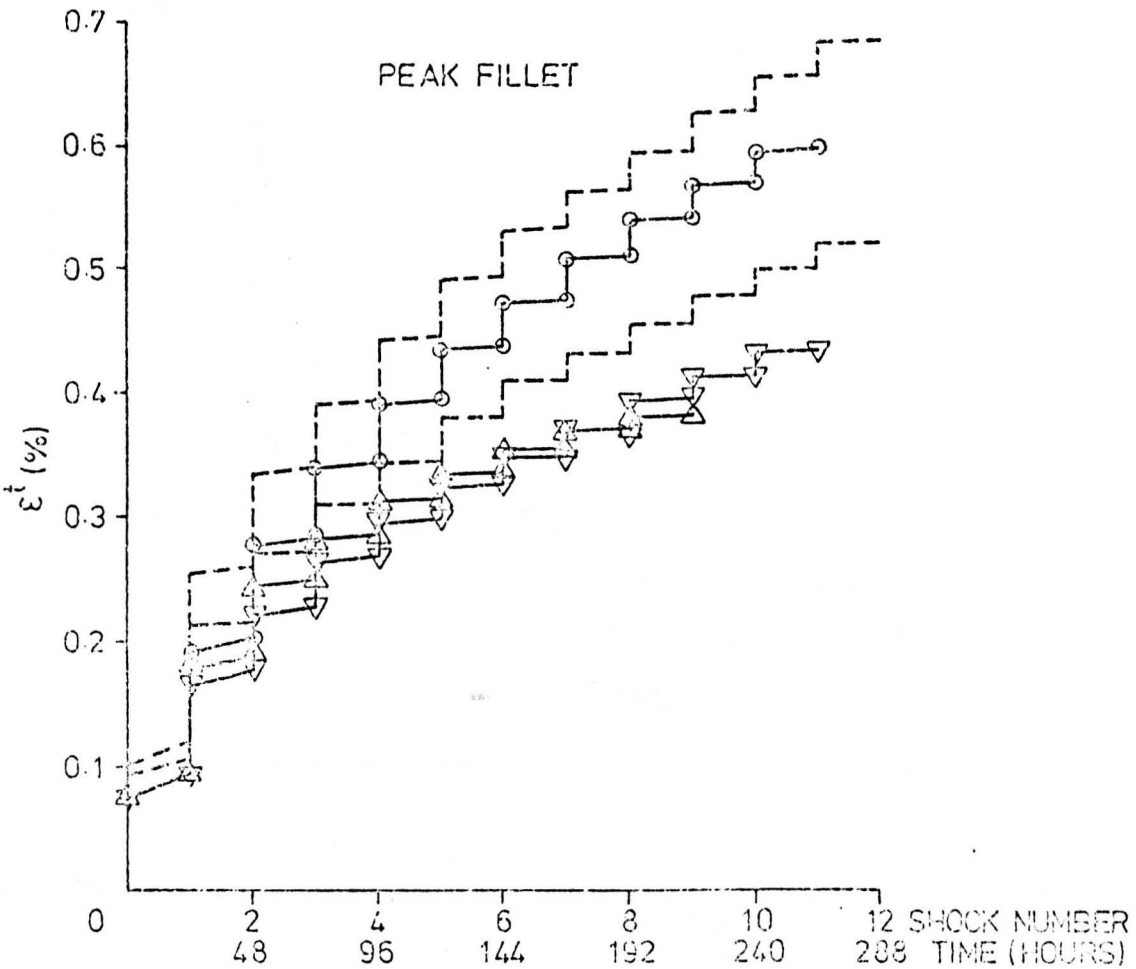
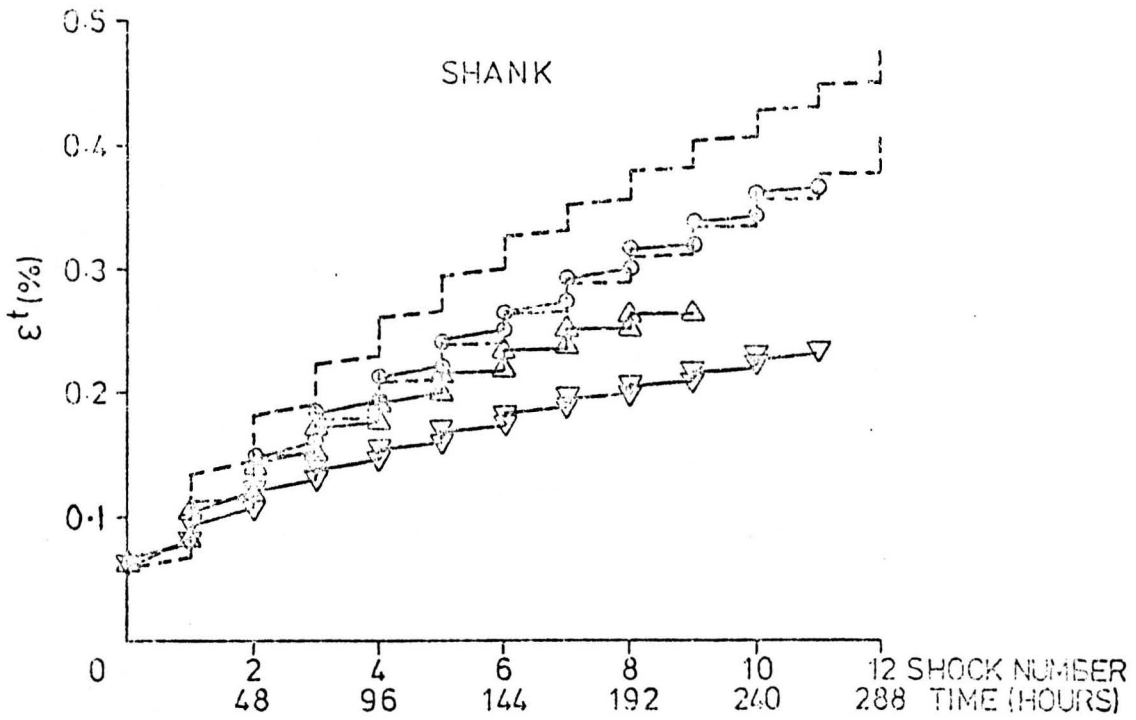


Figure 4.48(a) Flanged tube. ($P/P_L = 0.7$, 24 hour dwell periods). Comparison between experimental results and finite element predictions of total strain (see Figure 4.40 for notation).

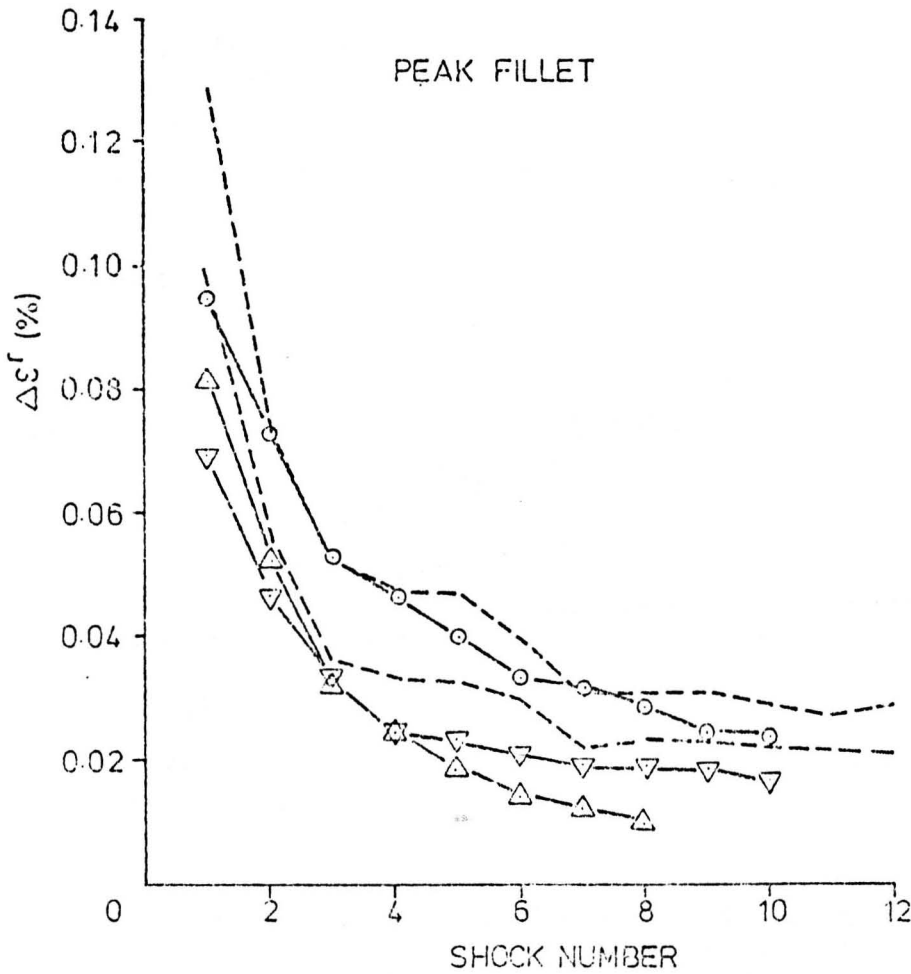
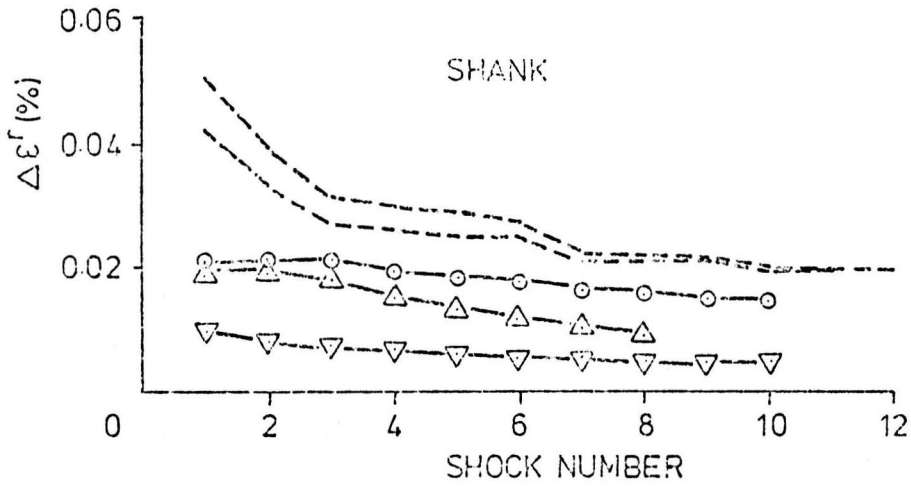


Figure 4.48(b) Flanged tube. ($P/P_L = 0.7$, 24 hour dwell periods). Comparison between experimental results and finite element predictions of ratchet strain (see Figure 4.40 for notation).

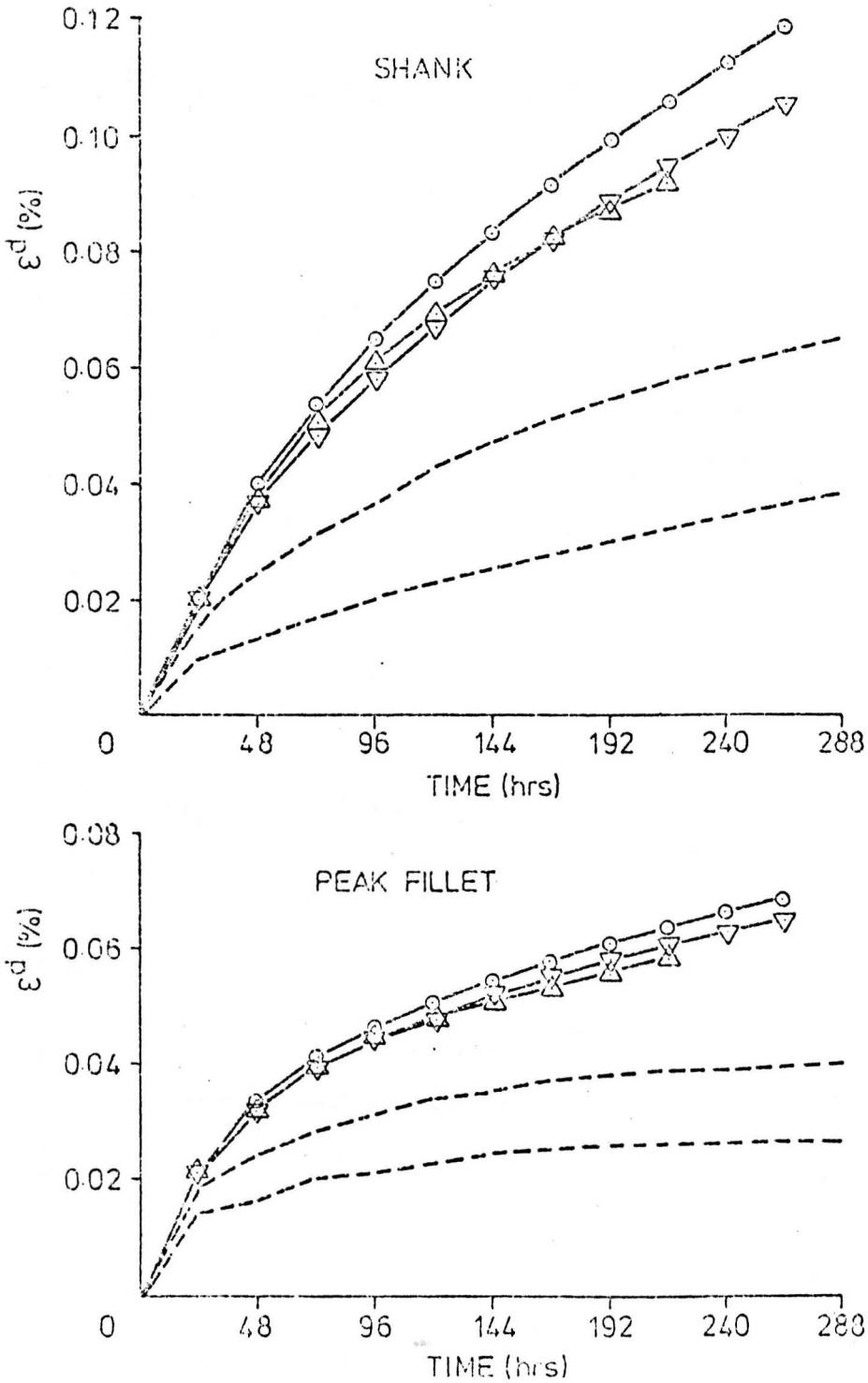


Figure 4.48(c) Flanged tube ($P/P_L = 0.7$, 24 hour dwell periods). Comparison between experimental results and finite element predictions of accumulated dwell period strain. (See Figure 4.40 for notation).

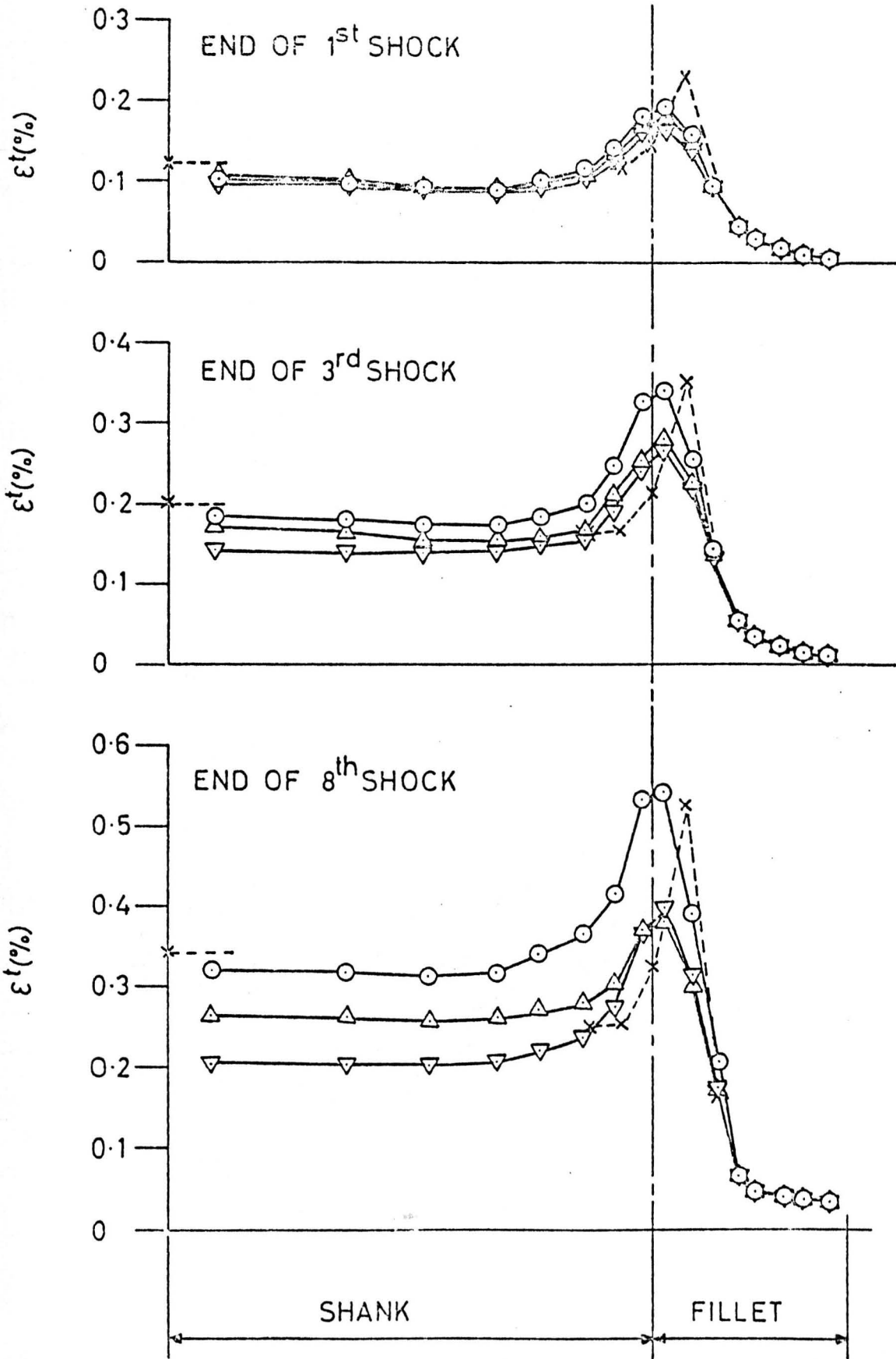


Figure 4.49 Flanged tube ($P/P_L = 0.7$, 24 hour dwell periods). Comparison between experimental results and finite element predictions of total strain distributions along the outside surface. (See Figure 4.40 for notation).

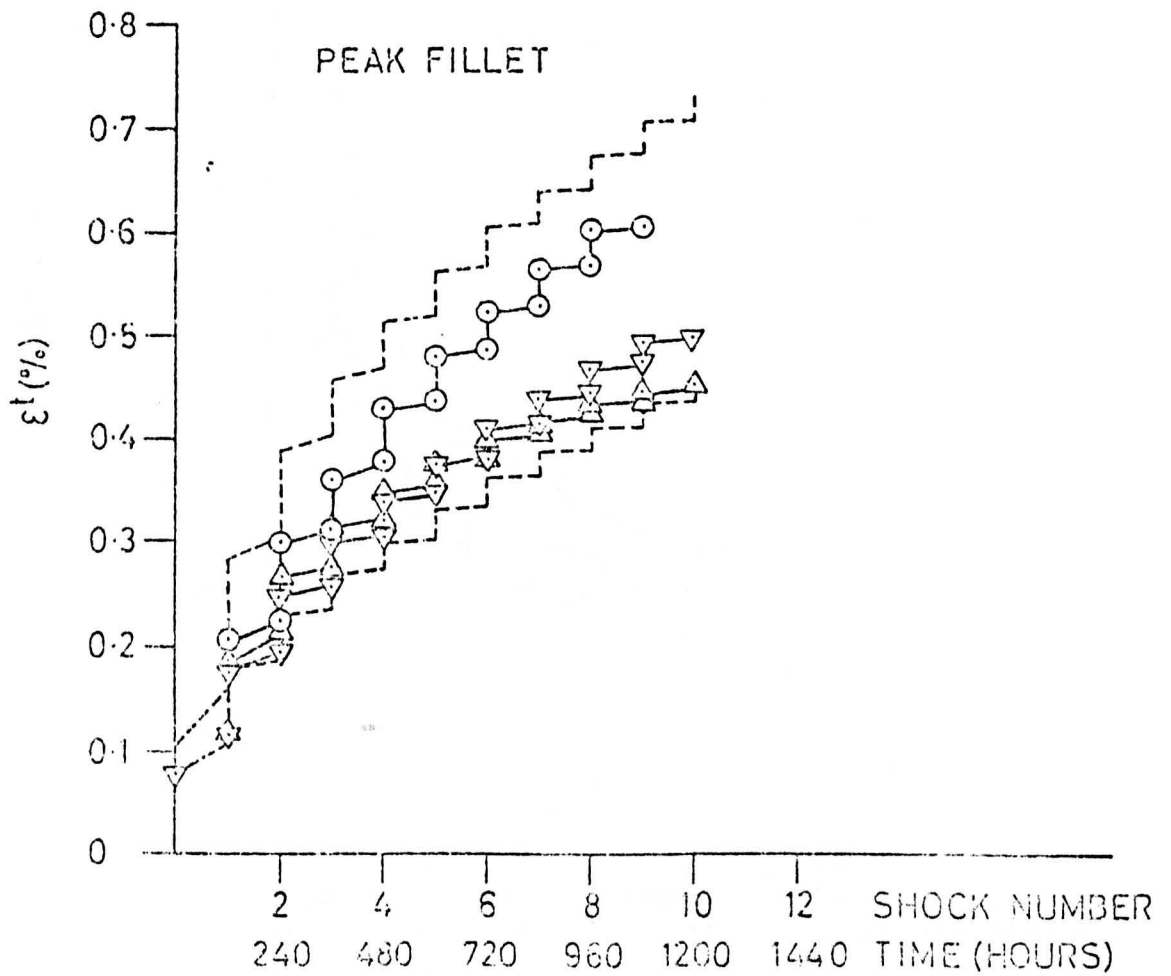
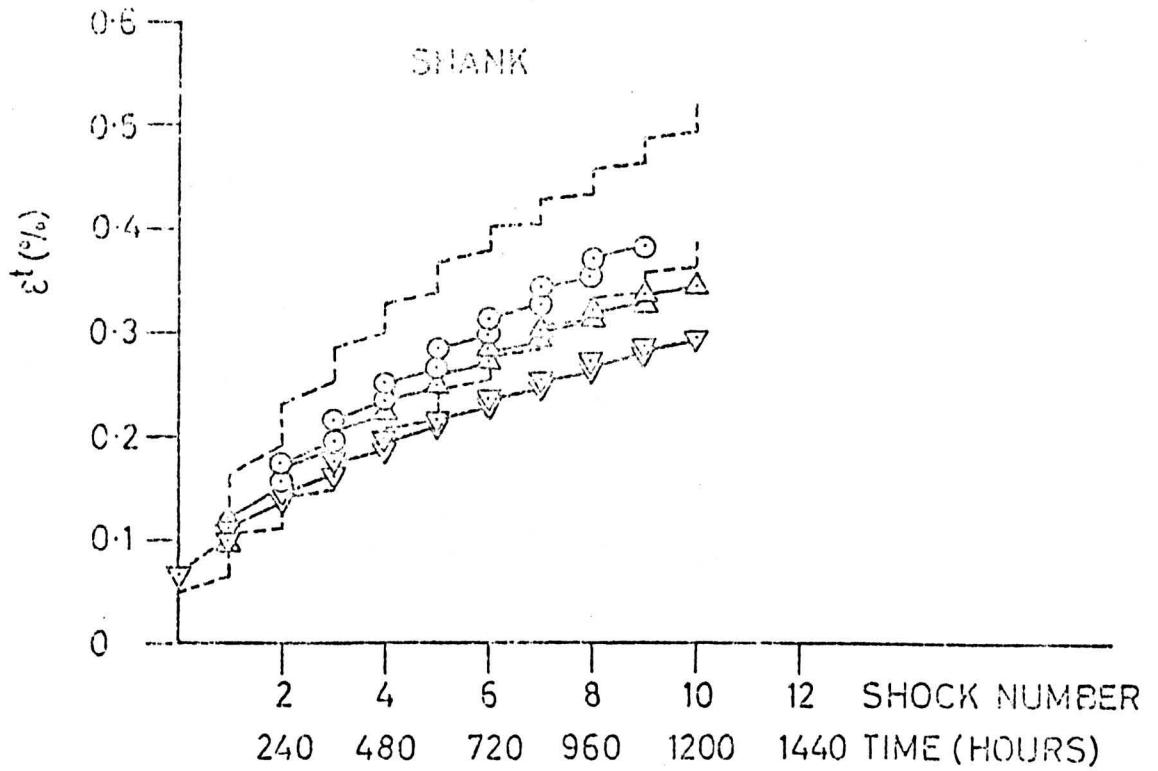


Figure 4.50(a) Flanged tube ($P/P_L = 0.7$, 120 hour dwell periods). Comparison between experimental results and finite element predictions of total strain (see Figure 4.40 for notation).

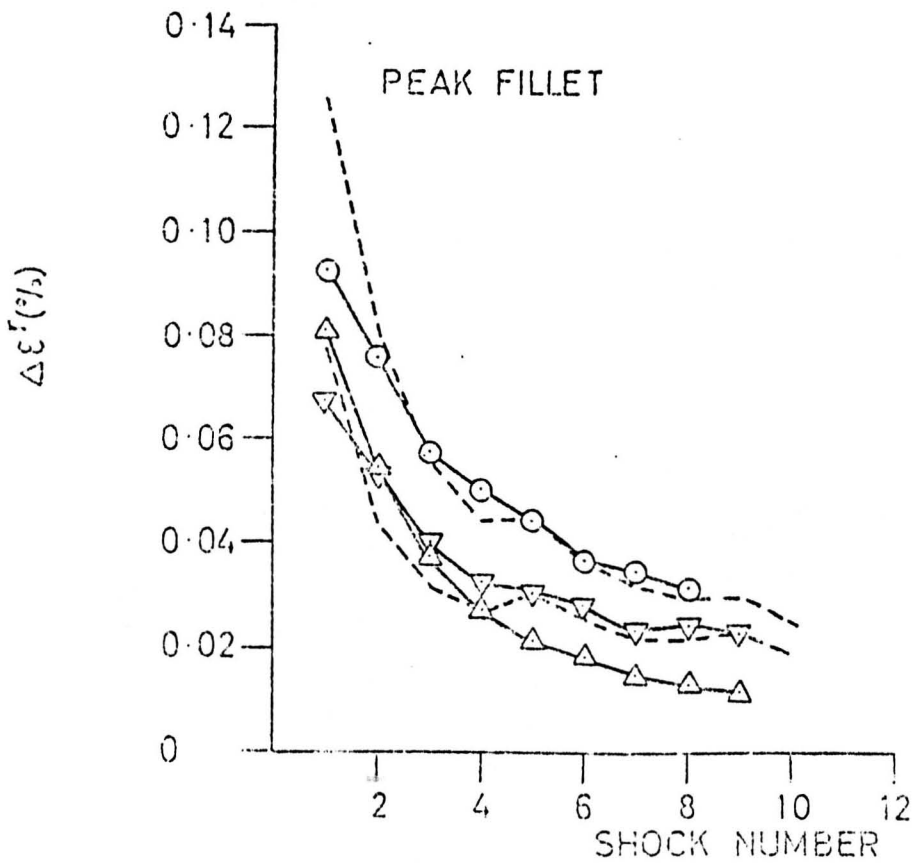
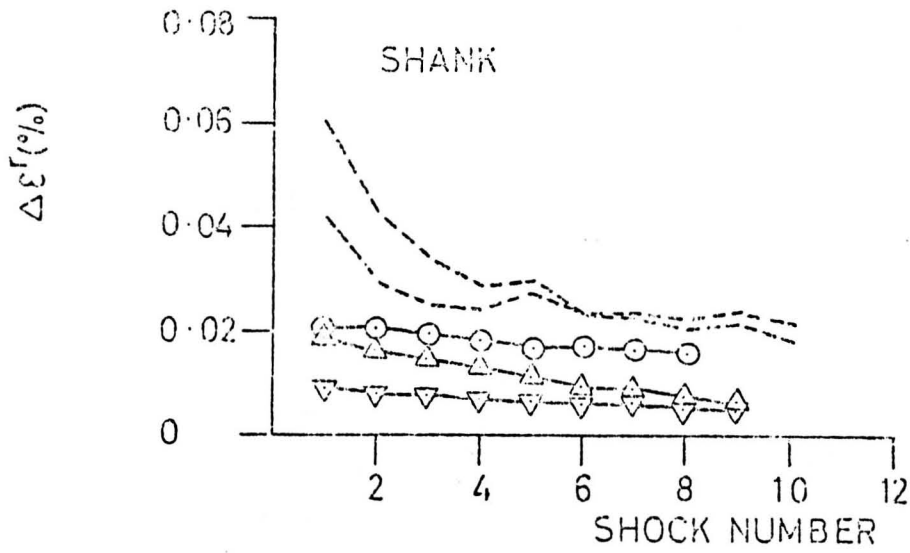


Figure 4.50(b) Flanged tube ($P/P_L = 0.7$, 120 hour dwell periods). Comparison between experimental results and finite element predictions of ratchet strain (see Figure 4.40 for notation).

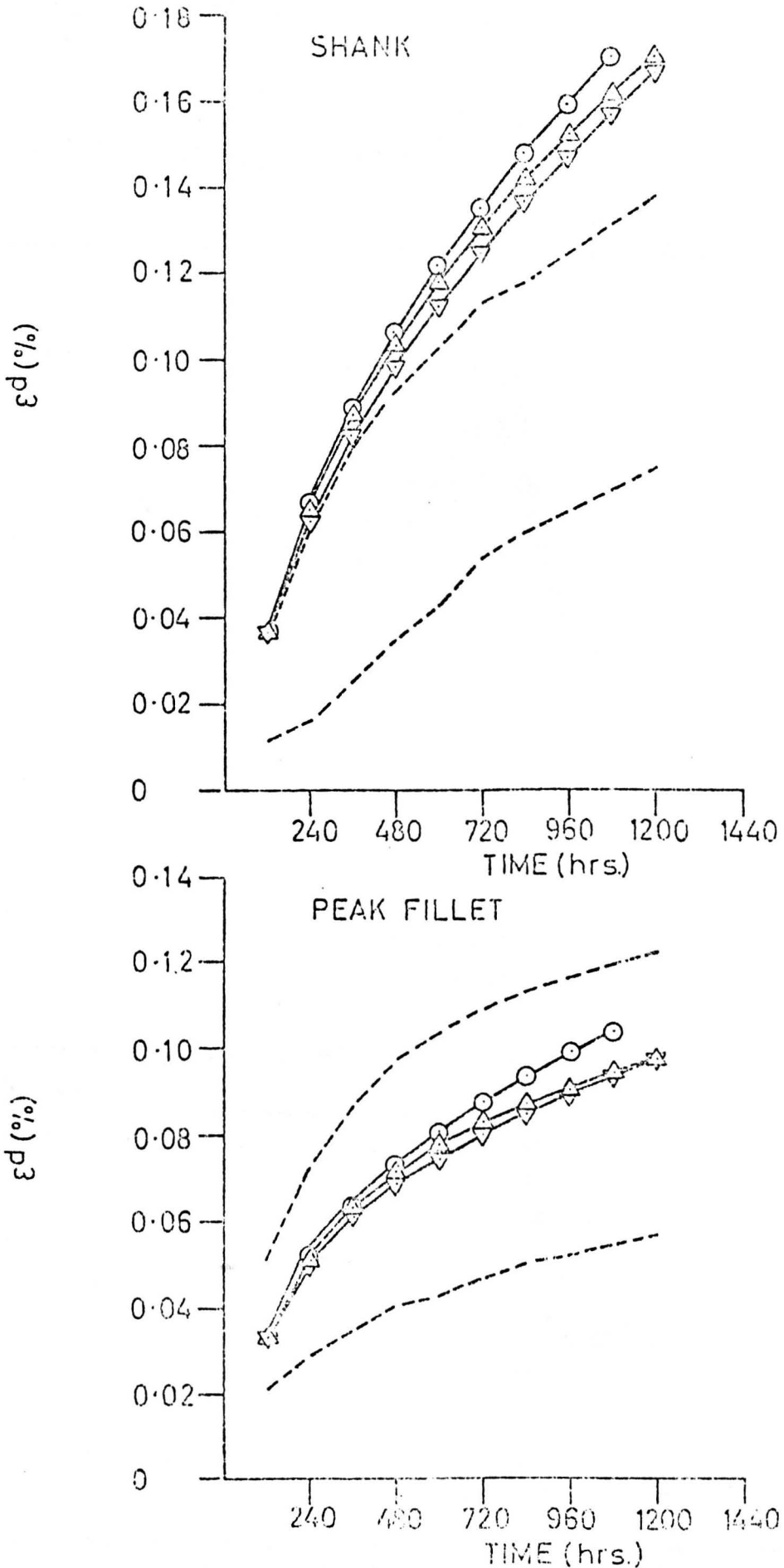


Figure 4.50(c) Flanged tube ($P/P_L = 0.7$, 120 hour dwell periods). Comparison between experimental results and finite element predictions of accumulated dwell period strain (see Figure 4.40 for notation)

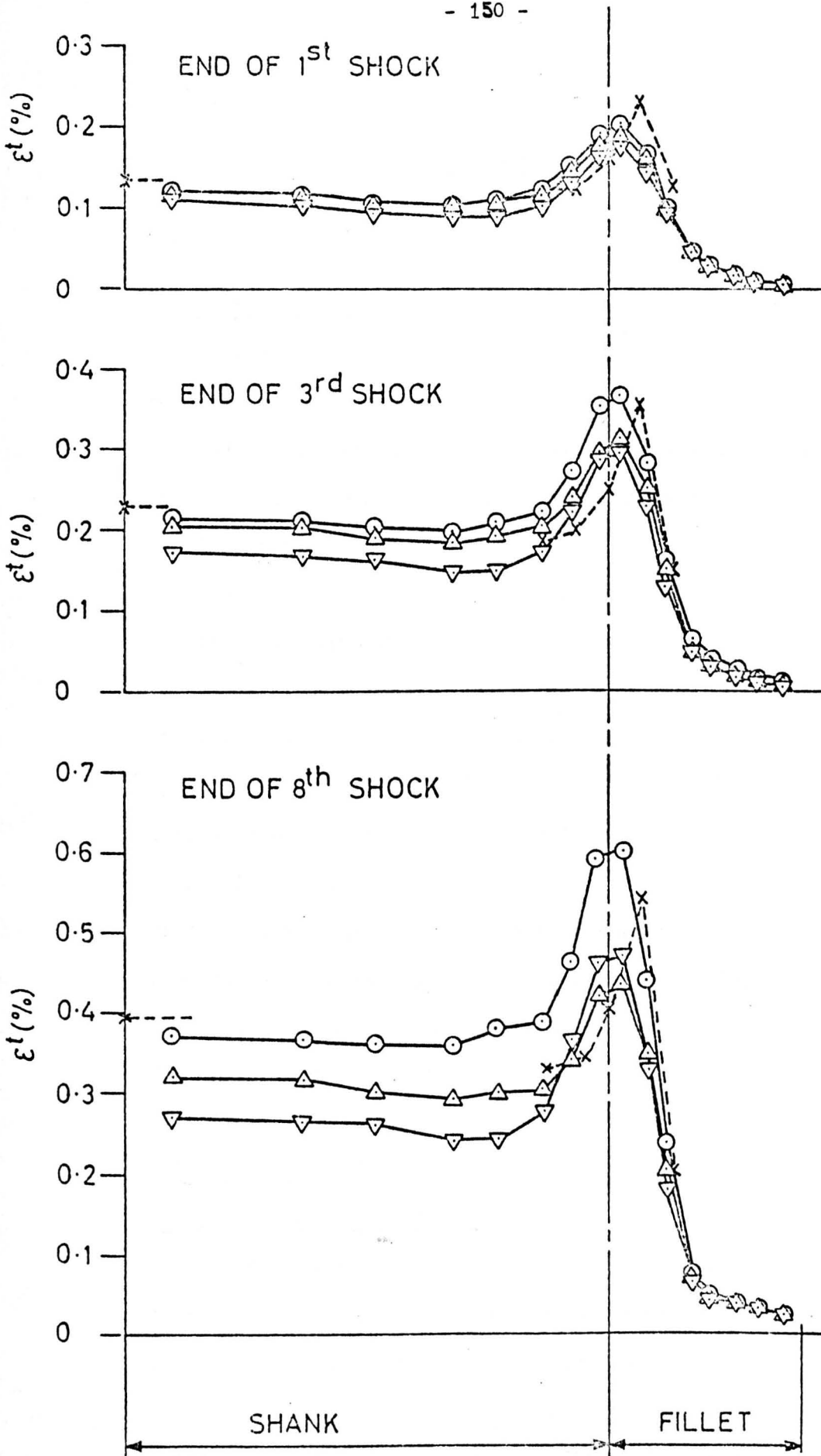


Figure 4.51 Flanged tube ($P/P_L = 0.7$, 120 hour dwell periods). Comparisons between experimental results and finite element predictions of total strain distribution along the outside surface. (See Figure 4.40 for notation).

CHAPTER FIVE

5. STEPPED BEAM

5.1 Introduction

The development of the stepped beam component (Figure 3.2) has been discussed in Section 3.2.1. This component has a uniform section (shank) and a stress concentration due to the fillet radius at the change of section. The component behaviour under conditions of

- i) steady mechanical axial load; and
- ii) pure bending

is discussed here. Ratchetting may occur when the two loading conditions are combined (i.e. steady mechanical axial load and cyclic bending) and creep in the dwell periods between successive cycles of bending will affect the behaviour. This chapter describes a detailed study of the shank behaviour in addition to the analysis of the whole component. Analysis of the whole component includes comparison with the experimental results of Yahiaoui (12). Section 5.4 investigates the validity of Ainsworth's (7) bounding technique for the stepped beam shank.

5.2 Shank Analysis

5.2.1 Finite element model

A three element model of a 10 mm length of shank is used together with three 'rigid' elements through which the loading is applied (see Figure 5.1). The purpose of the 'rigid' elements is to ensure that the section AB remains plane during deformation. Axial loading and bending is applied to the rigid elements with the constraint that the nodal displacements in the 'X' direction along AB are identical to the corresponding nodal displacements along the

left hand edge of the rigid elements. The nodes on the left hand edge of the shank model are constrained to have zero displacement in the 'X' direction. Nodes 4 and 33 are constrained to have the same displacement in the 'y' direction and node 15 is fixed. The six elements are two-dimensional plane-stress 8-noded isoparametric elements.

5.2.2 Data

The material data is the same as for the analysis of the flanged tube shank described in Section 4.2.2 and given in Table 4.1.

5.2.3 Bending cycle

A complete bending cycle consists of:-

- i) application of a 'hogging' moment, M
- ii) reversal of load to give an equal 'sagging' moment, -M
- iii) the removal of the moment.

The most severe conditions occur at the intermediate steady states of full positive and negative moment when the elastically calculated axial stress varies linearly through the section from $6M/bd^2$ to $-6M/bd^2$.

5.2.4 Cyclic bending with constant axial load

The creep ratchetting behaviour is bounded by the 'no-creep' condition (zero dwell period between cycles) and 'complete-redistribution' (where creep returns the residual stress distribution after each cycle to the stationary state stress distribution). Elastic-perfectly-plastic, isotropic hardening and kinematic hardening models are considered. Ratchet strains quoted are in the axial direction and at the top and bottom surfaces which are

identified as the first tensile and first compressive surfaces. The first tensile (FT) surface is defined as the surface which experiences a tensile stress for the first application of moment during the first cycle. The first compressive (FC) surface is the opposite surface which would have a compressive stress for the first application of moment during the first cycle with zero mean load.

5.2.4.1 'No creep' condition

5.2.4.1.1 Elastic-perfectly-plastic material model

Ratchetting mechanism

The axial stress distributions due to initial loading and during the first mechanical cycle are shown in Figure 5.2 for $P/P_L = 0.64$ and $M/M_y = 0.8$ (where P_L is the limit load in simple tension and M_y is the pure moment required to cause initial yielding on the top and bottom surfaces). This first cycle produces a linearly varying increment of ratchet strain across the section with a maximum at the first tensile surface. A steady cyclic state is established after the first cycle with the cyclic variation in stress distribution being identical to that shown in Figure 5.2. An equal amount of ratchet strain is produced in the second and subsequent cycles which is constant across the section and less than the mean centreline value for the first cycle. The accumulation of surface ratchet strains, ϵ^r (defined in equation 4.1), in the first ten cycles is shown in Figure 5.3. The initially straight beam experiences an increment of curvature and centreline growth during the first cycle. For the second and subsequent cycles there are no further incremental changes in curvature. The variation in curvature during the first three cycles is shown in Figure 5.4

where K/K_y is the normalised curvature and K_y is the curvature at first yield in the absence of mean load

$$\text{i.e. } K_y = 2 \epsilon_y / d.$$

This demonstrates the analogy between the stepped beam shank behaviour and that for Bree's (1,2) uniaxial model of a thin tube as the problem is equivalent to one of curvature control between a maximum for the first application of moment in a cycle and zero for the reversed moment. An analytical solution for the stepped beam shank is therefore available based on Bree's (1) analysis and has been used to obtain steady state ratchet strains.

For the 'no creep' ratchetting case, the whole section yields during the cycle and Figure 5.2 shows a 'plastic core' (i.e. a region in the centre of the beam which yields during both halves of the cycle) to be present. The 'plastic-core' is an essential feature of this ratchetting mechanism and the ratchet strain is related to the size of the 'plastic core'. The ratchetting boundary is defined by the combination of steady and cyclic load for which the plastic region just extends from the first tensile surface to the centreline during the first half of the first cycle (and hence from the first compressive surface to the centreline for the second half of the first cycle). The presence of an 'elastic core' (i.e. a region in the centre of the beam that is always elastic) means that shakedown will always occur after the first cycle.

Effects of mean load and cyclic bending load on ratchetting behaviour

Burgreen (5) has studied the cyclic behaviour of this component and the 'Burgreen diagram' shown in Figure 2.11 is equivalent to the 'Bree diagram' for a thin tube. The narrow band between shakedown and collapse (i.e. ratchetting regime) implies that ratchet

strains are very sensitive to small changes in applied load. The ratchetting behaviour of the stepped beam shank with an elastic-perfectly-plastic material model can be completely defined by three parameters:-

1. the first cycle first tensile surface ratchet strain
2. the first cycle first compressive surface ratchet strain
3. the steady state ratchet strain which is the same for both surfaces.

Figure 5.5 shows the variations in these ratchet strains with mean load and cyclic bending load. The analytical solution (1) was used to obtain steady state ratchet strains and finite element solutions provided the first cycle behaviour. Figure 5.5 illustrates the strong dependence of the ratchet strains on mean load.

5.2.4.1.2 Linear hardening models

A bilinear representation of the monotonic stress-strain curve was used with ratios of plastic to elastic modulus of 0.01, 0.05, 0.1. Isotropic and kinematic hardening models have been considered.

Ratchetting mechanism

The axial stress distributions due to initial loading and during the first cycle for $P/P_L = 0.8$, $M/M_y = 1.5$ for isotropic hardening with $E_p/E = 0.05$ are shown in Figure 5.6 together with an indication of the extent of the yield zone at the extremities of the cycle. A 'plastic core' is evident and there is a linearly varying increment of ratchet strain across the section at the end of the cycle, with a maximum at the first tensile surface. Unlike the elastic-perfectly-plastic case, the material has hardened and the 'instantaneous' yield stress varies in relation to accumulated strain across the section. The second cycle variation in axial stress

distribution is shown in Figure 5.7. The exact shape of the stress distributions cannot be obtained from the Gauss point values and the distributions are only approximate. The size of the 'plastic core' has reduced due to material hardening and there is a similar reduction in the ratchet strain. The size of 'plastic core' reduces with each successive cycle until the 'plastic core' disappears and ratchet strains are zero. Similarly the ratchet strains reduce monotonically to zero. The accumulation of surface ratchet strains during the first 10 cycles for these loading conditions and hardening assumptions are shown in Figure 5.8. The accumulated first tensile surface ratchet strain is dominated by the large first cycle increment which hardens the material significantly so that further ratchet strains are small and shakedown* occurs in ~ 6 cycles. The first compressive surface accumulated ratchet strain is always less than the first tensile surface and material hardening occurs at a slower rate with shakedown occurring in ~ 8 cycles. The residual curvature always has the same sign and is a maximum at the end of the first cycle. The residual curvature subsequently reduces to reach a steady state value when the component has completely 'shaken-down' in ~ 8 cycles.

The first cycle stress distributions for kinematic hardening with the same loading and plastic modulus are shown in Figure 5.9. The first application of moment produces an identical stress distribution to that for isotropic hardening (Fig. 5.6). However the 'constant yield range' associated with kinematic hardening results in a modification of the stress distribution during the second half of the first cycle as can be seen from figure 5.9. The approximate

* shakedown is defined as the point at which ratchet strains are zero. However under certain conditions of load and kinematic hardening cyclic plasticity may be evident.

stress distributions during the second cycle are shown in Figure 5.10. The axial stress/strain variations during the first cycle with isotropic and kinematic hardening assumptions are shown in Figures 5.11 and 5.12 for Gauss points nearest to the first tensile and first compressive surfaces respectively. For the first tensile surface, the kinematic hardening assumption results in more compressive yielding during the second half of the cycle and for the first compressive surface the kinematic hardening assumption leads to more tensile yielding during the second half of the cycle; the net result being a reversal in residual curvature at the end of the cycle. The accumulation of surface ratchet strains during the first 10 cycles is shown in Figure 5.13. The residual curvature always has the same sign which is opposite to the results with isotropic hardening. The overall growth, in terms of centreline strain, is greater than with an isotropic hardening model (compare Figure 5.13 for kinematic hardening with Figure 5.8 for isotropic hardening).

For this particular loading and plastic modulus, a reasonable estimate for maximum accumulated strain, for both hardening models, could be based on a finite element calculation for a single cycle, in which case the maximum ratchet strain across the section is the same for the two hardening models, although the behaviour is very different.

Effects of mean load, bending load, hardening assumption
and E_p/E on ratchetting behaviour

Finite element computations were performed for 10 cycles with a range of mean loads from $P/P_L = 0$ to 0.8 and 3 bending loads; $M/M_y = 1.0, 1.5$ and 2.0. The cyclic ratchetting behaviour of the

stepped beam shank for the range of mean loads, cyclic bending loads, hardening assumptions and E_p/E values is presented in the form of carpet plots, in Figures 5.14 to 5.19. These plots show the variation of accumulated surface ratchet strains with mean and cyclic load for the combinations of hardening assumption and E_p/E values given in Table 5.1.

The figures show the accumulation of surface ratchet strains after the 1st and 10th cycles. Also the accumulations after the 2nd and 5th cycles are given where there is a significant difference between 1st and 10th cycle values. For $E_p/E = 0.05$ and 0.1 (Figs. 5.16 - 5.19) shakedown always occurs in less than 10 cycles. The number of cycles to shakedown is given for the extremities of mean load; intermediate mean loads result in shakedown in a number of cycles between those quoted. The number of cycles to shakedown is different for the two surfaces and depends on the hardening assumption. For $E_p/E = 0.01$ shakedown had not occurred in 10 cycles except for low mean loads. In view of the convergence problems associated with high mean and cyclic loads (i.e. requiring the moments to be applied in a large number of small increments) it was not practical to continue the computation beyond 10 cycles to the shakedown or steady cyclic state.

Except for the cases below, the residual curvature is always positive for isotropic hardening and negative for kinematic hardening (positive curvature being defined as the curvature at the end of the first application of moment during the first cycle),

- (i) for $E_p/E = 0.05$ and 0.1 and $M/M_y = 1.0$, there is no difference in the results for both hardening models and residual curvatures are positive (i.e. no reverse plasticity with kinematic hardening)

- (ii) for $E_p/E = 0.1$, $M/M_y = 1.5$, isotropic hardening and zero mean load the curvature at the end of the first cycle is negative
- (iii) for $E_p/E = 0.01$, $M/M_y = 1.5$ and isotropic hardening, residual curvature is negative for $P/P_L < \sim 0.5$
- (iv) for $E_p/E = 0.01$, $M/M_y = 1.0$ and kinematic hardening, the sign of the residual curvature is both mean load and cycle number dependent.

There is a marked similarity in ratchetting behaviour between the first tensile surface with an isotropic hardening model and the first compressive surface with a kinematic hardening model. Accumulated ratchet strains increase with increases in both mean and cyclic loads and are dominated by the first cycle. The kinematic hardening model results in larger accumulated ratchet strains on the first compressive surface compared with the first tensile surface with isotropic hardening.

There is also a similarity in ratchetting behaviour between the first tensile surface with a kinematic hardening assumption and the first compressive surface with an isotropic hardening assumption for E_p/E values of 0.05 and 0.1. Ratchet strains increase with mean load but are a maximum for a bending load somewhere between 1.0 and 2.0 of the yield moment, and shakedown is more rapid for the first compressive surface with an isotropic hardening assumption.

Finally, the results can be used to identify combinations of loading and material behaviour which would result in unacceptably high accumulations of strain.

5.2.4.2 Complete redistribution

5.2.4.2.1 Elastic-perfectly-plastic material model

Ratchetting mechanism

The axial stress distributions due to initial loading and during the first bending cycle for $P/P_L = 0.64$ and $M/M_y = 0.8$ are identical to those shown in Figure 5.2. However between the end of the first bending cycle and the start of the second bending cycle, the stresses are allowed to completely redistribute to the stationary state stress distribution which is the same as the initial stress distribution. Redistribution is judged to be complete when the variation in axial stress is within 1% of the mean stress. With an assumption of zero interaction between plastic and creep strains, the second and subsequent cycles will be identical to the first cycle with both surfaces experiencing an amount of ratchet strain equal to the first cycle value. The accumulation of ratchet strains during the first ten cycles is compared with the equivalent 'no creep' behaviour in Figure 5.3. Each cycle produces an equal increment of centreline growth and curvature. For these particular loading conditions the 'complete redistribution' assumption gives an upper bound on ratchetting behaviour for both the maximum (first tensile surface) and the centreline accumulation of ratchet strain. The general observations for the flanged tube shank discussed in Section 4.2.4.2.1 are also applicable here, i.e.:-

1. plastic growth across the whole section during a cycle is not necessary for continued ratchetting under 'complete redistribution' conditions (i.e. a 'plastic core' is not essential); and

2. any plastic straining during the first cycle will lead to continued ratchetting thus causing a shift in the ratchetting boundary to the elastic/plastic boundary:-

$$\frac{P}{P_L} + \frac{M}{M_y} = 1.$$

The variation in curvature during the first three cycles is shown in Figure 5.4. There is a relatively 'small' increase in curvature during each dwell period and the cyclic variations in curvature for each cycle are identical (within the bounds of computational accuracy).

Effects of mean load and cyclic bending load on ratchetting behaviour

With complete redistribution between each cycle the ratchet strains on every cycle are identical and are the same as those for the 1st cycle without creep. This has been indicated in Figure 5.5 where the variations of the surface ratchet strains with mean load, for various values of the cyclic moment are plotted. It may be seen from Figure 5.5 that, for 'complete redistribution', the maximum steady state ratchet strains occur on the first tensile surface and are larger than those for the 'no creep' case, hence the 'complete redistribution' case provides an upper bound on maximum accumulated ratchet strains. The significant difference between the 'no creep' and 'complete redistribution' cases is that in the 'no creep' case there is no change in the residual curvature after the first cycle; in the 'complete redistribution' case, the ratchetting mechanism produces changes in curvature as well as changes in the mean strain. From Figure 5.5 it appears that for low values of M/M_y and high values of P/P_y the 'complete redistribution' case may not provide an upper bound for the mean ratchet strain and hence accumulated mean ratchet strain, although it does provide an upper bound for the maximum ratchet strain.

Creep during the dwell periods

The surface strains which accumulate during the first dwell period for $P/P_L = 0.7$ and $M/M_y = 0.7$ are shown in Figure 5.20 plotted against time function, Γ (defined by equation 4.2). As for the shank of the flanged tube, discussed in Section 4.2.4.2.1, the results are asymptotic to the 'virgin' creep curve at the same mean load and offset by an amount of strain due to stress redistribution, $\Delta \epsilon^d / \epsilon_y$, which is greater for the first tensile surface but is relatively small for both surfaces. The variation of $\Delta \epsilon^d / \epsilon_y$ at the surfaces with mean load and bending moment is shown in Figure 5.21. In all cases the increment of strain due to stress redistribution is small and although there appears to be some inconsistency in the results for $M/M_y = 1.2$ it must be remembered that the scatter is 'probably' within the computational accuracy of the program. The results for $M/M_y = 0.8$ are not included because it was found that sufficient time had not been allowed for redistribution to be complete. The general trend is for $\Delta \epsilon^d / \epsilon_y$ to be larger on the first tensile surface and to be more sensitive to changes in mean load when compared with the first compressive surface.

5.2.4.2.2 Linear hardening models

Ratchetting mechanism

The stress distribution due to initial loading and during the first cycle for $P/P_L = 0.8$, $M/M_y = 1.5$ and $E_p/E = 0.05$ are the same as those for the 'no creep' condition in Figures 5.6 and 5.9 for isotropic hardening and kinematic hardening respectively. Between the end of the first and the start of the second bending cycles 'complete redistribution' returns the residual stress distribution to the steady state uniform stress distribution due to initial loading. However the material has hardened and the next bending cycle produces less ratchet strain than the first at both surfaces for isotropic and kinematic hardening.

For isotropic hardening, the surface ratchet strains accumulated in 10 cycles are compared with the results for 'no creep' in Figure 5.8. There is an overall increase in the accumulation of surface ratchet strains compared with the 'no creep' behaviour but the ratchetting must eventually cease when the material has hardened sufficiently for cycling to be within the elastic range.

The accumulated surface ratchet strains in 10 cycles for kinematic hardening are compared with the 'no creep' results in Figure 5.13. Again, there is an increase in the ratchet strains which must reduce to zero when the material has fully hardened.

Effects of mean load, bending load, hardening assumption and E_p/E on ratchetting behaviour

Finite element computations were performed for 10 cycles with a range of mean loads of $P/P_L = 0.2$ to 0.8 and 3 bending loads; $M/M_y = 1.0, 1.5$ and 2.0 . The variation in the cyclic behaviour of the stepped beam shank with mean load, bending moment, hardening assumption and E_p/E is given in Figures 5.22 to 5.26. Carpet plots are used to show the variation of accumulated ratchet strain with mean and cyclic loads for the combinations of hardening assumption and E_p/E given in Table 5.2.

Results for $E_p/E = 0.01$ with kinematic hardening were not obtained because of the large amount of computation involved. The 10th cycle ratchet strains (values in parenthesis) for the extremities of mean load (i.e. $P/P_L = 0.2$ and 0.8) are given to indicate the cases where significantly more than 10 cycles are required to reach shakedown. For the 'complete redistribution' case shakedown is related to purely elastic cycling with no cyclic plasticity region. For intermediate values of load the 10th cycle ratchet strains fall within the extreme values quoted. The residual curvatures are similar in direction to the 'no creep' case being generally positive for isotropic hardening and negative for kinematic hardening. The

main exception to this behaviour is for $M/M_y = 1.0$ and $E_p/E = 0.05$ and 0.1 where there is no reverse plasticity for kinematic hardening and the results for isotropic hardening and kinematic hardening are therefore the same. In most cases, the accumulation of first tensile and first compressive surface ratchet strains under 'complete redistribution' conditions is equal or greater than for the 'no creep' case in Figures 5.14 to 5.19. The opposite effect is apparent on the first compressive surface for $E_p/E = 0.01$ and $M/M_y = 1.0$. For $E_p/E = 0.05$ and 0.1 , the effects of 'complete redistribution' on ratchet strains reduce with increasing bending load and for $M/M_y = 2.0$ the results for 'no creep' and 'complete redistribution' are very similar. For the first tensile surface with isotropic hardening and the first compressive surface with kinematic hardening the accumulation of strain, particularly for large bending loads, is dominated by the ratchet strain in the first cycle.

For $E_p/E = 0.05$ and 0.1 the 10th cycle ratchet strains are generally small (less than, and in most cases, very much less than, 0.23). However for $E_p/E = 0.01$ which is approaching an elastic-perfectly plastic model, 10th cycle ratchet strains up to the yield strain could be expected although the loading conditions would probably be unacceptable in view of the large first cycle ratchet strains of up to 50 times the yield strain.

Creep during the dwell periods

The dwell period behaviour with an elastic-perfectly-plastic material assumption has been discussed in Section 5.2.4.2.1. The dwell period behaviour for hardening materials is similar to that shown in Figure 5.20 with an asymptotically approached constant creep strain rate which is the same as for virgin material at the same load and an increment of strain due to stress redistribution, $\Delta \epsilon^d / \epsilon_y$. However the hardening of the material results in a reduction in the amount of stress redistribution for each successive

dwelling period as shown in Figure 5.27 for $P/P_L = 0.8$, $M/M_y = 1.5$, $E_p/E = 0.05$ and an isotropic hardening assumption. Differences between first tensile and first compressive surface dwelling period behaviour are seen to be insignificant after 10 cycles and the increment of dwelling period strain due to stress redistribution is relatively small after a few cycles. The variation in $\Delta \epsilon^d / \epsilon_y$ for the first dwelling period with bending load for the extremes of mean load ($P/P_L = 0.2$ and 0.8) for $E_p/E = 0.05$ are shown in Figure 5.28. The 1st cycle redistribution strains are relatively insensitive to the plastic modulus and values for the other plastic moduli are within $0.1 \epsilon_y$ of those in Figure 5.28.

The variation in time function for complete redistribution, Γ_R , is shown in Figure 5.29. For a particular mean load, a range of Γ_R values is given which indicates the variation with bending load and plastic modulus. In general the variation with bending load and plastic modulus is small and the redistribution time function is practically independent of mean load. From the definition of time function (equation 4.2) and Figure 5.29 it can be seen that the redistribution time depends mainly on the mean load. The large range for $P/P_L = 0.2$, where redistribution times are large and dwelling period strains small, is inconsistent with the results for higher mean loads and possibly relates to the accuracy criterion of the creep computation.

5.3 Analysis of the Whole Component

5.3.1 Finite element model

The 46 element mesh used to model a half section of the stepped beam is shown in Figure 5.30. Axial and bending loads are applied to 3 additional 'rigid' elements to maintain the 'plane-sections-remain-plane' criterion discussed in Section 5.2.1. The left hand

end of the beam is clamped. Two-dimensional, plane stress, 8-noded, isoparametric elements are used throughout. The justification for using this mesh is discussed in Appendix II. When surface stress or strain distributions are quoted, data has been obtained for the Gauss points nearest to the surface shown in Figure 5.30.

5.3.2 Data

The material data is generally the same as for the shank and discussed in Section 5.2.2. Elastic-perfectly-plastic, isotropic hardening, kinematic and non-linear kinematic hardening models are used to investigate the 'no creep' ratchetting behaviour of the component, including a comparison with the experimental results of Yahiaoui (12) for which the multilinear representations of the lead alloy uniaxial stress-strain and cyclic behaviour, shown in Figure 4.24, are used. The 'overlay method' (20) is used to model non-linear kinematic hardening using two sub-layers of elements for the shank and is based on Curve A in Figure 4.24. The overlay model is shown in Figure 5.31 and the individual element data is given in Table 5.3.

For the 'complete redistribution' case, an elastic-perfectly plastic material model is used. A time index of unity is assumed for the Norton Bailey creep law (other creep law constants from Table 4.1) together with an assumption of zero interaction between plastic and creep strains.

5.3.3 Axial loading

5.3.3.1 Elastic stresses

The elastic surface meridional stress distribution due to an axial load is shown in Figure 5.32, from which a mechanical stress concentration factor due to axial loading of 1.8 is predicted (compared with 1.66 from photoelastic results (55)). Figure 5.33

shows the 'exaggerated' deformed shape for a mean load of $0.7 P_L$. There is an overall thinning of the component but no obvious necking in the region of the stress concentration.

5.3.3.2 Elastic-plastic behaviour

The development of the plastic zone with increasing axial load up to collapse is shown in Figure 5.34, for an elastic-perfectly-plastic material assumption. The zone initiates in the fillet and moves into the shank with increasing load. At collapse, virtually the whole of the shank has yielded.

5.3.3.3 Creep at sustained mean load

The stationary state meridional stress distribution is compared with the meridional stress distribution due to an initial loading of $P/P_L = 0.7$ in Figure 5.35. The values plotted are for the Gauss points nearest to the surface. There is a shift in the position of peak stress towards the shank and a drastic reduction in the magnitude of the peak stress in the fillet.

5.3.4 Application of bending moment

5.3.4.1 Elastic stresses

The elastic surface meridional stress distribution due to bending is shown in Figure 5.36, from which a stress concentration factor in bending of 1.46 is predicted (compared with 1.38 from photoelastic results (55)).

5.3.4.2 Elastic-plastic behaviour

The development of the plastic zone with increasing moment towards collapse is shown in Figure 5.37, for an elastic-perfectly-plastic material assumption. The zone initiates in the fillet and spreads into the shank as load increases. Although yielding in the shank commences for $M/M_y = 1$, this is not predicted for $M/M_y = 1.11$ since the Gauss points nearest to the surface do not yield until $M/M_y = 1.13$.

Results for moments greater than $1.4 M_y$ (0.93 of the collapse moment) could not be obtained because of convergence problems with the finite element program. However it is clear that, at collapse, the plastic zone will have reached the centreline of the beam and the majority of the shank will have yielded.

5.3.5 Cyclic bending with sustained mean load

5.3.5.1 'No creep' condition

5.3.5.1.1 Elastic-perfectly-plastic material model

Ratchetting mechanism

The regions of yielding during the first and second cycles for $P/P_L = 0.7$ and $M/M_y = 0.7$ are shown in Figure 5.38.

At the first tensile and first compressive surface 'peak fillet' positions the ratchetting behaviour is 'similar' to that for the shank already discussed in Section 5.2.4.1.1. The first cycle produces increments of surface 'peak fillet' ratchet strain, the first tensile surface experiencing a larger increment of ratchet strain. A steady state condition is reached after the first cycle where first tensile and first compressive surface 'peak fillet' ratchet strains are equal, and less than those in the first cycle. From Figure 5.38 it is seen that the reduction in fillet ratchet strains between the first and subsequent cycles is associated with a reduction in the yield zone in the fillet region. There are no further changes in residual 'curvature' of the component. The accumulation of surface ratchet strains in the shank and at the 'peak fillet' positions during the first 10 cycles are shown in Figure 5.39. The distribution of steady state meridional ratchet strains, which is the same for both surfaces, is shown in Figure 5.40, from which it is clear that 'peak fillet' ratchet strains

occur very close to the shank/fillet intersection and are less than those in the shank.

Effects of mean load and bending load on ratchetting behaviour

The accumulations of first tensile and first compressive surface shank and 'peak fillet' meridional ratchet strains in 10 cycles for $P/P_L = 0.5$ and $M/M_y = 1.05$ are shown in Figure 5.41. Again steady state conditions exist after the first cycle and 'peak fillet' meridional ratchet strains are less than those in the shank. The results for this loading and $P/P_L = 0.7$, $M/M_y = 0.7$ are summarised in Table 5.4. The results are discussed in Chapter 7.

5.3.5.1.2 Linear hardening models

The accumulations of first tensile and first compressive surface shank and 'peak fillet' meridional ratchet strains in 10 cycles for $P/P_L = 0.54$ and $M/M_y = 1.30$ are shown in Figure 5.42 for 'no creep' conditions. The results are for the isotropic and kinematic hardening models of the lead alloy stress-strain behaviour shown in Figure 4.24 and are normalised with respect to the relevant yield stress (i.e. $\sigma_y = 19.8 \text{ MN/m}^2$). Both models predict shake-down in under 10 cycles for the shank and 'peak fillet' positions with the possible exception of the first compressive surface in the shank with isotropic hardening for which the results indicate shake-down in ~ 15 cycles. The reversal of residual curvature between isotropic and kinematic hardening models already identified for the shank is also apparent in the fillet region, although the term 'curvature' is not strictly applicable to the fillet since strain distributions through the thickness are not linear. In the fillet it is more reasonable to compare surface strains, i.e. accumulated ratchet strains at the 'peak fillet' position are always greater on the first tensile surface for isotropic hardening and on the

first compressive surface for kinematic hardening.

With the exception of the first cycle for the first tensile surface, the isotropic hardening model always predicts a greater accumulation of ratchet strains at the 'peak fillet' position compared with the shank, whereas the kinematic hardening model predicts greater accumulations in the shank. The same is true for ratchet strains prior to shakedown. An upper bound on total accumulated strains in the component can be obtained by considering the first compressive surface in the shank with kinematic hardening.

The accumulation of ratchet strains at the shank surface with kinematic hardening are compared with the equivalent results with a non-linear kinematic hardening model in Figure 5.43. The results for the two models deviate during the 3rd cycle which indicates that strains during this cycle exceed the breakpoint value between Curves A and B in Figure 4.24 (i.e. the normalised equivalent of 0.6% strain from Figure 4.24). For the 3rd and subsequent cycles prior to shakedown, the non-linear kinematic hardening model predicts ratchet strains which are larger than for kinematic hardening. However, 10th cycle ratchet strains with a non-linear kinematic hardening model are small and shakedown has almost occurred, whereas for kinematic hardening, the results indicate shakedown in ~ 8 cycles.

5.3.5.1.3 Comparison between experimental results and finite element predictions

This section discusses the comparison between experimental test data (12) and finite element predictions for a typical loading condition.

$$\text{i.e. } \frac{P}{P_L^*} = 0.5, \quad \frac{M}{M_y^*} = 1.2 \text{ (Nominal)}$$

where P_L^* and M_y^* are based on a 0.2% proof stress for the lead alloy of 21.5 MN/m^2 . The experimental moments were applied 'rapidly' (~ 6 mins per cycle) and a 'no creep' condition has been assumed for the finite element predictions.

It was found that the curvature of the beam had an effect on the applied moments because of an additional moment due to the eccentricity of the axial load. This additional moment has been quantified for the shank and found to be significant (12). Table 5.5 compares the nominal shank moments with the actual moments which vary during the first 5 cycles before reaching an approximate steady state of $\pm 1.061 M_y^*$. Finite element predictions with these actual moments are compared with the experimental shank results.

Actual moments in the fillet have also been quantified and found to be up to 5% greater than shank values (12). In view of the strong dependence of strain on bending load it was considered unrealistic to use the shank moments in Table 5.5 for an analysis of the whole component and comparison between experimental results and finite element predictions are made for the shank region only.

In addition to comparisons based on actual moments, experimental shank strains at the end of each quarter cycle are used to determine curvatures and finite element predictions in the shank based on curvature controlled loading have been obtained.

Actual moments

Finite element predictions of total strains and ratchet strains in the shank for $P/P_L^* = 0.5$ and the steady state bending load of $M/M_y^* = 1.061$ with an elastic-perfectly-plastic model (Curve C,

Figure 4.24) are compared with the experimental results in Figure 5.44. The model correctly predicts the 'sign' of the residual curvature except for the first cycle but cannot predict the increase in this parameter with cycle number. The model over-predicts the accumulation of strains because the steady state ratchet strain prediction of 0.074% per cycle is larger (and after a few cycles very much larger) than the experimental ratchet strains.

Comparison between the experimental results and finite element predictions of total strain and ratchet strain, using the actual moments from Table 5.5, with isotropic and kinematic hardening models are shown in Figures 5.45 and 5.46 respectively for the first 10 cycles. With both isotropic and kinematic hardening models, the first compressive surface total strains are greater than those for the first tensile surface, which is not the case from the experimental results. Also, both models predict shakedown in ~ 10 cycles. The reduction in first compressive surface strain during the 2nd to 4th cycles with kinematic hardening is an unexpected result. The experimental and predicted variations in total surface strain during the first two cycles are compared in Figure 5.47. The finite element predictions for the first tensile surface are always lower than the experimental results. The opposite effect occurs on the first compressive surface.

Curvature control

Finite element predictions based on curvature controlled loading for isotropic and kinematic hardening models are compared with the experimental results in Figures 5.48 and 5.49 respectively.

The 'incremental application of load' approach used in the finite element program made obtaining these results a slow and

tedious task and the predictions are therefore restricted to a few cycles. Obviously, both models will correctly predict the relative magnitudes of the surface strains but absolute values are over-predicted. However, the predictions, particularly with a kinematic hardening model, are in generally good agreement with the experimental results over the 6 cycles analysed. Since neither model can be used to predict material ratchetting, shakedown must eventually occur.

5.3.5.2 Complete redistribution (Elastic-perfectly-plastic material model)

Ratchetting mechanism

The regions of yielding during the first and second cycles for $P/P_L = 0.7$ and $M/M_y = 0.7$ are shown in Figure 5.50. There is a reduction in the yield zone in the fillet region between the first and second cycles. The component ratchet strains produced in the first cycle are identical to those for the 'no creep' condition. However between the end of the first cycle and the start of the second cycle, the residual stresses are allowed to completely redistribute to the stationary state stress distribution (shown in Figure 5.35). The behaviour of the shank under 'complete redistribution' conditions has been discussed in Section 5.2.4.2.1. At the 'peak fillet' positions, a steady state condition is reached after the first cycle and first tensile surface meridional ratchet strains are greater than those for the first compressive surface.

The whole component experiences an increment of 'curvature' and overall growth for each cycle. The accumulations of surface ratchet strains in the shank and at the 'peak fillet' positions during the first 10 cycles are compared with those for the 'no creep'

condition in Figure 5.39. The distributions of first tensile and first compressive surface steady state meridional ratchet strains are compared with the 'no creep' case in Figure 5.40. For the 'complete redistribution' case the 'peak fillet' ratchet strains are greater than those in the shank, whereas for 'no creep' the converse occurs.

Effects of mean load and bending load on ratchetting behaviour

The accumulations of shank and 'peak fillet' meridional ratchet strains in 10 cycles for $P/P_L = 0.5$ and $M/M_y = 1.05$ are compared with the 'no creep' case in Figure 5.41. The first cycle and steady state ratchet strains in the shank and fillet for this loading and $P/P_L = 0.7$, $M/M_y = 0.7$ are given in Table 5.4. The results are discussed in Chapter 7.

Creep during the dwell periods

The strains which accumulate during the first dwell period in the shank and at the 'peak fillet' positions, ϵ^d , are shown in Figure 5.51 for $P/P_L = 0.7$ and $M/M_y = 0.7$. The results are asymptotic to straight lines with an increment of normalised strain, $\Delta \epsilon^d / \epsilon_y$, due to redistribution of stresses. $\Delta \epsilon^d / \epsilon_y$ is positive in the shank and at the 'peak fillet' position on the first tensile surface. For the 'peak fillet' position on the first compressive surface, $\Delta \epsilon^d / \epsilon_y$ is negative. There is some scatter in the results for the 'peak fillet' positions and a least squares fit was applied to the relevant data. The results in Figure 5.51 are a truncated version of the first dwell period behaviour which explains why the 'peak fillet' least squares fit may not appear to be accurate for the data points given. For the shank identical results are obtained for each dwell period since the initial stress distribution is the same as the stationary state stress distribution.

In the fillet, steady state dwell period behaviour occurs after the first dwell period since the stationary state stress distribution is not the same as that due to axial load. The first and steady state dwell period constant strain rates, $d(\epsilon^d/\epsilon_y)/d\Gamma$, are identical but the amount of strain due to redistribution is constant after the first dwell period. The dwell period behaviour for this loading together with $P/P_L = 0.5$, $M/M_y = 1.05$ is summarised in Table 5.6. The fillet results for $P/P_L = 0.5$, $M/M_y = 1.05$ indicate that redistribution might not be complete. For all cases, the increment of strain due to redistribution, $\Delta\epsilon^d/\epsilon_y$, is small. The normalised gradient, $(d(\epsilon^d/\epsilon_y)/d\Gamma)/(P/P_L)$, is independent of mean load. These results are discussed further in Chapter 7.

5.4 Application of Ainsworth's Bounding Technique to the shank

Ainsworth's (7) bounding technique is used to obtain an upper bound on shank total centreline strain under 'complete redistribution' conditions with mean stress, σ , using the finite element results for a 'no creep' computation with the same bending loads and a higher mean stress, σ^* (results taken from the analysis of the shank discussed in Section 5.2). Ainsworth suggests an optimum value for this higher mean load

$$\sigma^* = \sigma \left(1 + \frac{1}{n}\right) \quad \text{where } n \text{ is the stress index in the creep law.}$$

The through thickness axial stress distribution at the end of each cycle, from the 'no creep' computations at mean stress σ^* , is used to predict centreline strain during the dwell period for the equivalent 'complete redistribution' condition at mean stress σ .

Upper bounds for two loading situations have been obtained:-

- (i) $\frac{P}{P_L} = 0.7, \frac{M}{M_y} = 1.0, \frac{E_p}{E} = 0.05$, Isotropic hardening, dwell period = 60 hrs,
- (ii) $\frac{P}{P_L} = 0.4, \frac{M}{M_y} = 2.0, \frac{E_p}{E} = 0.05$, Isotropic hardening, dwell period = 2000 hrs,

using the predictions for 'no creep' computations with the same bending load, plastic modulus, hardening assumption but with the following mean loads:-

- (i) $\frac{P^*}{P_L} = 0.8 \quad \left\{ \frac{P}{P_L} \left(1 + \frac{1}{n} \right) = 0.796 \right\}$
- (ii) $\frac{P^*}{P_L} = 0.5 \quad \left\{ \frac{P}{P_L} \left(1 + \frac{1}{n} \right) = 0.455 \right\}$

which are, as shown, reasonably close to Ainsworth's suggested optimum values.

The derived upper bounds for cases (i) and (ii) are compared with the finite element predictions in Figures 5.52 and 5.53 respectively.

In both cases, the upper bound is grossly in excess of the finite element results due to the over-prediction of dwell period strains. Creep strains across the section, based on the residual stress at each Gauss point are used in a volume integral of the creep dissipation function in order to obtain an upper bound on the centreline dwell period strains. Due to the 'peaky' form of the residual stress distribution and high value of the stress index (7.3), the volume integral is dominated by the creep strain values for the central Gauss points where the peak stresses occur. It should be noted that these particular results have no practical application because of the exceptionally large accumulations of strain (up to 240%) which are far in excess of design limitations.

$\frac{E_p}{E}$	Figure Number	
	Isotropic Hardening	Kinematic Hardening
0.01	5.14	5.15
0.05	5.16	5.17
0.1	5.18	5.19

Table 5.1 Shank Study, 'no creep' conditions. Key to Figure numbers

$\frac{E_p}{E}$	Figure Number	
	Isotropic Hardening	Kinematic Hardening
0.01	5.22	-
0.05	5.23	5.24
0.1	5.25	5.26

Table 5.2 Shank study, complete redistribution. Key to figure numbers.

	Hardening	E (GN/m ²)	σ_y (MN/m ²)	E _{p1} (GN/m ²)	E _{p2} (GN/m ²)
Material 1	Kinematic	44.90	38.32	0.4	-
Material 2	Kinematic	1.50	8.86	0.4	-
Composite Material	Non-linear Kinematic	23.20	19.80	0.949	0.4

Table 5.3 Stepped Beam Shank. Element data used in 'overlay' model for non-linear kinematic hardening

(see Figure 5.31)

$\frac{P}{P_L}$	$\frac{M}{M_y}$	Position	Normalised Ratchet Strain per cycle			
			'No-creep'		'Complete redistribution'	
			1st cycle	Steady State	1st cycle	Steady State
0.5	1.05	FT surface Shank	2.175	0.555	2.175	2.204
		FC surface	-0.010	0.555	-0.010	-0.031
		FT surface Fillet	3.293	0.322	3.293	2.417
		FC surface	1.573	0.322	1.573	1.040
0.7	0.7	FT surface Shank	2.611	1.500	2.611	2.613
		FC surface	1.175	1.500	1.175	1.182
		FT surface Fillet	3.973	1.025	3.973	2.902
		FC surface	1.335	1.025	1.335	1.347

Table 5.4 Stepped Beam Ratchetting Behaviour with an Elastic-perfectly Plastic Material Model

Cycle	Nominal M/M_y^*	Actual M/M_y^* in the shank
1	+M	+1.2
	0	0
	-M	-1.2
	0	0
2	+M	+1.2
	0	0
	-M	-1.2
	0	0
3	+M	+1.2
	0	0
	-M	-1.2
	0	0
4	+M	+1.2
	0	0
	-M	-1.2
	0	0
5-10	+M	+1.2
	0	0
	-M	-1.2
	0	0

Table 5.5 Effect of eccentricity on applied moments

$\frac{P}{P_L}$	$\frac{M}{M_y}$	Position	$\frac{a(\epsilon^d/\epsilon_y)}{a\Gamma}$	$\frac{a(\epsilon^d/\epsilon_y)/a\Gamma}{P/P_L}$	$\Delta\epsilon^d/\epsilon_y$	
					1st cycle	Steady State
0.5	1.05	FT surface Shank	0.502	1.004	0.302	0.302
		FC surface	0.500	1.000	0.218	0.218
		FT surface Fillet	0.479	0.959*	0.159	0.154
		FC surface	0.410	0.819*	0.217	0.209
0.7	0.7	FT surface Shank	0.700	1.000	0.237	0.237
		FC surface	0.699	0.998	0.079	0.079
		FT surface Fillet	0.704	1.005	0.077	0.116
		FC surface	0.718	1.026	-0.040	-0.041

* redistribution possibly not complete

Table 5.6 Stepped Beam. Dwell Period Behaviour.

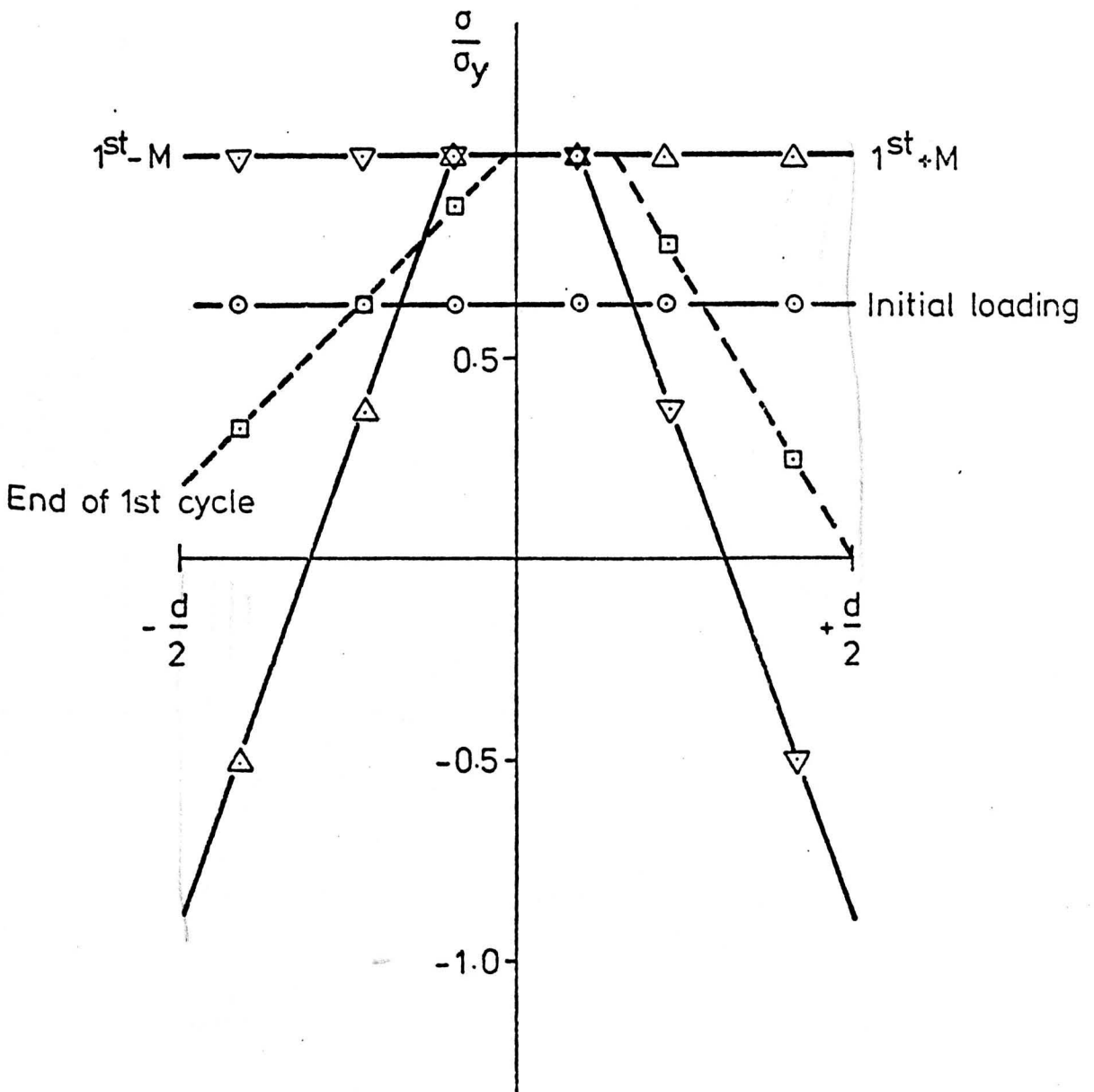


Figure 5.2 Stepped beam shank (elastic-perfectly-plastic, $M/M_y = 0.8$, $P/P_L = 0.64$, 'no creep' conditions). Axial stress distributions due to initial loading and during the first cycle.

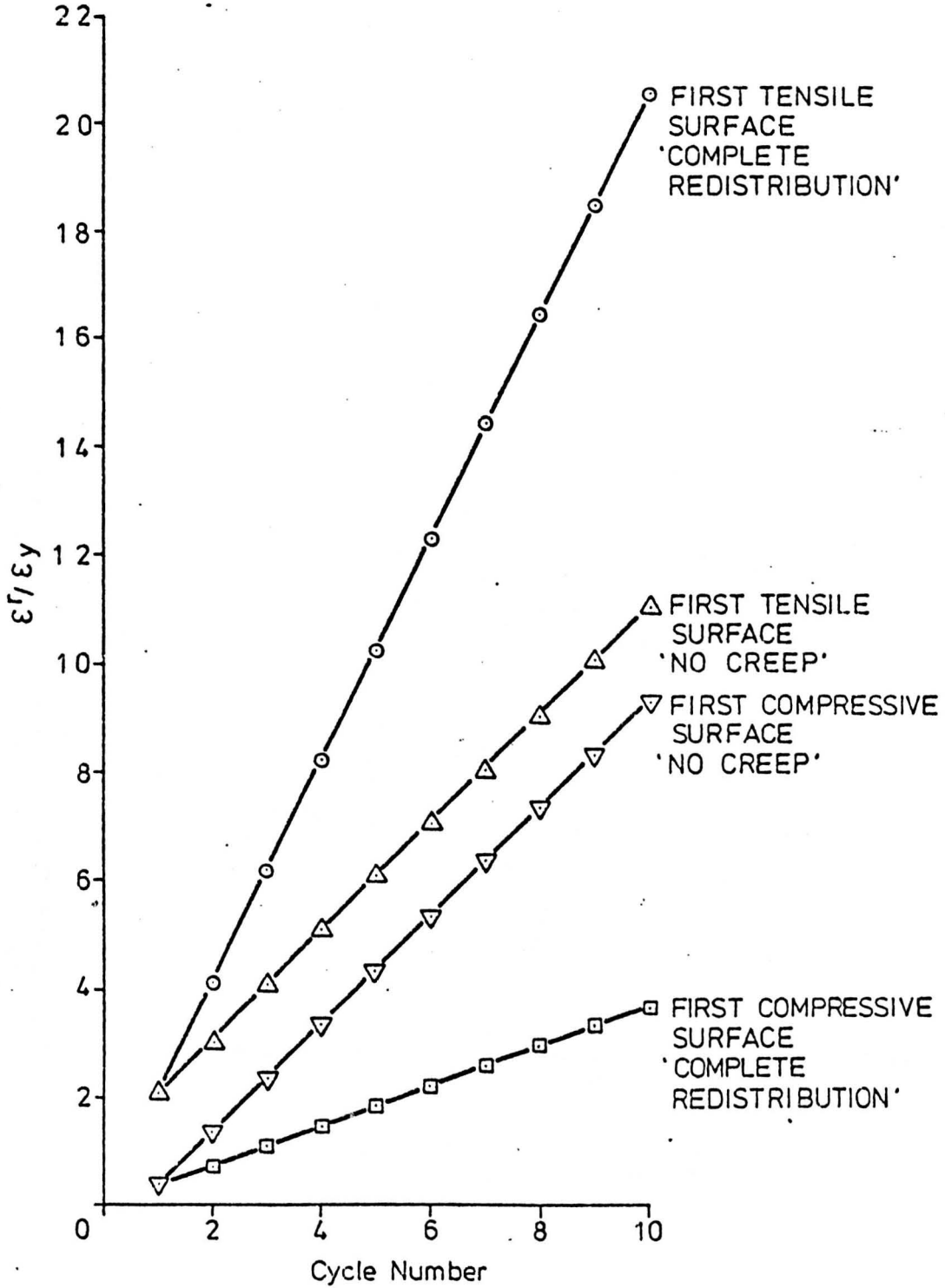


Figure 5.3 Stepped beam shank (elastic-perfectly-plastic, $M/M_y = 0.8$, $P/P_T = 0.64$). Accumulation of normalised ratchet strain during the first 10 cycles.

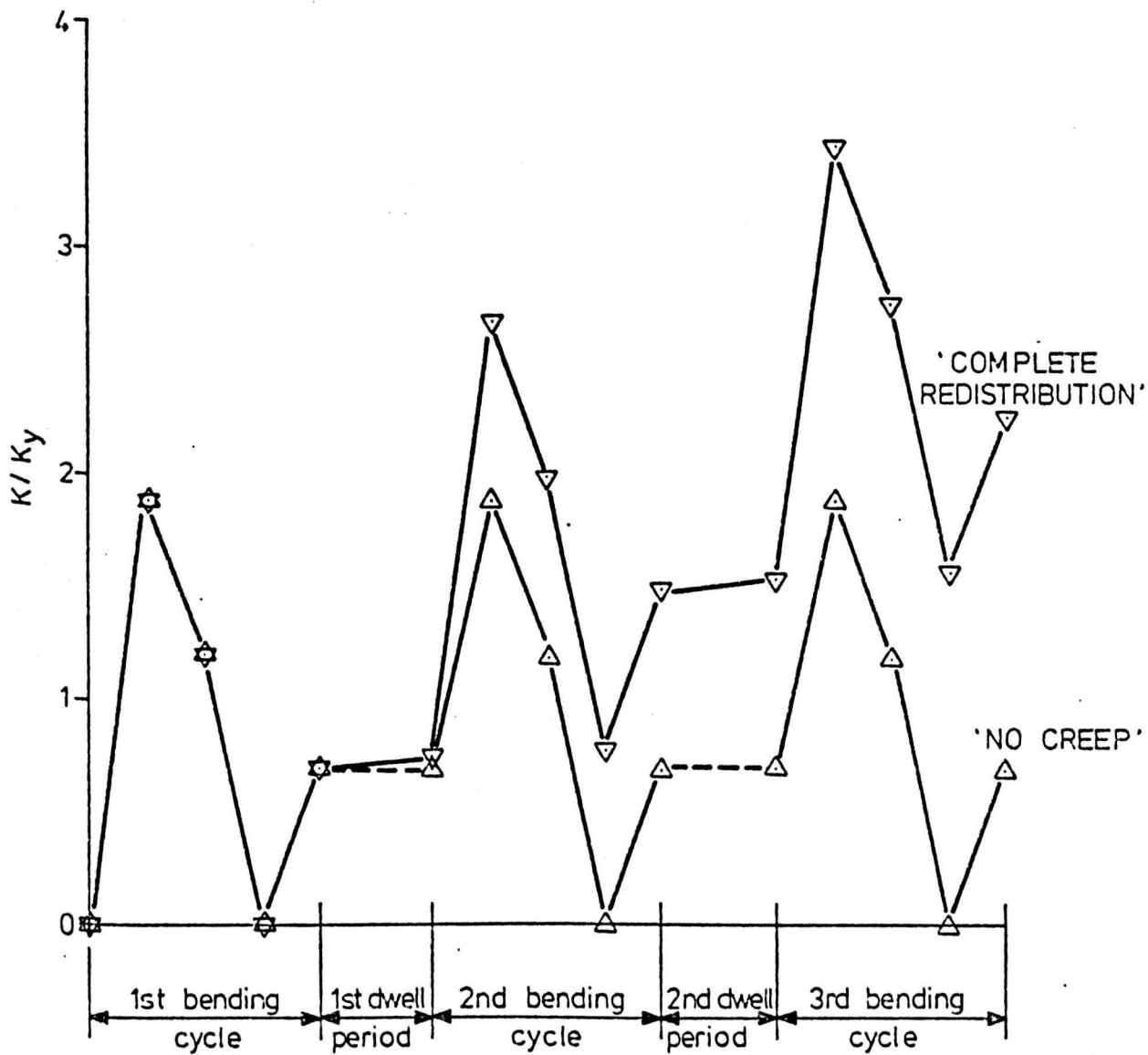


Figure 5.4 Stepped beam shank (elastic-perfectly-plastic, $M/M_y = 0.8$, $P/P_L = 0.8$). Variation in normalized curvature during the first 3 cycles.

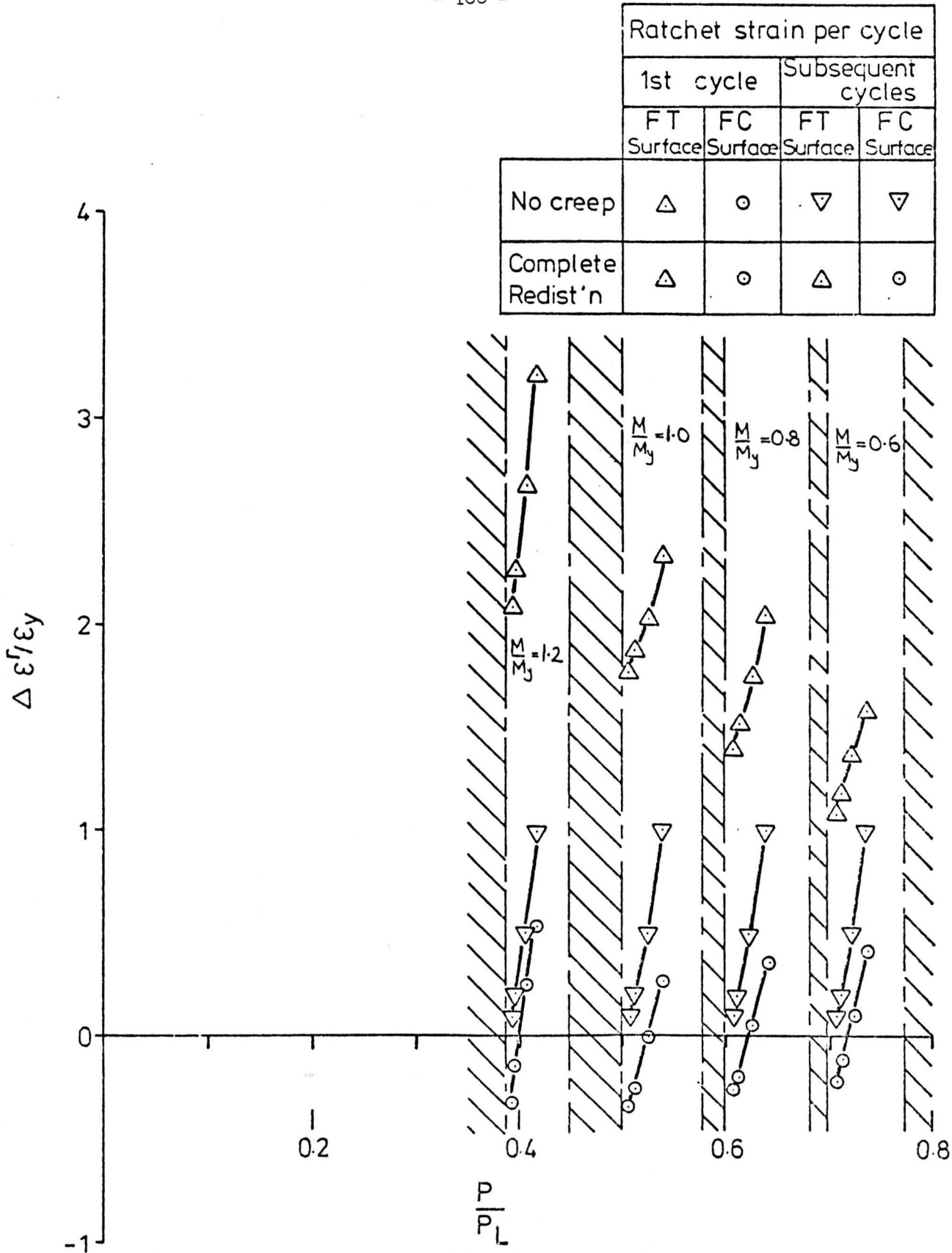


Figure 5.5 Stepped beam shank (elastic-perfectly-plastic). Variation in normalised ratchet strain for the first and subsequent cycles with mean load and bending load.

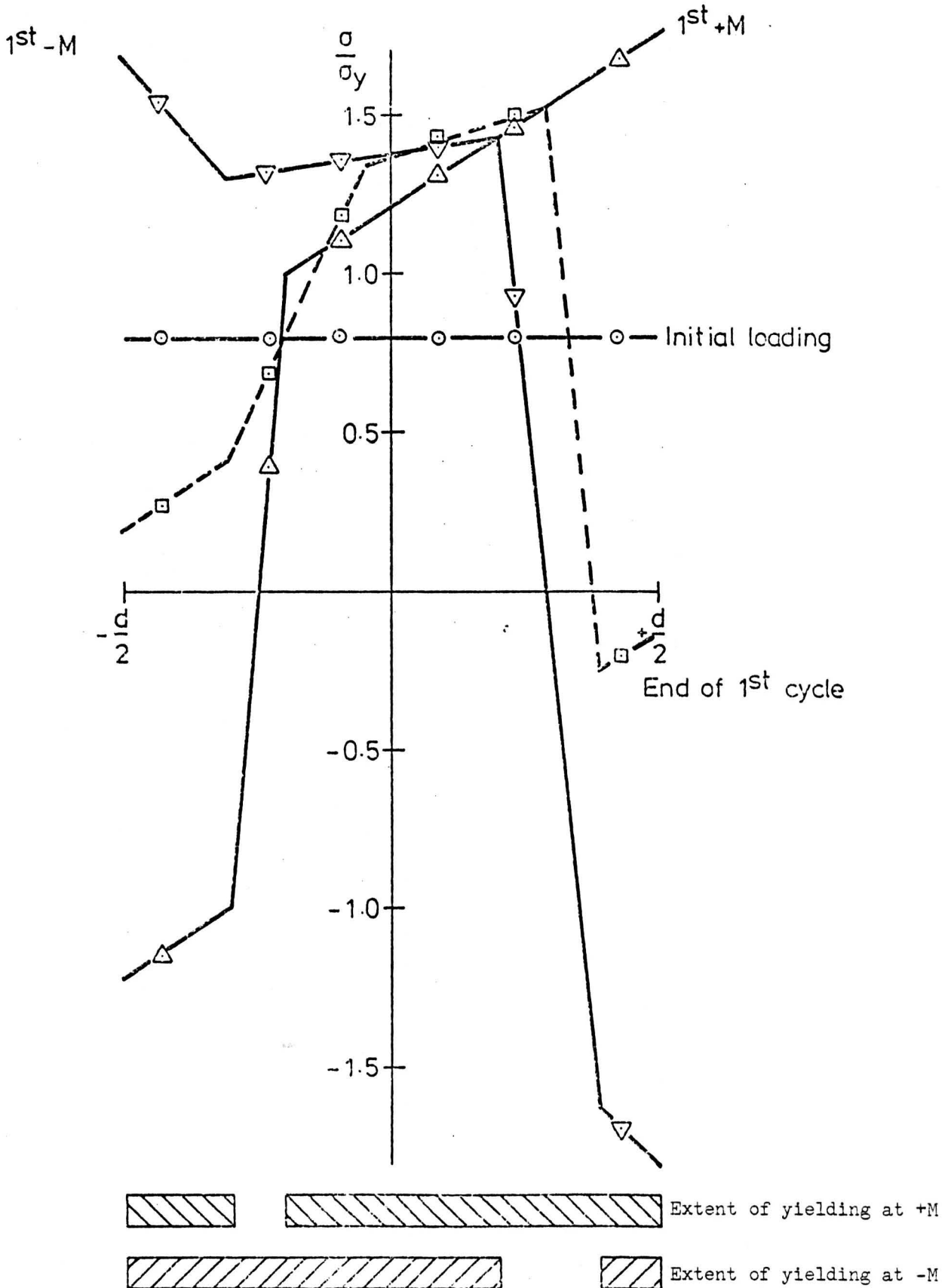


Figure 5.6 Stepped beam shank (Isotropic hardening, $E_p/E = 0.05$, $M/M_y = 1.5$, $P/P_L = 0.8$, 'no creep' conditions). Axial stress distributions due to initial loading and during the first cycle.

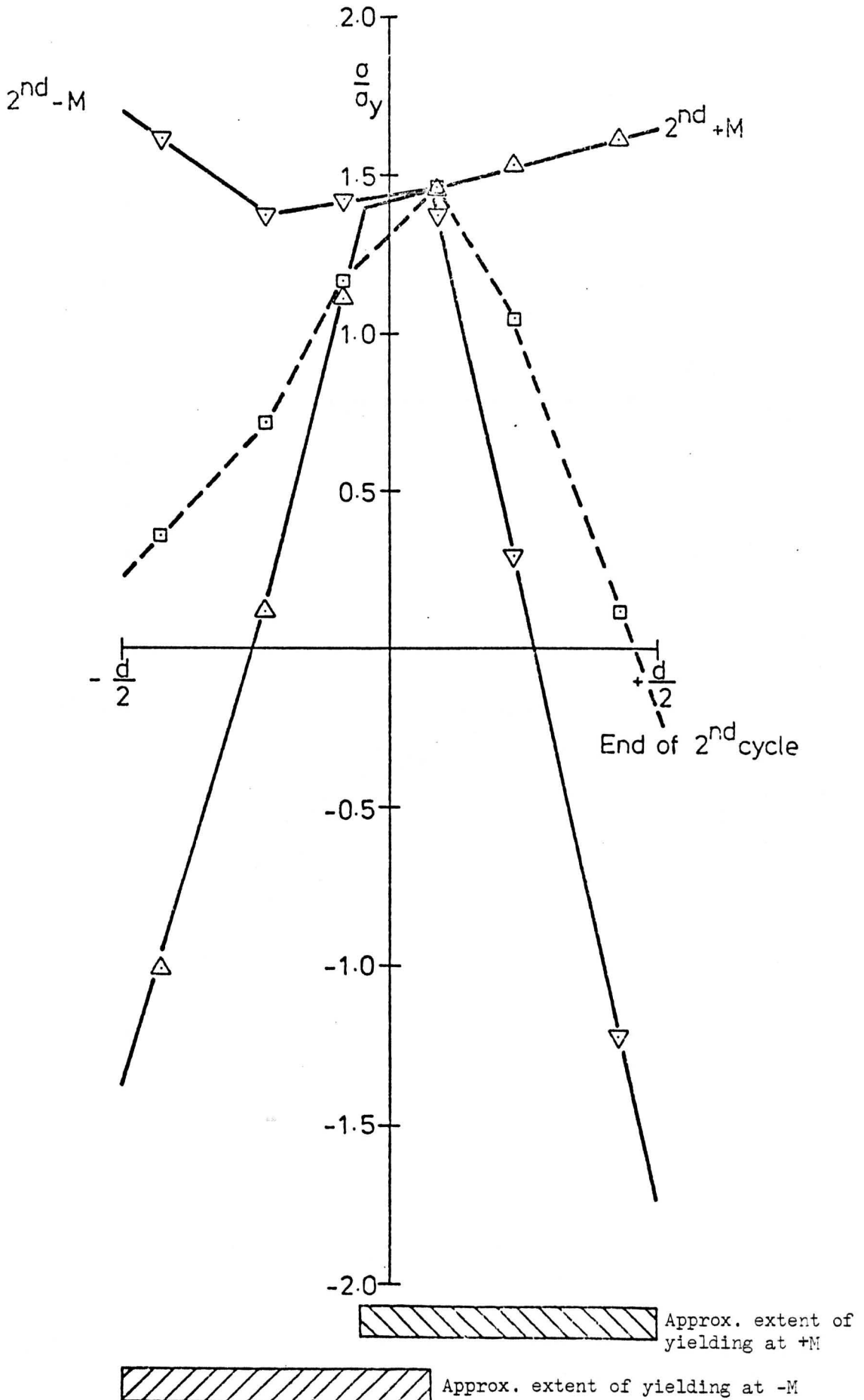


Figure 5.7 Stepped beam shank (Isotropic hardening, $E_p/E = 0.05$, $M/M_y = 1.5$, $P/R = 0.3$, 'no creep' conditions). Axial stress distributions during the 2nd cycle.

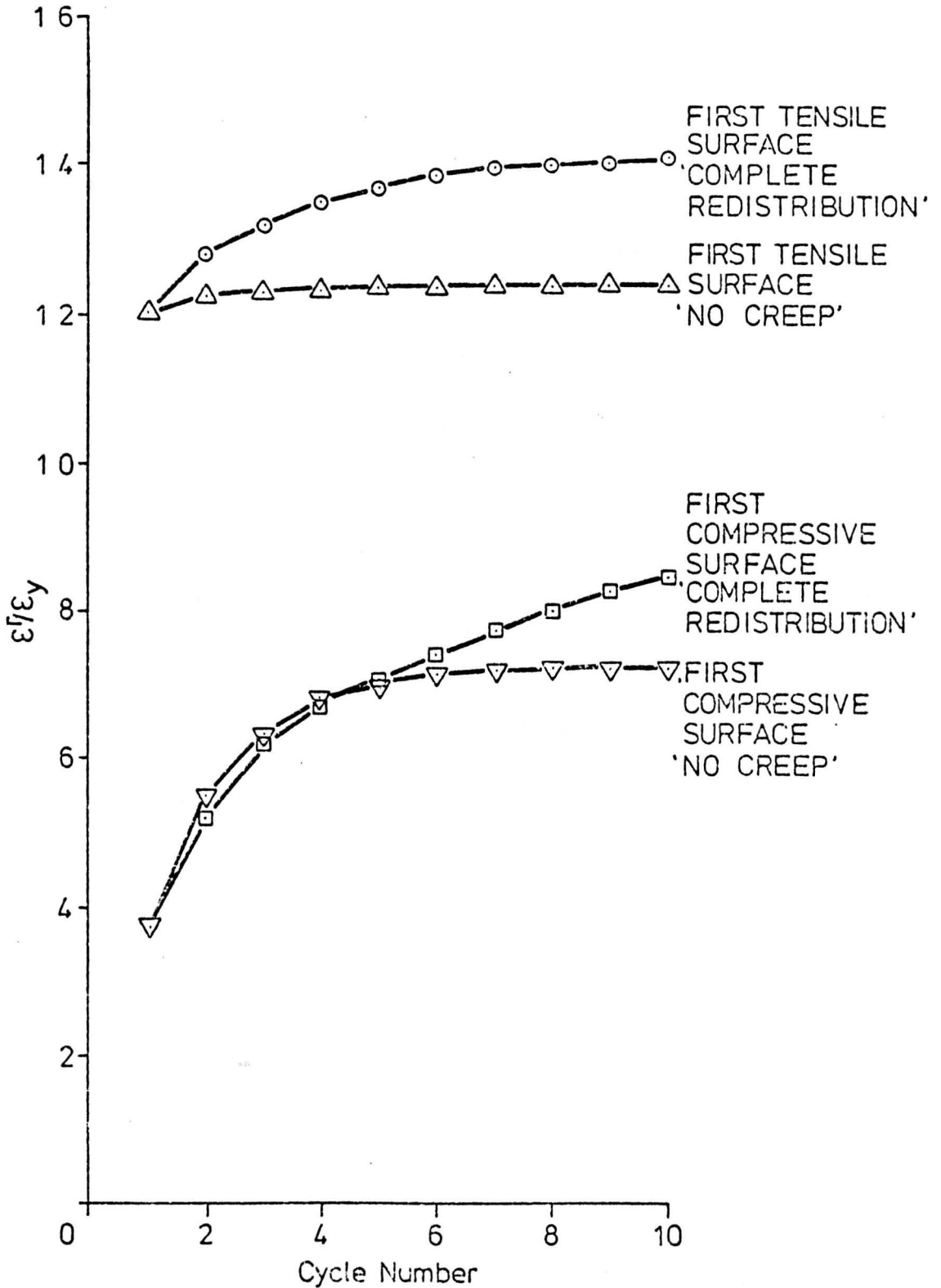


Figure 5.8 Stepped beam shank (Isotropic hardening, $E_p/E = 0.05$, $M/M_y = 1.5$, $P/P_L = 0.8$). Accumulation of normalised ratchet strain during the first 10 cycles.

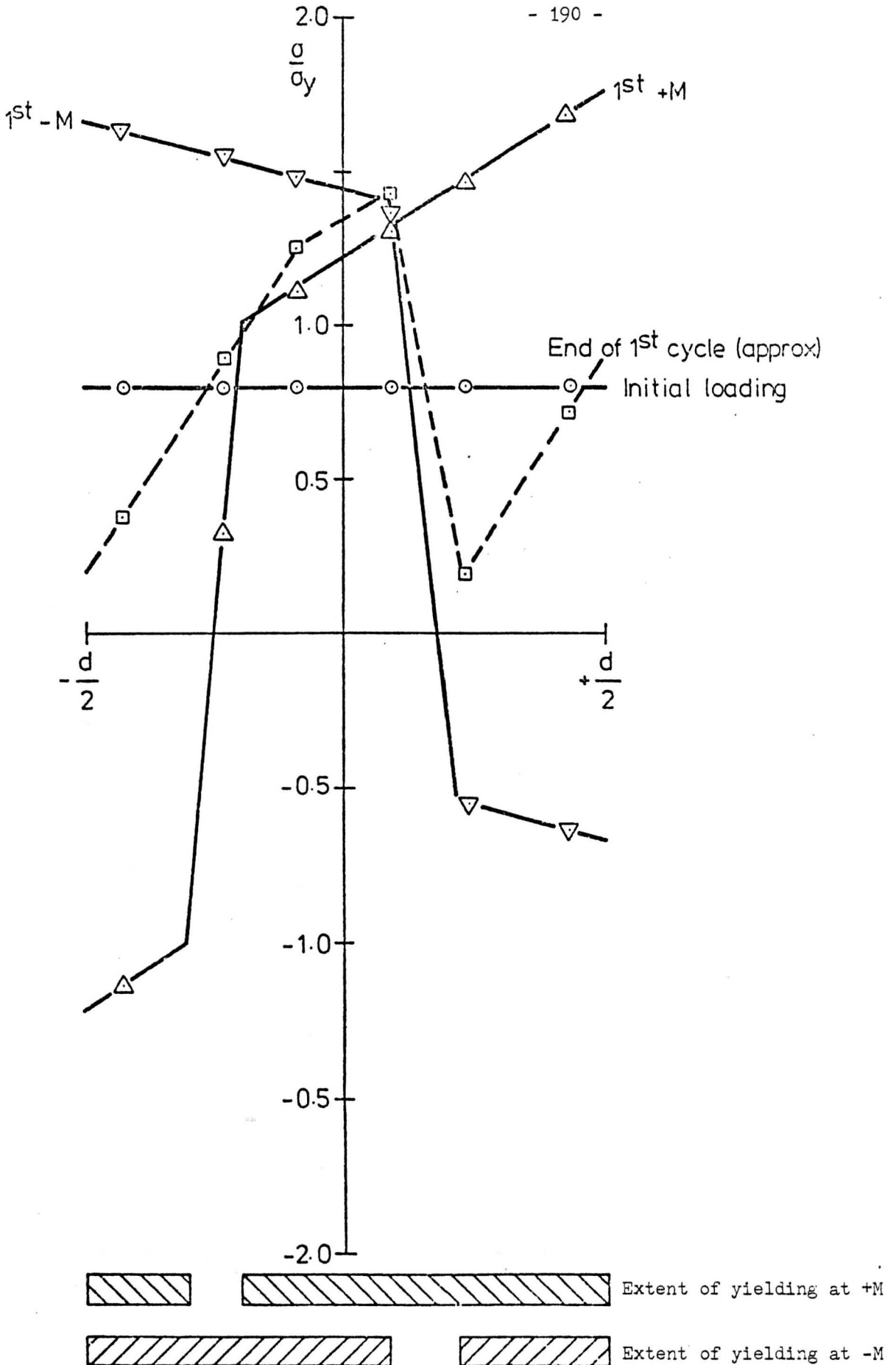
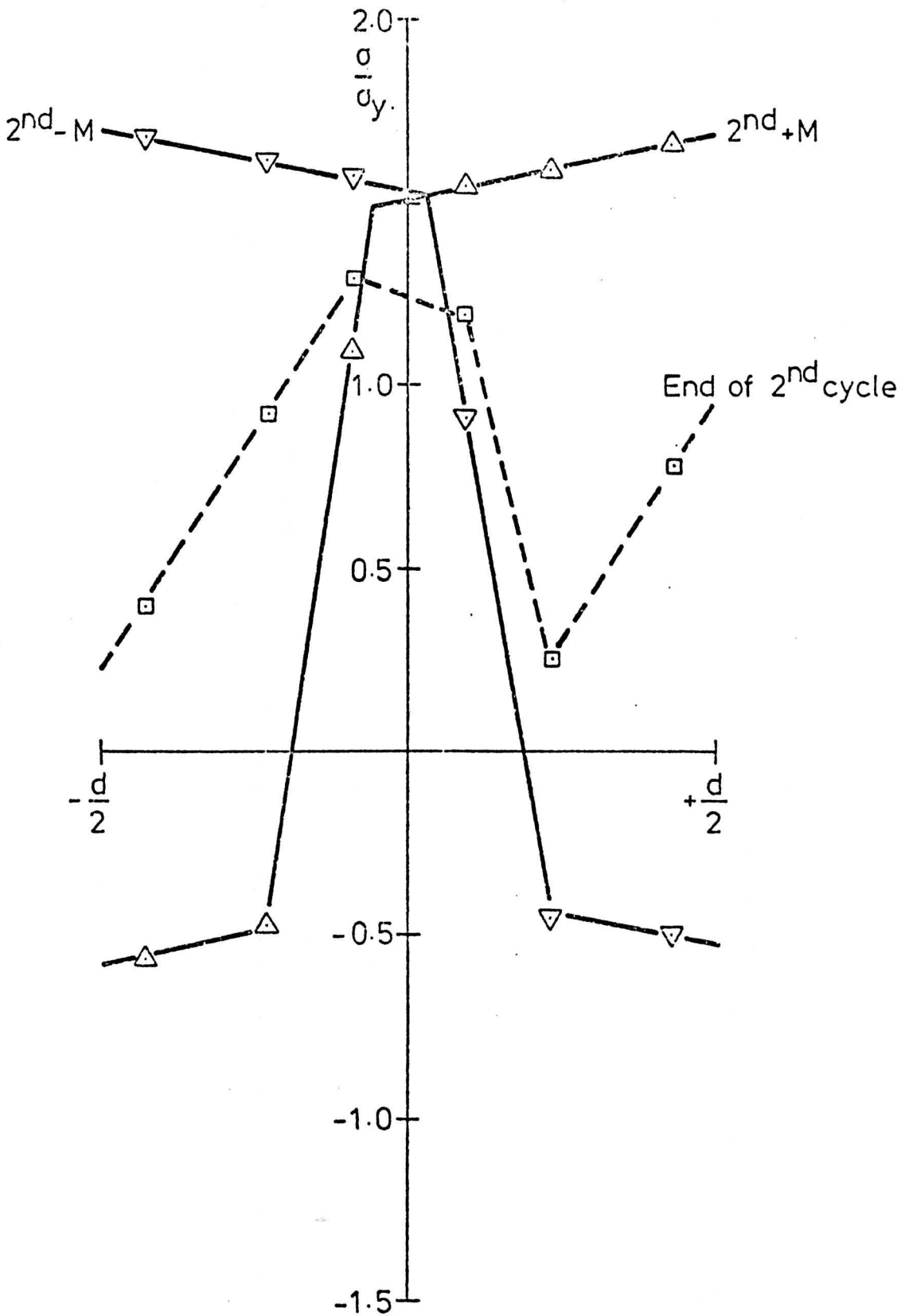
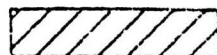
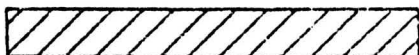


Figure 5.9 Stepped beam shank (Kinematic hardening, $E_p/E = 0.05$, $M/M_y = 1.5$, $P/P_L = 0.8$, 'no creep' conditions). Axial stress distributions due to initial loading and during the first cycle.



Approx. extent of yielding at +M



Approx. extent of yielding at -M

Figure 5.10 Stepped beam shank. (Kinematic hardening, $E_p/E = 0.05$, $M/M_y = 1.5$, $P/P_L = 0.8$, 'no creep' conditions). Axial stress distributions during the 2nd cycle.

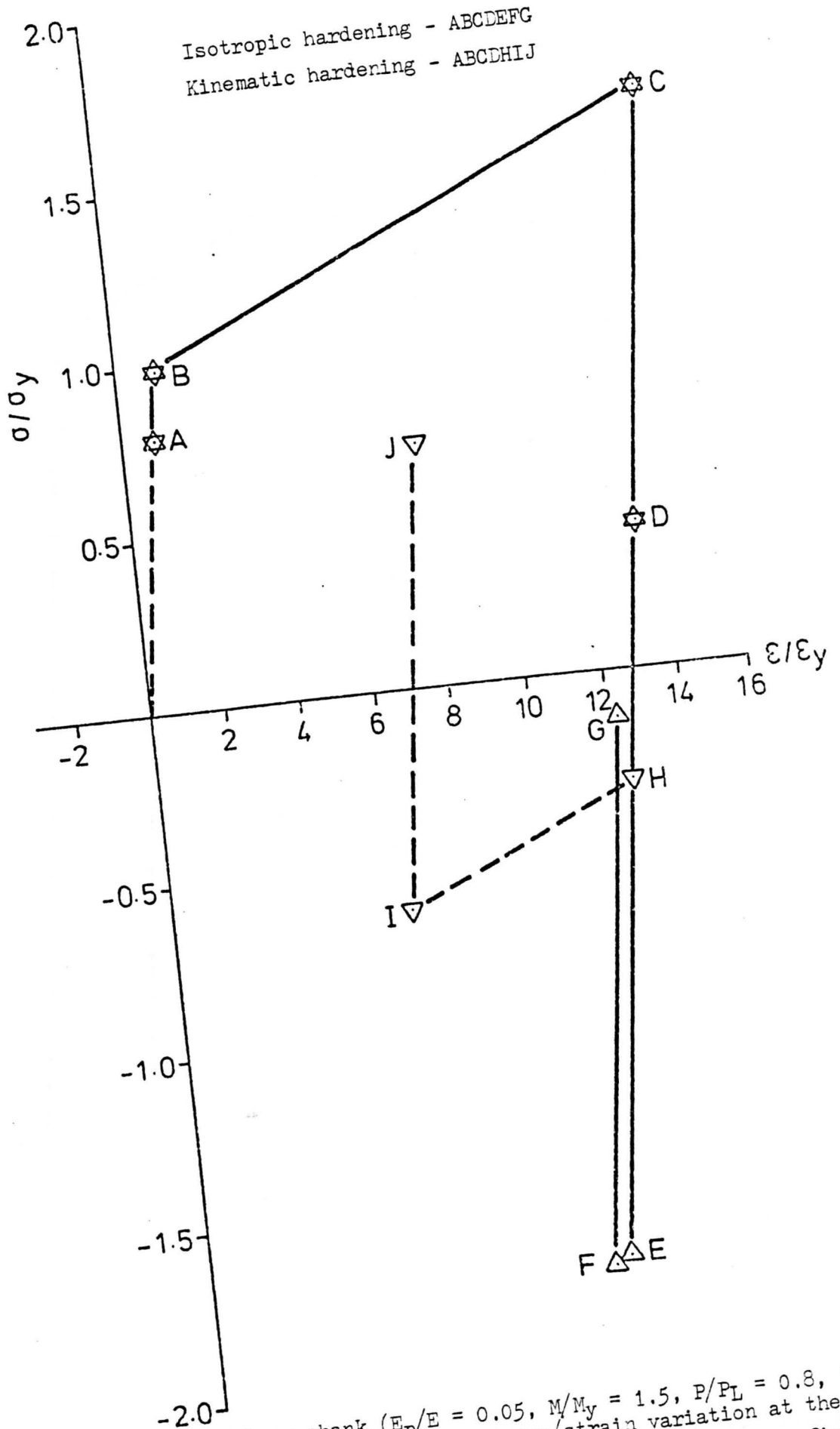


Figure 5.11 Stepped beam shank ($E_p/E = 0.05$, $M/M_y = 1.5$, $P/P_L = 0.8$, 'no creep' conditions). Axial stress/strain variation at the Gaussian point nearest to the first tensile surface during the first

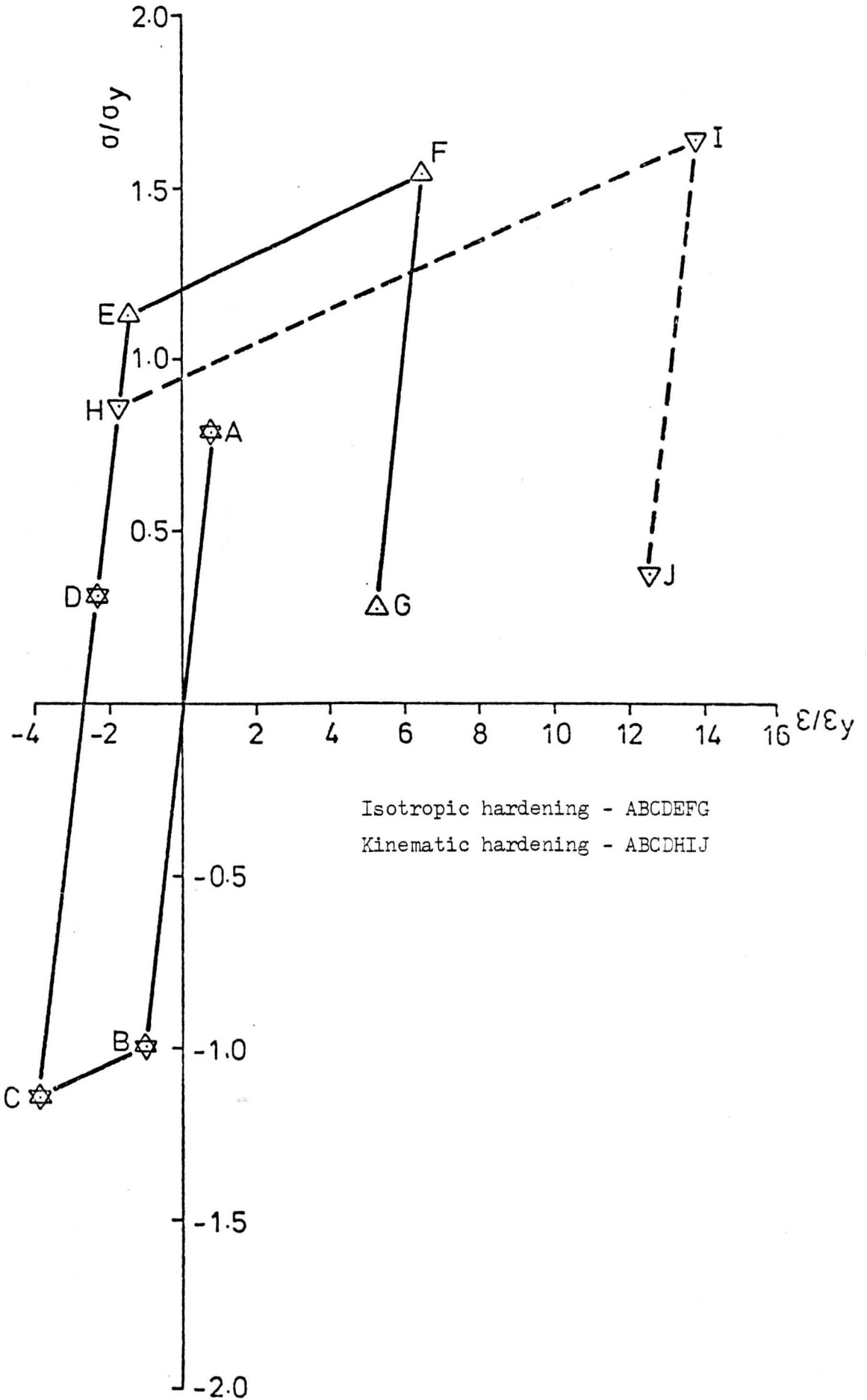


Figure 5.12 Stepped beam shank ($E_p/E = 0.05$, $M/M_y = 1.5$, $P/P_L = 0.8$, 'no creep' conditions). Axial stress/strain variation at the Gauss point nearest to the first compressive surface during the first cycle.

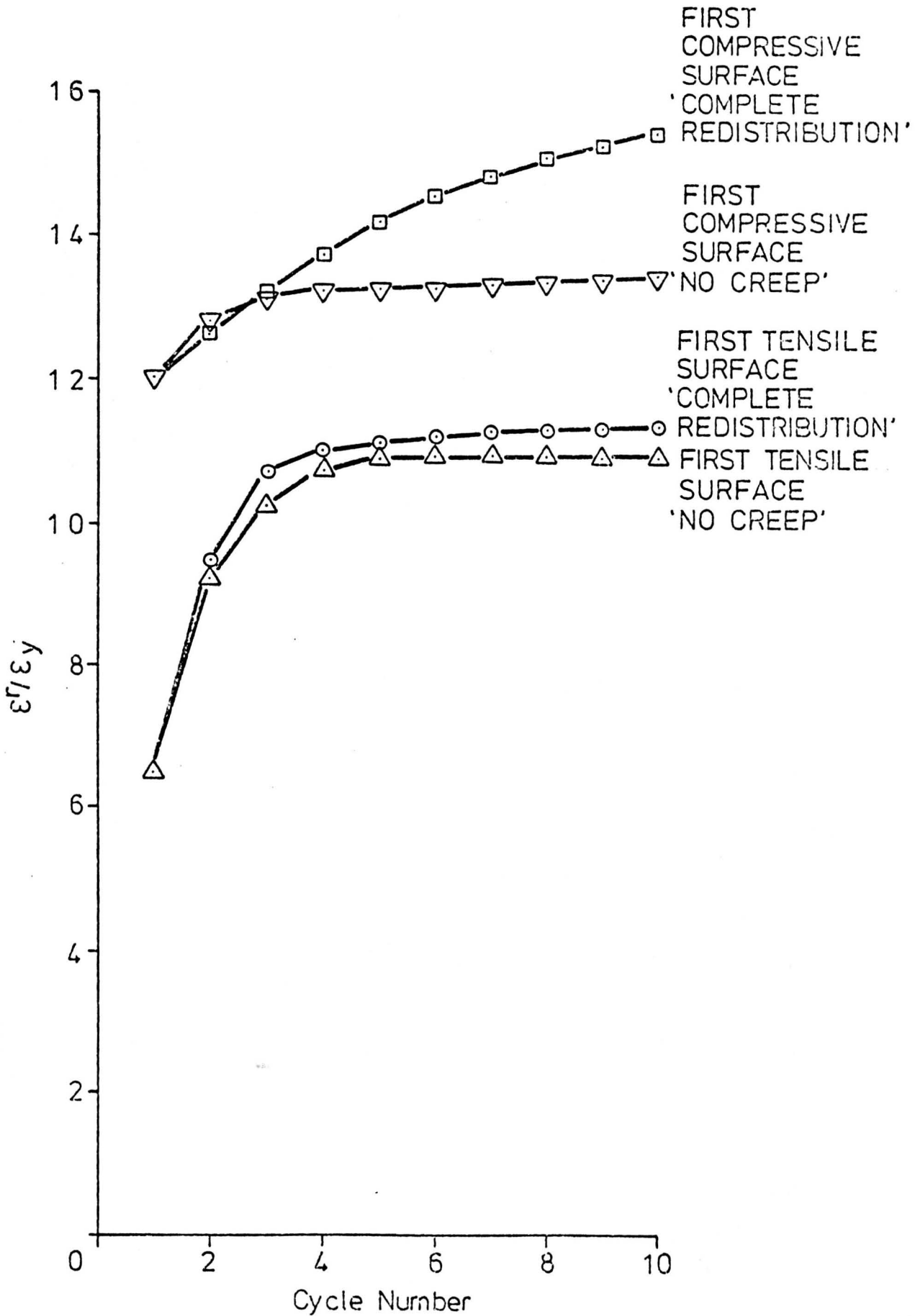


Figure 5.13 Stepped beam shank (Kinematic hardening, $E_p/E = 0.05$, $M/M_y = 1.5$, $P/P_L = 0.8$). Accumulation of normalised ratchet strain during the first 10 cycles.

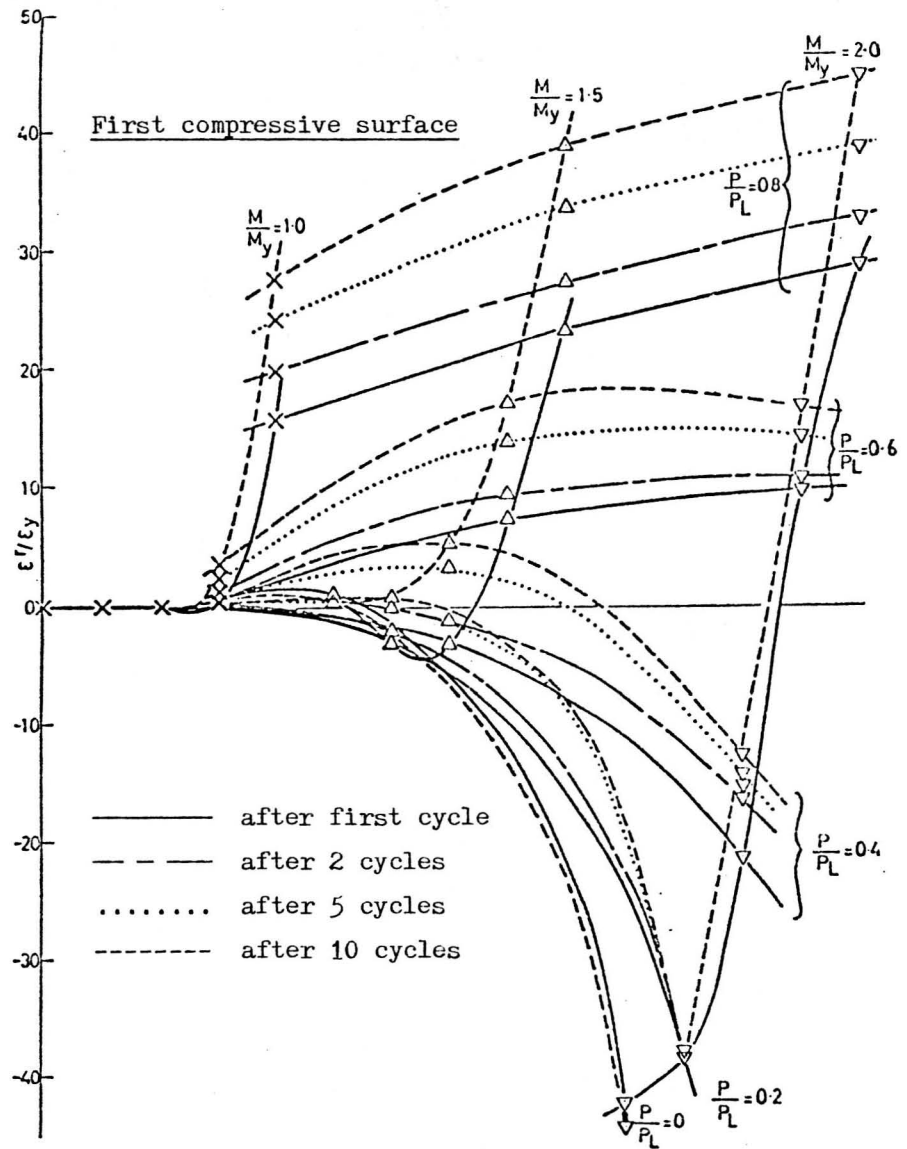
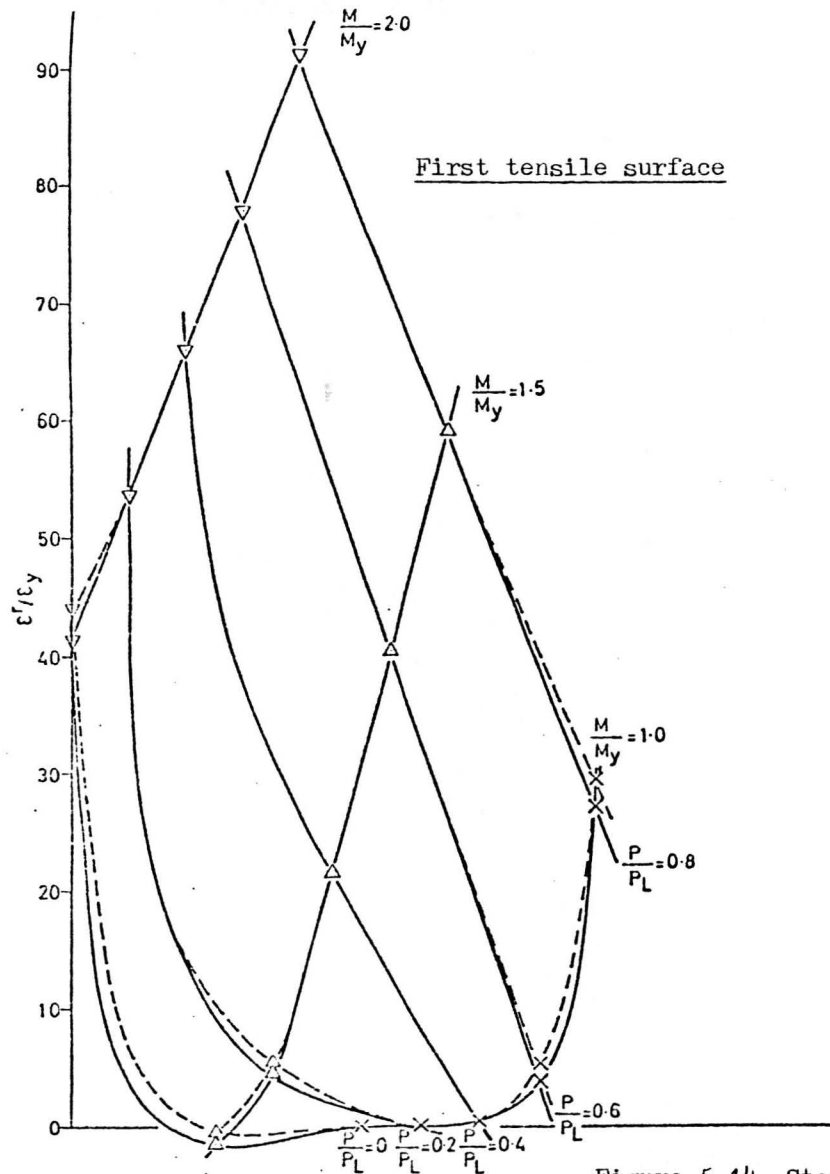


Figure 5.14 Stepped beam shank (Isotropic hardening, $E_D/E = 0.01$, 'no creep' conditions). Accumulation of normalized ratchet strain in 10 cycles.

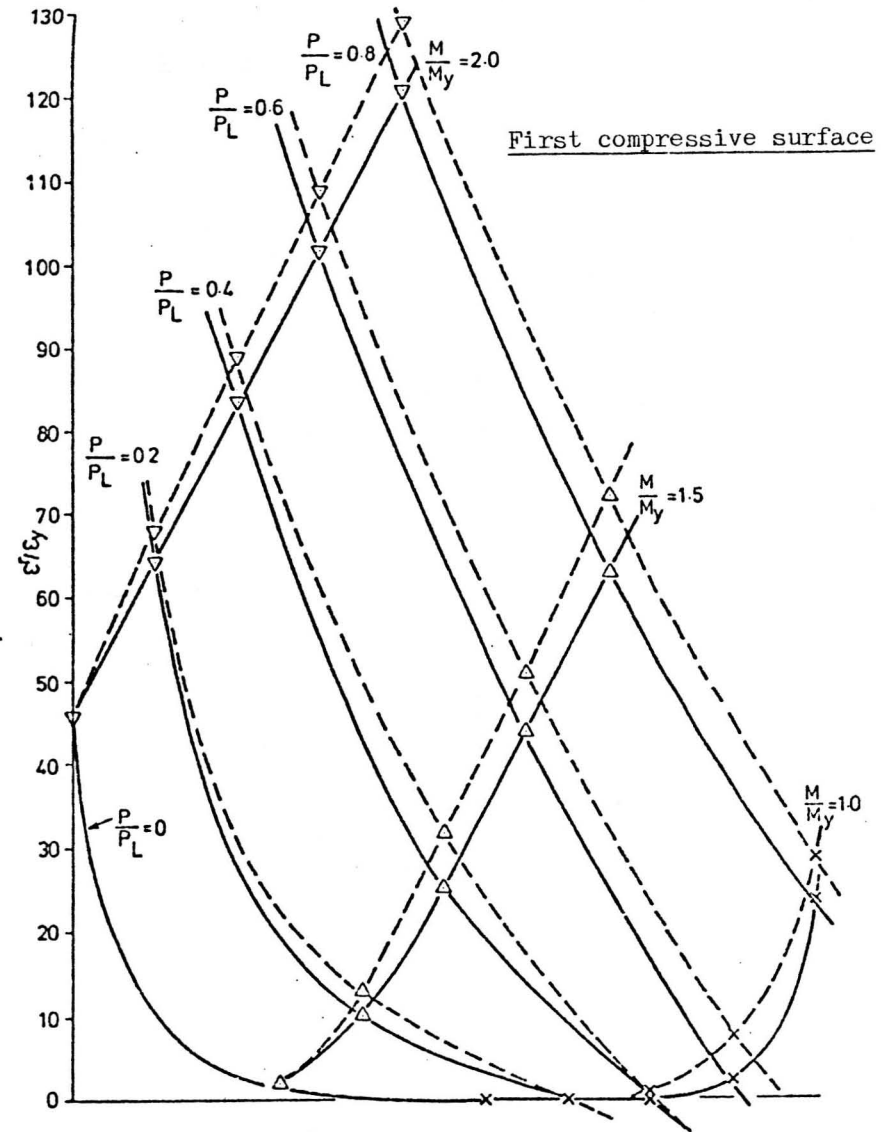
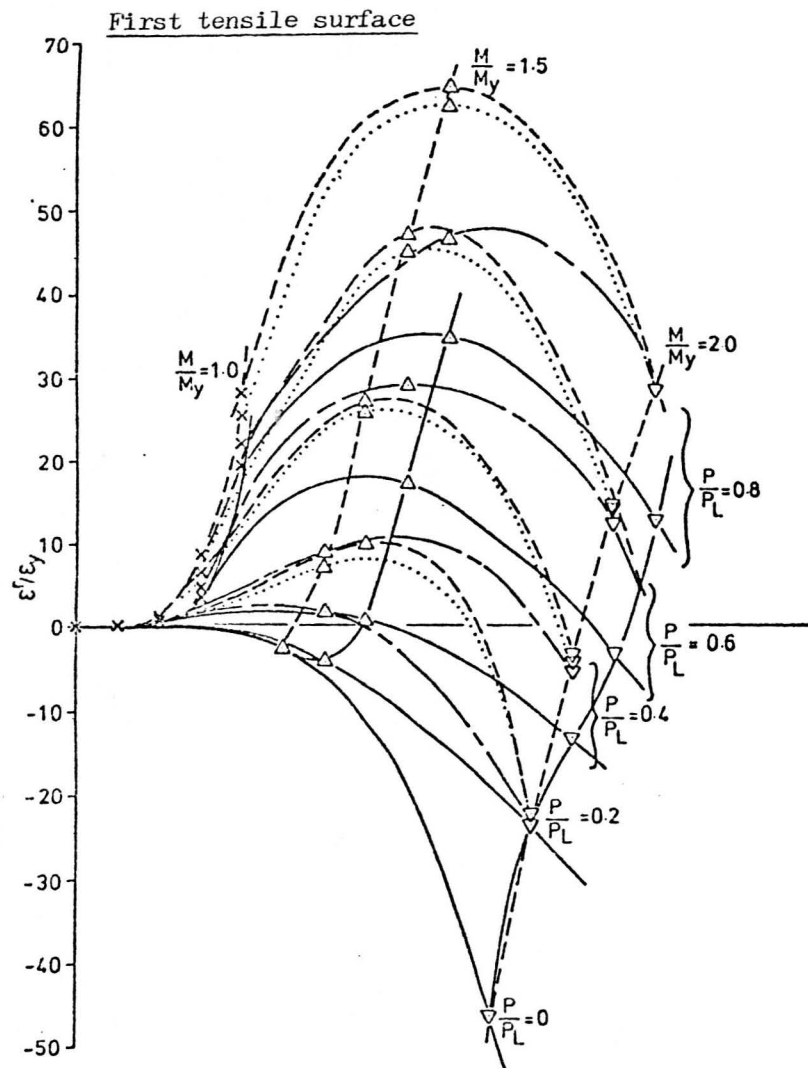
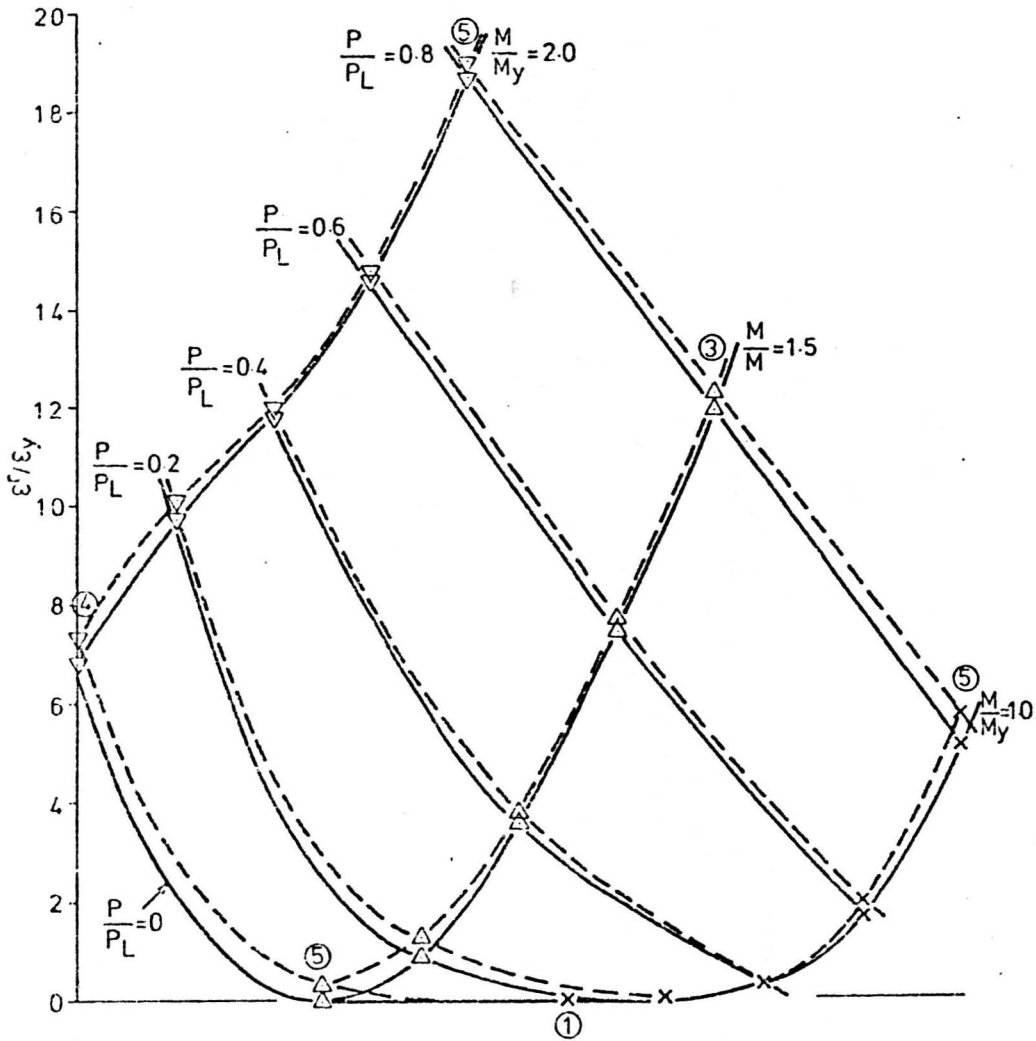


Figure 5.15 Stepped beam shank (Kinematic hardening, $E_T/E = 0.01$, 'no creep' conditions). Accumulation of normalised ratchet strain in 10 cycles - see Figure 5.14 for notation.

First tensile surface



First compressive surface

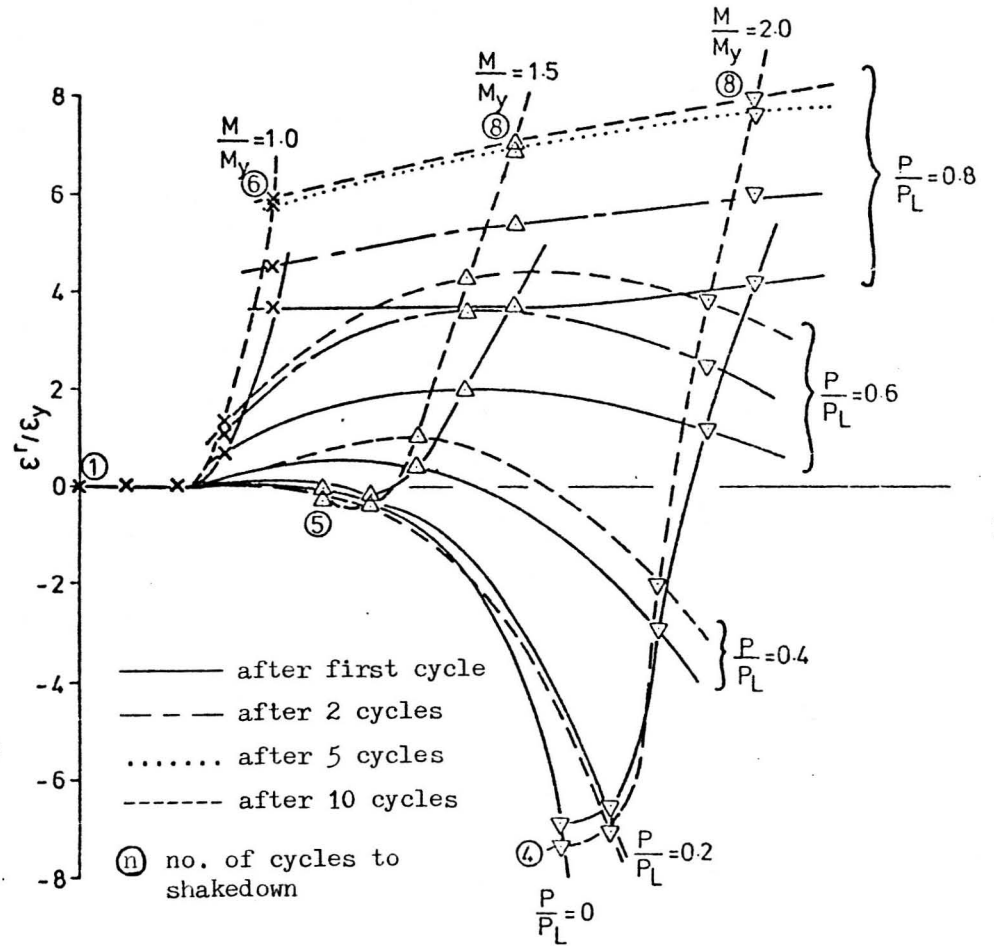


Figure 5.16 Stepped beam shank (Isotropic hardening, $E_p/E = 0.05$, 'no creep' conditions). Accumulation of normalised ratchet strain in 10 cycles.

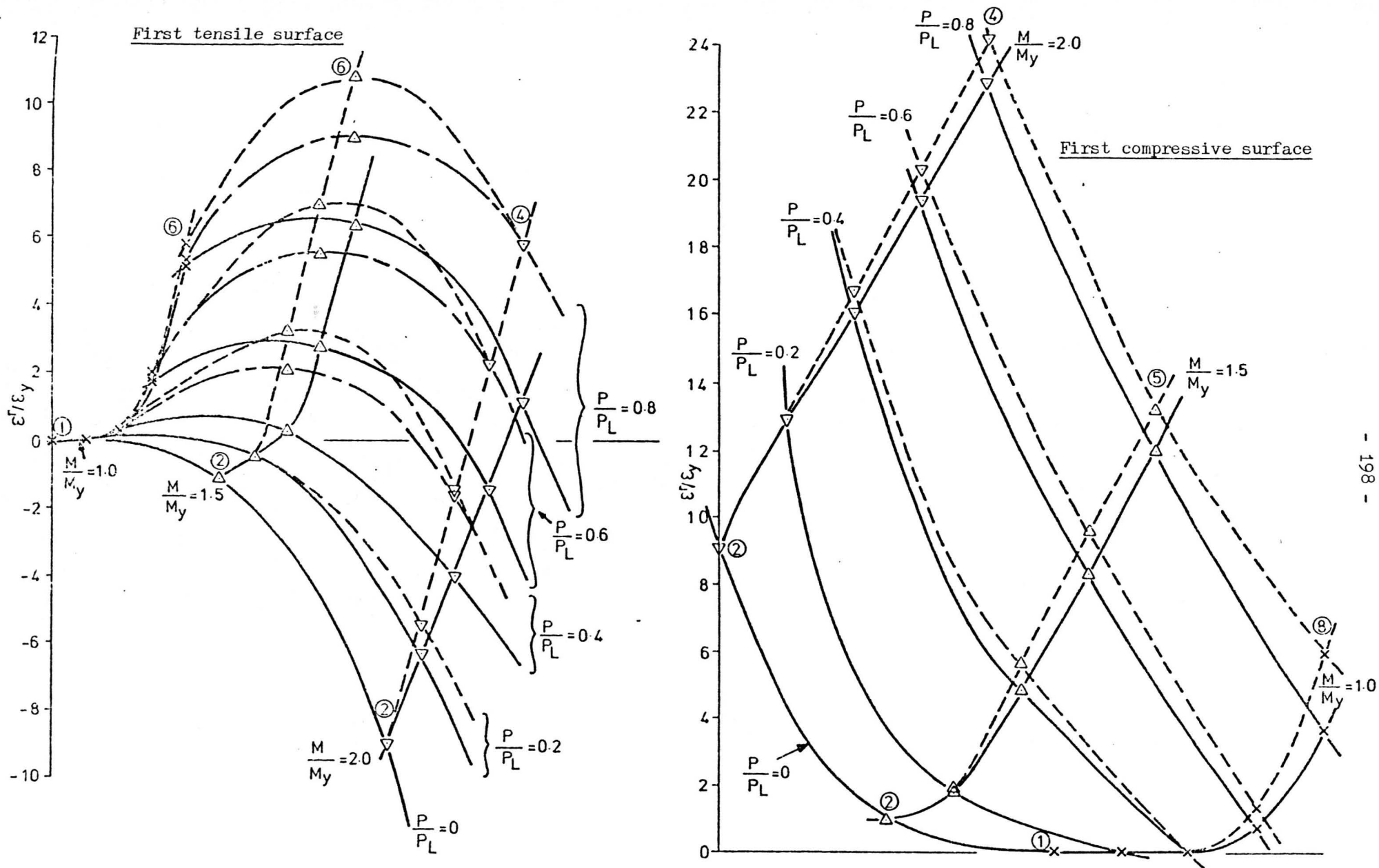


Figure 5.17 Stepped beam shank (Kinematic hardening, $E_p/E = 0.05$, 'no creep' conditions). Accumulation of normalised ratchet strain in 10 cycles - see Figure 5.16 for notation.

First tensile surface

First compressive surface

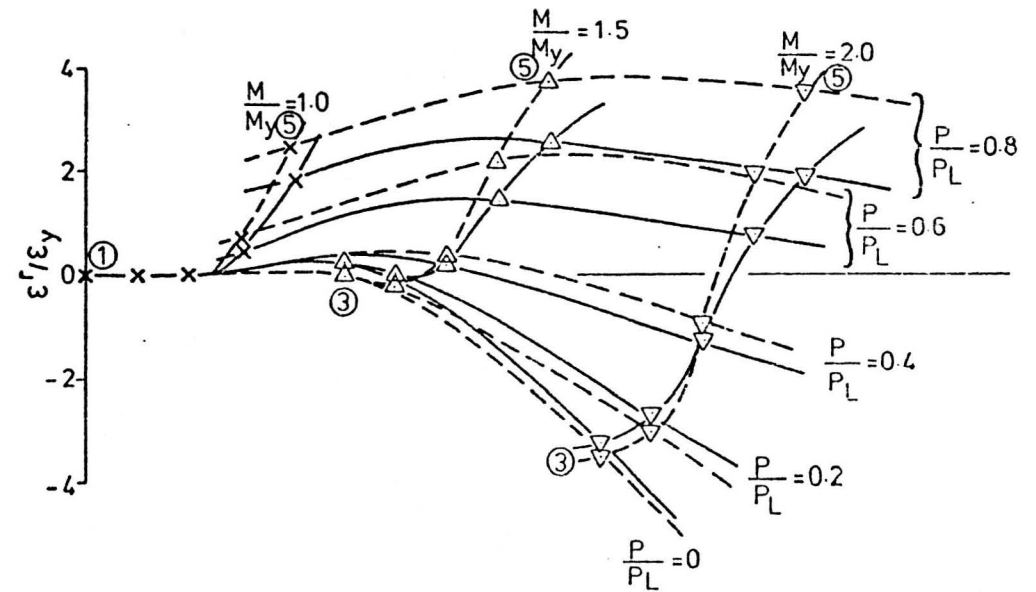
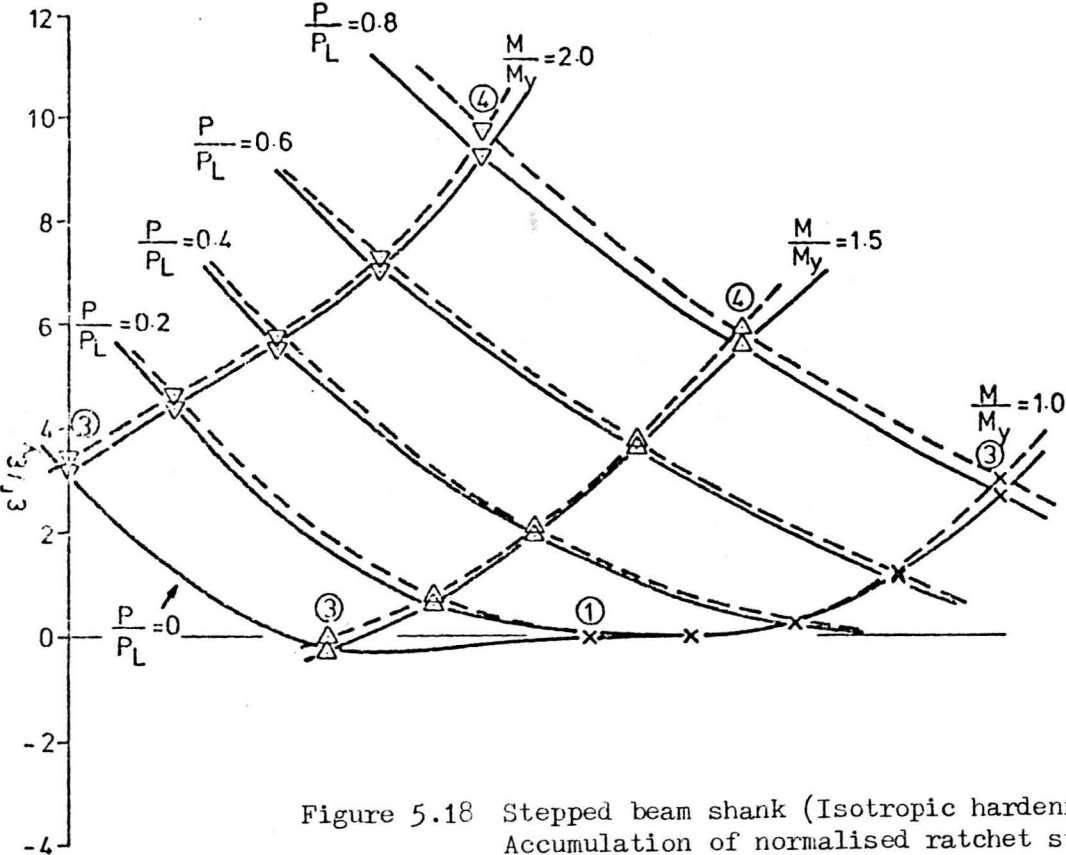
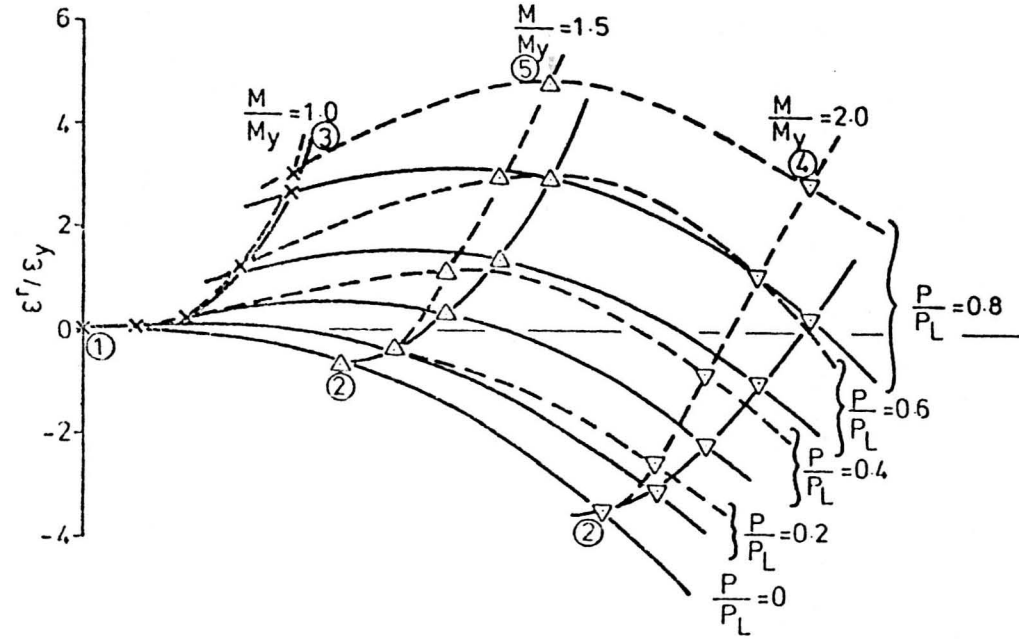


Figure 5.18 Stepped beam shank (Isotropic hardening, $E_p/E = 0.1$, 'no creep' conditions).
Accumulation of normalised ratchet strain in 10 cycles - see Figure 5.16 for notation.

First tensile surface



First compressive surface

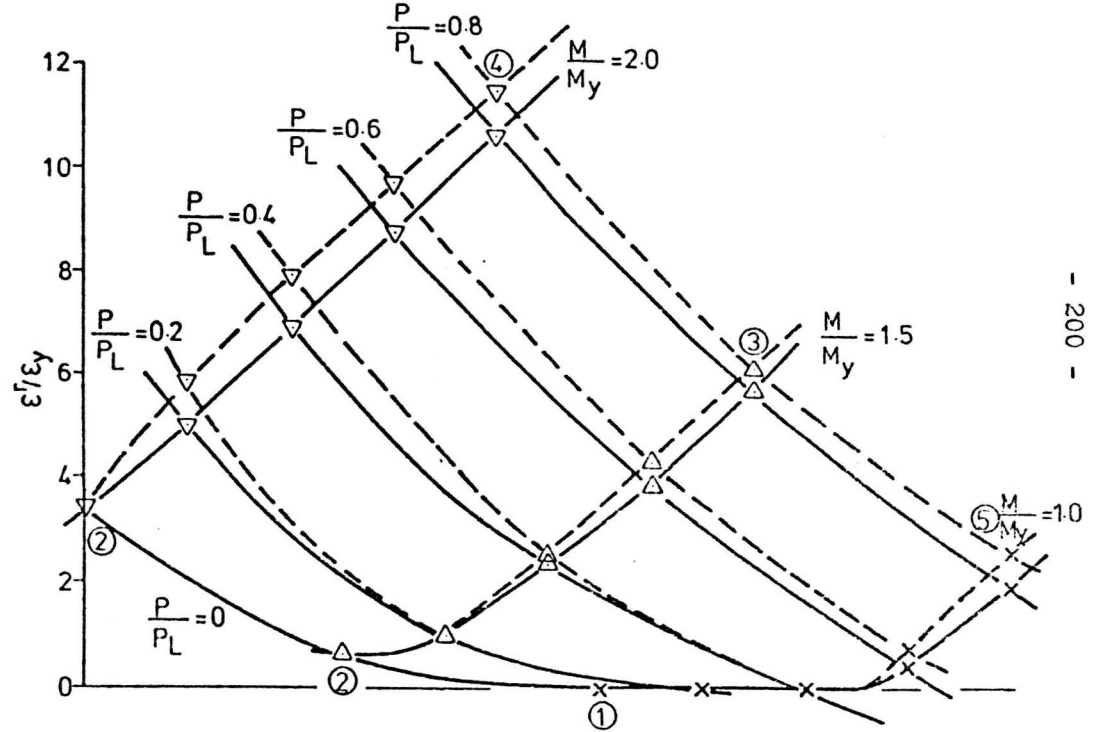


Figure 5.19 Stepped beam shank (Kinematic hardening, $E_p/E = 0.1$, 'no creep' conditions).
Accumulation of normalised ratchet strain in 10 cycles - see Figure 5.16 for notation.

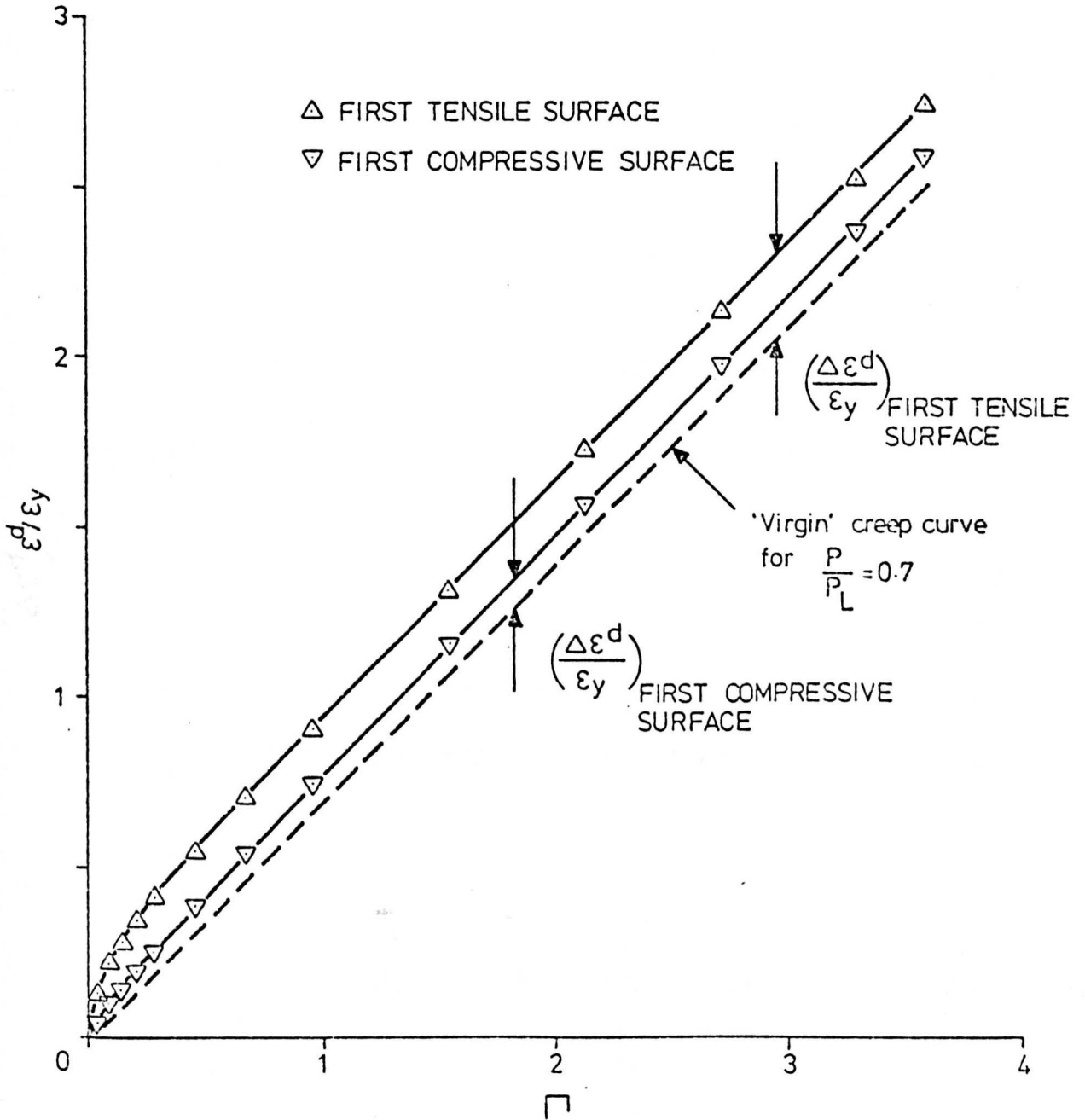


Figure 5.20 Stepped beam shank (elastic-perfectly-plastic, $M/M_y = 0.7$, $P/P_L = 0.7$, complete redistribution). Accumulations of normalised strain during the first dwell period.

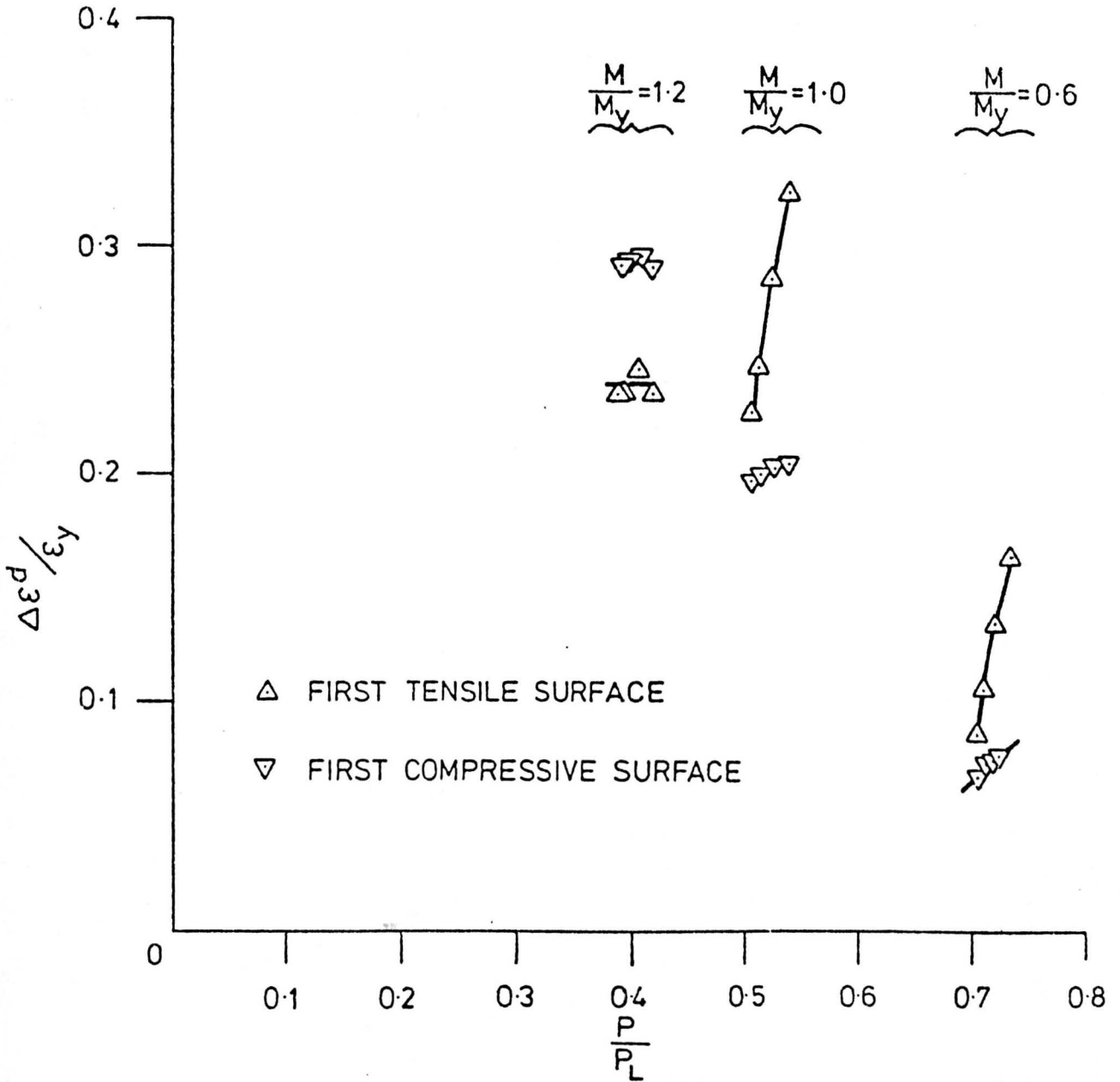


Figure 5.21 Stepped beam shank (elastic-perfectly-plastic, complete redistribution). Variation in increment of normalised strain due to stress redistribution with mean and bending loads.

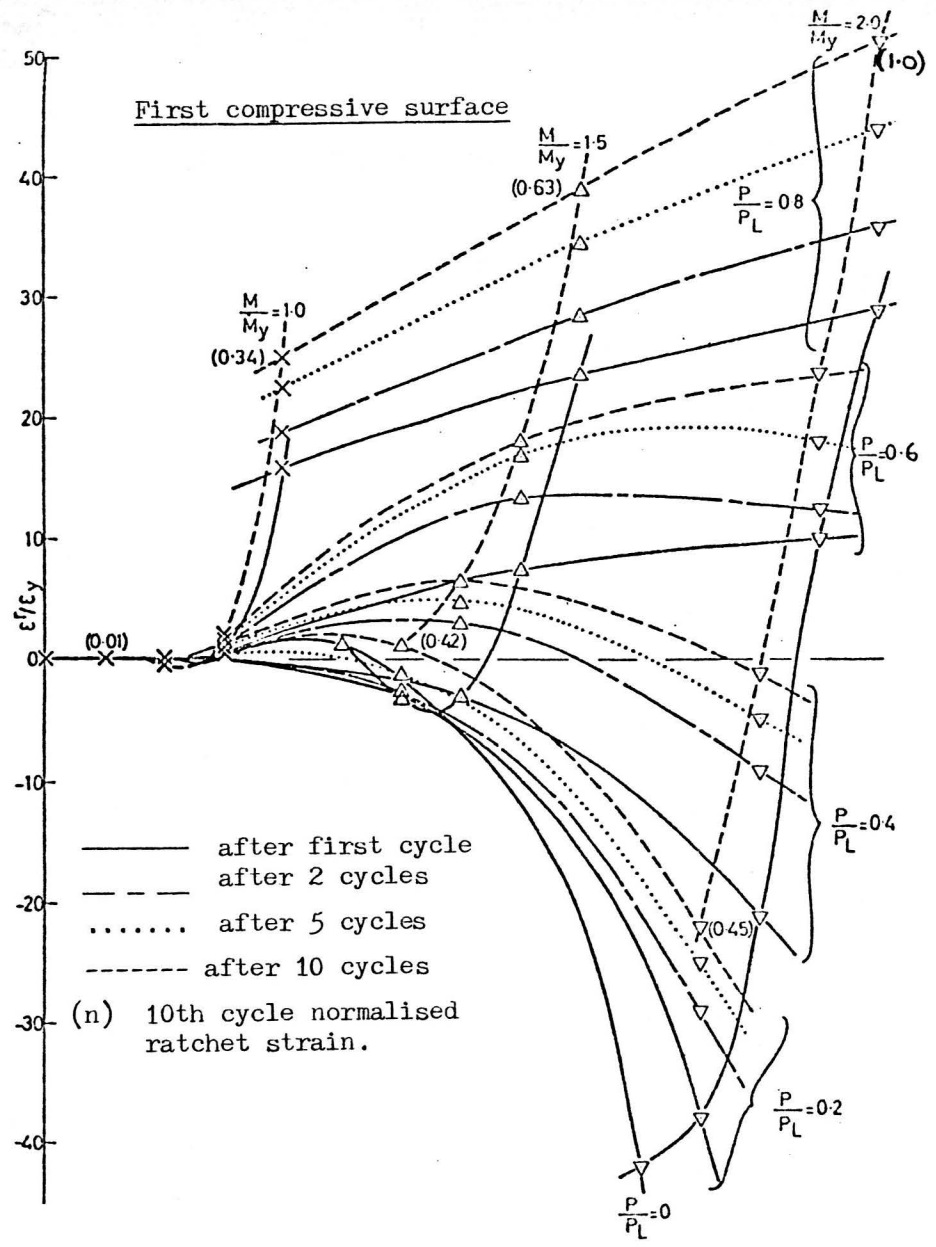
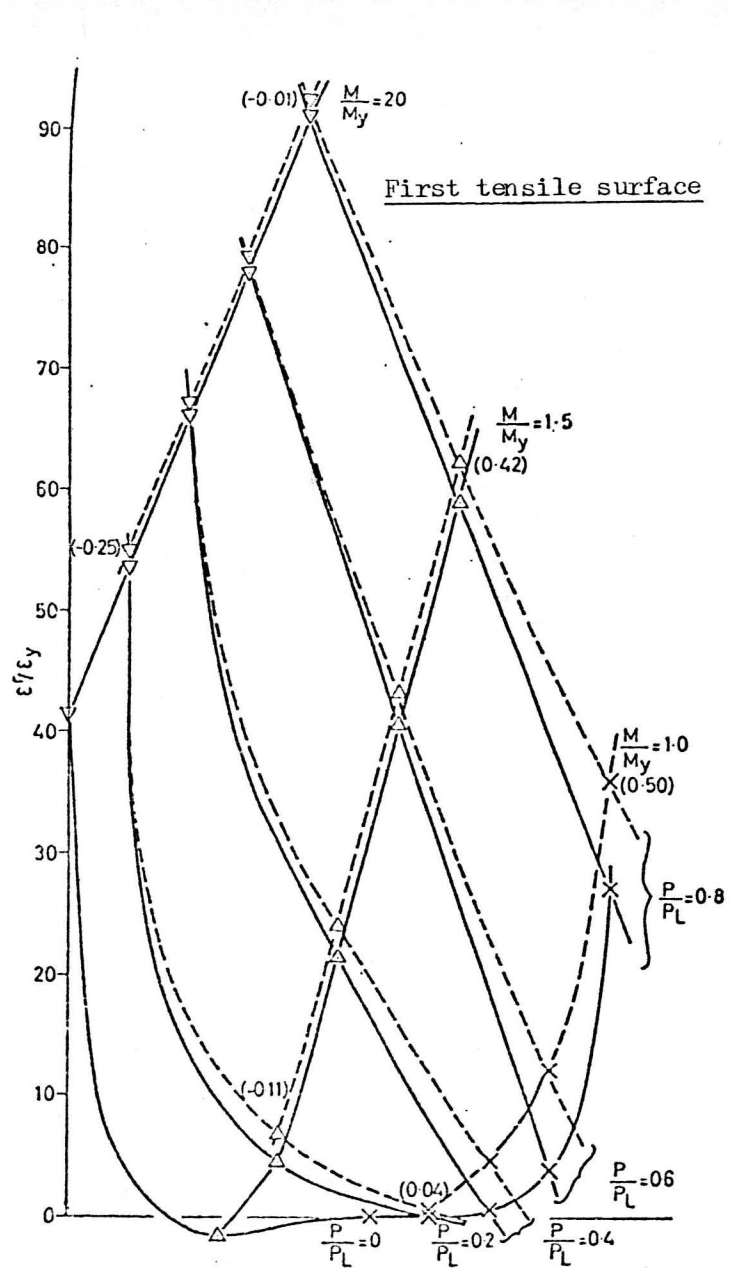


Figure 5.22 Stepped beam shank (Isotropic hardening, $E_p/E = 0.01$, complete redistribution). Accumulation of normalised ratchet strain in 10 cycles.

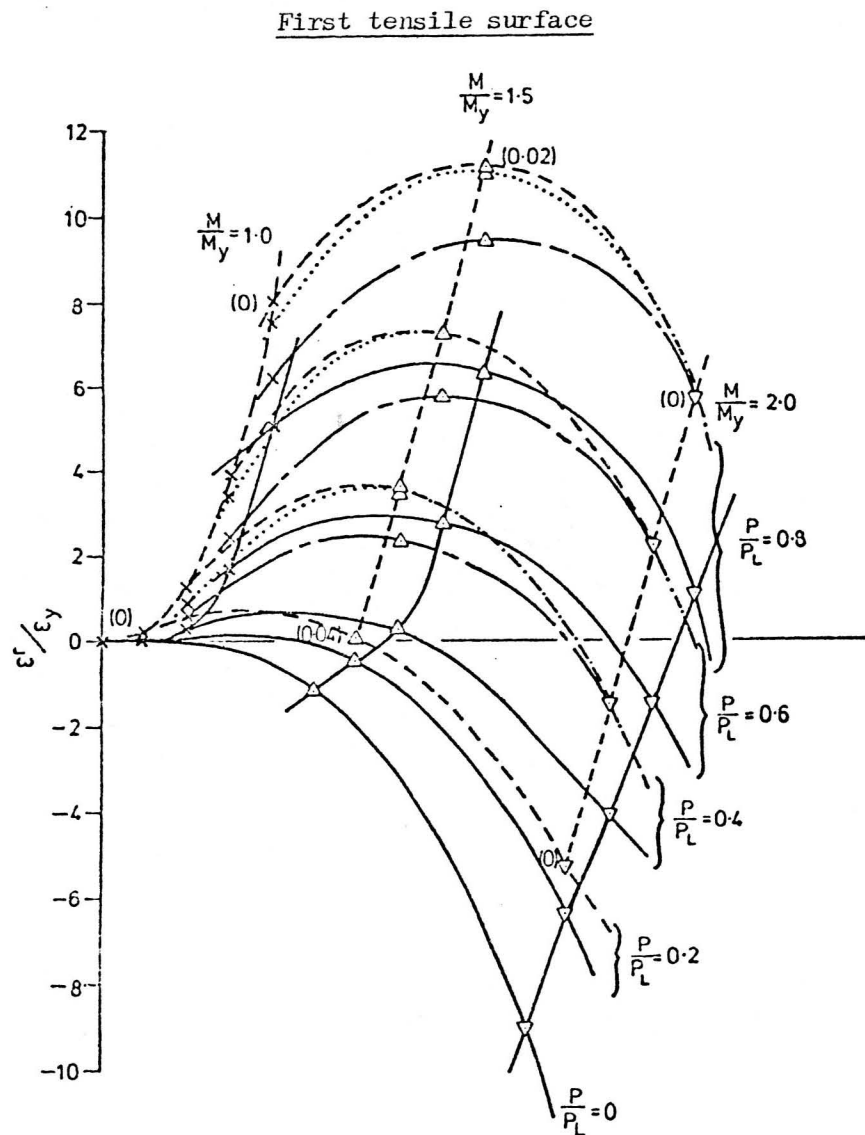


Figure 5.24 Stepped beam shank (Kinematic hardening, $E_p/E = 0.05$, complete redistribution).
 Accumulation of normalised ratchet strain in 10 cycles - see Figure 5.22 for notation.

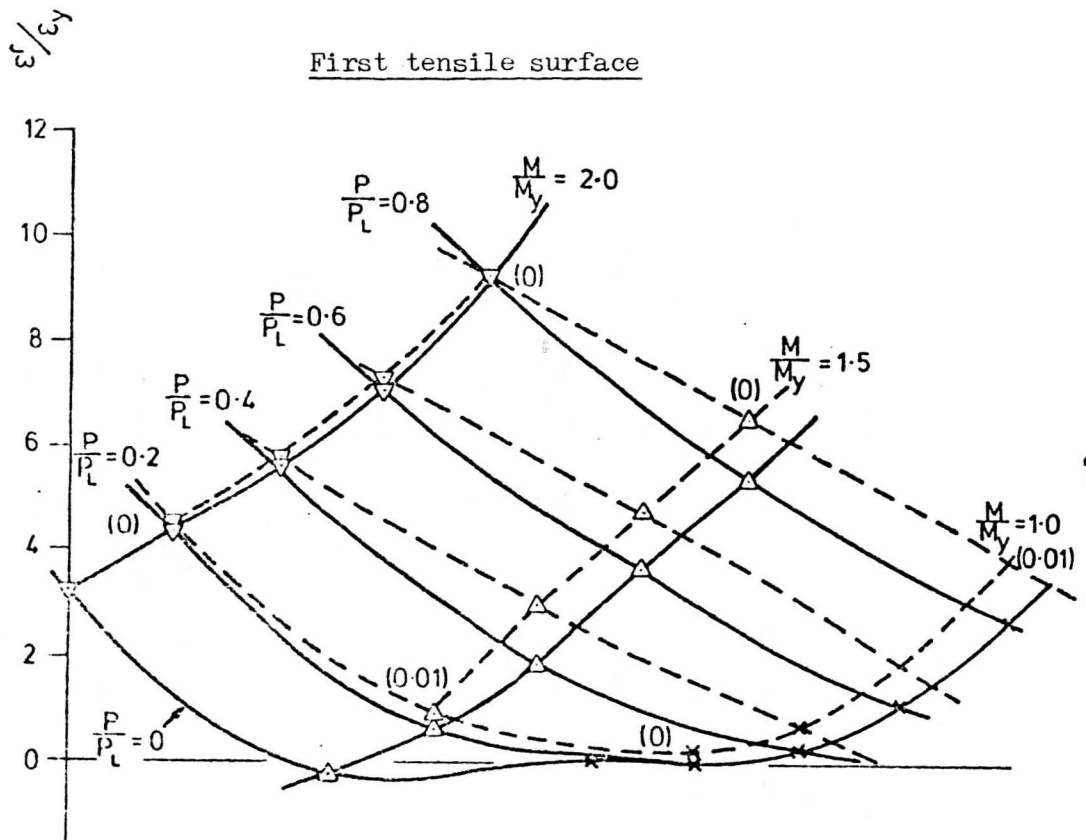
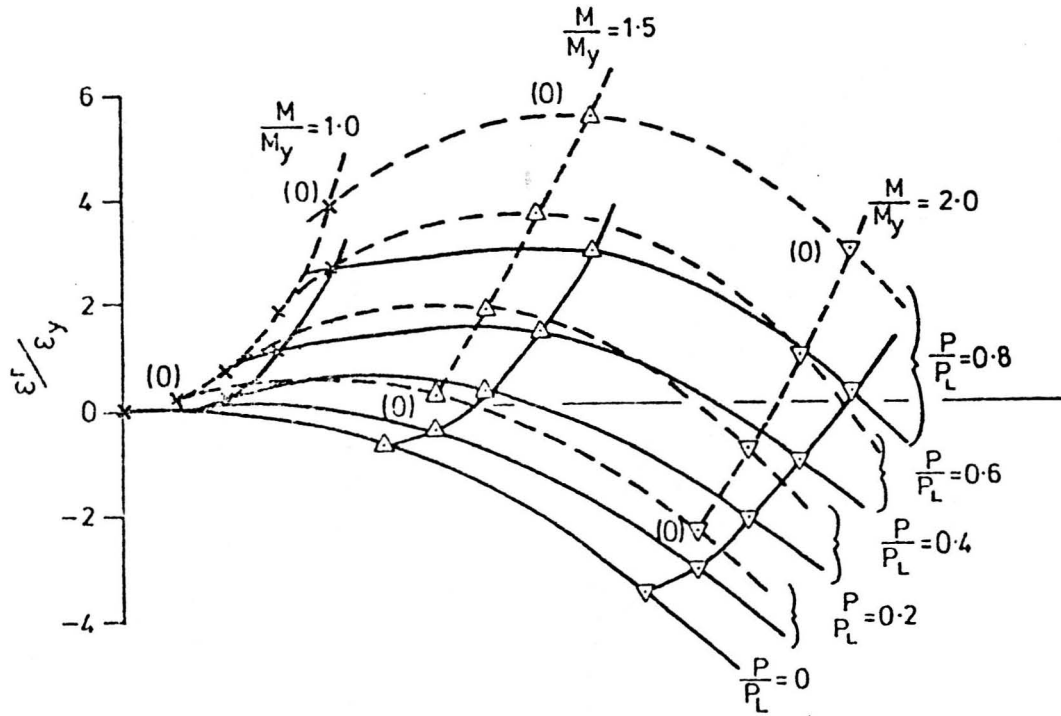


Figure 5.25 Stepped beam shank (Isotropic hardening, $E_p/E = 0.1$, complete redistribution).
 Accumulation of normalised ratchet strain in 10 cycles - see Figure 5.22 for notation.

First tensile surface



First compressive surface

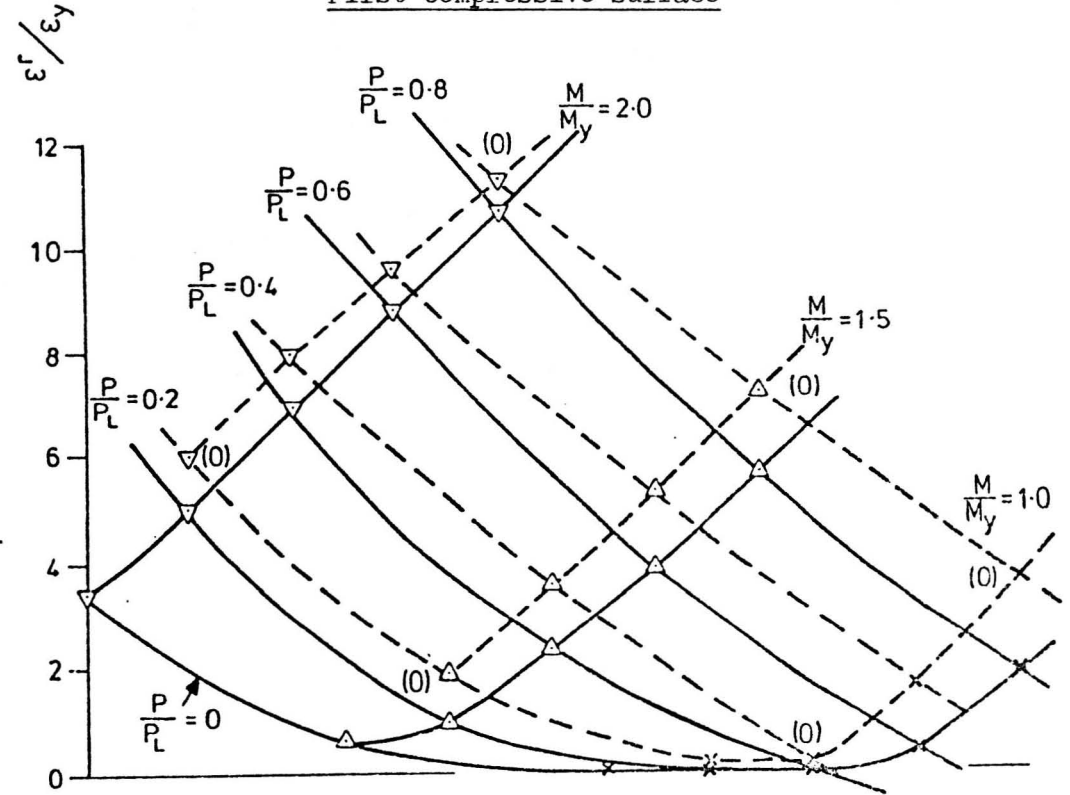


Figure 5.26 Stepped beam shank (Kinematic hardening, $E_p/E = 0.1$, complete redistribution).
Accumulation of normalised ratchet strain in 10 cycles - see Figure 5.22 for notation.

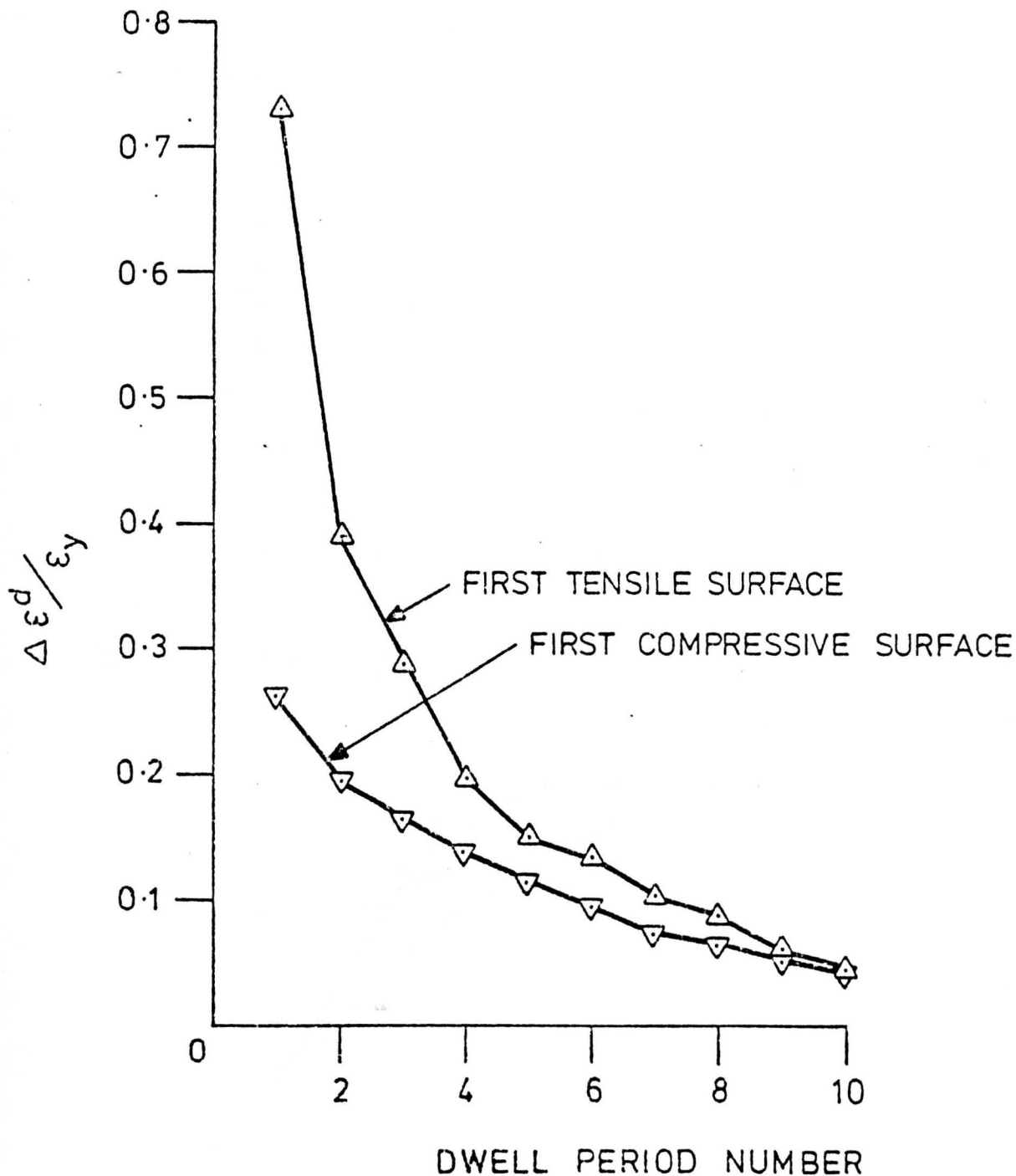


Figure 5.27 Stepped beam shank (Isotropic hardening, $E_p/E = 0.05$, $M/M_y = 1.5$, $P/P_L = 0.8$, complete redistribution). Variation in increment of normalised strain due to stress redistribution for the first 10 dwell periods.

- × ISOTROPIC HARDENING, FIRST TENSILE SURFACE
- △ ISOTROPIC HARDENING, FIRST COMPRESSIVE SURFACE
- KINEMATIC HARDENING, FIRST TENSILE SURFACE
- ▽ KINEMATIC HARDENING, FIRST COMPRESSIVE SURFACE

————— $P/P_L = 0.2$
 - - - - - $P/P_L = 0.8$

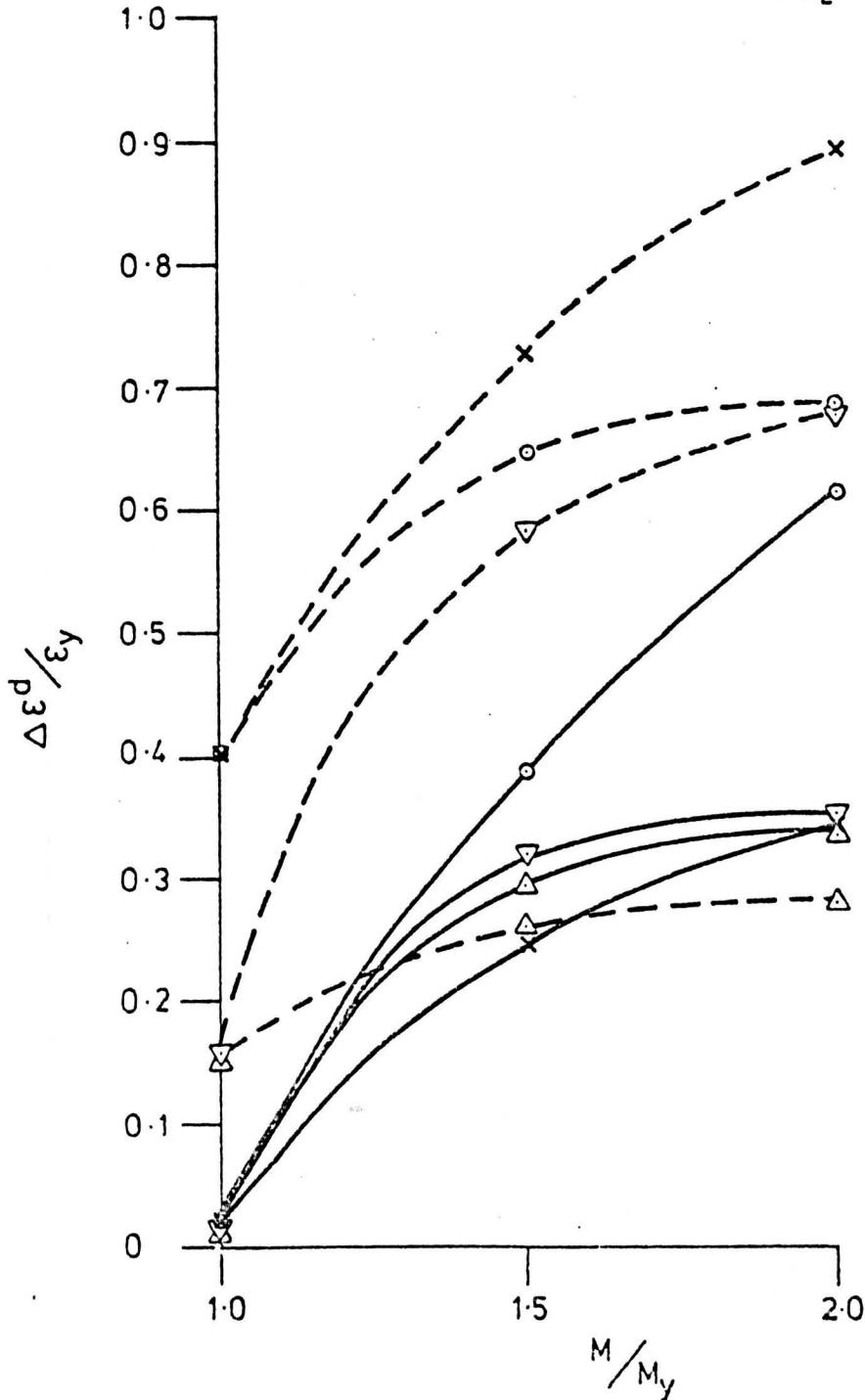


Figure 5.28 Stepped beam shank ($E_p/E = 0.05$, complete redistribution). Variation in increment of normalised strain due to stress redistribution during the first dwell period with mean and bending loads.

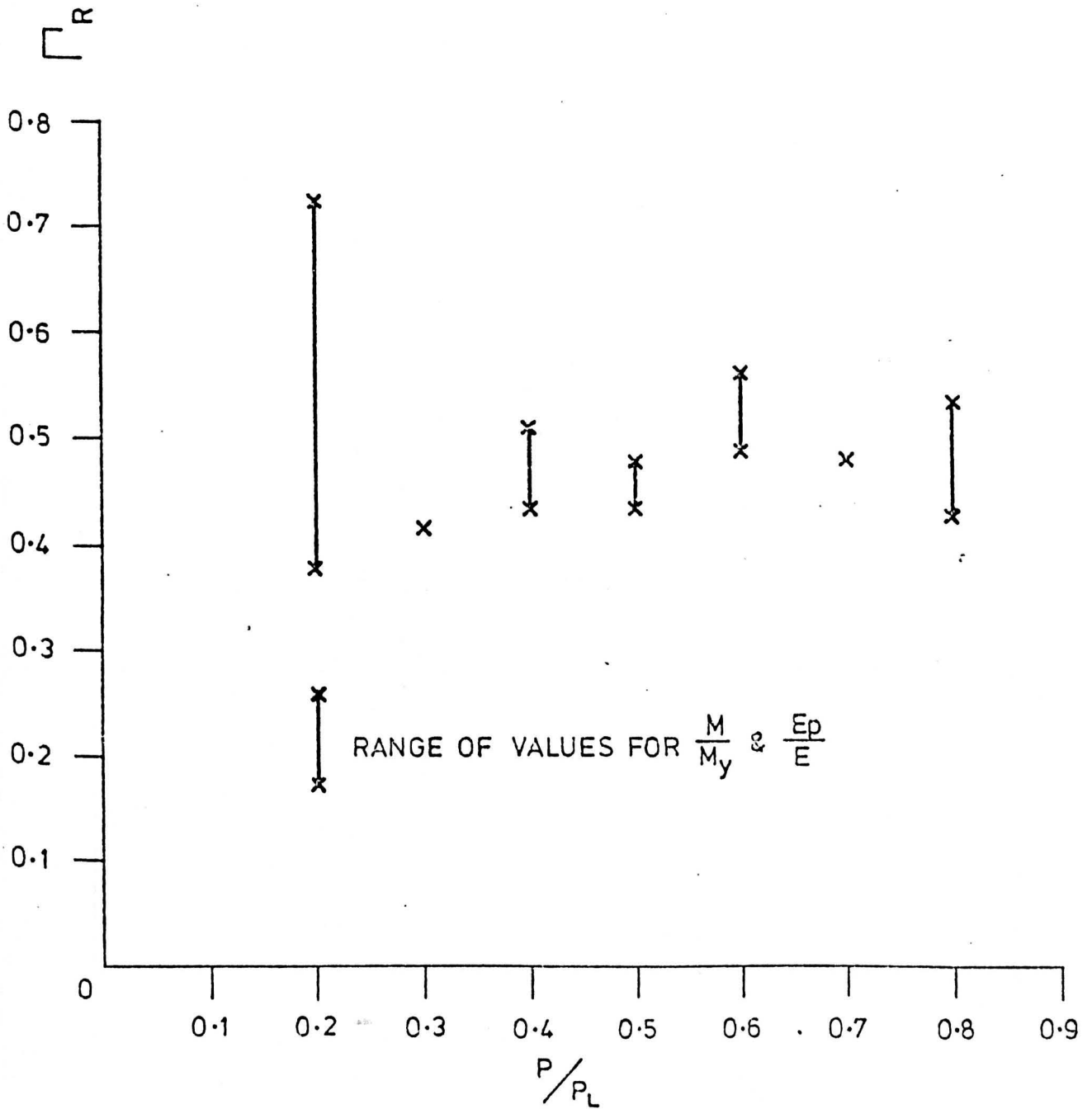


Figure 5.29 Stepped beam shank. Variation in time function for complete redistribution with mean load, bending load and E_p/E

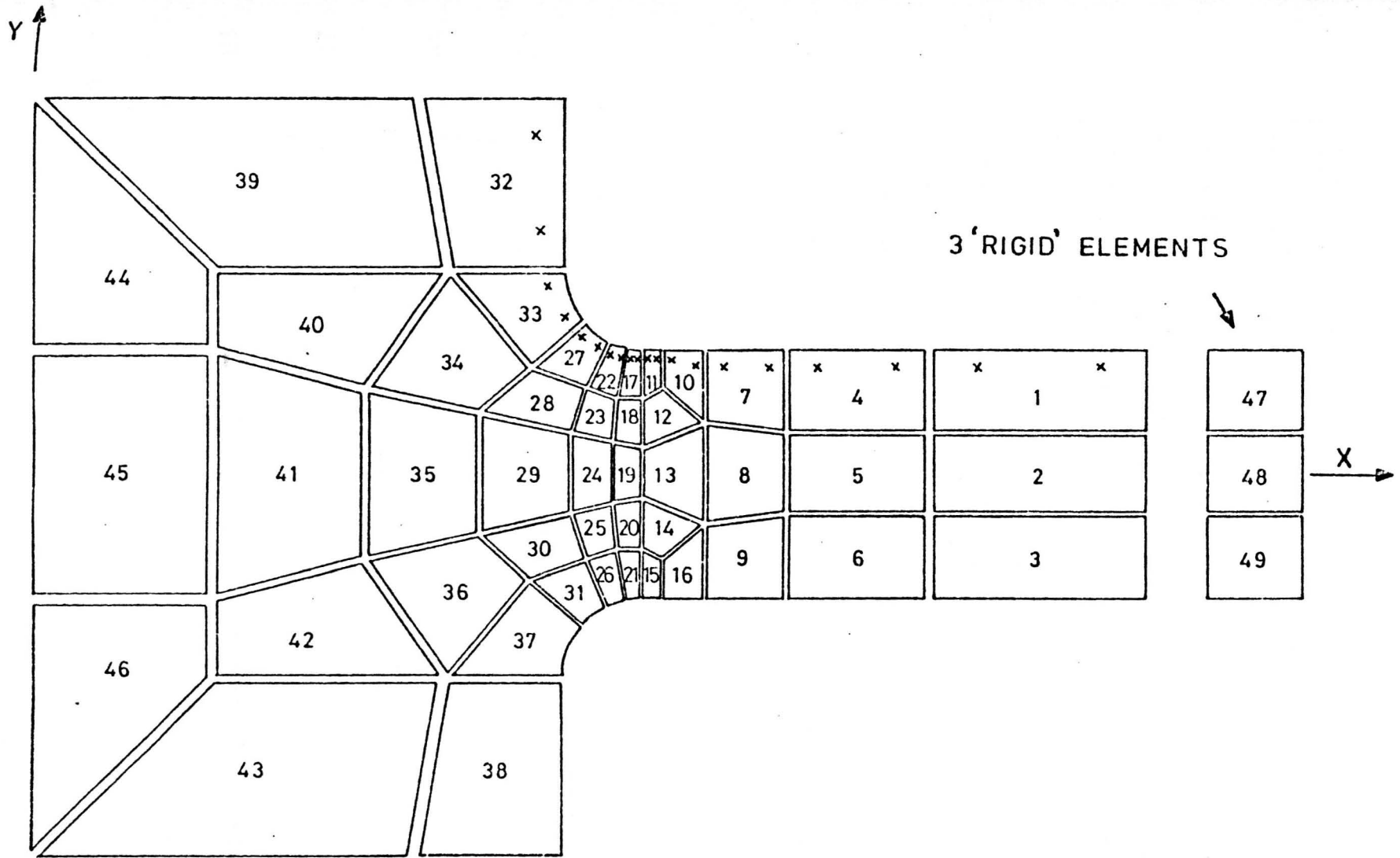


Figure 5.30 Stepped beam. Finite element mesh including 'rigid' elements showing the positions of the Gauss points nearest to the outside surface.

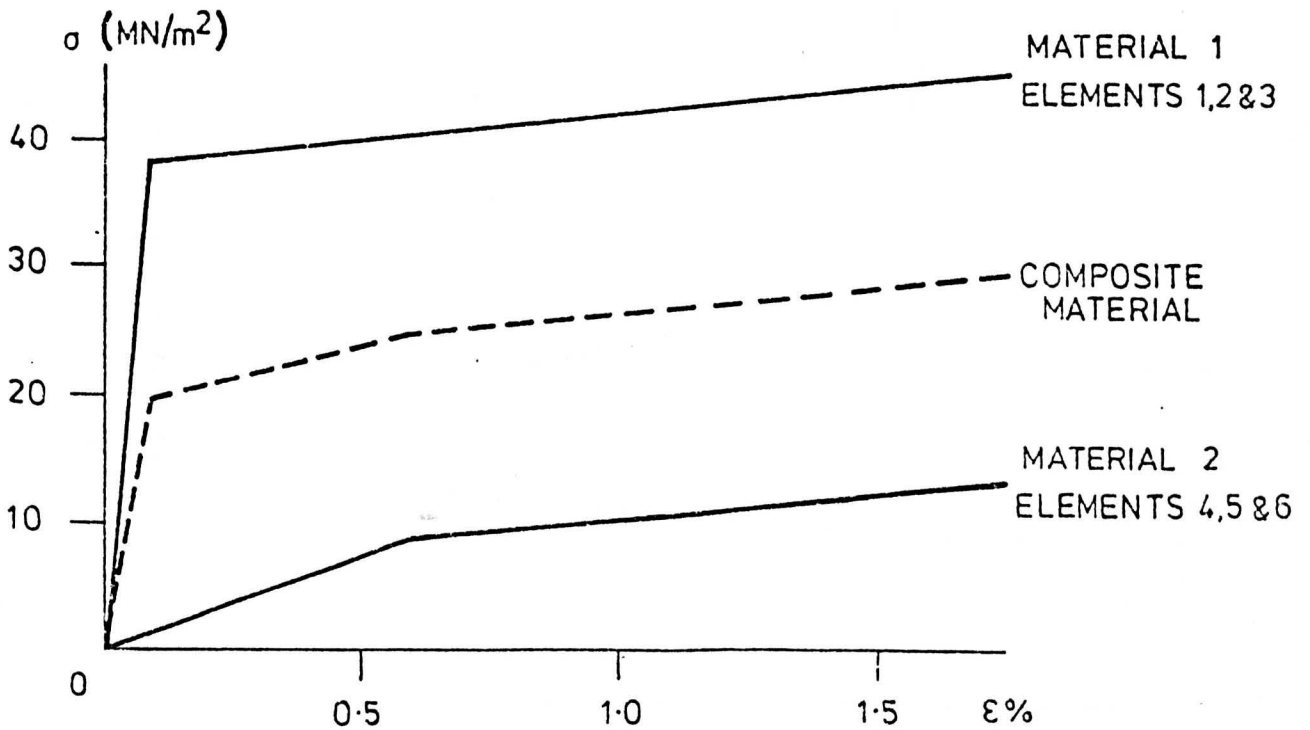
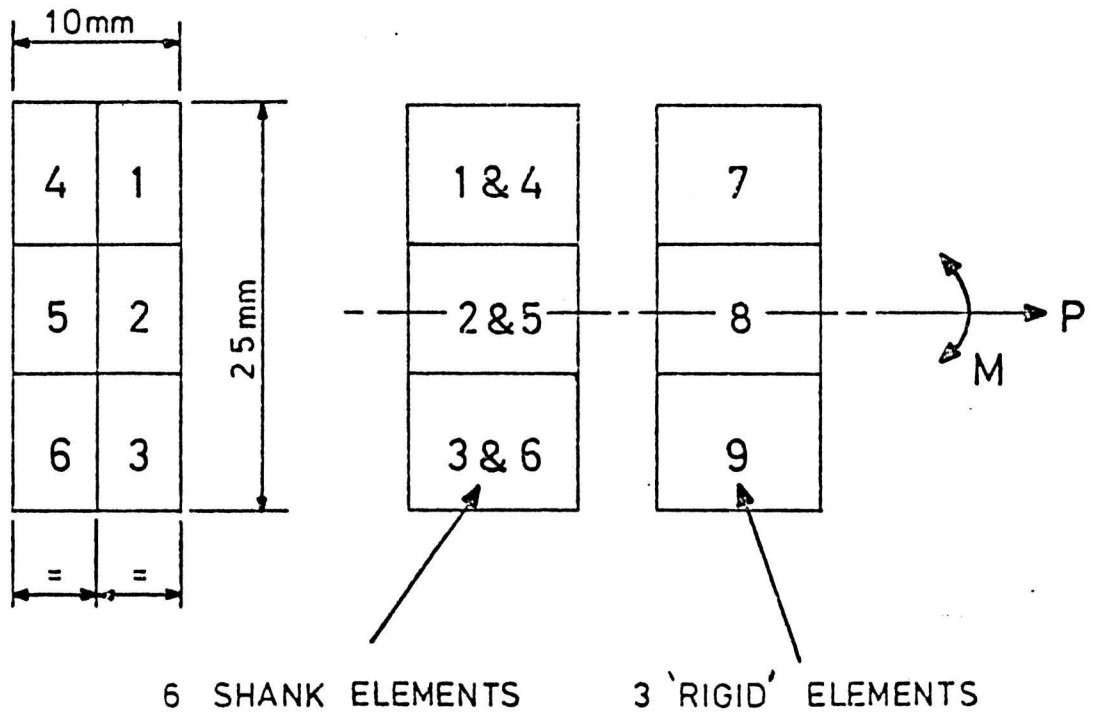


Figure 5.31 Stepped beam shank. Overlay model for non-linear kinematic hardening (see Table 5.3).

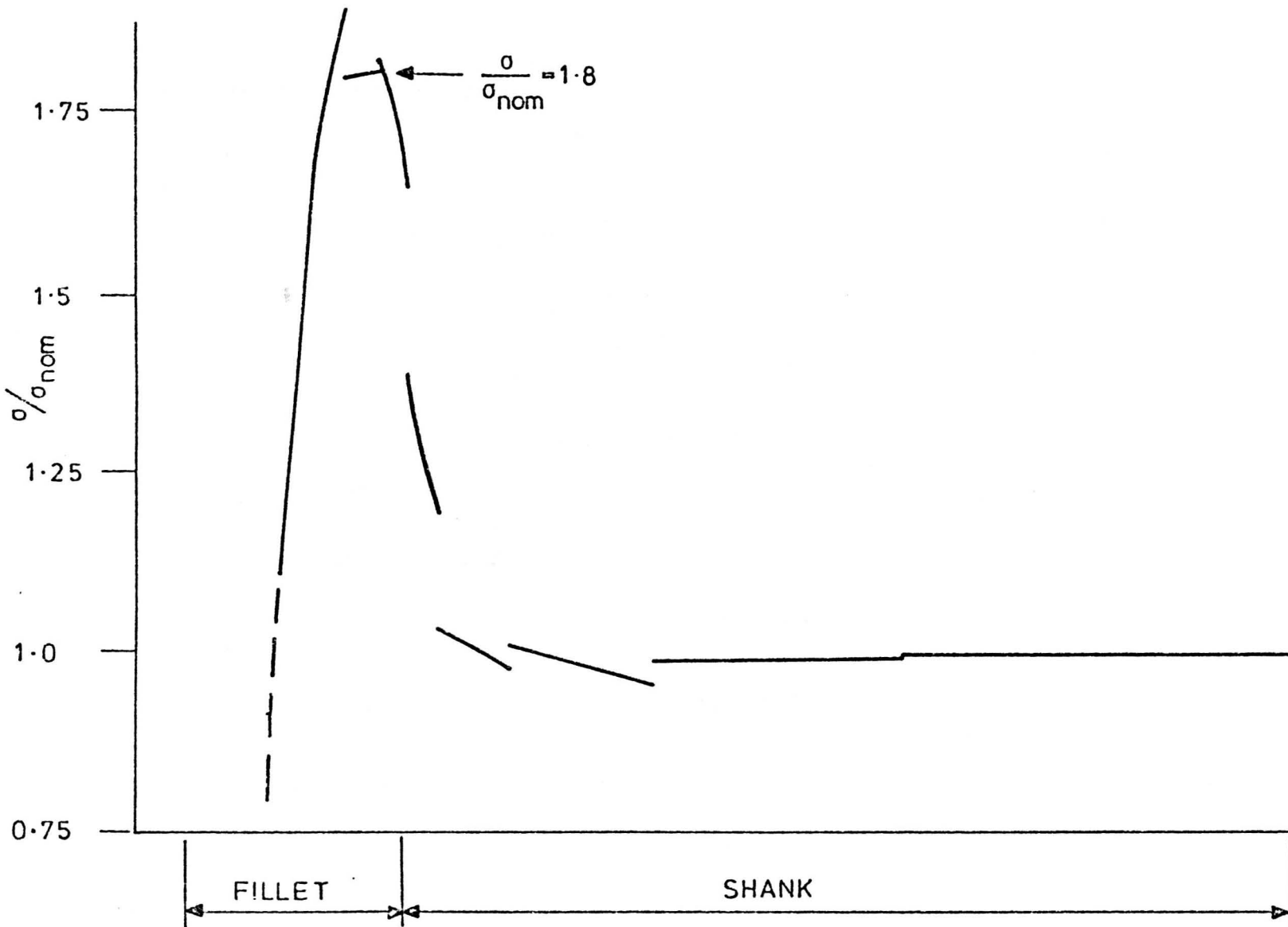


Figure 5.32 Stepped beam. Distribution of elastic surface stress along the shank and around the fillet due to an axial load.

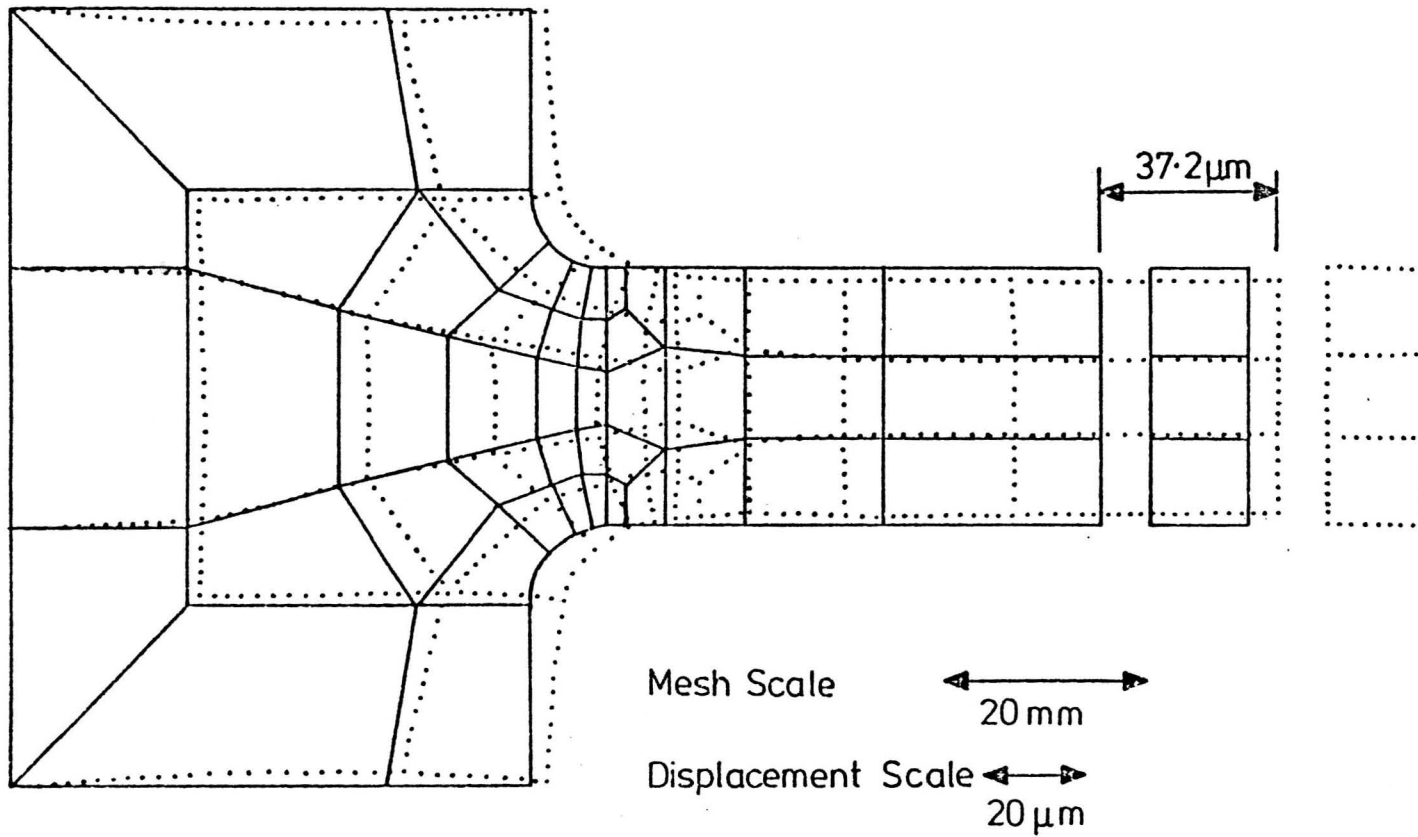


Figure 5.33 Stepped beam. 'Exaggerated' deformed shape for a mean load of 0.7 of the limit load.

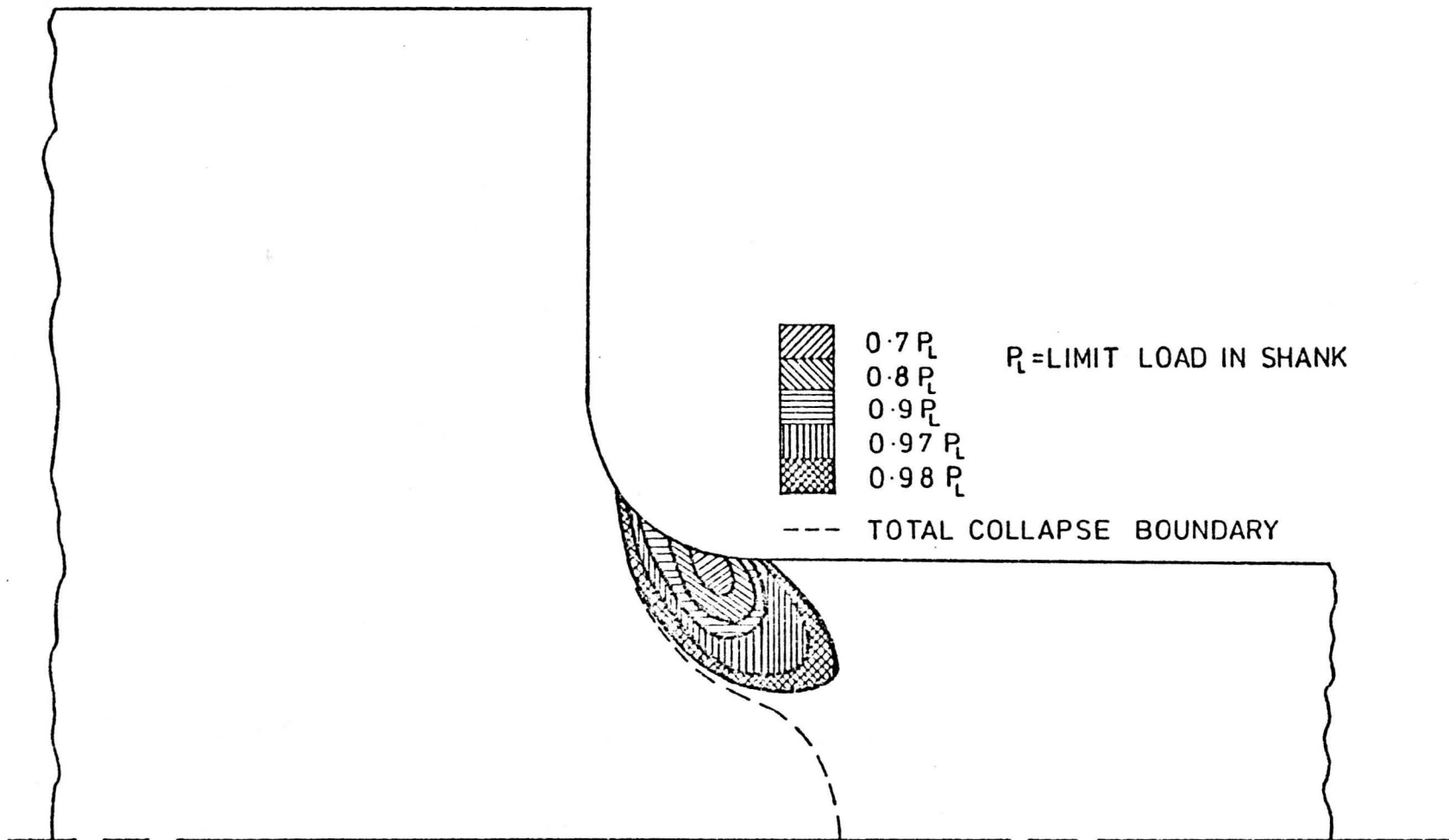


Figure 5.34 Stepped beam (elastic-perfectly-plastic). Growth of plastic zone with increasing axial load up to collapse.

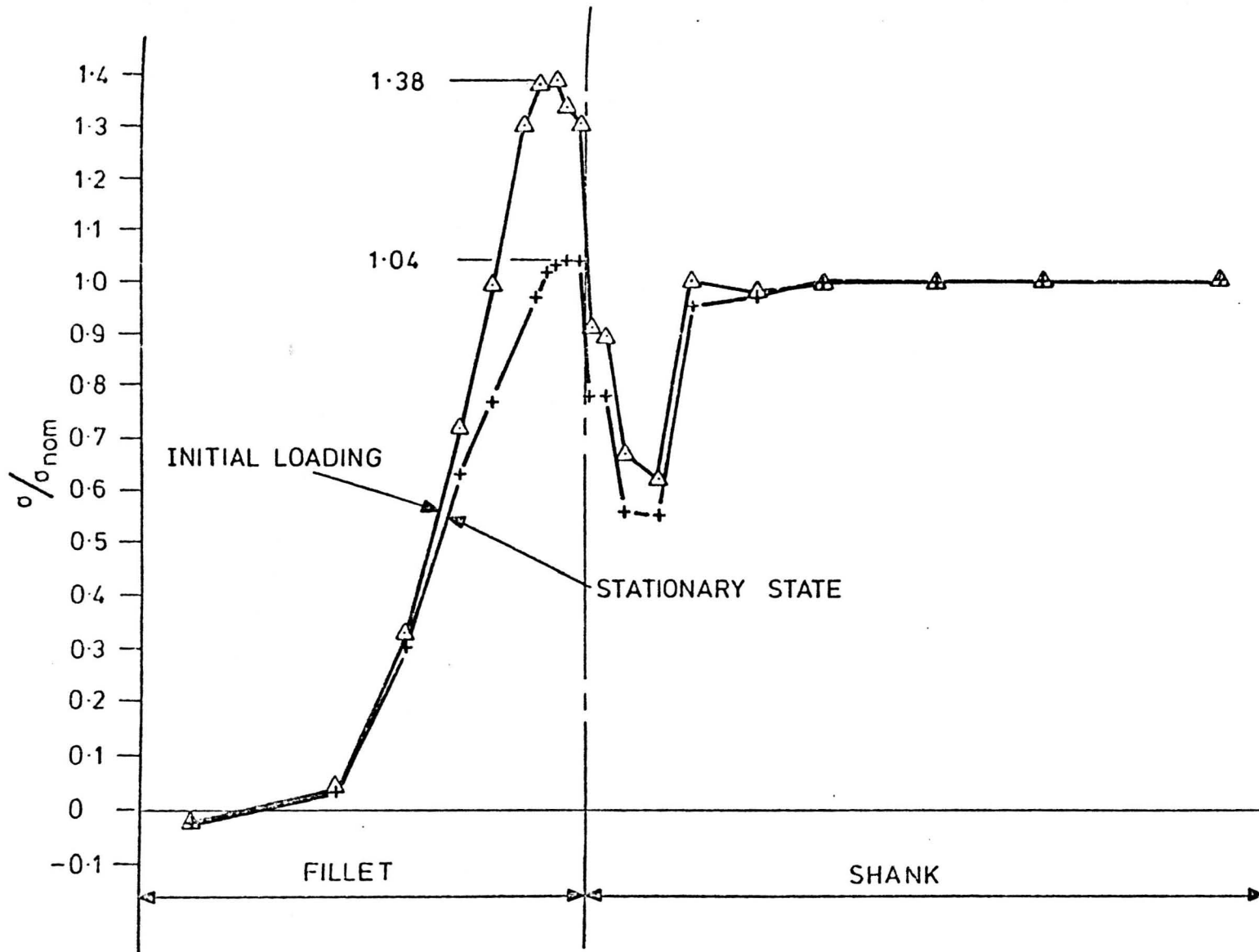


Figure 5.35 Stepped beam. Redistribution of meridional stress along outside 'surface' due to creep at sustained mean load. (see Figure 5.30).

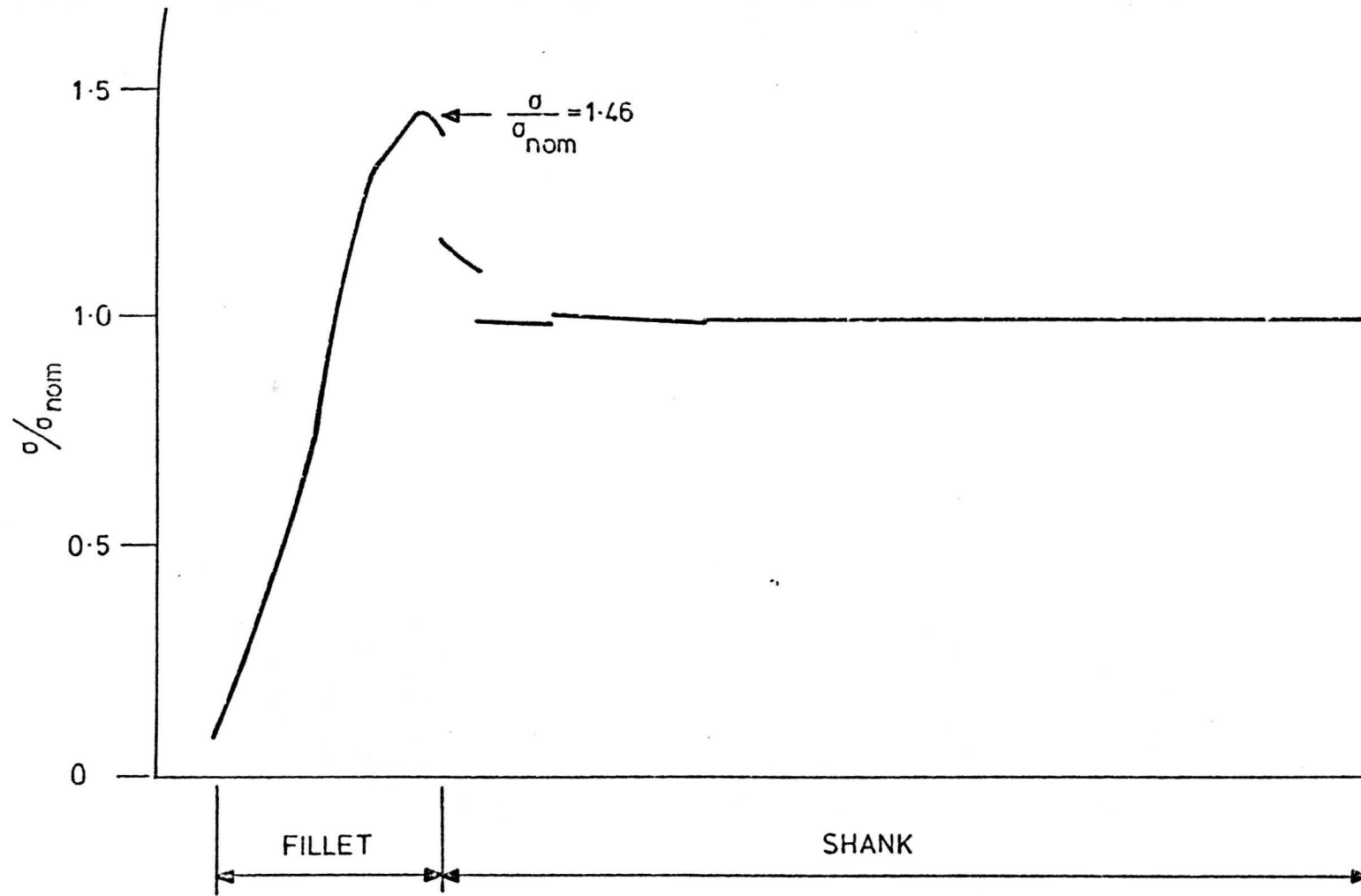


Figure 5.36 Stepped beam. Distribution of elastic surface stress along the shank and around the fillet due to pure bending.

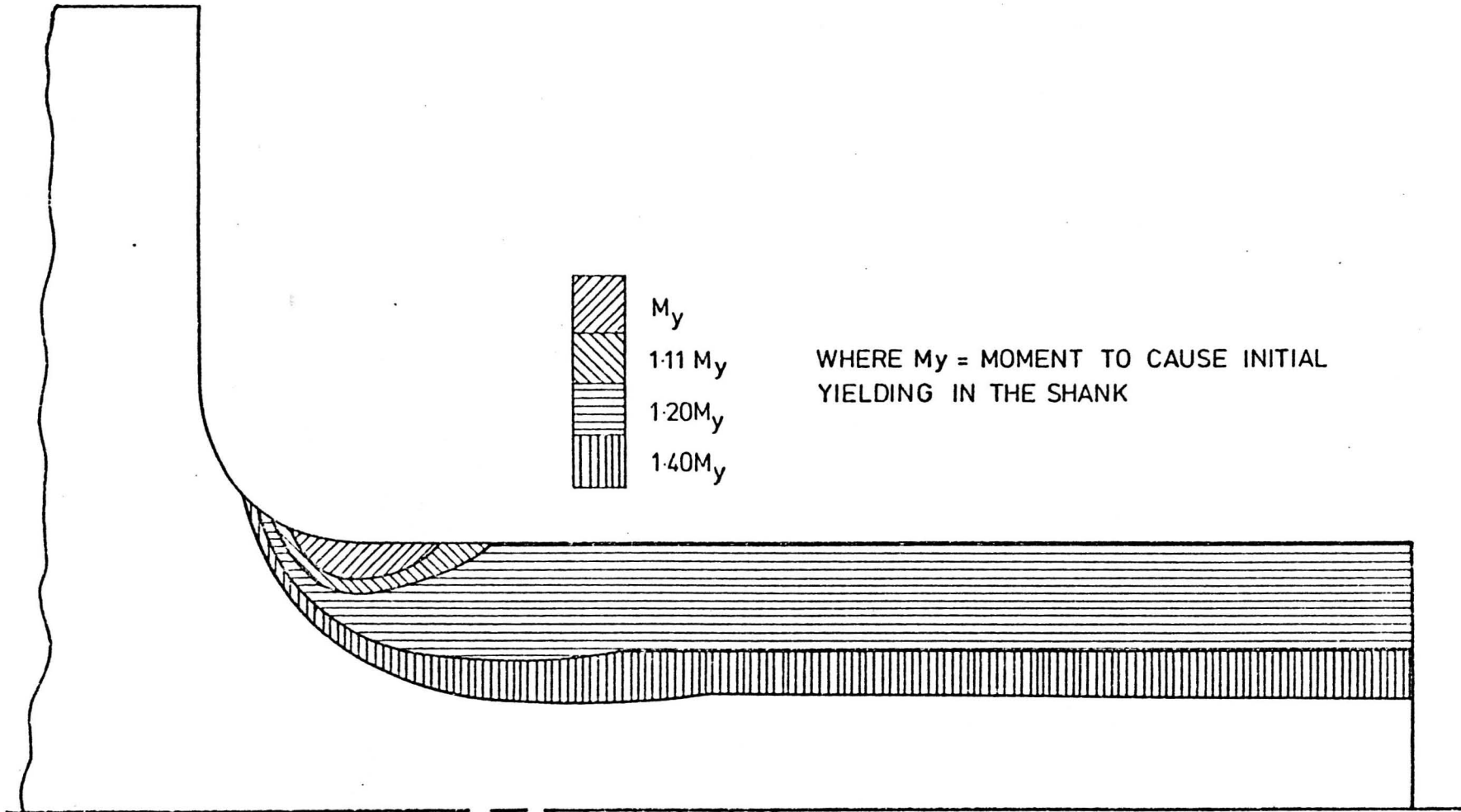


Figure 5.37 Stepped beam (elastic-perfectly-plastic). Growth of plastic zone with increasing bending moment towards collapse.

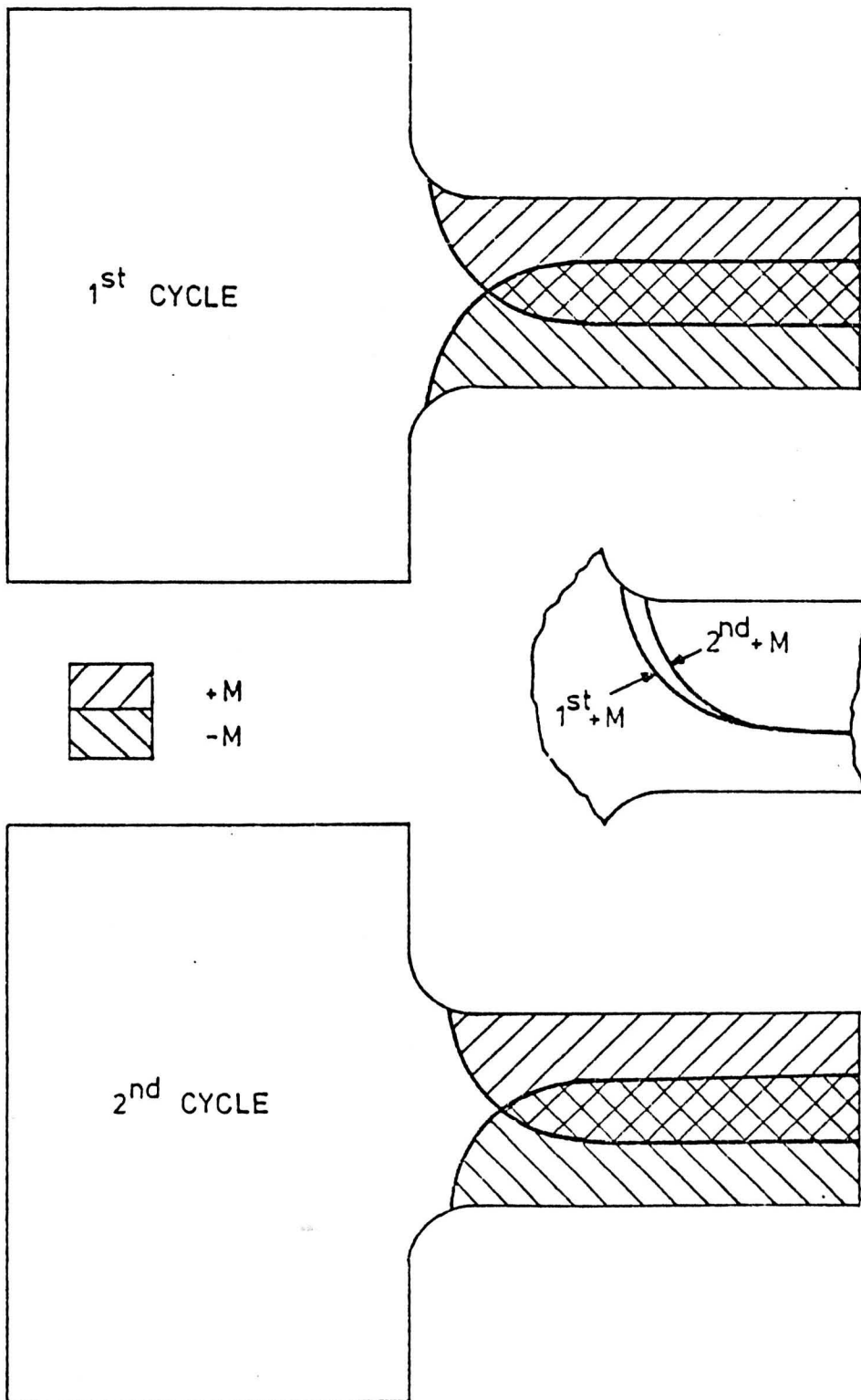


Figure 5.38 Stepped beam (Elastic-perfectly-plastic, $M/M_y = 0.7$, $P/P_L = 0.7$, 'no creep' conditions). Regions of yielding during the first and second cycles.

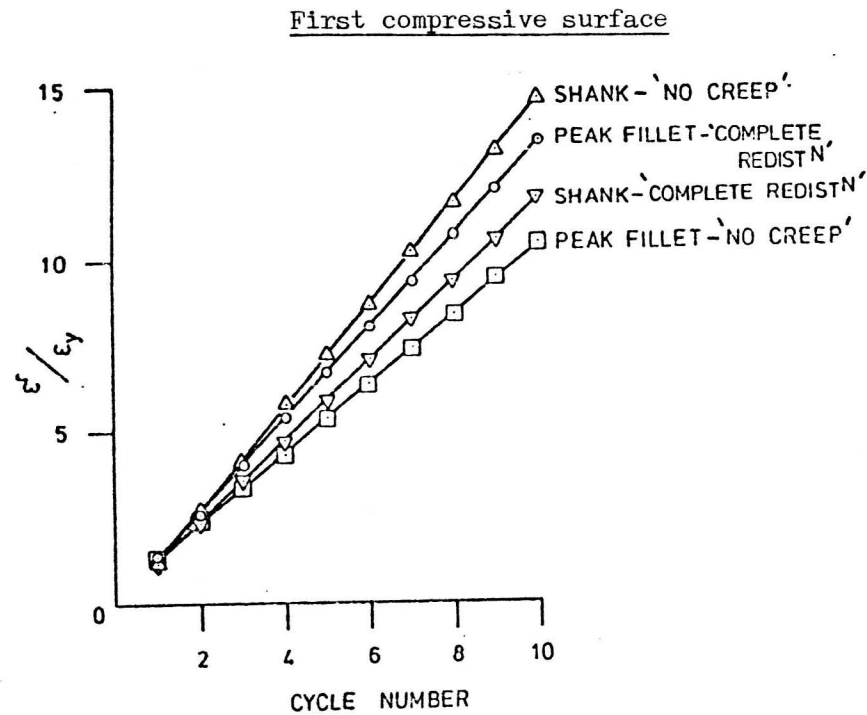
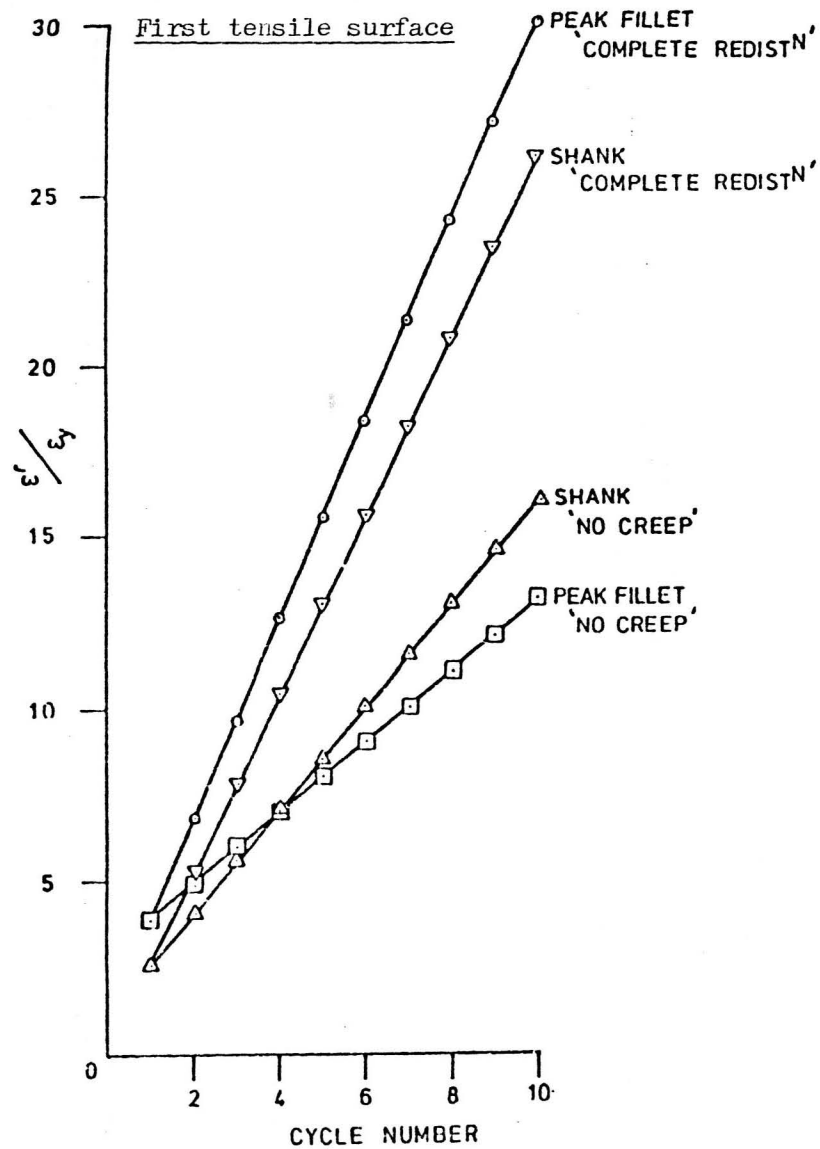


Figure 5.39 Stepped beam (Elastic-perfectly-plastic, $M/M_y = 0.7$, $P/P_L = 0.7$).
Accumulation of normalised ratchet strain during the first 10 cycles.

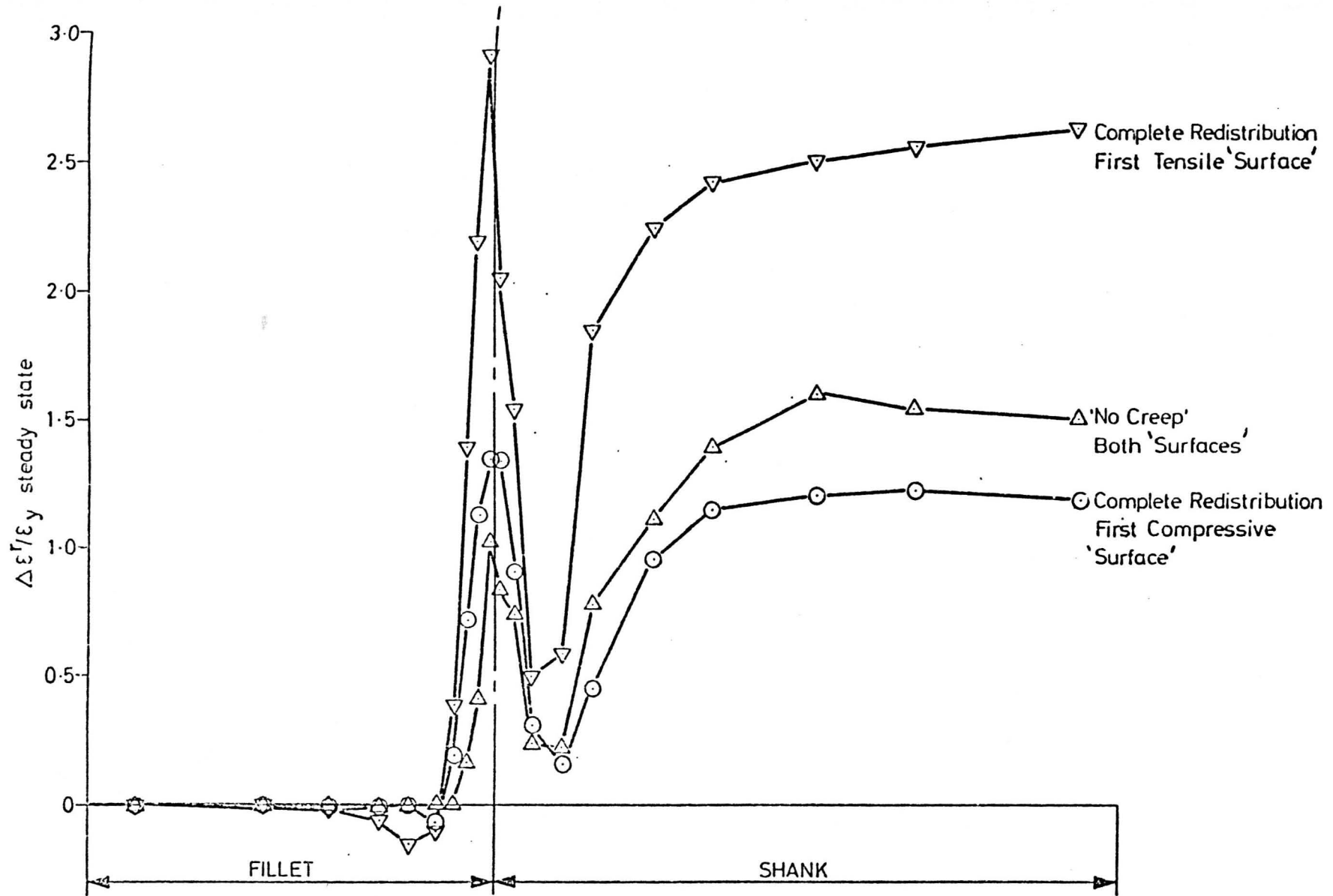


Figure 5.40 Stepped beam (Elastic-perfectly-plastic, $M/M_y = 0.7$, $P/P_L = 0.7$).
Distributions of steady state normalised meridional ratchet strain. (see Figure 5.30)

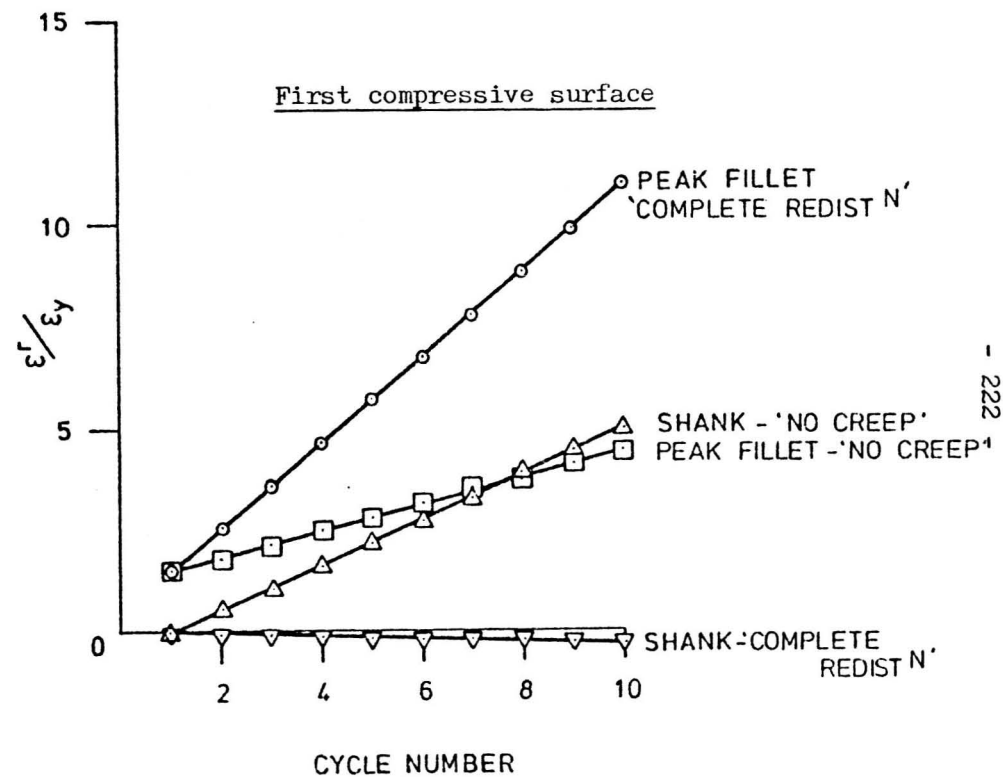
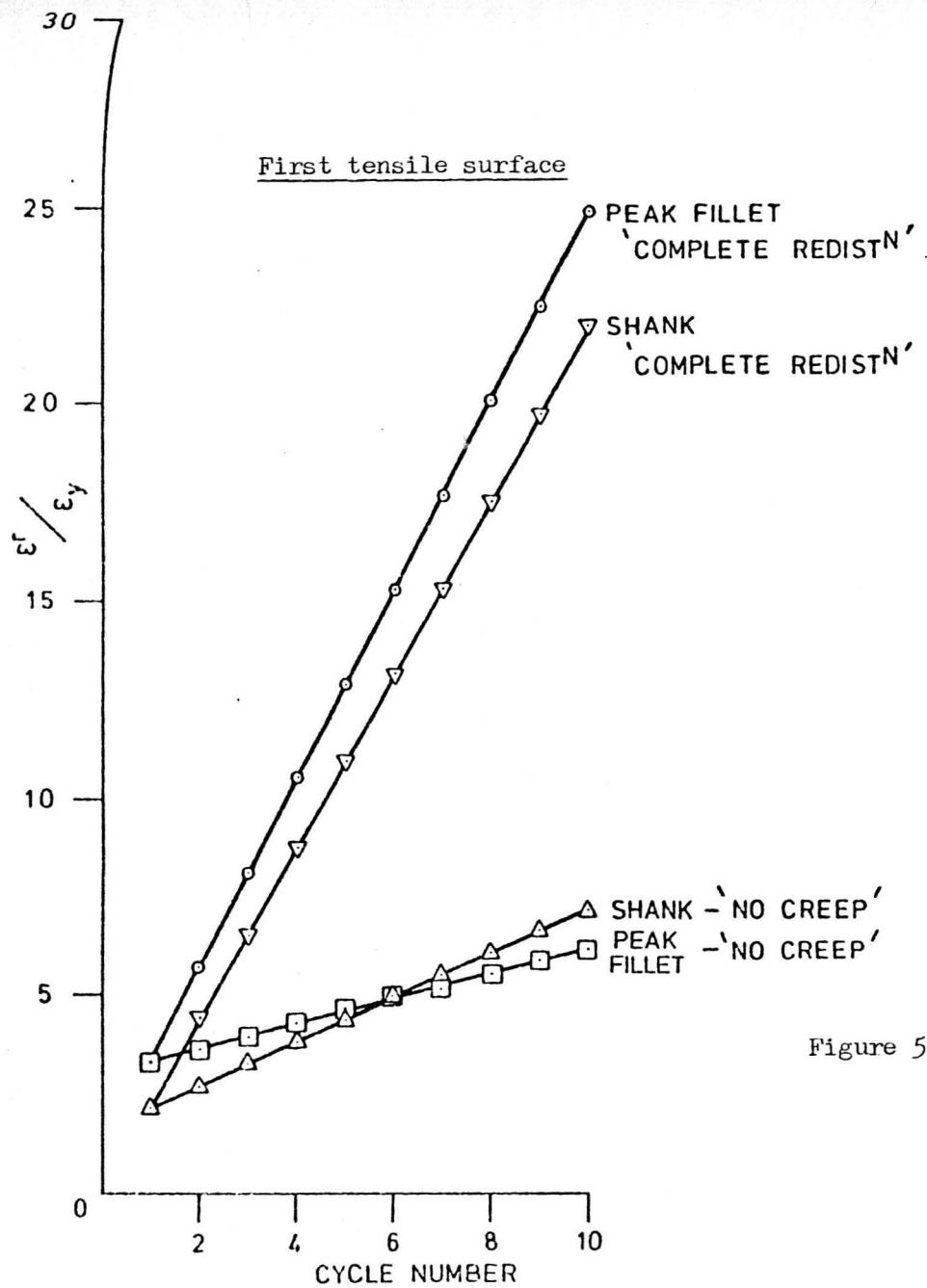


Figure 5.41 Stepped beam (Elastic-perfectly-plastic, $M/M_y = 1.05$, $P/P_L = 0.5$) Accumulation of normalised ratchet strain during the first 10 cycles.

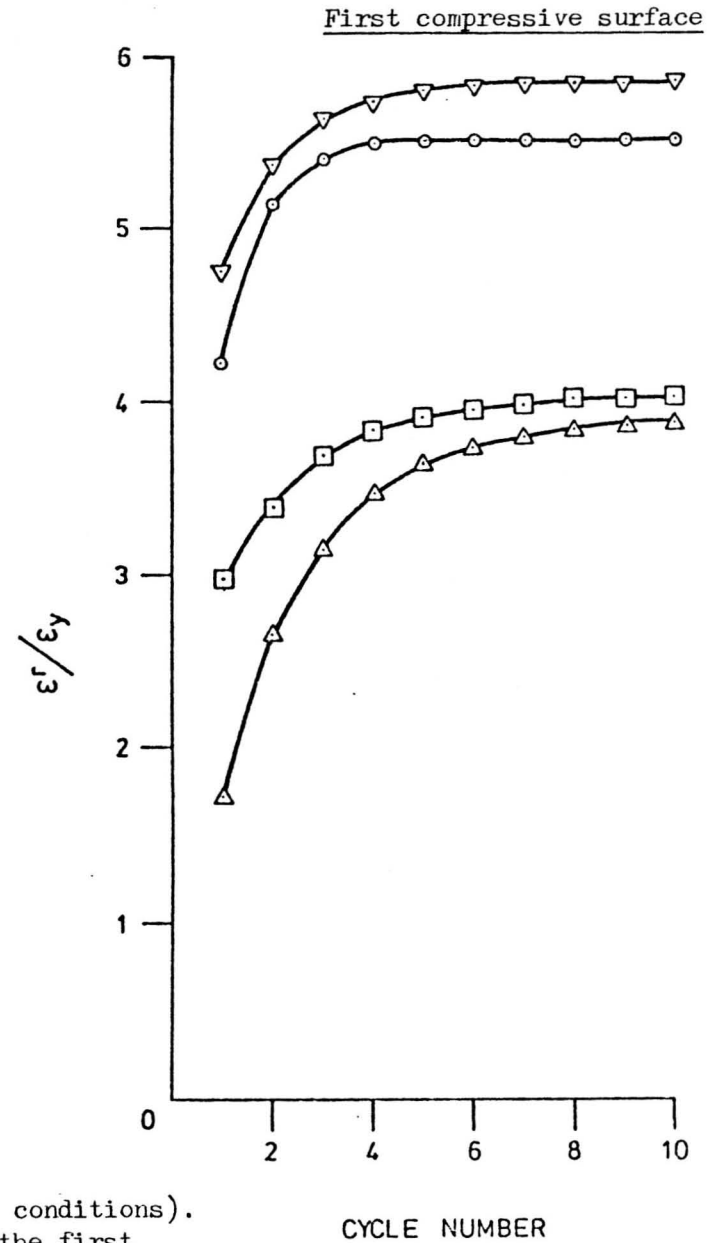
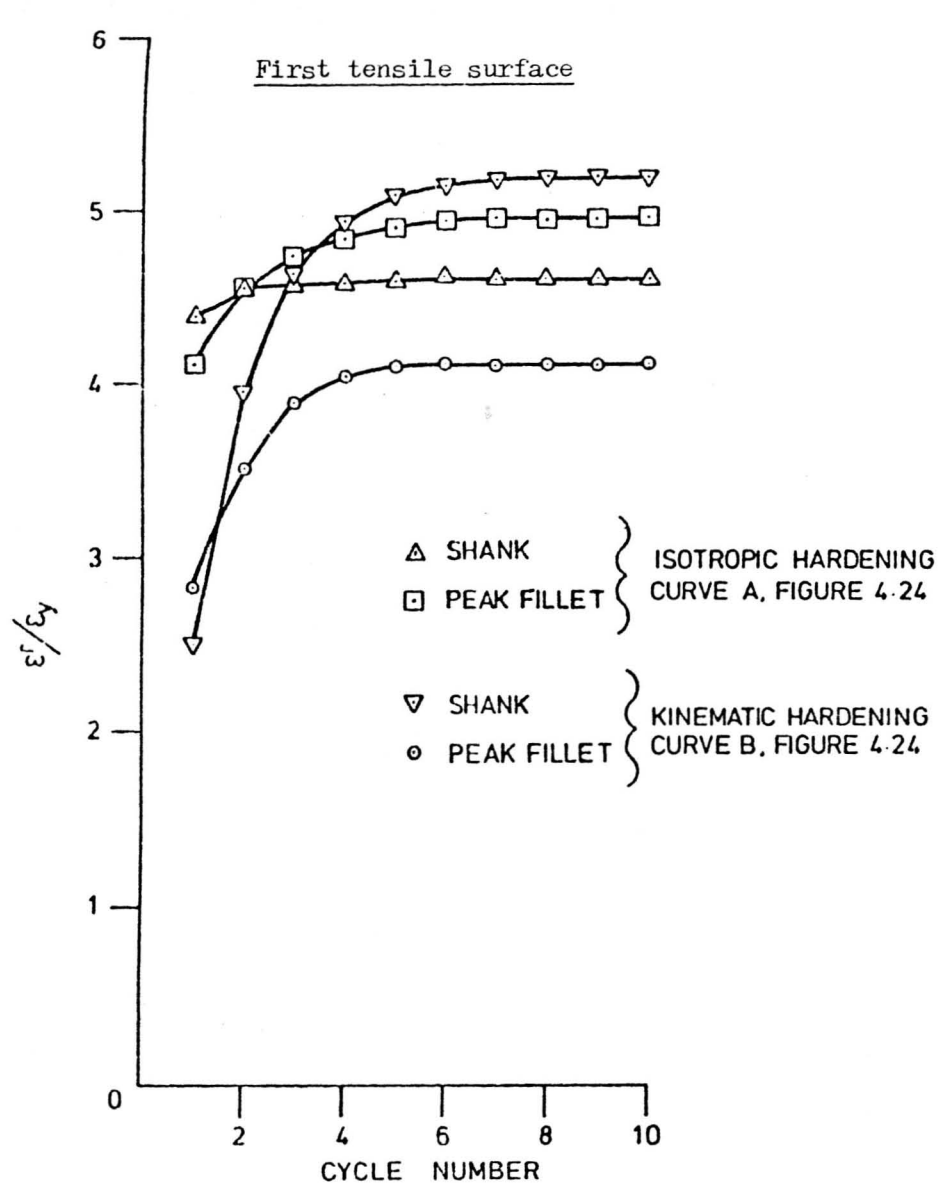


Figure 5.42 Stepped beam ($M/M_y = 1.3$, $P/P_L = 0.54$, 'no creep' conditions). Accumulation of normalised ratchet strain during the first 10 cycles.

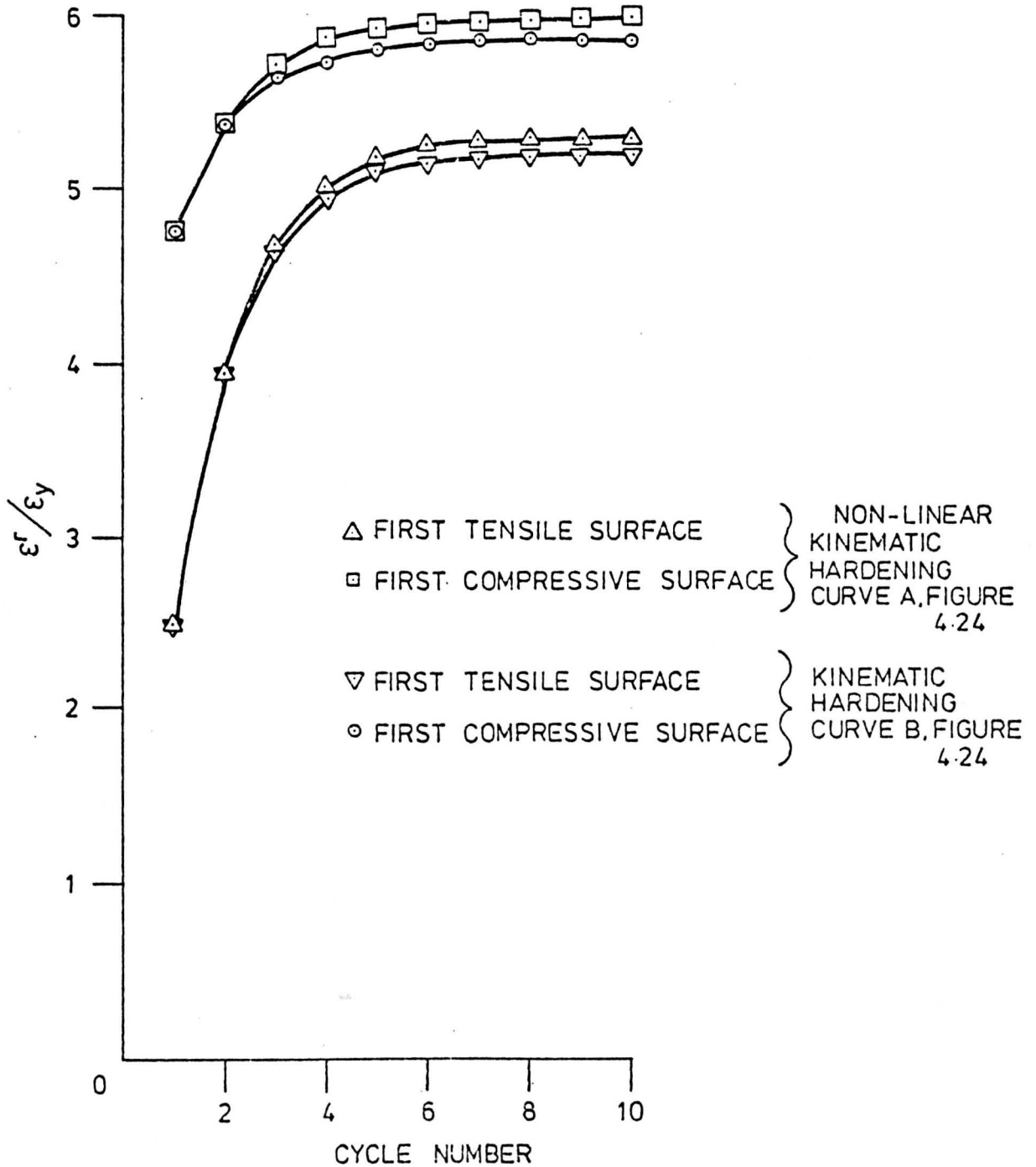


Figure 5.43 Stepped beam shank ($M/M_y = 1.3$, $P/P_L = 0.54$, 'no creep' conditions). Accumulation of normalised ratchet strain during the first 10 cycles.

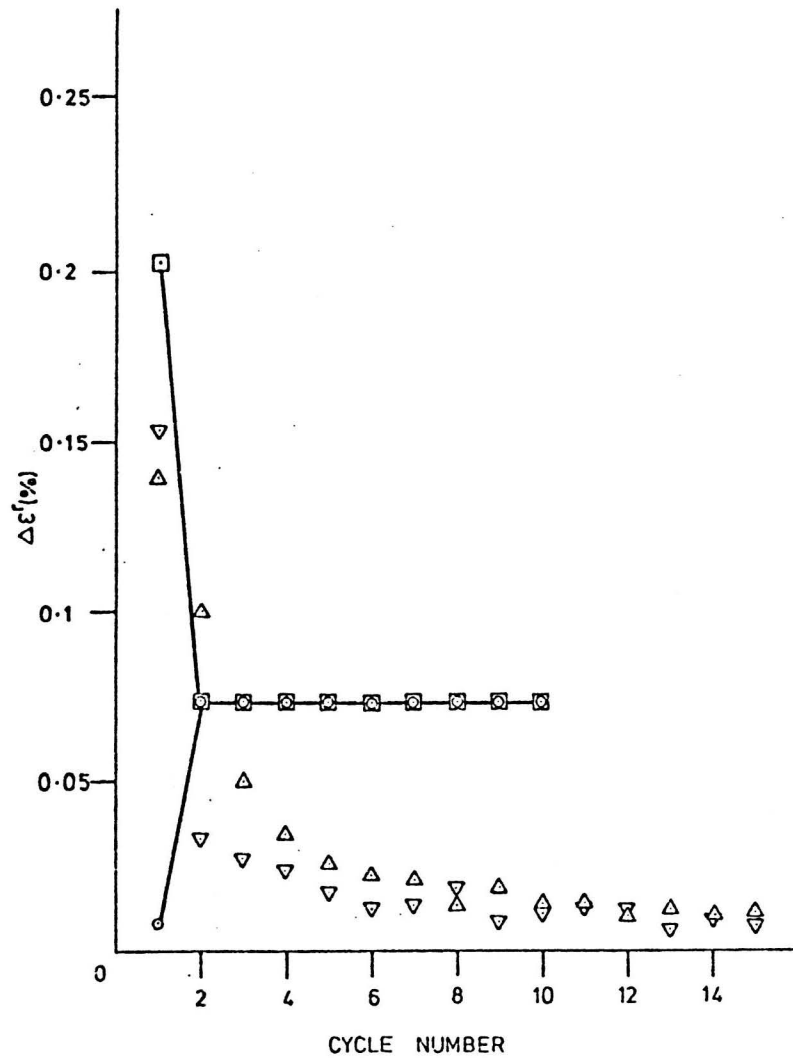
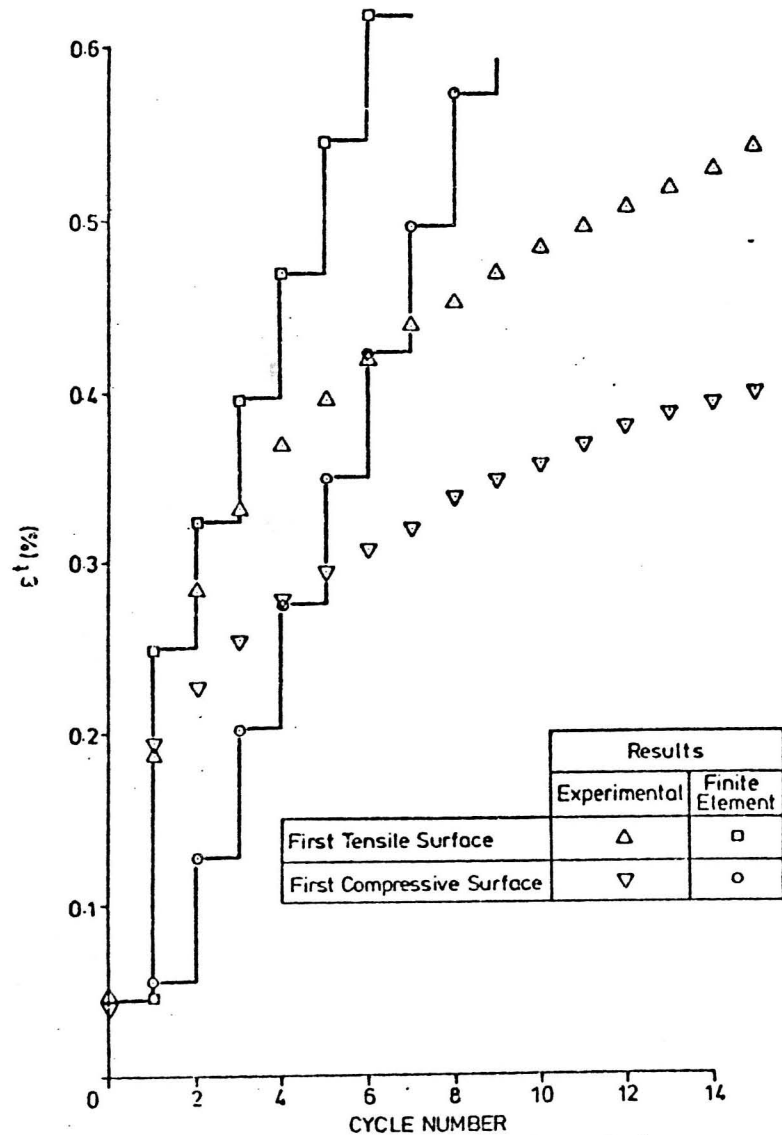


Figure 5.44 Stepped beam shank. Comparison between experimental results (nominal $M/M_y = 1.2$, $P/P_L = 0.5$, 'rapid' cycling) and finite element predictions (elastic-perfectly plastic curve C Figure 4.24, $M/M_y = 1.061$, $P/P_L = 0.5$, 'no creep' conditions).

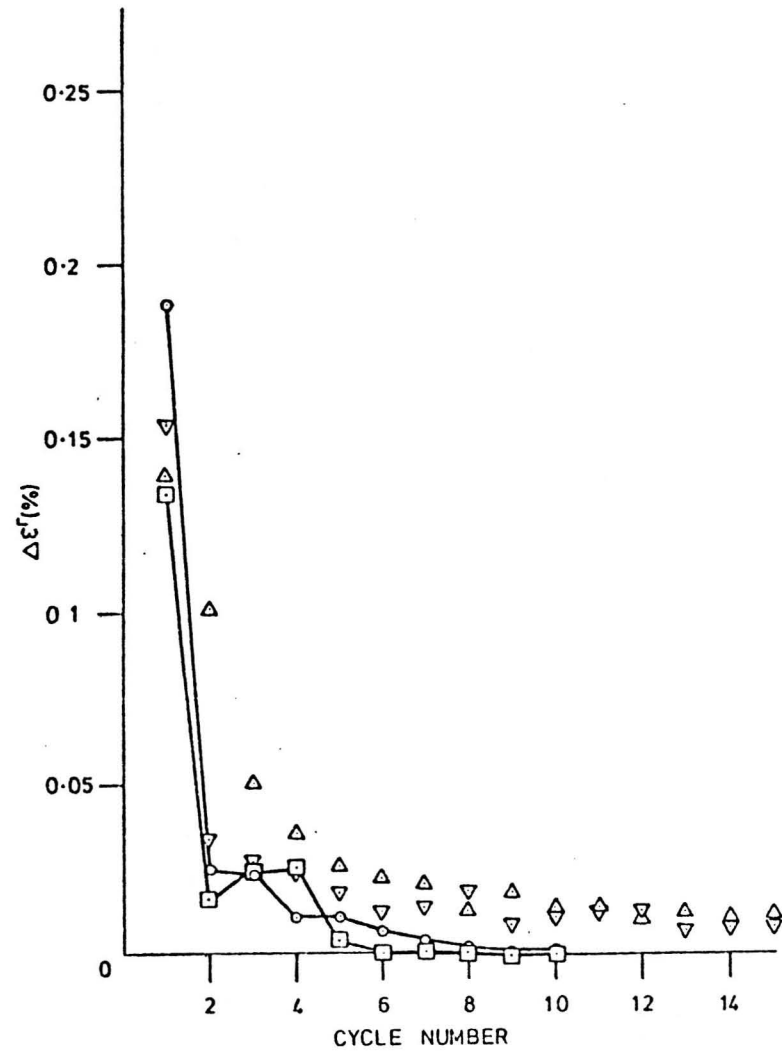
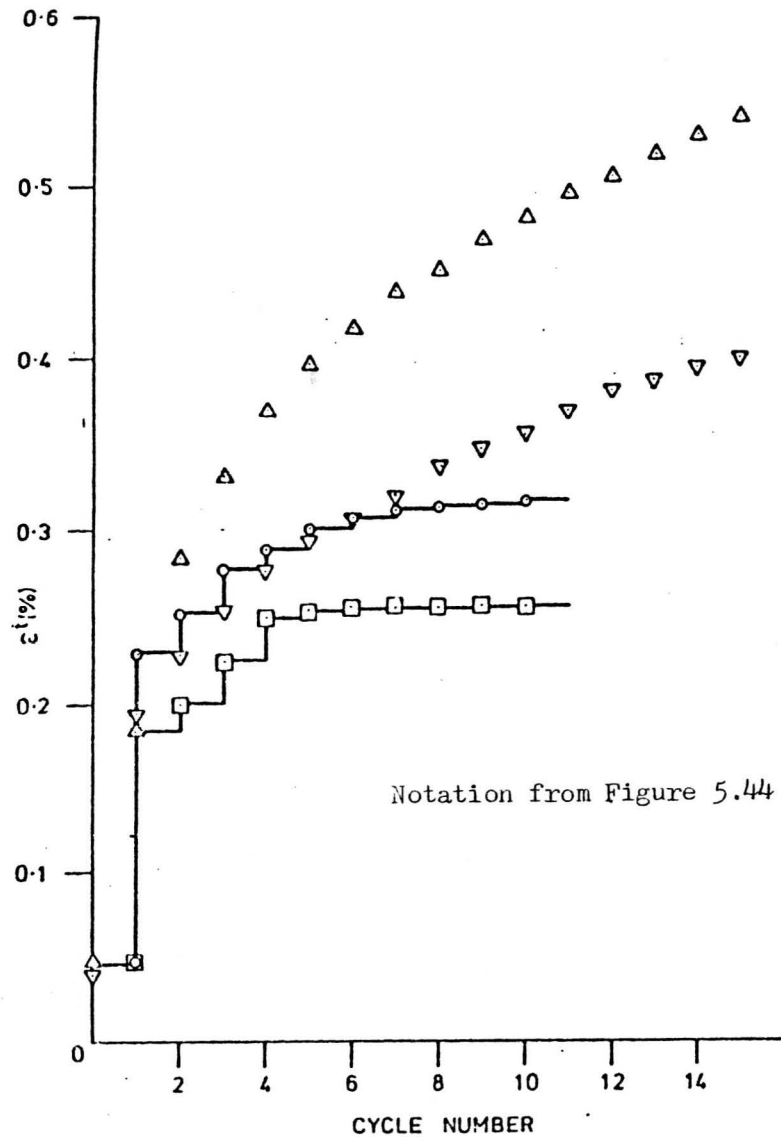


Figure 5.45 Stepped beam shank. Comparison between experimental results (nominal $M/M_y = 1.2$, $P/P_L = 0.5$, 'rapid' cycling) and finite element predictions (isotropic hardening curve A Figure 4.24, M/M_y from Table 5.5, $P/P_L = 0.5$ 'no creep' conditions).

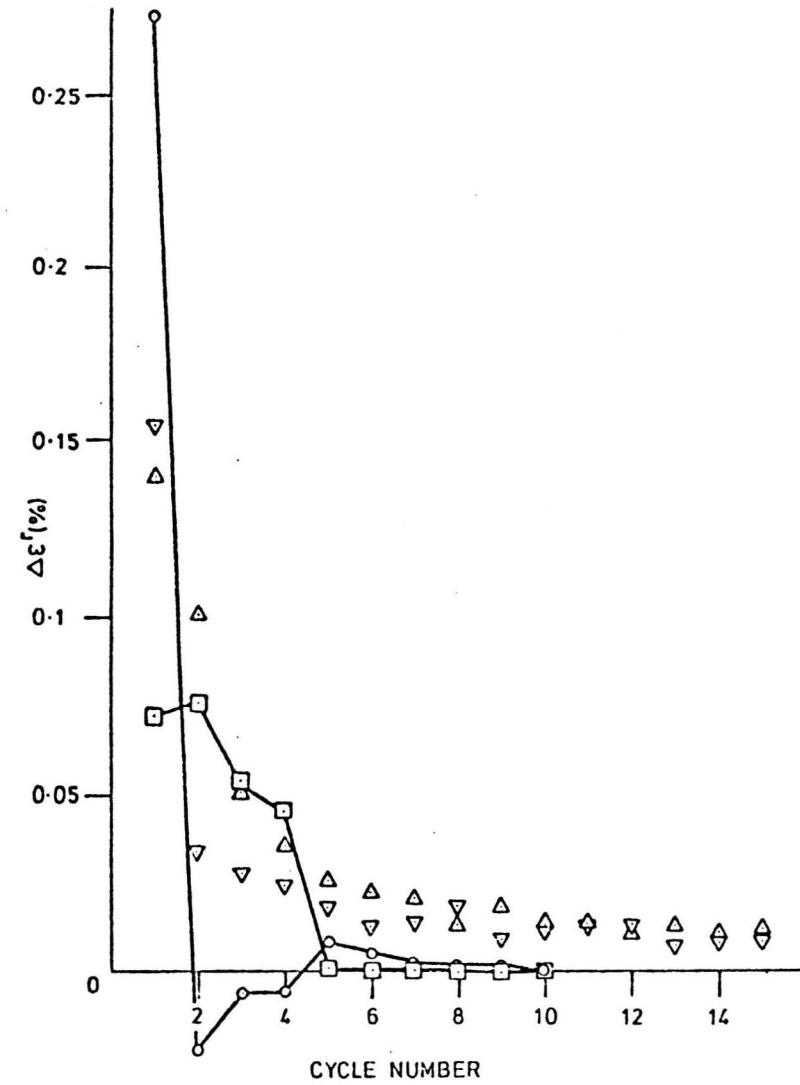
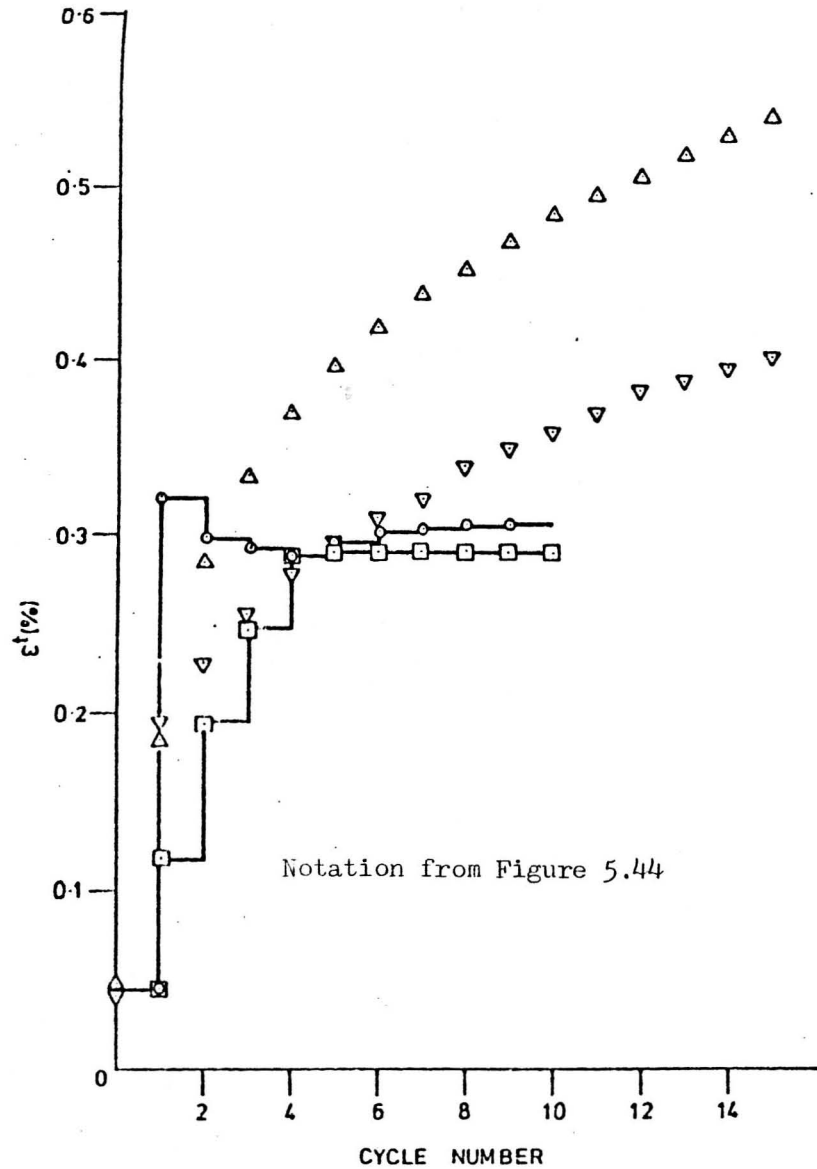


Figure 5.46 Stepped beam shank. Comparison between experimental results (nominal $M/M_y = 1.2$, $P/P_L = 0.5$, 'rapid' cycling) and finite element predictions (kinematic hardening curve B Figure 4.24, M/M_y from Table 5.5, $P/P_L = 0.5$, 'no creep' conditions)

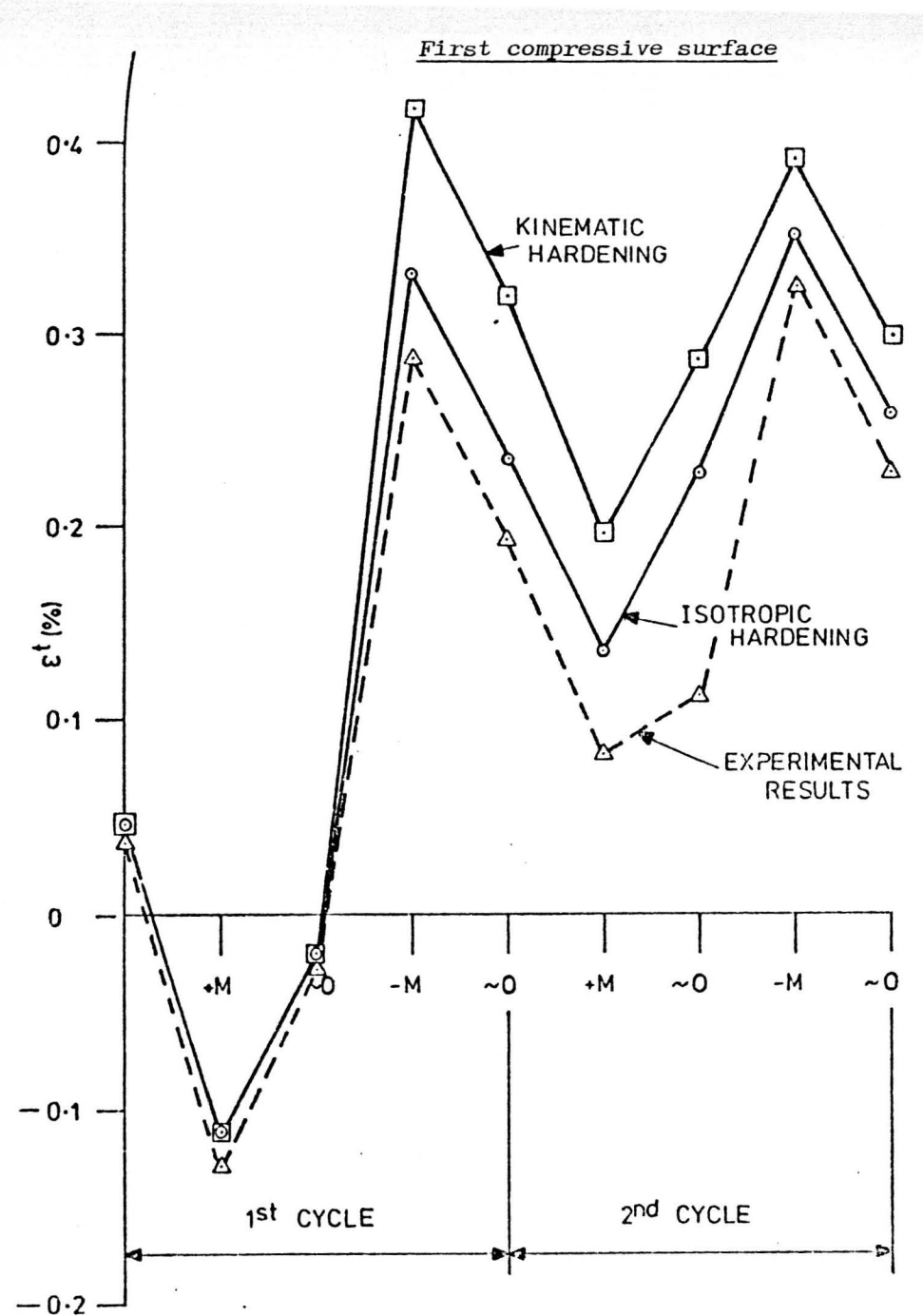
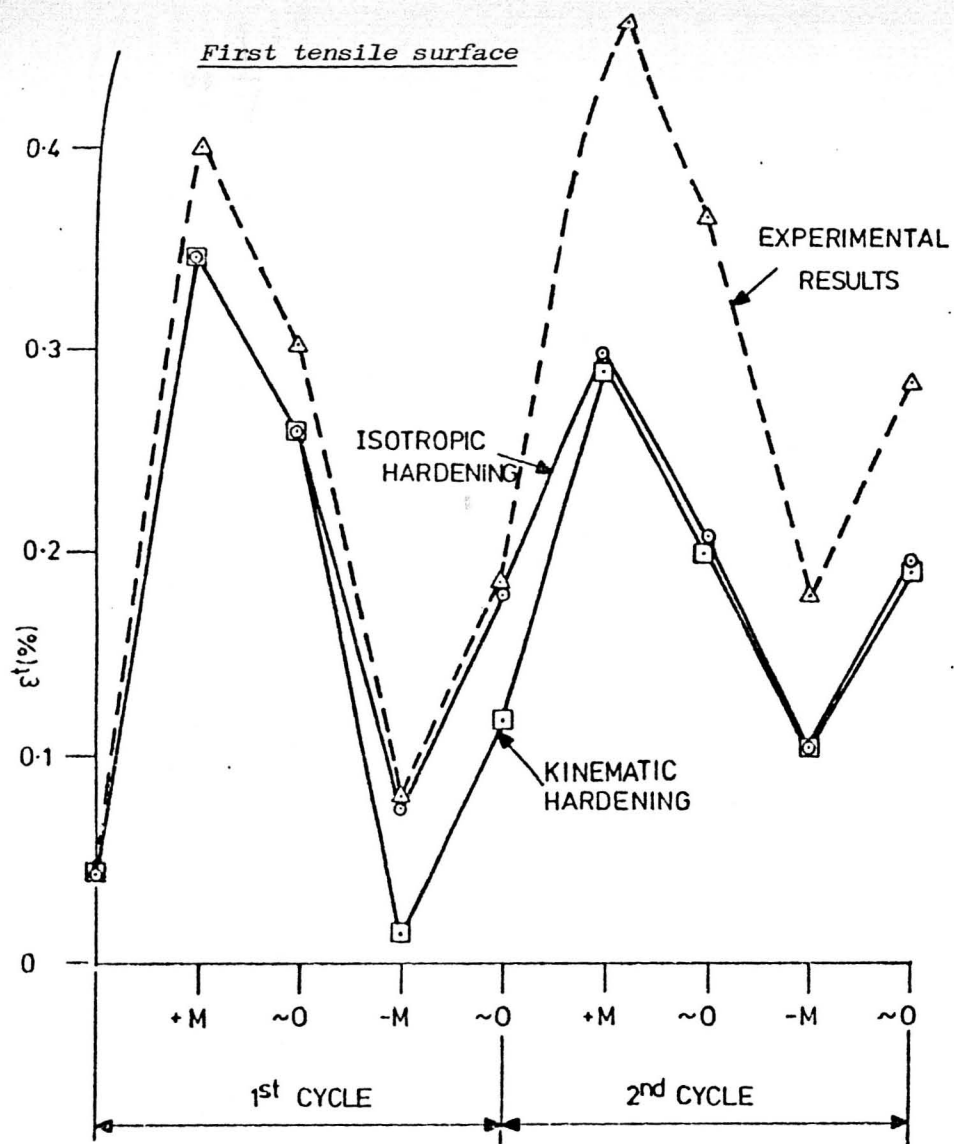


Figure 5.47 Stepped beam shank. Experimental and predicted variations in total surface strain during the first two cycles for the results shown in Figures 5.45 and 5.46.

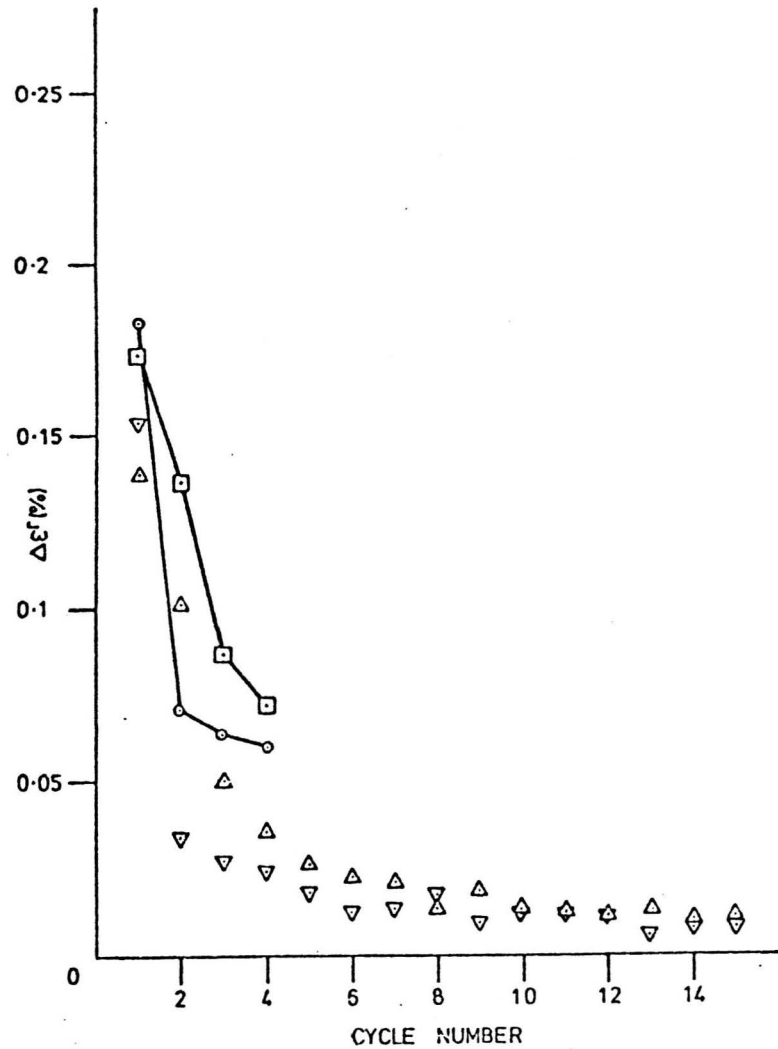
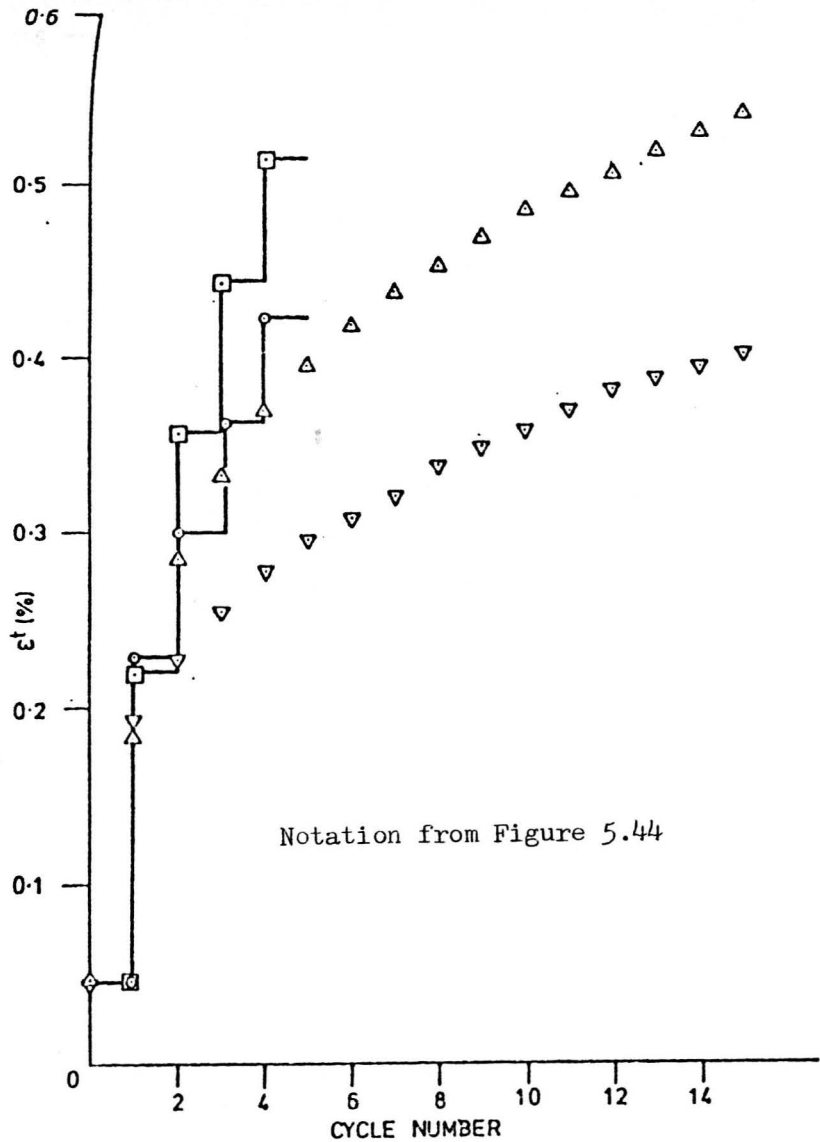


Figure 5.48 Stepped beam shank. Comparisons between experimental results (nominal $M/M_y = 1.2$, $P/P_L = 0.5$, 'rapid' cycling) and finite element predictions (isotropic hardening curve A Figure 4.24, curvature control, $P/P_L = 0.5$, 'no creep' conditions).

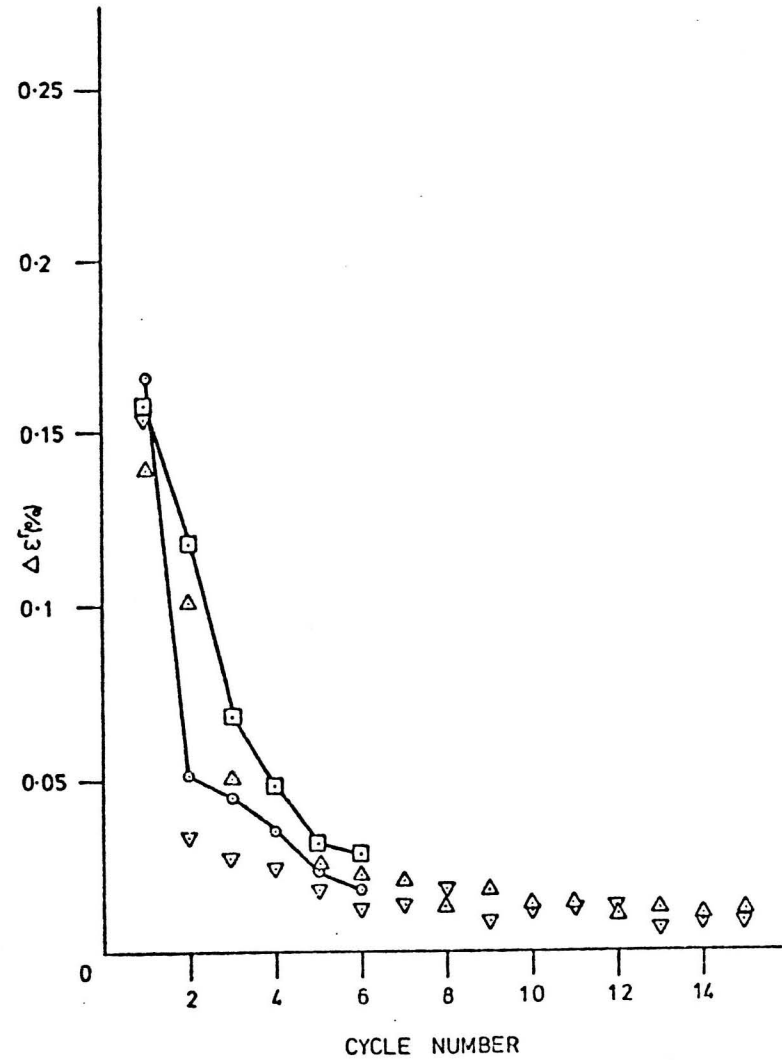
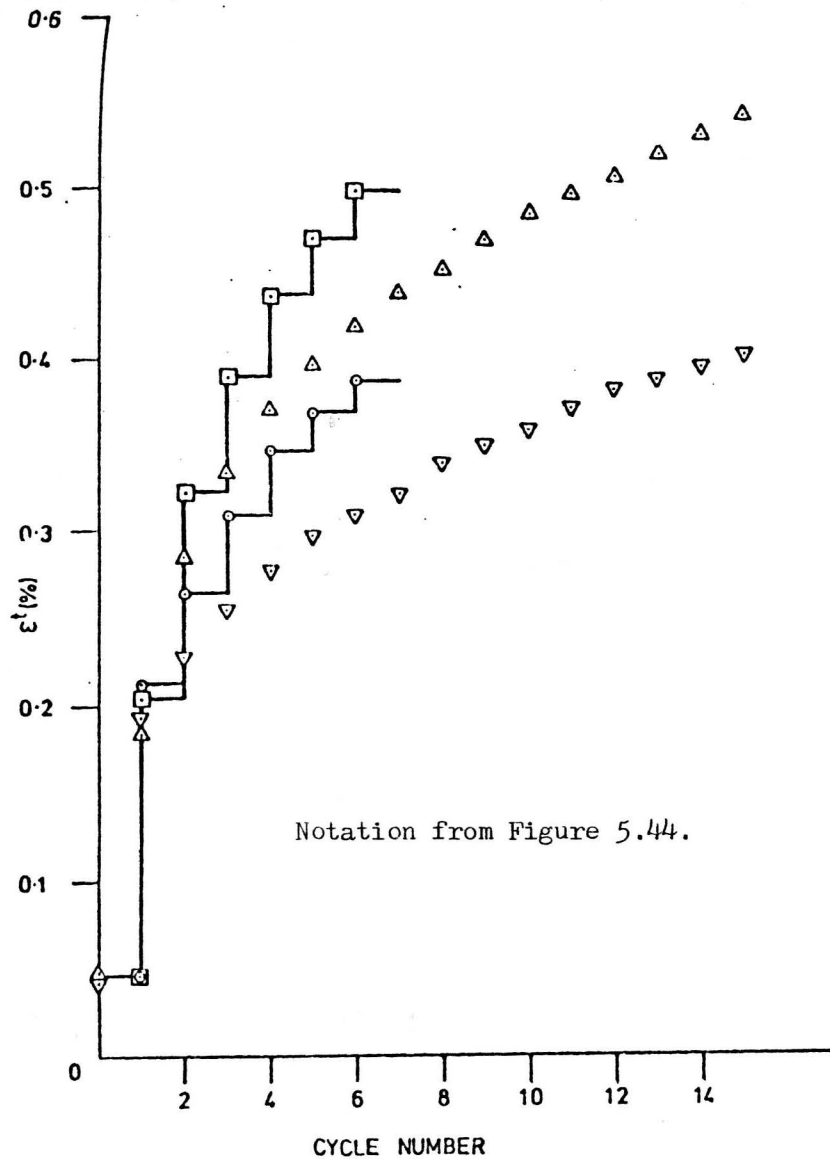


Figure 5.49 Stepped beam shank. Comparison between experimental results (nominal $M/M_y = 1.2$, $P/P_L = 0.5$, 'rapid' cycling) and finite element predictions (kinematic hardening curve B Figure 4.24, curvature control, $P/P_L = 0.5$, 'no creep' conditions).

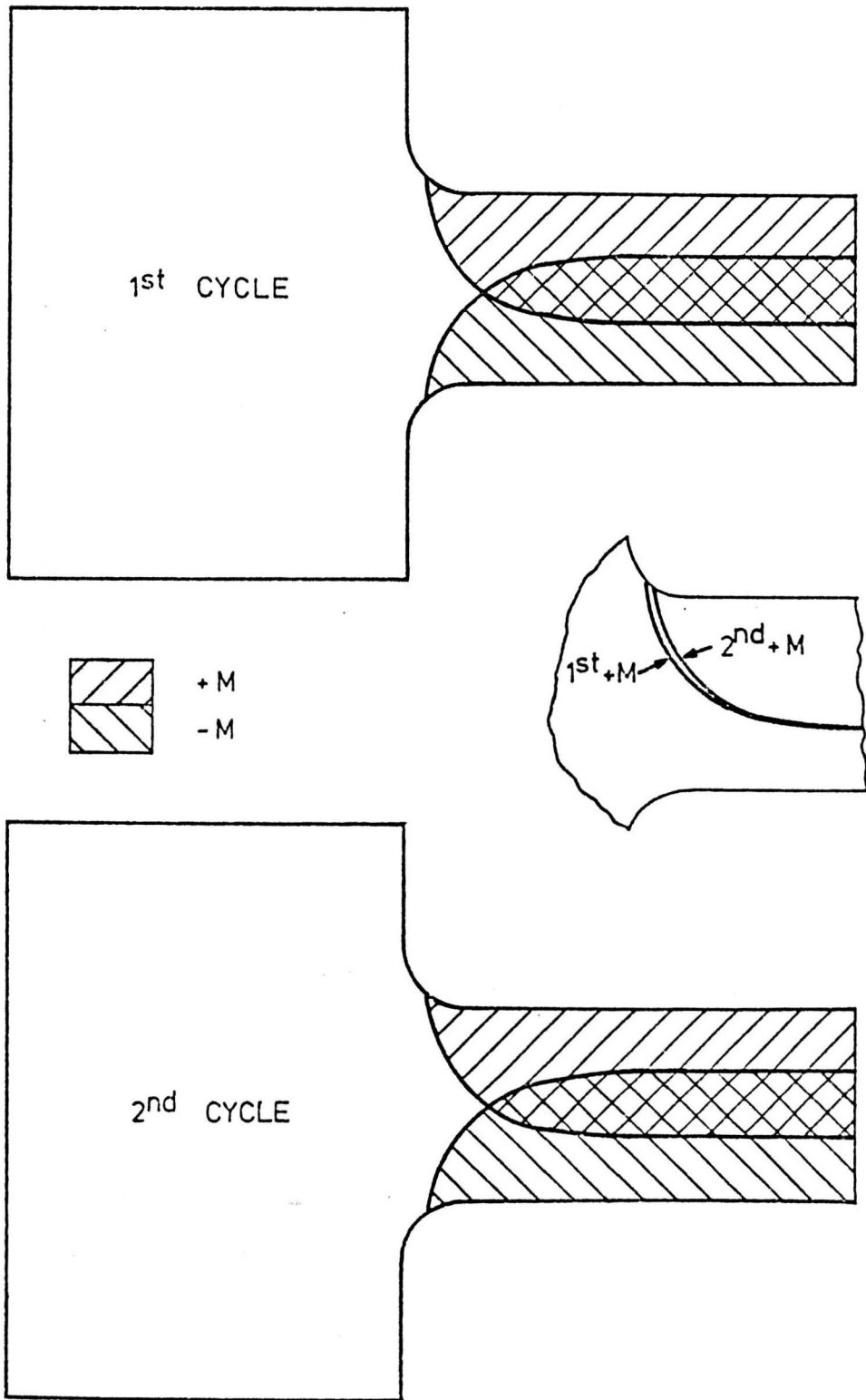


Figure 5.50 Stepped beam (elastic-perfectly-plastic, $M/M_y = 0.7$, $P/P_L = 0.7$, complete redistribution). Regions of yielding during the first and second cycles.

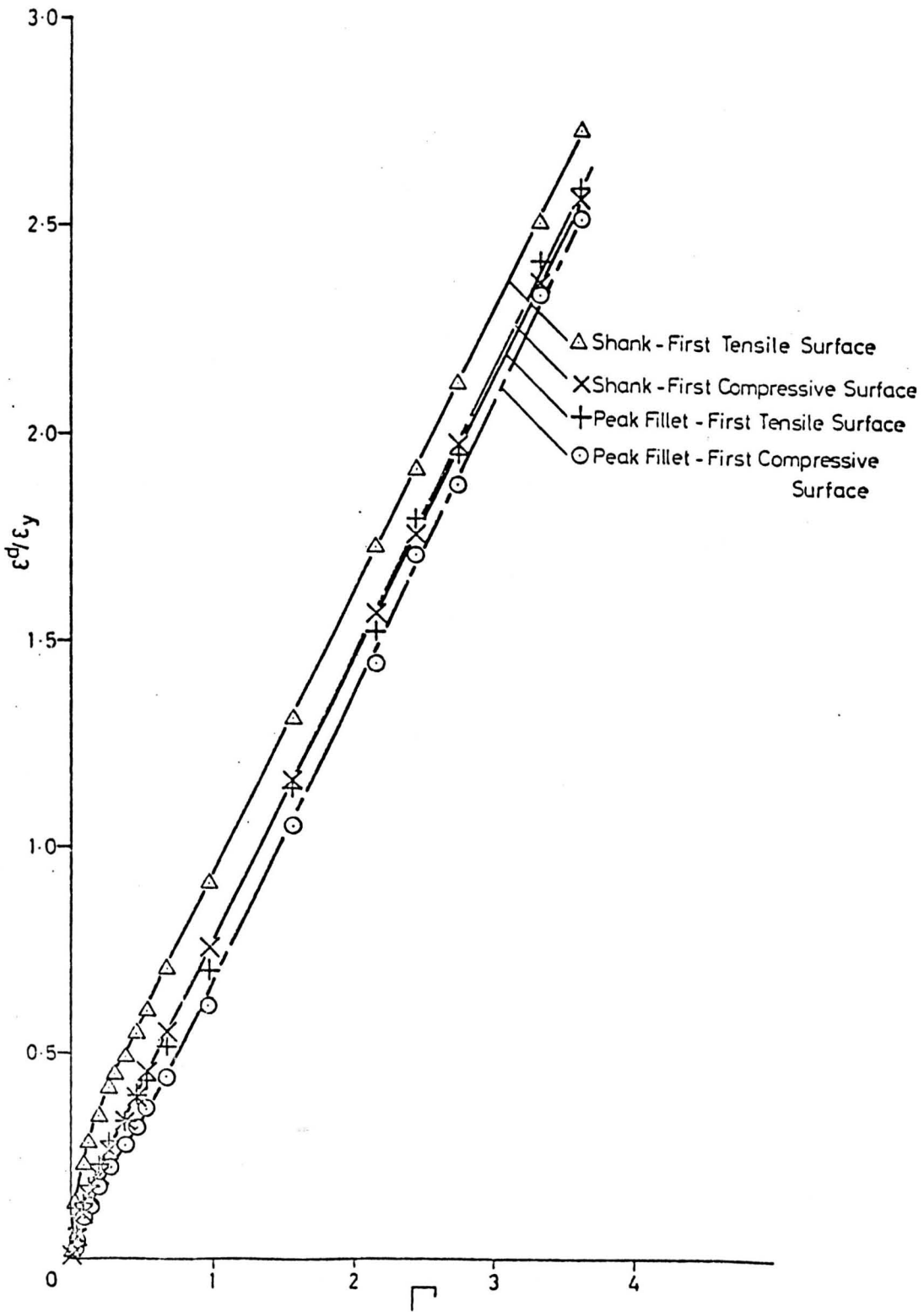


Figure 5.51 Stepped beam (elastic-perfectly-plastic, $M/M_y = 0.7$, $P/P_L = 0.7$, complete redistribution). Accumulations of normalised meridional strain during the first dwell period.

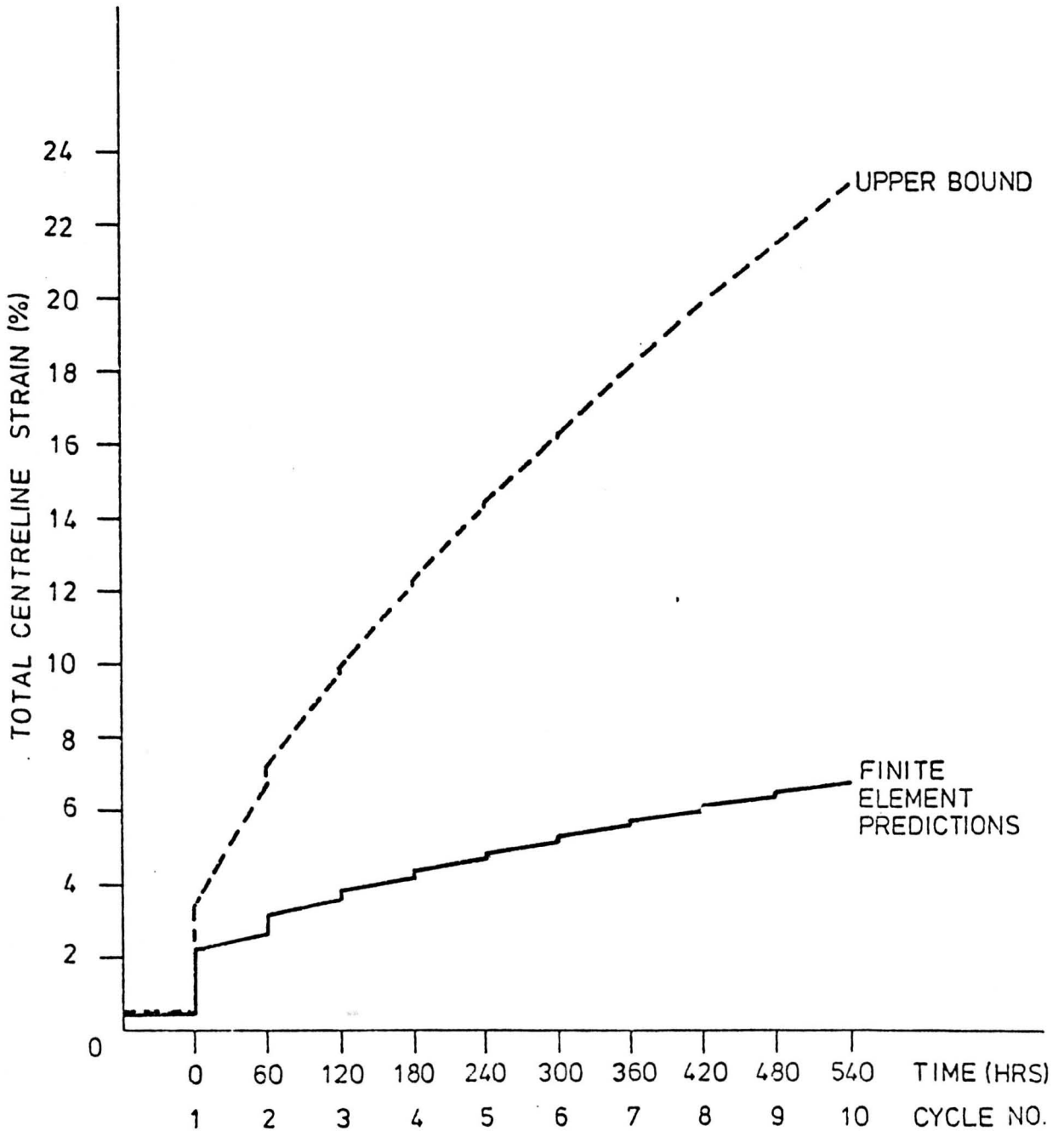


Figure 5.52 Stepped beam shank (isotropic hardening, $E_p/E = 0.05$, $M/M_y = 1.0$, $P/P_L = 0.7$). Comparison between finite element predictions and Ainsworth's upper bound predictions.

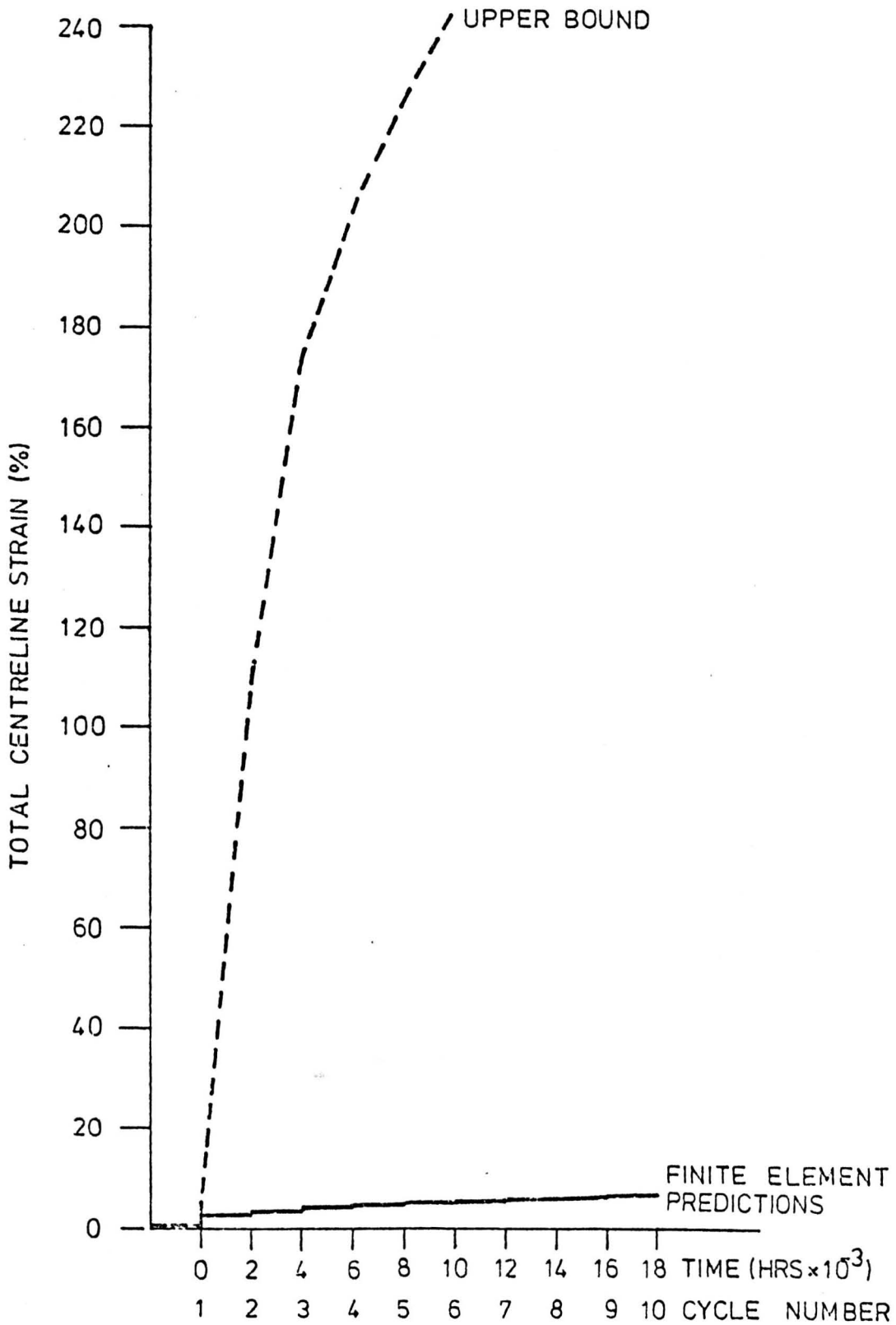


Figure 5.53 Stepped beam shank (isotropic hardening, $E_p/E = 0.05$, $M/M_y = 2.0$, $P/P_L = 0.4$). Comparison between finite element predictions and Ainsworth's upper bound predictions.

CHAPTER SIX

6. 'HOLE-IN-PLATE', CIRCULAR PLATE AND SHOULDERED TUBE COMPONENTS

6.1 Introduction

In this chapter, the analysis of the 'hole-in-plate', circular plate and shouldered tube components is described. Each component ratchets when subjected to steady mechanical and cyclic thermal loading. The effects of the steady mechanical and thermal loads are initially studied independently prior to the analysis of ratchetting. The effect of creep during dwell periods is bounded by consideration of the 'no creep' and 'complete redistribution' cases.

An elastic-perfectly-plastic material model is used throughout and the material data is given in Table 6.1. Appendix I lists the 'standard' input data used in the finite element analyses.

6.2 'Hole-in-plate' Component

6.2.1 Finite element model

The 27 element mesh used to model a quarter section of the 'hole-in-plate' component (see Figure 3.3) is shown in Figure 6.1. The axes of symmetry AB and CD are constrained to have no displacement in the global X and Y directions respectively and a mechanical load is applied to the right hand end of the mesh in the global X direction. Two-dimensional, plane stress, 8 noded isoparametric elements are used and the justification of this mesh is discussed in Appendix II. The Gauss points nearest to AB are also shown in Figure 6.1.

6.2.2 Mechanical loading

6.2.2.1 Elastic stresses

The elastic normal stress distribution across the section of maximum stress variation, AB, due to the mechanical loading is shown

in Figure 6.2 from which a maximum mechanical stress concentration factor of 2.43 is obtained at point A. The 'exaggerated' deformed shape for a mean load of 0.7 of the limit load is shown in Figure 6.3. The comparatively large deformation of the element nearest to point A is clear.

6.2.2.2 Elastic-plastic behaviour

The growth of the plastic zone in the component when subjected to increasing mechanical load up to collapse is shown in Figure 6.4. The plastic zone grows from the point of peak stress, A, and at collapse there is a band of yielded material with part of section AB remaining elastic.

6.2.2.3 Creep at sustained mean load

The effects of creep on the normal stress distribution along AB is shown in Figure 6.5, for Gauss points nearest to the axis of symmetry. The fully redistributed stress distribution is approximately linear and the reduced stress concentration factor is approximately 1.21.

6.2.3 Thermal loading cycle

The component is initially under isothermal conditions and is insulated except for the surface of the hole. A thermal shock consists of:-

- (i) a ramp increase in the temperature of the hole surface of 60°C in 2 seconds;
- (ii) a dwell period of 1000 seconds for conditions to stabilise at the increased temperature;
- (iii) a ramp reduction in the temperature of the hole surface of 60°C in 2 seconds; and

(iv) a further dwell period of 1000 seconds for the original isothermal conditions to be re-established.

The most severe stress conditions occur during the transient. The temperature response at points A, B, C, D and the variation in through thickness temperature difference across AB and CD are shown in Figure 6.6 for the first half of the transient (i.e. (i) and (ii)). The temperature files used to apply the thermal shocks were edited to an acceptable number of increments without affecting the severity of the transient. The times chosen and the temperature distributions along AB and CD during the first half of the thermal shock are given in Figure 6.7. The thermal stress conditions are more severe along AB than CD and Figure 6.8 shows the time variation in elastically calculated thermal stress normal to AB at the Gauss point nearest to A for the first 15 seconds of the first half of a thermal shock. This stress is negative and peaks at approximately 2.7 seconds after the start of the ramp change in temperature.

Equivalent linear temperature differences were obtained from the non-linear temperature distributions across AB, shown in Figure 6.7, by the approach suggested by Yamamoto et al (49) and a maximum value of 51.7°C was obtained. Using this value in the equation for maximum thermal stress, $\sigma_t = E\alpha\Delta T/2$, gives a maximum normalised thermal stress range, $\sigma_t/\sigma_y = 1.37$, for the complete cycle.

6.2.4. Cyclic thermal loading with sustained mean load

6.2.4.1 'No creep' condition

Ratchetting mechanism

The plastic zones due to an initial mechanical load of 0.7

of the limit load, at the end of the first half thermal cycle and at the end of the first complete thermal cycle are shown in Figure 6.9. The first thermal cycle generates an increment of plastic strain across part of the section AB and the maximum ratchet strain is at point A in the direction tangential to the hole.

After the first cycle a cyclic steady state is reached and the development and translation of the zones of additional plastic growth during a steady state thermal cycle are shown in Figure 6.10. The residual stress distributions across AB at the end of a steady state cycle are given in Figure 6.11. There is a peak value at an intermediate position between A and B. During the first half of a steady state thermal shock yielding initiates from this position (see Figure 6.10) and moves outwards to B. During the second half of the thermal shock, yielding initiates at A and moves outwards towards the centre of the section (Figure 6.10). The total regions of additional plastic growth during a steady state thermal cycle are given in Figure 6.12. The whole section experiences an increment of plastic strain. Since the steady state plastic zones are narrower near the hole (i.e. near A) than they are on the outside surface (i.e. near B), larger ratchet strains would be expected to occur near the hole. This is shown to be the case in Figure 6.13(a), which shows the distribution of steady state ratchet strains across AB in the direction normal to AB. The steady state ratchet strain at A is less than the first cycle value. Figure 6.13(b) shows the distribution of steady state ratchet strain along the outside surface and shows the peak value to be away from B but still significantly less than the ratchet strain at A.

The 'exaggerated' nodal displacements at the end of the 8th shock and the incremental 'exaggerated' nodal displacements due to the 9th shock are shown in Figure 6.14. There is a reduction in the section AB and an ovalisation of the hole which has a general

increase in diameter.

The accumulation of ratchet strains at point A during the first 10 cycles is shown in Figure 6.15.

Effect of mean load on ratchetting behaviour

The accumulation of peak ratchet strains (at point A) for a mean load of 0.5 of the limit load during the first 10 cycles is shown in Figure 6.16. In this case the steady state condition is achieved in approximately 5 cycles and the steady state ratchet strains are very small ($(\Delta \epsilon^r / \epsilon_y)_{SS} = 0.015$). A summary of the results for $P/P_L = 0.5$ and 0.7 is given in Table 6.2 and the results are discussed in Chapter 7.

6.2.4.2 Complete redistribution

Ratchetting mechanism

The plastic zones due to an initial mechanical load of 0.7 of the limit load, at the end of the first half thermal cycle and at the end of the first thermal cycle are identical to those for the 'no creep' case shown in Figure 6.9. Between the end of the first thermal cycle and the start of the second thermal cycle the stresses redistribute to the stationary state stress distribution which for the section AB is given in Figure 6.11. The variation of stress normal to AB, at A and B and at the point of peak residual stress, during the first dwell period is given in Figure 6.17. The stationary state stress distribution (Fig. 6.11) does not have a central peak value. Steady cyclic state conditions exist after the first cycle and the regions of additional plastic strain during a steady state cycle are shown in Figure 6.18. During the first half of the cycle, yielding is restricted to regions around A and B. The second half of the cycle is very similar to that for the

'no creep' case shown in Figure 6.10, where yielding initiates from the bore and extends over approximately one half of the section during the half cycle. The distribution of steady state ratchet strain in the direction of applied load across the section AB is compared with the 'no creep' case in Figure 6.13(a). The distribution is non-linear with a large increase in ratchet strains in the region close to A where the peak ratchet strain occurs. A relatively flat steady state distribution of ratchet strain along the outside surface is shown in Figure 6.13(b). Steady state ratchet strains at A are less than the first cycle and the accumulation of peak ratchet strains during the first 10 cycles is shown in Figure 6.15.

The 'exaggerated' displacements after 8 cycles, during the 9th thermal shock and during the 9th dwell period are shown in Figure 6.19. The reduction in section AB and ovality of the hole of the 'no creep' case is again apparent under 'complete redistribution' conditions but there is an overall reduction in hole diameter at A which results from the dwell period behaviour.

Effects of mean load on ratchetting behaviour

The accumulation of peak ratchet strains (at point A) for a mean load of 0.5 of the limit load during the first 10 cycles is compared with the 'no creep' case in Figure 6.16. With 'no creep' the ratchet strains are very small but with 'complete redistribution' resulting from creep, the component ratchets with a large accumulation of inelastic strain. A summary of the results for $P/P_L = 0.5$ and 0.7 is given in Table 6.2 and the results are discussed in Chapter 7.

Creep during the dwell periods

The tangential strain which accumulates during the first dwell period at point A for a mean load of $0.7 P_L$ is shown in Figure 6.20.

The steady state behaviour which occurs during the second and subsequent dwell periods is similar to that for the first dwell period. The normalised steady state strain rates and increments of normalised strain due to stress redistribution, $\Delta \epsilon^d / \epsilon_y$, for this load and $P/P_L = 0.5$ are given in Table 6.3. For both loads the increments of strain are negative because the stress at A increases during the redistribution. The dwell period results are discussed in Chapter 7.

6.3 Circular Plate Component

6.3.1 Finite element model

The 40 element, axisymmetric mesh used to model the circular plate component (see Figure 3.4) was previously used by Hyde (32) and is shown in Figure 6.21. The edge of the plate is constrained to have the same radial displacement at each node and the steady load consists of a transverse pressure applied to the top face. Axisymmetric 8-noded isoparametric elements are used. When stress and strain distributions are quoted, the results are for Gauss points nearest to faces (0.11 mm) or edges (0.44 mm).

6.3.2 Transverse pressure loading

6.3.2.1 Elastic stresses

The radial variation in elastic stress along the top (pressurised) and bottom faces is shown in Figure 6.22 for a transverse pressure load of 0.7 of the collapse load. The collapse load is based on the theory of Hopkins and Wang (56) for a circular plate with a 'built-in' edge and a uniformly distributed transverse load,

$$\text{i.e.} \quad \frac{P_{\text{col}}}{2\pi M_{\text{col}}} = 6.25$$

where P_{col} is the collapse load and M_{col} is the collapse moment for a beam of unit thickness and depth equal to the thickness of the circular plate. For the circular plate configuration used a collapse pressure of $4.25 \times 10^5 \text{ N/m}^2$ is obtained.

The results plotted in Figure 6.22 are for the Gauss points nearest to the surfaces. The clamping arrangement and effects of pressure on the top surface at the edge result in slightly lower radial and hoop stresses on the bottom face compared with the top pressurised face. The 'exaggerated' deformed shape for the same loading is shown in Figure 6.23.

6.3.2.2 Elastic-plastic behaviour

The elastic-plastic behaviour of the component when subjected to increasing transverse pressure load up to collapse is shown in Figure 6.24. Yielding initiates at the four 'corners' of the mesh and at collapse plastic hinges at the edge and centre of the plate are evident. The results also give an indication of the accuracy of the Hopkins and Wang (56) theory; in the finite element analysis collapse occurs at a pressure of 1.05 of the Hopkins and Wang collapse pressure.

6.3.2.3 Creep at sustained mean load

The effect of creep on the hoop and radial stress distributions on the centre line (AB in Figure 6.21) is shown in Figure 6.25 for a transverse pressure of 0.474 of the collapse pressure. There is no difference between hoop and radial stress components. The initially linear variation redistributes to a highly non-linear form with large stress gradients in the region of the 'neutral plane'. Creep has a similar effect on the hoop and radial

stress distributions at the edge (CD in Figure 6.21) as shown in Figures 6.26 and 6.27 respectively.

6.3.3 Thermal loading cycle

The component is initially under isothermal conditions and the edge is insulated. A thermal shock consists of:-

- (i) the application of a 40°C through thickness temperature gradient. This is obtained by reducing the temperature of the pressurised face by 40°C in 2 seconds at a constant rate with the temperature of the unpressurised face held constant;
- (ii) a period of time for the temperature gradient to stabilise;
- (iii) an equivalent ramp increase in the temperature of the pressurised face; and
- (iv) a further period of time for the initial isothermal conditions to be re-established.

The worst thermal conditions occur when the maximum temperature difference exists and using the Bree (1) equation for thermal stress, the maximum normalised thermal stress range, $\frac{\sigma_t}{\sigma_y}$, is 1.41 which was confirmed by the finite element elastic analysis.

The temperature files used to apply the thermal shocks were those developed by Hyde (32) for his analysis of the component.

6.3.4 Cyclic thermal loading with sustained transverse pressure

6.3.4.1 'No creep' condition

Ratchetting mechanism

The first thermal cycle produces ratchet strains which vary throughout the component. The largest value of tensile ratchet strain occurs at the bottom edge of the plate (position D in Figure 6.21) in the transverse direction. There is an equal

compressive ratchet strain at the same point in the radial direction. At the centre of the plate the maximum tensile ratchet strain occurs at point A in the transverse direction with an equal compressive ratchet strain at point B in the same direction. Ratchet strains quoted are tensile and for points A (centre) and D (edge) in the transverse direction. The accumulation of ratchet strains at the edge and centre of the plate during the first 10 cycles and the individual ratchet strains for a pressure of 0.7 of the collapse pressure are shown in Figure 6.28. Steady state conditions are not reached and ratchet strains continue to reduce during the 10 cycles analysed. Larger accumulations of ratchet strain occur at the edge. The regions of additional plastic straining for the two halves of the 2nd thermal shock and during the 10th thermal shock are shown in Figures 6.29 and 6.30 respectively. Plastic straining is apparent at the edge and centre of the plate (during the first and second halves of the shock respectively). The reduction in ratchet strain between the 2nd and 10th shocks corresponds to a reduction in the yield zone at the edge whereas there is no apparent reduction in the yield zone at the centre. Unlike the other components, ratchetting occurs in the absence of a 'plastic core'. The 'exaggerated' displacements at the end of the 10th thermal shock and during the 11th thermal shock are shown in Figure 6.31.

Effect of transverse pressure on ratchetting behaviour

The accumulation of edge and centre ratchet strains during the first 10 cycles and the individual ratchet strains for a pressure of 0.295 and 0.4 of the collapse pressure are shown in Figure 6.32 and for 0.474 of the collapse pressure in Figure 6.33. In all cases, shakedown occurs in less than 5 cycles. The results are summarised in Table 6.4 and are discussed in Chapter 7.

6.3.4.2 Complete redistribution

Ratchetting mechanism

The ratchet strains produced by the first thermal shock are identical to those for the 'no creep' condition. Between the end of the first thermal shock and the start of the second shock the residual stress field is allowed to completely redistribute to a stationary state stress distribution which is the same as the stress field developed by creep from the initial stress distribution with the applied pressure only, (see Figures 6.25 to 6.27). Unlike the 'no creep' case a steady cyclic state is reached after the first cycle where second and subsequent thermal shocks produce the same increment of ratchet strain which is less than the first cycle value. The regions of additional plastic straining during a steady state cycle are shown in Figure 6.34 for a pressure of 0.7 of the collapse pressure. Plastic straining is again apparent at the edge during the first half of the shock and at the centre during the second half of the shock and a 'plastic hinge' at the edge is evident when the 40°C linear temperature gradient is fully established. The accumulation of ratchet strains at the edge and centre of the plate during the first 10 cycles and the individual ratchet strains for a pressure of 0.7 of the collapse pressure are compared with those for the 'no creep' condition in Figure 6.28. The 'exaggerated' nodal displacements at the end of 10 cycles, during the 11th shock and during the 11th dwell period are shown in Figure 6.35 for the same loading.

Effect of transverse pressure on ratchetting behaviour

The accumulation of edge and centre ratchet strains during the first 10 cycles and the individual ratchet strains for a pressure

of 0.295 and 0.4 of the collapse pressure are compared with the 'no creep' behaviour in Figure 6.32 and for 0.474 of the collapse pressure in Figure 6.33. The results are summarised in Table 6.4 and are discussed in Chapter 7.

Creep during the dwell periods

The strains which accumulate during the first dwell period at the point of maximum tensile ratchet strain (i.e. point D in Figure 6.21) in the transverse direction for a pressure of 0.7 of the collapse pressure are shown in Figure 6.36. The behaviour is similar to that for the components already discussed and steady state conditions occur during the second and subsequent dwell periods. The normalised steady state strain rates and increments of normalised strain due to stress redistribution at point D for pressures of 0.295, 0.4, 0.474 and 0.7 of the collapse pressure are given in Table 6.5. These results are discussed in Chapter 7.

6.4 Shouldered Tube Component

6.4.1 Finite element model

The 50 element, axisymmetric mesh used to model the shouldered tube component (see Figure 3.5) was previously used by Hyde et al (10, 11) and is shown in Figure 6.37. The left hand end of the mesh (shank face) is constrained to have zero displacements in the axial direction. Axial loading is applied to the right hand end which is constrained to have constant displacement in the axial direction. Axisymmetric 8-noded isoparametric elements are used.

6.4.2 Axial mechanical loading

6.4.2.1 Elastic stresses

The elastic stress distributions along the outside surface and bore due to an axial load are shown in Figures 6.38 and 6.39. The meridional stress is dominant and peak conditions occur in the fillet. The results are for the Gauss points nearest to the surface. At the surface, a mechanical stress concentration factor of 1.59 has previously been obtained (10). The 'exaggerated' deformed shape for a mean load of 0.7 of the limit load is shown in Figure 6.40. There is a localised necking close to the shank/fillet transition.

6.4.2.2 Elastic-plastic behaviour

The elastic-plastic behaviour of the component subjected to increasing axial load up to collapse is shown in Figure 6.41. Yielding initiates in the fillet and the yielded zone is very localised even at high load ($P/P_L = 0.9$). At collapse a significant region of the shank remains elastic.

6.4.2.3 Creep at sustained mean load

The stationary state meridional stress distributions for the Gauss points nearest to the outside surface and bore are compared with the initial stress distributions in Figures 6.42 and 6.43 respectively. There is a significant reduction in the stress concentration factor in the fillet but the stationary state and initial stress distributions along the bore surface are very similar.

6.4.3 Thermal loading cycle

Initial isothermal conditions are maintained by fluid flowing through the bore and along the outside surface. The temperature of the bore fluid flow remains constant. A thermal shock consists of:-

- (i) a ramp reduction in the temperature of the fluid flowing along the outside surface of 56°C in 2 seconds;
- (ii) a period of 1.2 seconds for the temperature gradient to be fully established;
- (iii) a ramp increase in the temperature of the fluid flowing along the outside surface of 56°C in 2 seconds; and
- (iv) a further period of 1.2 seconds for the initial isothermal conditions to be re-established.

For this thermal load the most severe thermal conditions occur when the maximum temperature difference exists (i.e. (ii)) and an almost linear through thickness variation in temperature is established in the shank.

Results are obtained for two maximum normalised thermal stress ranges, 1.42 and 2.83, based on the Bree (1) equation for thermal stress.

i.e.
$$\frac{\sigma_t}{\sigma_y} = \frac{E \alpha \Delta T}{2(1 - \nu) \sigma_y}$$

The temperature files used to applied the thermal shocks were those obtained by Hyde et al (10, 11).

6.4.4 Cyclic thermal loading with sustained axial load

6.4.4.1 'No creep' condition

Ratchetting mechanism

The stress distributions in the shank due to initial loading, at the end of the first half of the first thermal cycle and at the end of the first complete thermal cycle for $P/P_L = 0.5$ and $\sigma_t/\sigma_y = 2.83$ are shown in Figure 6.44. There is an increment of ratchet strain in the first cycle and a steady cyclic state is

established after the first complete cycle. Maximum ratchet strains occur in the axial direction and are constant with radius. Steady state ratchetting will occur in the shank when there is a central region which experiences plasticity during both halves of the thermal cycle.

At the 'peak fillet' position, where the largest ratchet strains are accumulated, a steady cyclic state is also reached after the first cycle. The distribution of steady state, meridional ratchet strain along the outside surface of the component is shown in Figure 6.45 for $P/P_L = 0.5$ and $\sigma_t/\sigma_y = 2.83$. The accumulations of ratchet strain in the shank and at the 'peak fillet' position during the first 10 cycles for this loading are shown in Figure 6.46.

The ratchetting mechanism in the fillet for $P/P_L = 0.7$ and $\sigma_t/\sigma_y = 1.42$ is discussed below. The regions of additional plastic straining for a steady state cycle are shown in Figure 6.47 and the accumulation of ratchet strain in the shank and at the 'peak fillet' position during the first 10 cycles are shown in Figure 6.48. During the first half of the thermal shock, yielding initiates in the shank and fillet and the yield zone is fully developed by increment 11. The zone of plastic straining contracts as the steady state thermal gradient is established. During the second half of the thermal shock there is no further plastic straining in the shank but a plastic zone spreading from the bore in the region of the fillet is sufficiently large to produce a band of plastic growth through the section close to the fillet which in turn ensures an increment of plastic strain across the section. In the shank a substantial (approx. $2/3$ rds) part

remains elastic during the complete cycle and, in the absence of a 'plastic-core', ratchetting would not be expected after the first cycle. This is shown to be the case in Figure 6.48 where steady state ratchet strains in the shank are zero and there is no further accumulation of ratchet strains after the first cycle. In the fillet, from Figure 6.48, it would appear that the steady cyclic state is established after approximately 6 cycles. The 'exaggerated' deformed shapes after the 10th cycle and during the 11th cycle are shown in Figure 6.49. The absence of shank ratchetting is apparent from Figure 6.49(b). There is a reduction in cross-sectional area in the region of the fillet.

Effects of mean load and thermal load on ratchetting behaviour

The accumulations of shank and 'peak fillet' ratchet strains during the first 10 cycles for $P/P_L = 0.5$ and $\sigma_t/\sigma_y = 1.42$ are shown in Figure 6.50. Steady state ratchet strains are zero in the shank and very small in the fillet. The results for this load combination, $P/P_L = 0.7$, $\sigma_t/\sigma_y = 1.42$ and $P/P_L = 0.5$, $\sigma_t/\sigma_y = 2.83$ are summarised in Table 6.6. These results are discussed in Chapter 7.

6.4.4.2 Complete redistribution

Ratchetting mechanism

The ratchet strains in the shank and at the 'peak fillet' positions produced by the first thermal shock are identical to those for the 'no creep' condition. Between the end of the first thermal shock and the start of the second thermal shock the stresses completely redistribute to the stationary state stress

distributions shown in Figures 6.42 and 6.43. In the shank the ratchet strains in the second and subsequent cycles are the same and are equal to the first cycle ratchet strains. At the 'peak fillet' position a steady cyclic state is reached after the first cycle and ratchet strains produced in the second and subsequent cycles are the same but differ from the first cycle value because the stationary state stress distribution (which is the initial condition for the second and subsequent cycles) is different to the initial stress distribution due to axial loading. The ratchet strains accumulated in the shank and at the 'peak fillet' position during the first 10 cycles for $P/P_L = 0.5$ and $\sigma_t/\sigma_y = 2.83$ are compared with the 'no creep' case in Figure 6.46. The steady state ratchet strains and hence the accumulation of ratchet strains are greater for the 'complete redistribution' condition.

The regions of additional plastic straining during a steady state thermal cycle for $P/P_L = 0.7$ and $\sigma_t/\sigma_y = 1.42$ are shown in Figure 6.51. The accumulation of ratchet strains in the shank and at the 'peak fillet' positions for this loading are compared with the 'no creep' case in Figure 6.48. In the shank, the 'plastic-core' requirement for continued ratchetting is not applicable if creep occurs; all cycles are identical and any plastic straining during the first cycle will be repeated in each subsequent cycle. In the fillet, a band of yielded material is evident, as for the 'no creep' case, but not essential for ratchetting to continue. The 'exaggerated' deformed shapes after the 10th cycle, during the 11th shock and during the 11th dwell period for $P/P_L = 0.7$, $\sigma_t/\sigma_y = 1.42$ are shown in Figure 6.52. The radial displacements are zero in the rigid shoulder but inward radial displacements

occur in the shank. There is a reduction in cross section close to the fillet during the thermal shock.

Figure 6.52 shows that there is a greater reduction in bore diameter in the shank compared with the shoulder during the thermal cycle and the dwell period.

Effects of mean load and thermal load on ratchetting behaviour

The accumulation of ratchet strains for $P/P_L = 0.5$ and $\sigma_t/\sigma_y = 1.42$ are shown in Figure 6.50. The results for the various load combinations are summarised in Table 6.6 and are discussed in Chapter 7.

Creep during the dwell periods

The strains which accumulate in the shank and at the peak ratchetting position in the fillet during the first two cycles for $P/P_L = 0.5$ and $\sigma_t/\sigma_y = 2.83$ are shown in Figure 6.53. The results are asymptotic to straight lines; the gradient of the straight line is the same for the first and second (and hence subsequent) cycles. There is a greater accumulation of dwell period strains in the shank compared with the fillet. The steady state strain rates and increments of strain due to stress redistribution for this loading, $P/P_L = 0.5$, $\sigma_t/\sigma_y = 1.42$ and $P/P_L = 0.7$, $\sigma_t/\sigma_y = 1.42$ are given in Table 6.7 and discussed in Chapter 7.

Parameter		Hole-in-plate	Circular Plate	Shouldered Tube
Young's Modulus	(GN/m ²)	23.2	23.1	23.2
Yield Stress	(MN/m ²)	15.0	15.0	13.8 & 6.9
Coefficient of expansion	(°C ⁻¹)	1.71 x 10 ⁻⁵	2.57 x 10 ⁻⁵	2.88 x 10 ⁻⁵
Poisson's Ratio		0.44	0.44	0.44
Thermal Conductivity	(W/mK)	35.1	35.1	35.1
Surface heat Transfer coefficient	(kW/m ² K)	-	-	{ 26.4 bore 32.0 outside shank & fillet 15.7 outside shoulder
Specific heat/unit volume	(J/m ³ K)	1.43 x 10 ⁶	1.43 x 10 ⁶	1.43 x 10 ⁶
Creep Law constants	$\left\{ \begin{array}{l} A \\ n \\ m \end{array} \right.$	8.67 x 10 ⁻⁵⁸	8.67 x 10 ⁻⁵⁸	8.67 x 10 ⁻⁵⁸
		7.3	7.3	7.3
		1.0	1.0	1.0

Table 6.1 Material data for 'hole-in-plate', circular plate and shouldered tube components

$\frac{P}{P_L}$	Normalised Ratchet Strain per Cycle			
	'No creep'		'Complete redistribution'	
	1st cycle	Steady State	1st cycle	Steady State
0.5	1.902	0.015	1.902	1.071
0.7	3.312	1.737	3.312	2.441

Table 6.2 Ratchetting behaviour of 'hole in plate' component

$\frac{P}{P_L}$	$\frac{d(\epsilon^d/\epsilon_y)}{d\Gamma}$	$\frac{d(\epsilon^d/\epsilon_y)/d\Gamma}{P/P_L}$	$\Delta\epsilon^d/\epsilon_y$	
			1st cycle	Steady State
0.5	1.534	3.069	-0.183	-0.144
0.7	2.169	3.099	-0.371	-0.481

Table 6.3 Dwell period behaviour of 'hole in plate' component

		Normalised ratchet strain per cycle			
		'No creep'		'Complete Redistribution'	
$\frac{P}{P_{col}}$	Position	1st cycle	Steady State	1st cycle	Steady State
0.295	Centre	0.240	0	0.240	0.183
	Edge	1.503	0	1.503	1.225
0.4	Centre	0.408	0	0.408	0.290
	Edge	2.871	0	2.871	2.356
0.474	Centre	0.744	0	0.744	0.372
	Edge	3.924	0	3.924	3.293
0.7	Centre	2.994	0.560*	2.994	1.886
	Edge	7.712	1.078*	7.712	7.270

* 10th cycle values.

Table 6.4 Ratchetting behaviour of circular plate

$\frac{P}{P_{col}}$	Position	$\frac{d(\epsilon^d/\epsilon_y)}{d\Gamma}$	$\frac{d(\epsilon^d/\epsilon_y)/d\Gamma}{P/P_{col}}$	$\Delta\epsilon^d/\epsilon_y$	
				1st cycle	Steady State
0.295	D	0.474	1.607	0.093	-0.024
0.4	D	0.643	1.607	0.091	-0.078
0.474	D	0.769	1.623	0.077	-0.044
0.7	D	1.075	1.536	-0.156	-0.212

Table 6.5 Dwell period behaviour of circular plate

$\left[\frac{\sigma_t}{\sigma_y} \right]_{\text{NOM}}$	$\frac{P}{P_L}$	Position	Normalised Ratchet Strain per Cycle			
			'No creep'		'Complete Redistribution'	
			1st cycle	Steady State	1st cycle	Steady State
1.42	0.5	Shank	0.109	0	0.109	0.108
		Peak Fillet	1.648	0.012	1.648	1.518
1.42	0.7	Shank	0.235	0	0.235	0.239
		Peak Fillet	2.304	0.082	2.304	2.127
2.83	0.5	Shank	0.685	0.187	0.685	0.686
		Peak Fillet	3.701	1.558	3.701	3.748

Table 6.6 Ratchetting behaviour of shouldered tube

$\left[\frac{\sigma_t}{\sigma_y} \right]_{\text{NOM}}$	$\frac{P}{P_L}$	Position	$\frac{d(\epsilon^d/\epsilon_y)}{d\Gamma}$	$\frac{d(\epsilon^d/\epsilon_y)/d\Gamma}{P/P_L}$	$\Delta\epsilon^d/\epsilon_y$	
					1st cycle	Steady State
1.42	0.5	Shank	0.495	0.990	0.207	0.207
		Peak Fillet	0.259	0.518	0.425	0.400
1.42	0.7	Shank	0.704	1.006	0.262	0.262
		Peak Fillet	0.372	0.531	0.541	0.518
2.83	0.5	Shank	0.504	1.008	0.740	0.740
		Peak Fillet	0.269	0.538	0.817	0.841

Table 6.7 Dwell period behaviour of shouldered tube

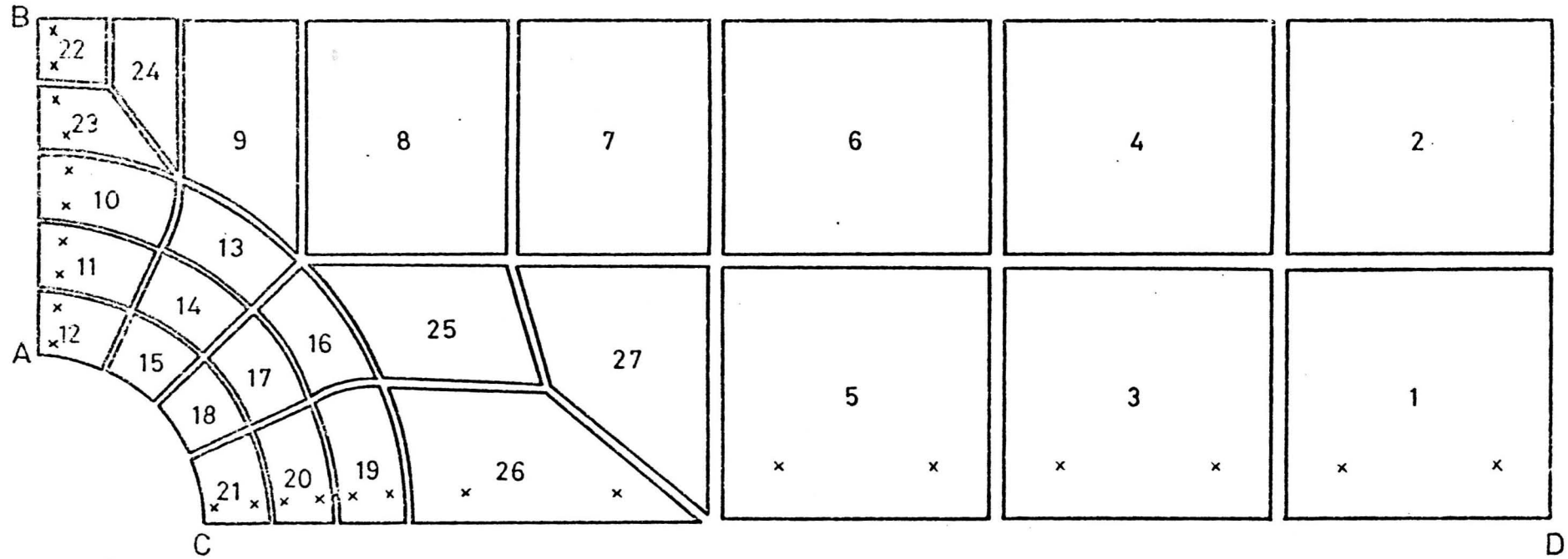
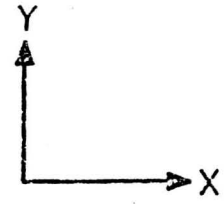


Figure 6.1 'Hole-in-plate'. Finite element mesh showing the positions of the Gauss points nearest to the AB and CD axes.

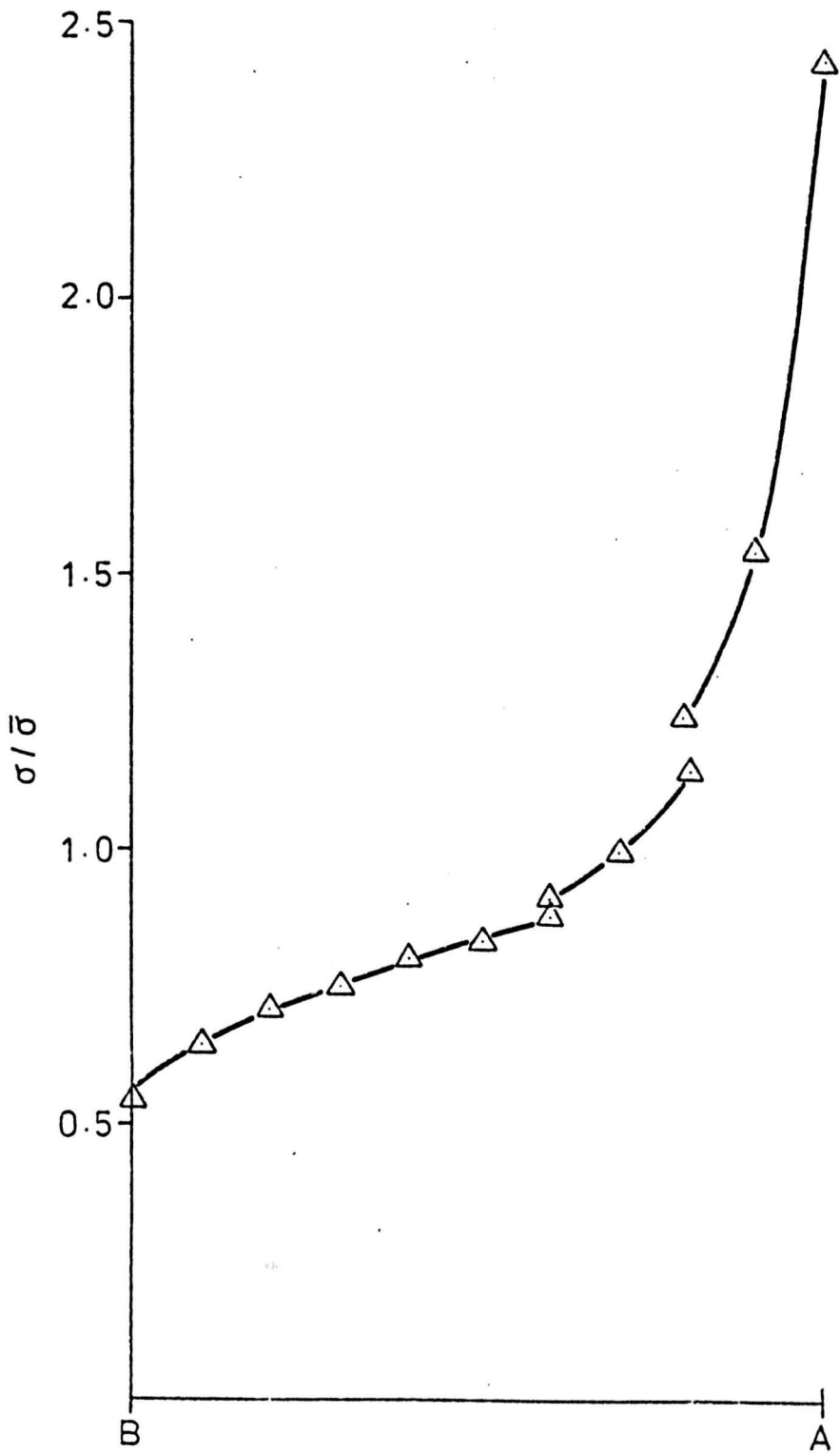


Figure 6.2 'Hole-in-plate'. Elastic normal stress distribution along AB due to mechanical loading.

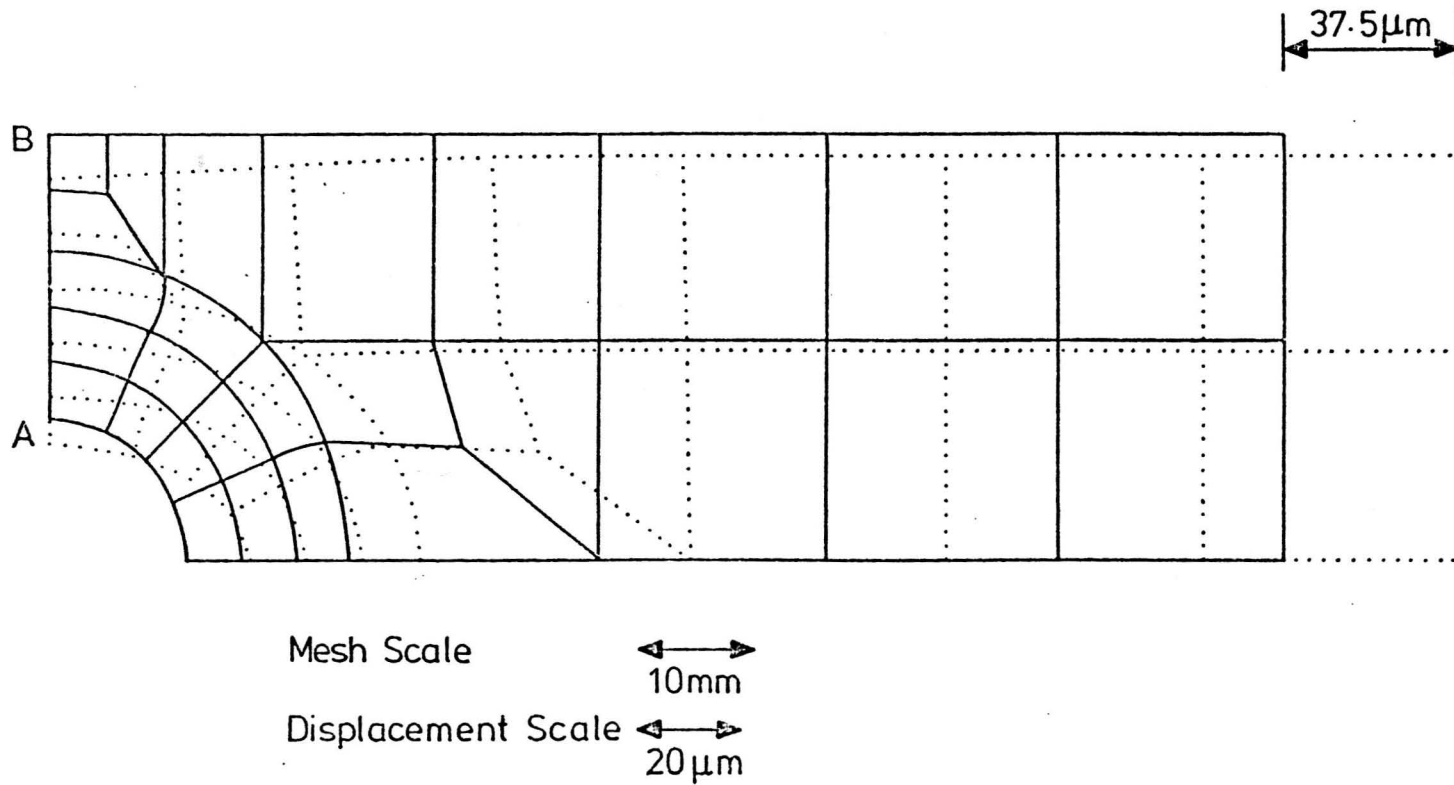
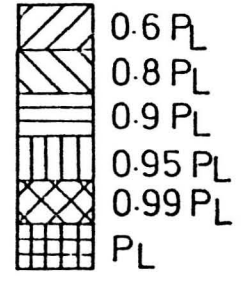


Figure 6.3 'Hole-in-plate'. 'Exaggerated' deformed shape for a mean load of 0.7 of the limit load.



WHERE $P_L = \text{LIMIT LOAD}$

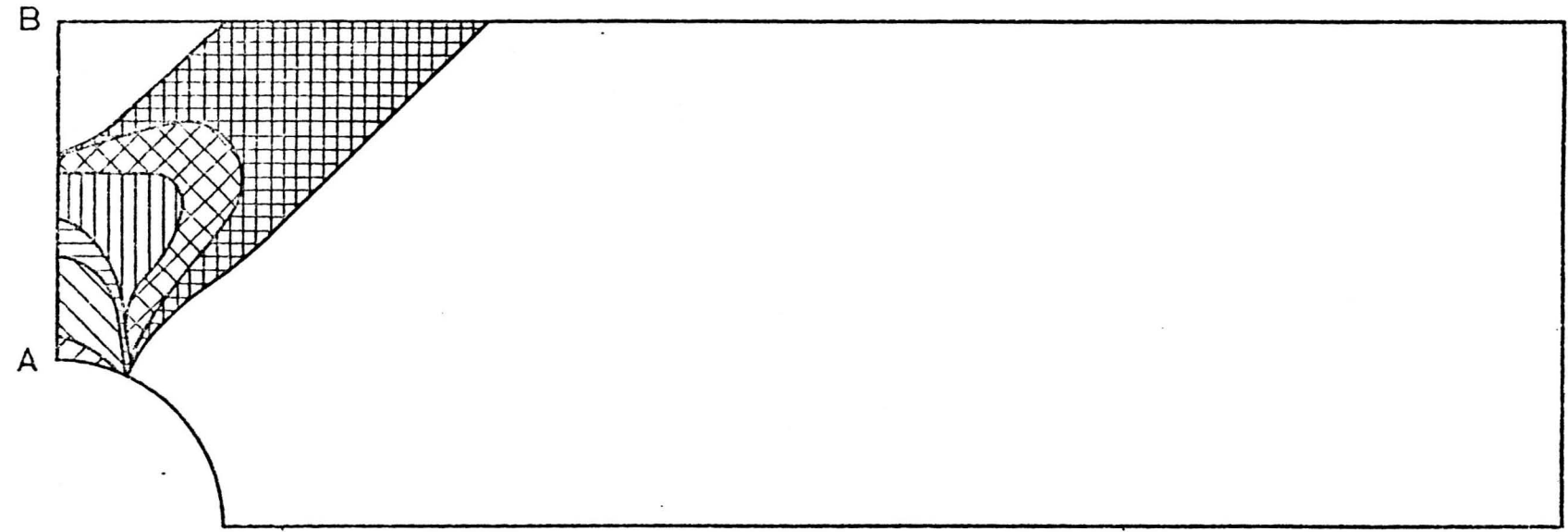


Figure 6.4 'Hole-in-plate' (elastic-perfectly-plastic). Growth of plastic zone with increasing mean load up to collapse.

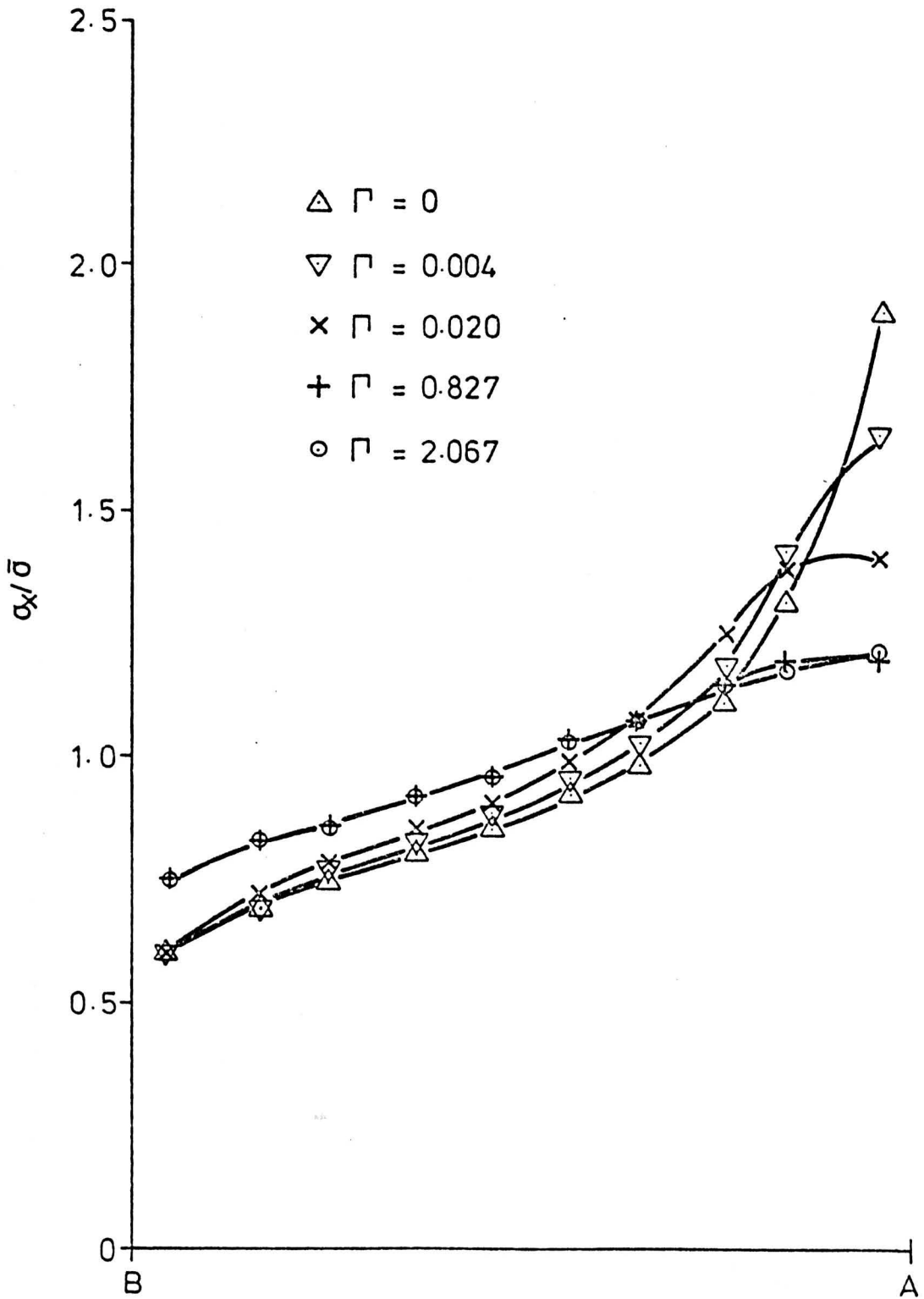


Figure 6.5 'Hole-in-plate'. Redistribution of normal stress 'along AB' due to creep at sustained mean load. (see Figure 6.1)

Figure 6.6(a) 'Hole-in-plate'. Temperature response across AB due to a ramp increase in bore surface temperature of 60°C in 2 secs.

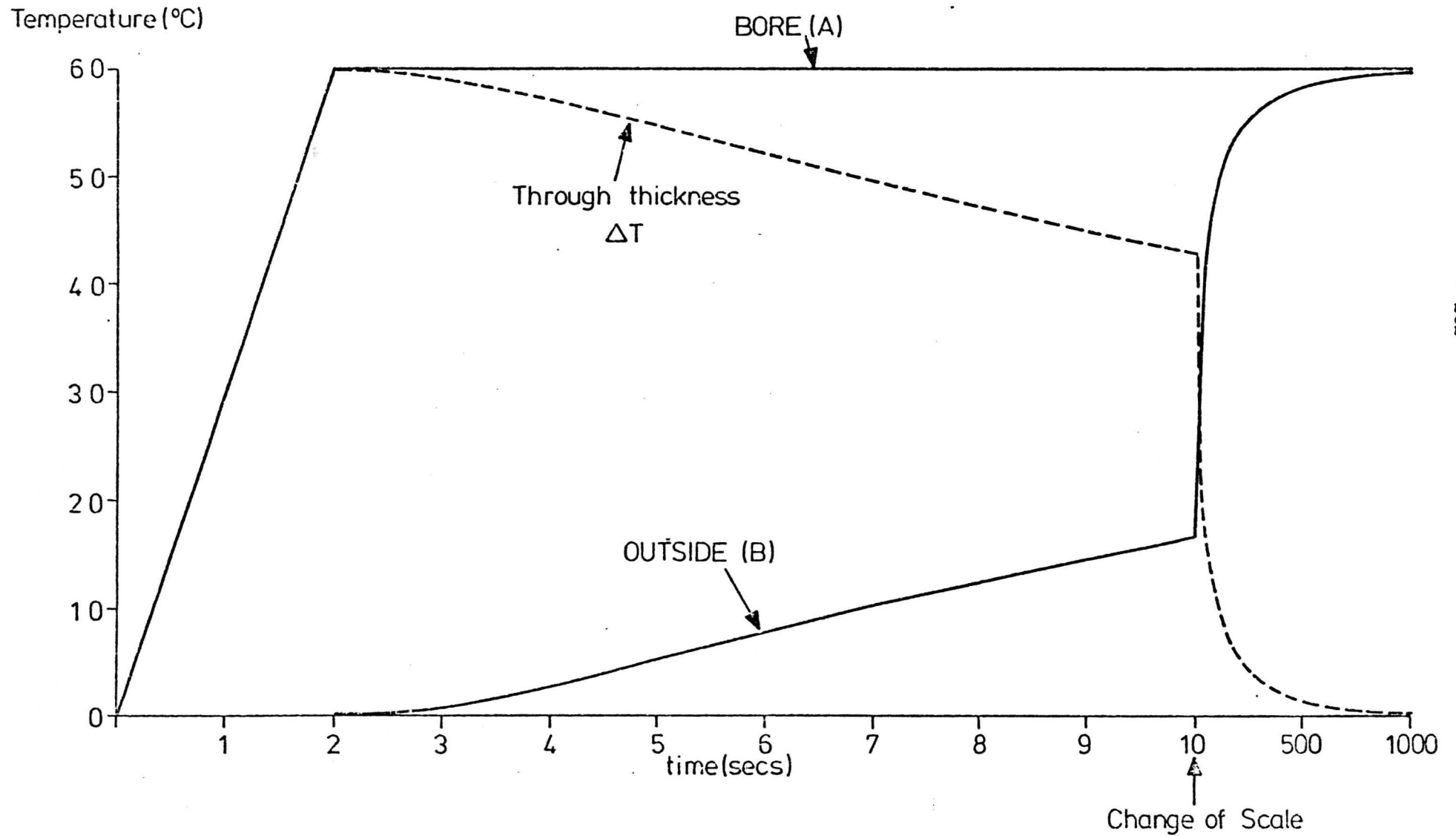
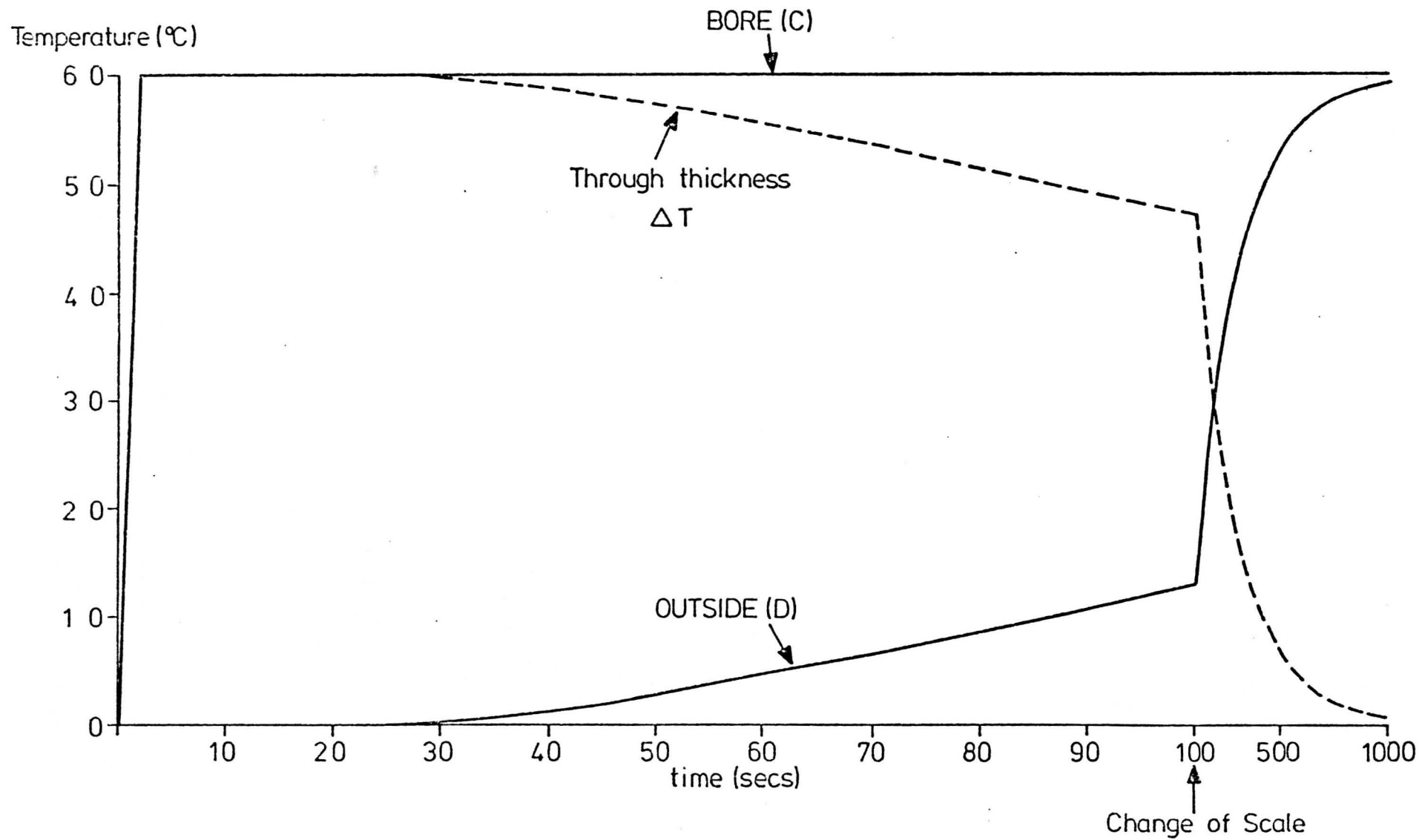


Figure 6.6(b) 'Hole-in-plate' Temperature response across CD due to a ramp increase in bore surface temperature of 60°C in 2 secs.



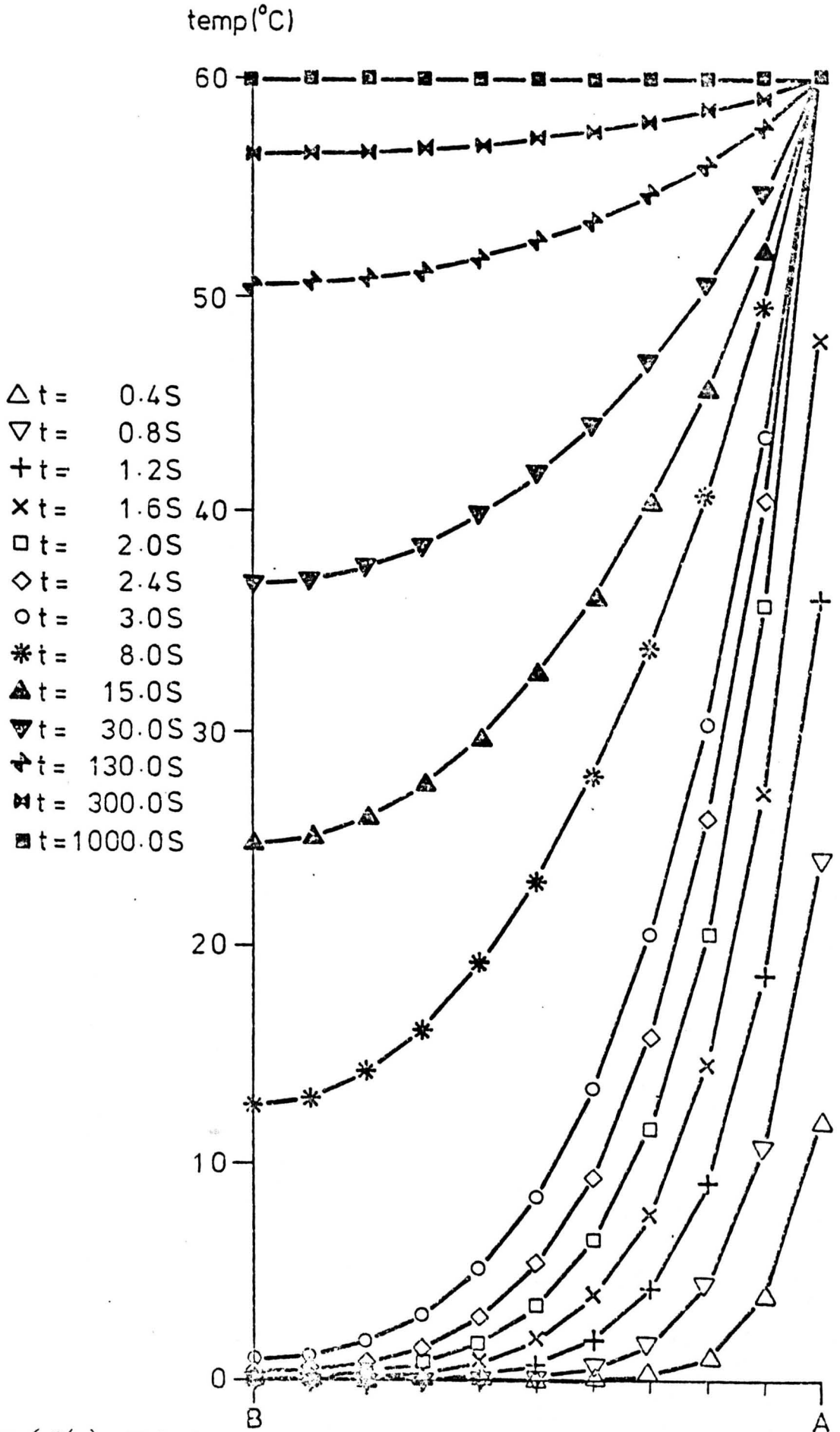
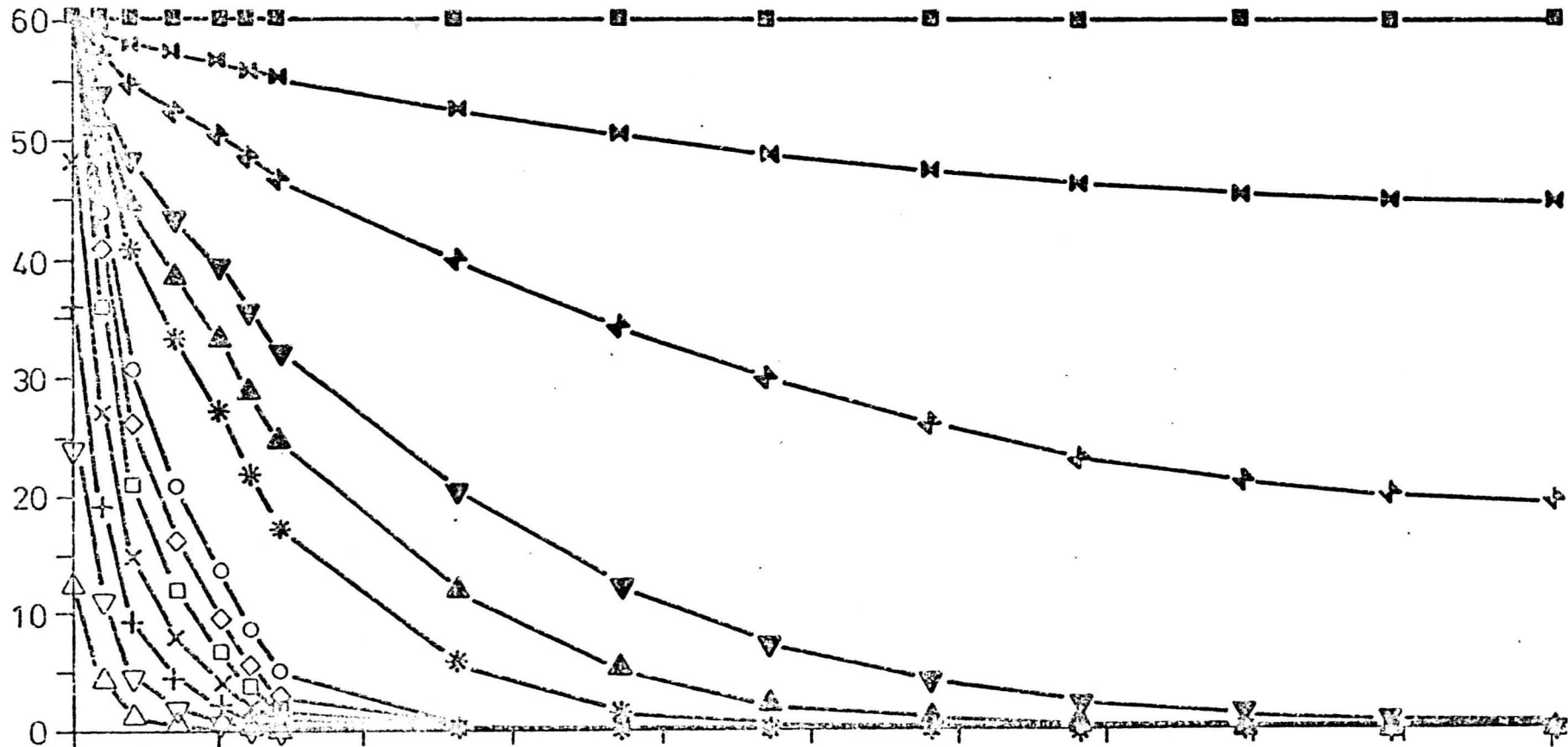


Figure 6.7(a) 'Hole-in-plate'. Temperature distribution along AB during a ramp increase in bore surface temperature of 60°C in 2 secs.

$\triangle t = 0.4S$	$\square t = 2.0S$	$\blacktriangle t = 15.0S$	$\blacksquare t = 1000.0S$
$\nabla t = 0.8S$	$\diamond t = 2.4S$	$\blacktriangledown t = 30.0S$	
$+ t = 1.2S$	$\circ t = 3.0S$	$\blacktriangleright t = 130.0S$	
$\times t = 1.6S$	$* t = 8.0S$	$\blacktriangleright t = 300.0S$	



C Figure 6.7(b). 'Hole-in-plate'. Temperature distributions along CD during a ramp increase in bore surface temperature of 60°C in 2 secs. D

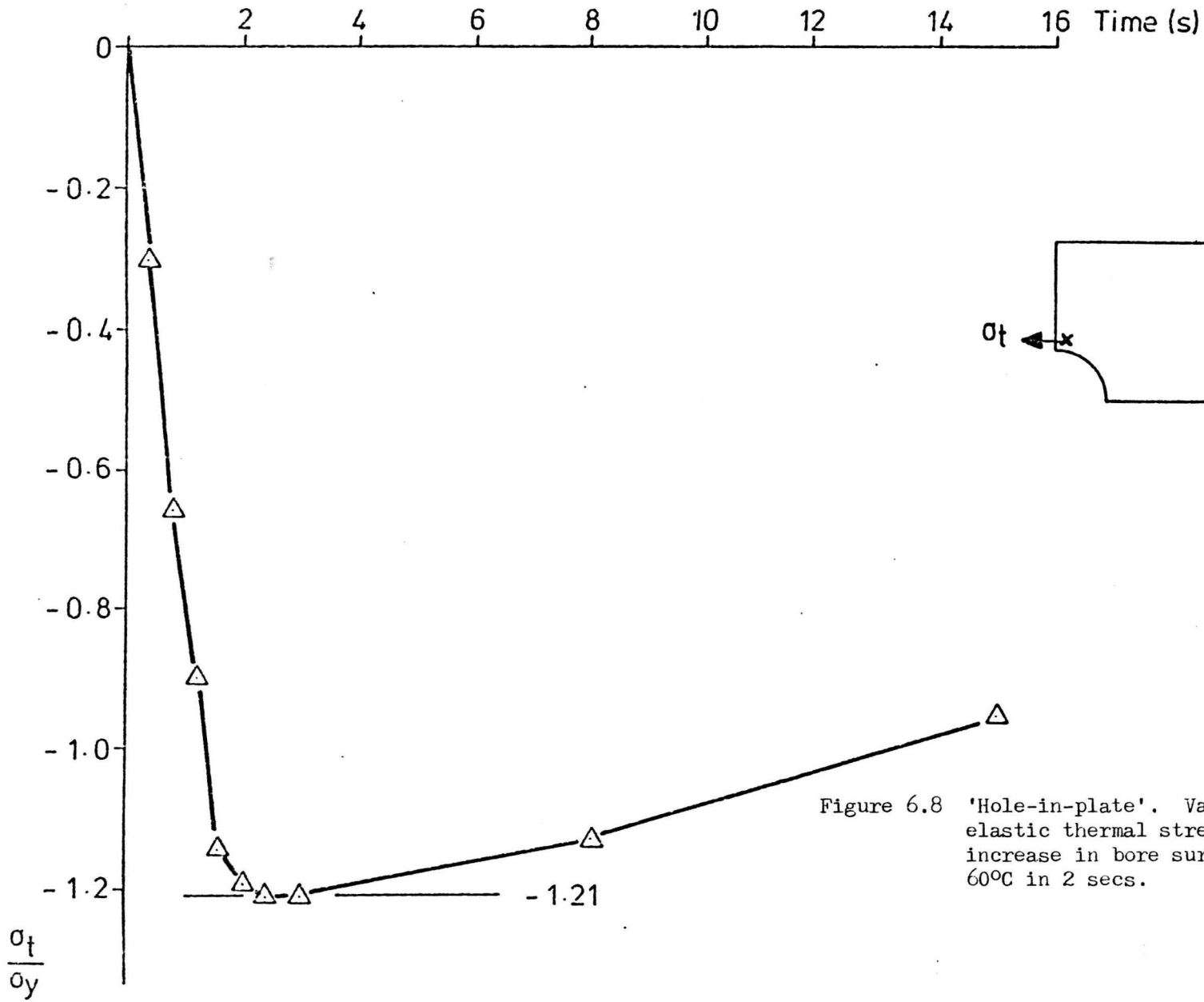


Figure 6.8 'Hole-in-plate'. Variation in maximum elastic thermal stress during a ramp increase in bore surface temperature of 60°C in 2 secs.

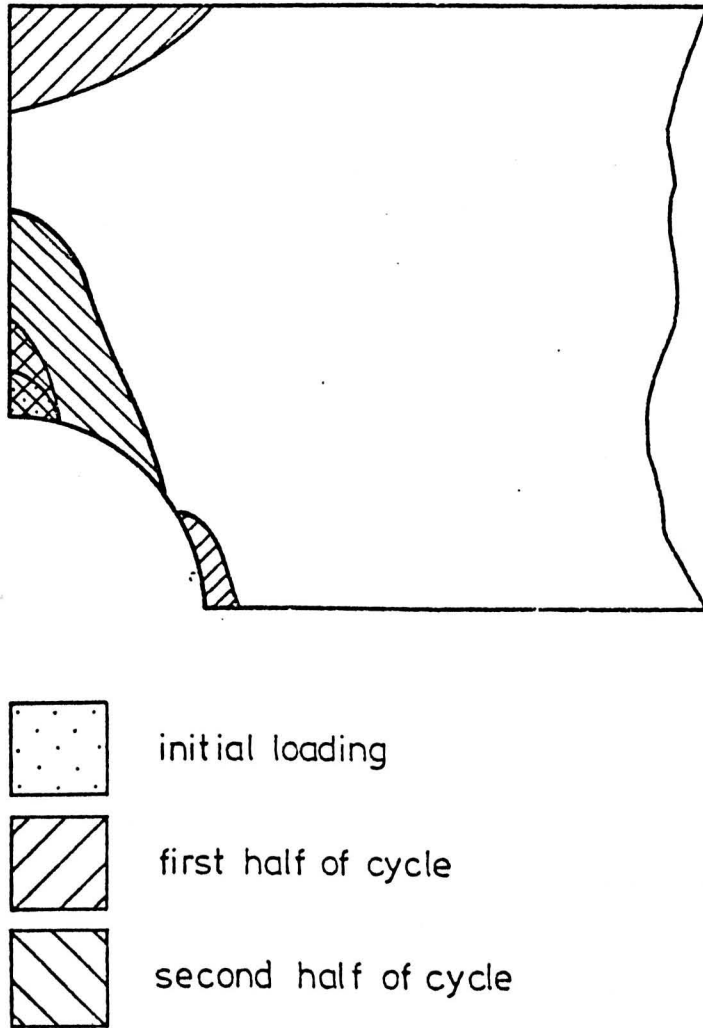


Figure 6.9 'Hole-in-plate' (elastic-perfectly-plastic, $\sigma_t/\sigma_y = 1.37$, $P/P_L = 0.7$, 'no creep' conditions). Regions of plastic straining due to initial loading and during the first thermal shock.

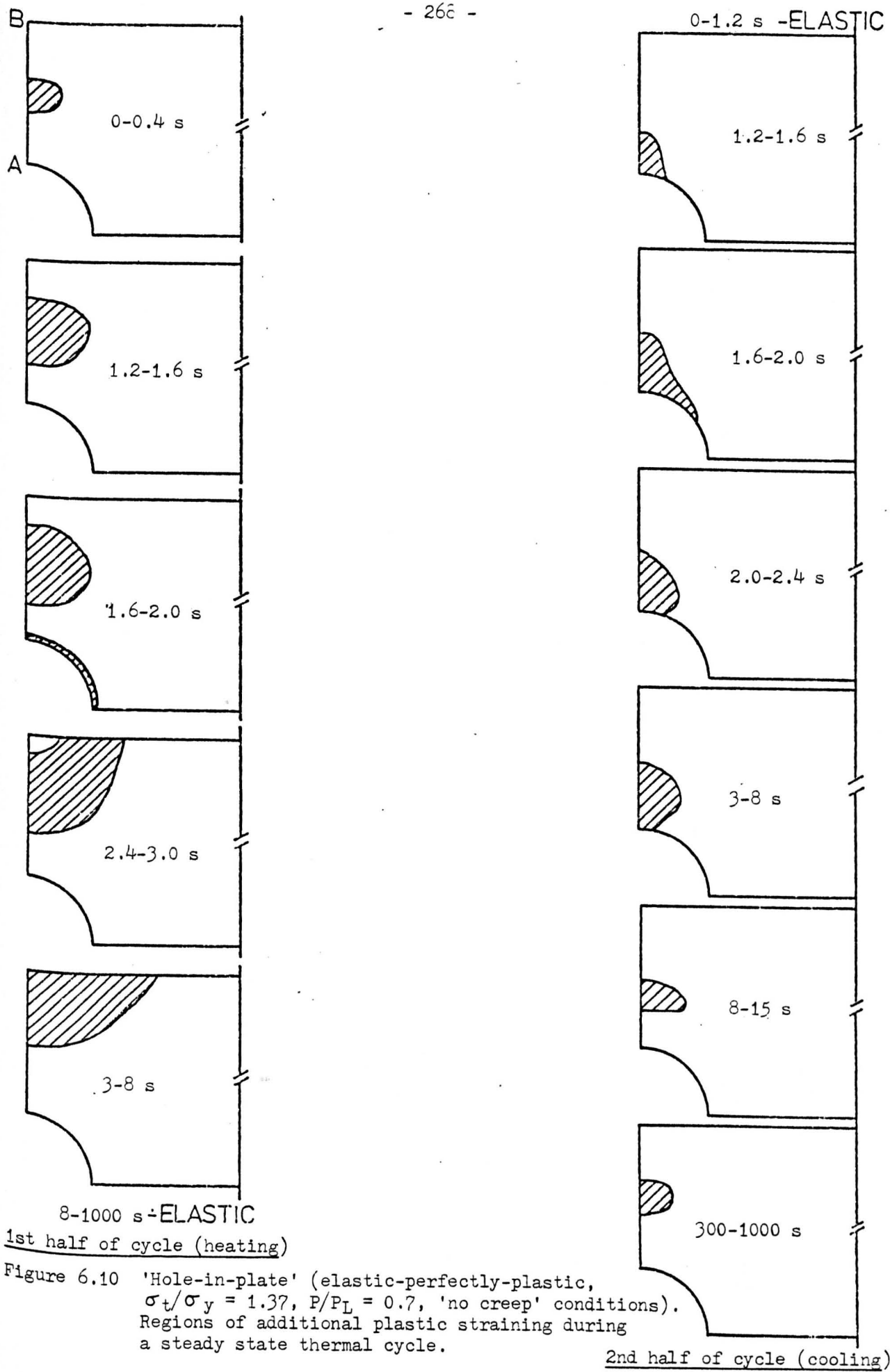


Figure 6.10 'Hole-in-plate' (elastic-perfectly-plastic, $\sigma_t/\sigma_y = 1.37$, $P/P_L = 0.7$, 'no creep' conditions). Regions of additional plastic straining during a steady state thermal cycle.

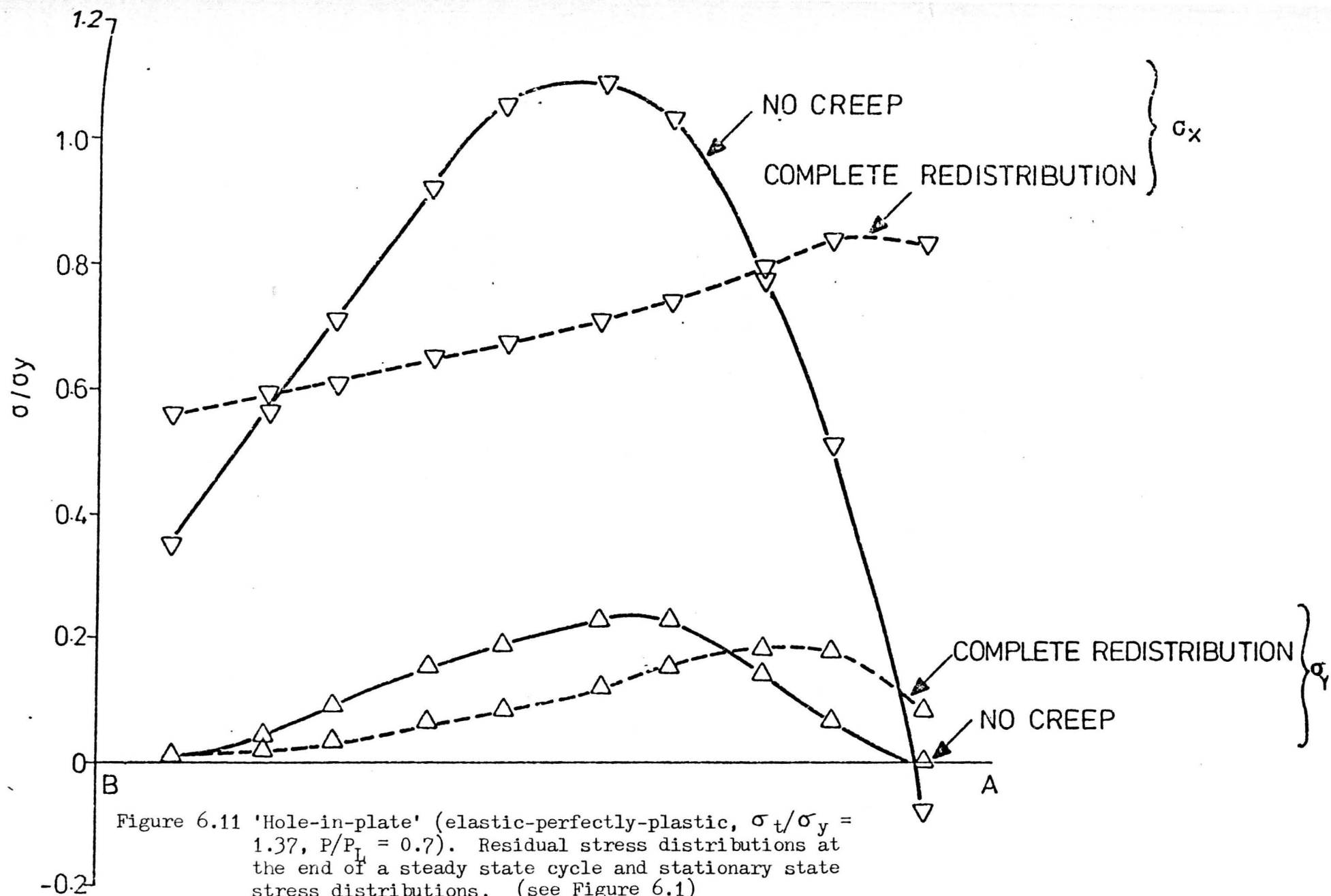


Figure 6.11 'Hole-in-plate' (elastic-perfectly-plastic, $\sigma_t/\sigma_y = 1.37$, $P/P_L = 0.7$). Residual stress distributions at the end of a steady state cycle and stationary state stress distributions. (see Figure 6.1)

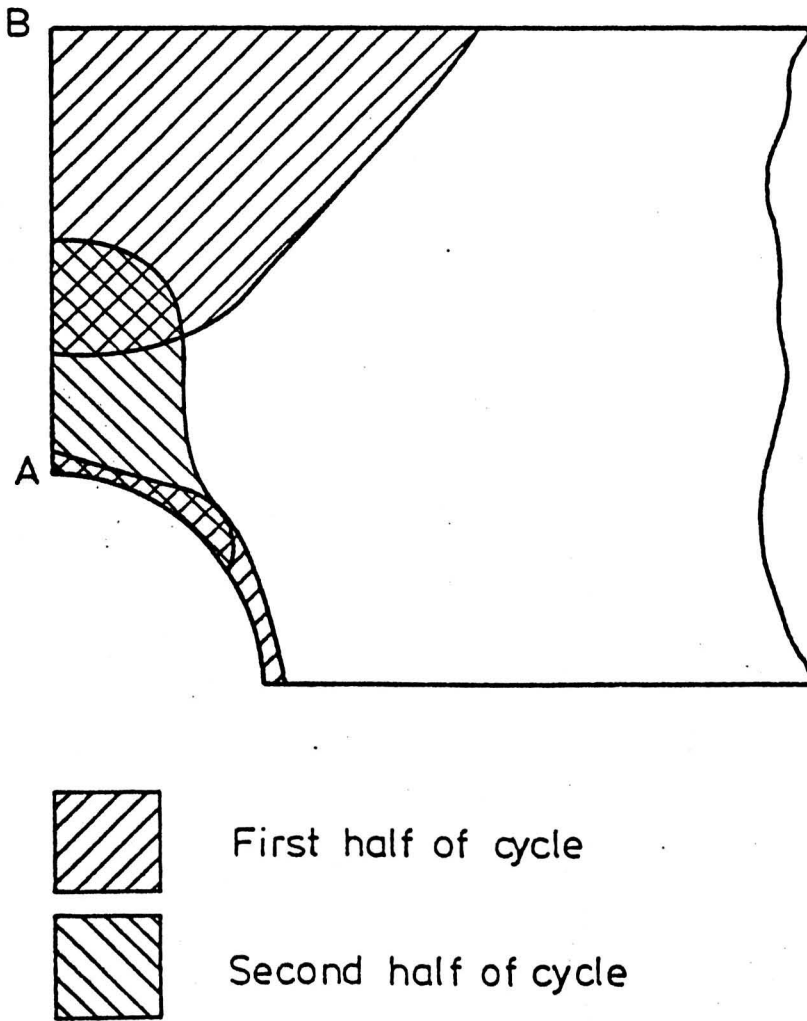


Figure 6.12 'Hole-in-plate' (elastic-perfectly-plastic, $\sigma_t/\sigma_y = 1.37$, $P/P_L = 0.7$, 'no creep' conditions). Regions of plastic straining during a steady state thermal cycle.

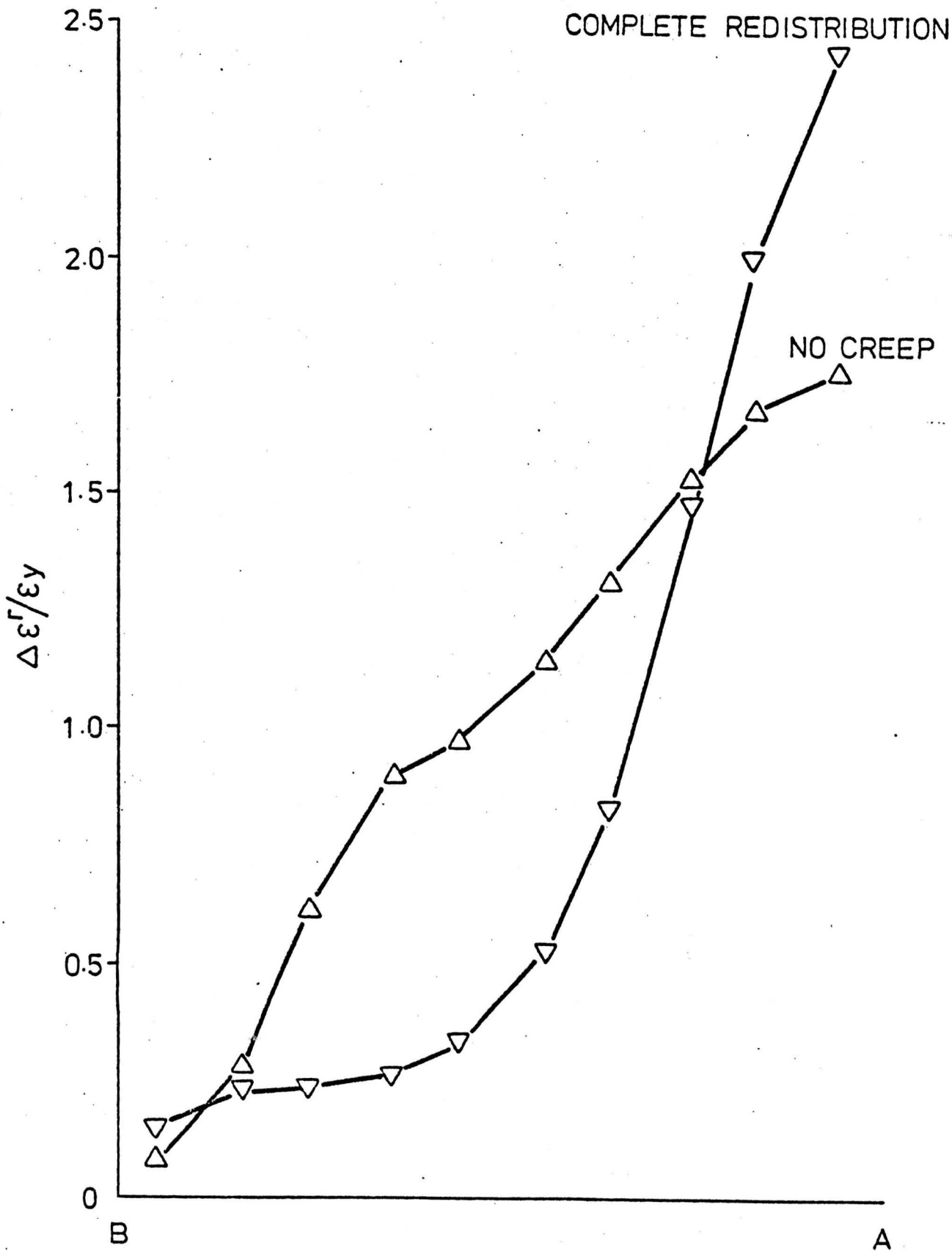


Figure 6.13(a) 'Hole-in-plate' (elastic-perfectly-plastic, $\sigma_t / \sigma_y = 1.37$, $P/P_L = 0.7$). Distribution of normalised steady state ratchet strains 'across AB' in the direction normal to AB (see Figure 6.1).

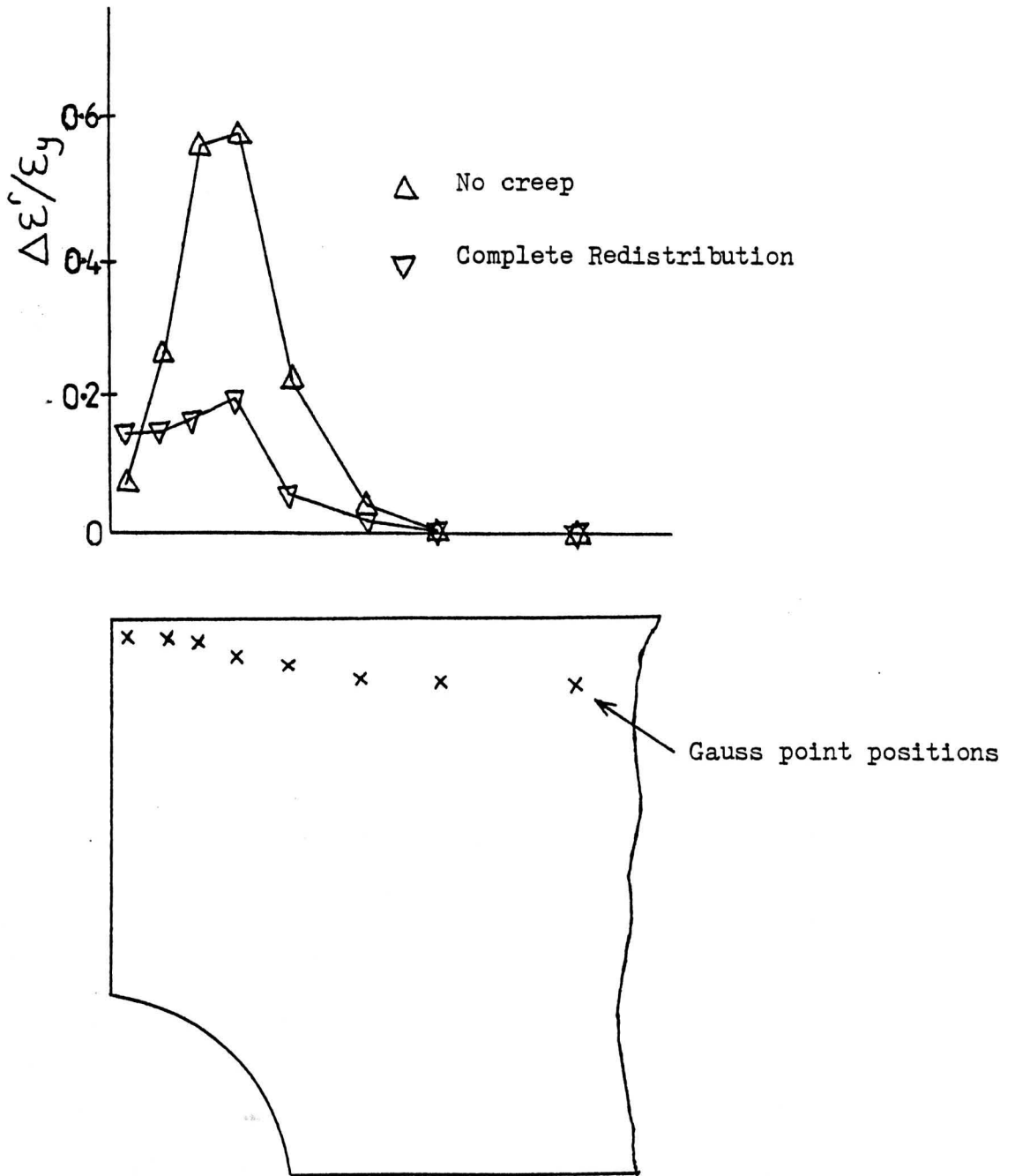


Figure 6.13(b) 'Hole-in-plate' (elastic-perfectly-plastic, $\sigma_t / \sigma_y = 1.37$, $P/P_L = 0.7$). Distribution of normalised steady state ratchet strains along the outside 'surface'.

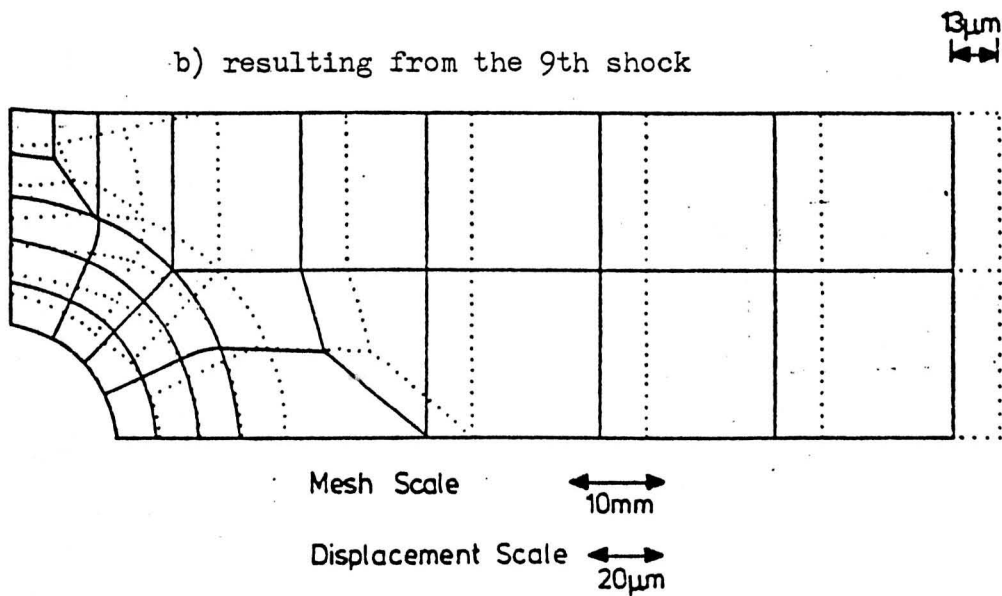
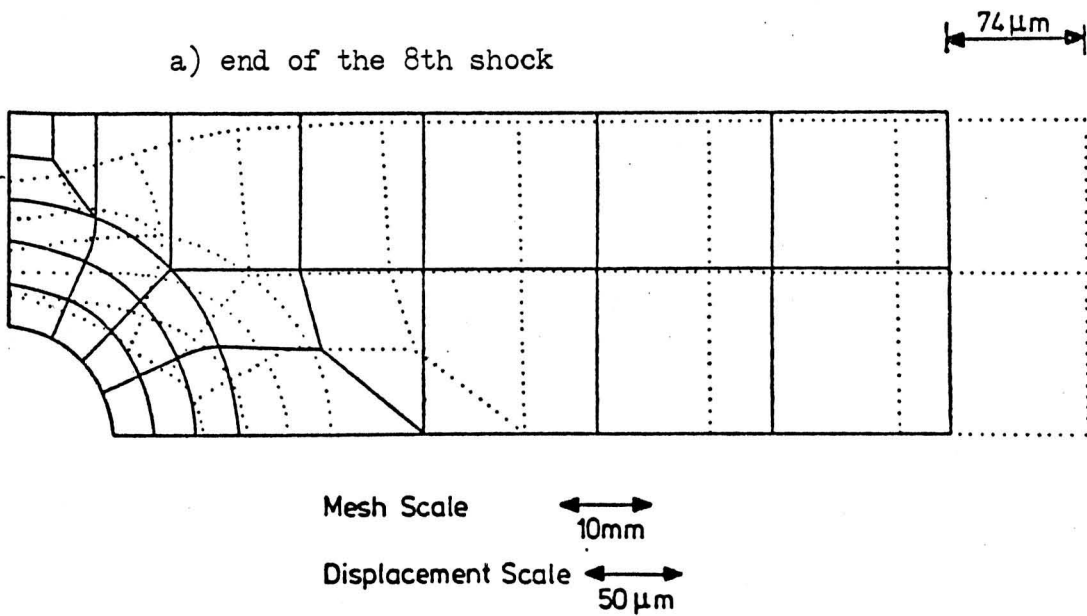


Figure 6.14 'Hole-in-plate' (elastic-perfectly-plastic, $\sigma_t/\sigma_y = 1.37$, $P/P_L = 0.7$, 'no creep' conditions). 'Exaggerated' nodal displacements.

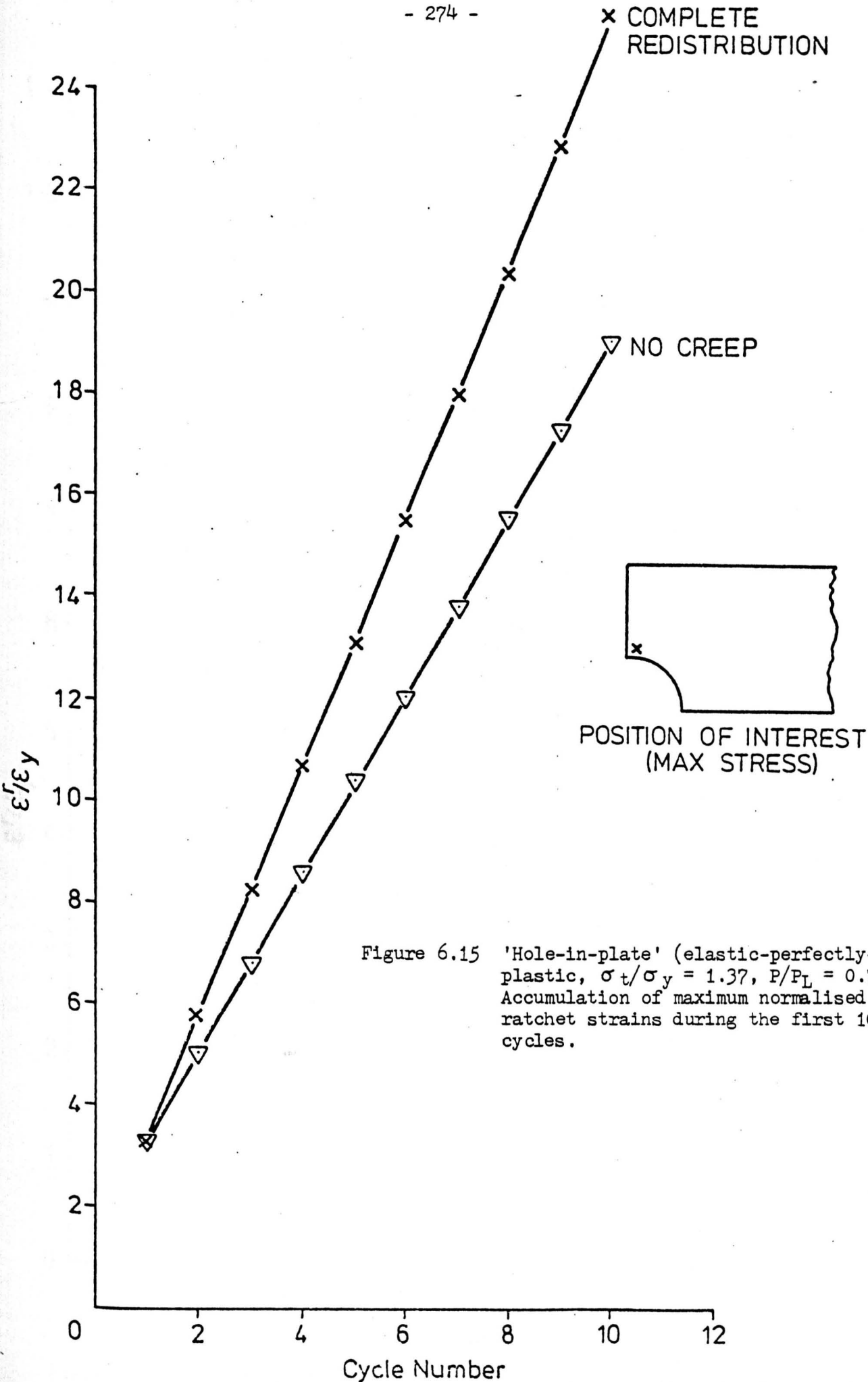


Figure 6.15 'Hole-in-plate' (elastic-perfectly-plastic, $\sigma_t/\sigma_y = 1.37$, $P/P_L = 0.7$). Accumulation of maximum normalised ratchet strains during the first 10 cycles.

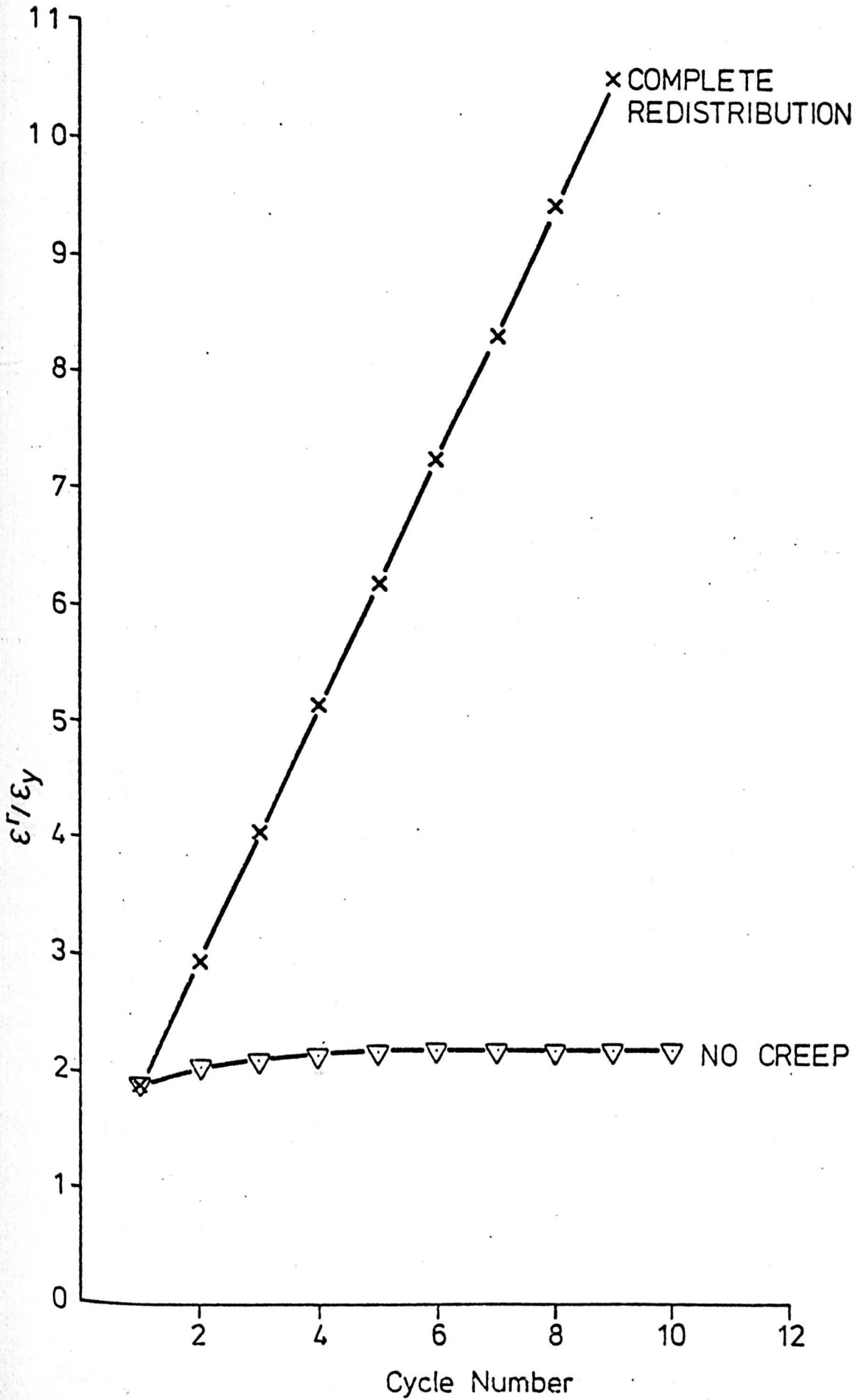


Figure 6.16 'Hole-in-plate' (elastic-perfectly-plastic, $\sigma_t/\sigma_y = 1.37$, $P/P_L = 0.5$). Accumulation of maximum normalised ratchet strains during the first 10 cycles.

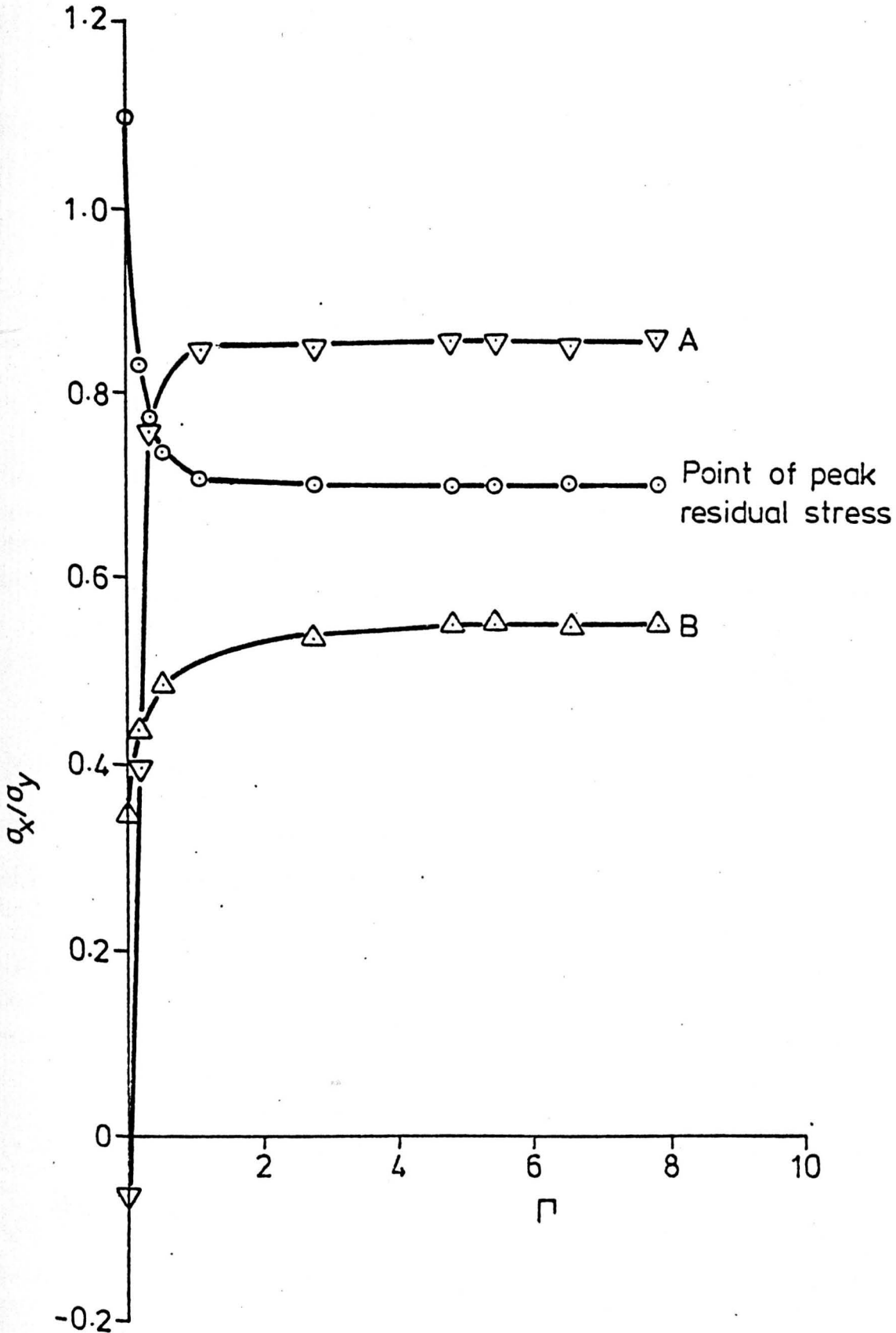


Figure 6.17 'Hole-in-plate' (elastic-perfectly-plastic, $\sigma_t/\sigma_y = 1.37$, $P/P_L = 0.7$, complete redistribution). Variation in stress normal to AB, at points across AB, during the first dwell period.

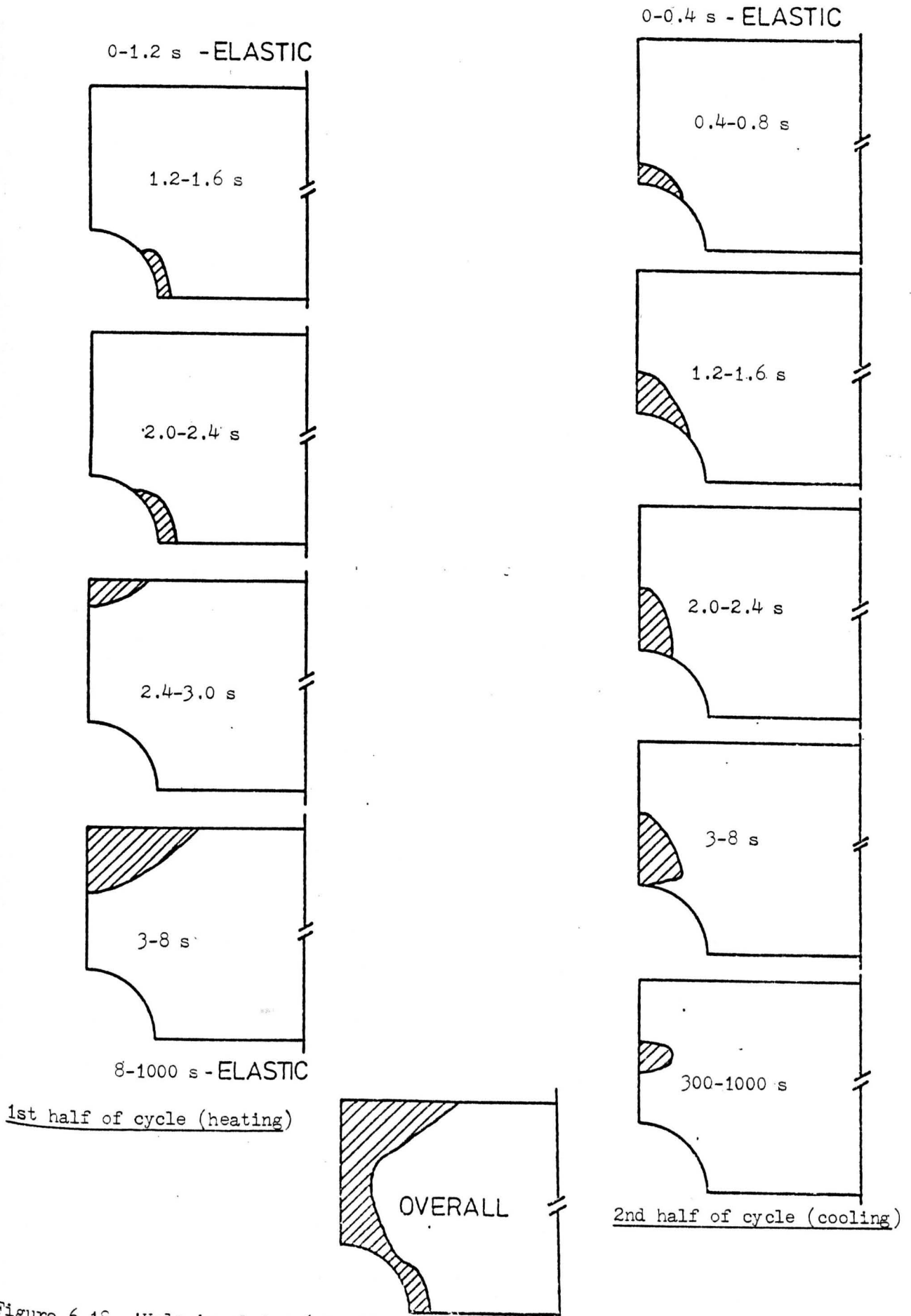
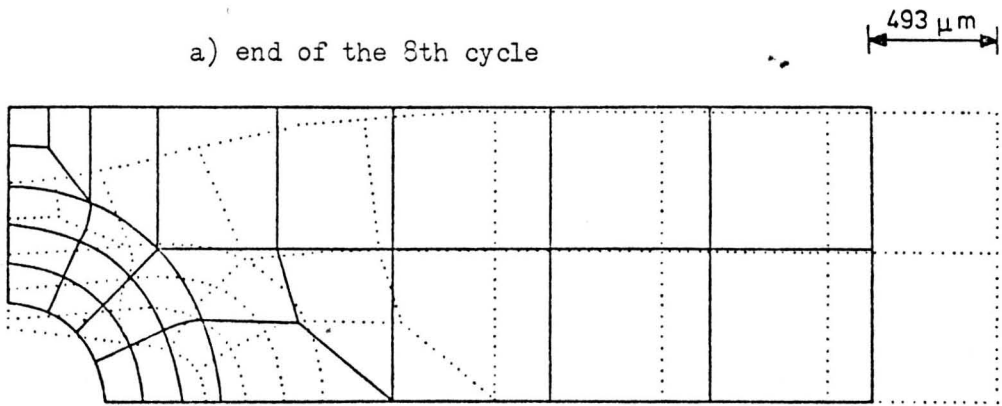
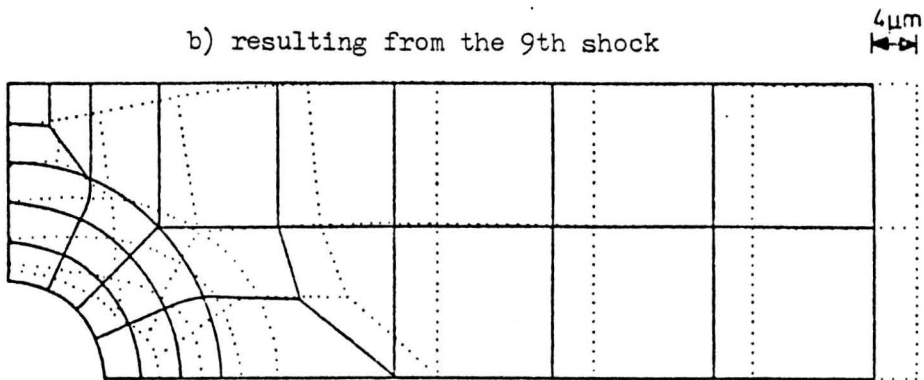


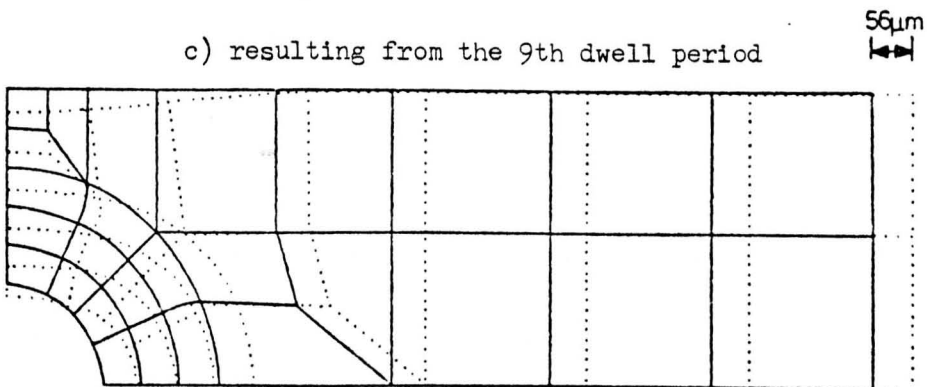
Figure 6.15 'Hole-in-plate' (elastic-perfectly-plastic $\sigma_t/\sigma_y = 1.37$, $P/P_L = 0.7$, complete redistribution). Regions of additional plastic straining during a steady state thermal cycle.



Mesh Scale \longleftrightarrow 10mm
Displacement Scale \longleftrightarrow 200 μm



Mesh Scale \longleftrightarrow 10mm
Displacement Scale \longleftrightarrow 10 μm



Mesh Scale \longleftrightarrow 10mm
Displacement Scale \longleftrightarrow 100 μm

Figure 6.19 'Hole-in-plate' (elastic-perfectly-plastic, $\sigma_t/\sigma_y = 1.37$, $P/P_L = 0.7$, complete redistribution). 'Exaggerated' nodal displacements.

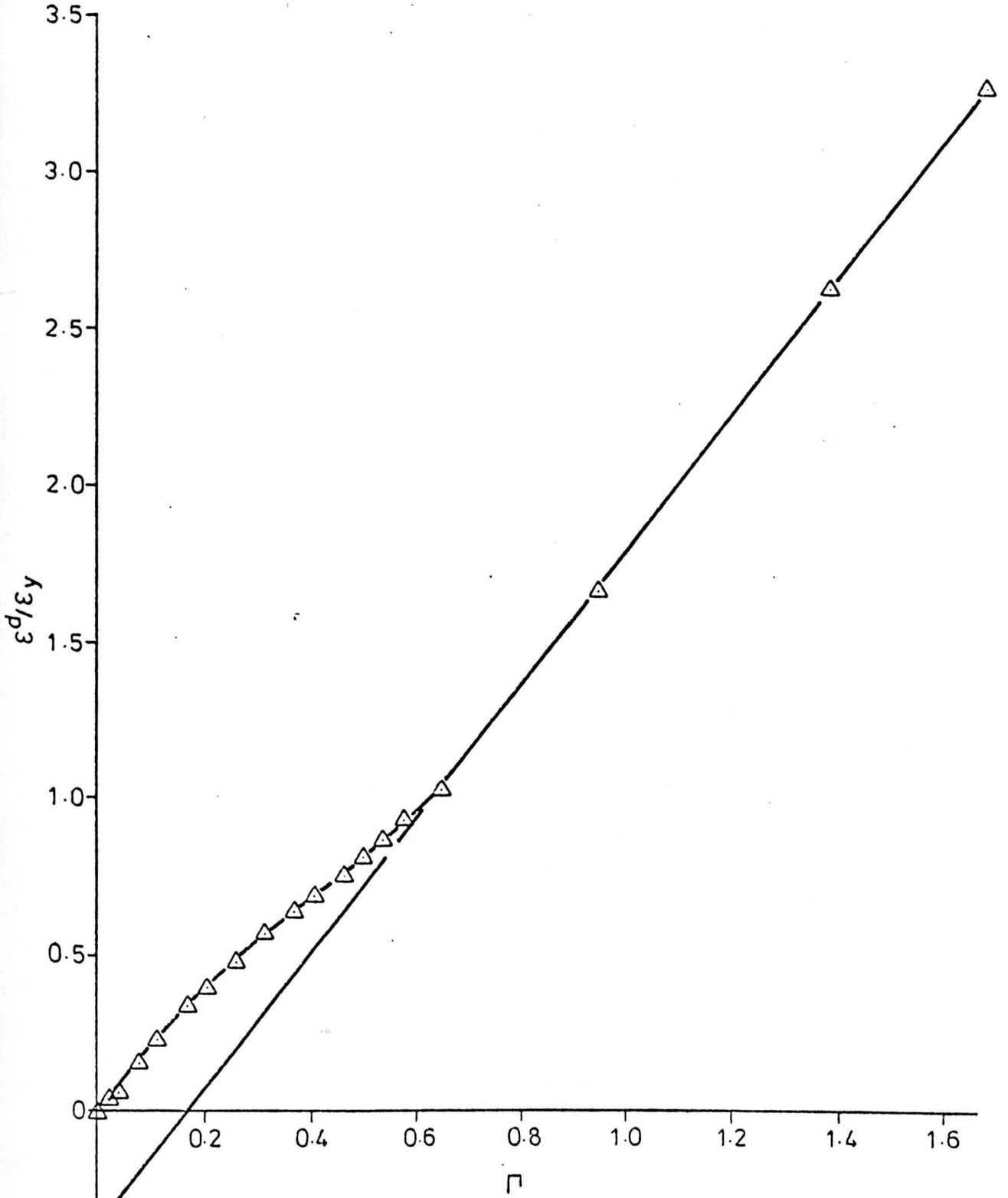


Figure 6.20 'Hole-in-plate' (elastic-perfectly-plastic, $\sigma_t/\sigma_y = 1.37$, $P/P_L = 0.7$, complete redistribution). Accumulation of normalised tangential strain at point A during the first dwell period.

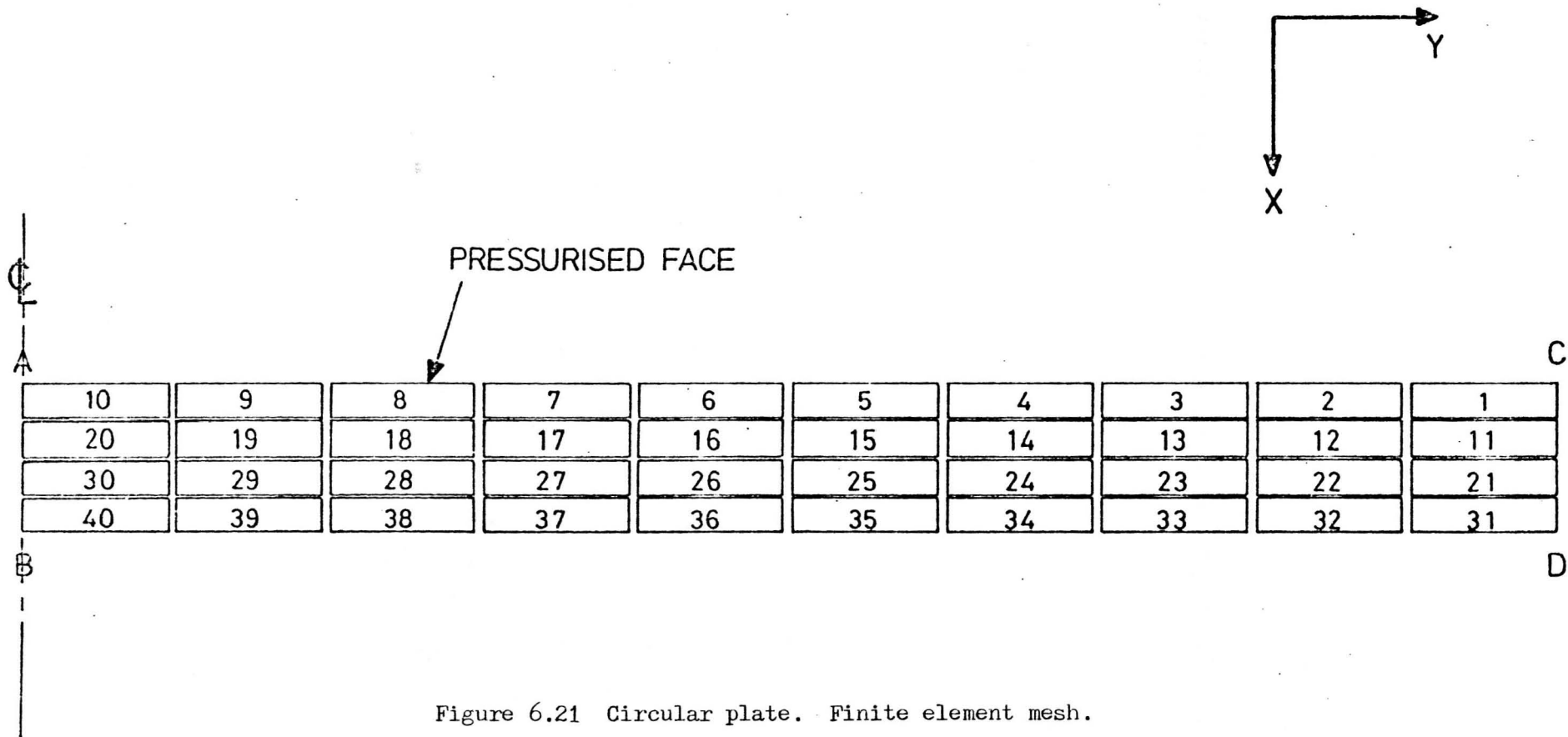


Figure 6.21 Circular plate. Finite element mesh.

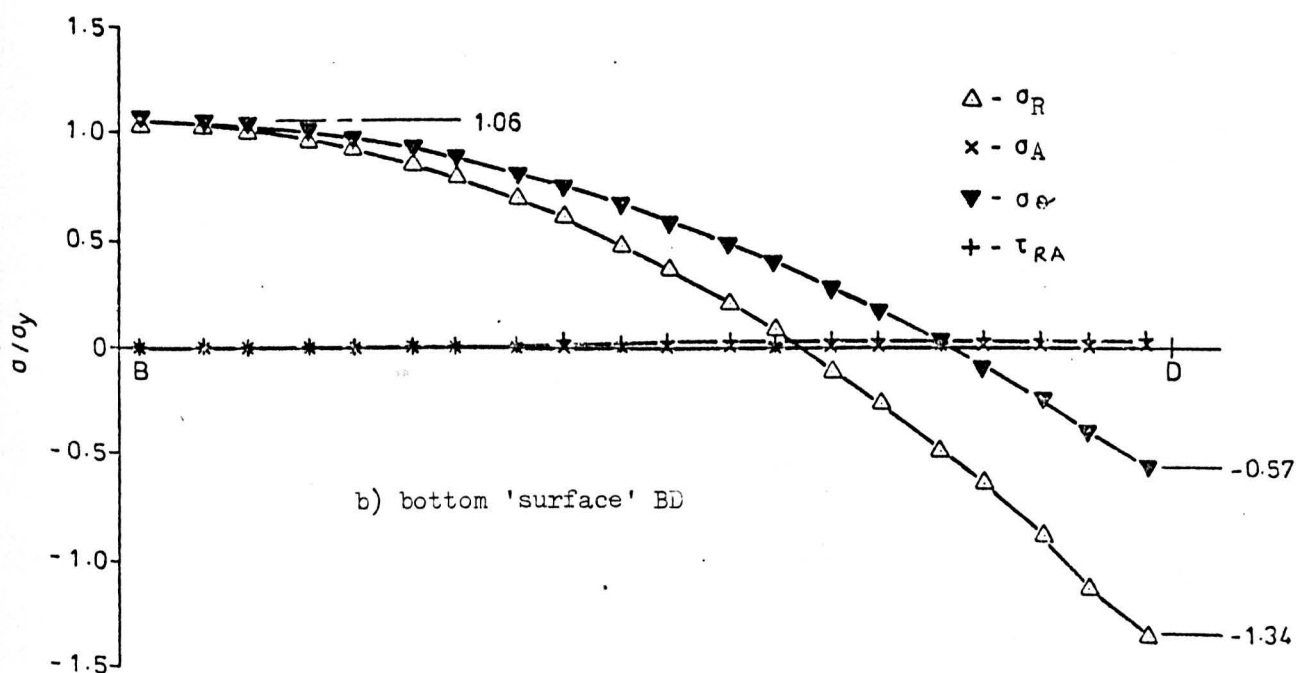
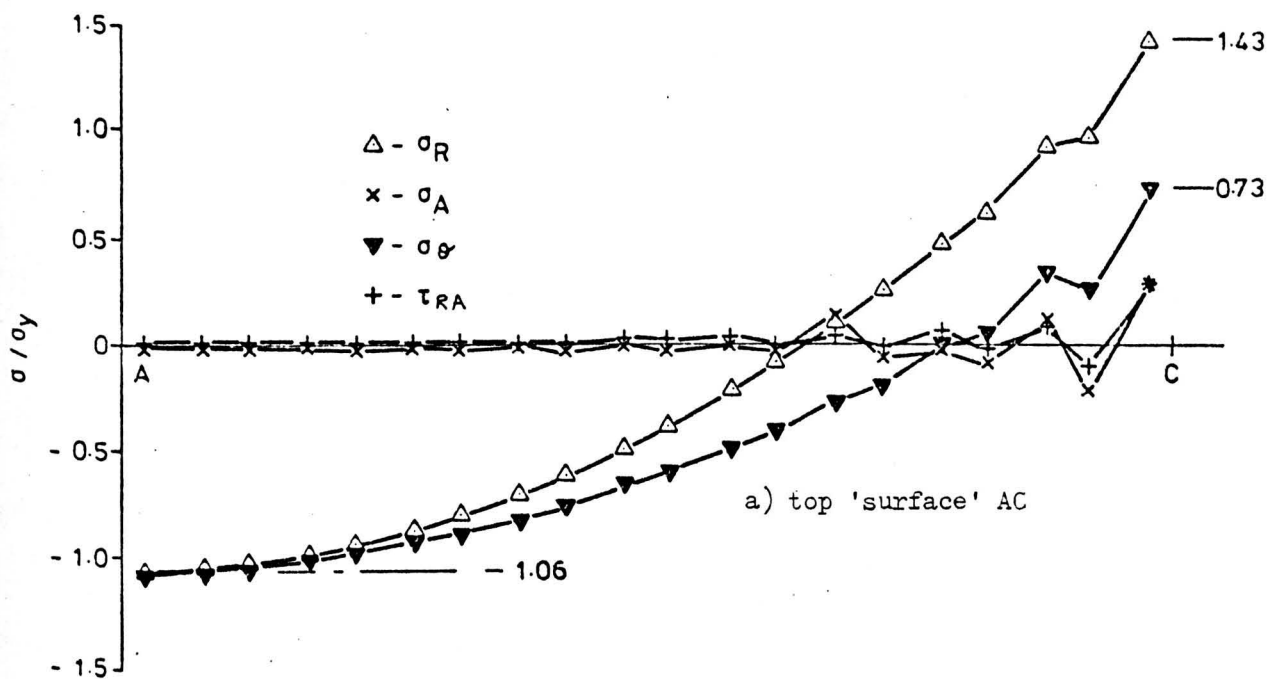


Figure 6.22 Circular plate. Elastic stress distributions due to a transverse pressure loading of 0.7 of the collapse pressure. (see Section 6.3.1)

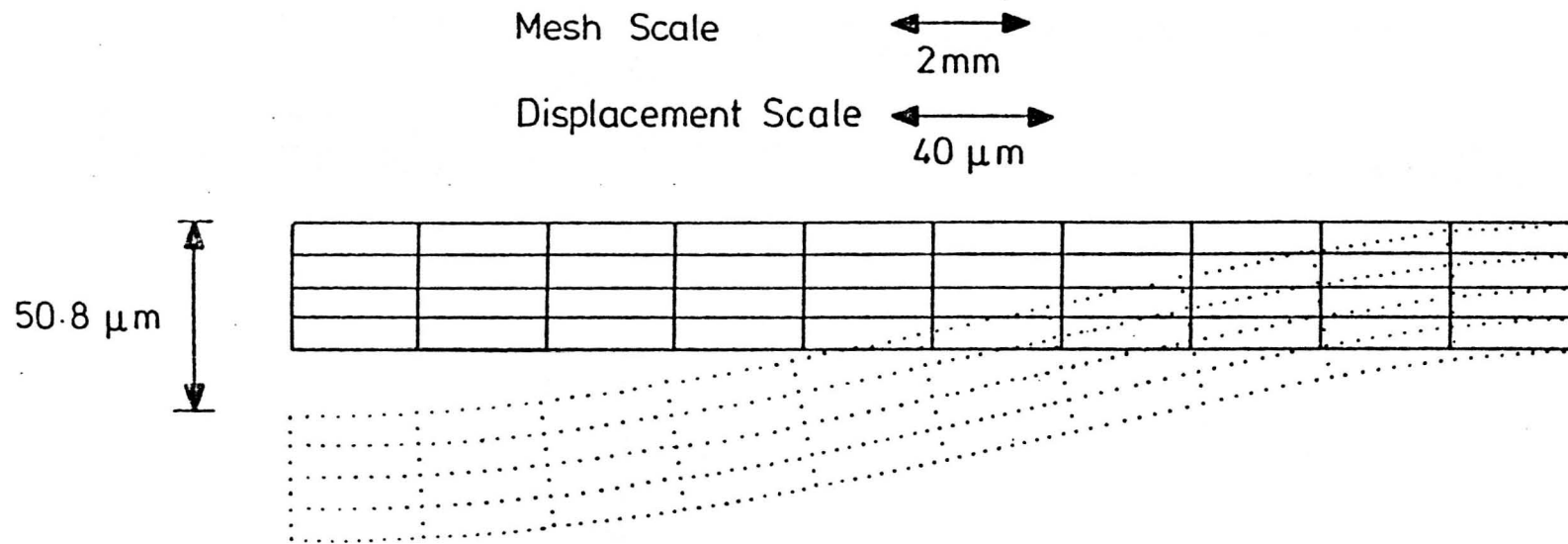
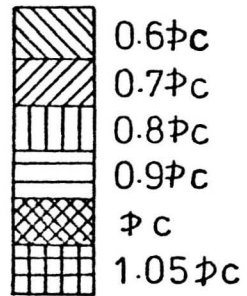
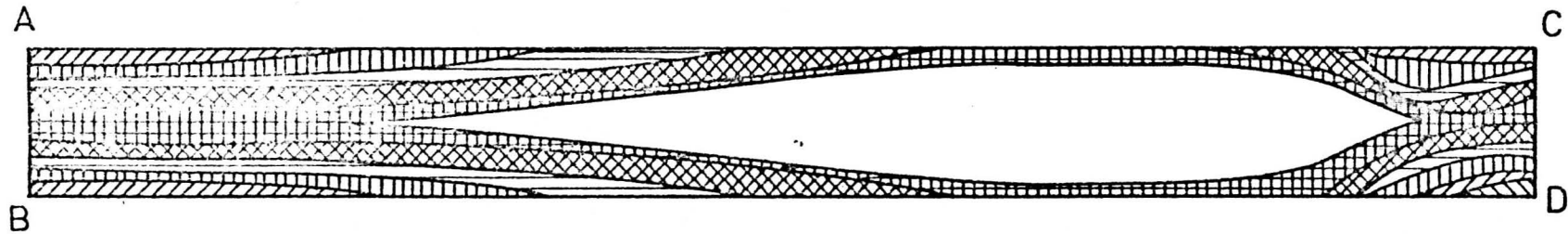


Figure 6.23 Circular plate. 'Exaggerated' deformed shape for a transverse pressure loading of 0.7 of the collapse pressure.



WHERE ϕ_c = COLLAPSE PRESSURE

Figure 6.24 Circular plate (elastic-perfectly-plastic). Growth of plastic zone with increasing transverse pressure up to collapse.

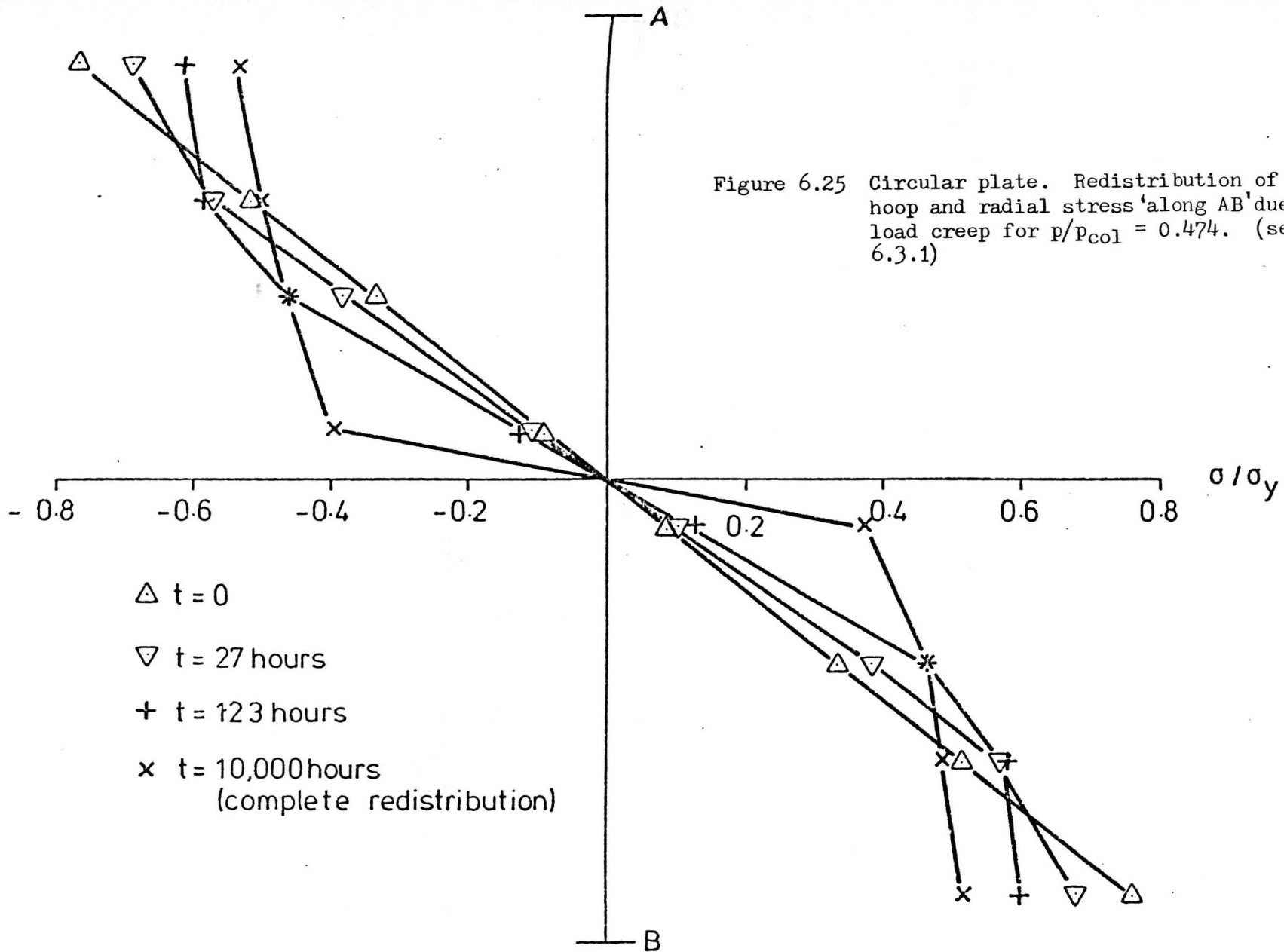


Figure 6.26 Circular plate. Redistribution of normalised hoop stress 'along CD' due to steady load creep for $p/p_{col} = 0.474$. (see Section 6.3.1)

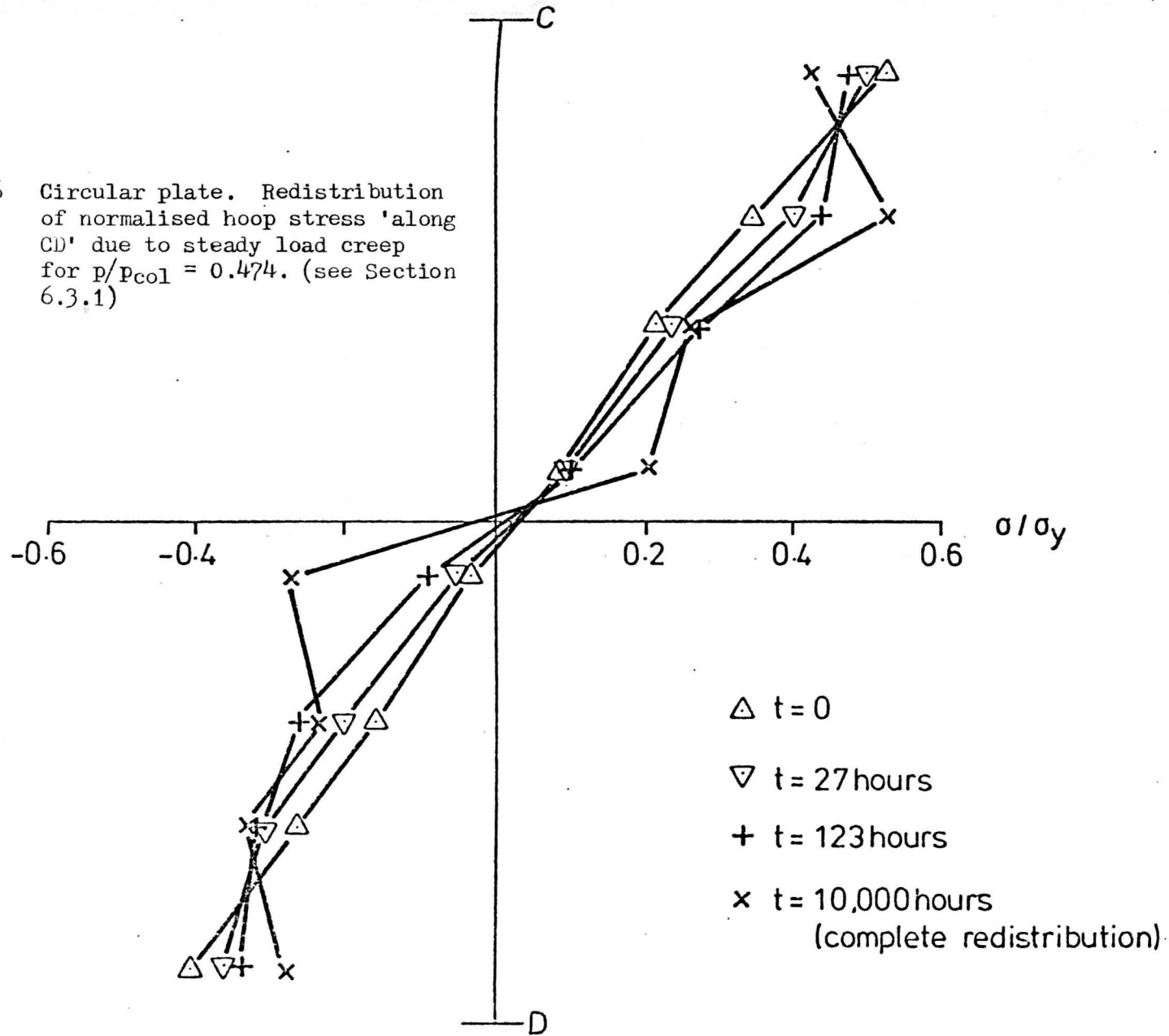
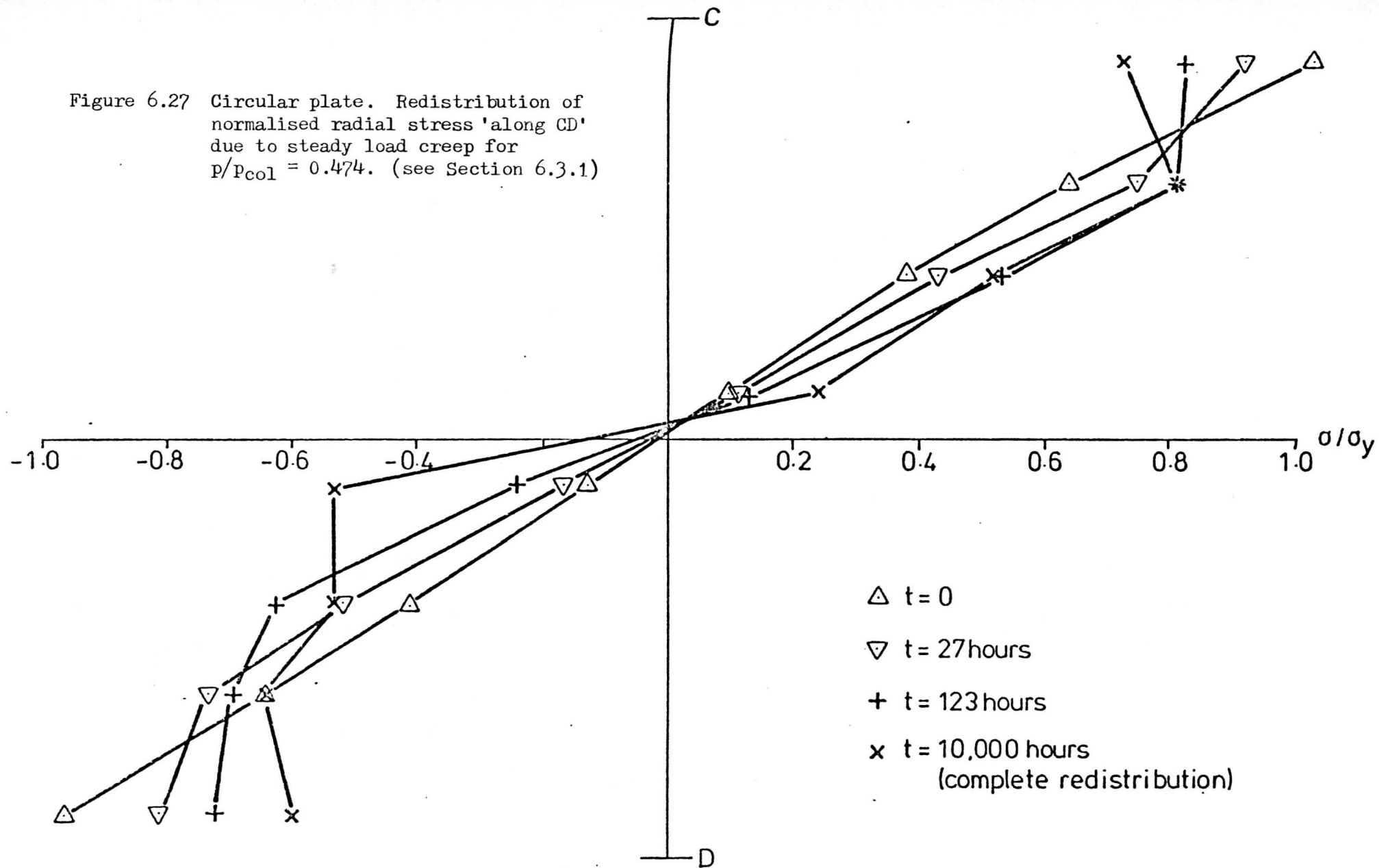


Figure 6.27 Circular plate. Redistribution of normalised radial stress 'along CD' due to steady load creep for $p/p_{col} = 0.474$. (see Section 6.3.1)



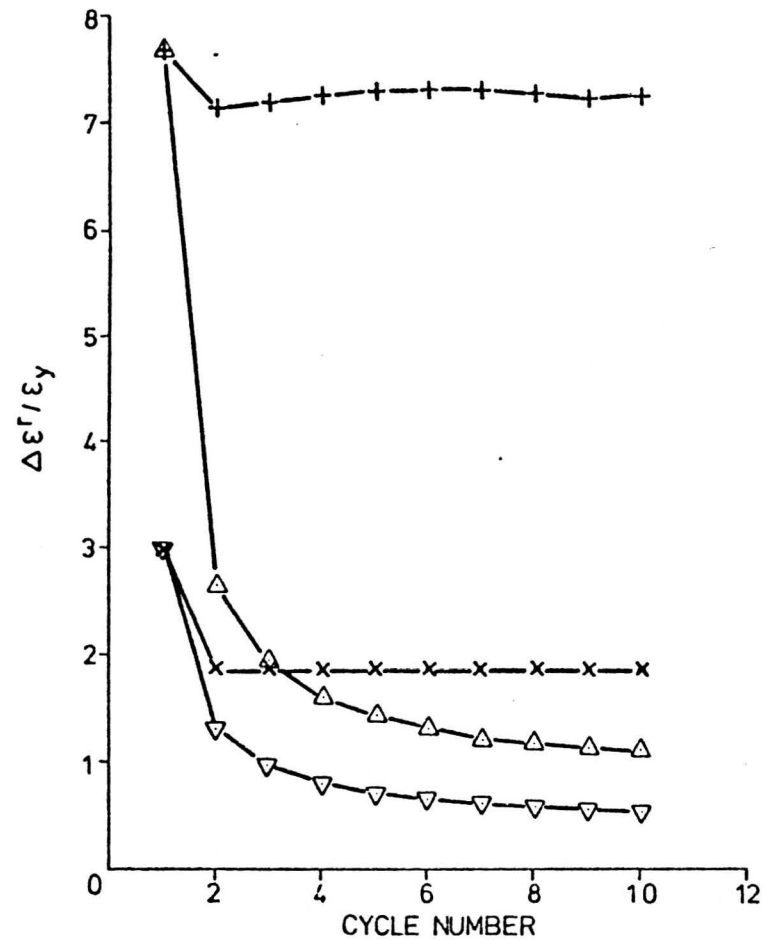
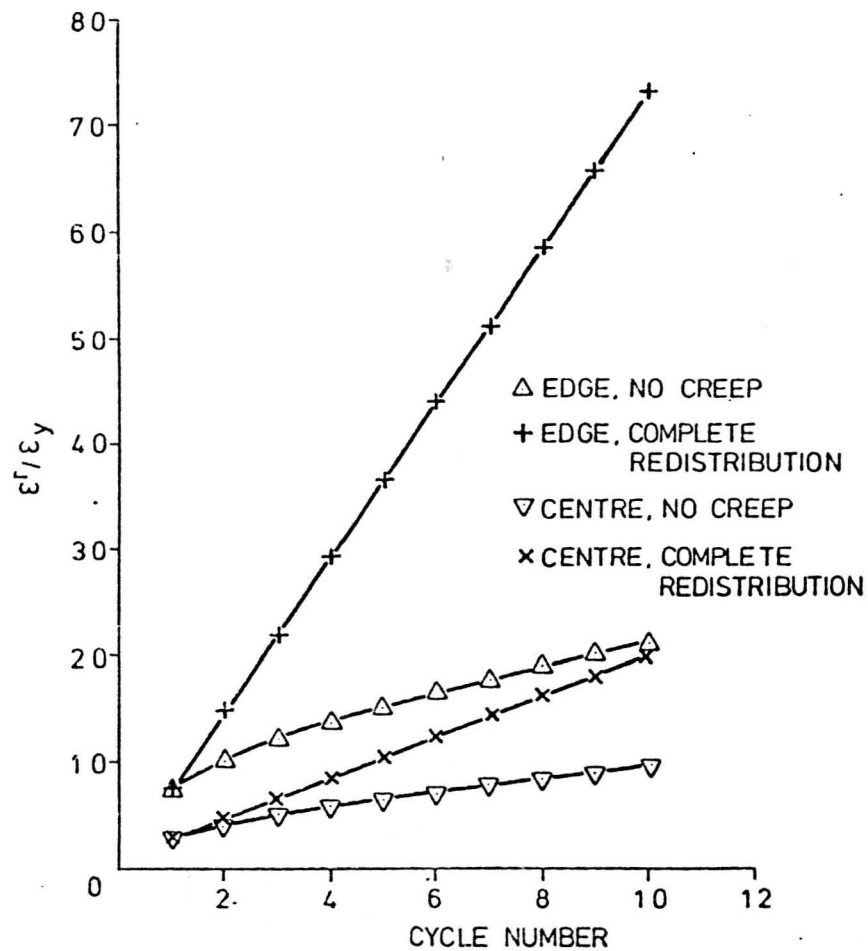
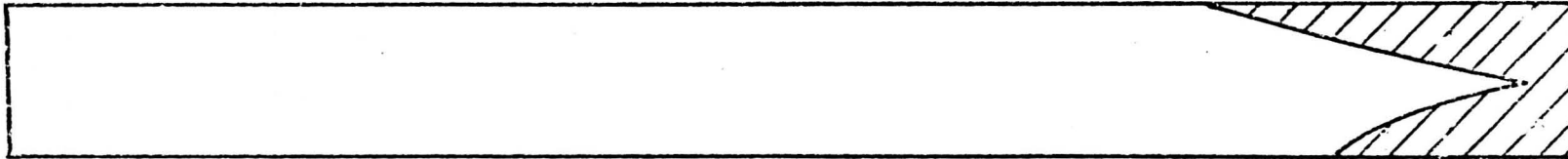


Figure 6.28 Circular plate (elastic-perfectly-plastic, $\sigma_t/\sigma_y = 1.41$, $p/p_{col} = 0.7$). Accumulated and individual maximum normalized ratchet strains at the edge and centre for the first 10 cycles.

a) First half of shock



b) Second half of shock

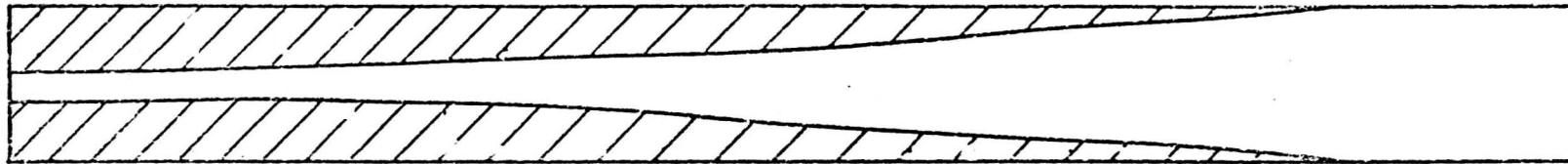
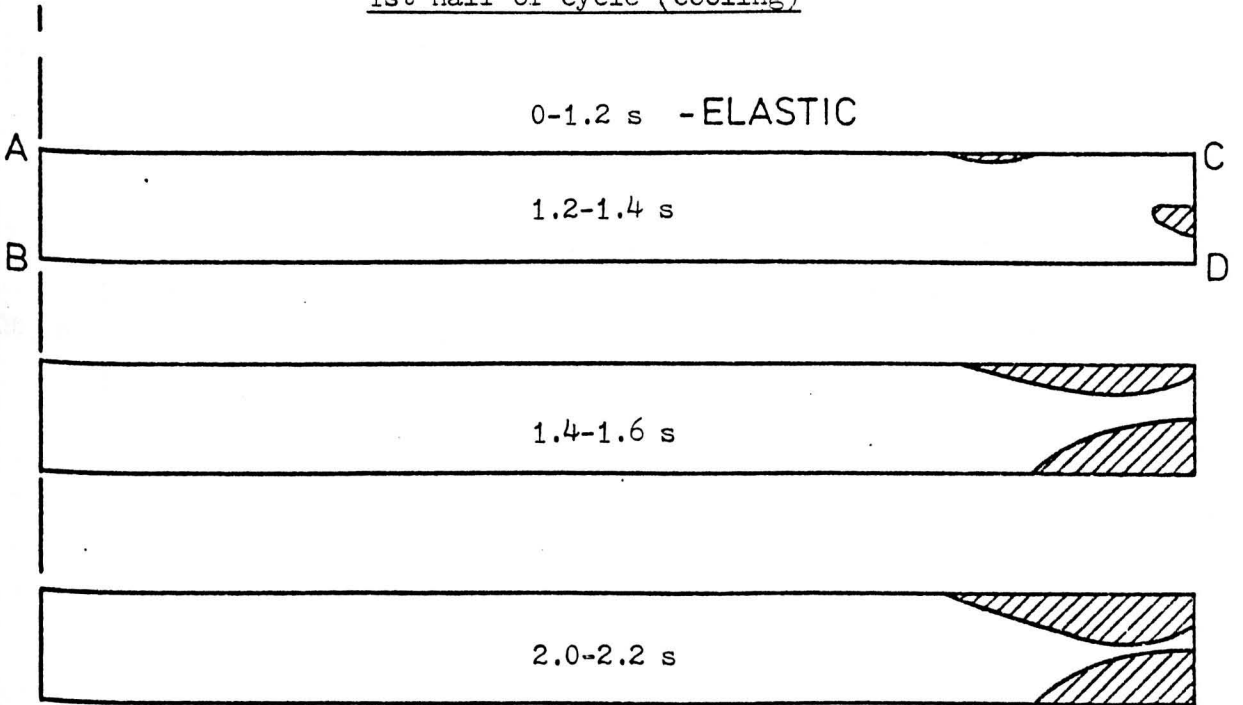


Figure 6.29 Circular Plate (elastic-perfectly-plastic, $\sigma_t/\sigma_y = 1.41$, $p/P_{col} = 0.7$, 'no creep' conditions). Regions of additional plastic straining for the two halves of the 2nd thermal shock.

1st half of cycle (cooling)



2nd half of cycle (heating)

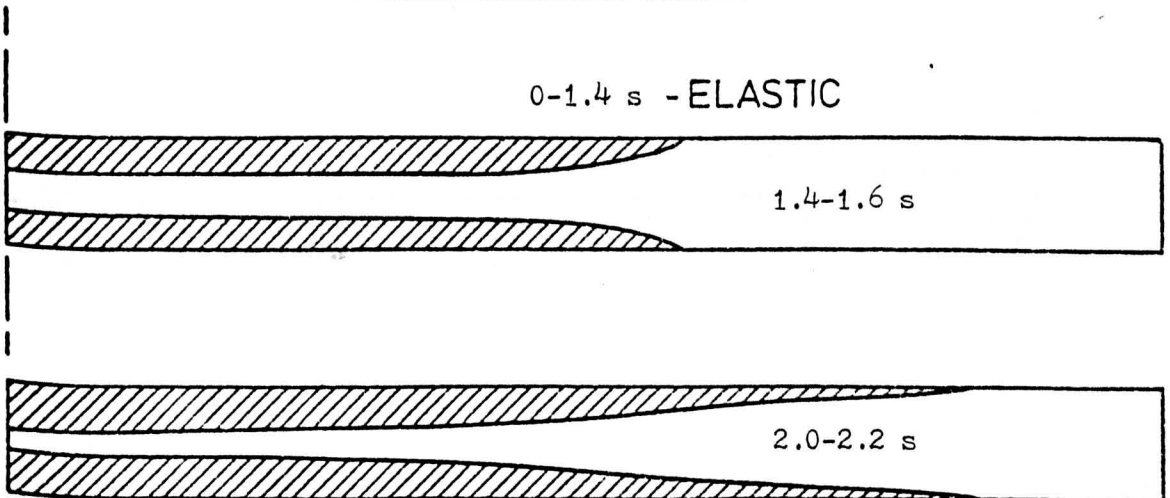
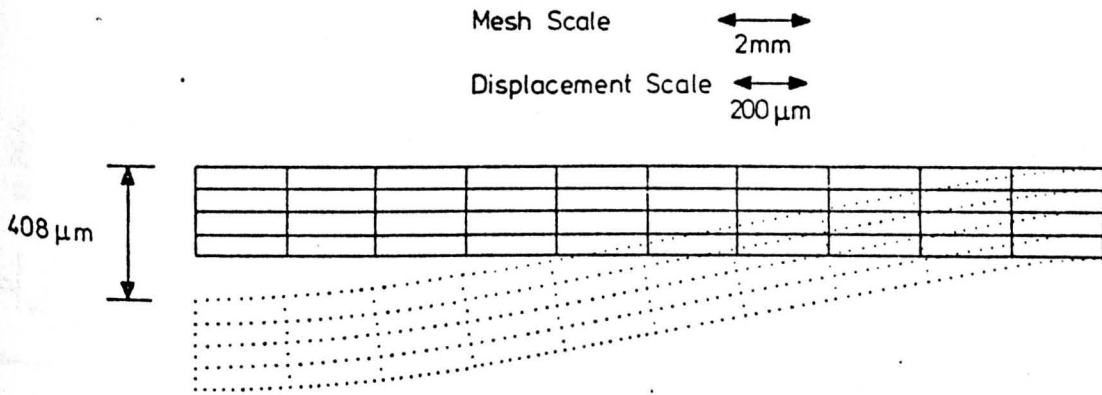


Figure 6.30 Circular plate (elastic-perfectly-plastic, $\sigma_t/\sigma_y = 1.41$, $p/p_{col} = 0.7$, 'no creep' conditions). Regions of additional plastic straining during the 10th thermal shock.

a) end of the 10th shock



b) resulting from the 11th shock

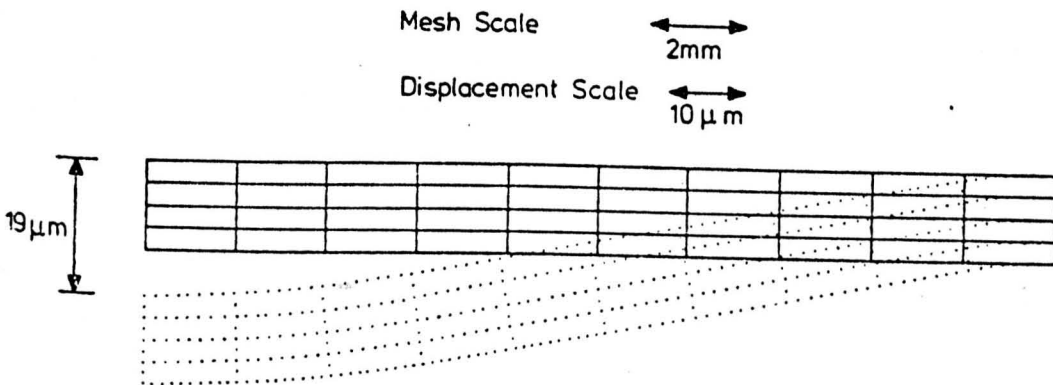
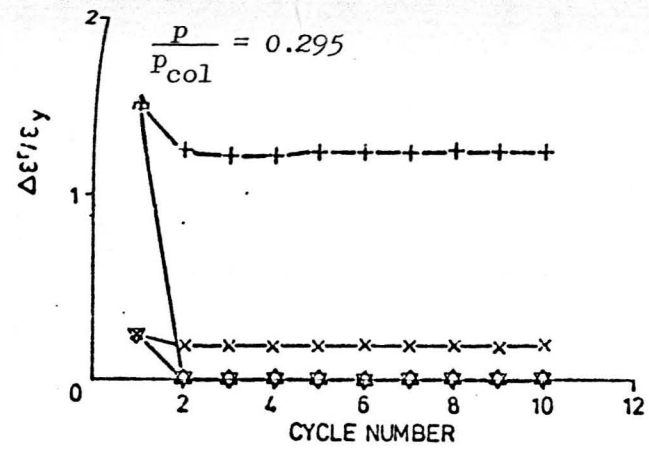
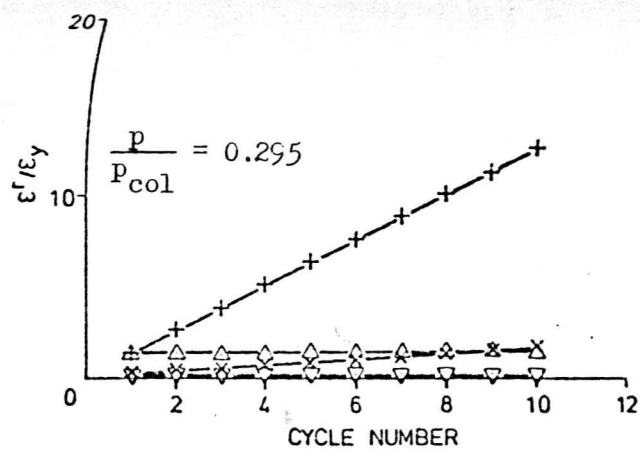


Figure 6.31 Circular plate (elastic-perfectly-plastic, $\sigma_t/\sigma_y = 1.41$, $p/p_{col} = 0.7$, 'no creep' conditions). 'Exaggerated' nodal displacements.



	'No Creep'	'Complete Redistribution'
Edge	△	+
Centre	▽	x

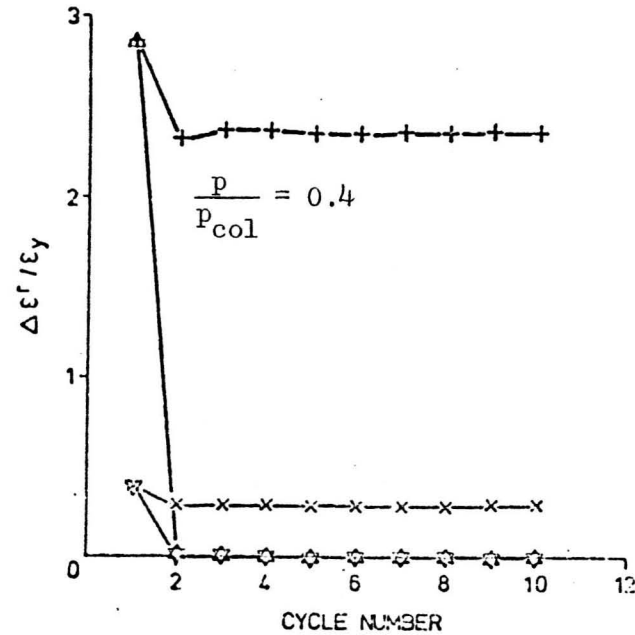
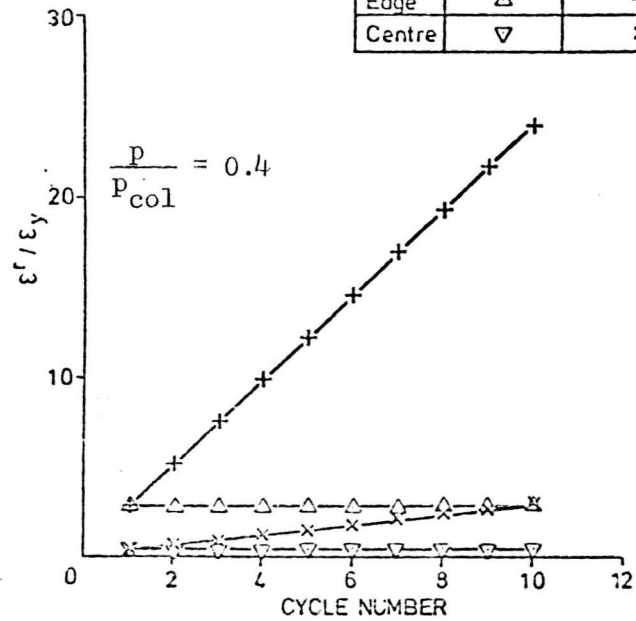


Figure 6.32 Circular plate (elastic-perfectly-plastic, $\sigma_t/\sigma_y = 1.41$, $p/p_{col} = 0.295$ and 0.4). Accumulated and individual maximum normalised ratchet strains at the edge and centre.

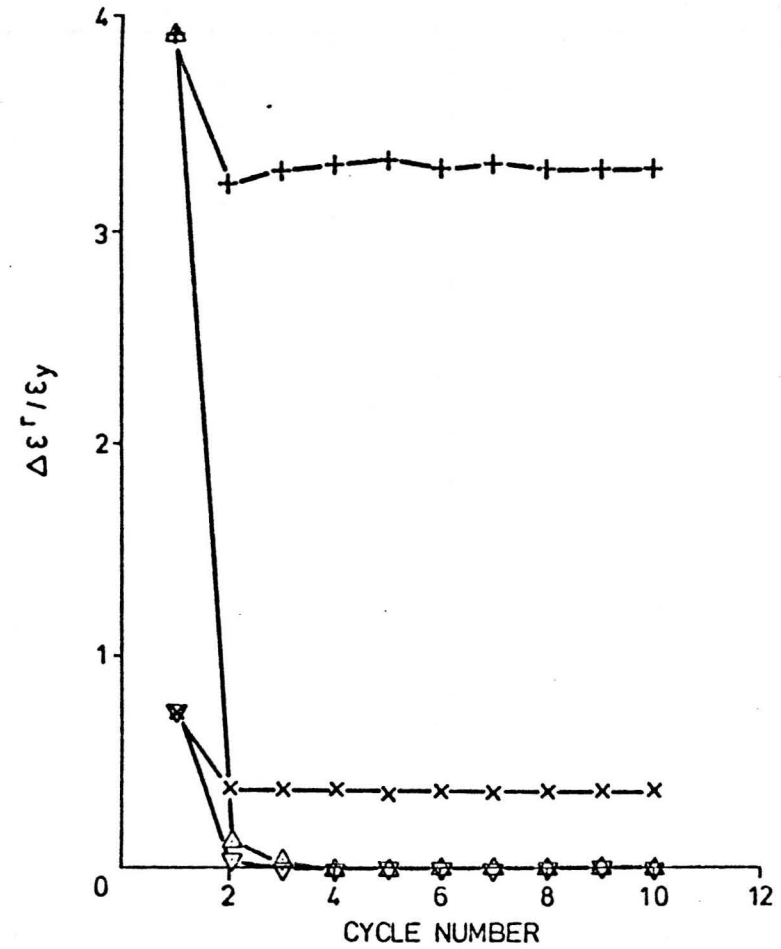
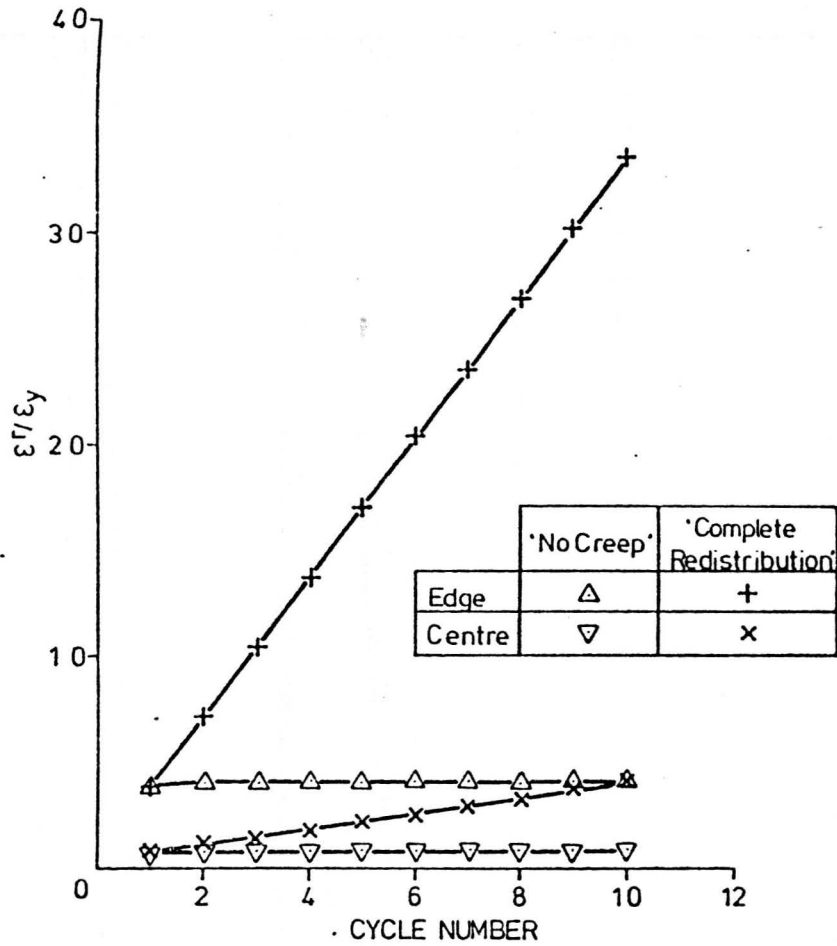


Figure 6.33 Circular plate (elastic-perfectly-plastic, $\sigma_t/\sigma_y = 1.41$, $p/p_{col} = 0.474$). Accumulated and individual maximum normalized ratchet strains at the edge and centre for the first 10 cycles.

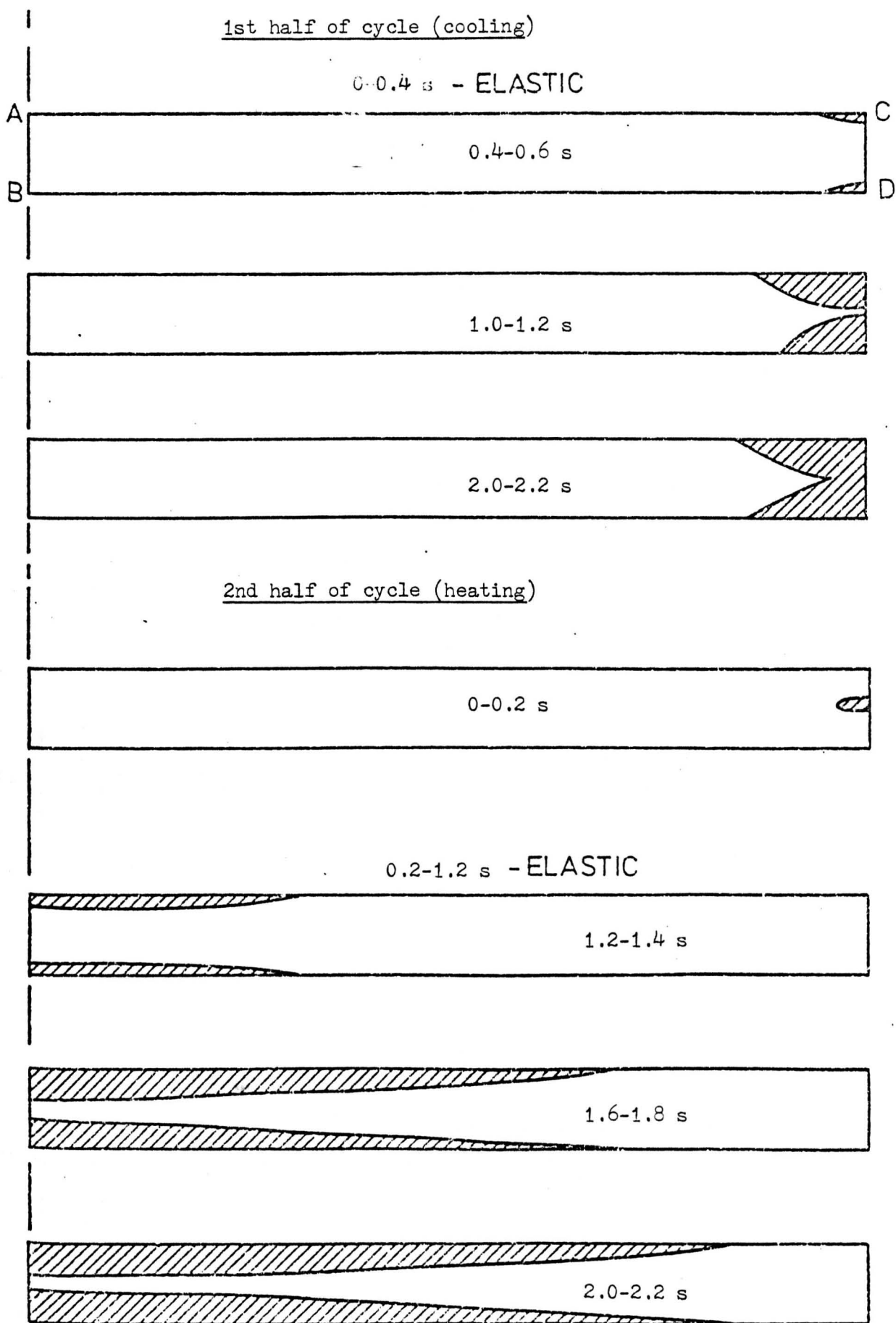
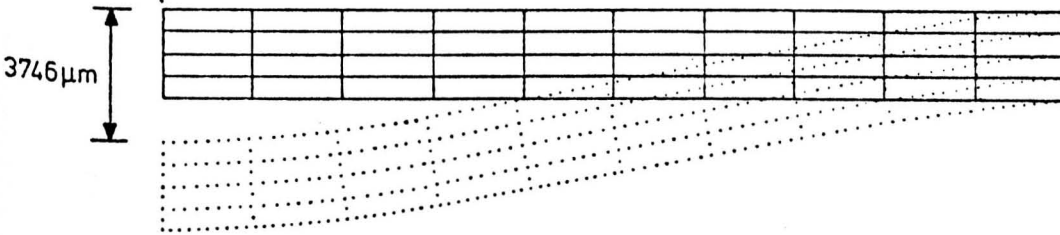


Figure 6.34 Circular plate (elastic-perfectly-plastic, $\sigma_t/\sigma_y = 1.41$, $P/P_{col} = 0.7$, complete redistribution). Regions of additional plastic straining during a steady state cycle.

a) end of the 10th cycle

Mesh Scale \longleftrightarrow
2mm

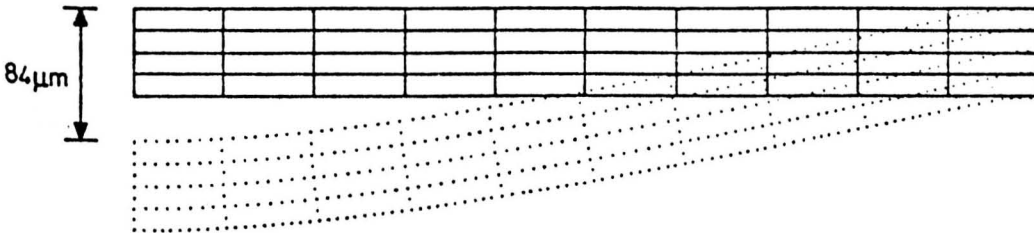
Displacement Scale \longleftrightarrow
2mm



b) resulting from the 11th shock

Mesh Scale \longleftrightarrow
2mm

Displacement Scale \longleftrightarrow
50 μm



c) resulting from the 11th dwell period

Mesh Scale \longleftrightarrow
2mm

Displacement Scale \longleftrightarrow
200 μm

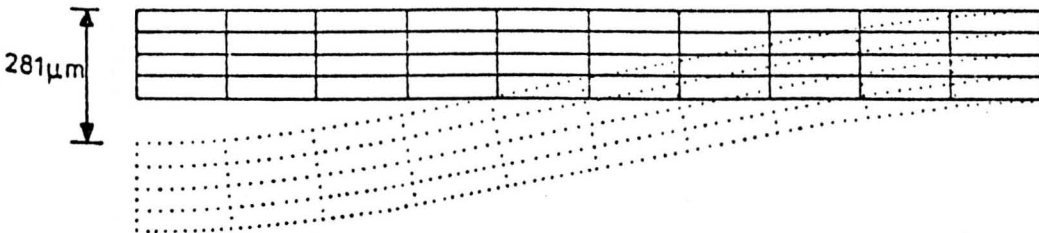


Figure 6.35 Circular plate (elastic-perfectly-plastic, $\sigma_t/\sigma_y = 1.41$, $p/p_{col} = 0.7$, complete redistribution). 'Exaggerated' nodal displacements.

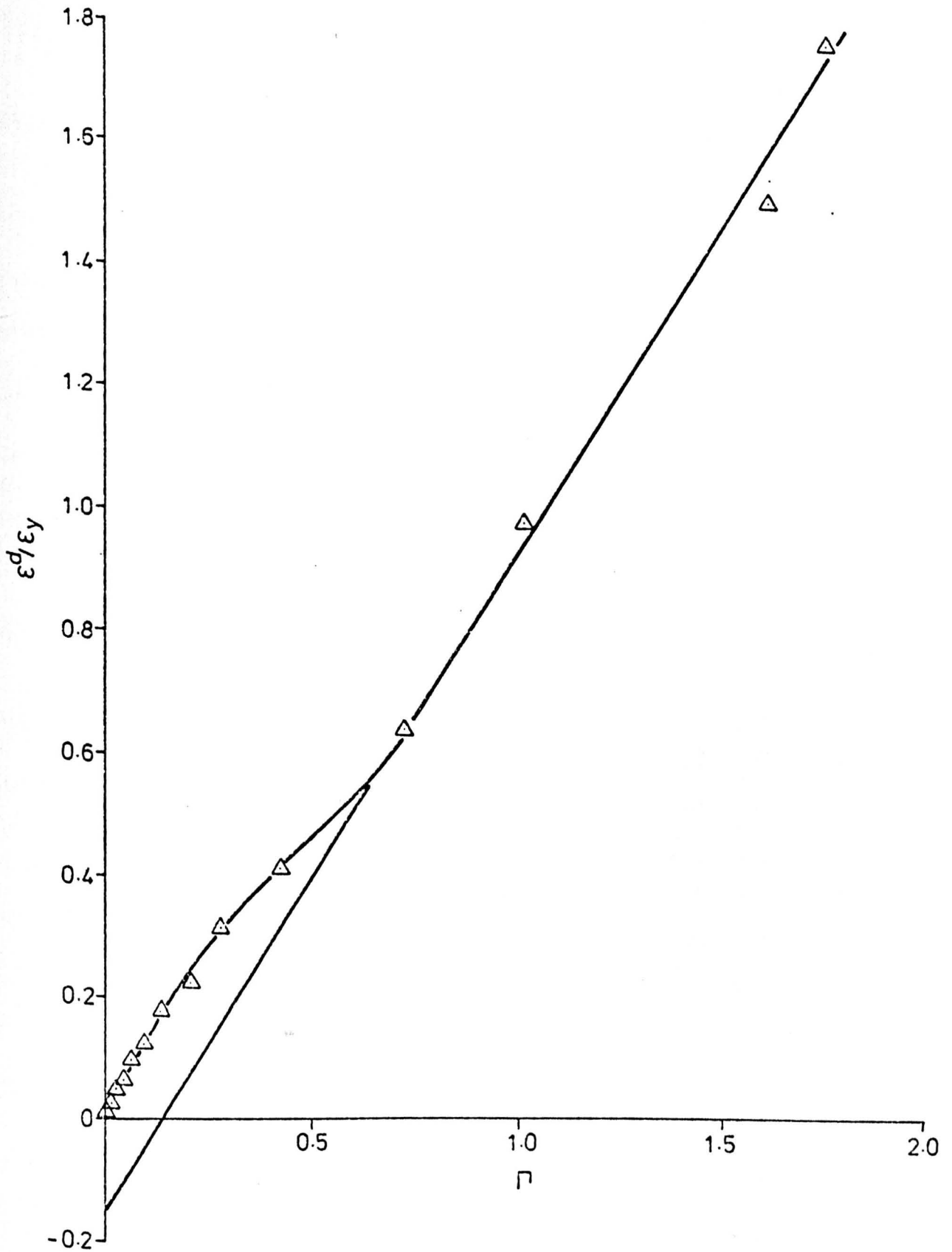


Figure 6.36 Circular plate (elastic-perfectly-plastic, $\sigma_t/\sigma_y = 1.41$, $p/p_{col} = 0.7$, complete redistribution). Accumulation of normalised strain in the transverse direction at point D during the first dwell period.

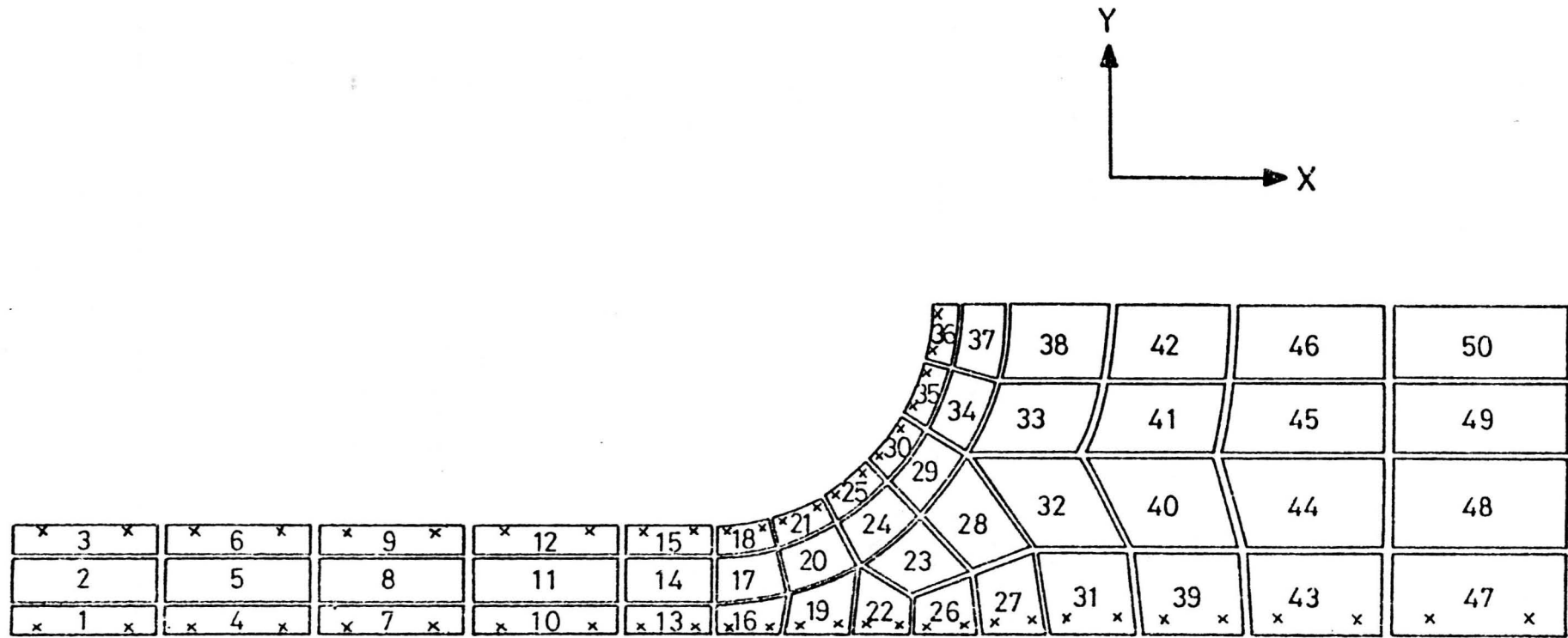


Figure 6.37 Shouldered tube. Finite element mesh showing the positions of the Gauss points nearest to the outside and bore surfaces.

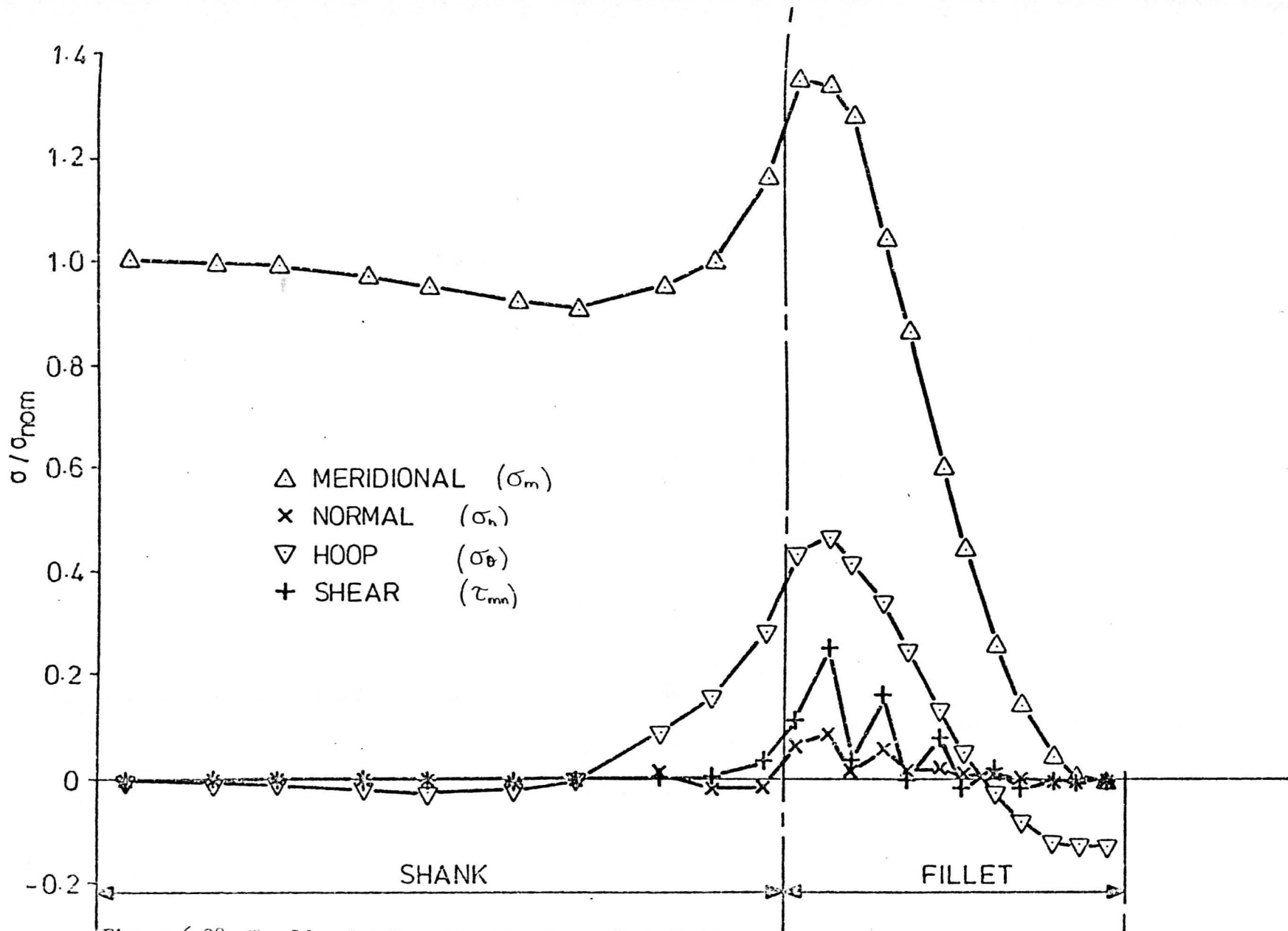


Figure 6.38 Shouldered tube. Elastic stress distributions along 'outside surface' due to an axial load.

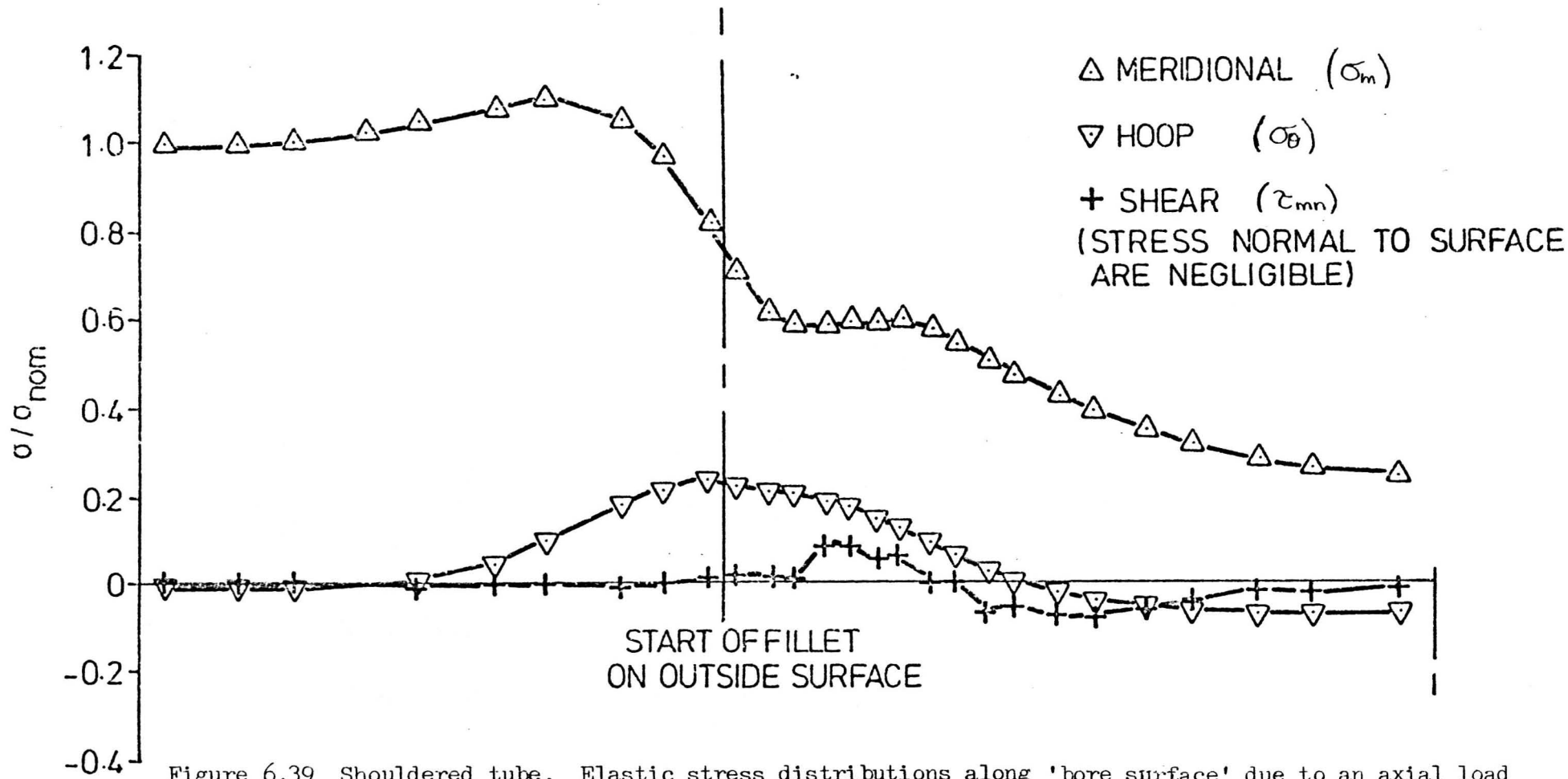


Figure 6.39 Shouldered tube. Elastic stress distributions along 'bore surface' due to an axial load (see Figure 6.37)

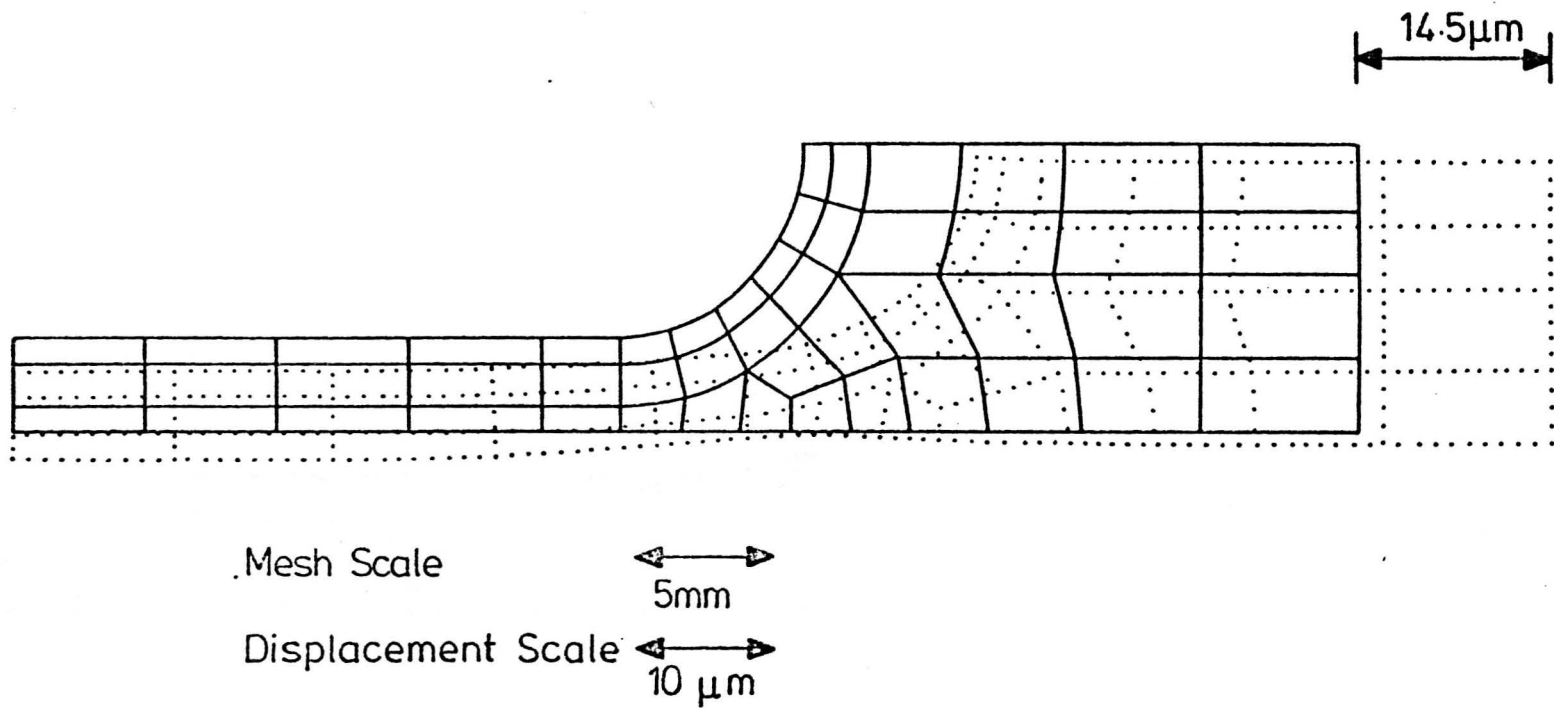
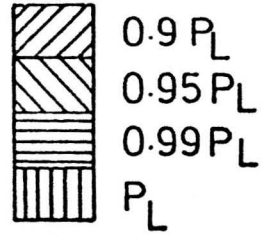


Figure 6.40 Shouldered tube. 'Exaggerated' deformed shape for a mean load of 0.7 of the limit load.



WHERE P_L = LIMIT LOAD IN SHANK

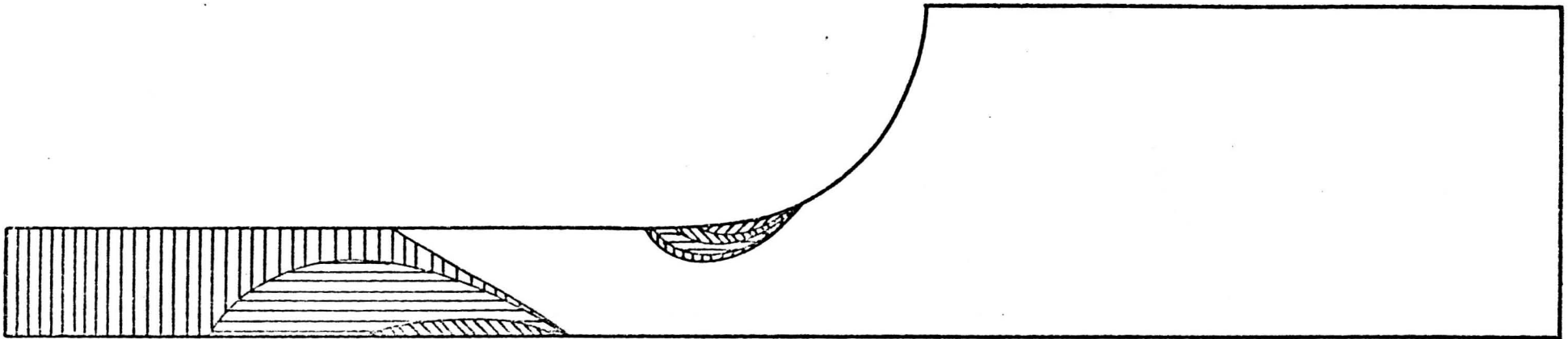


Figure 6.41 Shouldered tube (elastic-perfectly-plastic). Growth of plastic zone with increasing axial load up to collapse.

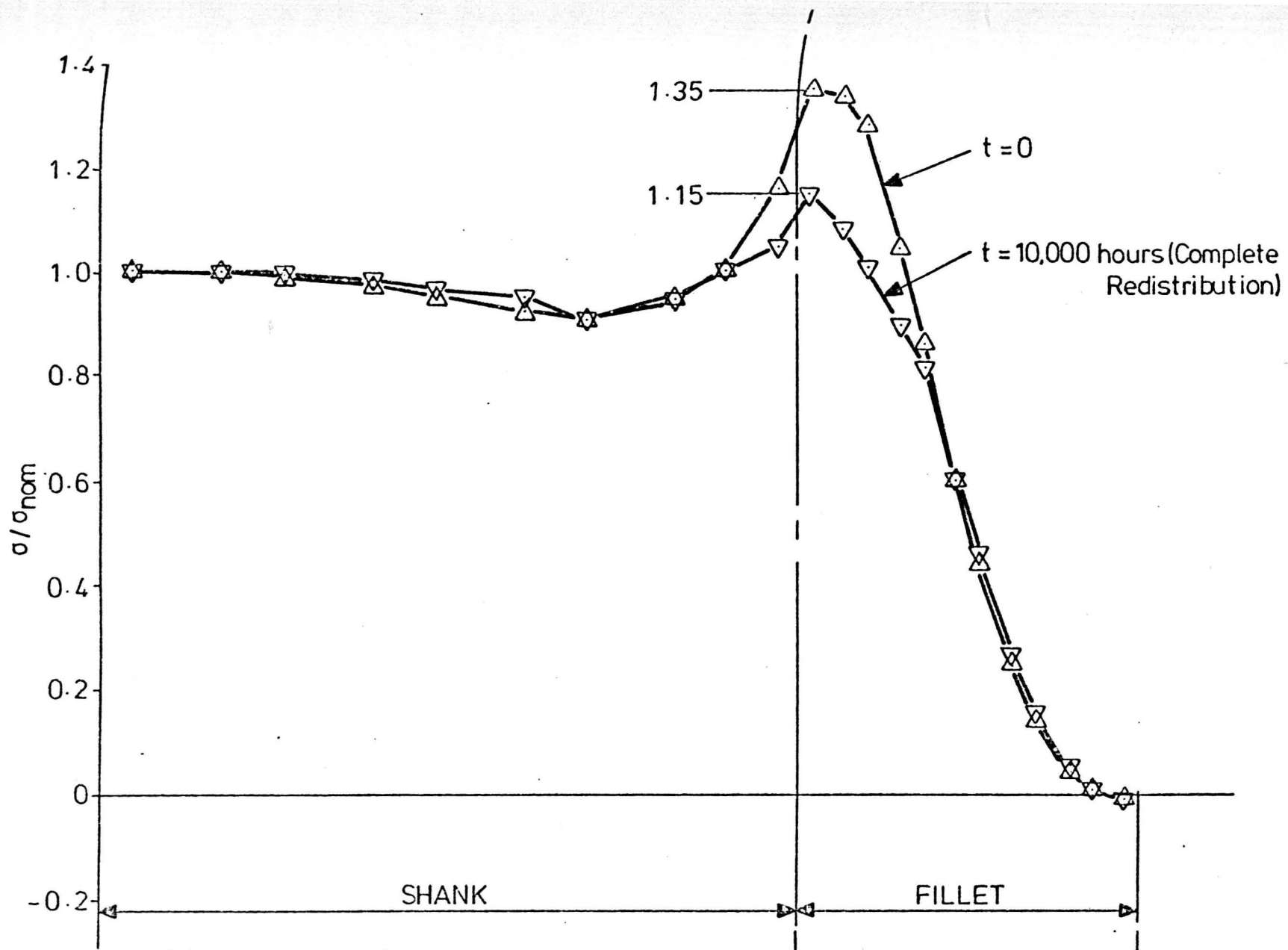


Figure 6.42 Shouldered Tube. Redistribution of meridional stress along the 'outside surface' due to steady load creep. (see Figure 6.37)

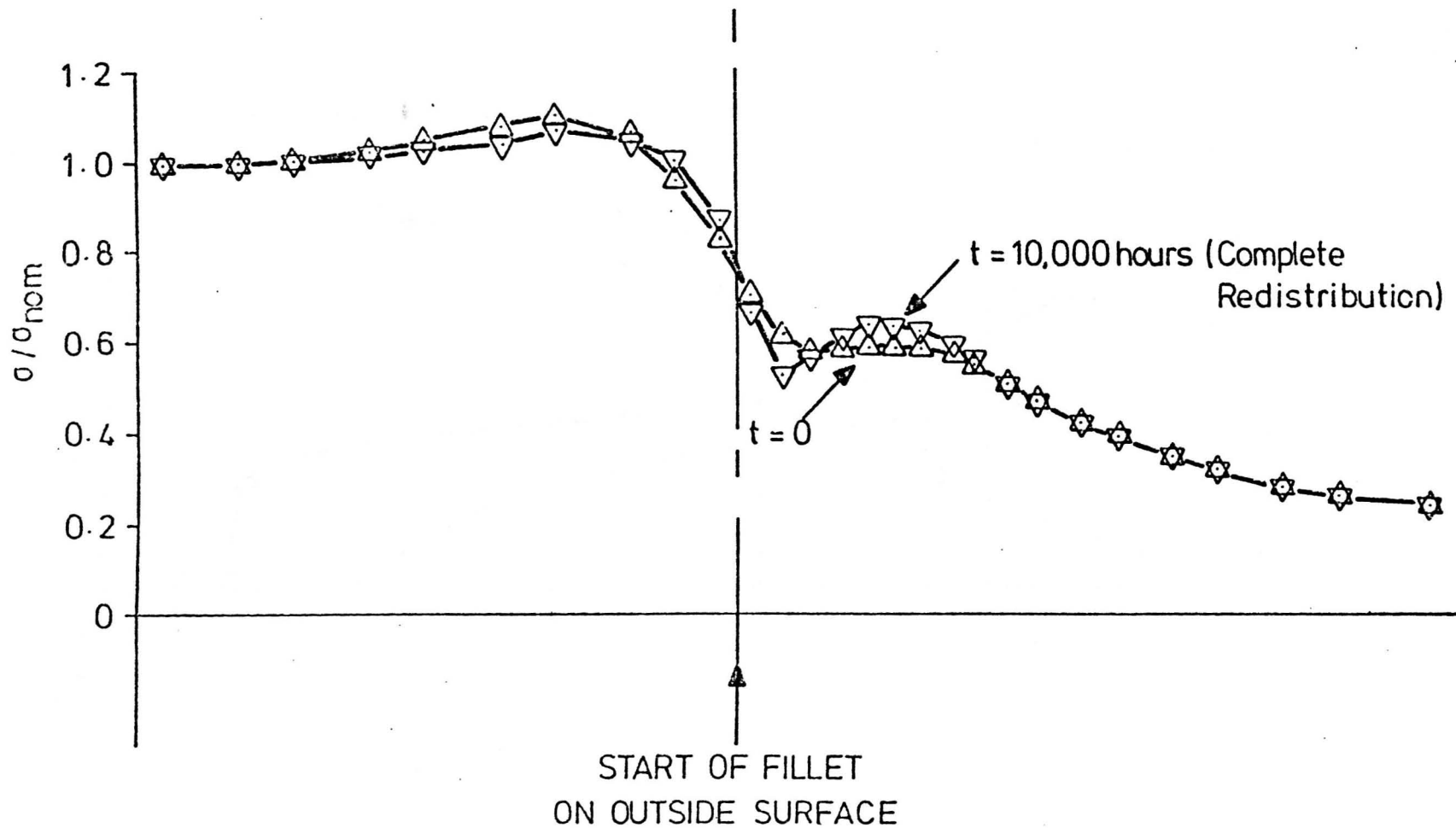


Figure 6.43 Shouldered tube. Redistribution of meridional stress along 'bore surface' due to steady load creep (see Figure 6.3?).

- AXIAL STRESS, INITIAL LOADING
- △ AXIAL STRESS, END OF HALF CYCLE
- ▽ HOOP STRESS, END OF HALF CYCLE
- ▲ AXIAL STRESS, END OF CYCLE
- ▼ HOOP STRESS, END OF CYCLE

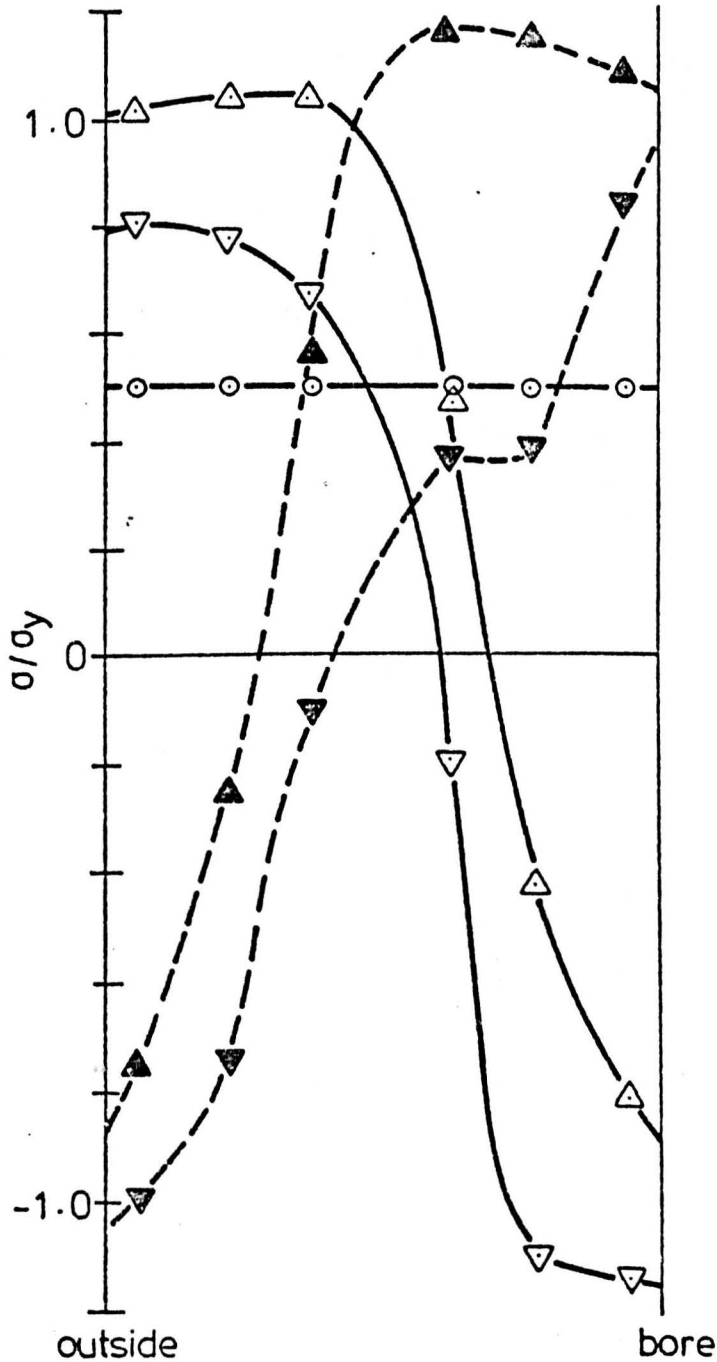


Figure 6.44 Shouldered tube (elastic-perfectly-plastic, $\sigma_t/\sigma_y = 2.83$, $P/P_L = 0.5$, 'no creep' conditions). Stress distributions in the shank due to initial loading and during the first thermal shock.

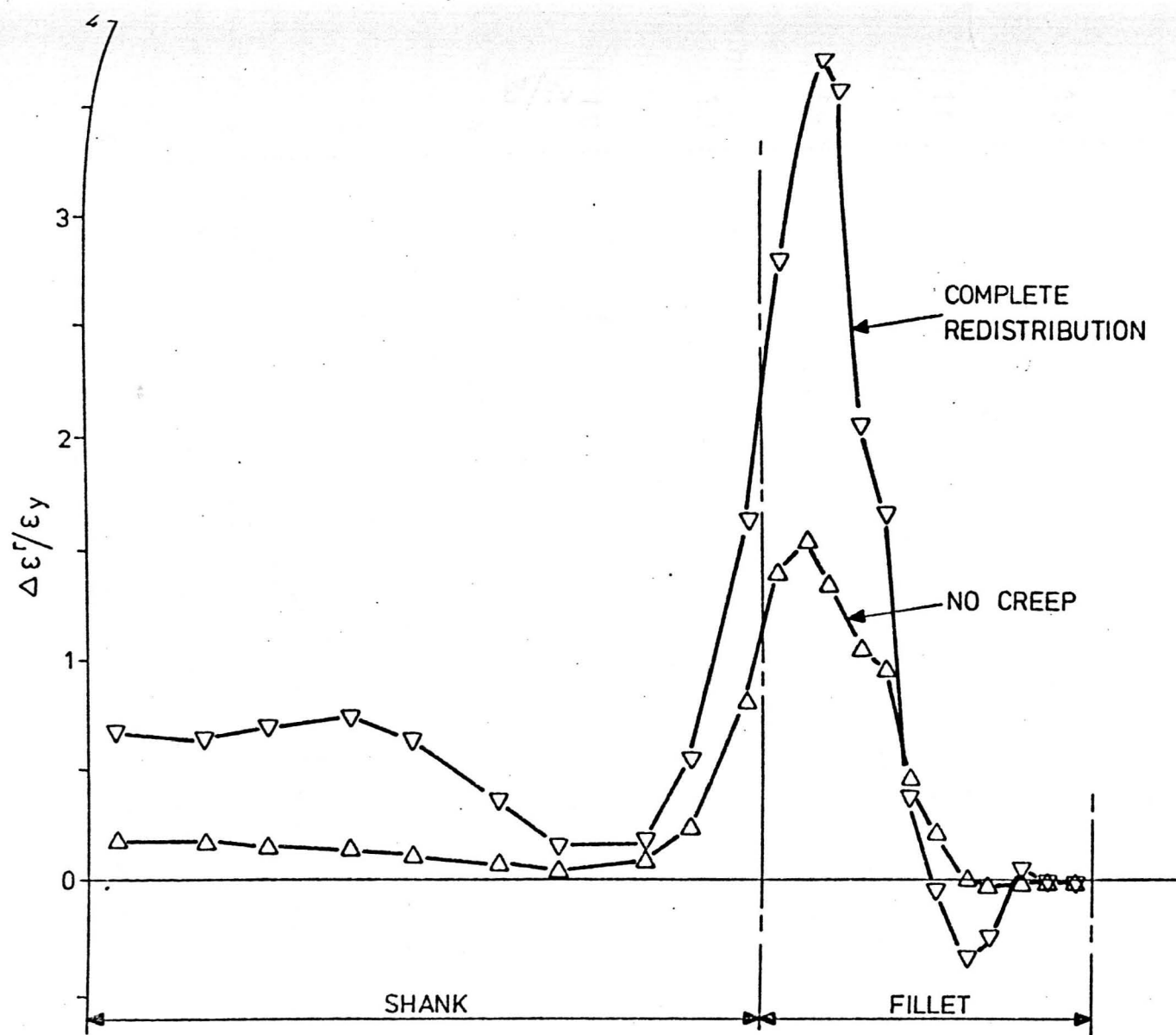


Figure 6.45 Shouldered tube (elastic-perfectly-plastic, $\sigma_t / \sigma_v = 2.83$, $P/P_L = 0.5$). Distribution of normalised steady state meridional ratchet strain along the 'outside surface' (see Figure 6.37).

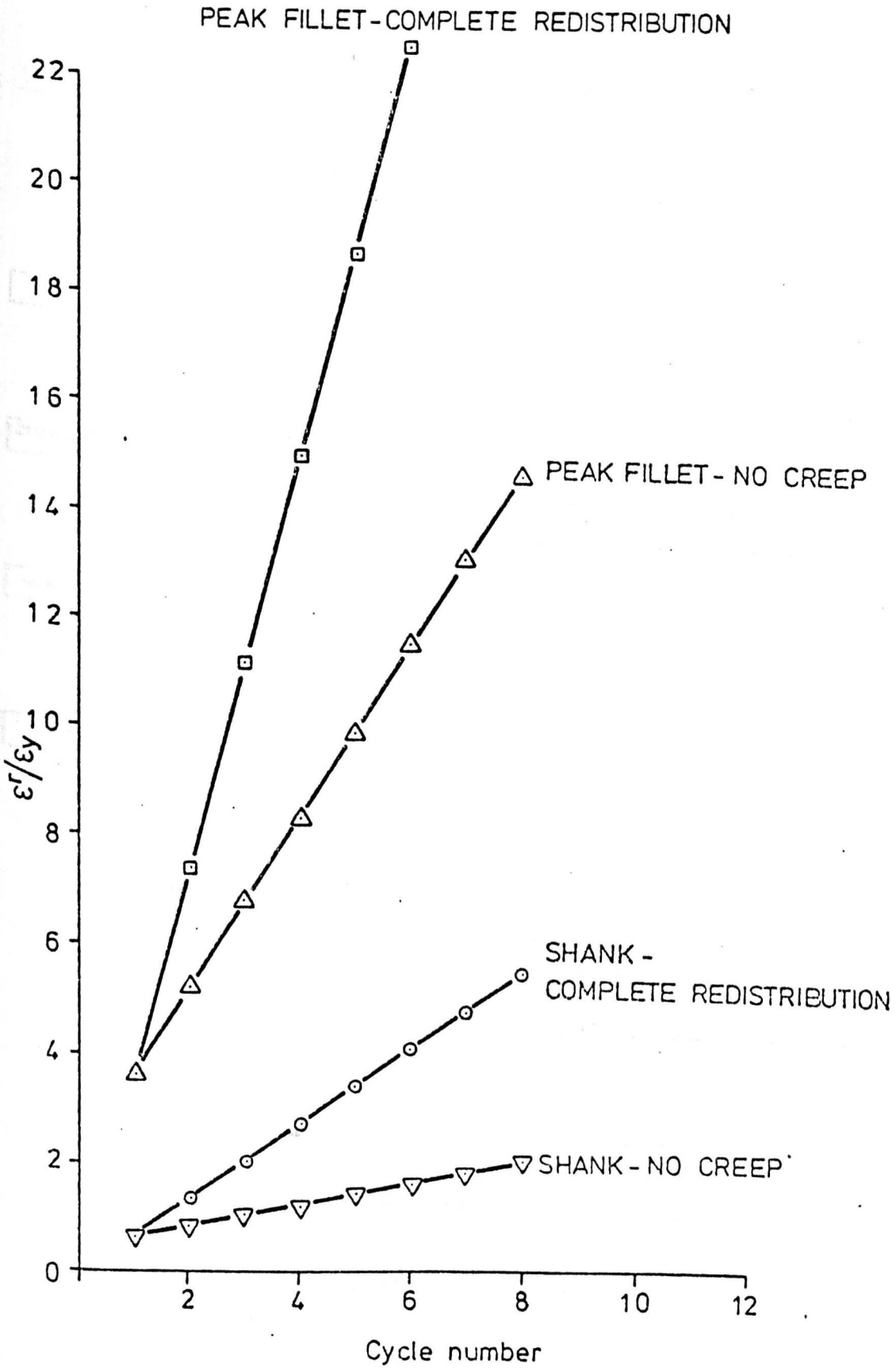


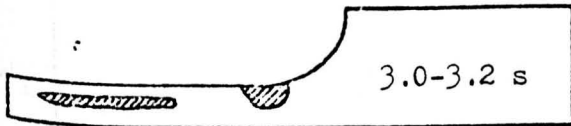
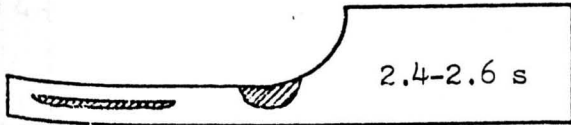
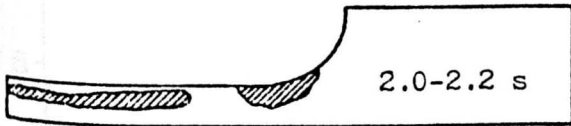
Figure 6.46 Shouldered tube (elastic-perfectly-plastic, $\sigma_t/\sigma_y = 2.83$, $P/P_L = 0.5$). Accumulations of normalised ratchet strain during the first 8 cycles.

1st half of cycle (cooling)

2nd half of cycle (heating)

0-1.8 s - ELASTIC

0-1.6 s - ELASTIC



OVERALL REGION OF PLASTICITY

Figure 6.47 Shouldered tube (elastic-perfectly-plastic, $\sigma_t/\sigma_y = 1.42$, $P/P_L = 0.7$, 'no creep' conditions). Regions of additional plastic straining during a steady state cycle.

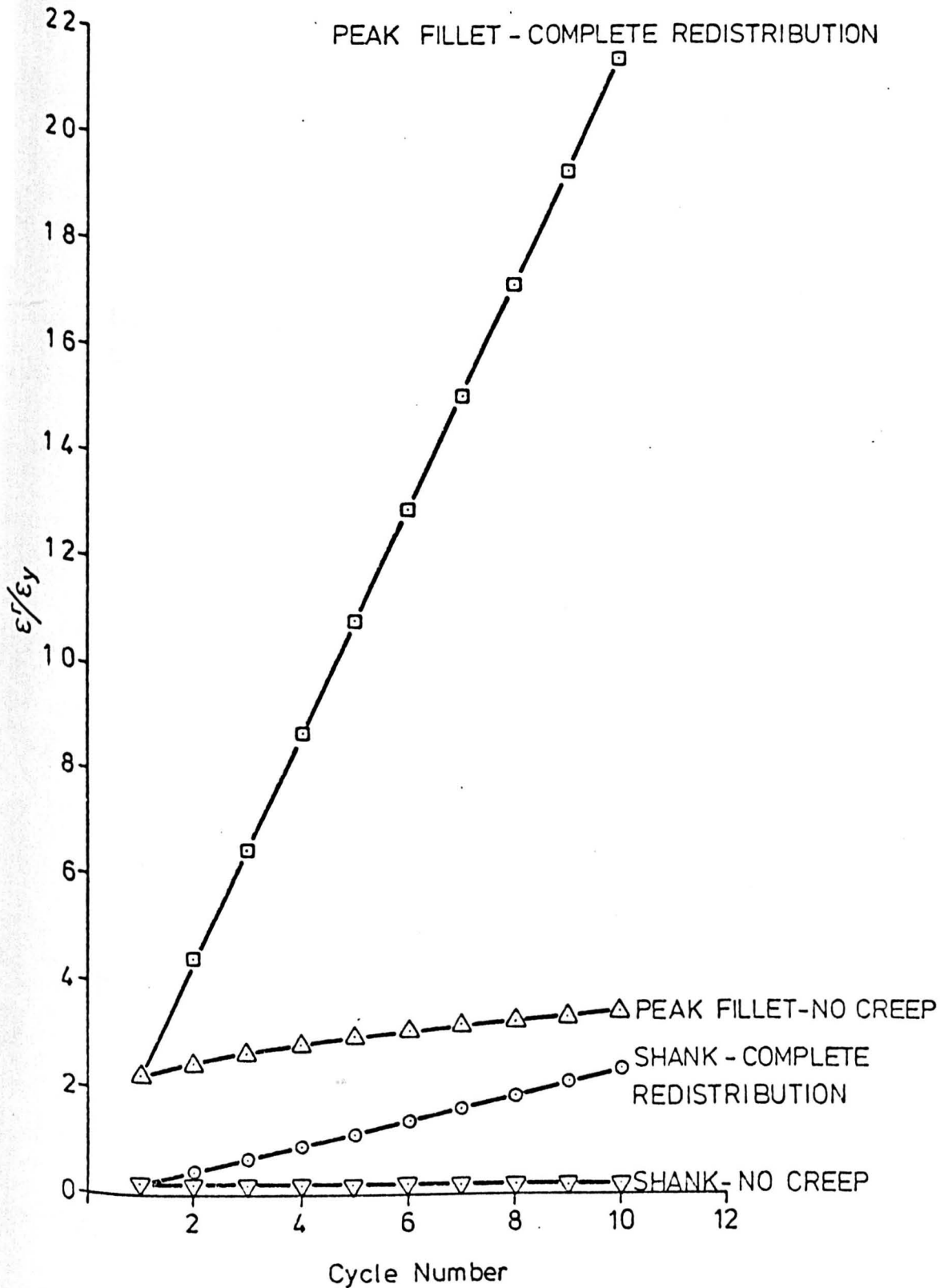
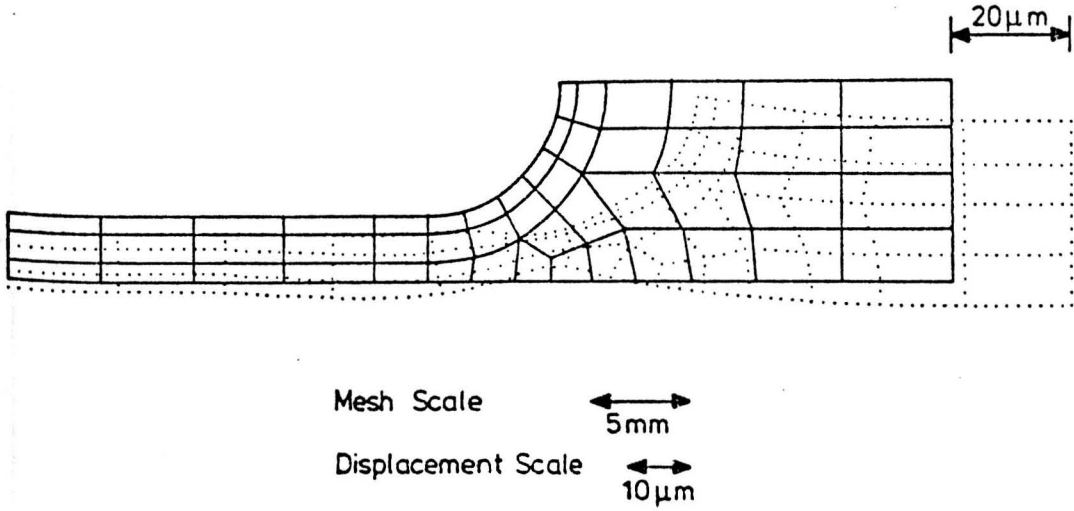


Figure 6.48 Shouldered tube (elastic-perfectly-plastic, $\sigma_t/\sigma_y = 1.42$, $P/P_L = 0.7$). Accumulations of normalised ratchet strain during the first 10 cycles.

a) end of the 10th shock



b) resulting from the 11th shock

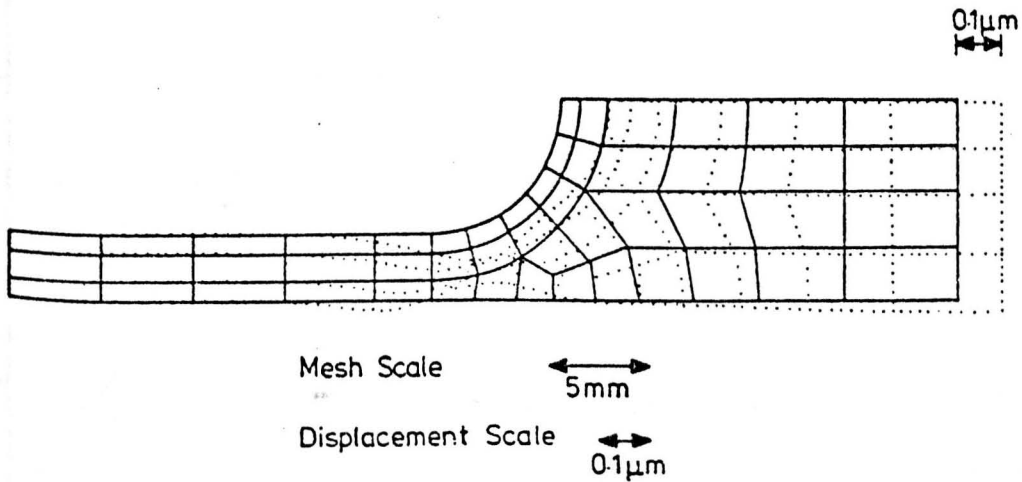


Figure 6.49 Shouldered tube (elastic-perfectly-plastic, $\sigma_t/\sigma_y = 1.42$, $P/P_L = 0.7$, 'no creep' conditions). 'Exaggerated' nodal displacements.

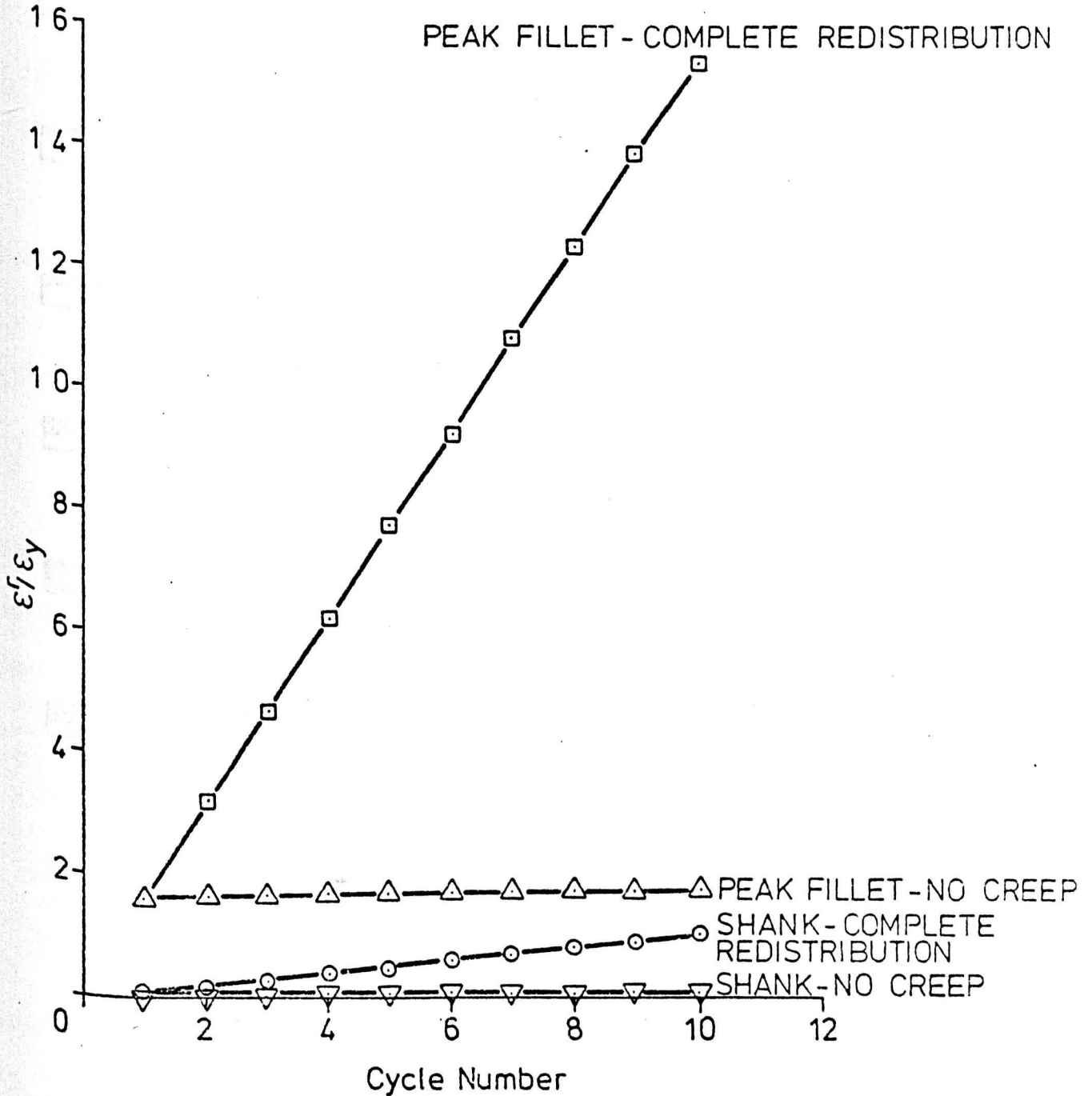
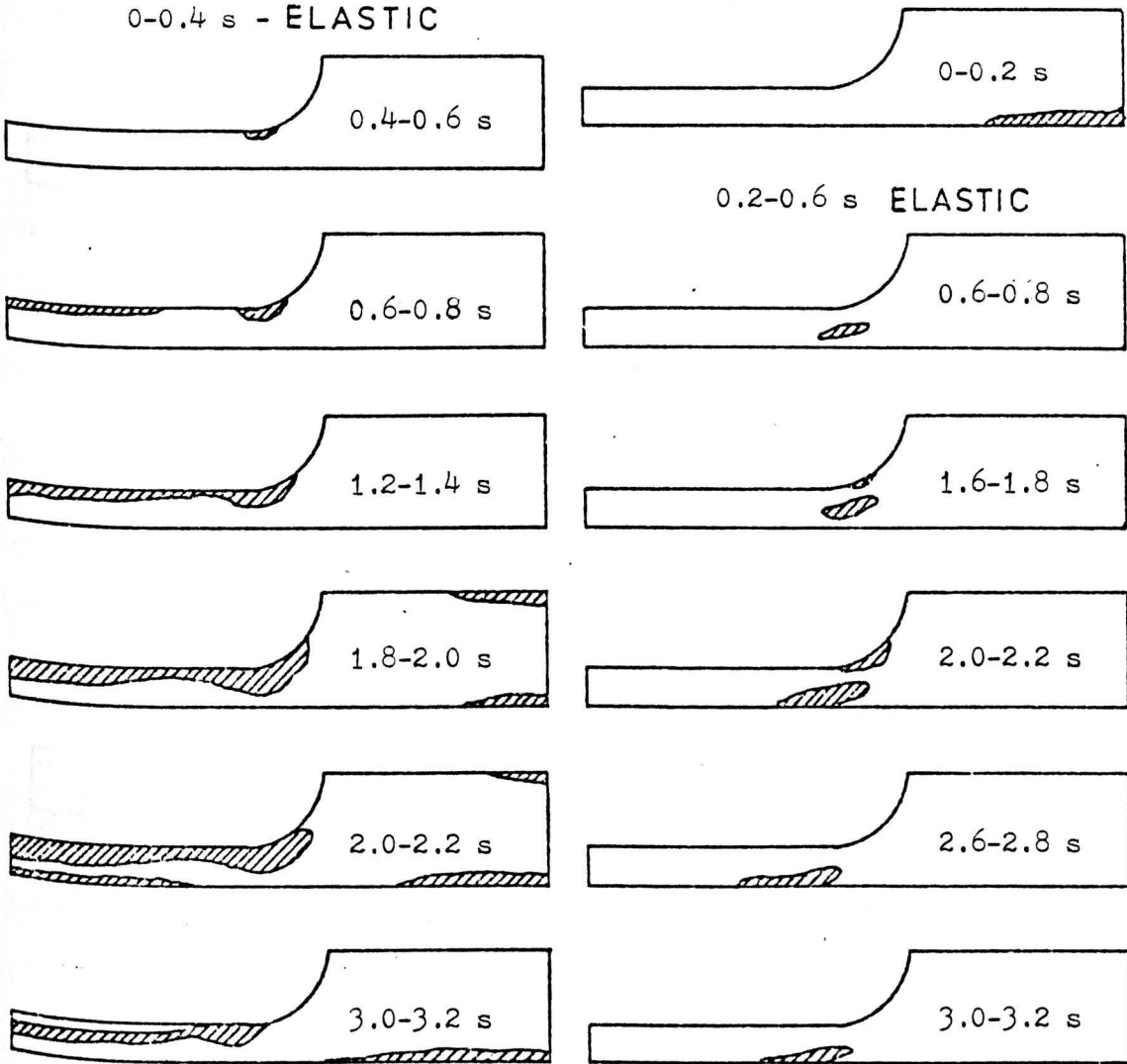


Figure 6.50 Shouldered tube (elastic-perfectly-plastic, $\sigma_t/\sigma_y = 1.42$, $P/P_L = 0.5$). Accumulations of normalised ratchet strain during the first 10 cycles.

1st half of cycle (cooling)

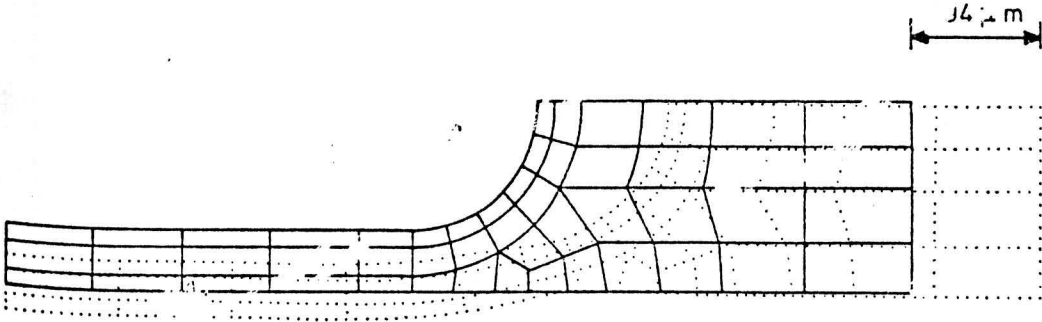
2nd half of cycle (heating)



OVERALL REGION OF PLASTICITY

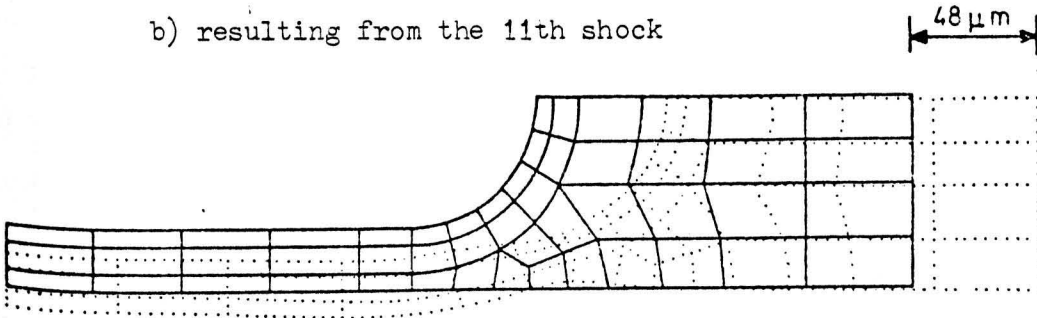
Figure 6.51 Shouldered tube (elastic-perfectly-plastic, $\sigma_t/\sigma_y = 1.42$, $P/P_L = 0.7$, complete redistribution). Regions of additional plastic straining during a steady state cycle.

a) end of the 10th cycle



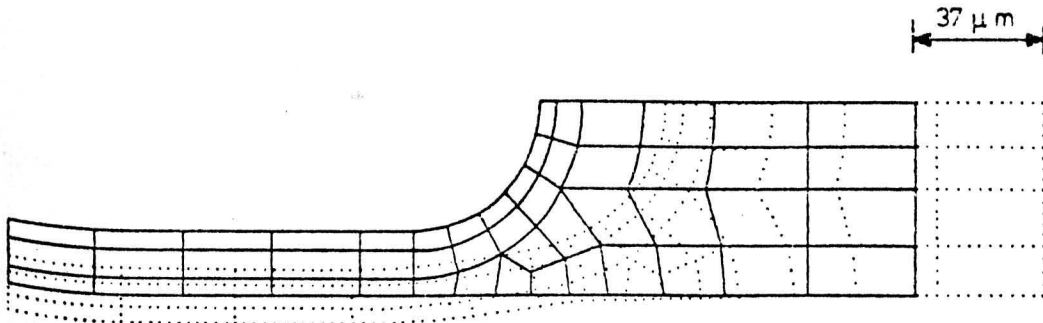
Mesh Scale \longleftrightarrow 5mm
Displacement Scale \longleftrightarrow 200 μm

b) resulting from the 11th shock



Mesh Scale \longleftrightarrow 5mm
Displacement Scale \longleftrightarrow 20 μm

c) resulting from the 11th dwell period



Mesh Scale \longleftrightarrow 5mm
Displacement Scale \longleftrightarrow 20 μm

Figure 6.52 Shouldered tube (elastic-perfectly-plastic, $\sigma_t/\sigma_y = 1.42$, $P/P_L = 0.7$, complete redistribution). 'Exaggerated' nodal displacements.

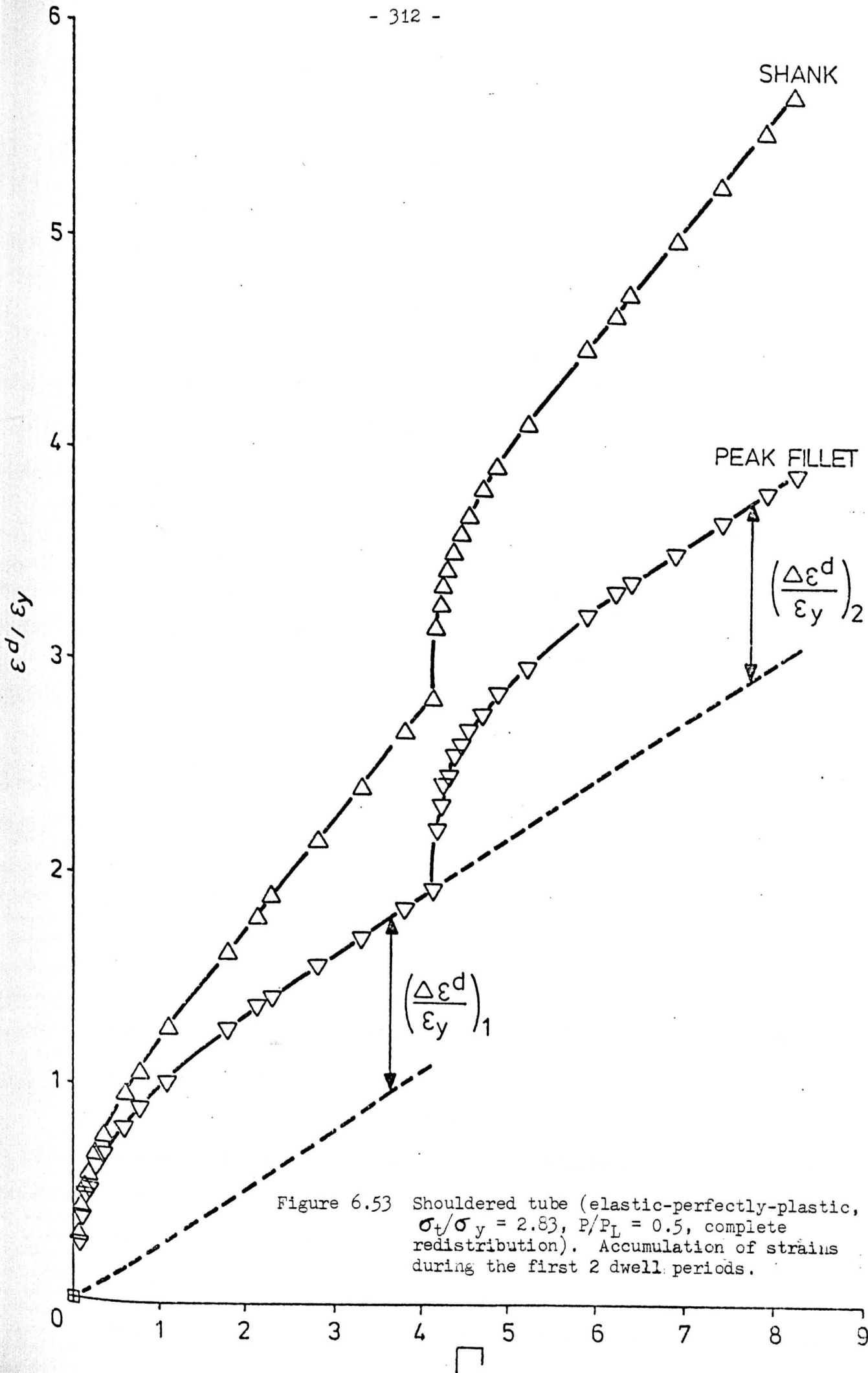


Figure 6.53 Shouldered tube (elastic-perfectly-plastic, $\sigma_t / \sigma_y = 2.83$, $P/P_L = 0.5$, complete redistribution). Accumulation of strains during the first 2 dwell periods.

CHAPTER SEVEN

7. A CORRELATION OF THE RATCHETTING AND DWELL PERIOD BEHAVIOUR
OF THE COMPONENTS

7.1 Introduction

The analysis of the 5 components has been described in Chapters 4-6. This Chapter presents a synopsis of the results. Section 7.2 compares in detail the behaviour of all 5 components when elastic-perfectly-plastic and zero plasticity/creep interaction models are assumed. This comparison is extended for the flanged tube and stepped beam results with material hardening and zero plasticity/creep interaction models in Section 7.3. The ratchetting mechanism, ratchet strains and dwell period strains are correlated and the implications for design are discussed in Chapter 8.

Characteristic ratchetting and dwell period behaviours are identified which will be used in Chapter 8 to recommend design procedures based on both limited finite element 'exact' solutions and approximate methods of solution. Ratchet strains for both the 'no creep' and 'complete redistribution' conditions are considered.

Finally, the effects of 'partial redistribution' of stresses during the dwell periods between cycles are assessed in Section 7.4.

7.2 Elastic-Perfectly-Plastic Material Model (All 5 Components)

7.2.1 Mechanical and thermal loading conditions

The mechanical and thermal loading conditions used in the analysis of the five components are summarised in Table 7.1, together with the thermal and mechanical stress concentration factors in regions of peak stress. Thermal conditions are defined by the Fourier number, $kt_c / \rho C_p L_c^2$, the Biot number, hL_c / k , and the nominal elastic thermal stress, σ_t / σ_y . The characteristic time,

t_c , is taken as the duration of the ramp temperature change (i.e. zero for a step change) and the characteristic length, L_c , is the bore diameter for the flanged tube and shouldered tube, the hole diameter for the 'hole-in-plate' component and the thickness for the circular plate. For the 'hole-in-plate' component and circular plate, where changes in metal surface temperature are used to define the transient, the surface heat transfer coefficient and hence the Biot number are taken as infinity. For components with cyclic thermal loading, nominal elastic thermal stresses are based on the Bree (1) equation, using an equivalent linear temperature distribution (49) for the flanged tube and 'hole-in-plate' components, as discussed in chapters 4-6. For the stepped beam, the analogy between the shank and the Bree thin tube is used to obtain an 'equivalent' nominal thermal stress based on cyclic changes in curvature. The 'equivalent' thermal stress concentration factor in the fillet is taken as the stress concentration factor due to pure bending.

7.2.2 Ratchetting mechanisms

The ratchetting mechanisms of the components can be classified into 4 categories:-

- (i) first cycle mechanism (all components);
- (ii) steady state, 'no creep' mechanism (all components except circular plate);
- (iii) continuous transient, 'no creep' mechanism (circular plate); and
- (iv) steady state, complete redistribution mechanism (all components).

The behaviour of the shanks and regions of stress concentration are generally similar.

7.2.2.1 First cycle mechanism

During the first cycle there will be an increment of growth at any point in the structure that experiences yielding. For components with uniform sections and stress concentrations the plastic zone initiates in the fillet and for 'low' loadings yielding in the fillet may not be accompanied by yielding in the shank.

7.2.2.2 Steady state, 'no creep' mechanism

For the uniform sections of the tubes and beam, steady state non zero ratchet strains are accumulated when the whole section suffers plastic deformation at some point during the cycle. The stress distributions at the start and end of the cycle are identical and the increment of plastic strain is constant across the section. For the stepped beam shank the development of the plastic zone during a cycle is similar to that of the 'Bree' beam (1). During the first half of the cycle, a plastic zone, initiating from a surface, spreads inwards towards the neutral axis and may be accompanied by a 'smaller' zone initiating from the other surface. During the second half of the cycle the plastic zone initiates from the opposite surface and the maximum depths of yielded material is the same as during the first half of the cycle. For ratchetting the 'major' plastic zone must cross the neutral axis during both halves of the cycle. A 'plastic core' (i.e. a region around the neutral axis which yields during both halves of the cycle) is an essential feature of ratchetting. Other mechanisms have been observed, for example in the case of the flanged tube shank, a plastic zone initiates from within the section and

spreads outwards during the first half of the cycle. During the second half of the cycle, the plastic zone initiates at the bore surface and spreads radially outwards. Again there is a requirement for a 'plastic core'.

In the fillet regions of the tubes and beam and the section AB for the 'hole in plate' component steady-state ratchetting may, depending on loading conditions, be accompanied by an initial transient effect. The existence of a 'plastic core' is also essential for steady state 'no creep' ratchetting and, again, the cyclic development of the plastic zones varies with components and loadings. For the tubes and beams the plastic zone initiates in the fillet and spreads into the shank and ratchet strains vary across the section. 'Peak fillet' ratchet strains are in the meridional direction. There is a 'necking' of the component across the section during a cycle when compared with the shank.

For the 'hole-in-plate' component, incremental plastic strains are accumulated across the whole of section AB during a cycle. The ratchet strains are a maximum at the hole surface (A) and produce an elongation of the hole in the direction of steady mechanical load.

7.2.2.3 Transient, 'no creep' mechanism

For the circular plate, ratchet strains reduce monotonically (in all but the highest load case to zero) and a steady state ratchetting condition does not exist. An increment of ratchet strain is produced by the development of plastic zones from the edge and centre of the plate during the first and second halves of the cycle respectively. The reduction in ratchet strain per cycle is associated with a reduction in the plastic zone between successive cycles which is apparent at the edge but not significant at the centre.

The presence of an 'elastic core' at all times during a cycle is a possible indication that shakedown will eventually occur as suggested by Townley et al (57) for pressure vessels.

7.2.2.4 Steady state, 'complete redistribution' mechanism

In all cases, ratchetting will occur if any plastic strains are produced during a steady state cycle. For the uniform sections of the tubes and beam, the ratchetting mechanism is identical to that for the first cycle, discussed in Section 7.3.1, since the initial stress distribution due to steady mechanical load is the same as the stationary state stress distribution. For the fillet regions of the tubes and beam, the 'hole in plate' component and the circular plate, steady state ratchetting occurs for the second and subsequent cycles if there is any plastic straining during the second cycle. For all components, with the possible exception of the circular plate, there is no requirement of a 'plastic core' for steady state ratchetting. For the circular plate, Figure 6.34 indicates a definite 'plastic hinge' at the edge although this 'plastic hinge' is not considered to be essential for continued ratchetting.

7.2.3 Ratchet strains

A summary of the ratchet strains obtained for the five components is given in Tables 7.2 and 7.3 for the 'no creep' and 'complete redistribution' conditions. The characteristic behaviour is found to fall into 3 categories:-

- A - equal ratchet strains for all cycles;
- B - equal ratchet strains for the second and subsequent cycles; and
- C(n) - steady state ratchet strains per cycle after n cycles.

7.2.3.1 Qualitative assessment

7.2.3.1.1 'No creep' condition

With the exception of the circular plate, a constant ratchet strain per cycle occurs after a small number of cycles (in many cases only one).

Uniform shank regions

In the shank regions of the tubes and beam a steady state situation is achieved after the first cycle (i.e. type B). The ratchet strains produced in the second and subsequent cycles are equal, in some cases zero, and less than the first cycle values (if maximum surface or centreline ratchet strains are considered for the stepped beam shank). Under these conditions, the initial uniform stress distribution due to steady mechanical load is 'more favourable' for ratchetting than the non-uniform residual stress distribution at the end of each cycle. The detailed studies of the flanged tube and stepped beam shanks have identified particular loadings for which 'more favourable' residual stress fields may or do exist, as follows:-

- (i) for the flanged tube shank with high mean load ($P/P_L > 0.75$)
- see Table 4.2
- (ii) for the stepped beam shank, Figure 5.5 indicates that steady state centreline ratchet strains may be greater than the first cycle ratchet strain for high mean loads and low bending loads, which are outside the range of loadings considered.

Regions of stress concentration

With the exception of the circular plate, steady cyclic state conditions are achieved after a few cycles (up to 6, i.e. type C) although for extreme loading conditions the steady cyclic state is

reached after the first cycle (i.e. type B).

For the circular plate, ratchet strains reduce monotonically with cycle number and, in all but the highest mean load case ($P/P_L = 0.7$), have reduced to zero in under 4 cycles. For the highest mean load peak ratchet strains are still reducing after 10 cycles. This monotonic reduction in ratchet strains is consistent with the results of Hyde (32) and Goodman and Goodall (21).

Comparison between shank and fillet

For the two axisymmetric, thermally loaded tubes the first cycle and steady state peak fillet ratchet strains are greater than the corresponding shank values. Furthermore the shouldered tube results for $\sigma_t/\sigma_y = 1.42$ show that the onset of ratchetting in the fillet occurs at reduced mean load compared with the shank.

For the mechanically cycled stepped beam, first cycle peak fillet ratchet strains are also greater than the corresponding shank values. However, the steady state peak fillet ratchet strains are less than the shank values. Since the tensile meridional strains in the fillet of the stepped beam are accompanied by compressive strains in the other two directions, the reduction in these compressive strains due to the constraints of the increased section will also contribute to a reduction in the tensile meridional strains. Alternatively, for the axisymmetric components, the hoop strains are tensile and due to Poisson's ratio effect reduce the overall tensile meridional strains. Hence a reduction in hoop strains due to the flange or shoulder constraint can have an adverse effect on the meridional strains.

7.2.3.1.2 'Complete redistribution'

A steady cyclic state, with constant ratchet strain per cycle, occurs in the first one or two cycles for uniform sections and stress concentration regions respectively.

Uniform shank regions

Each cycle produces an equal amount of ratchet strain (i.e. type A) since the initial stress distribution due to steady mean load is identical to the stationary state stress distribution. Any plastic strains produced in the first cycle will also be accumulated during each subsequent cycle. The implication is a shift in the shakedown and ratchetting boundary to the 'elastic limit' line (i.e. below which, cycling is purely elastic).

For the 'complete redistribution' case to be an upper bound on ratchet strains, the second cycle 'no creep' ratchet strain (i.e. the steady state value since the characteristic is type B) must not be greater than the first cycle ratchet strain. This is the case for all uniform sections in Tables 7.2 and 7.3 (if maximum surface or centreline ratchet strains are being considered for the stepped beam) and is generally so in all but the high mean load shank results (see Section 7.2.3.1.1 - Uniform shank regions).

Regions of stress concentration

For all components, including the circular plate, a steady cyclic state exists after the first cycle since the stationary state stress distribution is established after each cycle (i.e. Type B). Steady state ratchet strains are greater than the equivalent 'no creep' results and hence the 'complete redistribution' case is the upper bound. The results imply a reduction in the size of the shakedown region. Although continued ratchetting was found for all cases, it is conceivable that particular loadings could result in 'small' first cycle ratchet strains followed by shakedown. In this case the ratchetting boundary would not correspond to the elastic limit line and the shakedown region would be somewhat larger than the elastic region.

Comparison between shank and fillet

For all cases, including the stepped beam, peak fillet ratchet strains are greater than the equivalent shank values.

7.2.3.2 Quantitative correlation

7.2.3.2.1 Bree's analysis

'No creep' condition

The results for the five components and the elastic-perfectly-plastic results from the flanged tube shank study in Table 4.2 have been correlated on the basis of Bree's (1) analysis by plotting the results, using equivalent load values on a 'Bree' diagram in Figure 7.1 using the notation in Table 7.4. The full curves are the ratchetting boundary and lines of constant ratchet strain per cycle for the Bree problem. The points are plotted at the equivalent loading conditions for the various components and the numerical value adjacent to each 'blackened in' symbol is the steady state ratchet strain. Open symbols indicate a zero steady state ratchet strain (i.e. shakedown). The equivalent loads for the components are obtained as follows. In all cases the steady mechanical load, P/P_L , is taken as the nominal value (in the case of the 'peak fillet' regions of the stepped beam, flanged and shouldered tubes the nominal shank value is used). For the uniform regions of the flanged tube and shouldered tube, the elastic thermal stress range, σ_t/σ_y , is based on an 'equivalent' linear temperature distribution; the intermediate steady state temperature distribution through the shank of the shouldered tube is reasonably linear whereas the approach of Yamamoto et al (49) has been used to 'linearise' the most severe non-linear temperature distribution through the flanged tube shank. For the uniform region of the stepped beam the

'equivalent' elastic thermal stress range is based on cyclic changes in curvature using the analogy between the stepped beam shank and the Bree beam. For the fillet regions of the beam and tubes an estimate of the elastic thermal stress range is obtained by multiplying the shank value by the thermal stress concentration factor ('equivalent' thermal stress concentration factor for the stepped beam). This method of estimating the thermal stress in fillet regions is considered to be pessimistic since the high stress regions caused by geometric discontinuities are usually very localised whereas the cyclic thermal load factor for ratchetting is associated with the distribution through the whole section, as illustrated by the Yamamoto equivalent thermal stress approach.

The peak temperature distribution through the circular plate is linear and the elastic thermal stress range can be obtained directly from Bree's equation. The nominal elastic thermal stress range for the 'hole-in-plate' component is the equivalent linear value for the most severe temperature distribution during the transient. A thermal stress concentration factor due to geometry effects is not readily quantified for this problem. However for the tubes it is seen from Table 7.1 that the thermal stress concentration factor is greater than the mechanical stress concentration factor and, on this assumption, an elastic thermal stress range for the 'hole-in-plate' component has been obtained by multiplying the nominal value by the mechanical stress concentration factor. Using these methods of determining the equivalent steady and cyclic loads, the steady state ratchetting results are presented in Figure 7.1. It can be seen that, for all of the cases examined, the ratchetting boundary and lines of constant ratchet strain per cycle from Bree's

analysis are conservative. Therefore the use of 'equivalent' linear temperature distributions and thermal stress concentration factors, which can both be determined relatively easily, appears to offer a simple method of conservatively dealing with transient thermal loading and complex geometries for 'no creep' conditions.

'Complete redistribution'

The equivalent loading conditions for all components are identical to those described for the 'no creep' case. This is obviously true for cyclic thermal loading and figure 5.4 shows the same to be true for the stepped beam shank which experiences the same cyclic curvature range for both the 'no creep' and 'complete redistribution' cases. For the 'complete redistribution' case Bree suggests the elastic limit line as the 'new' ratchetting boundary with the disappearance of the shakedown region and this has been verified in the previous discussions in the studies of the flanged tube and stepped beam shanks. Alternatively, Leckie (45) suggests that: 'the effects of plasticity are likely to be small provided the load is less than $n/(n + 1)$ of the shakedown load'. The steady state ratchet strain results for the components for the 'complete redistribution' case are compared with the Bree boundary and the $n/(n + 1)$ boundary in Figure 7.2. For the stepped beam, the maximum surface ratchet strains are quoted.

In all cases the Bree boundary is conservative as expected since it allows for no plastic growth during a cycle. With the exception of the circular plate results, the $n/(n + 1)$ boundary is also conservative; the steady state ratchet strain for the shouldered tube shank with $P/P_L = 0.5$ (the only other point within this boundary) is small. The $n/(n + 1)$ boundary approach is not a satisfactory design criterion for the circular plate which has already been

shown to have a significantly different cyclic behaviour to the other components. With the exception of the circular plate, it is suggested that the 'no creep' ratchetting boundary also provides a reasonable design criterion for the 'complete redistribution' ratchetting behaviour of the components using the simple methods of estimating steady and cyclic loads. Furthermore for the flanged tube, 'hole in plate' and shouldered tube the lines of constant ratchet strain for the 'no creep' case in Figure 7.1 are either conservative or very similar to the results obtained for the 'complete redistribution' case.

7.2.3.2.2 Cousseran analysis

The 'efficiency diagram' (Figure 2.12) suggested by Cousseran et al (50) and the proposed method for limiting accumulated inelastic strains are discussed in Section 2.2.2.2. To obtain the efficiency index, V , and the secondary stress ratio, SR , suggested by Cousseran et al in order to compare the correlated results on the 'efficiency diagram' the following data is required:

- (i) the primary stress;
- (ii) the secondary stress;
- (iii) the accumulated inelastic strain; and
- (iv) the test (computation) duration.

The primary and secondary stress have been obtained in the same way as the steady mechanical load and elastic thermal stress range parameters respectively used for the correlation of the component results on the basis of Bree's analysis discussed in the previous section. For regions of stress concentration no account is taken of the mechanical stress concentration factor in the definition of primary stress and the secondary stress is obtained by multiplying

the nominal value (based on a linear or 'equivalent' linear temperature distribution) by the thermal stress concentration factor.

An 'equivalent' secondary stress and thermal stress concentration factor is used for the beams and, in the absence of a thermal stress concentration factor for the 'hole in plate' component, the mechanical stress concentration factor is used. The secondary stress ratio is therefore,

$$SR = \frac{\frac{\sigma_t}{\sigma_y} \times SCF_{th}}{\frac{P}{P_L} + \frac{\sigma_t}{\sigma_y} \times SCF_{th}}$$

where the thermal stress concentration factor, SCF_{th} , is unity for the uniform regions of the tubes and beam and for the circular plate.

The efficiency index, V , is obtained by dividing the primary stress by an effective stress, σ_{eff} (see Section 2.2.2.2.2). In a normalised form

$$V = \frac{P/P_L}{\sigma_{eff}/\sigma_y}$$

The normalised effective stress, σ_{eff}/σ_y , is based on the normalised accumulated inelastic strain (ratchet plus dwell period strain) and the duration of the test and is obtained from the normalised isochronous stress-strain curves. An example of the normalised isochronous stress-strain curves for the material data used in the analysis of the flanged tube is shown in Figure 7.3. These curves have been constructed by adding the normalised creep strain for a time duration, t , and steady stress, σ_{eff} , (based on the assumed creep law) to the normalised elastic strain associated with σ_{eff} . The $t = 0$ curve is the normalised elastic-perfectly

plastic material stress/strain model used for all the components. For the correlation of the component results on the basis of the 'efficiency diagram', the accumulated inelastic strain in 10 cycles has been used to obtain the effective stress.

A method of determining effective stress is explained with the aid of Figure 7.4. For a given test duration, t' , the effective stress corresponding to an accumulation of inelastic strain, ϵ^{ine} , is obtained from a line drawn parallel to the elastic line.

It will be shown that, for an elastic-perfectly-plastic material assumption, the effective stress can be obtained analytically for both the 'no creep' and 'complete redistribution' conditions.

'No creep' condition

The test duration is taken as zero since there are no dwell periods between cycles and hence for any accumulation of inelastic strain the normalised effective stress is always unity. The normalised effective stress is therefore independent of the number of cycles being computed. The results for the components are given in Table 7.5 and correlated on the basis of the 'efficiency diagram' in Figure 7.5 which also includes the relevant results from the flanged tube shank study taken from Table 4.2. The notation is the same as that for the Bree correlation. For all cases where the steady state ratchet strains are non-zero, the results fall within the cloud of data points presented by Cousseran et al (see Figure 2.12). This is not necessarily the case when shakedown occurs. The similarity between this correlation of the results and the representation of the results on a Bree diagram is clear since the points which are inside the shakedown boundary in Figure 7.1 are also within the equivalent Bree line in Figure 7.5. el pl ✓

For a given efficiency index it is possible to define a lower and mean value for the secondary stress ratio using either the equivalent Bree line or a mean line through the cloud of data. The efficiency indices in Table 7.5 for the components have been used to determine lower and mean value estimates for the thermal stress range which are compared with the assumed thermal stress range in Table 7.6. For the 'no creep' case this method shows no distinction between shank and peak fillet estimates of thermal stress range also the estimates vary with mean load. The discrepancies between the estimated and assumed thermal stress ranges reflect the positions of the data points in Figure 7.5 compared with the equivalent Bree line and the cloud of data points in Figure 2.12.

'Complete redistribution'

The test duration is taken as 10 x the dwell period since the accumulation of inelastic strains in 10 cycles is being used for the correlation. For the elastic-perfectly-plastic material assumption used, the method of evaluating effective stress from the isochronous curves proposed by Cousseran et al can be reduced to an analytical solution based on normalised inelastic strain, $\epsilon^{ine}/\epsilon_y$, and test duration, t. The inelastic strain is identical to the creep strain that would be accumulated in a uniaxial test at the effective stress for the same time duration. For the creep law used in the analysis

$$\epsilon^{ine} = A \sigma_{eff}^n t$$

and hence

$$\sigma_{eff}^n = \frac{\epsilon^{ine}}{At}$$

Therefore the normalised effective stress is given by:-

$$\frac{\sigma_{\text{eff}}}{\sigma_y} = \left[\frac{\epsilon^{\text{ine}}/\epsilon_y}{\frac{AE}{t} \sigma_y^{n-1}} \right]^{1/n}$$

The results for the components are given in Table 7.5 and correlated on the 'efficiency diagram' in Figure 7.6. The results fall within a band which is similar to the cloud of data in Figure 2.12 although some of the results, typically those for the stress concentrations, appear to be above that cloud. This is a possible indication of pessimism in evaluating peak thermal stress using a thermal stress concentration factor since a reduction in thermal stress would reduce the secondary stress ratio for these data points. For this 'pessimistic' thermal stress, the effective stress and, hence, accumulated inelastic strain estimate using a 'mean' line through the cloud of data is higher than the value predicted by the finite element method. The estimated lower and mean values of thermal stress range, obtained by the method described in the previous section, are compared with the assumed values in Table 7.6. The estimated values are generally low and vary with mean load. The estimates are low because the actual data points in Figure 7.6 are generally above a mean line through the cloud of data.

7.2.4 Dwell period strains

The dwell period behaviour for all components and loadings is found to be similar. When dwell period strains are plotted against time function, the response shows two distinct stages:-

- (i) an initial non-linear behaviour while stress redistribution occurs; and
- (ii) a steady state condition, once stress redistribution is complete, where additional dwell period strains are due to creep alone and linearly related to time function.

The dwell period behaviour can be characterised by three parameters:

- (i) the normalised increments of strain due to stress redistribution during the first dwell period, $(\Delta \epsilon^d / \epsilon_y)_1$;
- (ii) the normalised increments of strain due to stress redistribution during the second and subsequent dwell periods, $(\Delta \epsilon^d / \epsilon_y)_{\text{steady state}}$; and
- (iii) the steady state strain rate, $d(\epsilon^d / \epsilon_y) / d\Gamma$, which is the same for each dwell period.

A summary of these parameters for all the components and loadings considered is given in Tables 7.2 and 7.3.

For regions of uniform stress, the stress distribution at the end of each cycle is identical and the increments of strain due to stress redistribution during each dwell period are the same. In regions of stress concentration, the stress distribution at the end of the second and subsequent cycles is the same and different to the first cycle and equal increments of strain due to stress redistribution are accumulated during each dwell period after the first.

7.2.4.1 Steady state strain rates

In uniform regions it has been shown in Section 4.2.4.2.1 that the steady state strain rate is equal to the normalised mean load, P/P_L and hence the normalised steady state strain rates, $(d(\epsilon_x/\epsilon_y)/d\Gamma)/P/P_L$, are unity.

In the fillet regions of the tubes and beams and the peak ratchetting position of the 'hole in plate' component and circular plate the normalised steady state strain rates are independent of steady and cyclic loads. For the tubes and beam, the normalised steady state strain rates at the 'peak fillet' position are the same as (beam) or less than (tubes) the equivalent shank values. For the stepped beam with $P/P_L = 0.5$ and $M/M_y = \pm 1.05$, the difference between first tensile surface and first compressive surface normalised steady state strain rates in the fillet is a possible indication that redistribution was not complete particularly since these values differ from those for $P/P_L = 0.7$ and $M/M_y = \pm 0.7$. The normalised steady state strain rates can often be determined using the simple reference stress approach or the O'Donnell and Porowski method (6).

7.2.4.2 Normalised increments of strain due to stress redistribution

From Table 7.2, the normalised increments of strain due to stress redistribution are seen to be small (less than, and in most cases very much less than, 0.84) and in some cases negative. Also the first and steady state dwell period values are either identical (uniform sections) or very similar (non-uniform stress distribution where the maximum difference occurs in the circular plate and is 0.169).

7.3 Material Hardening Model (Flanged Tube and Stepped Beam)

The presence of material work hardening has a significant effect on component ratchetting and creep behaviour when compared with observations in the previous sections for an elastic-perfectly-plastic material model. This section reviews the results for the flanged tube and stepped beam with a material hardening model and compares the behaviour with that already described for an elastic-perfectly-plastic material model.

7.3.1 Ratchetting mechanisms

A steady state ratchetting condition is not reached due to the increase in yield stress. 3 categories of behaviour are noted.

- (i) first cycle mechanism (as described in Section 7.2.2.1);
- (ii) continuous transient, 'no creep' mechanism; and
- (iii) continuous transient, complete redistribution mechanism.

7.3.1.1 Transient 'no creep' mechanism

The 'plastic core' requirement for ratchetting in both uniform regions and stress concentrations described in Section 7.2.2.2 is applicable. The development of the plastic zones in the flanged tube and stepped beam is very similar to that described in Section 7.2.2.2; however due to hardening the size of the 'plastic core' reduces between successive cycles and ratchetting stops when the 'plastic core' disappears. For isotropic hardening further cycling is within the elastic range. For kinematic hardening either elastic range cycling or a stable cyclic loop is reached, depending on loading conditions.

7.3.1.2 Transient complete redistribution mechanism

Although the stationary state stress distribution is achieved after each cycle, the increase in yield stress is comparable to a

reduction in the severity of the subsequent cycle and there is a reduction in ratchet strain. A 'plastic core' is not essential for an increment of ratchet strain to be accumulated in a cycle. Isotropic and kinematic hardening models predict the same 'shakedown' behaviour to those discussed in Section 7.3.1.1.

7.3.2 Ratchet and dwell period strains

The predictions of ratchet and dwell period strains accumulated in the shanks of the flanged tube and stepped beam with work hardening material models have been described in detail in Sections 4.2 and 5.2 respectively. Some results for the stress concentration regions of the flanged tube (Sections 4.3.5.1.2 and 4.3.5.3) and stepped beam (Section 5.3.5.1.2) are also given. In this section, the accumulated inelastic strain results are compared on the 'efficiency diagram' (50).

For the flanged tube shank and peak fillet results, the secondary stress ratio, SR, is obtained by the method described in Section 7.2.3.2.2. The equivalent thermal stress range obtained for the stepped beam with an elastic-perfectly-plastic material model and described in Section 7.2.3.2.1 is based on a change in curvature during a cycle which does not vary with cycle number. This condition does not apply when the material hardens as can be seen for the example in Figure 7.7. The cyclic curvature range reduces and only achieves a constant value when ratchetting ceases. For this reason the stepped beam results are not included.

7.3.2.1 'No creep' condition

Figure 7.8 shows an example of the normalised isochronous stress-strain curves for a hardening material. For the 'no creep' condition ($t = 0$ curve) the normalised effective stress, $\sigma_{\text{eff}}/\sigma_y$,

for a normalised accumulated inelastic strain, $\varepsilon^{ine}/\varepsilon_y$, is given by:-

$$\frac{\sigma_{eff}}{\sigma_y} = \frac{\varepsilon^{ine}/\varepsilon_y}{(E/E_p - 1)} + 1$$

The flanged tube results are given on the 'efficiency diagram' in Figure 7.9. In most cases, the results fall within the cloud of data points presented by Cousseran et al (see Figure 2.12), the exception being the low mechanical load results from the flanged tube shank study (i.e. $V = 0.3$) where shakedown occurs in one or two cycles.

7.3.2.2 Ratchetting with creep

From Figure 7.8 it can be seen that two possible expressions for σ_{eff}/σ_y can be used depending on the accumulated inelastic strain:-

i.e. (i) if $\varepsilon^{ine} < A \sigma_y^{n_t m}$, $\varepsilon^{ine} = A \sigma_{eff}^{n_t m}$

$$\text{and } \frac{\sigma_{eff}}{\sigma_y} = \left[\frac{\varepsilon^{ine}/\varepsilon_y}{AE \sigma_y^{n-1} t^m} \right]^{1/n}$$

or (ii) if $\varepsilon^{ine} > A \sigma_y^{n_t m}$, $\varepsilon^{ine} = A \sigma_{eff}^{n_t m} +$

$$\frac{(\sigma_{eff} - \sigma_y)(E/E_p - 1)}{E}$$

$$\text{and } \varepsilon^{ine}/\varepsilon_y = AE \sigma_y^{n-1} t^m \left(\frac{\sigma_{eff}}{\sigma_y} \right)^n + \left(\frac{\sigma_{eff}}{\sigma_y} - 1 \right) \left(\frac{E}{E_p} - 1 \right)$$

which can be solved iteratively for σ_{eff}/σ_y .

The results are given on the 'efficiency diagram' in Figure 7.10.

Since the accumulated inelastic strain results from the flanged

tube shank survey with complete redistribution (using a high stress index) are dominated by the dwell period strains, which are in turn dominated by the steady state strain rate components, the normalised effective stress is slightly larger than the mean load, P/P_L , and the efficiency index is almost unity. The results do not fall within the Cousseran cloud of data points. Alternatively, the results for the flanged tube with 24 and 120 hour dwell periods, previously discussed in Section 4.3.5.3, compare well with the cloud of data points in Figure 2.12.

7.4 Effects of Partial Redistribution on Ratchet and Dwell

Period Strains

The discussion in the previous sections has been based on the results for the 'no creep' and 'complete redistribution' cases. The results for the 'complete redistribution' case are independent of time index. This section gives a brief summary of the likely behaviour of the components when stress redistribution between cycles is only partial and when a realistic time index is used. The relevant flanged tube results from Section 4.3.5.3 are referenced. For uniform regions of the tubes and beams, the residual stress field at the end of each cycle is modified during the dwell period but does not return to the constant stress field associated with the mean load. After a finite number of dwell periods, greater than one, a steady state residual stress field condition will be reached and from then on both ratchet strains and dwell period strains will be the same for each subsequent cycle and dwell period. This is indicated for the flanged tube from Figures 4.48 and 4.50.

For the 'peak fillet' positions of the tubes and beam and for the 'hole in plate' and circular plate components, the

residual stress field at the end of each cycle is modified during the dwell period but does not return to the stationary state stress distribution. Again a steady state condition of constant ratchet and dwell period strains is reached after a finite number of cycles and can be seen for the flanged tube component in Figure 4.48.

The ratchet and creep strains under conditions of partial redistribution are bounded by the 'no creep' and 'complete redistribution' cases. The proximity of the results to the bounds depends on the degree of redistribution (i.e. the length of the dwell period).

Table 7.1: Thermal and Mechanical Loading Conditions (Elastic-perfectly-plastic)

Component	Fo ($kt_c / \rho C_p L^2$)	Bi (hL/k)	$\frac{P}{P_L}$	Nominal elastic thermal stress $\div \sigma_y$	Thermal stress concentration factor	Mechanical stress concentration factor
Flanged Tube	0	12.87	0.5, 0.7	1.94	1.81	1.53
Stepped Beam	not applicable	not applicable	0.5	2.58	1.46	1.80
			0.7	2.51	1.46	1.80
Hole in Plate	0.08	∞	0.5, 0.7	1.37	-	2.43
Circular Plate	12.27	∞	0.295, 0.4 0.474 & 0.7	1.41	not applicable	not applicable
Shouldered Tube	0.11	15.80 (Bore) 19.15 (outside shank & fillet)	0.5, 0.7	1.42	1.96	1.59
		9.39 (outside shoulder)	0.5	2.83	1.96	1.59

Table 7.2 Summary of Flanged Tube, 'Hole-in-Plate', Circular Plate and Shouldered Tube results (Elastic-perfectly-plastic)

Component	$\frac{P}{P_L}$	Position	Normalised Ratchet Strain per Cycle ($\Delta\epsilon^r/\epsilon_y$)					$\frac{d(\epsilon^d/\epsilon_y)}{d\Gamma}$	$\frac{d(\epsilon^d/\epsilon_y)/d\Gamma}{\frac{P}{P_L}}$	$\Delta\epsilon^d/\epsilon_y$	
			1st cycle	No creep		Complete redistribution				1st cycle	Steady state
				Steady state	Characteristic behaviour	Steady state	Characteristic behaviour				
Flanged Tube	0.5	shank	0.048	0	B	0.044	A	0.527	1.054	0.110	0.110
		peak fillet	0.361	0	C(4)	0.275	B	0.350	0.701	0.250	0.176
Tube	0.7	shank	0.107	0.060	B	0.109	A	0.742	1.060	0.132	0.132
		peak fillet	0.852	0.128	C(6)	0.608	B	0.521	0.743	0.150	0.088
Hole-in plate	0.5	peak	1.902	0.015	C(5)	1.071	B	1.534	3.069	-0.183	-0.144
	0.7	peak	3.312	1.737	B	2.441	B	2.169	3.099	-0.371	-0.481
Circular Plate	0.295	outside edge	1.503	0	B	1.225	B	0.474	1.607	0.093	-0.024
	0.4	outside edge	2.871	0	B	2.356	B	0.643	1.607	0.091	-0.078
	0.474	outside edge	3.924	0	C(3)	3.293	B	0.769	1.623	0.077	-0.044
	0.7	outside edge	7.712	1.078**	C(10)**	7.270	B	1.075	1.536	-0.156	-0.212
Shouldered Tube $(\frac{\sigma_t}{\sigma_y} = 1.42)$	0.5	shank	0.109	0	B	0.108	A	0.495	0.990	0.207	0.207
		peak fillet	1.648	0.012	C(4)	1.518	B	0.259	0.518	0.425	0.400
	0.7	shank	0.235	0	B	0.239	A	0.704	1.006	0.262	0.262
		peak fillet	2.304	0.082	C(5)	2.127	B	0.372	0.531	0.541	0.518
Shouldered Tube $(\frac{\sigma_t}{\sigma_y} = 2.83)$	0.5	shank	0.685	0.187	B	0.686	A	0.504	1.008	0.740	0.740
		peak fillet	3.701	1.558	B	3.748	B	0.269	0.538	0.817	0.841

** Values quoted are 10th cycle ratchet strains. After 10 cycles the ratchet strain per cycle was still reducing.

Table 7.3 Summary of Stepped Beam Results (Elastic-perfectly-plastic)

$\frac{P}{P_L}$	$\frac{M}{M_y}$	Position	Normalised Ratchet Strain per Cycle				$\frac{d(\epsilon^d/\epsilon_y)}{d\Gamma}$	$\frac{d(\epsilon^d/\epsilon_y)d\Gamma}{P/P_L}$	$\Delta\epsilon^d/\epsilon_y$			
			1st cycle	No creep		Complete redistribution			1st cycle	Steady state		
				Steady state	Characteristic behaviour	Steady state					Characteristic behaviour	
0.5	± 1.05	FT	2.175	0.555	B	2.204	A	0.502	1.004	0.302	0.302	
		shank {										
		FC	-0.010	0.555	B	-0.031	A	0.500	1.000	0.218	0.218	
		fillet {										
		FT	3.293	0.322	B	2.417	B	0.479	0.959*	0.159	0.154	
		FC	1.573	0.322	B	1.040	B	0.410	0.819*	0.217	0.209	
0.7	± 0.7	FT	2.611	1.500	B	2.613	A	0.700	1.000	0.237	0.237	
		shank {										
		FC	1.175	1.500	B	1.182	A	0.699	0.998	0.079	0.079	
		fillet {										
		FT	3.973	1.025	B	2.902	B	0.704	1.005	0.077	0.116	
		FC	1.335	1.025	B	1.347	B	0.718	1.026	-0.040	-0.041	

FT - first tensile surface * redistribution possibly not complete

FC - first compressive surface

Component	Symbol		
	Shakedown	Ratchetting	
Flanged tube	shank	○	●
	peak fillet	□	■
Stepped beam	shank	×	✕
	peak fillet	+	➤
'Hole-in-plate'		▷	▶
Circular plate		◇	◆
Shouldered tube	shank	▽	▼
	peak fillet	△	▲

Table 7.4 Notation used in Figures 7.1, 7.2, 7.5 and 7.6.

Table 7.5 Evaluation of parameters for Cousseran diagram (elastic-perfectly-plastic)

Component	$\frac{\sigma_t}{\sigma_y}$	$\frac{P}{P_L}$	Position	(SCF) _{th}	SR	'No Creep'				Complete Redistribution			
						$\frac{\epsilon^R}{\epsilon_y}$ in 10 cycles	Duration (hrs)	$\frac{\sigma_{eff}}{\sigma_y}$	ν	$\frac{\epsilon^{ine}}{\epsilon_y}$ in 10 cycles	Duration (hrs)	$\frac{\sigma_{eff}}{\sigma_y}$	ν
Flanged tube	1.94	0.5	Shank	-	0.795	0.048	0	1.0	0.5	29.806	5,000	0.581	0.861
			Peak fillet	1.81	0.875	0.450	0	1.0	0.5	23.196	5,000	0.561	0.891
		0.7	Shank	-	0.735	0.647	0	1.0	0.7	15.632	200	0.826	0.847
			Peak fillet	1.81	0.834	2.492	0	1.0	0.7	16.539	200	0.833	0.840
Stepped beam	2.58	0.5	Shank	-	0.838	7.170*	0	1.0	0.5	30.485*	10,000	0.723	0.692
			Peak fillet	1.46	0.883	6.191*	0	1.0	0.5	31.741*	10,000	0.727	0.688
	2.51	0.7	Shank	-	0.782	16.111*	0	1.0	0.7	91.625*	10,000	0.841	0.832
			Peak fillet	1.46	0.840	13.198*	0	1.0	0.7	95.155*	10,000	0.845	0.828
'Hole in plate'	1.37	0.5	Peak	2.43	0.869	2.250	0	1.0	0.5	43.913	20,000	0.691	0.724
		0.7	Peak	2.43	0.826	18.945	0	1.0	0.7	119.328	5,000	0.958	0.731
Circular plate	1.41	0.295	Outside edge	-	0.827	1.503	0	1.0	0.295	31.188	900,000	0.392	0.753
		0.4	Outside edge	-	0.779	2.871	0	1.0	0.4	66.802	150,000	0.556	0.719
		0.474	Outside edge	-	0.748	4.084	0	1.0	0.474	63.492	50,000	0.642	0.738
		0.7	Outside edge	-	0.668	21.335	0	1.0	0.7	169.531	10,000	0.915	0.765
Shouldered tube	1.42	0.5	Shank	-	0.740	0.109	0	1.0	0.5	19.337	50,000	0.585	0.855
			Peak fillet	1.96	0.848	1.820	0	1.0	0.5	27.795	50,000	0.615	0.813
	0.7	Shank	-	0.670	0.235	0	1.0	0.7	27.993	6,000	0.823	0.851	
		Peak fillet	1.96	0.799	3.455	0	1.0	0.7	39.235	6,000	0.862	0.812	
2.83	0.5	Shank	-	0.850	2.368	0	1.0	0.5	17.585	500,000	0.767	0.652	
		Peak fillet	1.96	0.917	17.723	0	1.0	0.5	28.445	500,000	0.819	0.611	

* Max surface values

Component	$\frac{P}{P_L}$	Position	$\frac{\sigma_t}{\sigma_y}$ used	Estimated σ_t/σ_y			
				'No creep'		Complete Redistribution	
				Lower	Mean	Lower	Mean
Flanged Tube	0.5	Shank	1.94	2.00	3.07	0.32	0.69
		Peak Fillet	3.51	2.00	3.07	0.24	0.59
	0.7	Shank	1.94	1.17	2.10	0.48	1.00
		Peak Fillet	3.51	1.17	2.10	0.53	1.05
Stepped Beam	0.5	Shank	2.58	2.00	3.07	0.80	1.50
		Peak Fillet	3.77	2.00	3.07	0.79	1.46
	0.7	Shank	2.58	1.17	2.10	0.56	1.09
		Peak Fillet	3.77	1.17	2.10	0.53	1.07
'Hole-in-plate'	0.5	Peak	3.33	2.00	3.07	0.75	1.29
	0.7	Peak	3.33	1.17	2.10	1.05	1.82
Circular Plate	0.295	Outside Edge	1.41	3.18	5.07	0.38	1.00
	0.4	Outside Edge	1.41	2.46	4.04	0.62	1.08
	0.474	Outside Edge	1.41	2.05	3.32	0.65	1.16
	0.7	Outside Edge	1.41	1.17	2.10	0.86	1.56
Shouldered Tube	0.5	Shank	1.42	2.00	3.07	0.33	0.70
		Peak Fillet	2.78	2.00	3.07	0.44	0.85
	0.7	Shank	1.42	1.17	2.10	0.47	0.98
		Peak Fillet	2.78	1.17	2.10	0.62	1.19
	0.5	Shank	2.83	2.00	3.07	1.02	1.77
		Peak Fillet	5.55	2.00	3.07	1.22	2.06

Table 7.6 Comparison between assumed thermal stresses and estimated thermal stresses from the Cousseran diagram.

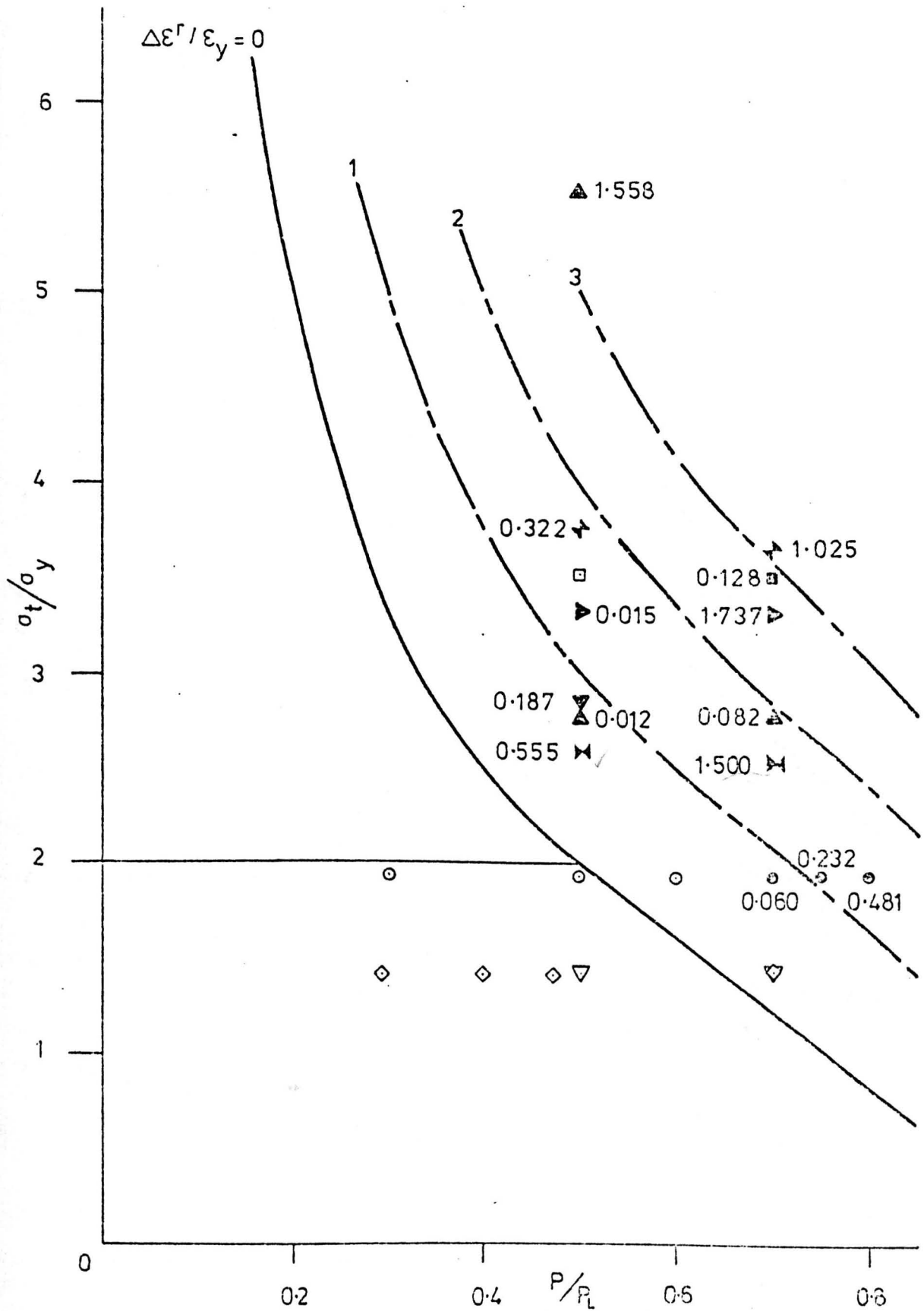


Figure 7.1 All 5 components (elastic-perfectly-plastic, 'no creep' conditions). Correlation of steady state ratchetting behaviour on a Bree diagram (see Section 7.4.2.1 and Table 7.4 for notation).

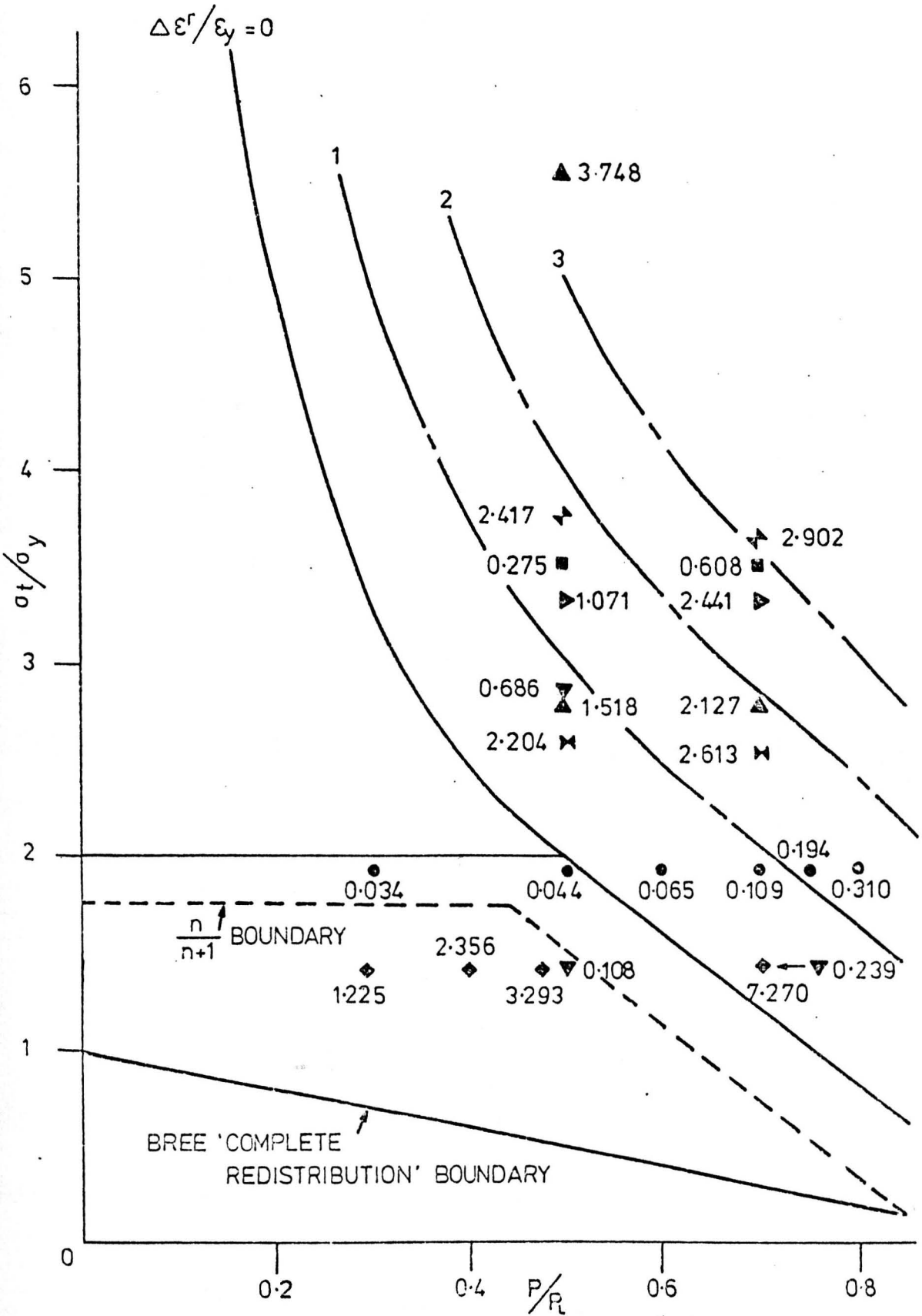


Figure 7.2 All 5 components (elastic-perfectly-plastic, complete redistribution). Correlation of steady state ratchetting behaviour on a Bree diagram (see Section 7.4.2.1 and Table 7.4 for notation).

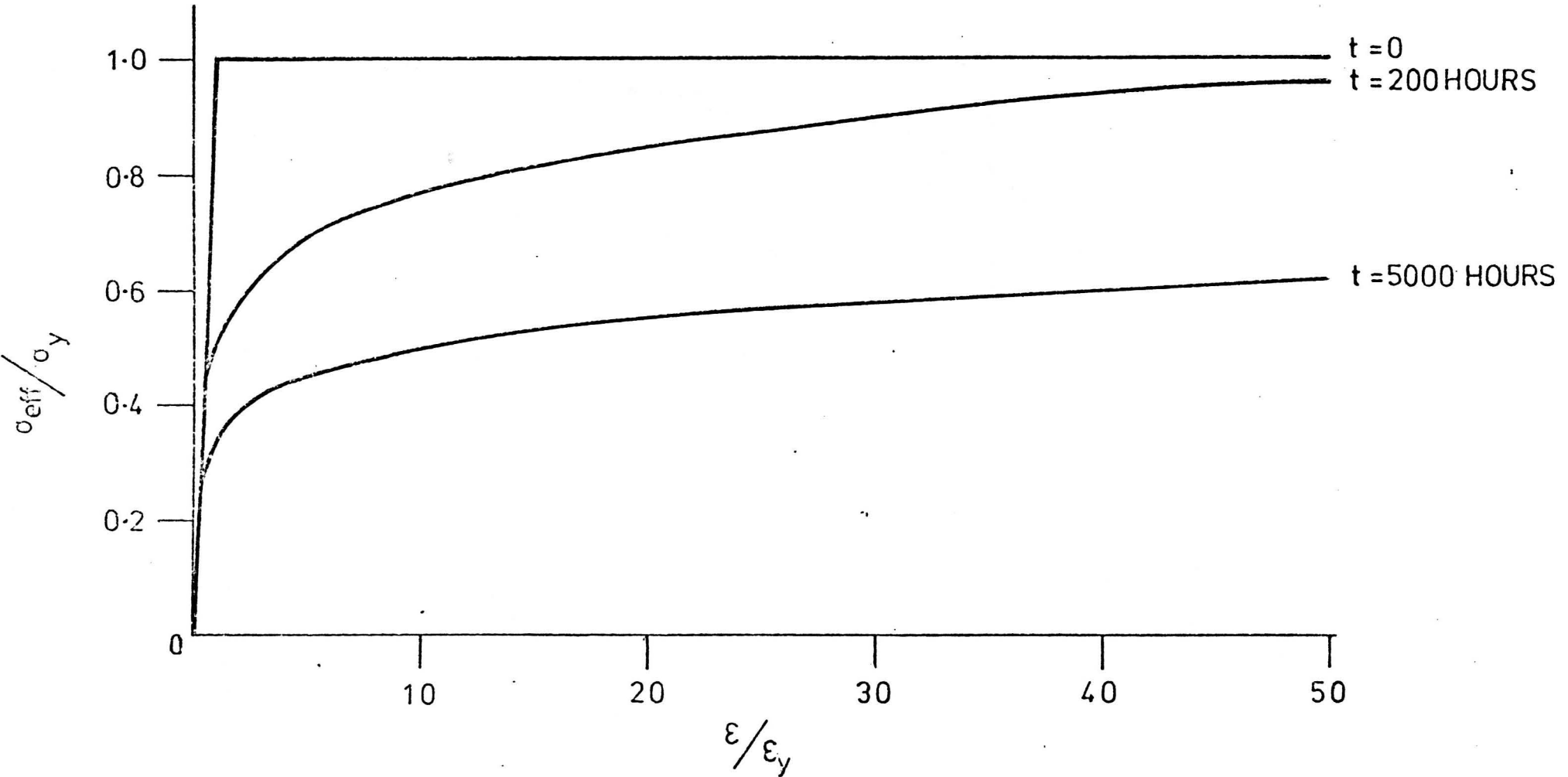


Figure 7.3 An example of the normalised isochronous stress-strain curves for the elastic-perfectly-plastic material data used in the flanged tube analysis.

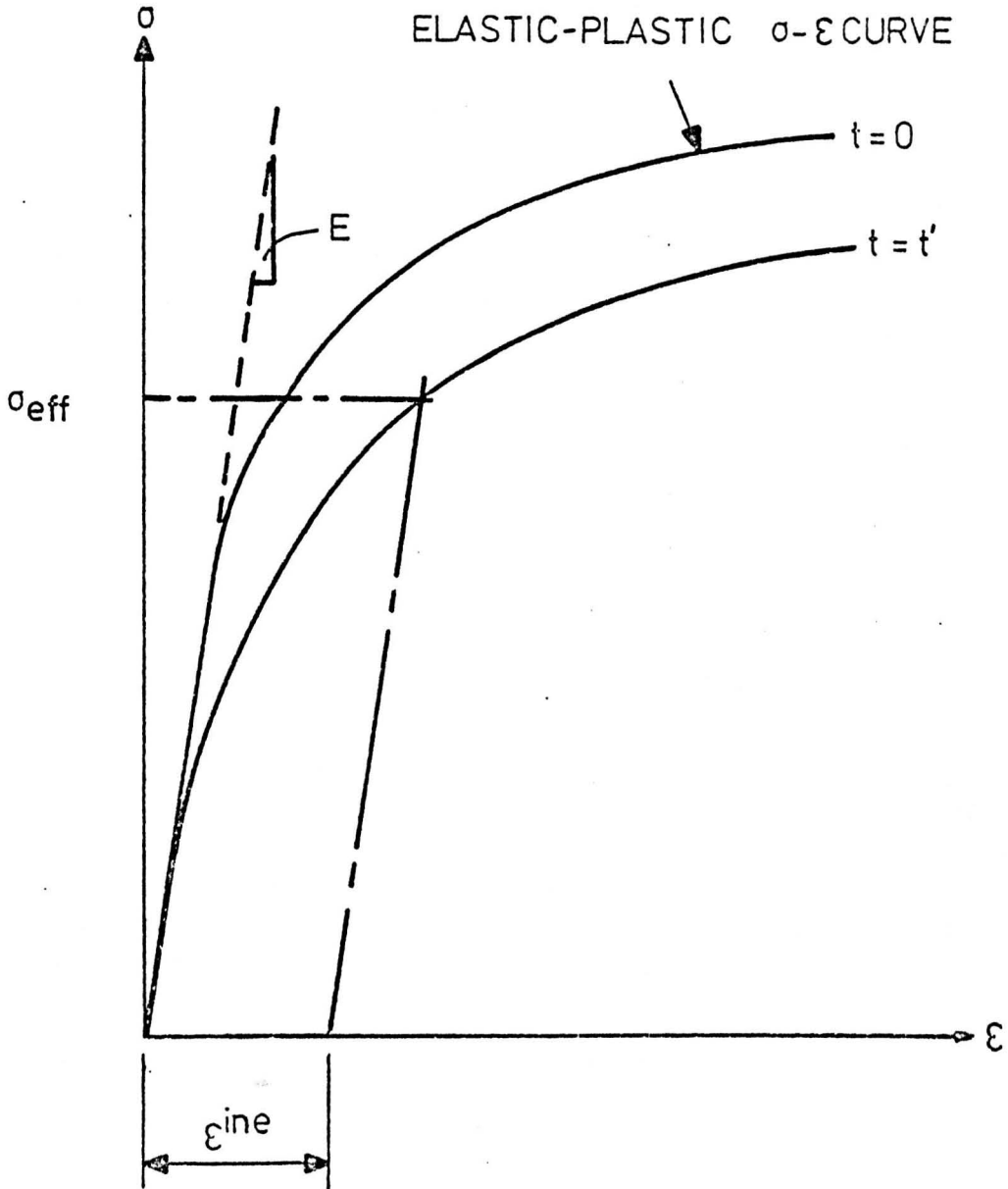


Figure 7.4 An example of the method used to determine the 'effective stress' in a Cousseran analysis.

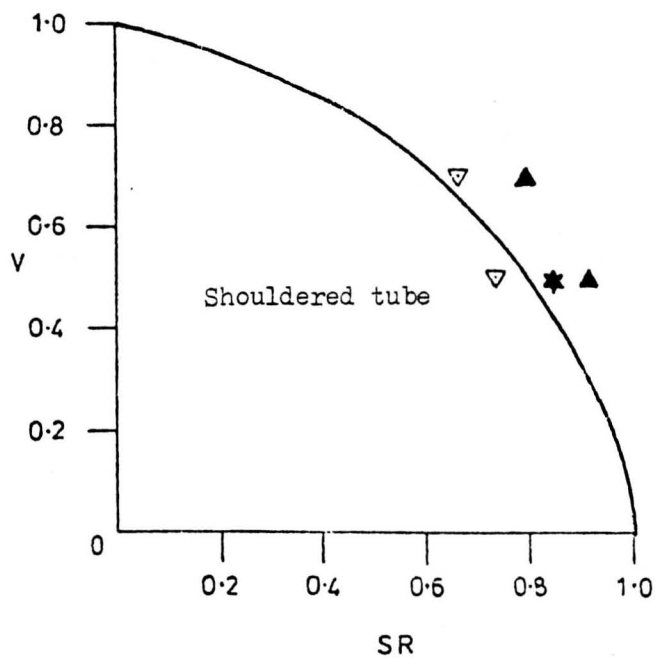
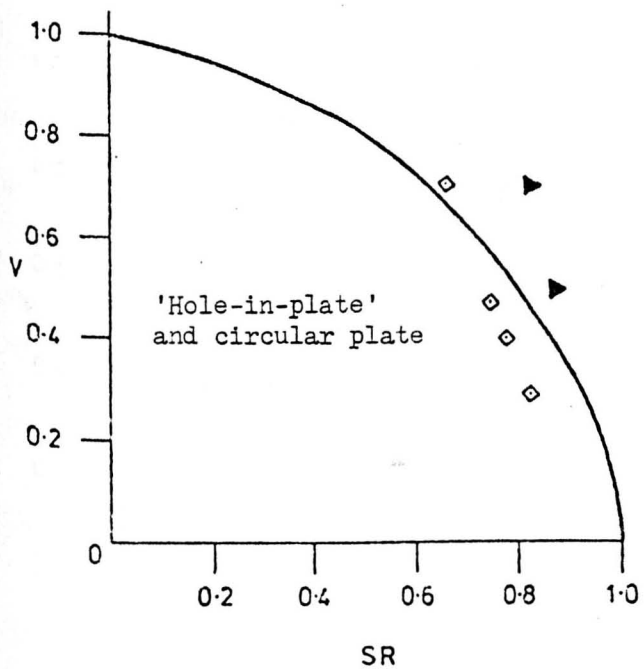
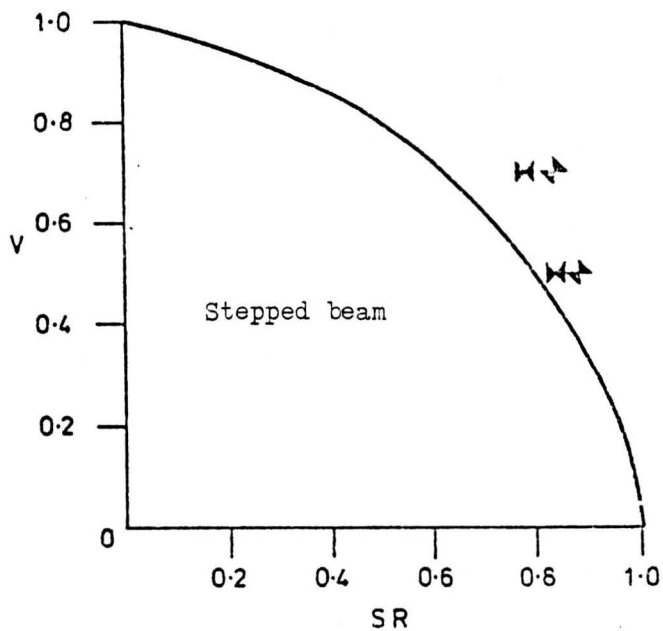
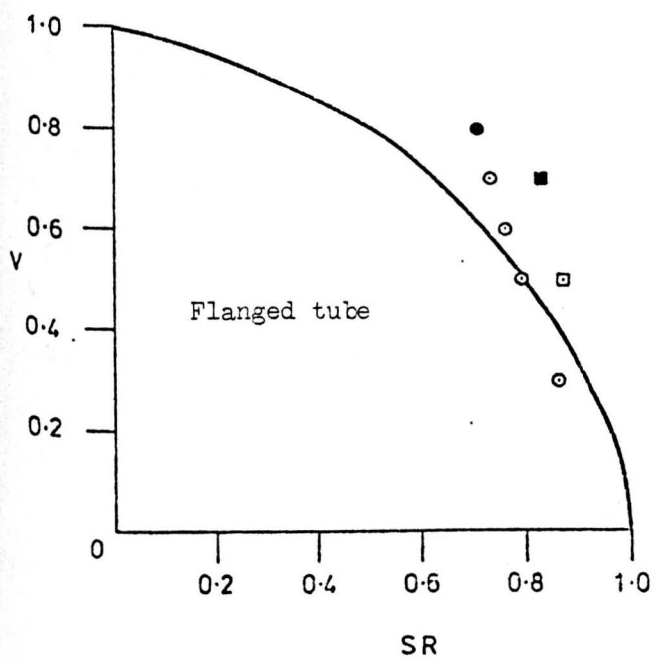


Figure 7.5 All 5 components (elastic-perfectly-plastic, 'no creep' conditions). Correlation of ratchetting behaviour on an Efficiency Diagram. (see Table 7.4 for notation).

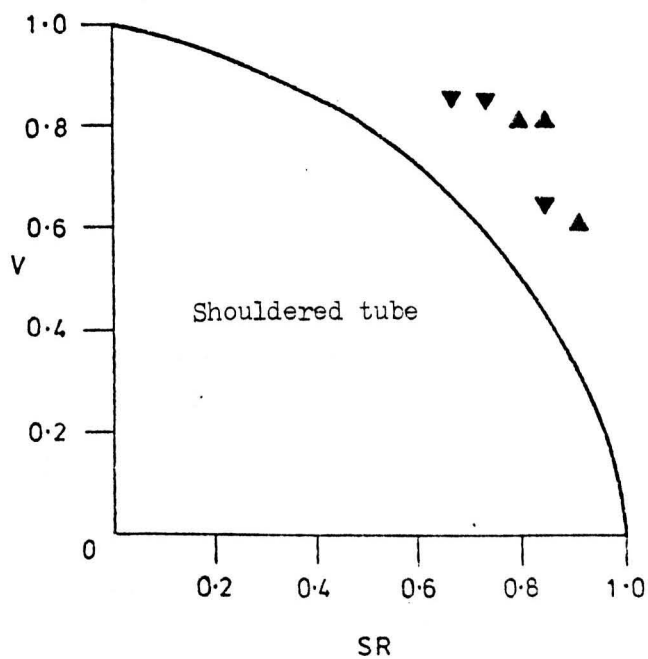
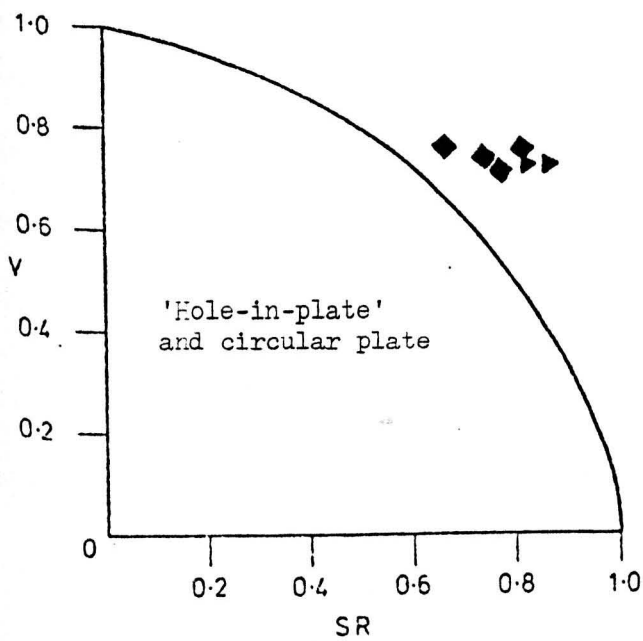
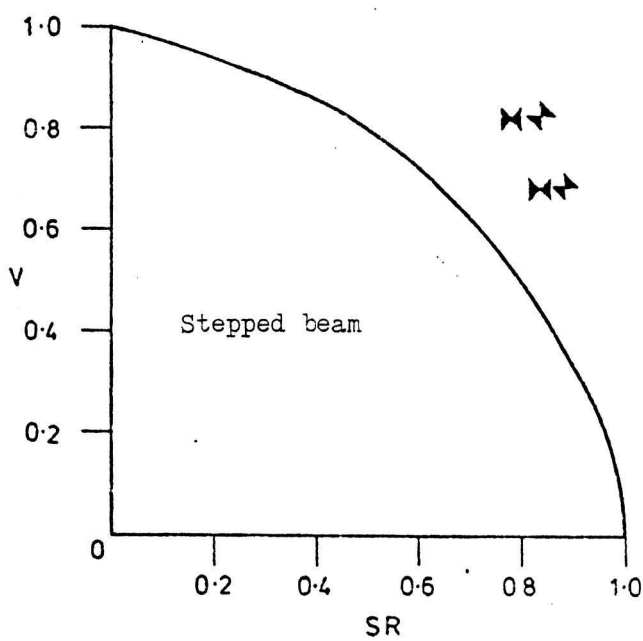
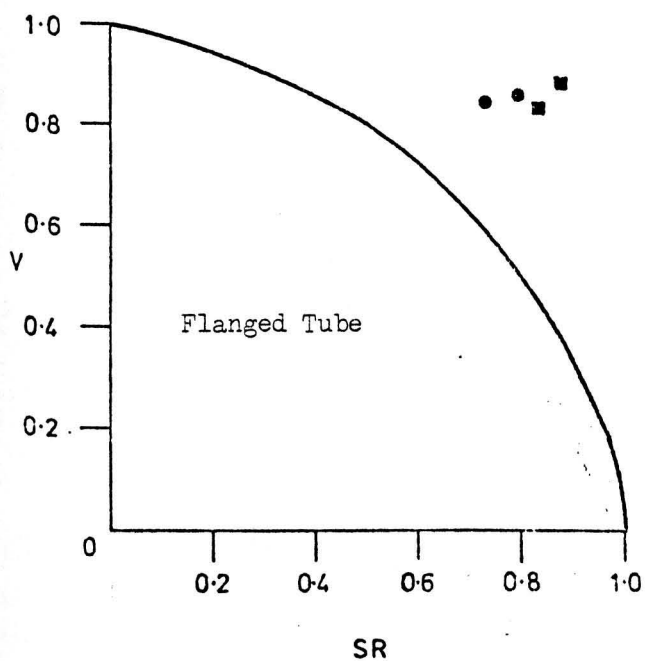


Figure 7.6 All 5 components (elastic-perfectly-plastic, complete redistribution). Correlation of ratchetting behaviour on an Efficiency Diagram (see Table 7.4 for notation).

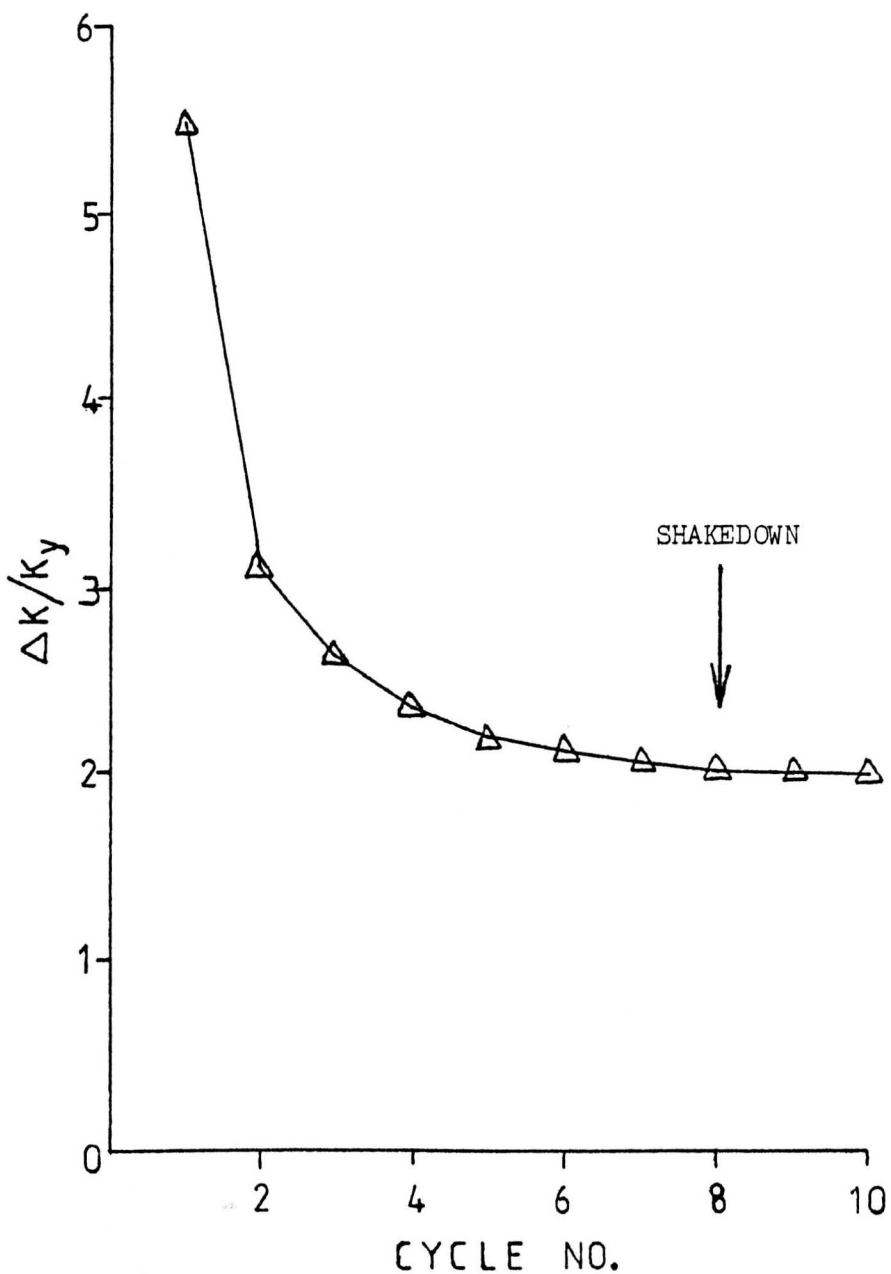


Figure 7.7 Stepped beam shank (Kinematic hardening, $E_p/E = 0.05$, $M/M_y = 1.0$, $P/P_L = 0.8$, 'no creep' conditions). Variation in normalised cyclic curvature range during the first 10 cycles.

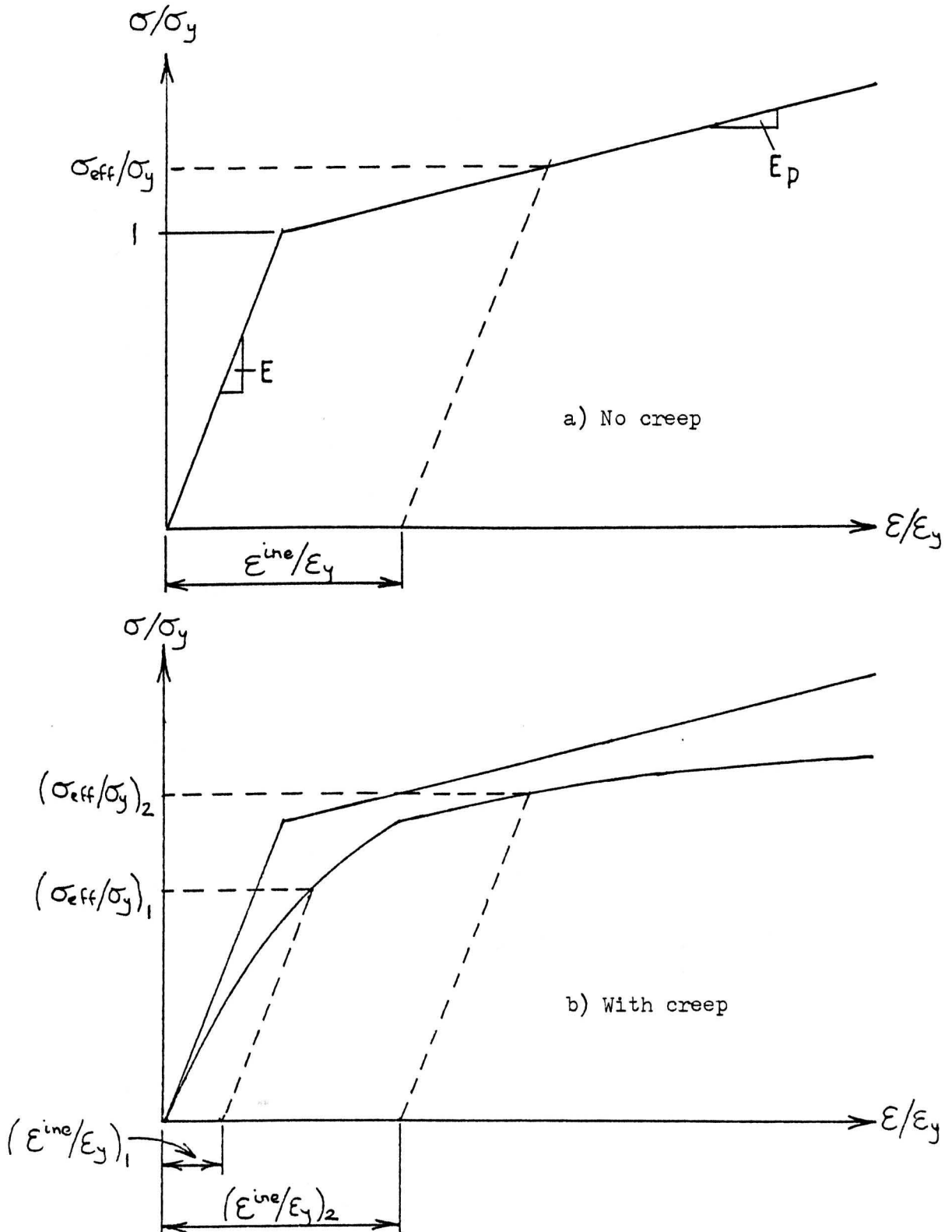
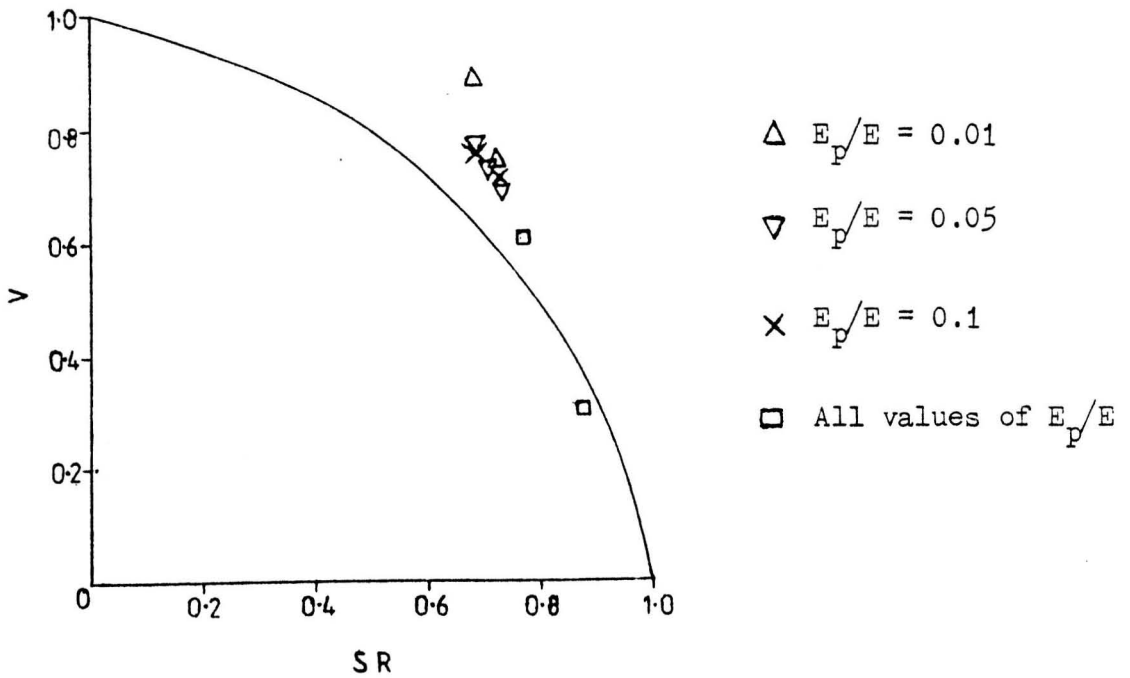
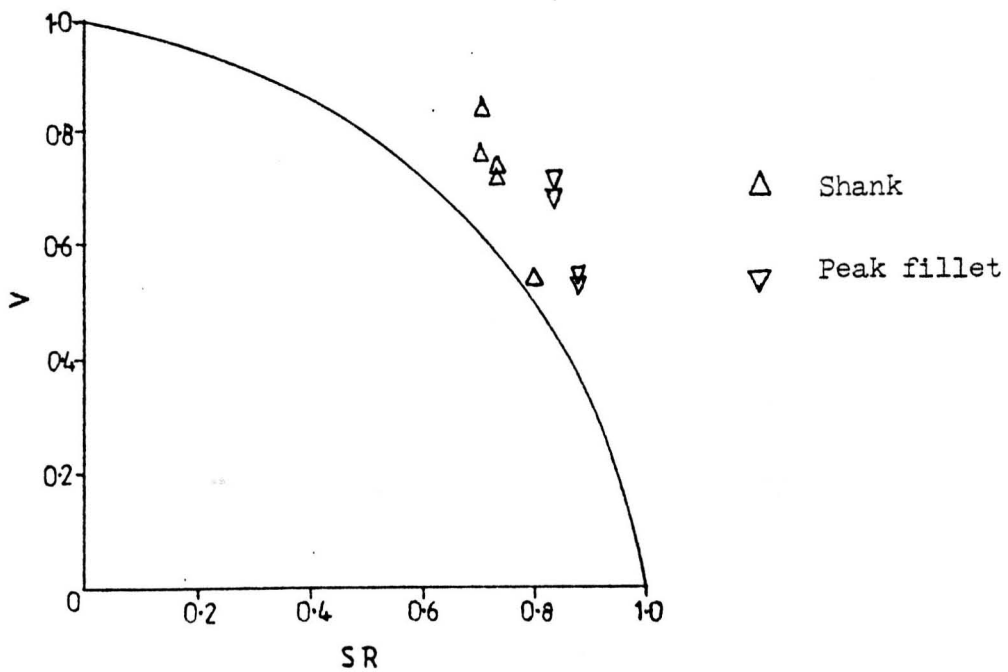


Figure 7.8 An example of the normalised isochronous stress-strain curves for a work hardening material.

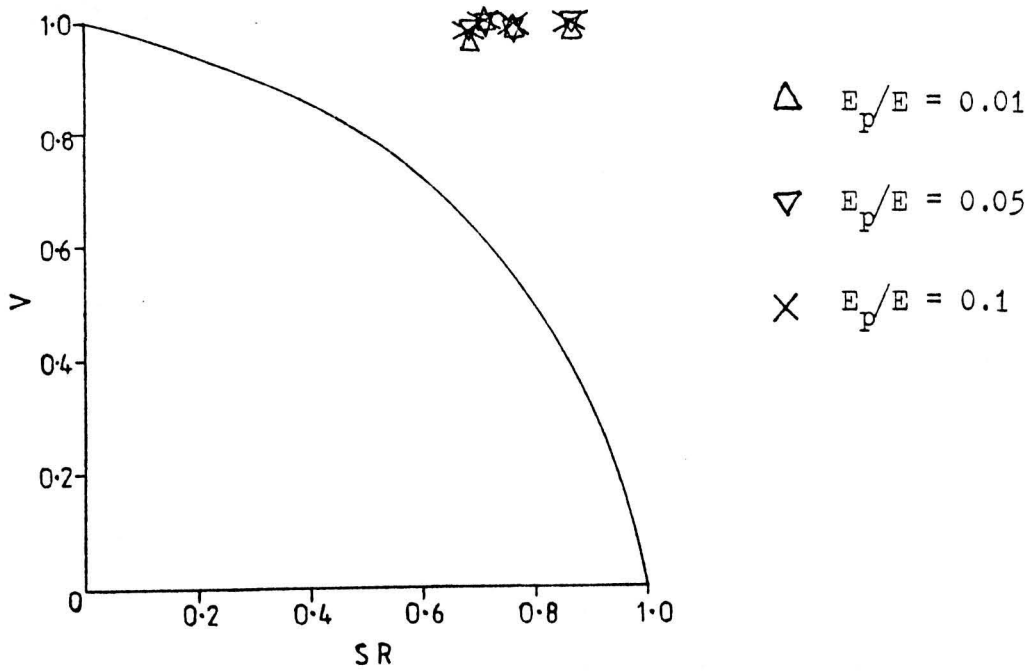


a) Shank study results.

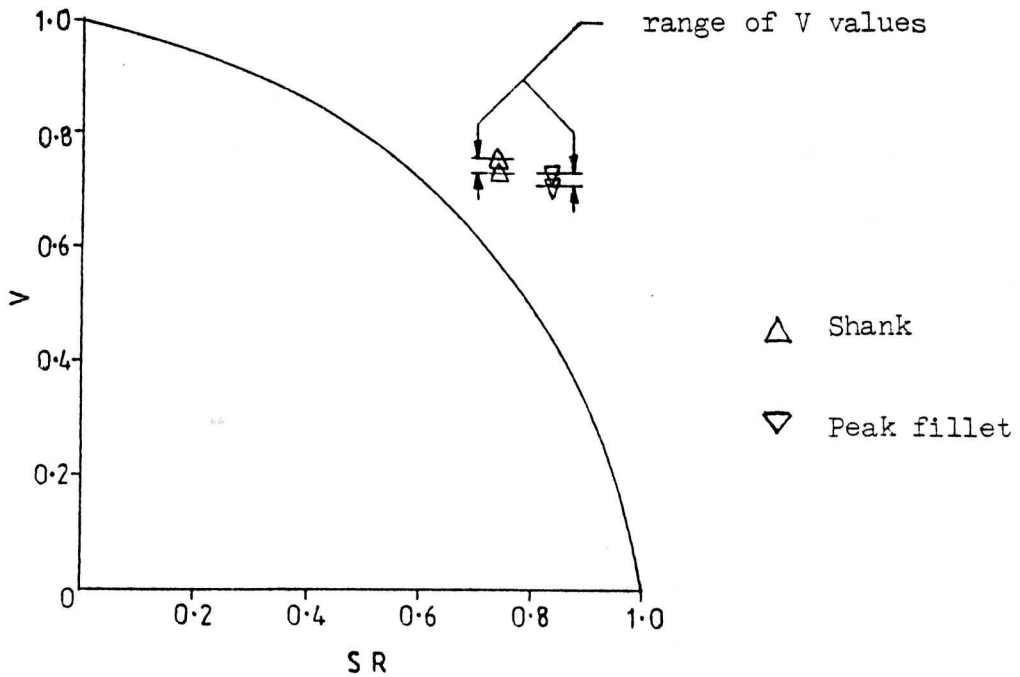


b) Whole component analysis results.

Figure 7.9 Flanged tube (material hardening, 'no creep' conditions). Correlation of the ratchetting behaviour on an Efficiency Diagram.



a) Shank study results (complete redistribution)



b) Whole component analysis results (24 and 120 hour dwell periods).

Figure 7.10 Flanged tube (material hardening, ratchetting with creep). Correlation of the ratchetting behaviour on an Efficiency Diagram.

CHAPTER EIGHT

8. DISCUSSION

8.1 Introduction

Potential problems of ratchetting with creep can be identified in components in conventional and nuclear power plant, chemical plant and aero engines. The design of components which are likely to experience severe loading conditions should include an assessment of the likelihood and effects of ratchetting.

Four main assessment techniques are:-

1. Experimental tests on actual components with loadings and temperatures typical of 'in service' conditions.
2. Model testing.
3. Finite element predictions.
4. Approximate analytical solutions.

A major disadvantage of experimental tests under 'in service' conditions is the high cost of rig manufacture for generally high operating temperatures and the difficulty in measuring deformations under experimental test conditions. Also long 'in service' timescales may inhibit the amount of useful information that can be obtained in an experimental test of limited duration.

Model materials such as lead and copper have been used to investigate the ratchetting and creep behaviour of components. These materials have relatively low melting temperatures and creep at temperatures which can be achieved experimentally at reasonable cost and at which measurements of deformation can be obtained with relative ease. Although, in some cases, the results from model testing may be used directly to predict the behaviour of actual engineering components, a more important aspect of model

testing, and directly related to this work, is the interaction between model tests and analytical prediction techniques. If model material behaviour can be accurately predicted using analytical methods then the same analytical methods can be used to predict the behaviour of actual components which may have different geometries but have similar material characteristics to the model material and similar loading conditions. Within the Department of Mechanical Engineering at this University, a lead alloy has been used extensively as a model material. The latest experimental tests have been carried out by Yahiaoui (12) who discusses the usefulness of the lead alloy as a model material.

The finite element method and approximate analytical solutions for predicting component behaviour form the basis of the investigations in this research. Valuable insights into the ratchetting and creep behaviour of components (particularly in regions of stress concentration where relevant research is very limited) have been obtained.

The finite element method has been used:-

1. to investigate the mechanisms of ratchetting;
2. to study in detail the effects of loading, material behaviour assumptions and stress redistribution on the ratchetting and dwell period behaviour of simple components;
3. to identify the characteristic ratchetting and dwell period behaviour of a number of complex components and loadings in order to suggest simplified design procedures based on
 - a) limited finite element computations,
 - b) approximate analytical techniques,
 - c) a combination of finite element solutions and approximate techniques.

4. to examine the accuracy to which the results of experimental tests can be predicted by finite element solutions using simplified material models and to identify the shortfalls of the models in order to suggest improvements in the modelling techniques.

The results of the detailed studies of the flanged tube and stepped beam shanks are discussed in section 8.2. The results of the comparative study of five components with significantly differing geometries and loadings have been discussed in Chapter 7. The implications of these results in terms of simplified design procedures are discussed in section 8.3.

The results and implications of the comparisons between experimental model testing (12) and finite element predictions are discussed in section 8.4.

8.2 Detailed Studies of the Flanged Tube and Stepped Beam Shanks

A major disadvantage of the finite element method for predicting the behaviour of complex components subjected to severe loadings, particularly where plasticity and creep effects are to be investigated, is the high cost of obtaining the necessary results. Not only are the 'runtime' and core storage requirements of the non-linear program large but also the manhours required to develop an adequate mesh, generate the data and investigate suitable material models. A considerable amount of useful data on the effects of loading conditions, material models and stress redistribution during dwell periods on cyclic behaviour can be obtained from simple models of the uniform regions within a component where a limited number of elements and simplified constraints can be used. The data preparation

and 'runtimes' for these simple models is relatively small. For example, finite element computations for the flanged tube with identical loading conditions and material assumption were performed for 9 cycles and the 'runtimes' were

shank model	-	239 secs
whole component model	-	5400 secs

The main disadvantage of the simple models is their inability to represent regions of stress concentration (which are often the most critical regions of the component).

The results for the uniform shanks of the flanged tube and stepped beam can be used in two ways. Firstly the normalised form of the results make them of direct relevance to components with the same geometry made from any material with the same behaviour characteristics. Secondly, since the components differ significantly in geometry and loading conditions, similar 'trends' in behaviour, which have been identified, may be applicable for a range of components and loadings.

There are two significant differences between the two components:-

1. The total axial strain of the flanged tube shank does not vary radially; the behaviour of this component can be defined by a single parameter, i.e. the maximum ratchet or dwell period strain. The stepped beam shank experiences changes in curvature as well as axial strain and the strain varies with through-thickness position. Two parameters are required to define the behaviour; maximum surface ratchet and dwell period strains are used in preference to centreline strain and curvature since they provide a direct measure of

the maximum strains in the component. However, some interesting behaviour can be more easily explained in terms of curvature.

2. The cyclic loading is load controlled for the beam but is strain controlled for the tube. As a result the limit load for the beam depends on both the steady axial load and the cyclic bending load but the limit load of the tube depends only on the steady load (i.e. the thermal load alone cannot cause collapse).

Usually the 'complete redistribution' case is the upper bound on incremental and accumulated ratchet strains although some cases have been identified for which the 'no creep' case provides the upper bound (i.e. high mean loads). Obviously the 'complete redistribution' case will always be the upper bound for total accumulated strains. The elastic-perfectly-plastic material model results in a cyclic steady state with equal ratchet strains after the first cycle for the 'no creep' case and for each cycle for the 'complete redistribution' case. The presentation of the data for the steady cyclic state behaviour with an elastic-perfectly-plastic material model is simple because the ratchet strains and dwell period strains are independent of cycle number. The ratchet strains predicted by the isotropic and kinematic hardening models will eventually reduce to zero. For the flanged tube shank a single magnitude of cyclic thermal load has been considered and in all the cases investigated there is no reverse plasticity with the kinematic hardening model; hence the results for isotropic and kinematic hardening are ideally the same- small differences in the results are due solely to variations in the programming technique for the two hardening models. For the stepped beam shank a range of cyclic

bending loads have been used and differences between the predictions with isotropic and kinematic hardening models are apparent.

Normalised ratchet strains per cycle and accumulated ratchet strains increase with mean load and decrease with increasing plastic modulus. However, it should be noted that for realistic material modelling, the yield stress used for an elastic-perfectly-plastic material model is likely to be higher than that for an equivalent hardening model (see Figure 4.24); in this case, predictions of accumulated ratchet strain with the hardening model may initially be greater than with an elastic-perfectly-plastic model. From the results of the stepped beam shank survey the maximum surface ratchet strains also increase with cyclic load. For high mean loads the 'no creep' case may provide the upper bound on total accumulated ratchet strains. For the beam shank this generalisation relates to centreline ratchet strains, but the maximum surface accumulated ratchet strains in the beam are always greater for the 'complete redistribution' case. For the 'no creep' case with an elastic-perfectly-plastic material model an analytical solution for steady state ratchet strains in the stepped beam shank is available. Alternatively cyclic change in curvature, which can be obtained from the analytical solution, is analogous to the thermal stress parameter used by Bree and can be used in the Bree equations to obtain ratchet strains. The narrow ratchetting band between shakedown and collapse regimes means that ratchet strains are very sensitive to small changes in steady and cyclic loads. The sensitivity of ratchet strains to load (for both elastic-perfectly-plastic and hardening material models) is of particular importance when comparisons between

finite predictions and experimental results are made (see section 8.4).

The effects of hardening model and dwell periods on the incremental changes in curvature of the stepped beam shank is an interesting feature of the results. With an elastic-perfectly-plastic material model the residual curvature at the end of each cycle is the same for the 'no creep' case. For the 'complete redistribution' case there are equal increments of centreline ratchet strain and curvature for each cycle and only small changes in curvature during the dwell periods. For a non-zero plastic modulus the curvature response depends on the cyclic bending load. For the lowest cyclic bending load (i.e. $M/M_y = 1.0$) the results for isotropic and kinematic hardening models are the same. The residual curvature is a maximum at the end of the first cycle and reduces towards a steady state value during the second and subsequent cycles for both the 'no creep' and 'complete redistribution' cases. For higher cyclic bending loads, the residual curvatures for each cycle are 'positive' for isotropic hardening and 'negative' for kinematic hardening for both the 'no creep' and 'complete redistribution' cases. Again changes in curvature during the dwell periods are small. The 'reversal' of residual curvature may provide a simple means of choosing between isotropic and kinematic hardening models for a finite element analysis based on the observed curvatures during a simple experimental test.

For hardening material models, the differences between the loading conditions for the two components has a significant effect on the accumulation of ratchet strains. The severe loading conditions for the stepped beam shank results in an accumulation of

ratchet strains which is dominated by the first cycle for both 'no creep' and 'complete redistribution' cases. The flanged tube shank loadings are less severe and total accumulated ratchet strains cannot be reasonably predicted from the results for a single cycle of load.

For the 'complete redistribution' case the value of the time function for redistribution is found to be virtually independent of mean and cyclic loads and the degree of hardening. The increments of dwell period strain due to stress redistribution are small in comparison to the total dwell period strains. For an elastic-perfectly-plastic material assumption this increment is the same for each dwell period and for hardening materials, the increment of strain due to stress redistribution is a maximum for the first dwell and reduces during the second and subsequent dwell periods

8.3 Comparative Study of Components - Implications on Design

The finite element method is a very powerful, but also very expensive, prediction technique for components subjected to ratchetting and creep. The results of the comparison of component behaviour, discussed in Chapter 7, provide information on how computations can be kept to a minimum and yet give exact or reasonable estimates of accumulated strain. Also, the results of the finite element analyses are used to test the validity of approximate methods for obtaining estimates of total strain.

The comparison of the results for the five components of differing geometries and loading conditions assumes an elastic-perfectly-plastic model with no interaction between plastic and creep strains. The elastic-perfectly-plastic material assumption is

used extensively to model the behaviour of engineering materials in preference to hardening assumptions and, except for the 'no creep' case for the circular plate, the characteristic steady cyclic state condition limits the number of cycles required for an exact solution. The results for the five components have been normalised so that they can be applied to other similarly shaped components which are made from materials with the same form of material behaviour and have similar loadings.

The effects of creep during the dwell periods on ratchet strains and the effects of the residual stress fields at the end of a cycle on the dwell period behaviour have been bounded by the 'no creep' and 'complete redistribution' cases. In practice, if dwell periods are not of sufficient duration for stress redistribution to be complete then the actual accumulation of strain will be between the two bounds. The 'complete redistribution' case always provides the upper bound on accumulated strain and in all but the high mean load cases (which would not generally occur in such components) provides the upper bound on accumulated ratchet strain.

8.3.1 'No creep' case - ratchet and total accumulated strains

Finite element solutions

For the uniform regions of the tubes and beam the steady cyclic state, with constant ratchet strain per cycle, occurs after the first cycle. Exact solutions for total accumulated strains are obtained from finite element predictions for two cycles only and an approximate solution based on one cycle only is unjustified in terms of the 'time saving'. However it is noted that, except for the high load cases for the flanged tube and stepped beam, the steady state ratchet strains are less than the first cycle ratchet strain.

At the 'peak fillet' positions for the tubes and beam and at the position of maximum strain for the 'hole-in-plate' component, the steady cyclic state is reached in a few (up to six) cycles. Furthermore for the shouldered tube with higher cyclic thermal load ($\sigma_t/\sigma_y = 2.83$), the steady cyclic state is reached after the first cycle, compared with four cycles for $\sigma_t/\sigma_y = 1.42$ and the same steady load. In all cases considered the steady state ratchet strain is less than the first cycle ratchet strain. In view of the likely 'in-service' conditions of low-medium steady loading and high cyclic loading it is suggested that exact solutions can be obtained from finite element solutions for two cycles. For lower cyclic loads it has been shown that steady state ratchet strains are smaller, but of the same order of magnitude, as the second cycle ratchet strains and in this case conservative estimates of accumulated strain can be obtained from a two cycle finite element analysis.

For the circular plate, the ratchet strains (in all but the high steady load case) reduce monotonically to zero. For the high steady load case the ratchet strains were still reducing after ten cycles. This difference in behaviour can possibly be explained by the way in which the stress distributions due to steady and cyclic loading interact. The steady pressure loading and cyclic through thickness temperature gradients imposed on the circular plate produce similar stress distributions, i.e. compressive on the top (pressurised) surface and tensile on the other surface. The other four components investigated have dissimilar stress distributions due to steady and cyclic loading and require a 'plastic-core' for continued ratchetting. For the circular plate,

a 'plastic-core' concept is not applicable since collapse would occur beforehand. An exact solution for the accumulated strain in a circular plate type component requires a complete analysis to shakedown which, for the cyclic load considered and for low-medium steady loading, is very rapid. A conservative estimate of accumulated strain could be based on finite element computations for two cycles. However, the degree of pessimism might be unrealistically high if a larger number of cycles were being considered.

Approximate methods of solution

The Bree diagram (1) including lines of constant ratchet strain per cycle can be used to obtain conservative estimates of steady state ratchet strains for all of the components which experience cyclic thermal loading, based on the definitions of equivalent steady and cyclic loads given in Chapter 7 which can be obtained from a relatively simple elastic thermal analysis. For the stepped beam shank exact values of ratchet strain can be obtained using an equivalent cyclic thermal load based on changes in curvature. For the tubes and beam the estimates for the shanks are better than for the 'peak fillet' positions which draws attention to the pessimism of the definition of cyclic load based on the thermal stress concentration factor. It was seen that, with the exception of the circular plate, the first cycle ratchet strains are 'reasonably' predicted by the lines of constant ratchet strain per cycle on the Bree diagram (e.g. the maximum surface strain in the beam shank is underestimated by approximately $1.5 \epsilon_y$) in which case a 'reasonable' estimate of accumulated strains can be made. Also the ratchetting boundary on the Bree diagram is found to be conservative for all the cases considered.

When the results for the components are correlated on the 'efficiency diagram' suggested by Couserran et al (50) they generally fall within the cloud of data points in figure 2.12; the exceptions being the combinations of primary and secondary stress which results in shakedown. However the 'efficiency diagram' cannot be used to estimate accumulated strains for the 'no creep' case with an elastic-perfectly-plastic material since for non-zero steady state ratchet strains the ratio of effective stress to yield stress is unity and the Couserran method would estimate accumulated strains which are either zero or indeterminate.

8.3.2 'Complete redistribution' case

8.3.2.1 Ratchet strains

Finite element solutions

For the uniform regions of the tubes and beam, each cycle produces an equal amount of ratchet strain and the exact solution for accumulated ratchet strain requires only 1 cycle to be computed. For non-uniform stress regions, including the circular plate, constant ratchet strains per cycle exist for the second and subsequent cycles and are very similar in magnitude to the first cycle ratchet strain. An exact prediction for accumulated ratchet strain is obtained from a finite element analysis for 2 cycles of load and a good, but not necessarily conservative, approximation can be based on the results for a single cycle.

Approximate methods of solution

With the exception of the circular plate, the lines of constant ratchet strain per cycle on the Bree diagram for a 'no creep' condition can be used to obtain an estimate (up to $\approx 0.5 \epsilon_y$ per cycle underestimate) of the steady state ratchet strain for the complete redistribution condition. The difference between the circular plate and the other components has already been discussed and the non-conformity is not unexpected. The load controlled, rather than strain controlled, character-

istic of the stepped beam shank is suggested as a possible explanation for the high first cycle (and hence steady state) ratchet strains.

The $n/(n + 1)$ ratchetting boundary suggested by Leckie (45) appears to be satisfactory for all of the components except the circular plate and provides a more acceptable design criteria than the very restrictive 'elastic line' ratchetting boundary suggested by Bree (1). In fact, with the exception of the circular plate, the 'complete redistribution' case ratchet strains for loadings within the 'no creep' boundary were relatively small ($\leq 0.108 \epsilon_y$).

8.3.2.2 Dwell period strains

Finite element solutions

For the uniform regions of the tubes and beam, the dwell period behaviour between each cycle is identical and the exact solution can be obtained from the results for a single dwell period. In regions of stress concentration the second and subsequent dwell periods produce identical results and the exact solution can be obtained after only 2 dwell period computations. A good approximation of accumulated dwell period strains can be obtained from the predictions for the first dwell period since there is only a slight difference in the increment of dwell period strain due to redistribution between the first and second (steady state) dwell periods. The normalised steady state creep rates, $(d(\epsilon^d/\epsilon_y)/d\Gamma)/(P/P_L)$, are independent of load, P/P_L , and can be obtained from a single steady load finite element creep solution at any value of mean load.

Approximate methods of solution

The normalised increment of dwell period strain due to stress redistribution, $\Delta\epsilon^d/\epsilon_y$, is small; less than and in most cases much less than 0.84. The strains accumulated during long dwell periods are therefore dominated by the contribution from the steady state creep rates and in cases of negative $\Delta\epsilon^d/\epsilon_y$, dwell period strains based on the steady state

creep rates are conservative. The reference stress approach can often be used to determine normalised creep rates and therefore offers a simple method of estimating dwell period strains. Alternatively the O'Donnell and Porowski method (6) may be suitable in order to obtain a bound on creep strain.

8.3.2.3 Total accumulated strains

Finite element solutions

From the preceding discussion of ratchet strains and dwell period strains it is clear that the exact solution for total accumulated strains can be obtained from finite element solutions for 2 cycles and dwell periods. Reasonable estimates of accumulated strain require only one cycle and dwell period to be computed.

Approximate methods of solution

A combination of approximate ratchet strains, based on a single cycle finite element solution or the Bree diagram, and estimated dwell period strains, using the Reference Stress Method or O'Donnell and Porowski, can be used to estimate accumulated strains. Alternatively, since the correlation of the results for 'complete redistribution' on the 'efficiency diagram' gives data points which generally lie within or slightly above the cloud of data presented by Cousseran et al (50), a reasonable approximation of accumulated strains can often be obtained from the efficiency diagram, for example using a mean line through the cloud of data.

The Ainsworth (7) upper bound approach has been used for the stepped beam shank with a hardening material assumption and in both of the cases considered the bound is extremely conservative. This unnecessarily large overestimate is shown to result from the high stress index of the lead material in which case it is anticipated that a similar degree of overestimation would be apparent with an elastic-perfectly-plastic material assumption. A major criticism of the Ainsworth approach is that it requires a full finite element analysis for an equivalent 'no creep' case together with some detailed processing of the output data. The additional computation

during the dwell periods for an exact solution may not have a significant effect on the overall cost (in terms of runtime and processing time) of obtaining a solution. Also the Ainsworth bound is based on a 'no-creep' solution at a higher mean load than the exact solution and must therefore require more iterations for the solution. A failing of the method is that it cannot be used to obtain strains in stress concentration regions.

8.3.3 Notes on failure

For both the 'no-creep' and 'complete redistribution' cases for the flanged tube and shouldered tube and for the 'complete redistribution' case for the stepped beam, the accumulation of strain is greater at the 'peak fillet' position than in the shank. Using a failure criterion based on total accumulated strain, the component life is limited by the accumulation of strain in the fillet, whereas for a uniaxial test, component failure in the shank is likely.

Fatigue failures may occur for combinations of steady and cyclic load which result in reverse plasticity. This aspect of failure has not been investigated but it is suggested that the 'position' of such a fatigue failure is not intuitively obvious since both steady and cyclic stresses are increased by a stress raiser.

8.4 Comparisons Between Experimental Results and Finite Element Predictions

The comparisons of finite element predictions with the experimental results for the flanged tube for 5 loading cases, have different degrees of success depending on mean load, position in the component and dwell period. In the shank, the predictions of accumulated ratchet strain are low compared with the experimental results. In particular the first cycle ratchet strain is grossly underpredicted although the predictions improve with increasing load. It is suggested that a possible reason for the underestimate, particularly for the first cycle, is the inaccurate modelling of the 'knee' of the stress-strain curve which is most noticeable for the

elastic-perfectly-plastic model and is reflected in the predictions with this model. At high mean load the effects of inaccurate 'knee' modelling would be less pronounced and this is confirmed by the predictions. Also the predictions of 'peak fillet' ratchet strains, where stress levels are obviously higher, are significantly improved. Furthermore the finite element predictions of ratchet strain for the 24 hour and 120 hour dwell period tests are in good agreement with the experimental results over the range of cycles considered. The tendency of the experimental shank and peak fillet ratchet strains to a steady state non-zero value, associated with material ratchetting, cannot ultimately be predicted by the hardening models. The elastic-perfectly-plastic material model will predict a steady cyclic state condition and reasonable estimates of steady state ratchet strain are obtained in the shank for $P/P_L = 0.8$ 'no-creep' and in the fillet for $P/P_L = 0.7$ with 24 hour and 120 hour dwell periods. The amount of material ratchetting is directly related to the degree of reverse plasticity and hence to the loading conditions. Since finite element predictions with isotropic and kinematic hardening models are nominally the same (i.e. no reverse plasticity with kinematic hardening) and considering the relatively low thermal loading it is suggested that material ratchetting is limited and the absence of a material ratchetting model is not a serious restriction on the ability to obtain reasonable predictions for the flanged tube. Over the range of cycles considered, the hardening model of the 76°C lead alloy stress strain data (Curve D Figure 4.24) provides the best estimates of ratchet strain accumulation. For the tests with 24 hour and 120 hour dwell periods between thermal shocks (i.e. $P/P_L = 0.7$) the predictions of individual dwell period strains and hence accumulated dwell period strains are generally higher

than the experimental results, with the exception of the 'peak fillet' predictions with 120 hour dwell period which are within the wide band of experimental data. Dwell period strain predictions reduce with reducing ratchet strain in the same way as the experimental results but the degree of overestimation is seen to increase with increasing inelastic strain. The greatest dwell period strains are predicted by the model which predicts the highest ratchet strains (i.e. Curve D Figure 4.24). Fessler, Hyde and Webster (25) have shown that, for a similar lead alloy, plastic pre-strain generally has a diminishing effect on creep strain compared with virgin creep data although at high stress levels the opposite effect was noted.

From the experimental results in Table 4.8 it would appear that the accumulated initial dwell period strains cause a reduction in the first cycle ratchet strain in the shank. The same effect may also occur in the fillet but the argument is qualitative since stress redistribution will contribute towards the reduction.

The following three improvements to modelling technique are suggested together with a qualitative assessment of their effect on predictions:-

- A. more accurate modelling of the knee of the uniaxial stress strain curve;
- B. a material ratchetting modelling; and
- C. a plasticity-creep interaction model

For the 'no-creep' predictions, A and B would result in higher accumulated ratchet strain predictions in the shank as required. At the 'peak fillet' position a material ratchetting model would again improve the predictions; the effects of more accurate knee modelling on 'peak fillet' ratchet strains are uncertain. For the finite element predictions with significant dwell periods the effects of A and B on ratchet strains are similar to

those for the 'no creep' condition. However an indirect effect of A and B is an anticipated increase in the dwell period strains. In contrast, it is suggested that a more realistic plasticity-creep interaction model could reduce the predictions of both ratchet and dwell period strains. In this case, the overall effect of the three suggested improvements is uncertain and in order to maintain good agreement between experimental and finite element results, the effects of A and B would need to be, to a large extent, counterbalanced by that of C. It must be pointed out, however, that although material ratchetting and plasticity-creep interaction are not modelled, the overall predictions of total strain using simple models generally compare favourably with the experimental results especially considering the spread of the experimental uniaxial data, particularly for creep, obtained by Yahiaoui (12).

From the comparisons between experimental and predicted strain distributions it would appear that the position of peak strain is not accurately predicted. A possible explanation is that machining inaccuracies in the mould used to produce the components results in a truncation of the fillet radius by $\sim 6^\circ$ at the shank/fillet interface (12). This would cause both a shift in the apparent position of peak strain and an increase in the stress concentration factor in the fillet.

The agreement between the experimental results for the 'load controlled' stepped beam and finite element predictions using load control is poor. The effect of the eccentricity of the axial load on the applied moments was not fully appreciated in the early stages of the project when a list of possible candidate components and loadings was drawn up and the two components chosen for detailed analysis. Having later quantified the effect of eccentricity, the actual moments were found

to be significantly different to the nominal values (for example, see table 5.5) and moments in the fillet were ~5% greater than the shank values. In view of the large changes in strain associated with relatively small changes in load, finite element predictions based on nominal moments, which had already been obtained, were not considered to be relevant for the comparison (e.g. compare shank predictions from figure 5.42, where P_L & M_y are based on $\sigma_y = 19.8 \text{ MN/m}^2$ rather than 0.2% proof stress, with predictions in figures 5.45 and 5.46). Also comparisons were restricted to the shank. The finite element predictions of ratchet strain with isotropic and kinematic hardening models are significantly lower than the experimental results and predict shakedown in ~10 cycles. A material ratchetting model would improve the predictions but the degree of improvement is unquantified at this time. In contrast, the elastic-perfectly-plastic model using steady state moments overpredicts the accumulation of ratchet strain and in particular the steady state ratchet strain. Finite element predictions based on curvature control are more accurate than those based on load control, in particular those with a kinematic hardening model. Both load and strain control problems arise in practice and the problems of prediction in each case have to be considered.

8.5 SUGGESTIONS FOR FURTHER WORK

Although good agreement between experimental results and finite element predictions for the flanged tube has been achieved with simple models of material behaviour, it is suggested that the implementation of both material ratchetting and plasticity-creep interaction models into the finite element program should be pursued. Material ratchetting has been shown to be significant from the experimental results for the high cyclic loading conditions of the stepped beam. Experimental data suggests that the cyclic behaviour of the lead alloy could be more

accurately predicted by a Goodman and Goodall model. Yahiaoui (12) reports on tests which have already been performed on the lead alloy to determine suitable constants for the Goodman and Goodall equations and to investigate the interaction between plastic and creep strains.

CHAPTER NINE

9. SUMMARY OF CONCLUSIONS

1. The finite element method has proved to be a very powerful, albeit expensive, technique for predicting the ratchetting and creep behaviour of components.
2. The detailed parameter survey of the flanged tube and stepped beam shanks has provided a valuable insight into the effects of loading conditions, material hardening and stress redistribution due to creep during the dwell periods between cycles of load on ratchetting and dwell period behaviour. These 'simplistic' models have highlighted effects that would not necessarily be recognised by 'whole component' analyses which, because of cost and time limitations, must be restricted in terms of the variation in the relevant parameters being investigated.
3. The flanged tube shank is a strain controlled cycling problem and ratchet strains are constant across the section. The uniform beam is load controlled and there may be variations in ratchet strain across the section and hence incremental growth in the direction of applied load may be accompanied by incremental changes in curvature.
4. For both models ratchet strains increase with mean load and are inversely related to the degree of the material hardening. For the uniform beam, the maximum surface ratchet strain also increases with cyclic bending load. Ratchet strains on the opposite surface are at a maximum for an intermediate cyclic bending load.
5. The elastic-perfectly-plastic material model predicts a ratchetting process which, above the shakedown limit, is continuous for both the plane tube and beam shank models with a constant ratchet strain per cycle. With material hardening, both isotropic and kinematic hardening models must ultimately predict shakedown to elastic

cycling or cyclic plasticity. When cyclic loads are relatively small (i.e. flanged tube) and no reverse yielding occurs the predictions from isotropic and kinematic hardening models are the same. For the higher cyclic loading conditions in the beam shank and particularly for a high plastic modulus, material hardening during the first cycle results in an accumulation of ratchet strain which is dominated by the first cycle.

6. The effects of stress redistribution due to creep in the dwell periods between cycles of load are bounded by the 'no creep' (rapid cycling) and complete redistribution (slow cycling) cases analysed. The complete redistribution case provides the upper bound on accumulated strain and in general on accumulated ratchet strain although situations have been identified where the 'no creep' case will predict the greater ratchet strains; typically for high mean load and relatively low cyclic load combinations which would not be expected in practise.
7. The accumulation of strain during the dwell periods is characterised by an initial transient stage due to stress redistribution superimposed on a steady state strain rate. The increments of strain due to redistribution are small compared with the total accumulation of dwell period strain. The steady state strain rates and redistribution times are directly related to steady load and are independent of cyclic load and hardening assumption.
8. The mechanisms of ratchetting have been investigated by considering 5 components with significantly different geometries and loading conditions using an elastic-perfectly-plastic material model and a zero plasticity-creep interaction rule for the 'no creep' and complete redistribution cases. 4 of the 5 components have very similar ratchetting mechanisms; the 'no creep' mechanism for the circular plate being the exception to the general rule. The similarity in

behaviour of these 4 components can be explained in the way that the stress distributions due to steady and cyclic loading interact.

9. For the 'no creep' case in uniform sections and regions of stress concentration a 'plastic core' (i.e. a portion of the ratchetting section which experiences plastic growth during both halves of a cycle) is required for ratchetting to be continuous. The 'plastic core' is not evident for the circular plate which will eventually shakedown under 'no creep' conditions. From the survey of the flanged tube and stepped beam shanks it has been shown that the monotonic reduction in ratchet strain due to material hardening is associated with a reduction in the size of the 'plastic core' and ratchetting ceases when the 'plastic core' disappears.
10. The 'plastic core' requirement is not essential for continued ratchetting with an elastic-perfectly-plastic material model and complete redistribution conditions. In plane regions, ratchetting is continuous for load combinations which produce any plastic strain during the first cycle. In regions of stress concentration, continued ratchetting was predicted for all components and loading conditions including the circular plate, although a small shakedown region would be expected.
11. For the range of components and loadings considered both shakedown and ratchetting conditions have been identified. With the elastic-perfectly-plastic material model, the accumulations of ratchet strains can be characterised by 3 categories which cover both the 'no creep' and complete redistribution conditions. In all of the cases considered ratchet strains are enhanced by complete redistribution in the dwell periods also ratchetting is evident under complete redistribution conditions for loadings which result in shakedown for the equivalent 'no creep' conditions.

12. For the two axisymmetric tube components having uniform sections and stress concentrations, the accumulations of meridional ratchet strain at the 'peak fillet' positions are greater than in the shank for all loadings and dwell period assumptions. Ratchetting at the 'peak fillet' position can occur for loadings that result in shakedown in the shank. For the 'plane stress' stepped beam, 'no creep' meridional ratchet strains in the fillet are less than in the shank due to the effects of the increased section on strains in the other two directions.
13. The increments of dwell period strain due to stress redistribution are always small and in some cases negative and the accumulated dwell period strain is dominated by the steady state component. The steady state strain rates in the fillet regions of the tubes are significantly less than in the shank and are directly proportional to mean load. For the stepped beam, steady state strain rates in the shank and fillet are similar and directly proportional to mean load.
14. With the exception of the 'no creep' case for the circular plate an elastic-perfectly-plastic material model will predict a cyclic steady state both in the plane sections and at points of high stress and this limits the number of computed cycles that are required for an exact solution. Similarly, exact steady state strain rates during the dwell periods for a range of mean loads can be obtained from a single load creep solution. Guidelines for the necessary computations for exact and approximate solutions are given and in general only two complete cycles, including dwell periods, have to be computed.

15. For the 'no creep' condition with an elastic-perfectly-plastic material model, the Bree ratchetting boundary and lines of constant ratchet strain per cycle are conservative for all of the components (uniform sections and stress concentrations) and loadings considered, with the exception of the circular plate, using simple definitions of the steady and equivalent cyclic loads. In regions of stress concentration, equivalent cyclic loads are related to 'nominal' values by the thermal or equivalent thermal stress concentration factor which is shown to be a pessimistic assumption.
16. With complete redistribution between cycles of load, the $n/n + 1$ boundary suggested by Leckie is satisfactory for all of the components and loadings except the circular plate and is far less restrictive than the elastic limit line boundary suggested by Bree. Furthermore the Bree ratchetting boundary for the 'no creep' condition provides a reasonable guideline for the 4 components.
17. The non-conformity of the circular plate component has been highlighted throughout the analysis. The approximate methods suggested are restricted to components subjected to loading conditions which are similar to Bree's thin tube. The ability to incorporate the effects of stress concentrations into approximate design calculations based on the Bree diagram is a significant feature of the results.
18. The correlation of the finite element results on the 'efficiency diagram' of Cousseran et al supports the theory that the accumulation of inelastic strain depends on the loading conditions and can be separated from the effects of material behaviour and test duration. The finite element results using the lead alloy material data generally correlate well with the cloud of data presented by Cousseran et al for a range of stainless steels.

19. The upper bound approach suggested by Ainsworth has proved to be an extremely conservative method of bounding strain accumulations in a situation of ratchetting with creep. The analysis is restricted to two examples for the stepped beam shank but suggests similar conclusions for the other components since the pessimism is associated with the high value of stress index in the creep law. The overall saving, in terms of computing costs and manhours, is also questionable. The approach cannot be used for SCF's.
20. The accumulation of strain during long dwell periods can be reasonably estimated from the steady state strain rate since the increment of strain due to stress redistribution is small compared with the total accumulation. For plane regions the steady state strain rate is equal to the creep strain rate associated with the mean stress. In regions of stress concentration steady state strain rates for a range of mean loads can be obtained from a single steady load creep finite element solution or alternatively the Reference Stress Method or O'Donnell and Porowski bound can often be used.
21. The comparison between experimental results and finite element predictions for the flanged tube has shown that generally good agreement can be obtained using simple models of material behaviour. This agreement is partially attributed to the relatively low magnitude of the cyclic thermal load under which conditions material ratchetting is limited.
22. A qualitative assessment of the likely effects of improved modelling techniques, including material ratchetting and plasticity-creep interaction models, confirms the anticipated improvement in predictions. However the implementation of improved models into existing finite element programs may not necessarily be cost effective, particularly in view of the flanged tube results. It

is also suggested that more accurate modelling of the uniaxial stress-strain curve is necessary for improved predictions in regions of 'nominal' stress. A non-linear kinematic hardening model may, therefore, be necessary and the overlay method can be used for such a model without the need for detailed program modification.

23. For high cyclic loads a material ratchetting model is required as shown by the comparison of results for the stepped beam shank, which also highlights the problems of modelling a load controlled cycling situation. Care must be taken to ensure that any interaction between steady and cyclic loads is accounted for in the definition of the problem to be solved.

ACKNOWLEDGEMENTS

The author wishes to thank the following:-

1. Dr. J. J. Webster and Dr. T. H. Hyde, his supervisors, for their guidance and support which has been readily available and gratefully received throughout the project.
2. Professor H. Fessler and Dr. K. Yahiaoui who complete the 'team' and who have made valuable contributions to the project.
3. The Science and Engineering Research Council for awarding the Research Assistantship.
4. The Head of the Department of Mechanical Engineering for providing the research facilities.
5. The in-mates of Research Room 3, particularly Dr. A. M. Rabie for his encouragement.
6. Caroline Brayley for the excellent tracings.
7. Janis Henshaw and Joanna Kelvey for the care and effort they have put into producing the typed thesis.
8. To his wife who, in the first instance, persuaded him to take on the research and who has suffered the consequences for the last three and a half years.

REFERENCES

1. BREE, J., 'Elastic-Plastic Behaviour of Thin Tubes Subjected to Internal Pressure and Intermittent High-Heat Fluxes with Application to Fast-Nuclear-Reactor Fuel Elements', Journal of Strain Analysis, Vol. 2, No. 3, 1967, pp 226-238.
2. BREE, J., 'Incremental Growth due to Creep and Plastic Yielding in Thin Tubes Subjected to Internal Pressure and Cyclic Thermal Stresses', Journal of Strain Analysis, Vol. 3, No. 2, 1968, pp 122-127.
3. ASME Code Case N.47-15 (1592-15), 'Class 1 Components in Elevated Temperature Service', ASME, New York, 1979.
4. MILLER, D.R., 'Thermal-Stress Ratchet Mechanism in Pressure Vessels', Journal of Basic Engineering, Vol. 81, No. 2, June 1959, pp 190-196.
5. BURGHEEN, D., 'Design Methods for Power Plant Structures', First Edition, C. P. Press, New York, 1975.
6. O'DONNELL, W.J. and POROWSKI, J., 'Upper Bounds of Accumulated Strains due to Creep Ratchetting', Welding Research Council Bulletin 195, 1971, pp 57-62.
7. AINSWORTH, R.A., 'A Note on Bounding Solutions for Creeping Structures Subjected to Load Variations above the Shakedown Limit', International Journal of Solids and Structures, Vol. 15, 1979, pp 981-986.
8. MARRIOTT, D.L., 'Approximate Analysis of Transient Creep Deformations', Journal of Strain Analysis, Vol. 3, No. 4, 1968.
9. PENNY, R.K. and MARRIOTT, D.L., 'Design for Creep', McGraw-Hill, Maidenhead, 1971.
10. HYDE, T.H. and WEBSTER, J.J., 'Predicting the Thermal Ratchetting and Creep Behaviour of a Component with a Stress Concentration', Journal of Strain Analysis, Vol. 17, No. 4, 1982.

11. HYDE, T.H., WEBSTER, J.J. and FESSLER, H., 'Thermal Ratchetting of Axially Loaded Tubes Operating in the Creep Range', *Journal of Strain Analysis*, Vol. 17, No. 4, 1982.
12. YAHIAOUI, K., 'Experimental Study of Creep and Ratchetting using Lead Alloy Model Components', Ph.D. Thesis, 1982, Nottingham University.
13. MENDELSON, A., 'Plasticity: Theory and Application', Macmillan Company, New York, 1968.
14. JOHNSON, W. and MELLOR, P.B., 'Engineering Plasticity', Van Nostrand Reinhold Co., London, 1973.
15. PRAGER, W., 'The Theory of Plasticity - A Survey of Recent Achievements', *Proceedings of the Institution of Mechanical Engineers*, London, Vol. 169, 1955, pp 41-57.
16. ZIEGLER, H., 'A Modification of Prager's Hardening Rule', *Quarterly Journal of Mechanics and Applied Mathematics*, Vol. 17, 1959, pp 55-65.
17. MASING, G., 'Eigenspannungen und Verfestigung beim Messing', *Proc. of the 2nd International Congress of Applied Mechanics*, Zurich, 1926, pp 332-335.
18. MROZ, Z., 'On the Description of Anisotropic Work-Hardening', *Journal of Mechanics and Physics of Solids*, Vol. 15, 1967, pp 163-175.
19. MROZ, Z., 'An Attempt to Describe the Behaviour of Metals under Cyclic Loads using a More General Work-Hardening Model', *Acta Mechanica*, Vol. 7, 1969, pp 199-212.
20. ZIENKIEWICZ, O.C., NAYAK, G.C. and OWEN, D.R.J., 'Composite and 'Overlay' Models in Numerical Analysis of Elasto-Plastic Continua', *Symposium on Foundations of Plasticity*, Warsaw, 1972.
21. GOODMAN, A.M. and GOODALL, I.W., 'Constitutive Relations for Stainless Steels', *Metals Society Conference*, Varese, May 1981.

22. JHANSALE, H.R., 'A New Parameter for the Hysteretic Stress-Strain Behaviour of Metals', Journal of Engineering Materials and Technology, Vol. 97, Jan. 1975, pp 33-38.
23. KRAUS, H., 'Creep Analysis', John Wiley and Sons, New York, 1980.
24. ODQVIST, F.K.G., 'Mathematical Theory of Creep and Creep Rupture', Oxford University Press, 1966.
25. FESSLER, H., HYDE, T.H. and WEBSTER, J.J., 'Some Tensile, Creep and Plasticity/Creep Interaction Data for the Lead Alloy which is to be used for the Shouldered Tubes', 3rd Progress Report to SRC on Creep and Plasticity Interaction, B/RG/7699.4, June 1978.
26. PARKES, E.W., 'Wings under Repeated Thermal Stress', Aircraft Engineering, Vol. 26, 1954, pp 402-406.
27. PARKES, E.W., 'Incremental Collapse due to Thermal Stress', Aircraft Engineering, Vol. 28, No. 333, Nov. 1956, pp 395-396.
28. PARKES, E.W., 'Effects of Repeated Thermal Loading', Aircraft Engineering, Vol. 32, 1960, pp 222-229.
29. PARKES, E.W., 'Structural Effects of Repeated Thermal Loading', Thermal Stress, ed. Benham et al., Pitman and Sons, London, 1964.
30. BURGEEEN, D., 'The Thermal Ratchet Mechanism', Journal of Basic Engineering, Vol. 90, No. 3, Sept. 1968, pp 319-324.
31. BURGEEEN, D., 'Structural Growth Induced by Thermal Cycling', Journal of Basic Engineering, Vol. 90, No. 3, Sept. 1968, pp 469-475.
32. HYDE, T.H., 'The Effect of Transverse Pressure Loading on the Thermal Ratchetting of Circular Plates', Journal of Strain Analysis, Vol. 15, No. 1, 1980.
33. GILL, S.S., 'A Simple Illustration of Incremental Collapse', Bull. Mechanical Engineering Education, Vol. 6, No. 1, 1967, pp 3-8.
34. RUIZ, C., 'The Inclusion of Incremental Collapse Problem in Undergraduate Courses', Bull. Mechanical Engineering Education, Vol. 6, No. 1, 1967, pp 9-21.

35. MEGAHED, M.M., 'Influence of Hardening Rule on the Elasto-Plastic Behaviour of a Simple Structure under Cyclic Loading', International Journal of Mechanical Sciences, Vol. 23, 1981, pp 169-182.
36. SAGAR, V. and PAYNE, D.J., 'Incremental Collapse of Thick-Walled Circular Cylinders under Steady Axial Tension and Torsion Loads and Cyclic Transient Heating', Journal of Mechanics and Physics of Solids, Vol. 23, 1975, pp 39-53.
37. EDMONDS, H.G. and BEER, F.J., 'Notes of Incremental Collapse in Pressure Vessels', Journal of Mechanical Engineering Sciences, Vol. 3, 1961, pp 187-199.
38. CALLADINE, C.R., 'Time-Scales for Redistribution of Stress in Creep of Structures', Proceedings of the Royal Society, London, series A, Vol. 309, 1969, pp 363-375.
39. BILL, I.M. and MACKENZIE, A.C., 'Reference Stress for Redistribution Time in Structures', Journal of Mechanical Engineering Sciences, Vol. 11, 1969, pp 429-431.
40. SODERBERG, C.R., 'Interpretation of Creep Tests for Machine Design', Trans. ASME, Vol. 58, No. 8, 1936, pp 733-743.
41. HYDE, T.H., 'Experimental Reference Stress Techniques for the Prediction of Creep Deformations using Lead Alloy Models', Ph.D. Thesis, 1976, Nottingham University.
42. LECKIE, F.A. and MARTIN, J.B., 'Deformation Bounds for Bodies in a State of Creep', Journal of Applied Mechanics, Vol. 34, No. 2, June 1967, pp 411-417.
43. LECKIE, F.A. and PONTER, A.R.S., 'Deformation Bounds for Bodies which Creep in the Plastic Range', Journal of Applied Mechanics, Vol. 37, No. 2, June 1970, pp 426-430.
44. PONTER, A.R.S., 'On the Relationship between Plastic Shakedown and the Repeated Loading of Creeping Structures', Journal of Applied Mechanics, Vol. 38, No. 2, June 1971, pp 437-440.

45. LECKIE, F.A., 'A Review of Bounding Techniques in Shakedown and Ratchetting at Elevated Temperatures', Welding Research Council Bulletin, 195, 1971, pp 1-56.
46. ANDERSON, W.F., 'Creep Ratchetting Deformation and Rupture Damage Induced by a Thermal Transient Stress Cycle', 1st National Congress on Pressure Vessel and Piping Technology, May 1971, San Francisco, pp 1-11.
47. INOUE, T. and TANAKA, K., 'Mechanical Ratchetting under Multiaxial Stresses at Elevated Temperatures', Mechanical Behaviour of Materials Symposium Proceedings, Kyoto, Japan, Aug. 1973, pp 55-63.
48. CORUM, J.M., YOUNG, H.C. and GRINDELL, A.G., 'Thermal Ratchetting in Pipes Subjected to Intermittent Thermal Downshocks at Elevated Temperatures', Pressure Vessels and Piping: Verification and Qualification of Inelastic Computer Programs, ASME, New York, 1975, pp 79-98.
49. YAMAMOTO, S., KANO, T. and YOSHITOSHI, A., 'Thermal Ratchetting Experiments of Type 304 Stainless Steel Pipes under Alternating Cold and Hot Thermal Shocks with Varying Axial Loads', Elevated Temperature Design Symposium, ASME, New York, 1976, pp 25-32.
50. COUSSERAN, P., LEBEY, J., MOULIN, D., CLEMENT, G. and ROCHE, R., 'Ratchetting-Experimental Tests and Practical Method of Analysis', 2nd International Conference on Engineering Aspects of Creep, Sheffield, Sept. 1980, pp 143-151.
51. FESSLER, H., HARDY, S.J., HYDE, T.H., WEBSTER, J.J. and YAHIAOUI, K., 'Cyclic Ratchetting Behaviour of Components Subject to Thermal and Mechanical Load', 1st Progress Report on Work Carried Out Under SRC Grant Ref. GR/A/8664.0, 1981.
52. DWIVEDI, V.S., FESSLER, H., HYDE, T.H. and WEBSTER, J.J., 'Elastic Steady-State Stresses in a Shouldered Tube', 1st Progress Report to SRC on Creep and Plasticity Interactions, Grant Ref. B/RG/7699.4, Sept. 1976.

53. DWIVEDI, V.S., FESSLER, H., HYDE, T.H. and WEBSTER, J.J., 'Elastic Transient, Thermal Stresses in a Shouldered Tube', 2nd Progress Report to SRC on Creep and Plasticity Interactions, Grant Ref. B/RG/7699.4, Feb. 1977.
54. FESSLER, H., HYDE, T.H. and WEBSTER, J.J., 'The Thermal Shock Rig', Fourth Progress Report on Creep and Plasticity Interactions, SRC Grant Ref. B/RG/7699.4, Dec. 1978.
55. PETERSON, R.E., 'Stress Concentration Design Factors', John Wiley and Sons, New York, 1953.
56. HOPKINS, H.G. and WANG, A.J., 'Load-Carrying Capacities for Circular Plates of Perfectly-Plastic Material with Arbitrary Yield Condition', Journal of the Mechanics and Physics of Solids, Vol. 3, 1954, pp 117-129.
57. TOWNLEY, C.H.A., 'The Application of Elastic/Plastic Analysis to the Design of Pressure Vessels', Berkeley Nuclear Laboratories, CEGB Report RD/B/N1105, July 1968.
58. DWIVEDI, V.S., 'Extensions to PAFEC 70+ for Creep and Plasticity Calculations', University of Nottingham, Mechanical Engineering Department Research Report, October 1977.
59. HARDY, S.J., 'Finite Element Program User Manual', University of Nottingham, Mechanical Engineering Department Research Report, March 1983.
60. ZIENKIEWICZ, O.C., 'The Finite Element Method', McGraw-Hill, (3rd Edition), 1977.
61. OWEN, D.R.J. and HINTON, E., 'Finite Elements in Plasticity - Theory and Practise', Pineridge, 1980.
62. MARCAL, P.V. and KING, I.P., 'Elastic-Plastic Analysis of Two-Dimensional Stress Systems by the Finite Element Method', International Journal of Mechanical Sciences, Vol. 9, 1967, pp. 143-155.

63. DAWSON, R.J., 'Finite Element Solution of Elastic-Plastic Problems',
M.Phil. Thesis, 1981, Nottingham University.
64. HENSHELL, R.D. (Editor), 'PAFEC 70+ with Extensions to Aug. 74',
University of Nottingham, 1974.
65. MANNION, J.J., 'Elastic-Plastic Behaviour of an Axisymmetric Component',
University of Nottingham, Mechanical Engineering Department
Third Year Project, 1980.
66. HULT, J., 'On the stationarity of stress and strain distribution
in creep', I.U.T.A.M. Symp., Haifa, 1962.

APPENDIX I

THE NON-LINEAR FINITE ELEMENT PROGRAM

AI.1 Introduction

Prior to 1979, the document giving details of the non-linear finite element creep and plasticity facilities within the Department of Mechanical Engineering was a manual written by Dwivedi (58). The manual also gives details of programming, job control and data input for programs run on the University's ICL 1900 series computer in operation at that time. The routines necessary for plasticity and creep computations were stored in a number of separate files and different combinations of these files were used depending on the type of analysis,

- i.e. a) mechanical and/or thermal plasticity only
b) creep only
c) plasticity and creep.

This resulted in unnecessary duplication of routines and the author's first action was to develop an 'all-embracing set of routines in a single file which combined all the existing facilities, some of which were only available with certain types of problem (e.g. a restart facility).

The facilities available in 1979 have been enhanced by modifications and the major modifications are described briefly in this Appendix. Full details of present program capabilities including data input and job control for running programs on the now fully operational ICL 2900 series computer (which replaced the 1900 in 1981-82) are given in a new manual (59), which also includes a flow chart for the program. This Appendix includes details of the 'standard' parameters (e.g. accuracy criteria) which have been used in the analyses.

Table A1.1 compares the present capabilities with those described by Dwivedi (58).

AI.2 Methods of Solution

Methods of solution for non-linear finite element analyses vary in complexity and are described in many references (e.g. 60, 61, 62). Dawson (63) describes the technique used for mechanical and thermal plasticity by the routines in this program. In brief, mechanical and thermal loads are applied incrementally up to their required values, and elastic-plastic solutions are obtained by the method of successive elastic solutions where the elastic stiffness matrix is used throughout. (For thermal loading, the final temperature distribution is reached incrementally using nodal temperature distributions stored in a file; having been obtained from a previous transient thermal analysis.) For each increment, solutions are obtained using a 'reverse gradient' iteration technique developed by Dawson (63). The von Mises yield criterion and Prandtl-Reuss flow rules are used to determine the increments of plastic strain and an elastic re-solution is used for stresses. Convergence is based on the equivalent stress at each Gauss point being within a specified tolerance using the equivalent strain and uniaxial stress-strain curve.

A time marching procedure is used for creep computations which is described by Dwivedi (58). For each time step, the equivalent creep strain increment is obtained by assuming a constant stress. The von Mises effective stress and Prandtl-Reuss flow rules are used to determine the components of incremental creep strain and the elastic re-solution process provides the stresses. Initially the time step is small in order to limit the change in stress to an

acceptable level. If the change in stress violates a specified criterion, the time step is halved and the creep strains re-calculated. If the criterion is met, the total creep strains are up-dated, the time step is doubled and the process is repeated until the final time is reached.

AI.3 Modifications to the Program

Modifications fall into 3 categories:-

1. consolidating existing facilities;
2. specific improvements for detailed component analysis; and
3. general improvements in the facilities.

Restart facility

The restart facility enables the user to divide a large computational problem into a number of more manageable units. On completing a series of plasticity and/or creep computations, information relating to the final conditions of the structure can be stored on a file and used to restart the problem, i.e. used as the initial conditions for a further series of computations.

Furthermore, restart information can be stored at any stage so that in the event of a job failure (hardware break, lack of convergence or maximum time limit) the program can be restarted from the last successfully completed computation.

Two independent loading cases

This modification is included for the analysis of the stepped beam component subject to a constant axial load and cyclic bending load although it permits analysis of any component subject to two independently varying load cases. A load case is defined as a series of nodal loads which remain in the same proportion during a

loading or unloading operation.

More than one period of creep

The single period of creep facility available prior to 1979 has been extended to allow computation of periods of creep interspaced with mechanical/thermal plasticity.

Element dependent properties

The plastic and creep properties can be varied within the elements of a structure which facilitates analysis of composite material structures and provides a basis for the 'overlay method' (20) to be used. (see Section 5.3.2). In addition, the user can specify the 'plastic' elements; the remainder will be assumed to be elastic during the computation.

Change in creep convergence criterion

A change in stress criterion based on the maximum stress in the structure is preferred to the previous criterion which compared change in stress at a Gauss point with the absolute value of stress at that point. Experience has shown that unnecessary computational time has been devoted to meeting the previous criterion at a point in the structure where stress levels are orders of magnitude below the mean stress since

$$\frac{\Delta \sigma}{\sigma} \longrightarrow \infty \quad \text{as} \quad \sigma \longrightarrow 0$$

Graph plotting facility

The graph plotting facilities, until now only available in conjunction with standard finite element calculations (64) have been extended so that stress and strain distributions (spacial or increment/time dependent) resulting from plastic and creep loadings

can be automatically plotted.

Obtaining the plots is a two-stage process, the creep and plasticity program being modified to allow the necessary information to be stored on a file.

The second stage, a simple FORTRAN program, extracts and manipulates the data into the required form for submission to the graph plotting routines.

General improvements to output

The output has been generally improved in four areas:-

1. omission of unwanted output;
2. removal of constant values (e.g. Gauss point co-ordinates) from the incremental output and replaced by a single listing of these parameters;
3. more detailed output - item 2. has allowed more 'space' in the incremental output for other useful data to be printed;
4. clearer headings.

AI.4 Additional data used in the analyses

In addition to the finite element mesh and material data described in the text, it is necessary to specify values for the parameters which control the incremental and time marching procedures. This data is given in Table AI.2. For thermal plasticity, the incremental temperature distributions are described in the relevant sections. For the stepped beam, the bending loads were generally applied in 10 equal increments although in some cases (i.e. high mean load, high bending load and low E_p/E) it was necessary to use 30 increments.

<u>Program Capabilities prior to 1979 (Ref. 58)</u>	<u>Existing Program Capabilities (Ref. 59)</u>
1. Mechanical and/or thermal plasticity only	Any combination of mechanical plasticity, thermal plasticity and creep computations.
2. Creep only	
3. Mechanical and/or thermal plasticity interspaced with one period of creep	
4. Thermal loading and unloading	Thermal loading and unloading
5. Restart facility available with plasticity program only (i.e. 1.)	Restart facility generally available
6. One loading case for mechanical plasticity	One or two independent loading cases
7. Material hardening assumptions Elastic-Perfectly-plastic Isotropic Hardening Kinematic Hardening	Elastic-Perfectly-plastic Isotropic Hardening Kinematic Hardening Non-linear Kinematic Hardening (via overlay method)
8. Material Creep behaviour Power law, Sinh law Strain and time hardening	Power law, Sinh law Strain and time hardening
9. -	Element dependent plastic and creep material data
10. -	Graph plotting

Table A1.1

Description	Variable name (59)	Value
Starting time interval for time marching creep computation	SCA	1.0
Max. number of iterations	MAXITN	30
Convergence accuracy for plasticity computation	TOL1	0.005
Iteration Modulus	YMOD	2 x Young's Mod.
Tolerance for creep computation	TOL	0.05

Table A1.2 Additional data used in the analysis

APPENDIX II

JUSTIFICATION OF THE FINITE ELEMENT MESHES

AII.1 Introduction

In designing finite element meshes it is necessary to balance accuracy and cost and this Appendix presents a justification for the finite element meshes of the flanged tube, stepped beam and 'hole in plate' components. The circular plate and shouldered tube component meshes have been inherited from previous projects and their justification is described elsewhere (see Chapter 6). Where necessary, reference is made to results already given in this document. Some results from a previous report (51) are reproduced.

AII.2 Flanged Tube

AII.2.1 Shank model

The acceptability of a four element through thickness shank model is confirmed by the small discontinuities in the axial stress distributions for the adopted shank length ($z = 40$ mm) in Figures AII.1 and AII.2 for mechanical and thermal loading respectively. These results are reproduced from an earlier document (51). A 2 x 2 Gauss array has been used in line with Dawson's (63) recommendations. The outermost Gauss points are 0.48 mm from their respective surfaces, compared with a 9 mm tube thickness (see Section AII.3.1).

AII.2.2 Whole component model

The 50 element mesh given in Figure 4.23 is a modified version of an earlier mesh which had been used to determine suitable dimensions for the final component (51). The original mesh is reproduced in Figure AII.3. Preliminary finite element computations with this mesh indicated a maximum discontinuity in stress at the shank/fillet

interface of $\sim 25\%$. The mesh was subsequently modified in this region (compare Figure 4.23 with Figure AII.3) and the discontinuity reduced to $\sim 15\%$, which was considered to be acceptable.

AII.3 Stepped Beam

AII.3.1 Shank model

An investigation was undertaken to determine a suitable finite element mesh for the shank. A 10 mm length of shank (25 mm deep by 10 mm thick) was modelled in several different ways by varying both the number of through thickness elements and the number of Gauss integration points per element. An axial load and bending moment was applied via an equal number of 'rigid' elements, in order to maintain a 'plane-sections-remain-plane' criterion (see Section 5.2.1) and the resulting elastic-plastic stress distributions for an elastic-perfectly-plastic material model are compared with the exact solution in Figure AII.4.

Although the results for a coarse mesh (2 elements and 2 by 2 Gauss array) are not significantly different from those for the more refined meshes, this configuration should be avoided because of the relatively large distance from the outer surfaces to the first Gauss point. Errors will occur when the plastic zone has not reached the outer Gauss point in which case the program will incorrectly predict an elastic solution.

A final choice of 3 elements with a 2 by 2 Gauss integration array was based on the following considerations:-

1. the required accuracy of the results;
2. the proximity of the outer Gauss points to the shank surfaces (1.8 mm);
3. the recommendation of a 2 by 2 Gauss array given by Dawson

(63) in his initial development of the elastic-plastic program; and

4. the compatibility between the shank model and the shank region of the whole component model and hence a 'reasonable' limit on the number of elements in the shank.

AII.3.2 Whole component model

The finite element mesh used is shown in Figure 5.30. The elastic stress distributions along the shank surface and around the fillet were computed for tension and pure bending and the results are given in Figures 5.32 and 5.36 respectively. Discontinuities in stress of up to 20% are apparent in the fillet region and, although large, were considered acceptable based on the following arguments:-

1. Gauss point values predicted by the elastic-plastic-creep program should be of acceptable accuracy;
2. similar discontinuities were present and had been accepted for an axisymmetric tube component of a previous project (65); and
3. good agreement between predicted stress concentration factors and those from photoelastic techniques had been obtained. i.e.

	Stress Concentration Factor	
	Finite Element	Photoelastic (55)
Tension	1.80	1.66
Bending	1.46	1.38

It is seen from Figures 5.32 and 5.36 that the chosen length of shank is sufficient to ensure uniform stress conditions in the mid-shank region.

AII.4 'Hole-in-plate'

The elastic stress distribution along the axis of symmetry with highest stress gradients (AB) due to axial load is shown in Figure 6.2 for the 27 element mesh in Figure 6.1. The 5 elements through the section AB result in acceptable levels of discontinuities in stress at element boundaries ($< 8\%$). A 2 x 2 Gauss array, giving 10 Gauss points across section AB, has been used. The extreme Gauss points are within 1 mm of A and B, compared with 25 mm across the section AB.

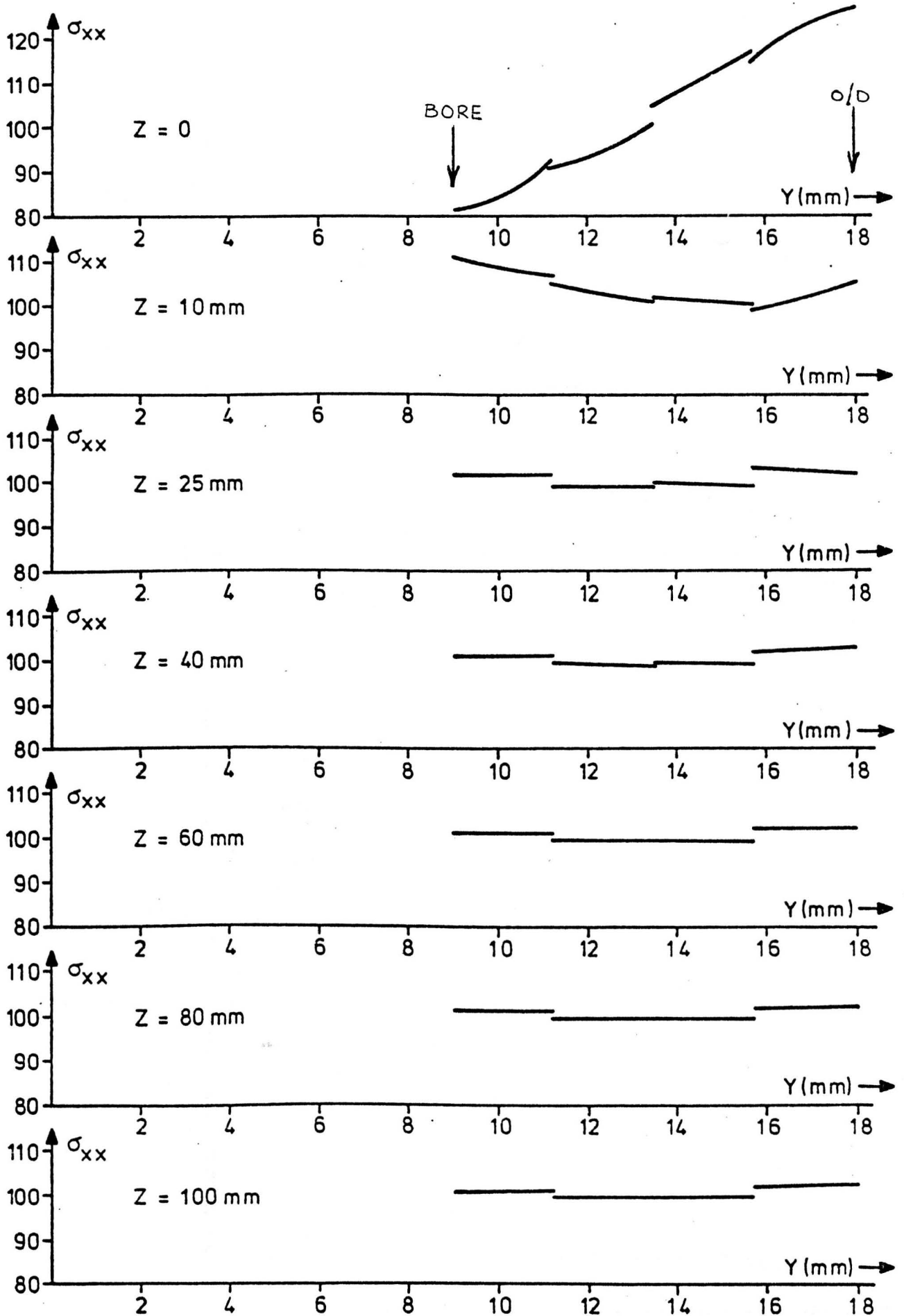


Figure AII.1 Axisymmetric component with fluid heating. Radial variation in axial stress in the shank due to an axial pressure of 100 N/m^2 as a function of shank length 'z'. (from reference 51)

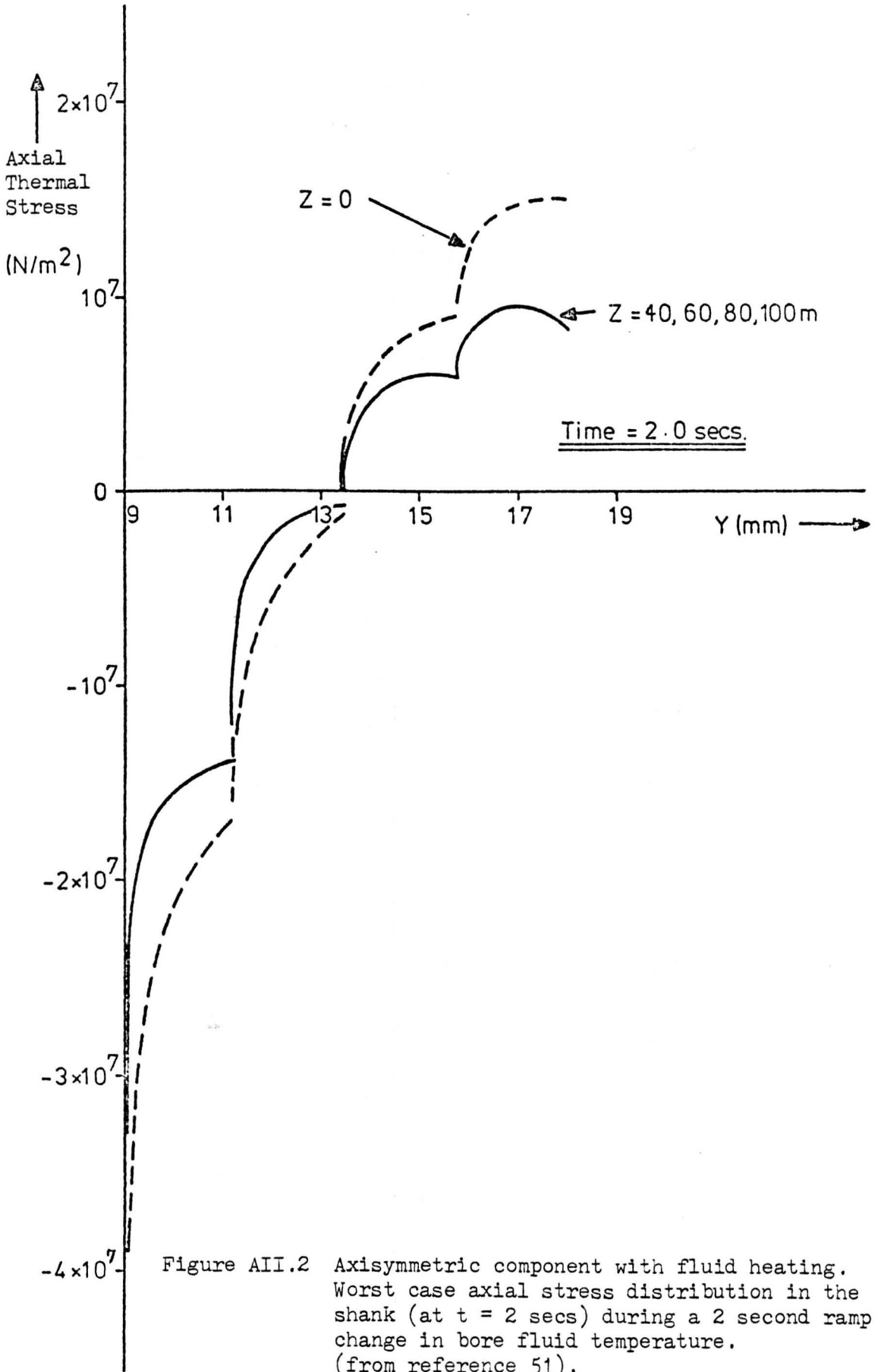


Figure AII.2 Axisymmetric component with fluid heating. Worst case axial stress distribution in the shank (at $t = 2$ secs) during a 2 second ramp change in bore fluid temperature. (from reference 51).

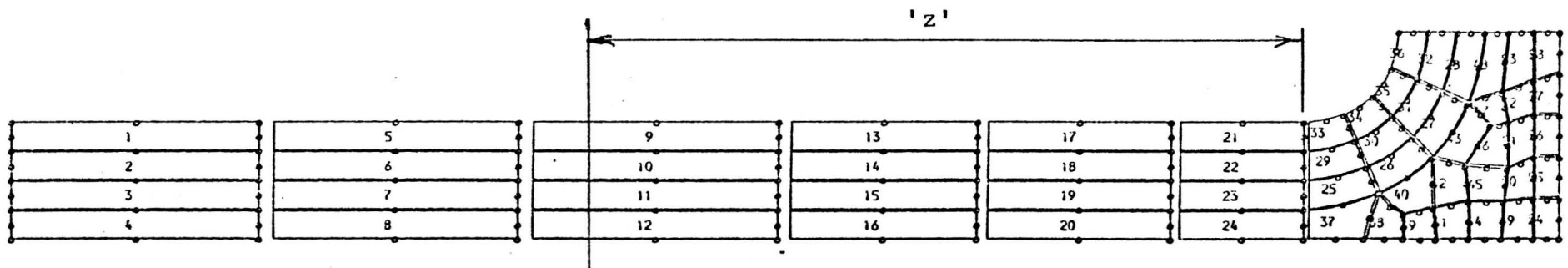


Figure AII.3 Flanged Tube. Preliminary finite element mesh (including element numbers) used to determine value for shank length, 'z'.

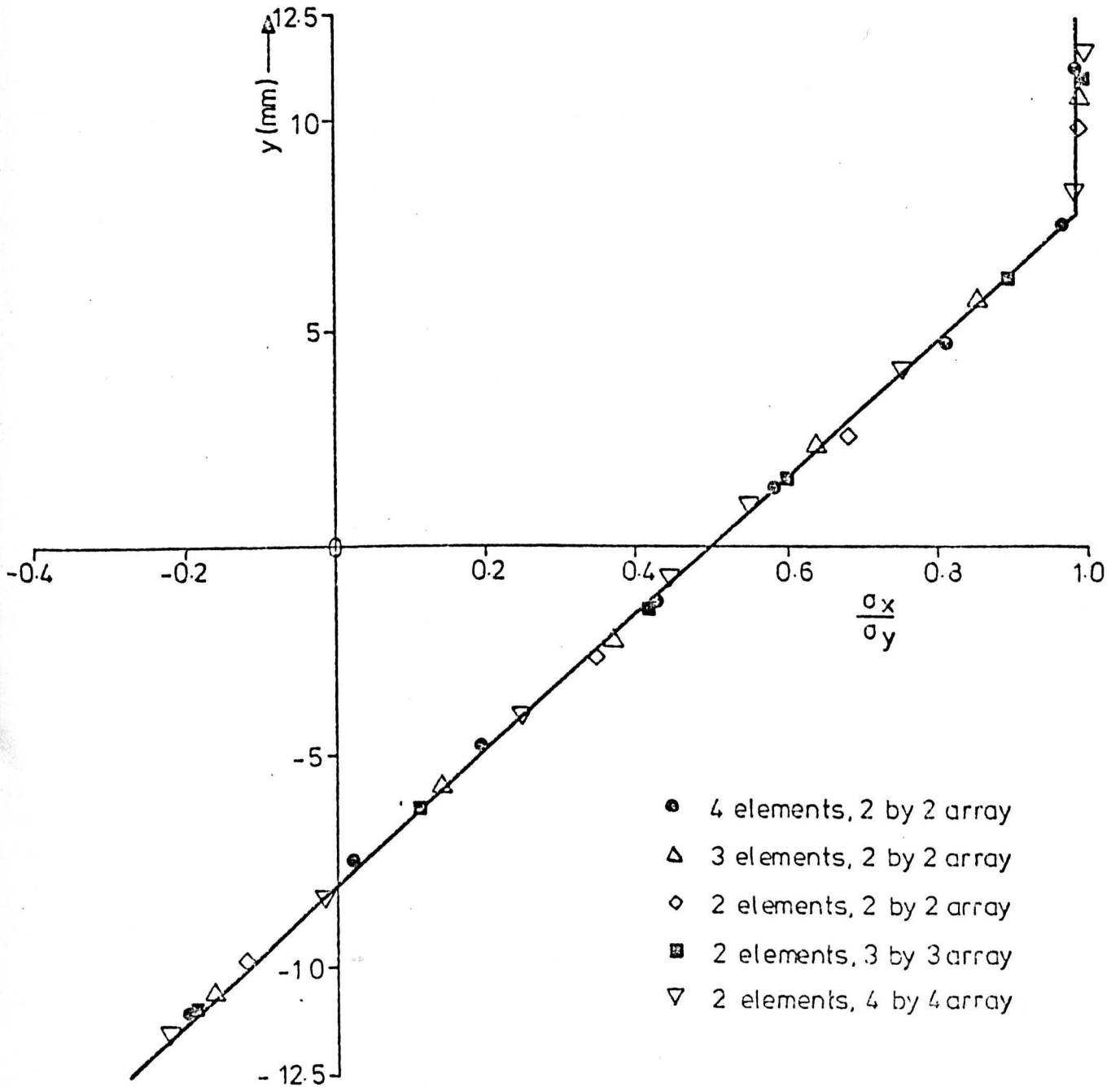


Figure AII.4 Stepped beam shank (elastic-perfectly-plastic, $P/P_L = 0.48$, $M/M_y = 0.72$). Comparison between exact solution and finite element predictions of axial stress distribution (from reference 51).